D 3715

[25]

EurJIC

European Journal of Inorganic Chemistry

25/2010
1st September Issue

Eur. J. Inorg. Chem. 2010, 3881–4048

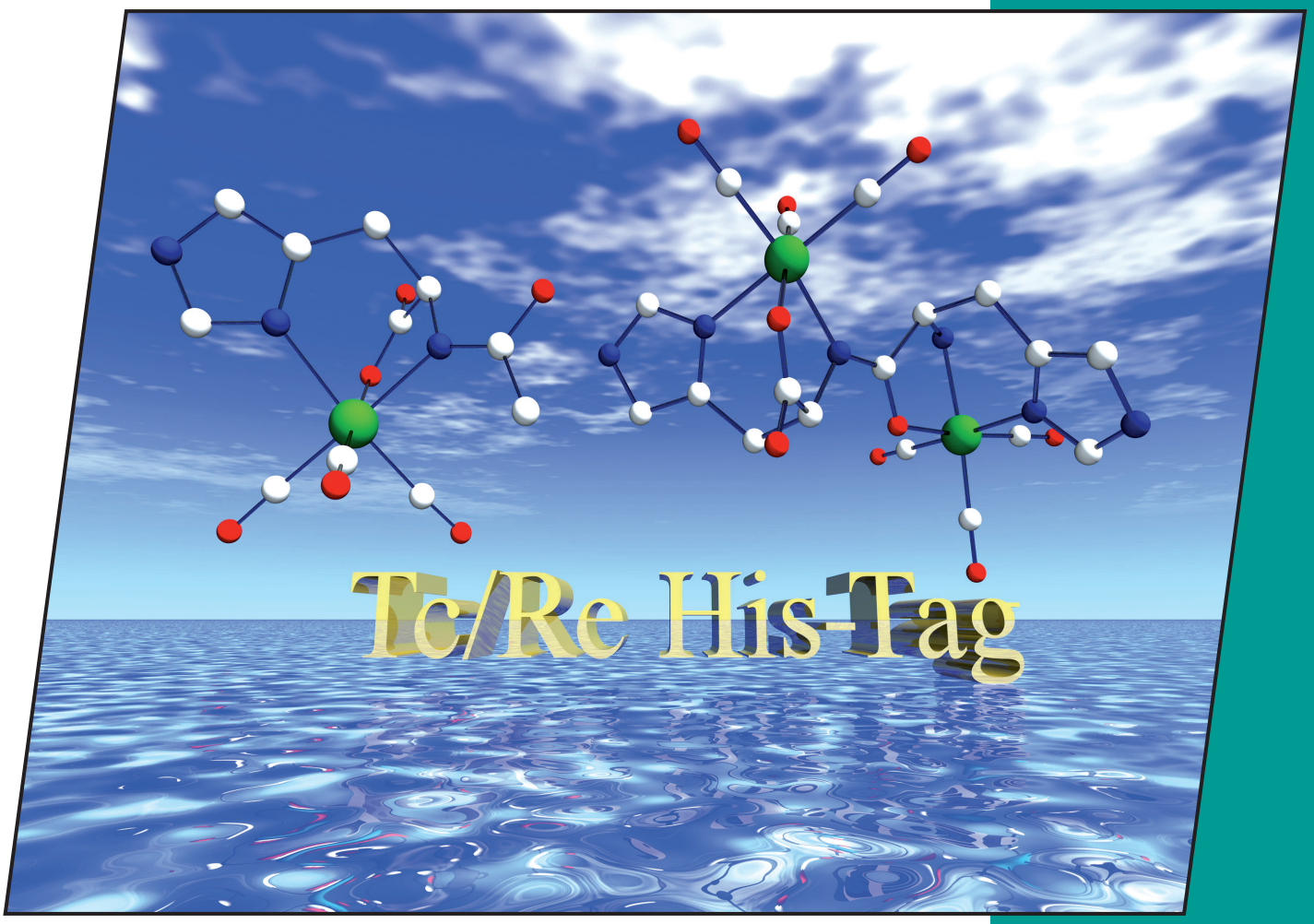

Cover Picture

Richard S. Herrick, Christopher J. Ziegler, and Americo Gambella

Reactions of $[Re(CO)_3]^+$ with Histidylhistidine and Modified Histidines

Microreview

Beth Anne McClure and Jeffrey J. Rack

Isomerization in Photochromic Ruthenium Sulfoxide Complexes

A Journal of

ChemPubSoc Europe

WILEY-VCH

www.eurjic.org

EJICFK (25) 3881–4048 (2010) · ISSN 1434-1948 · No. 25/2010

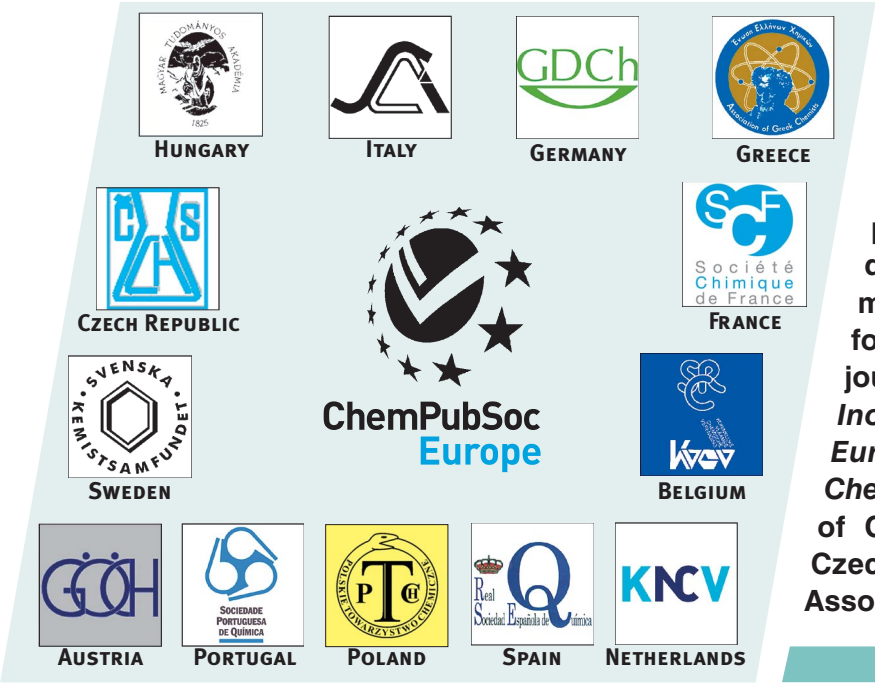

EurJIC is co-owned by 11 societies of ChemPubSoc Europe, a union of European chemical societies for the purpose of publishing high-quality science. All owners merged their national journals to form two leading chemistry journals, the *European Journal of Inorganic Chemistry* and the *European Journal of Organic Chemistry*. Three further members of ChemPubSoc Europe (Austria, Czech Republic and Sweden) are Associates of the two journals.

Other ChemPubSoc Europe journals are *Chemistry – A European Journal*, *ChemBioChem*, *ChemPhysChem*, *ChemMedChem*, *ChemSusChem* and *ChemCatChem.*

COVER PICTURE

The cover picture shows the crystal structures of two complexes that were prepared from aqueous reactions of histidine-based ligands with $Re(CO)_3(H_2O)_3^+$ and serve as models of $^{99m}Tc(CO)_3^+$/His-tag protein complexes. The complexes, similar to those found in certain enzymes, show unexpected peptide carboxamido-N donor bonds that underscore the stability of the labeled His-tag proteins as discussed in the Short Communication by R. S. Herrick, C. J. Ziegler et al. on p. 3905ff. Artwork: Christopher J. Ziegler.

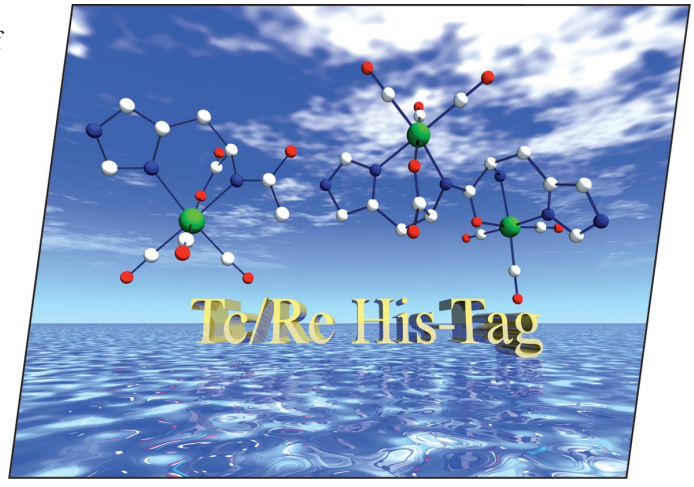

CONTENTS

MICROREVIEW

Photochromic Ru Complexes

B. A. McClure, J. J. Rack* 3895–3904

Isomerization in Photochromic Ruthenium Sulfoxide Complexes

Keywords: Photochromism / Ruthenium / Sulfoxide complexes / Photochemistry / Isomerization

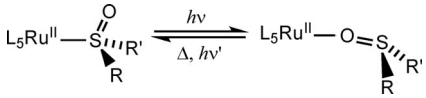

Details of spectroscopic results obtained from studies of photochromic ruthenium sulfoxide complexes are discussed. These results are compared and lead to the conclusion that different mechanisms for excited state isomerization exist for these compounds.

SHORT COMMUNICATIONS

Rhenium His-Tag Complexes

R. S. Herrick,* C. J. Ziegler,* A. Gambella 3905–3908

Reactions of $[Re(CO)_3]^+$ with Histidyl-histidine and Modified Histidines

Keywords: Medicinal chemistry / Radiopharmaceuticals / Rhenium

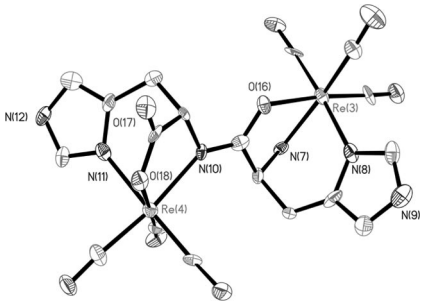

Reactions of His-tag models with $[Re(CO)_3(H_2O)_3]Br$ produce two compounds that display an unusual mode of binding. X-ray crystallography verifies that Ac-His-OH and His-His-OH (see figure) each produce a compound that has a peptide carboxamido-N donor group. Challenge experiments show that the complex with His-His-OH resists decomposition suggesting practical applications of complexed His-tags.

Chiral Luminescent Complexes

K. Saito, Y. Sarukawa, K. Tsuge, T. Konno* 3909–3913

Heterochiral vs. Homochiral Linkage of Emissive Iridium(III) Complexes with D-Penicillaminate: Drastic Change in Emission Induced by Silver(I) Linkage

Keywords: Chiral resolution / Iridium / Luminescence / S ligands / Substituent effects

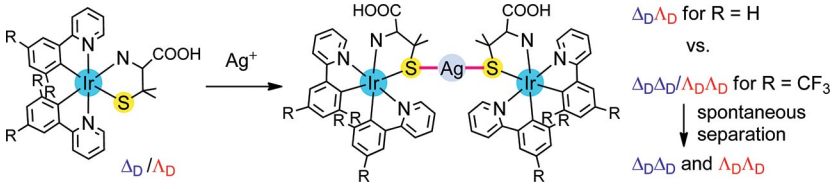

Emissive Ir^{III} complexes [Ir(D-Hpen)(ppy or ppy-CF_3)$_2$] were converted into $Ir^{III}Ag^{I}$-Ir^{III} complexes by linking with Ag^I, which led to a drastic blueshift of the emission bands. Whereas the $(ppy)Ir^{III}Ag^{I}Ir^{III}$ complex produced only the $\Delta_D\Lambda_D$ isomer, the ppy-CF_3 complex gave the $\Delta_D\Delta_D$ and $\Lambda_D\Lambda_D$ isomers that could completely be separated by crystallization. The emission quantum efficiencies for the $\Delta_D\Delta_D$ and $\Lambda_D\Lambda_D$ isomers were found to be markedly different, indicative of the importance of chirality in the control of emission properties.

FULL PAPERS

F-Containing Polyoxometalates

A. Banerjee, B. S. Bassil, G.-V. Röschenthaler,* U. Kortz* 3915–3919

Fluorine Tagging of Polyoxometalates: The Cyclic $[\{Mo^{V}_2O_4(H_2O)\}_4\{O_3PC(CF_3)(O)PO_3\}_4]^{12-}$

Keywords: Fluorine / Diphosphonates / Polyoxometalates / NMR spectroscopy

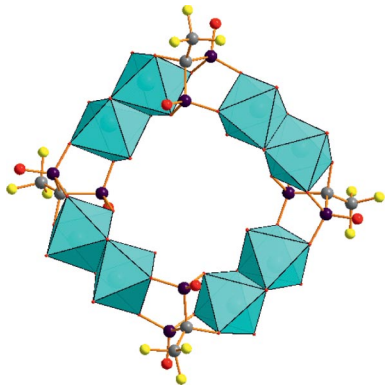

We have discovered a simple and efficient strategy to incorporate fluorine into polyoxometalates by reaction of the fluorinated diphosphonate $H_2O_3PC(CF_3)(OH)PO_3H_2$ with $[Mo^{V}_2O_4(H_2O)_6]^{2+}$ in aqueous medium (pH = 6.4) resulting in $[\{Mo^{V}_2O_4(H_2O)\}_4\{O_3PC(CF_3)(O)PO_3\}_4]^{12-}$ (**1**), which was structurally characterized in solution by multinuclear NMR spectroscopy and in the solid state by single-crystal X-ray diffraction.

Vibrations of Bridging Cyanides

S. F. A. Kettle,* E. Diana, E. M. C. Marchese, E. Boccaleri, G. Croce, T. Sheng, P. L. Stanghellini* 3920–3929

The Vibrational Spectra of the Cyanide Ligand Revisited: Double Bridging Cyanides

Keywords: Cyanides / Bridging ligands / Vibrational spectroscopy / Density functional calculations

Fundamental to a detailed understanding of the vibrational spectroscopy of Prussian Blues is an understanding of the interaction between *cis* and *trans* cyanide ligands connected through a metal atom. *cis* and *trans* M−CN−M′−NC−M complexes have been studied, which may be regarded as building blocks of Prussian Blue.

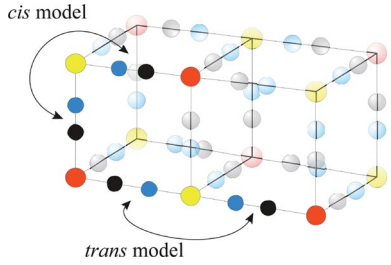

Dendritic Spin-Crossover Materials

Y. Wei, P. Sonar, M. Grunert, J. Kusz, A. D. Schlüter, P. Gütlich* 3930–3941

Iron(II) Spin-Transition Complexes with Dendritic Ligands, Part II

Keywords: Spin crossover / Iron / Dendrimers / Moessbauer spectroscopy / Magnetic properties

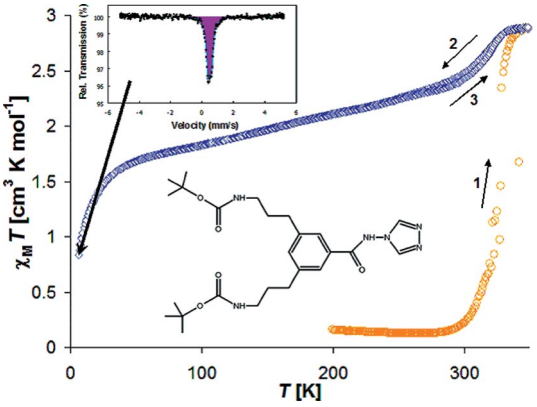

The study reports the synthesis and physical characterization of iron(II) complexes with G1-triazole-based dendritic ligands. Noncoordinated water molecules and different anions influence strongly the spin-state behaviour as reflected by Mössbauer, magnetic susceptibility, XRD, DSC and TG measurements.

Hydrogenase Models

F. Huo, J. Hou,* G. Chen, D. Guo, X. Peng* 3942–3951

[FeFe]-Hydrogenase Models: Overpotential Control for Electrocatalytic H_2 Production by Tuning of the Ligand π-Acceptor Ability

Keywords: Bioinorganic chemistry / Hydrogenase / Phosphanes / Carbonyldiiron compounds / Phosphane ligands

(Pyrrol-1-yl)phosphane-substituted diiron complexes [(μ-pdt)$Fe_2(CO)_5$L] [pdt = propanedithiolate, L = Ph_2PPyr (**2**), $PPyr_3$ (**4**); Pyr = pyrrolyl] and [(μ-pdt)$Fe_2(CO)_4L_2$] [L = Ph_2PPyr (**3**), $PPyr_3$ (**5**)] were prepared as functional models for the Fe-only hydrogenase. In the presence of HOAc, complexes **2**–**5** can catalyze proton reduction to H_2. Introduction of (pyrrol-1-yl)phosphane ligands shifts the reduction potentials of **2**–**5** to more positive values.

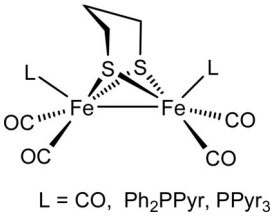

Functional Metallocenes

K. Döring, N. Ballav, M. Zharnikov,* H. Lang* 3952–3960

Synthesis, Electrochemical Behavior, and Self-Assembly of Metallocene-Functionalized Thiofluorenes

Keywords: Metallocenes / Thiols / Fused ring systems / Self-assembly / Monolayers / Cyclic voltammetry

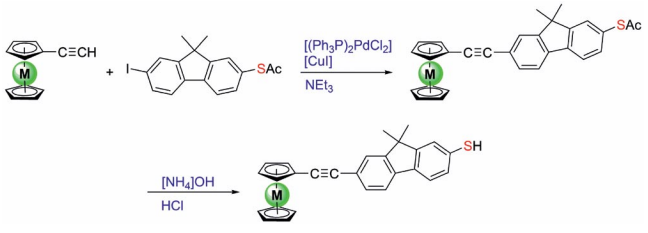

The synthesis and characterization of ferrocenyl- and ruthenocenyl-functionalized thiofluorenes are reported. These molecules can be immobilized in a self-assembled monolayer on a suitable substrate and used as molecular "devices" for electrochemical applications.

CONTENTS

Luminescence

D. Parker,* J. W. Walton, L. Lamarque, J. M. Zwier 3961–3966

Comparative Study of the Luminescence Properties and Relative Stability of a Series of Europium(III) Complexes Bearing One to Four Coordinated Azaxanthone Groups

Keywords: Europium / Luminescence / Lanthanides / Macrocycles

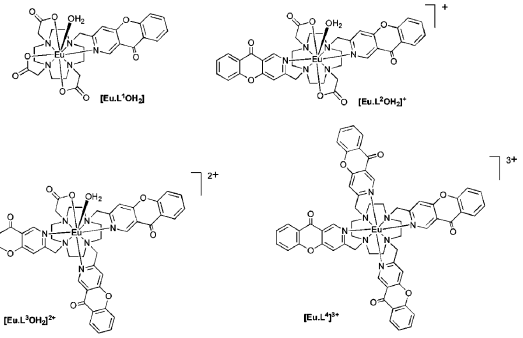

An emissive monocationic europium complex with two azaxanthone sensitising moieties shows the best stability profile in the series of four tested.

Dehydrogenation

G. R. Whittell, E. I. Balmond, A. P. M. Robertson, S. K. Patra, M. F. Haddow, I. Manners*..... 3967–3975

Reactions of Amine– and Phosphane–Borane Adducts with Frustrated Lewis Pair Combinations of Group 14 Triflates and Sterically Hindered Nitrogen Bases

Keywords: Amines / Boron / Dehydrogenation / Lewis acids / Lewis bases

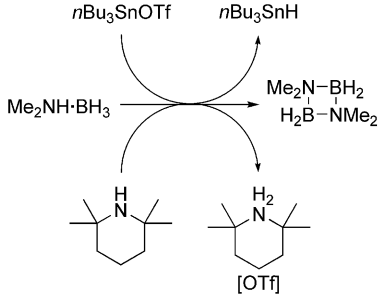

The "frustrated Lewis pairs" of trialkyl Group 14 triflates and sterically encumbered nitrogen bases promote the dehydrogenation of amine–borane adducts.

[FeFe]-Hydrogenases

M. K. Harb, H. Görls, T. Sakamoto, G. A. N. Felton, D. H. Evans,* R. S. Glass,* D. L. Lichtenberger,* M. El-khateeb, W. Weigand*... 3976–3985

Synthesis and Characterization of [FeFe]-Hydrogenase Models with Bridging Moieties Containing (S, Se) and (S, Te)

Keywords: Iron / Hydrogenases / Tellurium / Selenium / Sulfur / Electrocatalysis

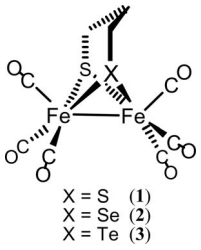

Diiron complexes containing mixed dichalcogenolato ligands (**2** and **3**) of the [FeFe]-hydrogenase active site have been synthesized and characterized. The electrochemistry of **2** and **3** reveal the ability of these complexes to be electrocatalysts for the reduction of the acetic acid proton to dihydrogen.

N-Substituted Ferrocenium Salts

D. Siebler, C. Förster, K. Heinze* 3986–3992

"Tail–Tail Dimerization" of Ferrocene Amino Acid Derivatives

Keywords: Anhydrides / Conformational analysis / Electrochemistry / Metallocenes / Mixed-valent compounds

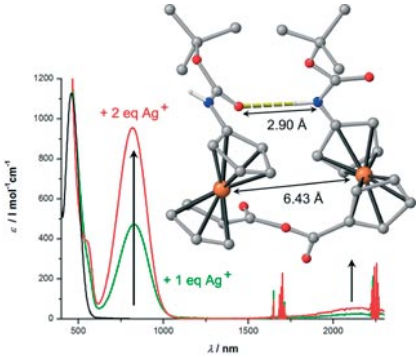

Acid anhydrides of N-protected 1′-aminoferrocene-1-carboxylic acid (Fca) form hydrogen-bonded rings in the solid state and in solution. Metal–metal interactions are probed by square-wave voltammetry, preparative oxidation, UV/Vis/NIR spectroscopy, and theoretical calculations.

Proton-Conducting Films

R. Supplit, A. Sugawara, H. Peterlik, R. Kikuchi, T. Okubo* 3993–3999

Supported and Free-Standing Sulfonic Acid Functionalized Mesostructured Silica Films with High Proton Conductivity

Keywords: Mesostructure / Self-assembly / Proton conductivity / Sol–gel processes / Conducting materials / Template synthesis

Free-standing and supported silica films with 2D-hexagonally structured sulfonic acid functionalized mesopores are prepared in a one-step synthesis. Humidified samples show exceptional proton conductivity of up to 0.18 Scm^{-1} at 60 °C and 95% relative humidity.

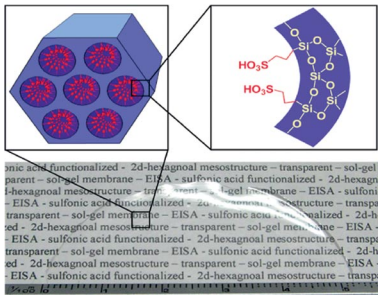

Nanofibers

J. Lu, L. Wu, J. Jiang,* X. Zhang* 4000–4008

Helical Nanostructures of an Optically Active Metal-Free Porphyrin with Four Optically Active Binaphthyl Moieties: Effect of Metal–Ligand Coordination on the Morphology

Keywords: Chirality / Porphyrinoids / Self-assembly / Optical activity / Nanostructures

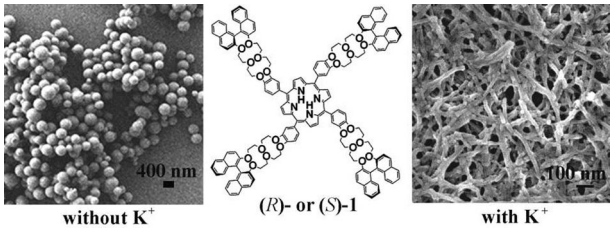

An optically active metal-free porphyrin decorated with four binaphthyl crown ether moieties linked through benzene units has been designed and synthesized. It self-assembles into nanoparticles in the absence of potassium ions. However, both enantiomers self-assemble into helixes first and then stack into a high-ordered supercoil with opposite helicity in the presence of potassium ions.

Phosphorescent Copper(I) Complexes

W. Sun, Q. Zhang, L. Qin, Y. Cheng,* Z. Xie, C. Lu,* L. Wang 4009–4017

Phosphorescent Cuprous Complexes with N,O Ligands – Synthesis, Photoluminescence, and Electroluminescence

Keywords: Copper / N,O ligands / Phosphane ligands / Phosphorescence / Electroluminescence

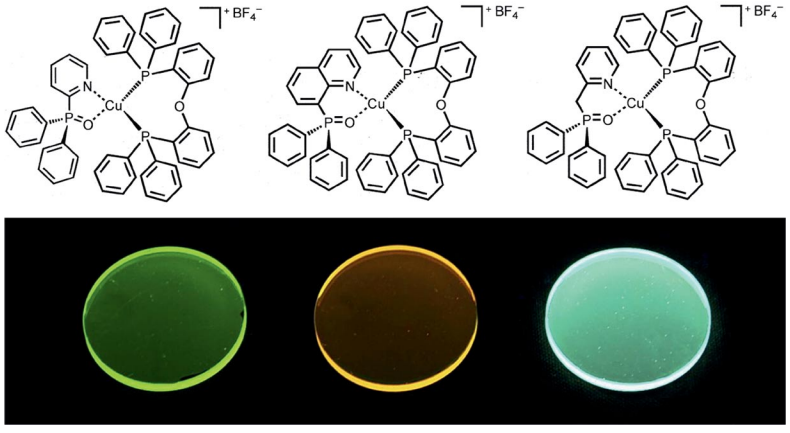

Phosphorescent Cu^{I} complexes containing phosphane oxide coordinating ligands are reported for the first time. In PMMA films, this class of complexes exhibits blue-green to orange emissions with quantum efficiencies of up to 0.72, indicating potential applications in electroluminescent devices.

Luminescent Cu(I) Complexes

M. G. Babashkina, D. A. Safin,* A. Klein,* M. Bolte 4018–4026

Synthesis, Characterisation and Luminescent Properties of Mixed-Ligand Copper(I) Complexes Incorporating *N*-Thiophosphorylated Thioureas and Phosphane Ligands

Keywords: Chelate complexes / Copper / Crystal Structure / Luminescence / Phosphanes / Thiourea

The potassium salts of HL^{I} or H_2L^{II} react with $[Cu(PPh_3)_3I]$ or a mixture of CuI and $Ph_2P(CH_2)_{1-3}PPh_2$ or $Ph_2P(C_5H_4FeC_5H_4)$-PPh_2 to give **1**–**10**. The crystal structures of H_2L^{II}, **1**, **3**–**6**, **8** and **10** were determined by single-crystal X-ray diffraction. The luminescent properties of complexes **1**–**10** in the solid state are reported.

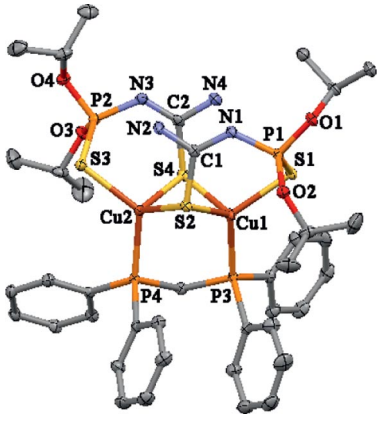

CONTENTS

MOF–POM Hybrids

X. Liu, Y. Jia, Y. Zhang, R. Huang* 4027–4033

Construction of a Hybrid Family Based on Lanthanide–Organic Framework Hosts and Polyoxometalate Guests

Keywords: Metal–organic frameworks / Polyoxometalates / Organic–inorganic hybrid composites / Lanthanides

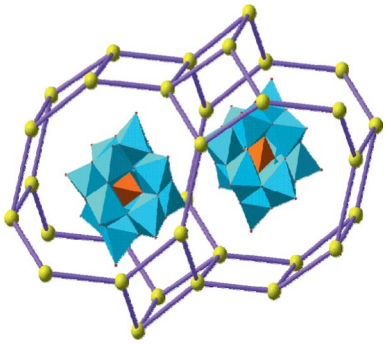

In this paper the synthesis, crystal structures, and properties of a series of 3D porous polyoxometalate (POM) based coordination polymers are discussed, namely, $Ln_4(pdc)_4[SiW_{12}O_{40}]\cdot xH_2O$ (Ln = Eu, Gd, Tb, Dy; x = 19, 13, 14, 18; H_2pdc = pyridine-2,6-dicarboxylate). These materials present striking thermostability, favorable catalytic properties, and satisfactory ethanol sorption.

Binuclear Pt Complexes

A. L. Fuller, F. R. Knight, A. M. Z. Slawin, J. D. Woollins* 4034–4043

Platinum Complexes of Aromatic Selenolates

Keywords: Platinum / Selenium / Heterocycles

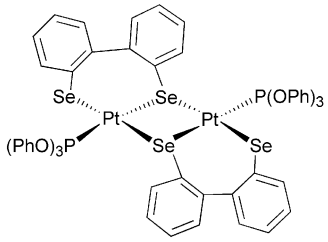

Aryl selenolates apart from forming simple mononuclear complexes also form binuclear Pt complexes, in fact mononuclear and binuclear species may be in equilibrium.

* Author to whom correspondence should be addressed.

Supporting information on the WWW (see article for access details).

On these pages, we feature a selection of the excellent work that has recently been published in our sister journals. If you are reading these pages on a computer, click on any of the items to read the full article. Otherwise please see the DOIs for easy online access through Wiley Online Library.

Coordination Chemistry

J. M. Lynam

Recent Mechanistic and Synthetic Developments in the Chemistry of Transition-Metal Vinylidene Complexes

How to tautomerise alkynes! Transition-metal vinylidene complexes are important synthetic intermediates for a range of transformations involving terminal alkynes. This article reviews a number of recent developments focused on understanding the alkyne/vinylidene tautomerisation mediated by transition-metal complexes. The coupling of experimental and theoretical methods has allowed for detailed insight into this process and the factors which control it.

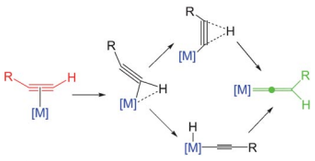

Chem. Eur. J.
DOI: **10.1002/chem.201000695**

Dendrimers

G. Bergamini, A. Sottilotta, M. Maestri, P. Ceroni,* F. Vögtle*

Cyclam-Cored Dendrimers Appended with Four Dendrons of Two Different Types: Intradendrimer Energy Transfer

The H effect! Two cyclam-cored dendrimers appended with dendrons of two different types, by proper protection/deprotection of the cyclam unit, are synthesized. Interdendron naphthyl-to-dansyl energy transfer takes place within the same dendrimer: its efficiency can be reversibly tuned by protonation/deprotonation of the cyclam core.

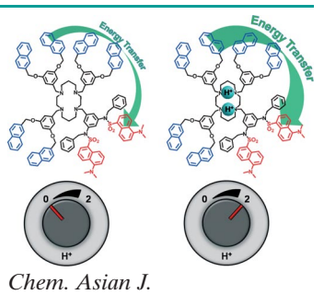

Chem. Asian J.
DOI: **10.1002/asia.201000170**

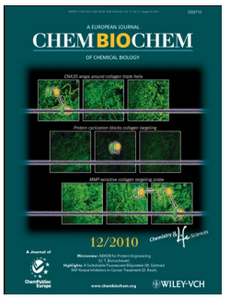

Drug Delivery

F. Marlin, P. Simon, T. Saison-Behmoaras, C. Giovannangeli*

Delivery of Oligonucleotides and Analogues: The Oligonucleotide Conjugate-Based Approach

Carrier conjugates: Oligonucleotide-based therapeutic strategies are moving closer to use in patients, but bench work is still needed. Although oligonucleotides are validated and powerful tools in basic research, their delivery is still the major issue impeding their use as therapeutics. Carrier–oligonucleotide conjugates currently in development are reviewed here.

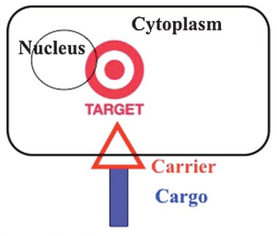

ChemBioChem
DOI: **10.1002/cbic.201000138**

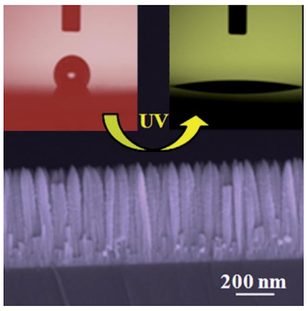

ChemPhysChem
DOI: **10.1002/cphc.201000333**

Nanostructures

D. Bekermann, A. Gasparotto,* D. Barreca, A. Devi, R. A. Fischer, M. Kete, U. Lavrenčič Štangar, O. I. Lebedev, C. Maccato, E. Tondello, G. Van Tendeloo

ZnO Nanorod Arrays by Plasma-Enhanced CVD for Light-Activated Functional Applications

Switch of the surface properties: Supported ZnO nanorod arrays with tailored roughness and aspect ratios are successfully synthesized by plasma-enhanced chemical vapor deposition. Such nanostructures exhibit significant superhydrophilic and photocatalytic properties tunable as a function of their morphological organization (see picture). This renders them promising building blocks for the fabrication of stimuli-responsive materials.

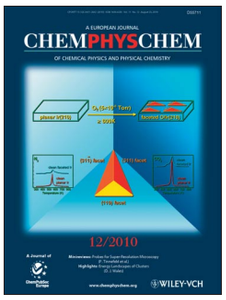

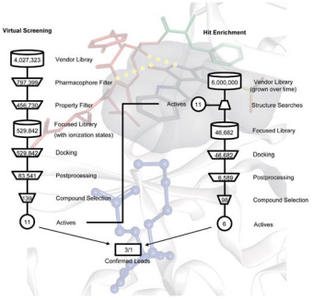

ChemMedChem
DOI: **10.1002/cmdc.201000157**

Bioinformatics

K. Engels, C. Beyer, M. L. Suárez Fernández, F. Bender, M. Gaßel, G. Unden, R. J. Marhöfer, J. C. Mottram, P. M. Selzer*

Inhibition of *Eimeria tenella* CDK-Related Kinase 2: From Target Identification to Lead Compounds

Targeting coccidiosis: Cyclin-dependant kinases (CDKs) of the protozoan parasite *Eimeria tenella*, which causes the severe poultry disease coccidiosis, were identified from genomic sequence data. The cell cycle and most well-characterized kinase (EtCRK2) of *E. tenella* were chemically validated as drug targets in enzyme and cell culture assays. Promising lead compounds were identified in a combined in silico/in vitro screening approach.

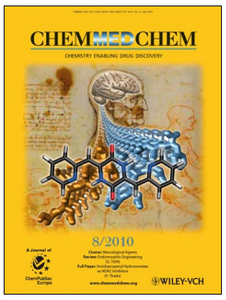

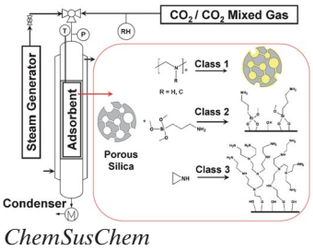

ChemSusChem
DOI: **10.1002/cssc.201000131**

Carbon Dioxide Capture

W. Li, S. Choi, J. H. Drese, M. Hornbostel, G. Krishnan, P. M. Eisenberger, C. W. Jones*

Steam-Stripping for Regeneration of Supported Amine-Based CO_2 Adsorbents

Amine-based solid CO_2 adsorbents have been investigated intensively in recent years. However, the focus has routinely been on their adsorption capacity and not on their regeneration. Here, a practical desorption process for supported amine adsorbents, steam-stripping, is demonstrated for the first time.

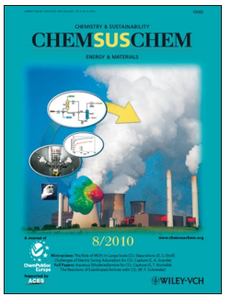

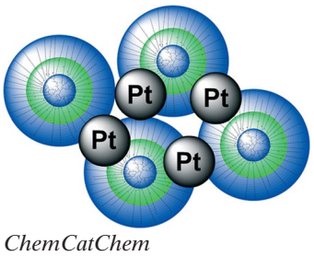

ChemCatChem
DOI: **10.1002/cctc.201000013**

Core–Shell Catalysts

J. Keilitz, M. Schwarze, S. Nowag, R. Schomäcker, R. Haag*

Homogeneous Stabilization of Pt Nanoparticles in Dendritic Core–Multishell Architectures: Application in Catalytic Hydrogenation Reactions and Recycling

Cores and effect: The synthesis and stabilization of Pt nanoparticles in dendritic core–multishell polymers and their application to hydrogenation reactions are described. The catalyst is reused 14 times (total TON = 22000) and can be recovered by ultrafiltration or phase separation with very low metal leaching into the product.

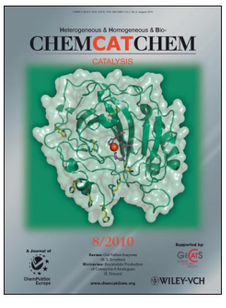

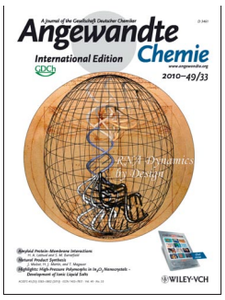

Nanoparticles

Y. Liu, C.-J. Jia, J. Yamasaki, O. Terasaki, F. Schüth*

Highly Active Iron Oxide Supported Gold Catalysts for CO Oxidation: How Small Must the Gold Nanoparticles Be?

The shape of gold: The title catalyst has been prepared through a colloidal deposition method. Scanning transmission electron microscopy studies confirmed that for the catalyst, gold clusters with a bilayer structure and a diameter of about 0.5 nm are not mandatory to achieve the high activity (see image).

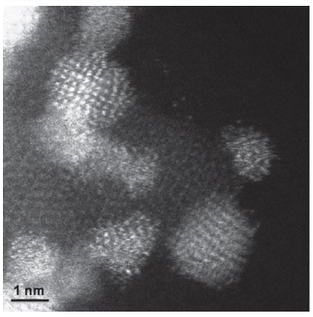

Angew. Chem. Int. Ed.
DOI: **10.1002/anie.201000452**

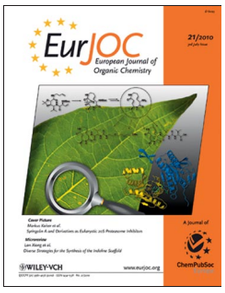

Pyrrolysine

T. Fekner, X. Li, M. K. Chan*

Pyrrolysine Analogs for Translational Incorporation into Proteins

A combination of crystallographic, biochemical, and synthetic studies related to pyrrolysine and its biochemical machinery led to the formulation of a set of principles for the design of successful analogs for site-specific modification of proteins. The journey leading to it and recent practical applications of the acquired knowledge are discussed.

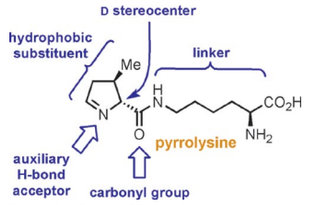

Eur. J. Org. Chem.
DOI: **10.1002/ejoc.201000204**

DOI: 10.1002/ejic.200900548

Isomerization in Photochromic Ruthenium Sulfoxide Complexes

Beth Anne McClure[a] and Jeffrey J. Rack*[a]

Keywords: Photochromism / Ruthenium / Sulfoxide complexes / Photochemistry / Isomerization

The spectroscopic properties of photochromic ruthenium sulfoxide complexes are reviewed. The mode of action is associated with an excited state S→O isomerization triggered by light. These complexes feature large, positive $Ru^{3+/2+}$ reduction potentials indicative of stabilization of the Ru dπ orbital set. In addition, these compounds feature large quantum yields of isomerization. In aggregate, the data argue against a promoting role for the LF states and suggest that isomerization occurs from the CT potential energy surface. Picosecond transient absorption experiments indicate a change in the isomerization mechanism between mondentate sulfoxide complexes and chelating sulfoxide complexes. These results as well as potential energy diagrams for certain complexes are discussed.

1. Introduction

Due to their favorable properties, photochromic compounds have found utility in a variety of areas. These properties include distinct electronic structures exhibited by ground and metastable states and fast switching times between these states. As such, these compounds have been employed in the formation of logic gates for molecular computing applications[1–5] as well as in biological applications.[6,7] These compounds have also been utilized in supramolecular or polymeric materials for the formation of photomechanical or opto-mechanical materials.[8–12] These are macroscopic films or crystals that change shape upon irradiation. The molecular basis for these applications lies in the creation of a new molecule following light irradiation. Photonic energy is transduced to potential energy, which is employed to break and make bonds on a femtosecond, picosecond or nanosecond timescale.

[a] Department of Chemistry and Biochemistry, Nanoscale and Quantum Phenomena Institute, Clippinger Laboratories, Ohio University
Athens, OH 45701, USA
Fax: +1-740-593-0148
E-mail: rackj@ohio.edu

By far, there are many more types of organic photochromic compounds and materials relative to their molecular inorganic counterparts. Stilbenes, azo-benzenes, fulgides, spiro-compounds and dithienylethenes and their many derivatives demonstrate the great diversity of structures featuring photochromism.[13–19] By contrast, molecular inorganic photochromic compounds and materials are more rare.[20–26] The most well-known example in this class is sodium nitroprusside (SNP), $Na_2[Fe(CN)_5(NO)]$.[22,23] When irradiated many transition metal nitrosyl compounds undergo an intramolecular linkage isomerization. For SNP, *O*-bonded nitrosyl, termed metastable state 1 (MS1), and an η^2-NO nitrosyl structure, termed metastable state 2 (MS2), are observed when crystalline material is irradiated at low temperature (< 100 K).[27,28] These compounds and related complexes have found utility in photorefractive applications.[29–33]

We have developed a class of simultaneously photochromic and electrochromic polypyridine ruthenium sulfoxide compounds.[34–50] The mode of action is due to an intramolecular isomerization of the sulfoxide from *S*-bonded to *O*-bonded. The isomerization is triggered either by light or by formal oxidation or reduction. The differential bonding characteristics of *S*- and *O*-bonded sulfoxides produces dis-

Beth Anne McClure received her B.S. degree with honors in chemistry from John Carroll University in 2006. Since then she has been pursuing her Ph.D. studies with Professor Jeffrey Rack at Ohio University, where she synthesizes and investigates mechanisms of photochromic action in ruthenium sulfoxide complexes. She is a National Defense Science and Engineering Graduate Fellow (2006–2009). When not in the lab or her kitchen, Beth enjoys music and the occasional game of euchre.
Jeffrey Rack received his B.S. degree in chemistry from Clemson University in 1991. He was awarded his Ph.D. in chemistry in 1996 by Colorado State University, where he worked with Steven Strauss on nonclassical metal carbonyl complexes. He accepted a joint postdoctoral appointment at Caltech in the laboratories of Thomas Meade (now at Northwestern University) and Harry Gray, where he studied electron transfer in DNA and spectroscopy of ruthenium complexes. After a postdoctoral appointment with Eva Birnbaum and Mark McCleskey at Los Alamos National Laboratory (2000–2001), he accepted a faculty position at Ohio University, where is now an associate professor.

tinct electronic structures and electrochemical $Ru^{3+/2+}$ reduction potentials. Herein, we describe important literature reports and highlight our spectroscopic findings from the study of these compounds since 2001.

2. Photochemical Isomerization in Ruthenium and Osmium dmso Complexes

Shown in Figure 1 are the absorption spectra of *S*- and *O*-bonded isomers of $[Ru(tpy)(pic)(dmso)]^+$, where tpy is 2,2′:6′,2′′-terpyridine, pic is 2-pyridinecarboxylate and dmso is dimethyl sulfoxide.[42,44,46] The lowest energy visible absorption maximum observed for both isomers is assigned to a Metal-to-Ligand Charge-Transfer (MLCT) transition based on its intensity and wavelength and in accord with many other ruthenium polypyridine complexes.[51] Irradiation of this complex by monochromatic laser light, white light, sunlight or typical fluorescent room lighting in many low donor or weakly basic solvents results in the formation of a new absorption spectrum. This spectrum is similar to that found for $[Ru(tpy)(pic)(OH_2)]^+$ and is thus consistent with an *O*-bonded donor.[52,53] Accordingly, we assign this new spectrum to the *O*-bonded isomer of $[Ru(tpy)(pic)(dmso)]^+$. These absorption changes are completely reversible at room temperature and mechanistic studies reveal the isomerization to be intramolecular. This reactivity has been found to be general for many ruthenium polypyridine sulfoxide complexes.

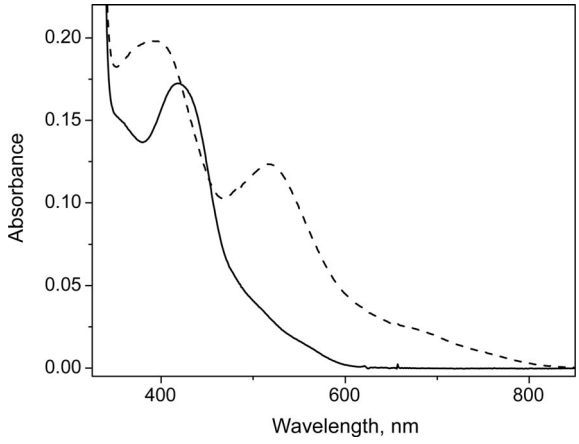

Figure 1. Absorption spectra of *S*-bonded (solid) and *O*-bonded (dashed) isomers of [Ru(tpy)(pic)(dmso)]+ in propylene carbonate.

Shown in Table 1 are quantum yields of isomerization ($\Phi_{S\rightarrow O}$) for a family of photochromic ruthenium sulfoxide complexes. From inspection of the table it can be seen that O-donor ligands such as malonate (mal), oxalate (ox) and acetylacetonate (acac), do not support dmso isomerization.[35] In contrast, N-donor ligands support dmso isomerization. These observations may be interpreted as a weaker ligand field leading to deactivation of the ^{3}MLCT state. Thus, O-donor ligand complexes feature a weaker ligand field and, in turn, smaller or non-existent $\Phi_{S\rightarrow O}$ values. Stronger field N-donor ligand complexes feature a greater energy difference between the deactivating ^{3}LF states and thermally-equilibrated ^{3}MLCT states thus favoring isomerization. This is a conventional argument to explain the photochemistry of ruthenium polypyridine complexes.[51]

Table 1. Photochemical and electrochemical data for $[Ru(tpy)L2(dmso)]^{n+}$ complexes.

L2	λ_{max}(S) /nm (ε /M^{-1} cm^{-1})	λ_{max}(O) /nm (ε /M^{-1} cm^{-1})	$E°'$(S) /V	$E°'$(O) /V	$\Phi_{s\rightarrow o}$
bpy	419 (8080)	490 (13668)	1.67	1.10	0.024
pic	421 (5347)	527 (4524)	1.38	0.63	0.25
tmen	429 (8161)	530 (7480)	1.65	1.03	0.007
acac	468 (5318)	–	0.95	–	<0.0001
ox	485 (4396)	–	0.86	–	–
mal	502 (5134)	–	0.82	–	–

However, close inspection of $\Phi_{S\rightarrow O}$ values in Table 1 reveals a separate trend. For example, if S→O isomerization involves the ligand field states then one expects the quantum yield to be similar to that observed for photosubstitution. Indeed, the isomerization might be thought of as an intramolecular photosubsitution reaction. The work of Ford, McMillin and others have shown that photosubstitution is a dissociative process involving the ligand field states and that photosubstitution quantum yields are on the order of 10^{-3}.[54–57] However, for $[Ru(tpy)(bpy)(dmso)]^{2+}$, $\Phi_{S\rightarrow O}$ = 0.024(±0.002) in propylene carbonate, an order of magnitude increase over the value determined for photosubstitution of CH_3CN by pyridine in $[Ru(tpy)(bpy)(CH_3CN)]^{2+}$ {Φ = 0.0016(±0.0002)}.[54] Moreover, $\Phi_{S\rightarrow O}$ = 0.25(±0.01) for $[Ru(tpy)(pic)(dmso)]^+$ and $\Phi_{S\rightarrow O}$ = 0.45(±0.01) for $[Ru(bpy)_2(OSO)]^{2+}$ (where OSO is 2-methylsulfinylbenzoate),[37,49] indicating an efficient conversion of photonic energy to potential energy. These large quantum yields indicate that the mechanism for photoisomerization may be different from that proposed for photosubstitution.

Additional evidence for an active role of LF states in photosubstitution on ruthenium(II) arises from studies showing that photosubstitution did not occur on analogous osmium(II) centers.[54] The ligand field splitting for Os^{2+} is estimated to be ca. 30% greater than for Ru^{2+}.[58] Therefore, although the LF states are thermally accessible from the MLCT states in Ru^{2+} complexes, these states are too high in energy to be accessible for the analogous Os^{2+} complexes, which presumably results in inactivity towards photosubstitution. For reasons of synthetic simplicity, $[Os(bpy)_2(dmso)_2]^{2+}$ was investigated for evidence of phototriggered dmso isomerization in order to further probe the role of ligand field states in phototriggered sulfoxide isomerization.[59] The structurally characterized complex features a bis-*S*-bonded ground state configuration and an absorption maximum at 355 nm, similar to that observed for photochromic $[Ru(bpy)_2(dmso)_2]^{2+}$.[45,60] The electrochemistry and photochemistry are consistent with isomerization, although it is apparent that only one dmso ligand isomerizes.[40] Steady state irradiation resulted in a decrease in absorbance at 355 nm concomitant with an increase at 403 nm. Reversion to the bis-*S*-bonded isomer from the mixed *S*,*O*-bonded metastable state is not observed at room temperature and requires modest heating for reversion (T =

60 °C). The isomerization quantum yield was determined to be 0.042(±0.001). Transient absorption studies suggest that isomerization does *not* occur from the emissive, thermally relaxed charge-transfer state, but rather from a higher-lying charge transfer state. Shown in Figure 2 is a state energy diagram of $[Os(bpy)_2(dmso)_2]^{2+}$. From these studies, it is clear that the LF states are not involved in isomerization. That $\Phi_{S\rightarrow O}$ is similar for ruthenium and osmium complexes indicates that isomerization involves different states from those utilized for photosubstitution.

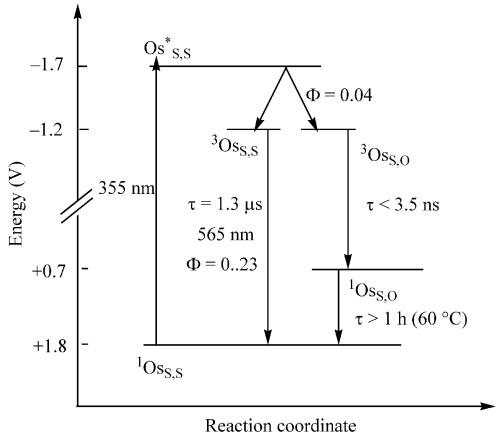

Figure 2. State diagram for $[Os(bpy)_2(dmso)_2]^{2+}$.

Since evidence of isomerization in osmium(II) sulfoxide complexes and a higher quantum yield for isomerization relative to photosubstitution argue against the involvement of the LF states, it appears that photochemical isomerization may proceed via the MLCT states. The involvement of the MLCT states is also supported by transient absorption spectroscopy. Shown in Figure 3 are the ground state absorbance and transient absorption spectra of [Ru(tpy)(bpy)(dmso)]$^{2+}$.[44] The 5 ps trace reveals a weak bleach feature near 450 nm, a sharp positive absorbance at ca. 550 nm and a broad featureless absorption at longer wavelengths (> 600 nm). Over the next 14 ps, the bleach feature becomes more pronounced concomitant with a disappearance of the sharp absorbance at 550 nm. For the 14 ps transient spectrum, the bleach feature is ascribed to depletion of the ground state MLCT transition for the *S*-bonded complex and the long wavelength absorption is attributed to an LMCT absorption, in accord with other studies.[61,62] Thus these spectral features have been interpreted as the formation of the ^{3}MLCT excited state of the *S*-bonded isomer. As time evolves, a new transient is revealed with the bleach centered at 475 nm and a modest decrease of the broad absorption at longer wavelengths. The time traces evince an isosbestic point indicating the formation of a new complex on a rapid timescale. The 242 ps transient spectrum does not represent an *O*-bonded Ru^{2+} ground state, as manifested by the absence of a strong absorption near 475 nm. Accordingly, we ascribe the new complex to an *O*-bonded ^{3}MLCT state. The spectral changes were fit to a bi-exponential decay with time constants of 2.4 ± 0.2 ps and 36 ± 0.2 ps. While the fast time constant is ascribed to relaxation of the Franck–Condon state to a thermally-equilibrated ^{3}MLCT *S*-bonded excited state, the slower time constant is attributed to both S→O isomerization along the CT excited state surface and to direct relaxation from the *S*-bonded CT state to *S*-bonded ground state. In conjunction with the quantum yield, this corresponds to a time constant for isomerization of 1.5 ns. An electronic state diagram summarizing isomerization and relaxation rates for [Ru(tpy)(bpy)(dmso)]$^{2+}$ is shown in Figure 4.

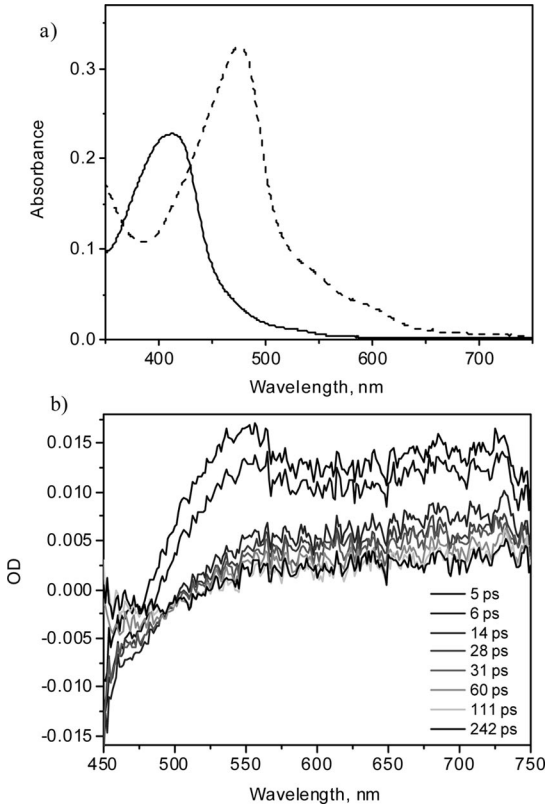

Figure 3. a) Ground-state absorbance spectra of *S*-bonded (solid) and *O*-bonded (dashed) [Ru(tpy)(bpy)(dmso)]$^{2+}$ b) Picosecond transient absorption spectra of S-[Ru(tpy)(bpy)(dmso)]$^{2+}$ in propylene carbonate solution.

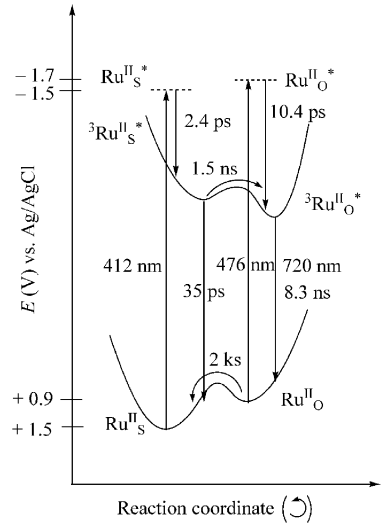

Figure 4. State diagram for [Ru(tpy)(bpy)(dmso)]$^{2+}$.

3. Adiabatic vs. Non-Adiabatic Photochemical Mechanisms

In order to gain further insight about this phototriggered isomerization, it is necessary to understand how excited state evolution is affected by coupling between vibrational and electronic components. Although vibronic coupling is often considered in the spectroscopy of transition metal complexes, it is typically employed in describing the probability of absorption of a photon rather than the events that occur following photon excitation.[63] McCusker's work on the temporal evolution of the ^{3}MLCT excited state of $[Ru(bpy)_3]^{2+}$ and its derivatives has indicated that non-thermally equilibrated excited states are important in the relaxation dynamics of such complexes.[61,62,64] Photochemical reactions involving these states inherently occur through the coherent motion of select vibrational modes that either are strongly coupled to the Franck–Condon state or other electronic potential energy surfaces. While we have found that some ruthenium sulfoxide complexes can store absorbed photonic energy in chemical bonds via formation of a metastable *O*-bonded isomer, we have barely begun to understand which vibrational modes are important to isomerization and how are they coupled to the ground and excited potential energy surfaces.[36]

According to the Born–Oppenheimer approximation, a potential energy surface (PES) of a molecule may be constructed by assuming that the electronic structure will rapidly change in response to small changes in nuclear configuration. These surfaces are frequently described as adiabatic and are generally well modelled by ab initio treatment, which separates electronic and nuclear components. The construction of such potential energy surfaces often provides valuable information concerning a reaction mechanism such as the relative energy levels and geometry of reactants, products, intermediates and transition states. Application of these approximations to photochemical reactions becomes inherently more complex as the reaction now includes a ground state and one or more excited states. Questions arise concerning not only how the PES may be modelled for an excited state species, but also how the molecule relaxes from one PES to another. If the vibronic coupling is weak, then the reaction may be modelled by considering changes in the nuclear configuration on the excited state PES separately from the ground state PES. Accordingly, relaxation to the ground state would be expected to occur following some change in nuclear configuration governed by the surface of the excited state PES. Such a mechanism may be described as adiabatic since non-adiabatic and other higher order terms may be neglected.

However, the weak coupling approximation has become increasingly inadequate for the description of many ultrafast photochemical processes. Advances in computational methods and ultrafast spectroscopic measurements have revealed that many systems are only accurately described when non-adiabatic and other higher order terms accounting for spin-orbit coupling or rotational modes are included.[65–68] Such systems typically result in conical intersections between adjacent PES's. These intersections are simply points at which the non-adiabatic coupling between two or more vibrational modes and the electronic components becomes singular. Thus, the conical intersection acts as a photochemical funnel that facilitates rapid non-radiative decay between two adjacent PES's. For example, the mechanism of *cis*-*trans* isomerization about a carbon-carbon double bond (C=C) can be described as a conical intersection involving rotation about the C=C as well as pyramidalization at one of the carbons.[69] These motions allow electronic decay to the ground state at a geometry which would otherwise be considered an avoided crossing on a femtosecond timescale. Another example is $[RuCl_5NO]^{2-}$, which features two photochemically-induced metastable isomers, MS1 (*O*-bonded NO coordination) and MS2 (η^2-NO coordination).[70] Using computational methods, conical intersections were found between the lowest energy excited state PES and ground state PES as well as between the two lowest energy excited state PES's. Such reactions may be considered non-adiabatic because separation of nuclear and electronic components does not permit an accurate description of the reaction coordinate.

As discussed above, the transient absorption spectra of $[Ru(tpy)(bpy)(dmso)]^{2+}$ show a direct conversion from the *S*-bonded ^{3}MLCT state surface to the *O*-bonded ^{3}MLCT state surface. That is, the isomerization occurs along the excited state ^{3}MLCT surface as depicted in Figure 4. Accordingly, it may be described as an adiabatic process in which progression along the reaction coordinate is maintained on the lowest electronically excited PES, analogous to any ground state thermal reaction. Isomerization precedes relaxation to the ground state PES. The driving force for isomerization may be viewed in parallel to the electrochemical reaction in which the CT state is described as a formally oxidized metal center (Ru^{3+}) and formally reduced ligand ($tpy^{\cdot-}$), resulting in the *O*-bonded state being thermodynamically stable relative to the *S*-bonded state.[42]

In comparison, $[Ru(bpy)_2(OSO)]^+$ has also been investigated by picosecond transient absorption spectroscopy (Figure 5).[37] In panel a are shown the spectra of *S*- and *O*-bonded isomers with transient spectra of each isomer shown in panels b and c, respectively. In b, the spectra of the *S*-bonded isomer reveal a bleach near 450 nm in the first few picoseconds concomitant with a broad featureless absorption at lower energy. In accord with $[Ru(tpy)(bpy)(dmso)]^{2+}$, these features have been interpreted as the formation of a ^{3}MLCT state of *S*-bonded character. However, as the spectra evolve through time, the bleach at 450 nm decreases in intensity concomitant with a decrease of the broad absorbance at lower energy culminating in the formation of a positive absorbance feature at 500 nm. The spectrum at 500 ps strongly resembles the ground state absorbance of the *O*-bonded isomer (panel a). The *O*-bonded transient absorption spectrum features a bleach feature centered at 500 nm, which decays over time to a spectrum which does not differ from the original ground state spectrum (panel c). Thus unlike $[Ru(tpy)(bpy)(dmso)]^{2+}$, irradiation of S-$[Ru(bpy)_2(OSO)]^+$ triggers an excited state isom-

erization that occurs not along the ^{3}MLCT surface, but rather directly from the *S*-bonded ^{3}MLCT excited state to the *O*-bonded singlet ground state in 150 ps. In accord with the above definitions, we have described this reactivity as non-adiabatic and therefore suggest the presence of a conical intersection between the CT PES of the *S*-bonded complex with the *O*-bonded ground state PES. These features with time constants for certain events are displayed in Figure 6.

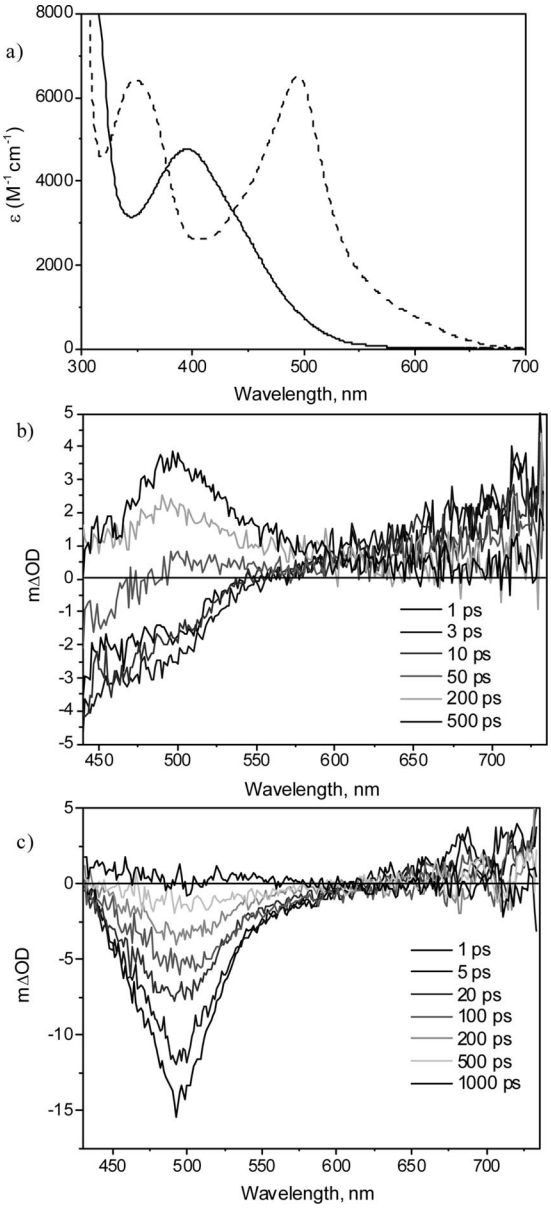

Figure 5. a) Ground-state absorption spectra of *S*-bonded (solid) and *O*-bonded (dashed) $[Ru(bpy)_2(OSO)]^+$. b) Picosecond transient absorption spectra of S-$[Ru(bpy)_2(OSO)]^+$ in methanol. c) Picosecond transient absorption spectra of O-$[Ru(bpy)_2(OSO)]^+$ in methanol.

In order to rationalize why this complex exhibits a different mechanism from previously studied dmso complexes, the energy level diagrams in Figures 4 and 6 may be compared. Emission measurements for $[Ru(bpy)_2(OSO)]^+$ reveal

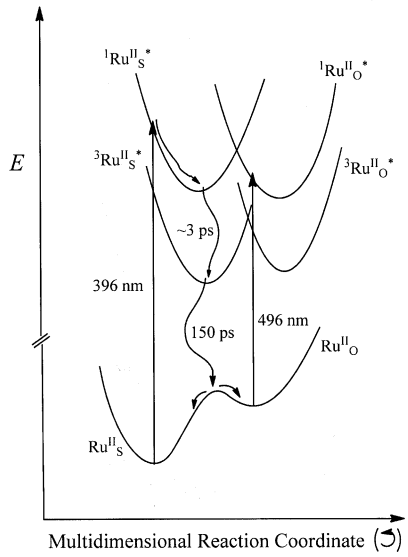

Figure 6. State diagram for $[Ru(bpy)_2(OSO)]^+$.

an unusually large Stokes' shift of ca. 8000 cm^{-1} for the *S*-bonded isomer as compared to ca. 5800 cm^{-1} for $[Ru(bpy)_3]^{2+}$. We expect that this Stokes' shift corresponds to a larger reorganization energy and hence a significant change in nuclear configuration between the Franck–Condon and thermally equilibrated ^{3}MLCT PES minimum. However, this is not unique to $[Ru(bpy)_2(OSO)]^+$ as a similarly large Stokes' shift has been observed for $[Ru(tpy)(bpy)(dmso)]^{2+}$. In both complexes, we have interpreted the geometry of this thermally equilibrated state to have either an η^2 or asymmetric η^2 coordination of the sulfoxide group. This geometry is intermediate between the *S*-bonded and *O*-bonded structures of the ground state isomers. Unlike $[Ru(tpy)(bpy)(dmso)]^{2+}$, the *O*-bonded ^{3}MLCT state of $[Ru(bpy)_2(OSO)]^+$ appears to be thermodynamically unstable relative to the η^2-excited state (Figure 6). Therefore, rapid relaxation occurs from the η^2 geometry on the excited state PES to the ground state PES where it branches between the *S*-bonded and *O*-bonded isomers accordingly. As observed in the comparison of the ground state absorbance spectra, the chelating sulfoxide complex exhibits particularly large stabilization of the Ru dπ orbitals relative to other $Ru(bpy)_2$-type complexes. It may be that this extra stabilization afforded by the chelating sulfoxide translates into additional stabilization of the excited state structure as well to a point where its energy level falls below that of the *O*-bonded excited state structure.

4. Excited-State Distortion

In an effort to more quantitatively determine the magnitude of distortion between the ground state and ^{3}MLCT state equilibrium geometries, we have recently analyzed the absorption and emission spectra of a series of complexes analogous to $[Ru(bpy)_2(OSO)]^+$, in which the methyl group on the sulfur has been replaced by a benzyl, naphthyl, or

pentafluorobenzyl group (R = Bn, Nap, BnF_5).[36] As shown in Figure 7, the absorbance spectrum for $[Ru(bpy)_2(OSOBnF_5)]^+$ is significantly broader than $[Ru(bpy)_3]^{2+}$. The full width at half maximum (*fwhm*) is directly proportional to the distortion or nuclear displacement (ΔQ) and proportional to the square root of the reorganization energy ($\lambda^{*1/2}$).[63] The reorganization energy is comprised of an outer sphere or solvent contribution (λ_o), and inner sphere contribution which may be further classified into intraligand (λ_{IL}) and metal–ligand (λ_{ML}) constituents. The relative contributions of these terms is shown in Equation (1), in which $h\nu_{ML}$ and $h\nu_{IL}$ are metal-ligand (Ru–N, Ru–S, Ru–O) vibrational modes and intraligand (bpy) vibrational modes respectively.[71] Values of 500, 1300, 500 and 1350 cm^{-1} were assumed for $h\nu_{ML}$, $h\nu_{IL}$, λ_o, and λ_{IL} based on previous studies of $[Ru(bpy)_3]^{2+}$ and other ruthenium polypyridine complexes.[71,72] It was assumed that the significantly broader spectra were due to a greater contribution from the metal-ligand modes. The results of this analysis are summarized in Table 2. Notably, the metal-ligand reorganization predicted for $[Ru(bpy)_3]^{2+}$ was 510 cm^{-1}, which agrees well with previous results;[71] whereas values for $[Ru(bpy)_2(OSOR)]^+$ were found to be significantly greater with values of 10,800 cm^{-1}, 14,400 cm^{-1}, and 14,800 cm^{-1} for R = Nap, BnF_5 and Bn, respectively.

$$\frac{(fwhm)^2}{5.55} = \lambda_o(2kT) + \lambda_{ML}\left(h\nu_{ML}\coth\left(\frac{h\nu_{ML}}{2kT}\right)\right) + \lambda_{IL}(h\nu_{IL}) \quad (1)$$

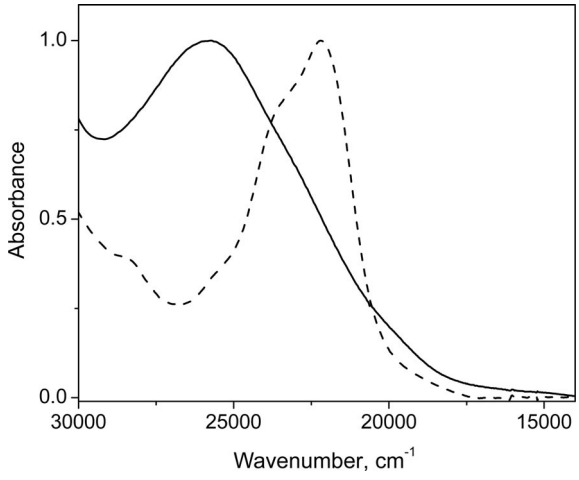

Figure 7. Normalized absorbance spectra of $[Ru(bpy)_3]^{2+}$ (dashed) and $[Ru(bpy)_2(OSOBnF_5)]^+$ (solid), $OSOBnF_5$ is 2-pentafluorophenylmethanesulfinylbenzoate.

Table 2. Absorption fitting values.

Complex	*fwhm* /cm^{-1}	λ_{ML} /cm^{-1}
$[Ru(bpy)_3]^{2+}$	3550	510
$[Ru(bpy)_2(OSOBn)]^+$	7360	14,800
$[Ru(bpy)_2(OSONap)]^+$	6380	10,800
$[Ru(bpy)_2(OSOBnF_5)]^+$	7250	14,400

Following methods described previously, corrected emission spectra were obtained at 77 K in 4:1 EtOH/MeOH glass and fit to Equation (2), in which $h\nu_m$ and $h\nu_l$ are medium and low frequency vibrational modes, S_m and S_l are Huang–Rhys parameters, and E_0 is the zero-zero splitting energy.[73] The parameters $h\nu_m$ and $h\nu_l$ are analogous to the intraligand and metal-ligand vibrational modes in Equation (1). The results are summarized in Table 3. Unlike the spectrum for $[Ru(bpy)_3]^{2+}$, which required the inclusion of a low frequency vibrational mode to adequately fit the spectrum,[74] the spectra for these complexes were fit with a single vibrational mode. Furthermore, the medium frequency mode is shifted to lower values of 1150–1300 cm^{-1} compared to 1400 cm^{-1} in $[Ru(bpy)_3]^{2+}$. These values are in relatively close agreement with the *S*-bonded ν(S=O) stretches observed for these complexes (1093 cm^{-1}, 1097 cm^{-1}, 1105 cm^{-1} for R = Nap, Bn, and BnF_5, respectively). This suggests that the ν(S=O) stretching mode is strongly coupled to excited state decay and is consistent with the absorption spectral analysis in that intraligand bpy vibrations are no longer the dominant mode coupling the excited and ground state potential energy surfaces.

$$I_\nu = \sum_{m=0}^{5}\sum_{l=0}^{15}\left(\frac{E_0 - mh\nu_m - lh\nu_l}{E_0}\right)^3 \frac{S_m^m S_l^l \exp\left[-4\ln 2\cdot\left(\frac{\nu - E_0 + mh\nu_m + lh\nu_l}{fwhm}\right)^2\right]}{m!l!} \quad (2)$$

Table 3. Corrected (77 K) emission spectra fitting parameters.

Complex	E_0 /cm^{-1}	$h\nu_m$ /cm^{-1}	$h\nu_l$ /cm^{-1}	S_m	S_l	*fwhm* /cm^{-1}
$[Ru(bpy)_3]^{2+}$	17,500	1400	400	0.8	1.0	600
$[Ru(bpy)_2(OSOBn)]^+$	17,200	1150	–	1.4	–	1450
$[Ru(bpy)_2(OSONap)]^+$	17,200	1150	–	1.4	–	1450
$[Ru(bpy)_2(OSOBnF_5)]^+$	17,300	1300	–	1.2	–	1600

5. Two-Color Photochromes

We recently reported two examples of photochromic ruthenium compounds that feature two-color reversible photochromism.[38,41] While this behavior has been observed in certain organic photochromes notably dithienylethenes, it remains rare in transition metal chemistry. We know of only a few examples of reversible, two color photochromic action in transition metal complexes. The pentacyanonitrosylmetallates show this behavior and Burkey and Heilweil have reported one such organometallic example.[75] The metal nitrosyl compounds feature phototriggered isomerization of the bound nitrosyl ligand from *N*-bonded to η^2-NO to *O*-bonded (isonitrosyl). Each isomer is observable by X-ray crystallography and infrared spectroscopy with different decay temperatures.[23] The lack of transient data detailing the isomerization complicates mechanistic interpretation.

The difficulty in preparing complexes with this behavior can be explained by examining Figure 4. The ground state isomerization from S to O is thermodynamically uphill; production of O-$[Ru(tpy)(bpy)(dmso)]^{2+}$ is only possible

through excitation of S-$[Ru(tpy)(bpy)(dmso)]^{2+}$ followed by isomerization and then relaxation. That is, isomerization and relaxation are exothermic reactions; the reverse reaction is thus not favorable. Referencing Kasha's rule, excitation of O-$[Ru(tpy)(bpy)(dmso)]^{2+}$ will always yield an *O*-bonded excited state which will necessarily relax to an *O*-bonded ground state. This is indeed observed. The only pathway to avoid this eventuality is to surface cross from the *O*-bonded manifold of states to the *S*-bonded manifold of states during IVR. Alternatively, isomerization from O to S may be achieved by accessing different transition states in the two reactions.[75]

The complex $[Ru(bpy)_2(OSSO)]^{2+}$,where OSSO is dimethylbis(methylsulfinylmethyl)silane, features three minima on the Ru^{II} ground state potential energy surface.[41] The ground state is a bis-*S*-bonded ground state, a metastable *S*,*O*-bonded isomer and a metastable bis-*O*,*O*-bonded isomer. The ground state exhibits an MLCT absorption at 350 nm, the *S*,*O*-bonded isomer absorbs at 400 nm, and the *O*,*O*-bonded isomer absorbs at 348 and 489 nm. The absorption maxima for each isomer are similar to that observed for $[Ru(bpy)_2(dmso)_2]^{2+}$ and $[Os(bpy)_2(dmso)_2]^{2+}$. Charge-Transfer excitation of the S,S isomer yields the S,O isomer and then the O,O-isomer in sequential photochemical reactions. Quantum yields of isomerization are $\Phi_{SS\rightarrow SO} = 0.55\ (\pm 6)$ and $\Phi_{SO\rightarrow OO} = 0.035(\pm 5)$ with 327 nm excitation. These absorption changes are reversible at room temperature in the absence of light. The bis-*O*,*O*-bonded isomer reverts to the S,O-isomer slowly at room temperature with a rate constant of $2.5(\pm 2) \times 10^{-4}\ s^{-1}$; reversion to the S,S isomer is much slower occurring over the period of several days. The slow reversion rates permit independent study of each of the three isomers.

Emission spectroscopy reveals strong evidence for a photochemical excited state O→S isomerization. Irradiation of the S,O-isomer with 355 nm or 400 nm irradiation, but not 532 nm, shows an emission spectrum with a maximum 600 nm and a lifetime of 2 ns. The emission quantum yield (Φ_{EM}) is 0.009 (±5). Presumably, the weak absorbance of the S,O-isomer at 532 nm prevents observance of the 600 nm emission feature. Irradiation of the O,O-isomer with 532 nm or longer wavelength shows a similar emission at 600 nm, though of a weaker intensity. Indeed, the emission quantum yield is $1.7(\pm 3) \times 10^{-4}$ with a lifetime of 2 ns. These data indicate that O→S isomerization occurs in the excited state. Mechanistic details for this reaction are not presently available.

We have recently reported the photochemistry of $[Ru(bpy)_2(pySO)]^{2+}$, where pySO is 2-(isopropylsulfinylmethyl)pyridine. This complex is reminiscent of a report from Meyer regarding $[Ru(bpy)_2(py)(dmso)]^{2+}$ (py is pyridine),[76] where both *S*- and *O*-bonded isomers are observed from reaction of $[(bpy)_2(py)Ru^{IV}{=}O]^{2+}$ with dimethylsulfide. In this example, the *O*-bonded isomer is initially formed and then thermally isomerizes to yield the *S*-bonded isomer. The *S*- and *O*-bonded isomers absorb at 400 and 476 nm, respectively. For the chelating complex, S-$[Ru(bpy)_2(pySO)]^{2+}$ absorbs at 370 nm indicating that the chelate provides additional stabilization of the dπ set relative to $[Ru(bpy)_2(py)(dmso)]^{2+}$, since the excited states of both complexes are MLCT bpy localized. Irradiation of propylene carbonate solutions of $[Ru(bpy)_2(pySO)]^{2+}$ with 355 nm light results in a decrease in the absorbance at 370 nm and an increase at 472 nm in accord with phototriggered S→O isomerization of the sulfoxide [$\Phi_{S\rightarrow O} = 0.11(2)$; Figure 8].[38] The infrared spectrum provides structural evidence for isomerization. The ground state *S*-bonded isomer exhibits $\nu(S{=}O) = 1090\ cm^{-1}$ which yields $\nu(S{=}O) = 1060\ cm^{-1}$ upon irradiation. Consistent with the absorption data, this new feature is ascribed to the *O*-bonded isomer.

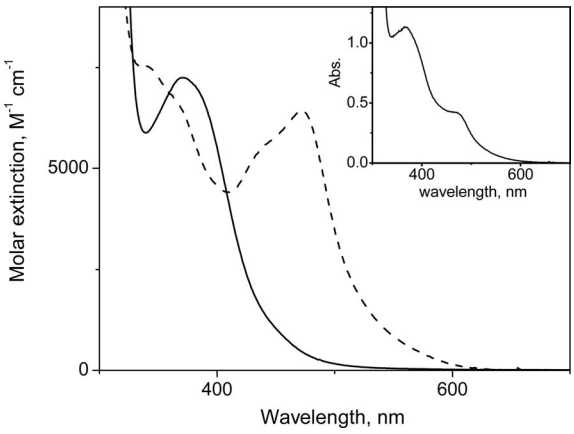

Figure 8. UV/Vis spectra of *S*-bonded (solid) and *O*-bonded (dashed) isomers of $[Ru(bpy)_2(pySO)]^{2+}$. Inset shows spectrum obtained following irradiation of *S*-bonded isomer with white light source.

Strikingly, charge transfer excitation ($\lambda \approx 475$ nm) of O-$[Ru(bpy)_2(pySO)]^{2+}$ results in a decrease of the absorbance at 472 nm and a return to a spectrum similar to the original *S*-bonded spectrum [$\Phi_{O\rightarrow S} = 0.027(6)$]. A reversible photochemical reaction with similar quantum yields indicates that a photostationary state may be found. The inset of Figure 8 shows the resultant spectrum from irradiation of S-$[Ru(bpy)_2(pySO)]^{2+}$ with a white light source. Indeed, the spectrum is a linear combination of *S*- and *O*-bonded isomers suggestive of a photostationary state. Transient absorption spectra of both *S*- and *O*-bonded spectra show that isomerization follows formation of thermally relaxed ^{3}MLCT states. Thus, we conclude that O→S and S→O isomerizations are not the microscopic reverse of one another, but rather that they access different transition states.

A Jablonski-type diagram summarizing our spectroscopic and electrochemical data are shown in Figure 9. The *S*- and *O*-bonded ground states are separated by 0.6 eV ($4735\ cm^{-1}$) as revealed from cyclic voltammetry. Excitation of *S*-bonded produces a ^{1}MLCT state which relaxes to a thermally equilibrated ^{3}MLCT state (CT_S in figure) in ca. 2 ps. The geometry of this state is quite different from that of the ground state. This complex may relax directly to the *S*-bonded ground state or isomerize to produce the *O*-bonded ground state. The S→O isomerization time constant is 1.5 ns. Excitation of the *O*-bonded ground state produces a ^{1}MLCT state which relaxes to a thermally equilibrated

^{3}MLCT state (CT_O in figure) in 7.4 ps. We propose that the geometry of this state is different from both the *O*-bonded ground state and the thermally equilibrated *S*-bonded ^{3}MLCT state. This complex may either isomerize to the *S*-bonded ground state with a time constant of 6.3 ns or to the *O*-bonded ground state. The relative energy levels of the ^{3}MLCT states are estimated from 77 K emission spectra. Additional studies are underway to better understand this unusual reactivity; in particular the mixing of S- and *O*-bonded excited state surfaces near the intersection region and early dynamics for the formation of these excited states.

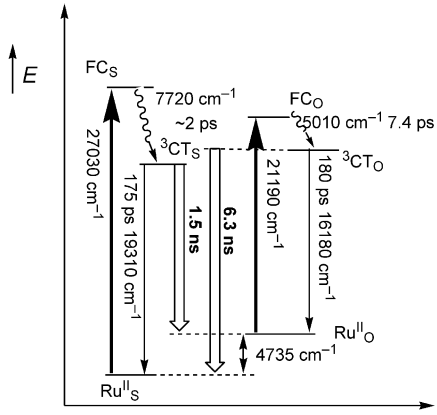

Figure 9. Jablonski-type diagram depicting energy levels and kinetics for relaxation and isomerization in $[Ru(bpy)_2(pySO)]^{2+}$.

6. SO_2 Isomerizations

At present, there are no crystallographic data available for metastable states of metal sulfoxide complexes. However, results from a number of crystallographic and spectroscopic studies of metal sulfur dioxide provide some valuable insight.[77–79] The first report of a photogenerated SO_2 metastable state was from Johnson and Dew.[80] On the basis of infrared spectroscopy, they found that irradiation of $[Ru(NH_3)_4Cl(SO_2)]Cl$ in the solid state at low temperature produced ultimately two isomers. The first isomer was confidently ascribed to an η^2-SO_2 isomer based on differences between symmetric and asymmetric ν(S=O) stretches and ^{18}O isotopic studies. A second isomer was observed in the infrared spectrum that appeared to be formed as a product following irradiation of the side-bonded SO_2 adduct. This isomer was tentatively assigned as an *O*-bonded SO_2 complex.

Coppens later reported the first structural data of the η^2-SO_2 isomer through photocrystallographic techniques.[78] Short wavelength irradiation of crystalline $[Ru(NH_3)_4Cl(SO_2)]Cl$ showed evidence of this metastable isomer. As expected, the Ru–S bond length increases from 2.080(1) Å to 2.32(2) Å concomitant with a decrease in the Ru–Cl bond from 2.407(1) Å to 2.32(1) Å. Similar changes have been observed in the molecular structures of metastable states of metal nitrosyl complexes.[27,28] An important nuance of this experiment is the low optical density of the crystalline material. The visible electronic transitions for this and related complexes are Laporte-forbidden Ligand Field transitions, which are characteristically weak. This feature facilitates bulk conversion from the ground state to the metastable state by permitting more light to penetrate the crystal. Even so, the population of the η^2-SO_2 complex is just 11.1(1)%, indicating the difficulty of this experiment. In addition, these metastable states are thermally unstable requiring these experiments to be performed at liquid nitrogen and lower temperatures.

Visible irradiation of crystalline $[Ru(NH_3)_4(OH_2)(SO_2)]^{2+}$ at 13 K produces a second metastable isomer assigned to the *O*-bonded SO_2 complex.[79] X-ray analysis of the irradiated crystal reveals contributions from the *S*-bonded ground state, two η^2-SO_2 states and two separate *O*-bonded SO_2 metastable isomers. At this temperature, the new *O*-bonded isomers were found at 36% total contribution. This report confirms the initial observation by Johnson and Dew in 1979. Unfortunately, accurate metrical data regarding bond lengths are not available due to the number of isomers formed upon irradiation. Nevertheless, it is remarkable that these isomerizations occur with retention of the crystal group and that there is no significant degradation of the crystal upon irradiation.

Importantly, these data indicate that the η^2-SO_2 complex can be observed as a metastable isomer, despite that it is the obvious transition state in the isomerization from *S*-bonded to *O*-bonded SO_2. The transition states accessed in the formation of these isomers must be described as "slipped" or asymmetric η^2 coordination, which is not unusual for other double-bonded donors. It indicates at the very least that the excited state potential energy surface is soft or, more precisely, that large changes in nuclear geometry occur with small energy changes. With regards to sulfoxide isomerizations, we interpret the presence of these metastable states to support our assignment of an η^2-SORR' in the photochemistry of chelating sulfoxides.

7. Summary

We have found that polypyridine ruthenium complexes of monodentate and chelating sulfoxides display intramolecular excited state S→O isomerization triggered by MLCT irradiation. The lowest energy ground state isomers of these complexes are *S*-bonded and feature large, positive $Ru^{3+/2+}$ reduction potentials due to an apparent stabilization of the Ru dπ orbital set. Remarkably, the excited state isomerization occurs on a nanosecond to picosecond timescale for these complexes. Transient absorption studies have revealed different mechanisms for isomerization for monodentate sulfoxides vs. chelating sulfoxides. Future studies of these complexes will involve exploitation of these properties in molecule-based devices as well as exploration of additional complexes that feature this reactivity.

Acknowledgments

We thank all the postdoctoral (pd), graduate (g) and undergraduate students that have contributed to the success of this project: Melanie Heying (pd), Aaron A. Rachford (g), Nicholas V. Mockus (g), Yuhuan Jin (g), Komal Garg (g) Carl P. Myers, Amy M. Shelker, Seth Marquard, Dennis P. Butcher Jr., Michelle Cooperrider, Christine Schultz, Tod Grusenmeyer, Eric Abrams, Ryan O'Donnell, Brianne Porter, Justin Henthorn, Krystyna Chisholm, Preston Roeper, Justin Reagh and Erika Thomas. B. A. M. thanks the National Defense Science and Engineering Graduate (NDSEG) Fellowship for a graduate fellowship. J. J. R. thanks Ohio University, Condensed Matter and Surface Science, NanoBioTechnology Initiative and National Science Foundation (NSF) (CHE-0809669; CHE-0947031) for partial funding of this work.

[1] S. Bonnet, J.-P. Collin, J.-P. Sauvage, *Inorg. Chem.* **2006**, *45*, 4024.
[2] S. D. Straight, J. Andreasson, G. Kodis, S. Bandyopadhyay, R. H. Mitchell, T. A. Moore, A. L. Moore, D. Gust, *J. Am. Chem. Soc.* **2005**, *127*, 9403.
[3] S. D. Straight, J. Andreasson, G. Kodis, A. L. Moore, T. A. Moore, D. Gust, *J. Am. Chem. Soc.* **2005**, *127*, 2717.
[4] S. Silvi, E. C. Constable, C. E. Housecroft, J. E. Beves, E. L. Dunphy, M. Tomasulo, F. M. Raymo, A. Credi, *Chem. Eur. J.* **2009**, *15*, 178.
[5] W. R. Browne, B. L. Feringa, *Ann. Rev. Phys. Chem.* **2009**, *60*, 407.
[6] U. Al-Atar, R. Fernandes, B. Johnsen, D. Baillie, N. R. Branda, *J. Am. Chem. Soc.* **2009**, *131*, 15966.
[7] P. Gorostiza, E. Y. Isacoff, *Science* **2000**, *322*, 395.
[8] R. Eelkema, M. M. Pollard, J. Vicario, N. Katsonis, B. S. Ramon, C. W. M. Bastiaansen, D. J. Broer, B. L. Feringa, *Nature* **2006**, *440*, 163.
[9] T. Hugel, N. B. Holland, A. Cattani, L. Moroder, M. Seitz, H. E. Gaub, *Science* **2002**, *296*, 1103.
[10] L. V. Schafer, E. M. Muller, H. E. Gaub, H. Grubmuller, *Angew. Chem. Int. Ed.* **2007**, *46*, 2232.
[11] Y. Yu, M. Nakano, T. Ikeda, *Nature* **2003**, *425*, 145.
[12] A. Natansohn, P. Rochon, *Chem. Rev.* **2002**, *102*, 4139.
[13] J. A. Delaire, K. Nakatani, *Chem. Rev.* **2000**, *100*, 1817.
[14] B. L. Feringa, R. A. van Delden, N. Koumura, E. M. Geertsema, *Chem. Rev.* **2000**, *100*, 1789.
[15] K. Ichimura, *Chem. Rev.* **2000**, *100*, 1847.
[16] M. Irie, *Chem. Rev.* **2000**, *100*, 1685.
[17] S. Kawata, Y. Kawata, *Chem. Rev.* **2000**, *100*, 1777.
[18] S. Nagashima, M. Murata, H. Nishihara, *Angew. Chem. Int. Ed.* **2006**, *45*, 4298.
[19] N. Tamai, H. Miyasaka, *Chem. Rev.* **2000**, *100*, 1875.
[20] J. J. Rack, *Z. Kristallogr.* **2008**, *223*, 356.
[21] J. J. Rack, *Coord. Chem. Rev.* **2009**, *253*, 78.
[22] T. E. Bitterwolf, *Coord. Chem. Rev.* **2006**, *250*, 1196.
[23] P. Coppens, I. Novozhilova, A. Kovalevsky, *Chem. Rev.* **2002**, *102*, 861.
[24] P. Gutlich, Y. Garcia, T. Woike, *Coord. Chem. Rev.* **2001**, *219*, 839.
[25] T. T. To, C. B. Duke, C. S. Junker, C. M. O'Brien, C. R. Ross, C. E. Barnes, C. E. Webster, T. J. Burkey, *Organometallics* **2008**, *27*, 289.
[26] S. Kume, H. Nishihara, *Dalton Trans.* **2008**, 3260.
[27] M. D. Carducci, M. R. Pressprich, P. Coppens, *J. Am. Chem. Soc.* **1997**, *119*, 2669.
[28] M. R. Pressprich, M. A. White, Y. Vekhter, P. Coppens, *J. Am. Chem. Soc.* **1994**, *116*, 5233.
[29] M. Imlau, R. Schieder, R. A. Rupp, T. Woike, *Appl. Phys. Lett.* **1999**, *75*, 16.
[30] M. Imlau, T. Woike, R. Schieder, R. A. Rupp, *Europhys. Lett.* **2001**, *53*, 471.
[31] D. Schaniel, M. Imlau, T. Weisemoeller, T. Woike, K. W. Kramer, H.-U. Gudel, *Adv. Mater.* **2007**, *19*, 723.
[32] J. Schefer, D. Schaniel, V. Petricek, T. Woike, *Z. Kristallogr.* **2008**, *223*, 259.
[33] M. Fally, M. Imlau, R. A. Rupp, M. A. Ellabban, T. Woike, *Phys. Rev. Lett.* **2004**, *93*, 243903.
[34] V. Dieckmann, S. Eicke, J. J. Rack, T. Woike, M. Imlau, *Opt. Exp.* **2009**, *17*, 15052.
[35] D. A. Lutterman, A. A. Rachford, J. J. Rack, C. Turro, *J. Phys. Chem. A* **2009**, *113*, 11002.
[36] B. A. McClure, E. R. Abrams, J. J. Rack, *J. Am. Chem. Soc.* **2010**, *132*, 5428.
[37] B. A. McClure, N. V. Mockus, D. P. Butcher, D. A. Lutterman, C. Turro, J. L. Petersen, J. J. Rack, *Inorg. Chem.* **2009**, *48*, 8084.
[38] B. A. McClure, J. J. Rack, *Angew. Chem. Int. Ed.* **2009**, *48*, 8556.
[39] N. V. Mockus, S. Marquard, J. J. Rack, *J. Photochem. Photobiol. A: Chem.* **2008**, *200*, 39.
[40] N. V. Mockus, J. L. Petersen, J. J. Rack, *Inorg. Chem.* **2006**, *45*, 8.
[41] N. V. Mockus, D. Rabinovich, J. L. Petersen, J. J. Rack, *Angew. Chem. Int. Ed.* **2008**, *47*, 1458.
[42] A. A. Rachford, J. L. Petersen, J. J. Rack, *Inorg. Chem.* **2005**, *44*, 8065.
[43] A. A. Rachford, J. L. Petersen, J. J. Rack, *Inorg. Chem.* **2006**, *45*, 5953.
[44] A. A. Rachford, J. J. Rack, *J. Am. Chem. Soc.* **2006**, *128*, 14318.
[45] J. J. Rack, N. V. Mockus, *Inorg. Chem.* **2003**, *42*, 5792.
[46] J. J. Rack, A. A. Rachford, A. M. Shelker, *Inorg. Chem.* **2003**, *42*, 7357.
[47] J. J. Rack, J. R. Winkler, H. B. Gray, *J. Am. Chem. Soc.* **2001**, *123*, 2432.
[48] A. A. Rachford, J. L. Petersen, J. J. Rack, *Dalton Trans.* **2007**, 3245.
[49] D. P. Butcher, A. A. Rachford, J. L. Petersen, J. J. Rack, *Inorg. Chem.* **2006**, *45*, 9178.
[50] T. A. Grusenmeyer, B. A. McClure, C. J. Ziegler, J. J. Rack, *Inorg. Chem.* **2010**, *49*, 4466.
[51] A. Juris, V. Balzani, F. Barigelletti, S. Campagna, P. Belser, A. Von Zelewsky, *Coord. Chem. Rev.* **1988**, *84*, 85.
[52] A. Dovletoglou, S. A. Adeyemi, T. J. Meyer, *Inorg. Chem.* **1996**, *35*, 4120.
[53] T. Norrby, A. Borje, B. Akermark, L. Hammarstrom, J. Alsins, K. Lashgari, R. Norrestam, J. Martensson, G. Stenhagen, *Inorg. Chem.* **1997**, *36*, 5850.
[54] C. R. Hecker, P. E. Fanwick, D. R. McMillin, *Inorg. Chem.* **1991**, *30*, 659.
[55] J. R. Kirchhoff, D. R. McMillin, P. A. Marnot, J.-P. Sauvage, *J. Am. Chem. Soc.* **1985**, *107*, 1138.
[56] D. A. Chaisson, R. E. Hintze, D. H. Stuermer, J. D. Petersen, D. P. McDonald, P. C. Ford, *J. Am. Chem. Soc.* **1972**, *94*, 6665.
[57] H. F. Suen, S. W. Wilson, M. Pomerantz, J. L. Walsh, *Inorg. Chem.* **1989**, *28*, 786.
[58] J. V. Caspar, T. J. Meyer, *J. Am. Chem. Soc.* **1983**, *105*, 5583.
[59] E. M. Kober, J. V. Caspar, B. P. Sullivan, T. J. Meyer, *Inorg. Chem.* **1988**, *27*, 4587.
[60] M. K. Smith, J. A. Gibson, C. G. Young, J. A. Broomhead, P. C. Junk, F. R. Keene, *Eur. J. Inorg. Chem.* **2000**, 1365.
[61] N. H. Damrauer, G. Cerullo, A. Yeh, T. R. Boussie, C. V. Shank, J. K. McCusker, *Science* **1997**, *275*, 54.
[62] N. H. Damrauer, J. K. McCusker, *J. Phys. Chem. A* **1999**, *103*, 8440.
[63] E. I. Solomon, A. B. P. Lever, *Inorganic Electronic Structure adn Spectroscopy*, John Wiley & Sons, New York, **1999**.
[64] J. K. McCusker, *Acc. Chem. Res.* **2003**, *36*, 876.
[65] T. A. Barckholtz, T. A. Miller, *Int. Rev. Phys. Chem.* **1998**, *17*, 435.
[66] S. Matsika, D. R. Yarkony, *J. Chem. Phys.* **2002**, *116*, 2825.
[67] M. Mayer, L. S. Cederbaum, *J. Chem. Phys.* **1996**, *105*, 4938.

[68] G. A. Worth, L. S. Cederbaum, *Annu. Rev. Phys. Chem.* **2004**, *55*, 127.
[69] B. G. Levine, T. J. Martinez, *Annu. Rev. Phys. Chem.* **2007**, *58*, 613.
[70] V. I. Baranovskii, O. V. Sizova, *J. Struct. Chem.* **2008**, *49*, 803.
[71] J. R. Winkler, T. L. Netzel, C. Creutz, N. Sutin, *J. Am. Chem. Soc.* **1987**, *109*, 2381.
[72] E. M. Kober, T. J. Meyer, *Inorg. Chem.* **1984**, *23*, 3877.
[73] K. R. Barqawi, Z. Murtaza, T. J. Meyer, *J. Phys. Chem.* **1991**, *95*, 47.
[74] J. V. Caspar, T. D. Westmoreland, G. H. Allen, P. G. Bradley, T. J. Meyer, W. H. Woodruff, *J. Am. Chem. Soc.* **1984**, *106*, 3492.
[75] T. T. To, E. J. Heilweil, C. B. Duke, K. R. Ruddick, C. E. Webster, T. J. Burkey, *J. Phys. Chem. A* **2009**, *113*, 2666.
[76] L. Roecker, J. C. Dobson, W. J. Vining, T. J. Meyer, *Inorg. Chem.* **1987**, *26*, 779.
[77] A. Y. Kovalevsky, K. A. Bagley, J. M. Cole, P. Coppens, *Inorg. Chem.* **2003**, *42*, 140.
[78] A. Y. Kovalevsky, K. A. Bagley, P. Coppens, *J. Am. Chem. Soc.* **2002**, *124*, 9241.
[79] K. F. Bowes, J. M. Cole, S. L. G. Husheer, P. R. Raithby, T. L. Savarese, H. A. Sparkes, S. J. Teat, J. E. Warren, *Chem. Commun.* **2006**, 2448.
[80] D. A. Johnson, V. C. Dew, *Inorg. Chem.* **1979**, *18*, 3273.

Received: June 17, 2009 (revised June 17, 2010)
Published Online: July 26, 2010

DOI: 10.1002/ejic.201000532

Reactions of $[Re(CO)_3]^+$ with Histidylhistidine and Modified Histidines

Richard S. Herrick,*[a] Christopher J. Ziegler,*[b] and Americo Gambella[a]

Keywords: Medicinal chemistry / Radiopharmaceuticals / Rhenium

Ac-His-OH and His-His-OH were treated with $[Re(CO)_3(H_2O)_3]^+$ to yield two new compounds, which were structurally characterized. Each displays a peptide carboxamido-N donor. The complex formed with His-His-OH uses this group as a bridging, bidentate ligand; the complex resists challenge experiments showing that His-tags are a good way to deliver the $[M(CO)_3]^+$ core (M = ^{99m}Tc, Re).

Introduction

The development of a clinically useful protocol for preparing $[^{99m}Tc(CO)_3(H_2O)_3]^+$ in aqueous solution directly from $[^{99m}TcO_4]^-$,[1] combined with superior characteristics of the $[Tc(CO)_3]^+$ core, makes the search for $[^{99m}Tc(CO)_3L]$ complexes as candidates for radiopharmaceuticals a logical research objective.[2] As no stable nuclides of technetium exist, cold rhenium congeners are an attractive way to pursue exploratory tests on promising candidates. Recently, clinically useful β^--emitting $^{186/188}$Re nuclides have become available, increasing the interest in the study of rhenium derivatives.[3] A typical strategy for preparing a target-specific[4] radiopharmaceutical is to synthesize a bifunctional chelating agent (BFCA) that chelates the metal core at one end and incorporates a receptor-targeting biomolecule at the other end.

Many BFCAs are prepared by a complex multistep procedure, so we were intrigued by the possibility of developing BFCAs, which require little or no synthetic preparation. Histidine can be modified to act as a BFCA; $[M(CO)_3(\kappa^3\text{-}N_\alpha,N_\delta,O^-\text{-His})]$ (M = ^{99m}Tc, Re) is readily prepared and is stable in the presence of biological nucleophiles.[5] Modified versions of these complexes, each with a linker arm coupled to the N_ε amine nitrogen atom, have been prepared, extending possible uses of this ligand.[6] $[M(CO)_3]^+$ has also been used to bind N_α-, CO_2H-, or N_α-His-acetyl-modified histidines attached to peptides.[7,8] One prominent study examined the feasibility of attaching $[M(CO)_3]^+$ to a His-tag fused to antibody, single-chain Fv fragments.[9] Each study demonstrated that the radiolabeled biomolecules are stable and resist serum and other challenges. However, the size and complexity of the molecules prevented the researchers from obtaining specific information on the bonding, structure or stoichiometry of these interactions.

Results and Discussion

Herein, we report surprising initial results of studies of reactions of modified histidines as models for His-tags and histidine conjugates with $[Re(CO)_3]^+$. We initiated the study of reactions of $[Re(CO)_3(H_2O)_3]Br$[10] (actually, $[Re(CO)_3(H_2O)_3][Re_2(CO)_6(\mu_2\text{-}Br)_3]\cdot 6H_2O$[11]) with His-OMe, Ac-His-OH and His-His-OH to obtain specific information difficult or impossible to obtain in larger molecules and to explore the possibilities of using histidine peptide conjugates as the chelating portion of a BFCA. Treatment of aqueous $[Re(CO)_3(H_2O)_3]^+$ with His-OMe under mild conditions in different solvents and at a variety of pHs produced only previously characterized $[Re(CO)_3(\kappa^3$-

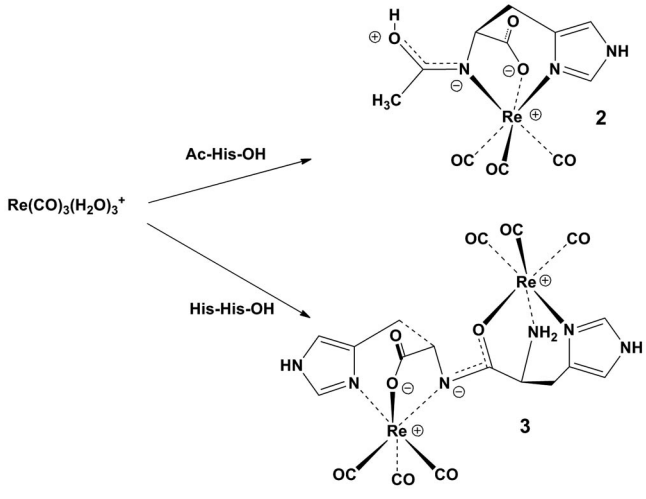

Scheme 1. Reaction scheme showing the preparation of the new compounds discussed in this article.

[a] Department of Chemistry, College of the Holy Cross
Worcester, MA 01610, USA
Fax: +1-508-793-3530
E-mail: Rherrick@holycross.edu
[b] Department of Chemistry, University of Akron
Akron, OH 44325, USA

N_α,N_δ,O^--His)] (**1**).[5] The hydrolysis of the ester bond is promoted by the lowered pK_a of water bound to [Re(CO)$_3$]$^+$.[5] In contrast, reactions with Ac-His-OH and His-His-OH gave new compounds **2** and **3**, respectively (Scheme 1); each compound has unusual bonding features discussed below.

Complex **2** forms when Ac-His-OH is treated with 1 equiv. of aqueous [Re(CO)$_3$(H$_2$O)$_3$]$^+$. Unexpectedly, the peptide conjugate is bound as a tridentate ligand via the carboxylate oxygen atom, the N_δ atom of the imidazole, and a deprotonated amide nitrogen atom (Figure 1).[12]

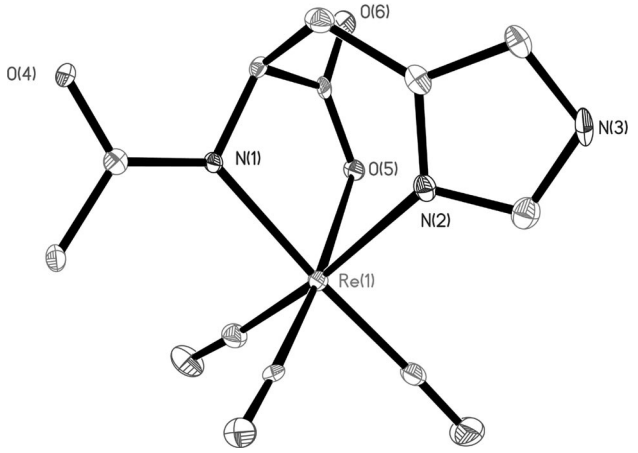

Figure 1. Molecular structure of **2** showing 35% ellipsoids. Solvent water molecules and hydrogen atoms have been omitted for clarity.

We believe that this is the first reported structure of an organometallic compound with a peptide carboxamido-N donor ligand. Since both the carboxylate and amide groups of Ac-His-OH are deprotonated, charge balance requires an additional proton for a neutral complex. We observe this proton in the difference map on the acyl oxygen atom of the amide group, an unusual location for protonation. We can confirm the presence of this proton by the increased C–O bond length of the acyl unit [1.306(6) Å], a corresponding decrease in the adjacent C–N bond length [1.315(6) Å], and by the presence of a clear hydrogen bond to a neighboring carboxylate acyl oxygen atom, with an O–O distance of 2.514(6) Å. The acyl C–O bond length of the carboyxlate group is as expected [1.236(6) Å], and thus we believe that this oxygen atom is not the site of protonation. ^{1}H and ^{13}C NMR spectra of **2** each show pairs of peaks in unequal populations due to restricted rotation around the amide bond.

Reaction of His-His-OH with 2 equiv. of [Re(CO)$_3$(-H$_2$O)$_3$]-Br produced **3**. Crystallographic elucidation (Figure 2) revealed that there are two nearly identical molecules in the asymmetric unit.[13] In each molecule, each histidine residue binds one [Re(CO)$_3$]$^+$ fragment. Previously, it was suggested that His-tagged proteins bind to [M(CO)$_3$]$^+$ ions through two imidazole rings on contiguous histidines.[9] This was found to be the bonding framework used for copper ions binding to a modified His-His dipeptide to model active-site Cu ions bound by adjacent His residues in certain oxygen-activating copper proteins.[14] In contrast, **3** was the only product observed even when a 1:1 metal/ligand stoichiometry was employed during synthesis. This compound also features a deprotonated amide nitrogen atom; the deprotonated peptide bond unit spans the two metal centers with the carboxamido nitrogen atom binding one rhenium center and the adjoining carbonyl oxygen atom binding the other rhenium center. As the N-terminal histidine is N_α,N_δ,O-bound, while the C-terminal histidinate is N_α^-,N_δ,O^--bound, the compound is formally a zwitterion.

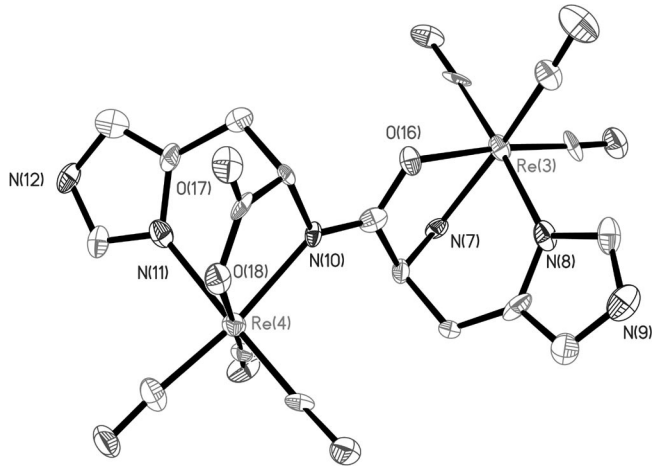

Figure 2. Molecular structure of one of two structurally similar molecules of **3** showing 35% ellipsoids. Hydrogen atoms have been omitted for clarity.

Selected bond lengths for **2** and **3** along with literature values for **1**[5] are collected in Table 1. Also included are selected bond lengths for [Re(CO)$_3$(κ^3-PN$_2$-{PPh$_2$C$_6$H$_4$-*o*-C(O)NCH$_2$CH$_2$NH$_2$})][7e] (**4**),[15] which is the most closely related Re^I compound with a carboxamido nitrogen donor atom.

Table 1. Selected bond lengths [Å] for compounds **1**–**4**.

Bond	**1**	**2**	**3**[a]	**4**
Re–N_δ	2.192	2.200(4)	2.17(2)[b]	–
Re–N_δ	–	–	2.193(7)[c]	–
Re–NH_2	2.188	–	2.195(7)	–
Re–OCO	2.147	2.169(3)	2.14(2)	–
Re–NC(O)	–	2.159(4)	2.16(2)	2.192
Re–O=C	–	–	2.130(6)	–
C–$N_{carboxamido}$	–	1.315(6)	1.303(9)	1.314
C–$O_{carboxamido}$	–	1.306(6)	1.300(6)	1.278

[a] Average of two measurements. There are two identical molecules in the asymmetric unit. Errors cover the observed range. [b] Imidizaole on N-terminal histidine. [c] Imidazole on C-terminal histidine.

The Re–NC(O) bond lengths in **2** and **3** are each close to 2.16 Å. Compound **4**,[15] which has a tridentate ligand with neutral P- and N-donor atoms and an N-donor carboxamido ligand, has an Re–NC(O) bond length of 2.192 Å. The significantly shorter bond lengths in **2** and **3** indicate a stronger bond for the peptide carboxamido ligands. Similar C–O and C–N bond lengths between 1.30

and 1.33 Å in the protonated acyl-carboxamido-N unit for **2** and **3** suggests that each has a bond order midway between 1 and 2 as illustrated in Scheme 1. Further evidence of resonance stabilization of the deprotonated amide in each compound (Scheme 2) is the fact that either a proton or an adjacent $[Re(CO)_3]^+$ fragment is bound to the carbonyl oxygen atom in **2** and **3**; this balances the formal negative charge the oxygen atom would otherwise collect in the imidate resonance form. Also, peaks in the IR spectra at 1570 and 1561 cm^{-1} for **2** and **3**, respectively, can be attributed to the C–O stretch of the carboxamido carbonyl group being lowered by resonance stabilization. Compound **4** shows a similar shortening of the C–N bond to 1.314 Å; however, the C=O bond is lengthened only slightly from a formal double-bond length to 1.278 Å. Unlike structures **2** and **3**, the carboxamido oxygen atom in **4** does not have an H^+ or $[Re(CO)_3]^+$ unit appended to it.

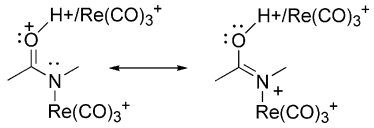

Scheme 2. Resonance stabilization of deprotonated amides for compounds **2** and **3**.

While peptide carboxamido-N donors are a somewhat unusual motif, they occur in at least one important metalloenzyme. The A-cluster, site of acetyl coenzyme A synthase activity in a variety of enzymes, has a Cys-Gly-Cys structure with two deprotonated amide groups and two thiolate groups binding the metal ions.[16] The enzyme structure has been elucidated,[16,17] and the structure of a small-molecule model of this enzyme with nickel complexes has been reported.[18]

Imidazole imine, carboxylate and amine donor groups have each been observed frequently in $[Re(CO)_3]^+$ compounds, with the imidazole rings binding most tightly.[19] Selective binding of $[Re(CO)_3(H_2O)_2]^+$ and $[Re(CO)_3(L–L)]^+$ to proteins has been observed to occur via the imine nitrogen atom of a surface histidine.[20,21] When combined in histidine, they make for a tightly binding tridentate ligand whose compounds resist challenges at 37 °C by biomolecular nucleophiles.[22] Comparison of imidazole Re–N_δ bond lengths of **1**–**3** shows they are mostly similar, except that the Re–N_δ bond length of the imidazole rings on the N-terminal histidine **3** is shorter by about 0.02 Å; presumably, this offsets the relatively weaker bonding of the amine group and the acyl oxygen atom. The Re–OCO distance is slightly longer in **2** than in **1** or **3**.

Compounds **2** and **3** were challenged in solutions at 37 °C with 100% excess of *N*-methylimidazole in [D_6]dmso. Compound **2** decomposed within 24 h; **3** showed no sign of decomposition after 2 weeks under these conditions. Despite the unusual binding observed in this compound, it is resistant to the presence of biological nucleophiles.

Conclusions

In this study, we report fundamental information regarding the type of binding and the binding strength of His-tags toward the $[Re(CO)_3]^+$ core by using simple peptide conjugates as models. Each conjugate was found to bind using an unexpected carboxamido N-donor group; the carboxamido group functioned as a bridging, bidentate N,O-donor group in **3**. Despite the unusual bonding mode, **3** resisted challenge by biological nucleophiles supporting the use of His-tags as a means of delivering the $[M(CO)_3]^+$ core. Nonetheless, it is extremely unlikely that two $[^{99m}Tc(CO)_3]^+$ cations will bind a HisHis conjugate due to the very low concentration of $[^{99m}Tc(CO)_3(H_2O)_3]^+$ available under clinical conditions. However, the novel binding mode and strength of binding observed are leading us to pursue further studies.

Experimental Section

General: Starting materials were obtained from commercial sources and were used without further purification. Distilled water was used as solvent, and reactions were run in air with no special precautions. $[Re(CO)_3(H_2O)_3]Br$ was prepared and isolated according to a literature procedure.[10] NMR spectra were recorded with a Varian 400 MHz spectrometer. IR spectra were recorded with a Nicolet Series II Magna-IR 750 spectrometer. Elemental analyses were performed by Atlantic Microlab of Norcross, GA 30091.

2: $[Re(CO)_3(H_2O)_3]Br$ (0.100 g, 0.247 mmol), and acetyl-L-histidine (0.797 g, 3.71 mmol) were heated to reflux in water (10 mL) for 60 min. A white solid formed during the reaction. The solid was filtered, washed with cold water, dried and washed with diethyl ether. Crystals suitable for X-ray diffraction were grown by diffusion of water into a methanol solution of **2**. Yield 37.3%. IR: $\tilde{\nu}$ = 3189 [ν(NH)]; 2019, 1924, 1896, 1871 [ν(C≡O)]; 1656 [ν(C=O)]; 1570 [$\nu(C{=}O)_{carbox}$] cm^{-1}. $C_{11}H_{10}N_3O_6Re$ (466.42): calcd. C 28.26, H 2.16, N 8.99; found C 28.23, H 2.08, N 8.89. ^1H NMR ([D_6]dmso): δ = 12.90 (major, s, 1 H, $N_{Im}H$), 12.86 (minor, br., 1 H, $N_{Im}H$), 8.14 (major, s, 1 H, $C_{Im}H$), 8.06 (minor, s, 1 H, $C_{Im}H$), 7.07 (minor, s, 1 H, $C_{Im}H$), 7.04 (major, s, 1 H, $C_{Im}H$), 4.67 (major, t, J = 3.6 Hz,1 H, α-*H*,), 4.41 (minor, t, J = 3.8 Hz, 1 H, α-*H*), 3.15 (minor, m, 1 H, CH_2), 3.12 (major, dd, J = 13.2, 4.4 Hz, 1 H, CH_2), 2.91 (minor, m, 1 H, CH_2), 2.86 (major, dd, J = 13.2, 4.8 Hz, 1 H, CH_2), 2.39 (s, 3 H, CH_3) ppm. ^{13}C NMR ([D_6]dmso): δ = 179.9, 170.4 (minor), 169.8 (major), 140.4 (major), 140.3 (minor), 134.4, 116.3, 59.9 (minor), 57.7 (major), 28.3 (minor), 24.2 (major), 17.4 ppm.

3: $[Re(CO)_3(H_2O)_3]Br$ (0.075 g, 0.186 mmol), and L-histidyl-L-histidine (0.027 g, 0.093 mmol) were heated to reflux in water (10 mL) for 30 min. A white solid formed during the reaction. The solid was filtered, washed with cold water and dried. Crystals suitable for X-ray diffraction were grown by diffusion of water into a methanol solution of **3**. IR: $\tilde{\nu}$ =, 3240, 3154 [ν(NH)]; 2012, 1866, 1853 [ν(C≡O)]; 1627 [ν(C=O)]; 1561 [$\nu(C{=}O)_{carbox}$] cm^{-1}. $C_{18}H_{14}N_6O_9Re_2{\cdot}H_2O$ (848.77): calcd. C 25.41, H 1.89, N 9.88; found C 25.33, H 1.57, N 10.00. ^1H NMR ([D_6]dmso): δ = 13.06 (s, 1 H, $N_{im}H$), 12.82 (s, 1 H, $N_{im}H$), 8.22 (s, 1 H, $C_{im}H$), 8.13 (s, 1 H, $C_{im}H$), 7.17 (s, 1 H, $C_{im}H$), 7.00 (s, 1 H, $C_{im}H$), 6.18 (br., 1 H, NH_2), 5.39 (d, J = 11.6 Hz, 1 H, NH_2), 4.47 (m, 1 H, α-C*H*), 4.38 (t, J = 3.8 Hz, 1 H, α-C*H*), 3.41 (br., 1 H, β-CH_2), 3.27 (br., 1 H, β-CH_2), 3.02 (dd, J = 16.4 Hz, 1 H, CH_2, 2.4 Hz), 2.84 (dd,

J = 16.6 Hz, 1 H, CH_2, 4.8 Hz) ppm. ^{13}C NMR ([D_6]dmso): δ = 180.9, 180.5, 141.0, 140.1, 134.9, 133.1, 116.7, 116.2, 57.6, 54.4, 28.2, 28.2 ppm.

Acknowledgments

Financial support from the Research Corporation (CC6663/6616), the Richard Fisher Foundation, and the National Science Foundation (CHE-0116041) for support of this research is gratefully acknowledged.

[1] R. Alberto, K. Ortner, N. Wheatley, R. Schibli, A. P. Schubiger, *J. Am. Chem. Soc.* **2001**, *123*, 3135–3136.
[2] R. Alberto in *Bioorganometallics* (Ed.: G. Jaouen), Wiley-VCH, Weinheim, **2006**, pp. 97–124.
[3] U. Abram, R. Alberto, *J. Braz. Chem.* **2006**, *17*, 1486–1500.
[4] S. Liu, *Chem. Soc. Rev.* **2004**, *33*, 445–461.
[5] R. Alberto, R. Schibli, R. Waibel, U. Abram, A. P. Schubiger, *Coord. Chem. Rev.* **1999**, *190–192*, 901–919.
[6] J. K. Pak, P. Benny, B. Spingler, K. Ortner, R. Alberto, *Chem. Eur. J.* **2003**, *9*, 2053–2061.
[7] a) R. S. Herrick, in *New Developments in Organometallic Research* (Ed.: M. A. Cato), Nova Science Publishers, Inc., New York, **2006**, pp. 117–149; b) K. E. Bullok, M. Dyszlewski, J. L. Prior, C. M. Pica, V. Sharma, D. Piwnica-Worms, *Bioconjugate Chem.* **2002**, *13*, 1226–1237; c) A. Egli, R. Alberto, L. Tannahill, R. Schibli, U. Abram, A. Schaffland, R. Waibel, D. Tourwe, L. Jeannin, K. Iterbeke, P. A. Schubiger, *J. Nucl. Med.* **1999**, *40*, 1913–1917; d) D. Psimadas, M. Fani, C. Zikos, S. Xanthopoulos, S. C. Archimandritis, A. D. Varvarigou, *Appl. Radiat. Isot.* **2006**, *64*, 151–159; e) R. Schibli, P. A. Schubiger, *Eur. J. Nucl. Med. Mol. Imaging* **2002**, *29*, 1529–1542.
[8] I. U. Khan, D. Zwanziger, I. Boehme, M. Javed, H. Naseer, S. W. Hyder, A. G. Beck-Sickinger, *Angew. Chem. Int. Ed.* **2010**, *49*, 1155–1158.
[9] R. Waibel, R. Alberto, J. Willuda, R. Finnern, R. Schibli, A. Stichelberger, A. Egli, U. Abram, J.-P. Mach, A. Plückthun, P. A. Schubiger, *Nat. Biotechnol.* **1999**, *17*, 897–901.
[10] N. Lazarova, S. James, J. Babich, J. Zubieta, *Inorg. Chem. Commun.* **2004**, *7*, 1023–1026.
[11] R. S. Herrick, C. J. Ziegler, A. Çetin, B. R. Franklin, *Eur. J. Inorg. Chem.* **2007**, 1632–1634.
[12] Crystallographic data was collected at 100 K (Bruker KRYOFLEX) with a Bruker SMART APEX CCD-based X-ray diffractometer (Mo-K_α radiation, λ = 0.71073 Å). The structures were refined by using the Bruker SHELXTL Software Package (Version 6.10) and were solved until the final anisotropic full-matrix, least-squares refinement of F^2 converged. Crystallographic summary for **2**: $C_{11}H_{10}N_3O_6Re$; M_r = 466.42; colorless block 0.18 × 0.15 × 0.10 mm; orthorhombic, $P2(1)2(1)2(1)$; Z = 4; a = 8.9203(13), b = 11.1562(16), c = 13.4957(19) Å; V = 1343.0(3) Å^3, ρ = 2.307 Mg m^{-3}. A total of 11191 reflections were collected (3004 independent reflections). $F(000)$= 880, $R1$ = 0.0233, $wR2$ = 0.0387 [for 3004 I_o, $I_o > 2\sigma(I_o)$]. CCDC-767070 contains the supplementary crystallographic data for **2**. Data for **2** can be obtained free of charge from The Cambridge Crystallographic Data Centre via www.ccdc.cam.ac.uk/data_request/cif.
[13] Crystallographic data was collected at 100 K (Bruker KRYOFLEX) with a Bruker SMART APEX CCD-based X-ray diffractometer (Mo-K_α radiation, λ = 0.71073 Å). The structures were refined by using the Bruker SHELXTL Software Package (Version 6.10) and were solved until the final anisotropic full-matrix, least-squares refinement of F^2 converged. Crystallographic summary for **3**: $C_{36}H_{35.25}N_{12}O_{21.50}Re_4$; M_r = 1724.81; colorless block 0.10 × 0.08 × 0.08 mm; orthorhombic, $P2(1)2(1)2(1)$; Z = 4; a = 13.4740(17), b = 13.8927(18), c = 25.751(3) Å; V = 4820.3(11) Å^3, ρ = 2.377 Mg m^{-3}. A total of 40942 reflections were collected (10981 independent reflections). $F(000)$= 3229, $R1$ = 0.0389, $wR2$ = 0.0511 [for 10981 I_o, $I_o > 2\sigma(I_o)$]. CCDC-767071 contains the supplementary crystallographic data for **3**. Data for **3** can be obtained free of charge from The Cambridge Crystallographic Data Centre via www.ccdc.cam.ac.uk/data_request/cif.
[14] R. A. Himes, G. Y. Park, A. N. Barry, N. J. Blackburn, K. D. Karlin, *J. Am. Chem. Soc.* **2007**, *129*, 5352–5353.
[15] J. D. G. Correia, A. Domingos, I. Santos, R. Alberto, K. Ortner, *Inorg. Chem.* **2001**, *40*, 5147–5151.
[16] C. Darnault, A. Volbeda, E. J. Kim, P. Legrand, X. Vernede, P. A. Lindahl, J. C. Fontecilla-Camps, *Nat. Struct. Biol.* **2003**, *10*, 271–279.
[17] T. I. Doukov, T. M. Iverson, J. Seravalli, S. W. Ragsdale, C. L. Drennan, *Science* **2002**, *298*, 567–572.
[18] R. Krishnan, C. G. Riordan, *J. Am. Chem. Soc.* **2004**, *126*, 4484–4485.
[19] S. R. Banerjee, M. K. Levadala, N. Lazarova, L. Wei, J. F. Valliant, K. A. Stephenson, J. W. Babich, K. P. Maresca, J. Zubieta, *Inorg. Chem.* **2002**, *41*, 6417–6425.
[20] A. M. Blanco-Rodriguez, M. Busby, K. Ronayne, M. Towrie, C. Gradinaru, J. Sudhamsu, J. Sykora, M. Hof, S. Zalis, A. J. Di Bilio, B. R. Crane, H. B. Gray, A. Vlcek, *J. Am. Chem. Soc.* **2009**, *131*, 11788–11800.
[21] S. L. Binkley, C. J. Ziegler, R. S. Herrick, R. S. Rowlett, *Chem. Commun.* **2010**, *46*, 1203–1205.
[22] D. Rattat, K. Eraets, B. Cleynhens, H. Knight, H. Fonge, A. Verbruggen, *Tetrahedron Lett.* **2004**, *45*, 2531–2534.

Received: May 13, 2010
Published Online: July 20, 2010

DOI: 10.1002/ejic.201000689

Heterochiral vs. Homochiral Linkage of Emissive Iridium(III) Complexes with D-Penicillaminate: Drastic Change in Emission Induced by Silver(I) Linkage

Keisuke Saito,[a] Yuta Sarukawa,[a] Kiyoshi Tsuge,[a] and Takumi Konno*[a]

Keywords: Chiral resolution / Iridium / Luminescence / S ligands / Substituent effects

Reactions of [{Ir(ppy or ppy-CF_3)$_2$}$_2$(μ-Cl)$_2$] {Hppy = 2-phenylpyridine, Hppy-CF_3 = 2-[3,5-bis(trifluoromethyl)phenyl]-pyridine} with D-penicillamine (D-H_2pen) afforded emissive Ir^{III} mononuclear complexes [Ir(ppy or ppy-CF_3)$_2$(D-Hpen-*N*,*S*)] as a 1:1 mixture of the Δ_D/Λ_D isomers. These complexes were converted into $Ir^{III}Ag^{I}Ir^{III}$ trinuclear structures in [Ag{Ir(D-pen-*N*,*S*)(ppy or ppy-CF_3)$_2$}{Ir(D-Hpen-*N*,*S*)(ppy or ppy-CF_3)$_2$}] by treatment with $AgNO_3$, which led to a drastic blueshift of the emission bands. Whereas the (ppy)$Ir^{III}Ag^{I}Ir^{III}$ complex produced the heterochiral $\Delta_D\Lambda_D$ isomer, the ppy-CF_3 complex gave the homochiral $\Delta_D\Delta_D$ and $\Lambda_D\Lambda_D$ isomers that could completely be separated by crystallization. It was found that the quantum efficiency of the emission band for the $\Delta_D\Delta_D$ isomer is much lower than that for the $\Lambda_D\Lambda_D$ isomer.

Introduction

Emissive metal complexes have been extensively investigated for many years due to their potential applications including artificial photosynthesis systems,[1] light-emitting devices,[2] and luminescent sensors.[3] In particular, increasing attention has been directed toward emissive complexes that possess chiralities, because they are promising candidates as chiral luminescent sensors and potential sources of polarized light.[4–6] Representative compounds of this class involve octahedral ruthenium(II) species containing 2,2′-bipyridine (bpy), 2-phenylpyridinate (ppy), or their derivatives, and some of them have been isolated as optically active forms by means of column chromatography and/or diastereomeric fractional crystallization.[4,7,8] It has been recognized that octahedral iridium(III) complexes with these ligands are commonly highly emissive and readily color-tuned by modification of the ligands.[2a,2b,9] However, much less efforts have been devoted to the isolation of optically active, emissive iridium(III) complexes to date.[10] Thus, as part of our recent project on the development of chiral mononuclear and polynuclear complexes with sulfur-containing amino acids,[11] we investigated the coordination of D-penicillamine (D-H_2pen) to $[Ir(ppy)_2]^+$ and $[Ir(ppy\text{-}CF_3)_2]^+$ {ppy-CF_3 = 2-[3,5-bis(trifluoromethyl)phenyl]-pyridinate} cores, with the aim of isolating highly emissive iridium(III) species in optically pure forms. Whereas desirable mononuclear complexes with a chelating D-Hpen ligand, [Ir(D-Hpen-*N*,*S*)(ppy)$_2$] and [Ir(D-Hpen-*N*,*S*)(ppy-CF_3)$_2$], were successfully obtained from [{Ir(ppy or ppy-CF_3)$_2$}$_2$(μ-Cl)$_2$] and D-H_2pen, they were isolated as a 1:1 mixture of the Δ_D/Λ_D isomers, showing no diastereoselectivity. To our surprise, the linkage of two [Ir(D-Hpen-*N*,*S*)(ppy)$_2$] molecules with an Ag^+ ion exclusively gave the heterochiral $\Delta_D\Lambda_D$ isomer of an *S*-bridged $Ir^{III}Ag^{I}Ir^{III}$ trinuclear complex, whereas the linkage of [Ir(D-Hpen-*N*,*S*)(ppy-CF_3)$_2$] produced only the homochiral $\Delta_D\Delta_D$ and $\Lambda_D\Lambda_D$ isomers that spontaneously separated by crystallization (Scheme 1).

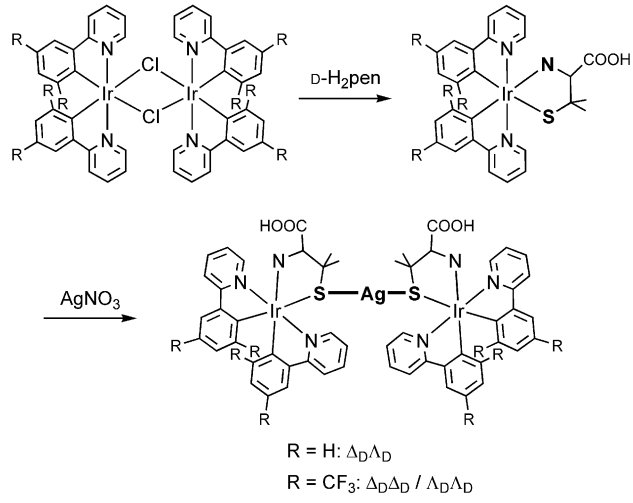

Scheme 1. Preparation of D-penicillaminato complexes.

In this communication, we report on these remarkable stereochemical results, together with the drastic change in the emission spectra upon the mononuclear/trinuclear conversion.

Results and Discussion

Treatment of an ethanolic suspension of [{Ir(ppy)$_2$}$_2$(μ-Cl)$_2$] with 1 mol-equiv. of D-H_2pen in the presence of so-

[a] Department of Chemistry, Graduate School of Science
Osaka University, Toyonaka, Osaka 560-0043, Japan
Fax: +81-6-6850-5766
E-mail: konno@chem.sci.osaka-u.ac.jp

Supporting information for this article is available on the WWW under http://dx.doi.org/10.1002/ejic.201000689.

dium acetate under reflux gave a clear orange solution, from which an orange powder (**1**) was isolated by adding water.[12] Complex **1** is poorly soluble in water, but well soluble in polar organic solvents such as methanol, ethanol, and dmso. The elemental analytical data of **1** are consistent with the formula of [Ir(D-Hpen)$(ppy)_2$], and its neutral charge was implied by the molar conductivity in methanol (7.5 $S cm^2 mol^{-1}$). Furthermore, **1** exhibits a $\nu_{C=O}$ band at 1702 cm^{-1} in the IR spectrum, indicative of the presence of a COOH group.[13] From these results, **1** is assigned to a neutral iridium(III) complex having a free COOH group, [Ir(D-Hpen-*N*,*S*)$(ppy)_2$], in which a D-Hpen ligand coordinates to an Ir^{III} center through amine and thiolate groups. The electronic absorption spectrum of **1** in methanol is characterized by a broad, intense CT band at about 400 nm with vague shoulders at longer wavelengths and a more intense π-π* band at about 260 nm (Figure 1).[14] In the ^1H NMR spectrum in [D_6]dmso, **1** gives two sets of proton signals with nearly the same intensities (4 methyl and 2 methine signals due to D-Hpen and 32 aromatic signals due to ppy),[12] suggesting that **1** is a 1:1 mixture of the Δ_D/Λ_D isomers. Consistent with this, the CD spectrum of **1** in methanol is almost silent over the whole region.

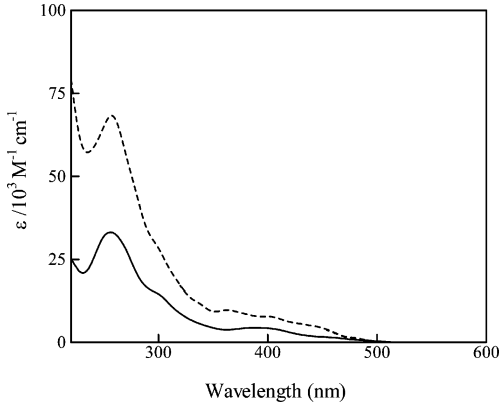

Figure 1. Absorption spectra of **1** (solid line) and **2** (broken line) in methanol.

When **1** was treated with 0.5 mol-equiv. of $AgNO_3$ in acetonitrile/water, the orange solution quickly turned to yellow, and yellow needle-like crystals (**2**) were obtained from the solution.[12] Whereas **2** is rather insoluble in water and common organic solvents, the addition of acid ($HClO_4$) or base (triethylamine) to a methanolic suspension of **2** gave a clear solution. Its absorption spectral features resemble those of **1**, showing MLCT and π-π* transition bands at similar wavelengths (Figure 1). X-ray fluorescence spectrometry indicates the presence of Ir and Ag atoms in **2**, and its elemental analytical data are consistent with the formula of [Ag{Ir(D-$H_{0.5}$pen)$(ppy)_2$}$_2$].[12]

The structure of **2** was determined by single-crystal X-ray crystallography.[15] As shown in Figure 2a, **2** is a neutral complex molecule consisting of two octahedral Ir^{III} units that are linearly linked by an Ag^I atom through S atoms to form an $Ir^{III}Ag^{I}Ir^{III}$ trinuclear structure [av. Ag–S 2.351(4) Å, S–Ag–S 169.62(11)°]. Each Ir^{III} unit has a *trans*(N_{ppy}) configuration and is chelated by two bidentate-*C*,*N* ppy ligands and a bidentate-*N*,*S* D-pen ligand [av. Ir–$C_{trans(S)}$ 1.999(13) Å, Ir–$C_{trans(N)}$ 1.997(13) Å, Ir–N_{ppy} 2.044(10) Å, Ir–N_{pen} 2.162(8) Å, Ir–S 2.432(4) Å]. Of three possible isomers, $\Delta_D\Delta_D$, $\Delta_D\Lambda_D$, $\Lambda_D\Lambda_D$, crystals of **2** contain only the heterochiral $\Delta_D\Lambda_D$ isomer with the opposite Δ and Λ configurational Ir^{III} units. In **2**, two carboxy groups are in an equatorial position such that N,S-chelate rings adopt an *ob* (*δ*) conformation for the Δ_D unit and a *lel* (*δ*) one for the Λ_D unit. No counterion exists in **2**, and thus **2** is formulated as [Ag{Ir(D-pen-*N*,*S*)$(ppy)_2$}{Ir(D-Hpen-*N*,*S*)$(ppy)_2$}], in which one of two carboxy groups is deprotonated. This is compatible with the IR spectrum of **2** that displays C=O stretching bands at 1719 cm^{-1} and 1620 cm^{-1} due to COOH and COO^-, respectively.[13] It is noted that the COOH group in **2** forms a strong intermolecular hydrogen bond with an adjacent COO^- group [O···O 2.399(10) Å], thereby constructing a 1D chain structure.[12]

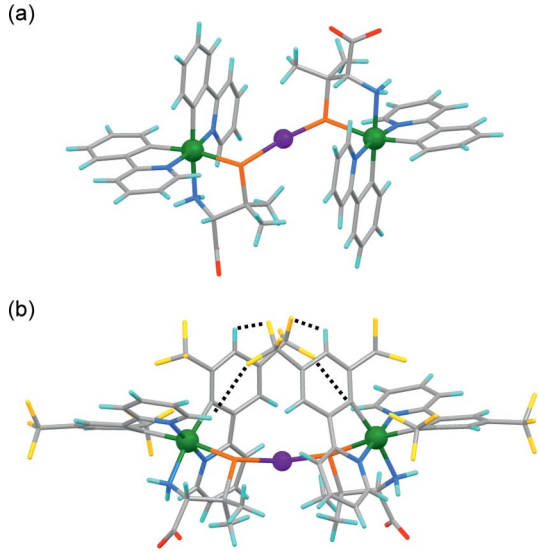

Figure 2. Perspective views of **2** (a) and **4a** (b). Ag: purple, Ir: green, S: orange, F: yellow, O: red, N: blue, C: gray, H: light blue.

Complexes **1** and **2** are both emissive in the solid state and in solution at room temperature. As shown in Figure 3a, the emission spectrum of **1** in the solid state shows a broad band at about 610 nm, whereas the emission band for **2** appears at much shorter wavelengths (540 nm). To examine the large blueshift of the emission band for **2**, preliminary molecular orbital calculations were performed by using density functional theory (DFT).[16] The DFT calculations revealed that the HOMO of **1** is mainly composed of dπ(Ir) mixed with p(S) and its HOMO-1 and HOMO-2 are dπ(Ir) mixed with π(ppy).[12] Since the LUMO of **1** is π*(ppy), the lowest transition is considered to be dominated by a dπ(Ir)/p(*S*)-to-π*(ppy) charge transfer. For **2**, the HOMO and HOMO-1 are both composed of dπ(Ir) mixed with π(ppy), and the HOMO-2 is dπ(Ir) mixed with p(S), whereas its LUMO is π*(ppy) as in the case of **1**. This is indicative of the stabilization of p(S) orbitals on binding to Ag^+. Thus, the lowest excited state for **2** is assigned as an

MLCT transition bearing a π(ppy)-π*(ppy) character with a larger HOMO–LUMO gap, which is responsible for the blueshift of the emission band for **1** compared to that for **2**.

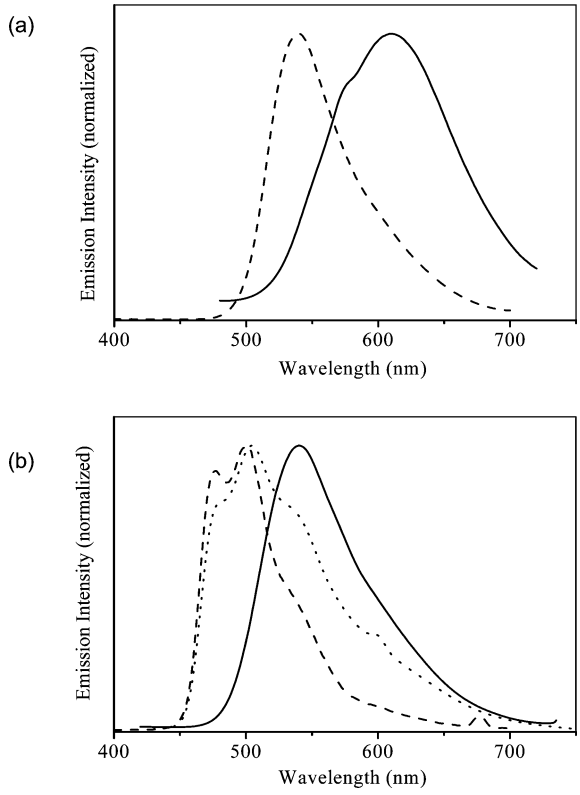

Figure 3. Emission spectra of **1**–**4** in the solid state at room temperature excited at 337 nm. (a): complexes with ppy (**1**: solid line, **2**: broken line). (b): complexes with ppy-CF_3 (**3**: solid line, **4a**: broken line, **4b**: dotted line).

Similar treatment of $[\{Ir(ppy\text{-}CF_3)_2\}_2(\mu\text{-}Cl)_2]$ with D-H_2pen afforded a yellow orange powder (**3**),[12] which is soluble in common organic solvents. This complex is confidently assigned as a neutral mononuclear complex, [Ir(ppy-$CF_3)_2$(D-Hpen)], analogous to **1**, based on the elemental analysis and the molar conductivity in methanol (18.8 $S\,cm^2\,mol^{-1}$), together with the IR spectrum that shows a $\nu_{C=O}$ band at 1720 cm^{-1}. The ^1H NMR and CD spectral measurements indicated that **3** is also a 1:1 mixture of the Δ_D/Λ_D isomers.[12] Complex **3** readily reacted with 0.5 mol-equiv. of $AgNO_3$ in acetonitrile to give a yellow solution, as in the case of **1**. However, two kinds of species (**4a** and **4b**) were separately isolated from the reaction solution; yellow needle-like crystals of **4a** appeared at first, and then a yellow powder of **4b** was precipitated after the removal of **4a**.[12] Whereas the absorption spectra of **4a** and **4b** are very similar to each other, their CD spectra that show large Δε values are nearly enantiomeric to each other (Figure 4). In addition, **4a** and **4b** exhibit a single set of signals at magnetic fields different from each other in the ^1H NMR spectra.[12] From these spectral features, together with the X-ray fluorescence and elemental analyses, it is concluded that **4a** and **4b** are the homochiral isomers ($\Delta_D\Delta_D$ or $\Lambda_D\Lambda_D$) of an $Ir^{III}Ag^{I}Ir^{III}$ trinuclear complex, $[Ag\{Ir(D\text{-}pen)(ppy\text{-}CF_3)_2\}\{Ir(D\text{-}Hpen)(ppy\text{-}CF_3)_2\}]$, the structure of which is analogous to that of **2**.

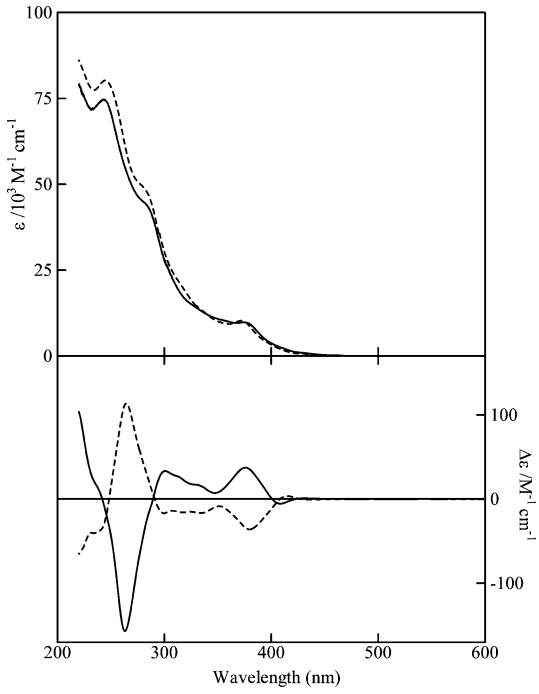

Figure 4. Absorption and CD spectra of **4a** (solid line) and **4b** (broken line) in methanol.

The direct structural information of **4a** was gained by single-crystal X-ray analysis.[15] As shown in Figure 2b, **4a** has an *S*-bridged $Ir^{III}Ag^{I}Ir^{III}$ structure, in which two octahedral Ir^{III} units are linearly linked by an Ag^{I} atom through S atoms [Ag–S 2.390(3) Å, Ir–S 2.432(3) Å, S–Ag–S = 171.82(18)°]. This *S*-bridged trinuclear structure in **4a** corresponds well with that in **2**, but both the two Ir^{III} units adopt the Δ configuration. Thus, **4a** is the $\Delta_D\Delta_D$ isomer, whereas **4b**, which shows a CD spectrum enantiomeric to that of **4a**, is the $\Lambda_D\Lambda_D$ isomer. A remarkable structural feature in **4a** is the presence of interunit C–H···F contacts [H···F 2.843(14) Å, 3.044(19) Å] between CF_3 groups and aromatic rings. Molecular model examinations revealed an interunit steric repulsion in the $\Delta_D\Delta_D$ or $\Lambda_D\Lambda_D$ isomer, which explains the selective formation of the $\Delta_D\Lambda_D$ isomer for the ppy $Ir^{III}Ag^{I}Ir^{III}$ complex (**2**). Thus, it is assumed that the stabilization due to the interunit C–H···F interaction overcomes the interunit steric repulsion, resulting in the formation of the homochiral $\Delta_D\Delta_D$ and $\Lambda_D\Lambda_D$ isomers when ppy is replaced by ppy-CF_3. In **4a**, two carboxy groups are in equatorial position with an *ob* (*δ*) conformational N,S-chelate ring. Like in **2**, COOH···OOC hydrogen bonds [O···O 2.54(2) Å] that connect the trinuclear molecules are also found in **4a**. However, this connection does not construct a 1D chain structure but a unique 1D double helix structure.[12]

Complexes **3** and **4** (**4a** and **4b**) are also emissive in the solid state and in solution. As shown in Figure 3b, **3** gives an emission band at about 540 nm, which is blueshifted by

ca. 70 nm relative to the band for **1**. A similar blueshift of emission bands by replacing ppy by ppy-CF_3 has been observed for other emissive iridium(III) systems.[14d,17] Each of **4a** and **4b** gives a 0–0 emission band at about 480 nm, which is blueshifted by 60 nm relative to the band for **2**. Comparison of the emission spectra of **4a** and **4b** with that of **3** reveals that the emission bands for **4a** and **4b** are considerably blueshifted. This is in parallel with the emission spectral correlation between **1** and **2** (Figure 3a). It should be noted that the quantum efficiency of the emission band for **4a** (Φ_{em} = 0.034) in solution (methanol, room temperature) is much lower than that for **4b** (Φ_{em} = 0.12), although their emission spectral features are quite similar to each other.[12] Such a drastic change in quantum efficiencies for emission bands due to diastereoisomerism has not been reported to date. The difference in the conformational flexibility of D-pen between **4a** and **4b**, which arises from the relative stability of the conformations (*lel* vs. *ob*) of an N,S-chelate ring and that of the orientations (equatorial vs. axial) of a pendent carboxy group, is most likely responsible for this result.[18]

Conclusions

We prepared new (ppy)- and (ppy-CF_3)Ir^{III} mononuclear complexes containing an N,S-chelating D-penicillaminate (**1** and **3**), which were converted into *S*-bridged $Ir^{III}Ag^{I}Ir^{III}$ trinuclear complexes (**2** and **4**) by linking with Ag^{I}. These mononuclear and trinuclear complexes are all emissive, and it was found that the mononuclear/trinuclear conversion leads to the drastic blueshift of emission bands despite the quite similarity of their absorption spectra. Remarkably, the linkage of **1** with Ag^{I} afforded only the heterochiral $\Delta_D\Lambda_D$ isomer (**2**), whereas the linkage of **3** produced the homochiral $\Delta_D\Delta_D$ and $\Lambda_D\Lambda_D$ isomers (**4a** and **4b**) that were easily, completely separated by fractional crystallization. Thus, a rare example of optically pure compounds with highly emissive properties was successfully obtained by the introduction of achiral Ag^{I}, in combination with a modification of ppy. Finally, the emission quantum efficiencies for **4a** and **4b** were found to be markedly different from each other, which indicates for the first time that the chirality at a metal center plays an important role in the control of emission properties of metal complexes.

Experimental Section

Experimental details, together with spectroscopic data, are given in the Supporting Information.

Supporting Information (see footnote on the first page of this article): Experimental details, NMR spectra, packing diagrams, and contour plots of MOs.

[1] a) E. Baranoff, J.-P. Collin, L. Flamigni, J.-P. Sauvage, *Chem. Soc. Rev.* **2004**, *33*, 147–155; b) A. J. Esswein, D. G. Nocera, *Chem. Rev.* **2007**, *107*, 4022–4047; c) P. Renaud, P. Leong, *Science* **2008**, *322*, 55–56; d) S. Fukuzumi, *Eur. J. Inorg. Chem.* **2008**, 1351–1362; e) J. J. Concepcion, J. W. Jurss, M. K. Brennaman, P. G. Hoertz, A. O. T. Patrocinio, N. Y. Murakami Iha, J. L. Templeton, T. J. Meyer, *Acc. Chem. Res.* **2009**, *42*, 1954–1965.

[2] a) P.-T. Chou, Y. Chi, *Chem. Eur. J.* **2007**, *13*, 380–395; b) V. Marin, E. Holder, R. Hoogenboom, U. S. Schubert, *Chem. Soc. Rev.* **2007**, *36*, 618–35; c) J. A. G. Williams, *Chem. Soc. Rev.* **2009**, *38*, 1783–1801.

[3] a) M. H. Keefe, K. D. Benkstein, J. T. Hupp, *Coord. Chem. Rev.* **2000**, *205*, 201–228; b) J. N. Demas, B. A. DeGraff, *Coord. Chem. Rev.* **2001**, *211*, 317–351; c) K. K.-W. Lo, W.-K. Huia, C.-K. Chunga, K. H.-K. Tsanga, D. C.-M. Nga, N. Zhub, K.-K. Cheungb, *Coord. Chem. Rev.* **2005**, *249*, 1434–1450; d) M. Kato, *Bull. Chem. Soc. Jpn.* **2007**, *80*, 287–294; e) J.-C. G. Bunzli, *Chem. Lett.* **2009**, *38*, 104–109; f) V. Fernandez-Moreira, F. L. Thorp-Greenwood, M. P. Coogan, *Chem. Commun.* **2010**, *46*, 186–202.

[4] H. Amouri, M. Gruselle, *Chirality in Transtion Metal Chemistry*, John Wiley & Sons, Chichester, UK, **2008**.

[5] a) S. H. Chen, D. Katsis, A. W. Schmid, J. C. Mastrangelo, T. Tsutsui, T. N. Blanton, *Nature* **1999**, *397*, 506–508; b) M. Grell, D. D. C. Bradley, *Adv. Mater.* **1999**, *11*, 895–905; c) J. E. Field, G. Muller, J. P. Riehl, D. Venkataraman, *J. Am. Chem. Soc.* **2003**, *125*, 11808–11809.

[6] C. M. Dupureur, J. K. Barton, *J. Am. Chem. Soc.* **1994**, *116*, 10286–10287.

[7] A. von Zelewsky, *Stereochemistry of Coordination Compounds*, John Wiley & Sons, New York, **1996**.

[8] a) T. J. Rutherford, M. G. Quagliotto, F. R. Keene, *Inorg. Chem.* **1995**, *34*, 3857–3858; b) X. Hua, A. von Zelewsky, *Inorg. Chem.* **1995**, *34*, 5791–5797; c) R. T. Watson, J. L. Jackson Jr., J. D. Harper, K. A. Kane-Maguire, L. A. P. Kane-Maguire, N. A. P. Kane-Maguire, *Inorg. Chim. Acta* **1996**, *249*, 5–7; d) J. Lacour, S. Torche-Haldimann, J. J. Jodry, C. Ginglinger, F. Favarger, *Chem. Commun.* **1998**, 1733–1734; e) B. T. Patterson, F. R. Keene, *Inorg. Chem.* **1998**, *37*, 645–650; f) F. R. Keene, *Chem. Soc. Rev.* **1998**, *27*, 185–194; g) D. Hesek, Y. Inoue, S. R. L. Everitt, H. Ishida, M. Kunieda, M. G. B. Drew, *Chem. Commun.* **1999**, 403–404; h) M. Chavarot, S. Ménage, O. Hamelin, F. Charnay, J. Pécaut, M. Fontecave, *Inorg. Chem.* **2003**, *42*, 4810–4816; i) P. Sun, A. Krishnan, A. Yadav, S. Singh, F. M. MacDonnell, D. W. Armstrong, *Inorg. Chem.* **2007**, *46*, 10312–10320.

[9] a) I. M. Dixon, J.-P. Collin, J.-P. Sauvage, L. Flamigni, S. Encinas, F. Barigelletti, *Chem. Soc. Rev.* **2000**, *29*, 385–391; b) M. S. Lowry, S. Bernhard, *Chem. Eur. J.* **2006**, *12*, 7970–7977; c) J. A. G. Williams, A. J. Wilkinson, V. L. Whittle, *Dalton Trans.* **2008**, 2081–2099.

[10] a) C. Schaffner-Hamann, A. von Zelewsky, A. Barbieri, F. Barigelletti, G. Muller, J. P. Riehl, A. Neels, *J. Am. Chem. Soc.* **2004**, *126*, 9339–9348; b) A. Auffrant, A. Barbieri, F. Barigelletti, J. Lacour, P. Mobian, J.-P. Collin, J.-P. Sauvage, B. Ventura, *Inorg. Chem.* **2007**, *46*, 6911–6919; c) R. S. Walters, C. M. Kraml, N. Byrne, D. M. Ho, Q. Qin, F. J. Coughlin, S. Bernhard, R. A. Pascal Jr., *J. Am. Chem. Soc.* **2008**, *130*, 16435–16441; d) F. J. Coughlin, M. S. Westrol, K. D. Oyler, N. Byrne, C. Kraml, E. Zysman-Colman, M. S. Lowry, S. Bernhard, *Inorg. Chem.* **2008**, *47*, 2039–2048.

[11] a) M. Taguchi, A. Igashira-Kamiyama, T. Kajiwara, T. Konno, *Angew. Chem. Int. Ed.* **2007**, *46*, 2422–2425; b) T. Aridomi, K. Takamura, A. Igashira-Kamiyama, T. Kawamoto, T. Konno, *Chem. Eur. J.* **2008**, *14*, 7752–7755; c) A. Igashira-Kamiyama, J. Fujioka, S. Mitsunaga, M. Nakano, T. Kawamoto, T. Konno, *Chem. Eur. J.* **2008**, *14*, 9512–9515; d) T. Aridomi, A. Igashira-Kamiyama, T. Konno, *Inorg. Chem.* **2008**, *47*, 10202–10204; e) M. Tamura, M. Yamagishi, T. Kawamoto, A. Igashira-Kamiyama, K. Tsuge, T. Konno, *Inorg. Chem.* **2009**, *48*, 8998–9004; f) Y. Sameshima, N. Yoshinari, K. Tsuge, A. Igashira-Kamiyama, T. Konno, *Angew. Chem. Int. Ed.* **2009**, *48*, 8469–8472.

[12] See the Supporting Information.

[13] K. Nakamoto, *Infrared and Raman Spectra of Inorganic and Coordination Compounds*, 5th ed., Wiley, Chichester, **1997**.

[14] a) S. Lamansky, P. Djurovich, D. Murphy, F. Abdel-Razzaq, H.-E. Lee, C. Adachi, P. E. Burrows, S. R. Forrest, M. E. Thompson, *J. Am. Chem. Soc.* **2001**, *123*, 4304–4312; b) A. B. Tamayo, B. D. Alleyne, P. I. Djurovich, S. Lamansky, I. Tsyba, N. N. Ho, R. Bau, M. E. Thompson, *J. Am. Chem. Soc.* **2003**, *125*, 7377–7387; c) J. Li, P. I. Djurovich, B. D. Alleyne, M. Yousufuddin, N. N. Ho, J. C. Thomas, J. C. Peters, R. Bau, M. E. Thompson, *Inorg. Chem.* **2005**, *44*, 1713–1727; d) I. Avilov, P. Minoofar, J. Cornil, L. De Cola, *J. Am. Chem. Soc.* **2007**, *129*, 8247–8258.

[15] Crystal data of **2**·CH_3CN·$2.5H_2O$ ($C_{56}H_{59}AgIr_2N_7O_{6.5}S_2$): M_r = 1490.6. crystal dimensions 0.45× 0.10× 0.10 mm, monoclinic, $P2_1$, a = 14.2408(6) Å, b = 9.7406(4) Å, c = 22.6729(10) Å, β = 94.8690(13)°, V = 3133.7(2) Å^3, Z = 2, $\rho_{calcd.}$ = 1.580 g cm^{-3}, μ = 4.6734 mm^{-1}, Mo-K_α radiation (λ = 0.71075 Å), T = 200(2) K, $2\theta_{max}$ = 55°, 31096 reflections measured of which 14278 unique (R_{int} = 0.084). 651 parameters, R_1 = 0.0574 [$I > 2\sigma(I)$], wR_2 = 0.1489 (all data), flack parameter –0.011(10), residual electron density 1.97/–2.44 e Å^{-3}. Crystal data of **4a**·$2H_2O$ ($C_{62}H_{47}AgF_{24}Ir_2N_6O_6S_2$): M_r = 1984.48. crystal dimensions 0.30× 0.10× 0.05 mm, orthorhombic, $I222$, a = 10.4391(14) Å, b = 28.204(4) Å, c = 32.179(6) Å, V = 9474(2) Å^3, Z = 4, $\rho_{calcd.}$ = 1.391 g cm^{-3}, μ = 3.1447 mm^{-1}, Mo-K_α radiation (λ = 0.71075 Å), T = 200(2) K, $2\theta_{max}$ = 55°, 45465 reflections measured of which 10881 unique (R_{int} = 0.218). 475 parameters, $R1$ = 0.0864 [$I > 2\sigma(I)$], $wR2$ = 0.2150 (all data), flack parameter 0.025(12), residual electron density 2.42/–0.89 e Å^{-3}. CCDC-770673 and -770674 contain the supplementary crystallographic data for this paper. These data can be obtained free of charge from The Cambridge Crystallographic Data Centre via www.ccdc.cam.ac.uk/data_request/cif.

[16] M. J. Frisch, G. W. Trucks, H. B. Schlegel, G. E. Scuseria, M. A. Robb, J. R. Cheeseman, J. A. Montgomery Jr., T. Vreven, K. N. Kudin, J. C. Burant, J. M. Millam, S. S. Iyengar, J. Tomasi, V. Barone, B. Mennucci, M. Cossi, G. Scalmani, N. Rega, G. A. Petersson, H. Nakatsuji, M. Hada, M. Ehara, K. Toyota, R. Fukuda, J. Hasegawa, M. Ishida, T. Nakajima, Y. Honda, O. Kitao, H. Nakai, M. Klene, X. Li, J. E. Knox, H. P. Hratchian, J. B. Cross, V. Bakken, C. Adamo, J. Jaramillo, R. Gomperts, R. E. Stratmann, O. Yazyev, A. J. Austin, R. Cammi, C. Pomelli, J. W. Ochterski, P. Y. Ayala, K. Morokuma, G. A. Voth, P. Salvador, J. J. Dannenberg, V. G. Zakrzewski, S. Dapprich, A. D. Daniels, M. C. Strain, O. Farkas, D. K. Malick, A. D. Rabuck, K. Raghavachari, J. B. Foresman, J. V. Ortiz, Q. Cui, A. G. Baboul, S. Clifford, J. Cioslowski, B. B. Stefanov, G. Liu, A. Liashenko, P. Piskorz, I. Komaromi, R. L. Martin, D. J. Fox, T. Keith, M. A. Al-Laham, C. Y. Peng, A. Nanayakkara, M. Challacombe, P. M. W. Gill, B. Johnson, W. Chen, M. W. Wong, C. Gonzalez, J. A. Pople, *Gaussian 03*, revision C.02, Gaussian, Inc., Wallingford, CT, **2004**.

[17] P. Coppo, E. A. Plummer, L. De Cola, *Chem. Commun.* **2004**, 1774–1775.

[18] When each carboxy group is oriented in a favorable equatorial position, the N,S-chelate ring adopts a thermodynamically more stable *lel* (δ for Λ) conformation in the $\Lambda_D\Lambda_D$ isomer (**4b**) and a less stable *ob* (δ for Δ) conformation in the $\Delta_D\Delta_D$ isomer (**4a**). Thus, the D-pen in **4a** is considered to be more flexible than that in **4b**, which is compatible with the lower emission quantum efficiency for **4a** compared with that for **4b**. A similar tendency of emission quantum efficiencies between the $\Delta_D\Delta_D$ isomer (Φ_{em} = 0.12) and the $\Lambda_D\Lambda_D$ isomer (Φ_{em} = 0.22) was recognized for the corresponding $Ir^{III}Au^{I}Ir^{III}$ complex, [Au{Ir(D-pen)(ppy-CF_3)$_2$}{Ir(D-Hpen)(ppy-CF_3)$_2$}], which were derived from **4a** and **4b**, respectively, by metal replacement reactions with Au^{I}.

Received: June 24, 2010
Published Online: July 16, 2010

DOI: 10.1002/ejic.201000468

Fluorine Tagging of Polyoxometalates: The Cyclic $[\{Mo^{V}_2O_4(H_2O)\}_4\{O_3PC(CF_3)(O)PO_3\}_4]^{12-}$

Abhishek Banerjee,[a] Bassem S. Bassil,[a] Gerd-Volker Röschenthaler,*[a] and Ulrich Kortz*[a]

Keywords: Fluorine / Diphosphonates / Polyoxometalates / NMR spectroscopy

We have discovered a simple and efficient strategy to incorporate fluorine into polyoxometalates by reaction of the fluorinated diphosphonate $H_2O_3PC(CF_3)(OH)PO_3H_2$ with $[Mo^{V}_2O_4(H_2O)_6]^{2+}$ in aqueous medium (pH = 6.4) resulting in $[\{Mo^{V}_2O_4(H_2O)\}_4\{O_3PC(CF_3)(O)PO_3\}_4]^{12-}$ (**1**), which was structurally characterized in solution by multinuclear NMR spectroscopy and in the solid state by single-crystal X-ray diffraction, infrared, thermogravimetric and elemental analyses. Polyanion **1** crystallizes as the mixed sodium/guanidinium salt $Na_{6.5}[(H_2N)_3C]_{5.5}[\{Mo^{V}_2O_4(H_2O)\}_4\{O_3PC(CF_3)(O)PO_3\}_4]\cdot 8H_2O$ (**1a**) in the monoclinic system, space group $C2/c$ with the unit-cell parameters a = 34.0685(95) Å, b = 8.0874(19) Å, c = 34.4101(10) Å, β = 100.20(2)°, V = 9331.02(4) Å^3 and Z = 2. The novel polyanion **1** has a cyclic, saddle-like structure with four $\{Mo_2O_4(H_2O)\}$ units linked by four fully deprotonated diphosphonate moieties. In addition, the $(CF_3)C$–OH moiety is deprotonated, due to the electronic effects of the neighboring CF_3 group, leading to the formation of an Mo–O(C) bond. Solution ^{31}P and ^{19}F NMR studies of **1** indicate magnetic inequivalence of the two phosphorus atoms in each diphosphonate moiety. The solid-state packing of the title polyanions in **1a** by loosely bound Na^+ counterions leads to an AAA-type arrangement.

Introduction

The class of polyoxometalates (POMs) is a well-established and expanding area of inorganic chemistry, mostly due to the tremendous compositional and structural variety combined with a multitude of interesting properties covering essentially all areas of physical and chemical sciences.[1] Diphosphonate-based polyanions have been structurally investigated only in the 1990s, and hence they represent a rather new area of study in the very wide arena of POM chemistry.[2] These compounds usually exhibit an open-structure type with the ditetrahedral hetero group(s) situated on the outside of the polyanion structure, in sharp contrast to POM structures based on Keggin or Wells–Dawson ions.[3] Such structural flexibility allows tuning of the polyanion properties such as stability, solubility and polarity by modifying the nature of the hetero groups. Recently, a new class of polyoxopalladates(II) and -aurates(III) has been discovered with hetero groups also situated in external positions.[4] It is also worth mentioning that diphosphonates as such have found extensive use as therapeutic drugs for the treatment of several bone-loss diseases.[5]

In 1994 Pope's group reported the folded dodecameric heteropolytungstate $[(O_3PXPO_3)_4W_{12}O_{36}]^{16-}$ (X = CH_2, O) containing four diphosph(on)ate hetero groups.[2a] Both compounds also showed high inhibitory activity towards HIV-1 reverse transcriptase.[6] This class of compounds was further explored, in particular to develop novel and more potent derivatives by modifying the diphosphonate functionality and as a result the POM structure. Pope's group prepared the methylenediphosphonate-based hexamolybdate $[(O_3PCH_2PO_3)Mo_6O_{18}(H_2O)_4]^{4-}$, the functionalised diphosphonate-based, polymeric polytungstate $[\{(O_3PCHN(CH_3)_2PO_3)W_2O_6\}^{4-}]_\infty$ and the diphosphate-containing 18-molybdate $[(P_2O_7)Mo_{18}O_{54}]^{4-}$.[2b–2d] Kortz reported the diphosphate-containing hexamolybdate $[(O_3POPO_3)Mo_6O_{18}(H_2O)_4]^{4-}$ and the 30-molybdate $[\{(P_2O_7)Mo_{15}O_{45}\}_2]^{8-}$.[2e,2f]

Mialane, Dolbecq and co-workers elaborated upon the work of Pope and Kortz by synthesizing a new family of methylenediphosphonate-based polyoxomolybdates(V) based on the $\{Mo^{V}_2O_4\}^{2+}$ moiety, formed with or without capping or templating agents such as formate, acetate, carbonate and sulfite.[7] Sevov and co-workers have also reported a methylenediphosphonate-containing mixed-valent Mo^{VI}/Mo^{V} species synthesized hydrothermally and with two different protonated amines as stabilizing.[8]

Fluorinated compounds have found applications in medicine, materials science and catalysis largely due to some special properties of the fluorine atom such as small size and high electronegativity.[9] There are previous reports on fluorine incorporation into "classical" POM frameworks, but these structures are difficult to prepare and in addition

[a] School of Engineering and Science, Jacobs University, P. O. Box 750561, 28725 Bremen, Germany
E-mail: u.kortz@jacobs-university.de
g.roeschenthaler@jacobs-university.de

Supporting information for this article is available on the WWW under http://dx.doi.org/10.1002/ejic.201000468.

only a few, internal sites could be fluorinated.[10] Now we have discovered a simple and elegant strategy to prepare fluorinated POMs by incorporation of fluorinated diphosphonate hetero groups. Here we report on the reactivity of 2,2,2-trifluoro-1-hydroxyethylidenediphosphonic acid (F3-Etidronic acid), $H_2O_3PC(CF_3)(OH)PO_3H_2$, towards the dinuclear, cationic Mo^V moiety $\{Mo^V_2O_4(H_2O)_6\}^{2+}$.

Results and Discussion

Synthesis and Structure

Polyanion **1** was prepared by reaction of the fluorinated diphosphonate $H_2O_3PC(CF_3)(OH)PO_3H_2$ with the dinuclear cationic Mo^V unit $[Mo^V_2O_4(H_2O)_6]^{2+}$ in aqueous medium (pH = 6.4) and isolated as the mixed sodium/guanidinium salt $Na_{6.5}[(H_2N)_3C]_{5.5}[\{Mo^V_2O_4(H_2O)\}_4\{O_3PC(CF_3)(O)PO_3\}_4]\cdot 8H_2O$ (**1a**). Single-crystal X-ray diffraction revealed that polyanion **1** is composed of four $\{Mo^V_2O_4(H_2O)\}$ units, which are linked by four fully deprotonated F3-Etidronate moieties leading to a cyclic, saddle-like assembly (see Figure 1). The P–C–P bond angle in **1** is 110°, which is in agreement with previously reported methylenediphosphonate-containing POMs.[2a,2c,2d] The electronic effect of the CF_3 group becomes apparent by the deprotonation of the adjacent C–OH group and bonding to the metal center, resulting in the $\{Mo_2O_4(H_2O)\}$ unit (unlike the more common $\{Mo_2O_4\}$ unit). The different electronic effects of the CH_3 vs. CF_3 groups of Etidronate and F3-Etidronate, respectively, towards the formation of cyclic heteropolymolybdates(V) can be demonstrated by comparing **1** with the recently reported cyclic compounds of Compain et al.[11] Thus, in the latter cyclic polyanions, the C–OH group of the diphosphonate moiety is left dangling outside, non-bonded to the metal center. However, in **1** the strong electron-withdrawing CF_3 group enforces deprotonation of the hydroxy group of the diphosphonate unit followed by bonding to the Mo center. Such a bonding mode of the diphosphonate unit has a marked effect on the nature of the polyanion structure and solution stability. As discussed earlier, it leads to the formation of the $\{Mo_2O_4(H_2O)\}$ units, and the C–O–Mo bonds actually prevent the polyanion to adopt an even more bent ring structure. Also, not unexpectedly the additional C–O–Mo bond imparts polyanion **1** with extra solution stability. The known cyclic Etidronate/Mo^V compounds were shown to be unstable in solution and to disintegrate into unknown fragments, in sharp contrast to **1**, which shows a markedly improved solution stability as observed by multinuclear NMR spectroscopy. An exception is the non-cyclic, Etidronate-containing $\{Mo^V_4O_{16}\}$ cluster of Compain et al., which also exhibits a deprotonated and bound C–OH group and solution stability.[11]

An analysis of the solid-state structure of **1a** reveals that the guanidinium and sodium countercations are located all around **1**, being coordinated to peripheral polyanion oxygen and fluorine atoms and crystal water molecules. The cavity of **1** is not stabilized by countercations in the solid state, which indicates that its cyclic structure is a result of covalent bonding within the polyanion (rather than a template effect involving the countercations). The solid-state packing mode of **1a** reveals an AAA-type stacking of individual polyanions connected to each other by weak Na···O interactions (see Figure 2). An extended packing profile of

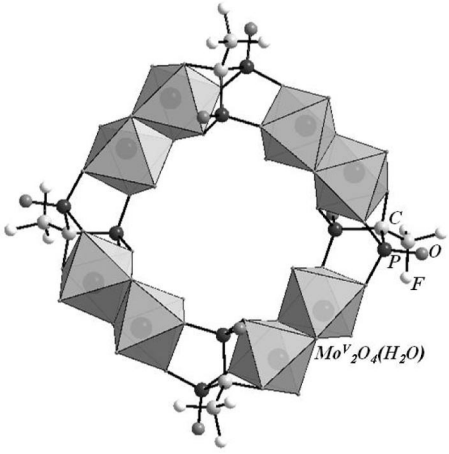

Figure 1. Combined ball-and-stick/polyhedral representation of **1**.

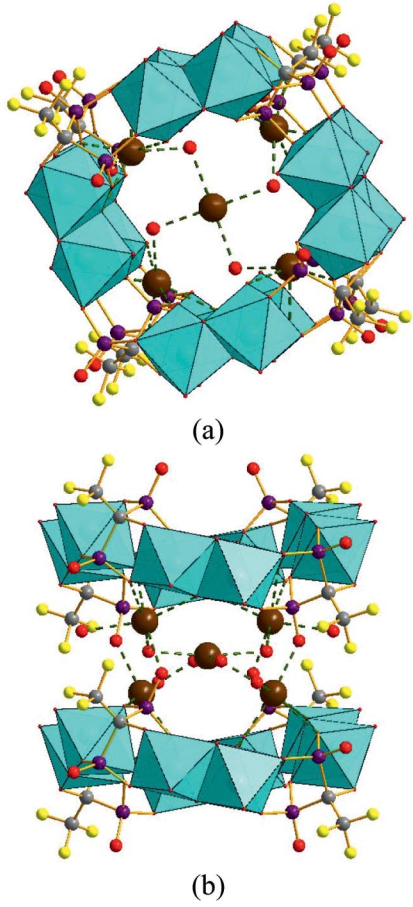

Figure 2. Packing diagrams of **1a** in the solid state viewed along the *b*-axis (a) and *a*-axis (b), respectively. Color code: MoO_6 octahedra turquoise, P purple, F yellow, O red, C grey, Na brown.

1a with both Na^+ and $[C(NH_2)_3]^+$ counterions reveals that the latter occupy spaces between two adjacent polyanions participating in extensive N–H···O(P) hydrogen-bonding interactions (Figure S1), unlike the Na^+ ions, which occupy positions between two stacked polyanions. Interestingly, the F atoms do not participate in any hydrogen bonding. The precise number of crystal water molecules in **1a** was determined by thermogravimetric analysis (see Figure S2).

NMR Spectroscopy

We have also studied the solution properties of redissolved **1a** by multinuclear NMR spectroscopy. The $^{31}P\{^{19}F\}$ NMR spectrum of **1** (see Figure 3, top) shows a pair of doublets at δ = 18.88 and 23.15 ppm ($^2J_{PP}$ = 12.4 Hz), respectively, indicating magnetic inequivalence of the two P atoms within each diphosphonate moiety, in complete agreement with the solid-state structure (Figure 1). Such magnetic inequivalence can be explained by taking into account the different bonding modes of the two P atoms in each of the four diphosphonate units. For one of the P atoms both P–O(Mo) bonds are in equatorial positions with respect to the two edge-shared MoO_6 octahedra, whereas the other P atom has an equatorial and an axial P–O(Mo) bond (see Figure 4). The non-decoupled ^{31}P NMR spectrum of **1** (see Figure 3a inset) shows the expected splitting of each of the phosphorus signals due to ^{19}F coupling ($^3J_{PF}$ = 6.3 Hz). The ^{19}F NMR spectrum of **1** (see Figure 3b) shows a triplet at δ = –67.34 ppm ($^3J_{FP}$ = 6.3 Hz), indicating very similar coupling constants for the interaction with the two inequivalent P atoms. The NMR signals

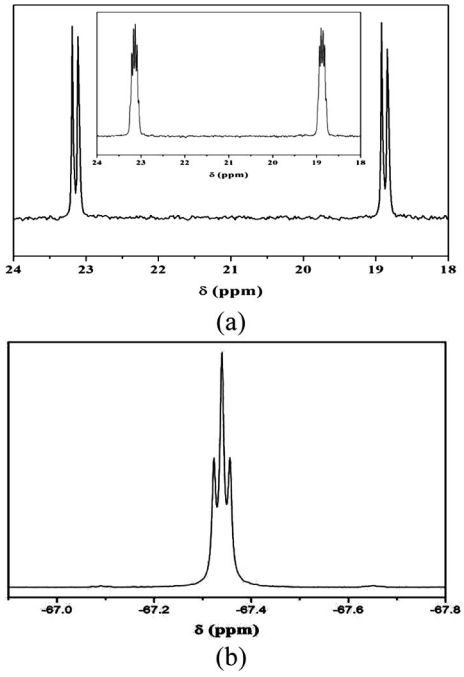

Figure 3. (a) $^{31}P\{^{19}F\}$ NMR spectrum of **1a** redissolved in D_2O (inset shows the non-decoupled spectrum), (b) ^{19}F NMR spectrum of **1a** redissolved in D_2O. Both spectra were measured at room temperature.

are all narrow as expected for a diamagnetic Mo^V is observed, due to antiferromagnetic coupling in the dimolybdenum(V) pairs.[7]

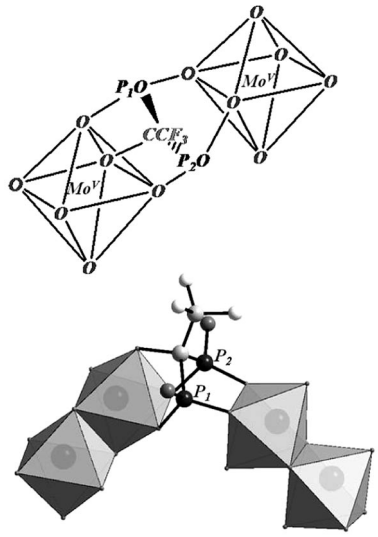

Figure 4. Structural fragment of polyanion **1** indicating the different bonding modes of the two P atoms within each diphosphonate unit, resulting in structural and hence magnetic inequivalence as shown by ^{31}P NMR spectroscopy. The atomic shading code is the same as in Figure 1.

FT-IR

In the IR spectrum of **1a**, the characteristic peaks at 918, 747 and 715 cm^{-1} are attributed to ν(Mo–O) of the polyanion and the characteristic bands at 1669, 1168, 1057, 1006 and 955 cm^{-1} can be assigned to the diphosphonate moieties in **1** (see Figure S3).

Conclusions

We have developed a simple strategy for the covalent F-tagging of polyanions. One-pot self-assembly of preformed F3-Etidronic acid, $H_2O_3PC(CF_3)(OH)PO_3H_2$, with the cationic $\{Mo_2O_4(H_2O)_6\}^{2+}$ resulted in the title polyanion **1**, which was structurally characterized in the solid state and in solution. The presence of the highly electron-withdrawing CF_3 group imparts unique structural features as well as solution stability to the molecule. Our work opens the door for the facile preparation of a multitude of fluorine-tagged POMs, especially cyclic polymolybdates, which are expected to be stable in solution. Currently, we explore the reactivity of F3-Etidronic acid with polyoxomolybdates, -tungstates and -vanadates. In addition, we are in the process of synthesizing other fluorinated diphosphonates, which are expected to give rise to novel and unexpected POM structures. We also plan to test the medicinal properties of our compounds.

Experimental Section

General: All reagents were purchased from commercial suppliers and used without further purification. All solvents were freshly distilled before use from appropriate drying agents. Reactions for the synthesis of the diphosphonate were performed under dry N_2 by using Schlenk techniques. The elemental analysis for **1a** was performed by Kanti Labs, Tirupathi (India). Infrared spectra were recorded on KBr pellets with a Nicolet Avatar spectrophotometer. Thermogravimetric analyses were carried out by using a TA Instruments SDT Q600 thermobalance with a 100 mL/min flow of nitrogen, and the temperature was ramped from 20 to 700 °C at a rate of 10 °C/min. All NMR spectra were recorded at 298 K on 15 mM solutions of **1a** redissolved in H_2O/D_2O with a 400 MHz JEOL ECS instrument. The ^{19}F NMR measurements were recorded at a working frequency of 376.9 MHz, and the chemical shifts were referenced to $CFCl_3$ as external standard. The ^{31}P NMR measurements were recorded at a working frequency of 162.1 MHz by using 85% H_3PO_4 in H_2O as external reference.

F3-Etidronic Acid: F3-Etidronic acid was synthesized according to a published procedure.[12] Tris(trimethylsilyl) phosphite[13] (3.16 g, 10 mmol) in dry THF (10 mL) and trifluoroacetyl chloride (0.66 g, 5 mmol) were allowed to react at –70 °C for 1 h, and the reaction mixture was stirred at room temperature overnight. Removal of all volatile materials in vacuo yielded the tris(trimethylsilyl) ester of F3-Etidronic acid. Hydrolysis of the ester by H_2O/MeOH (1:1) and subsequent removal of all volatile materials in vacuo yielded 1.2 g (90%) of F3-Etidronic acid as a viscous liquid. A 2 M stock solution of F3-Etidronic acid in H_2O was prepared and used for subsequent reactions.

$[Mo^V_2O_4(H_2O)_6]^{2+}$: The $[Mo^V_2O_4(H_2O)_6]^{2+}$ cation was also prepared according to the literature by using MoO_3 as the Mo source.[7b] To a suspension of MoO_3 (2.30 g, 16.0 mmol) in 4 M HCl (80 mL), N_2H_5OH (210 μL, 4.29 mmol) was added. The mixture was then stirred at 80 °C for 3 h to result in a deep red solution. This solution was cooled to room temp. and then used for subsequent reactions.

$Na_{6.5}[C(NH_2)_3]_{5.5}[\{Mo^V_2O_4(H_2O)\}_4\{O_3PC(CF_3)(O)PO_3\}_4]\cdot 8H_2O$ (1a): To a solution of $[Mo_2O_4(H_2O)_6]^{2+}$ in 4 M HCl (6.25 mL, 0.63 mmol) was added a 2 M aqueous solution of F3-Etdronic acid (315 μL, 0.63 mmol). The pH of the resultant solution mixture was adjusted to 6.4 with 8 M NaOH. Subsequently, guanidinium chloride (1 g, 10.4 mmol) was added and the solution stirred for ca. 15 min to result in the formation of a precipitate, which was filtered off. The filtrate was left overnight resulting in a red amorphous solid of **1a**, which was filtered off, washed with a 4 M NaCl solution and then air-dried. Slow concentration of this filtrate at room temperature resulted in red, needle-like crystals of **1a** after 3 d. Yield: 0.26 g (61% based on Mo). IR: $\tilde{\nu}$ = 1669 (s), 1362 (w), 1279 (m), 1168 (s), 1085 (s), 1057 (w), 1006 (w), 955 (s), 942 (sh), 918 (sh), 747 (m), 715 (w) cm^{-1}. $C_{12}H_{46}F_{12}Mo_8N_{12}Na_8P_8O_{55}$ (2665.81): calcd. F 8.55, Mo 28.8, Na 6.90, P 9.30; found F 8.12, Mo 28.8, Na 7.13, P 9.35.

X-ray Crystallography: A single crystal of **1a** was mounted on a glass fiber for indexing and intensity-data collection at 296 K with a Bruker X8 SMART APEX II CCD single-crystal diffractometer by using Mo-K_α radiation (λ = 0.71073 Å). Direct methods were used to solve the structures and to locate the heavy atoms. The remaining atoms were found from successive Fourier syntheses. Mo, P and two sodium atoms (Na2, Na3) were refined anisotropically, whereas the other atoms (C, N, O, F) as well as Na1 and Na4 were refined isotropically. Hydrogen atoms were placed in calculated positions. Routine Lorentz and polarization corrections were applied, and an absorption correction was performed by using the SADABS program.[14] Crystallographic data are summarized in Table 1. Figures 1, 2 and 4 were generated by Diamond Version 3.2c (© Crystal Impact GbR). CCDC-775102 contains the supplementary crystallographic data for this paper. These data can be obtained free of charge from The Cambridge Crystallographic Data Centre via www.ccdc.cam.ac.uk/data_request/cif.

Table 1. Crystallographic data for compound **1a**.

Empirical formula	$C_{12}H_{46}F_{12}Mo_8N_{12}Na_8P_8O_{55}$
Formula mass	2665.81
Crystal system	monoclinic
Space group	*C*2/*c* (no. 15)
a [Å]	34.069(10)
b [Å]	8.0874(19)
c [Å]	34.410(10)
β [°]	100.20(2)
V [Å^3]	9331(4)
Z	4
$\rho_{calcd.}$ [g cm^{-3}]	1.898
μ [mm^{-1}]	1.330
Reflections:	
collected	29295
unique (R_{int})	4857 (0.1657)
observed [$I > 2\sigma(I)$]	3180
Parameters	329
GoF	1.021
R [$I > 2\sigma(I)$][a]	0.0689
R_w (all data)[b]	0.2102

[a] $R = \Sigma||F_o| - |F_c||/\Sigma|F_o|$. [b] $R_w = [\Sigma w(F_o^2 - F_c^2)^2/\Sigma w(F_o^2)^2]^{1/2}$.

Supporting Information (see footnote on the first page of this article): Packing diagram of **1a**, infrared spectra of amorphous and crystalline **1a**, thermogram for **1a**.

Acknowledgments

U. K. and G.-V. R. thank Jacobs University for research support. A. B. thanks Drs. Natalya Kalinovich, Olesya Kazakova, Dipl.-Chem. Katja Vlasov and Dr. Maxim Ponomarenko for assistance during the synthesis of fluorinated diphosphonates.

[1] a) M. T. Pope, *Heteropoly and Isopoly Oxometalates*, Springer-Verlag, Berlin, **1983**; b) C. L. Hill, C. M. Prosser-McCartha, *Coord. Chem. Rev.* **1995**, *143*, 407–455; c) M. T. Pope, A. Müller, *Angew. Chem. Int. Ed. Engl.* **1991**, *30*, 34–48; d) *Chem. Rev.* **1998**, *98* (Special Issue on Polyoxometalates; Ed.: C. L. Hill); e) A. Müller, S. Roy, *Coord. Chem. Rev.* **2003**, *245*, 153–166; f) E. Coronado, P. Day, *Chem. Rev.* **2004**, *104*, 5419–5448; g) L. Cronin, in *Compr. Coord. Chem. II*, vol. 7 (Eds.: J. A McCleverty, T. J. Meyer), Elsevier, Amsterdam, **2004**, pp. 1–57; h) C. L. Hill, *J. Mol. Catal. A* **2007**, *262*, 2–6; i) U. Kortz, A. Müller, J. van Slageren, J. Schnack, N. S. Dalal, M. Dressel, *Coord. Chem. Rev.* **2009**, *253*, 2315–2327; j) *Eur. J. Inorg. Chem.* **2009**, *34* (Issue dedicated to Polyoxometalates; Guest Ed.: U. Kortz).

[2] a) U. Kortz, G. B. Jameson, M. T. Pope, *J. Am. Chem. Soc.* **1994**, *116*, 2659–2660; b) U. Kortz, M. T. Pope, *Inorg. Chem.* **1994**, *33*, 5643–5646; c) U. Kortz, M. T. Pope, *Inorg. Chem.* **1995**, *34*, 2160–2163; d) U. Kortz, M. T. Pope, *Inorg. Chem.* **1995**, *34*, 3848–3850; e) U. Kortz, *Inorg. Chem.* **2000**, *39*, 623–624; f) U. Kortz, *Inorg. Chem.* **2000**, *39*, 625–626.

[3] a) U. Kortz, F. Hussain, M. Reicke, *Angew. Chem. Int. Ed.* **2005**, *44*, 3773–3777; b) S. S. Mal, U. Kortz, *Angew. Chem. Int. Ed.* **2005**, *44*, 3777–3780; c) L.-H. Bi, M. H. Dickman, U.

Kortz, I. Dix, *Chem. Commun.* **2005**, 3962–3964; d) B. S. Bassil, S. S. Mal, M. H. Dickman, U. Kortz, H. Oelrich, L. Walder, *J. Am. Chem. Soc.* **2008**, *130*, 6696–6697.

[4] a) E. V. Chubarova, M. H. Dickman, B. Keita, L. Nadjo, F. Miserque, M. Mifsud, I. W. C. E. Arends, U. Kortz, *Angew. Chem. Int. Ed.* **2008**, *47*, 9542–9546; b) N. V. Izarova, M. H. Dickman, R. Ngo Biboum, B. Keita, L. Nadjo, V. Ramachandran, N. S. Dalal, U. Kortz, *Inorg. Chem.* **2009**, *48*, 7504–7506; c) N. V. Izarova, R. Ngo Biboum, B. Keita, M. Mifsud, I. W. C. E. Arends, G. B. Jameson, U. Kortz, *Dalton Trans.* **2009**, 9385–9387; d) N. V. Izarova, N. Vankova, T. Heine, R. Ngo Biboum, B. Keita, L. Nadjo, U. Kortz, *Angew. Chem. Int. Ed.* **2010**, *49*, 1886–1889.

[5] a) R. Bartl, B. Frisch, E. Tresckow, C. Bartl, *Bisphosphonates in Medical Practice*, Springer-Verlag, Berlin, Heidelberg, **2007**; b) H. Fleisch, *Bisphosphonates in Bone Diseases: From the Laboratory to the Patient*, Academic Press, San Diego, California, USA, **2000**; c) H. Fleisch, *Breast Cancer Res.* **2002**, *4*, 30–34; d) D. Wysowski, J. Chang, *Arch. Intern. Med.* **2005**, *165*, 346–347; e) D. M. Black, P. D. Delmas, R. N. Eastell, *Engl. J. Med.* **2007**, *356*, 1809–1822; f) S. R. Heckbert, G. Li, S. R. Cummings, N. L. Smith, B. M. Psaty, *Arch. Intern. Med.* **2008**, *168*, 826–831.

[6] S. G. Sarafianos, U. Kortz, M. T. Pope, M. J. Modak, *Biochem. J.* **1996**, *319*, 619–626.

[7] a) P. Peloux, A. Dolbecq, P. Mialane, J. Marrot, F. Sécheresse, *Dalton Trans.* **2004**, 1259–1263; b) A. Dolbecq, L. Lisnard, P. Mialane, J. Marrot, M. Benard, M. M. Rohmer, F. Sécheresse, *Inorg. Chem.* **2006**, *45*, 5898–5910.

[8] E. Dumas, C. Sassoye, K. D. Smith, S. C. Sevov, *Inorg. Chem.* **2002**, *41*, 4029–4032.

[9] a) G.-V. Röschenthaler, *Nachr. Chem.* **2005**, *53*, 743–746; b) P. Kirsch, *Modern Fluoroorganic Chemistry*, Wiley-VCH Verlag, Weinheim, **2004**; c) K. Uneyama, *Organofluorine Chemistry*, Blackwell Publishing, UK, **2006**; d) I. Ojima, *Fluorine in Medicinal Chemistry and Chemical Biology*, Wiley-Blackwell, UK, **2009**; e) S. Poonam, W. D. Andrew, *J. Enzym. Inhib. Med. Chem.* **2007**, *22*, 527–540.

[10] a) S. H. Wasfi, W. L. Johnson, *Synth. React. Inorg. Met. Org. Chem.* **1999**, *29*, 697–724; b) S. H. Wasfi, W. L. Johnson, D. L. Martin, *Synth. React. Inorg. Met. Org. Chem.* **1998**, *28*, 223–244; c) S. H. Wasfi, W. L. Johnson, D. L. Martin, *Synth. React. Inorg. Met. Org. Chem.* **1997**, *27*, 535–549; d) S. H. Wasfi, C. E. Costello, A. L. Rheingold, B. S. Haggerty, *Inorg. Chem.* **1991**, *30*, 1788–1792; e) A. K. Stover, J. R. Gutnick, A. N. Sarjeant, A. J. Norquist, *Inorg. Chem.* **2007**, *46*, 4389–4391; f) A. Michailovski, F. Hussain, B. Spingler, J. Wagler, G. R. Patzke, *Cryst. Growth Des.* **2009**, *9*, 755–765.

[11] J. D. Compain, A. Dolbecq, J. Marrot, P. Mialane, F. Sécheresse, *Compt. Rend. Chim.* **2010**, *13*, 329–335.

[12] R. M. Schoth, E. Lork, F. U. Seifert, G.-V. Röschenthaler, *Naturwissenschaften* **1996**, *83*, 571–574.

[13] M. Sekine, K. Okimoto, K. Yamada, T. Hata, *J. Org. Chem.* **1981**, *46*, 2097–2107.

[14] G. M. Sheldrick, *SADABS*, University of Göttingen, Göttingen, Germany, **1996**.

Received: April 27, 2010
Published Online: July 21, 2010

DOI: 10.1002/ejic.201000265

The Vibrational Spectra of the Cyanide Ligand Revisited: Double Bridging Cyanides

Sidney F. A. Kettle,*[a] Eliano Diana,[b] Edoardo M. C. Marchese,[b] Enrico Boccaleri,[c] Gianluca Croce,[c] Tianlu Sheng,[d] and Pier Luigi Stanghellini*[c]

Keywords: Cyanides / Bridging ligands / Vibrational spectroscopy / Density functional calculations

The vibrational behaviour of complexes of general formula $[(ML_5CN)_2M'L'_4]$ with either a *cis* or *trans* geometry has been studied. The ν(CN) modes have been assigned on the basis of both infrared and Raman intensities. The CN vibrators are but weakly coupled, particularly so in the *cis* arrangement. The spectroscopic analysis offers insights into the interpretation of the spectra of Prussian Blue species as *cis* and *trans* M–CN–M′–NC–M complexes may be regarded as building blocks of Prussian Blue. The structure of the complex $[(CO)_5MoCNNi(Bipy)_2NCMo(CO)_5]$ confirms the expected *cis* geometry of the metal core. The complex $[Cp(dppe)FeNCRu(4EtPy)_4CNFeCp(dppe)]^{3+}[PF_6^-]_3$ was prepared by oxidising the reduced form (2+ cation) and its crystal structure was determined and compared with that of the starting complex. Analysis of the structural and spectroscopic data led to the conclusion that the two iron atoms in the oxidised form have different charges and that the vibrations of the two CN groups are essentially independent. DFT calculations indicate that although π-bonding and antibonding occur, electrostatic effects (as described by the IVSE model) are probably more important.

Introduction

Although there has been continuing interest in Prussian Blue (in its idealised formulations given as $KFe^{II}[Fe^{III}(CN)_6]$, $Fe^{II}_3[Fe^{III}(CN)_6]_2$ or $Fe^{III}_4[Fe^{II}(CN)_6]_3$, omitting water) and related species,[1] it cannot be said that they are always well understood. Of particular interest to us is a detailed interpretation of their vibrational spectra, particularly in the ν(CN) region. Given the report of single-crystal studies many years ago,[2] it may be surprising that aspects of the interpretation of the vibrational spectra of Prussian Blues (PBs) remain unclear. The reasons mainly lie in the uncertainty associated with the correct characterisation of a typical material. Ostensibly identical preparations giving products that are analytically different, changes in spectral properties with time, the variable effects of trapped species in lattice holes and variations in the combinations of II and III valent metal species (perhaps by the incorporation of I valent metal) are just some of the difficulties, with all leading to changes in the vibrational spectra.[3]

For a better understanding of the vibrational spectra of PB-type compounds, we have carried out vibrational studies on well-characterised species that may be regarded as PB building blocks. The schematic structures of these species are illustrated in Figure 1 and show the typical *cis* and *trans* geometry of the M–CN–M′–NC–M core. In Figure 2 is illustrated the idealised crystal frame of the PB-type compounds, that is, an infinite network of hexacoordinate metal

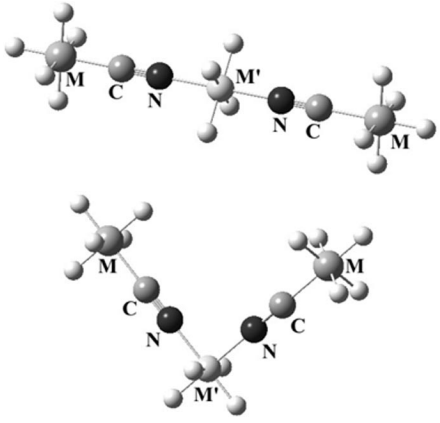

Figure 1. Schematic structures of the double bridging complexes: upper: *trans* or linear complexes; lower: *cis* or angular complexes. The ligand coordination around the M atoms is variable; the **E** and **F** series, *trans* complexes, show a reversed CN coordination.

[a] School of Chemical Sciences and Pharmacy, University of East Anglia,
Norwich NR4 7TJ, UK
[b] Dipartimento di Chimica IFM, Università di Torino,
Via P. Giuria 7, 10125 Torino, Italy
[c] Dipartimento di Scienze e Tecnologie Avanzate and Centro NanoSi.S.T.E.M.I., Università del Piemonte Orientale "A. Avogadro",
Viale Teresa Michel 17, 15121 Alessandria, Italy
Fax: +39-0131-360250
E-mail: pierluigi.stanghellini@mfn.unipmn.it
[d] Fujian Institut of Research on the Structure of Matter, Chinese Academy of Sciences,
Fujian 350002, China

Supporting information for this article is available on the WWW under http://dx.doi.org/10.1002/ejic.201000265.

atoms linked by bridging cyanides. It is evident that the present complexes can be regarded as ideal subunits of this crystalline network.

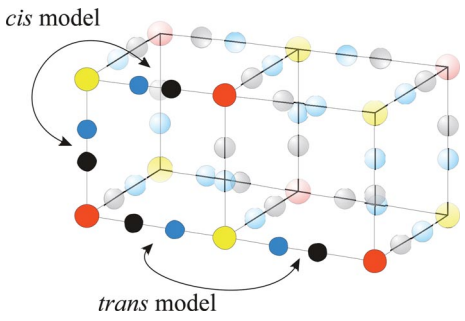

Figure 2. Idealised crystal frame of the PB-type compound showing the *cis* and *trans* M–CN–M′–NC–M cores as building blocks.

One of the less evident problems is that there may be a tendency to expect vibrational similarity between the isoelectronic CN^- and CO and to be guided by the interpretation of the latter. Unfortunately, this expectation is usually misplaced.[4] Although both are strong-field, π-bonding ligands that are present in complexes with superficial similarities, vibrationally the CO and CN^- ligands show significant differences. In $[M(CX)_6]$ species, whereas the values of f_{C-X} and f_{M-C} are almost the same, the most significant interaction constants involving C–X (the *cis* and *trans* C–X/C–X coupling constants) are smaller for X = N than for X = O. However, interaction constants involving M–C are either the same (*trans*) or larger (*cis*, but it is much smaller than the *trans*). Because there will be a large G matrix coupling between M–C and C–X of M–C–X, we expect that the M–C modes will exert a greater influence on the ν(CN) features than the ν(CO). Indeed, some authors have ignored the CN–CN coupling.[5] The ν(CN) infrared-Raman separations observed spectrally in $[M(CN)_6]$ anions in large measure arise indirectly from the coupling between M–C stretches. There is another difference. When CN^- is a terminal ligand in high-symmetry species, the totally symmetric vibration is not always at the highest frequency (the pattern invariably observed for CO).[6] It seems that a vibronic interaction, which influences only the totally symmetric vibration, is sometimes involved.

These differences as terminal ligands caution us not to expect too many similarities as bridging ligands either. Historically, the two ligands have been treated differently. For CN, so-called kinematic effects, the G matrix consequences of the constraints imposed by the bonding of a second metal atom, have been held to be important. For CO, they have never been mentioned, even for species geometrically similar to those found for CN.[7] However, this distinction has been made less evident by the recent finding that kinematic effects are much smaller for cyanides than previously believed.[8] Important has been the availability of high-quality DFT calculations that we believe to provide valuable insights. We have also made use of DFT calculations in this study.

Results and Discussion

The trimetallic (M–M′–M) compounds that are the subject of the present report are listed in Table 1 and their schematic structures are illustrated in Figure 1.

Table 1. List of the double-bridging CN complexes.

Identification number[a]	M fragment	M′ fragment	Charge	Anion
A1[b] *cis*	$[(CO)_5MoCN]$	$[Ni(bipy)_2]$	0	–
A2 *cis*	$[(CO)_5WCN]$	$[Ni(bipy)_2]$	0	–
A3 *cis*	$[(CO)_5CrCN]$	$[Ni(bipy)_2]$	0	–
A4 *cis*	$[(CO)_5MoCN]$	$[Co(bipy)_2]$	0	–
A5 *cis*	$[(CO)_5WCN]$	$[Co(bipy)_2]$	0	–
A6 *cis*	$[(CO)_5CrCN]$	$[Co(bipy)_2]$	0	–
A7 *cis*	$[(CO)_5MoCN]$	$[Mn(bipy)_2]$	0	–
A8 *cis*	$[(CO)_5WCN]$	$[Mn(bipy)_2]$	0	–
A9 *cis*	$[(CO)_5MoCN]$	$[Ni(phen)_2]$	0	–
A10 *cis*	$[(CO)_5WCN]$	$[Ni(phen)_2]$	0	–
A11 *cis*	$[(CO)_5MoCN]$	$[Co(phen)_2]$	0	–
A12[b] *cis*	$[(CO)_5WCN]$	$[Co(phen)_2]$	0	–
A13 *cis*	$[(CO)_5MoCN]$	$[Mn(phen)_2]$	0	–
A14 *cis*	$[(CO)_5WCN]$	$[Mn(phen)_2]$	0	–
B1[c] *cis*	[Cp(dppe)FeCN]	$[Ni(bipy)_2]$	+2	PF_6
B2[c] *cis*	[Cp(dppe)FeCN]	$[Co(bipy)_2]$	+2	PF_6
B3[c] *cis*	$[Cp(CO)_2FeCN]$	$[Mn(bipy)_2]$	+2	PF_6
C1 *trans*	$[(CO)_5MoCN]$	$[Ni(py)_4]$	0	–
C2[b] *trans*	$[(CO)_5WCN]$	$[Ni(py)_4]$	0	–
C3 *trans*	$[(CO)_5MoCN]$	$[Co(py)_4]$	0	–
C4[b] *trans*	$[(CO)_5WCN]$	$[Co(py)_4]$	0	–
C5 *trans*	$[(CO)_5MoCN]$	$[Mn(py)_4]$	0	–
C6 *trans*	$[(CO)_5WCN]$	$[Mn(py)_4]$	0	–
D1[b] *trans*	[Cp(dppe)FeCN]	$[Ni(py)_3(H_2O)]$	+2	ClO_4
D2[b] *trans*	$[Cp(PPh_3)_2RuCN]$	$[Ni(py)_4]$	+2	PF_6
D3[b] *trans*	$[Cp(PPh_3)_2RuCN]$	$[Co(py)_4]$	+2	PF_6
D4 *trans*	$[Cp(PPh_3)_2RuCN]$	$[Mn(py)_4]$	+2	PF_6
D5[b] *trans*	$[Cp(PPh_3)_2RuCN]$	$[Fe(py)_4]$	+2	PF_6
D6 *trans*	$[Cp(CO)_2FeCN]$	$[Ni(py)_3(H_2O)]$	+2	ClO_4
E1 *trans*	[Cp(dppe)FeNC]	$[Ru(py)_4]$	+2	PF_6
E2[b] *trans*	[Cp(dppe)FeNC]	$[Ru(4\text{-}MePy)_4]$	+2	PF_6
E3[b] *trans*	[Cp(dppe)FeNC]	$[Ru(4\text{-}EtPy)_4]$	+2	PF_6
E4 *trans*	[Cp(dppe)FeNC]	$[Ru(Me_2Py)_4]$	+2	PF_6
E5 *trans*	[Cp(dppe)FeNC]	$[Ru(3\text{-}MePy)_4]$	+2	PF_6
F1 *trans*	[Cp(dppe)FeNC]	$[Ru(py)_4]$	+3	PF_6
F2 *trans*	[Cp(dppe)FeNC]	$[Ru(4\text{-}MePy)_4]$	+3	PF_6
F3[b] *trans*	[Cp(dppe)FeNC]	$[Ru(4\text{-}EtPy)_4]$	+3	PF_6
F4 *trans*	[Cp(dppe)FeNC]	$[Ru(Me_2Py)_4]$	+3	PF_6

[a] The label indicates the series **A**–**F**, which are characterised on the basis of geometry and charge (see text for details). [b] The X-ray structure has been reported. [c] The structure is suggested by the method of preparation, but has not been confirmed by X-ray diffraction studies on a member of the series.

The compounds were first prepared by Vahrenkamp coworkers.[9–12] All contain two bridging CN groups, either in a *cis* or *trans* arrangement, bonded to a common metal atom. The species selected for the study show a systematic variation of the geometry, the M and M′ atoms, the ligands bonded to them and the formal charge of the complexes. Although infrared data have been reported, we have both repeated the measurements and augmented them with Raman data wherever possible. Crystal structure data are available for several species[9,10] and have been extrapolated to give the structures of similar compounds. To facilitate the interpretation of the spectra we have grouped the complexes into sets, each characterised by three common fea-

tures: similar geometries, similar ligand types bonded to M and M′ and identical formal ionic charges. To facilitate comparisons, the sets **A**–**F** in Table 1 are such that the differences are listed as systematically as possible.

Group **A** consists of uncharged *cis* complexes each containing two identical $M(CO)_5$ groups (M = Cr, Mo, W) and a central metal with two bidentate N ligands. The structure of one of them (**A12** in Table 1) has been reported in the literature,[10] that of another one (**A1**) has been characterised by us and is described later. Group **B** contains *cis* species, two with FeCp(dppe) groups and one with two $FeCp(CO)_2$ groups, each molecule carrying a formal 2+ charge. Group **C** resembles group **A** except that four pyridine-ligands are bonded to the central metal; the *trans* arrangement for two of the structures was confirmed by X-ray analysis. Like **A**, all members contain $M(CO)_5$ groups as the terminal ligands. Group **D** contains *trans* species carrying a formal 2+ charge. They all have a Cp group and two other ligating atoms as terminal ligands and a central metal with four pyridines (or three pyridines and one water). Group **E** also contains *trans* molecules with FeCp(dppe) terminal groups. They are noteworthy because the CN ligands are C-bonded to the central metal. Each complex carries a formal 2+ charge. Group **F** is similar to group **E** except the complexes carry a formal 3+ charge; the *trans* arrangement, previously suggested,[9] was determined by us for one of the structures by X-ray analysis.

Description of the Structures

Structure of Complex A1

The structure of the complex $[(CO)_5MoCNNi(bipy)_2NCMo(CO)_5]$ illustrated in Figure 3 shows the expected *cis* geometry of the complexes of the **A** series. The central nickel has a quasi-ideal octahedral coordination with bond angles ranging from 78 to 95°. The Ni–C(bipy) bonds show an average distance of 2.094 Å and the Ni–NC bond lengths are estimated to be around 2.047 Å. The molybdenum atoms are surrounded by CO ligands with an average distance of 2.033 Å, whereas the Mo–CN bond lengths are around 2.185 Å. The Ni–N–C–Mo is close to linearity with Ni–N–C and Mo–C–N angles of 170.5 and 176.9°, respectively.

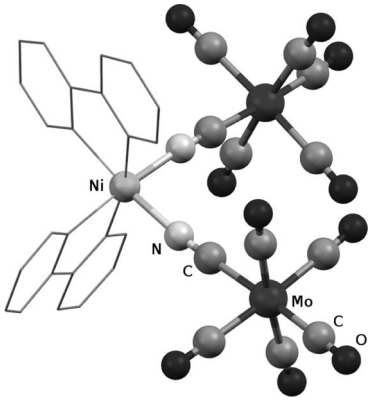

Figure 3. Molecular structure of the complex $[(CO)_5MoCNNi(Bipy)_2NCMo(CO)_5]$.

Structure of the Complex F3

Figure 4 illustrates the structure of the complex **F3**, which is part expected and part unusual. As expected, the core skeleton is almost linear, the NC–Ru–CN angle is 177.21° and the Fe–N–C angles lie in the range 176–178°. The hexacoordinate Ru central atom bears four ancillary ethylpyridine ligands and maintains a nearly octahedral arrangement (the angles around the Ru range from 88 to 92°). The iron atoms are surrounded by Cp and diphenylphosphanylethane ligands. Because of the imperfect quality of the diffraction data, anomalous electron density peaks appear around the CN groups and the CN bond lengths have

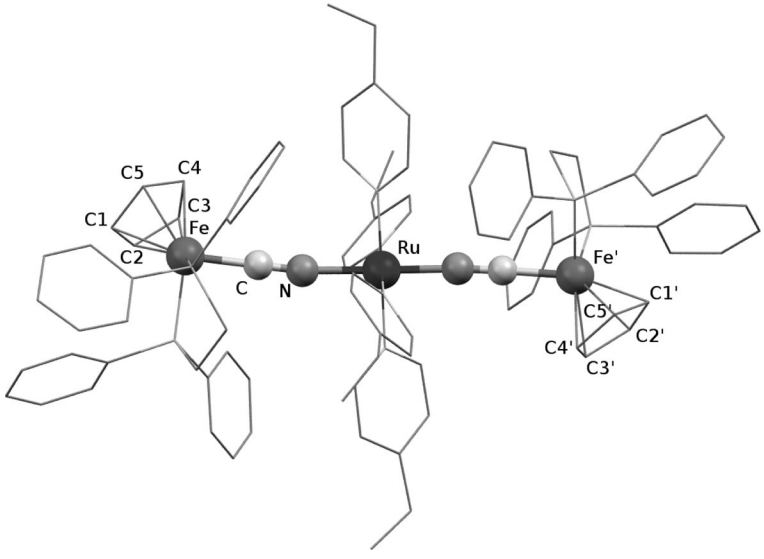

Figure 4. Molecular structure of the complex $[Cp(dppe)FeNCRu(4\text{-}EtPy)_4CNFeCp(dppe)]^{3+}[PF_6^-]^3$.

a significant uncertainty. Nevertheless, an (unexpected) structural difference between the two CN groups is both evident and significant. Selected bond lengths and angles are reported in Table 2 in which the two coordinated iron fragments are separately detailed.

Table 2. Selected bond lengths and angles of the complex [Cp(dppe)FeNCRu(4-EtPy)$_4$CNFeCp(dppe)]$^{3+}$[PF_6^-]$_3$ (**F3**) (in parentheses, the standard deviation). For a better comparison, the two moieties Ru–CN–Fe(Cp)(dppe) of the complex are separately considered.

	Fragment α[a]	Fragment β[a]
Ru–C(CN) [Å]	Ru–C′ 2.041(17)	Ru–C 1.992(14)
Fe–N(CN) [Å]	Fe′–N′ 1.941(15)	Fe–N 1.892(12)
C–N [Å]	C′–N′ 1.15(2)	C–N 1.17(2)
Fe–C(Cp) [Å]	Fe′–C2′ 2.070(14)	Fe–C2 2.089(17)
	Fe′–C1′ 2.076(15)	Fe–C1 2.097(17)
	Fe′–C4′ 2.101(14)	Fe–C4 2.142(15)
	Fe′–C3′ 2.115(16)	Fe–C3 2.110(16)
	Fe′–C5′ 2.112(15)	Fe–C5 2.167(15)
Fe–P [Å]	Fe′–P av. 2.208(5)	Fe–P av. 2.258(5)
C–Ru–N(py) [°]	C′–Ru–N av. 90.1(5)	C–Ru–N av. 90.0(5)
Ru–C–N [°]	Ru–C′–N′ 174.3(12)	Ru–C–N 176.0(12)
Fe–N–C [°]	Fe′–N′–C′ 178.0(12)	Fe–N–C 176.5(11)
Fe···Ru distance [Å]	Fe′···Ru 5.12(2)	Fe···Ru 5.04(2)
Ru–N(py) [Å]	Ru–N av. 2.109(12)	
N–Ru–N [°]	N–Ru–N av. 90.0(5)	
C–Ru–C [°]	C–Ru–C′ 177.2(5)	

[a] Figure 3 identifies the two fragments.

The data clearly show that the Ru–C and Fe–N bond lengths are shorter in fragment **β** than in fragment **α**. On the other hand, the coordination of the ligands around Fe is slightly weaker in fragment **β**, indicated by an increase in the average Fe–C(Cp) and Fe–P distances. Further, in both fragments, two of the Fe–C bond lengths are greater than the other three, which suggests that the Cp is somewhat η^3-allylic coordinated.

It is of interest to compare the key results arising from a crystallographic study of **F3** with the corresponding data for complex **E3**, which is the reduced form of **F3**.[9] Table 3 reports the most significant data, the two peripheral CpFe(dppe) units being separately considered. It is clear and significant that the two CpFe(dppe) units of the complex **E3** are very similar, which indicates that the electron distribution, or the formal oxidation states, of the two Fe atoms are the same in this species. In contrast, the two units of the complex **F3** are intrinsically different, only one of them, fragment **α** in Table 3, replicates the structural values found for the reduced form complex **E3**. The conclusion seems straightforward: the electron that has been withdrawn during the **E3**→**F3** oxidation process is localised in the peripheral unit **β**, the Fe atom of which has therefore acquired a higher oxidation state.

Table 3. Averaged bond lengths and angles of [Cp(dppe)FeNCRu(4-EtPy)$_4$CNFeCp(dppe)]$^{3+}$[PF_6^-]$_2$ (**E3**, reduced form)[9] and of [Cp(dppe)FeNCRu(4-EtPy)$_4$CNFeCp(dppe)]$^{3+}$[PF_6^-]$_3$ (**F3**, oxidised form) complexes (in parentheses, the standard deviation). For a better comparison, the two moieties Ru–CN–Fe(Cp)(dppe) of the complexes are separately considered.

Structural data	E3		F3	
	Fragment 1	Fragment 2	Fragment α	Fragment β
Ru–C(CN) [Å]	2.034(3)	2.034(3)	2.041(17)	1.992(14)
Fe–N(CN) [Å]	1.923–1.931(3)	1.923–1.931(3)	1.941(15)	1.892(12)
C–N [Å]	1.164(4)	1.164(4)	1.15(2)	1.17(2)
Fe–C(Cp) [Å]	2.085(8)	2.091(6)	2.095(15)	2.121(16)
Fe–P [Å]	2.207(1)	2.203(1)	2.208(5)	2.258(5)
C–Ru–N(py) [°]	88.7–91.7(1)	88.7–91.7(1)	90.1(5)	90.0(5)
Ru–C–N [°]	176.3–177.5(3)	176.3–177.5(3)	174.3(12)	176.0(12)
Fe–N–C [°]	170.9–174.8(3)	170.9–174.8(3)	178.0(12)	176.5(11)
Ru–N(py) [Å]	2.097(3)		2.109(12)	
Fe···Ru distance [Å]	5.113(5)		5.12(2)	5.04(2)
N–Ru–N [°]	86.4–91.7(1)		90.0(5)	
C–Ru–C [°]	177.9(1)		177.2(5)	

CN Vibrational Spectra

As far as the ν(C–N) vibrations are concerned, the expected vibrational behaviour is as follows: (i) for the *cis* complexes, with an approximate local C_{2v} symmetry, two ν(CN) modes, symmetric (A_1) and antisymmetric (B_1), both being infrared and Raman-allowed; (ii) for the *trans* complexes, with an approximate local $D_{\infty h}$ symmetry, two ν(CN) modes, the symmetric (σ_g^+) Raman-allowed and the antisymmetric (σ_u^+) infrared-allowed.

All the spectroscopic data are collected in Table 4. The infrared data are for species in the solid state and in solution. The Raman spectra are mostly of samples in the solid state. Solution Raman spectra were obtained for only a limited number of complexes.

Among the **A** series, the spectroscopic data of complex **A5**, which includes data from infrared and Raman spectra both in solution and in the solid state, can be considered typical of the spectroscopic behaviour of the *cis* complexes. Two infrared absorptions in the ν(CN) region are expected, one is found at 2115 cm^{-1} in CH_2Cl_2 solution. Two Raman bands are expected but only one is found at 2121 cm^{-1} (Figure 5). The assignment is clear: the Raman band is the symmetric mode, the infrared band, the antisymmetric. The data for complex **A5** suggest two generalisations that are applicable to all of the species in the present study: (i) the frequency of the symmetric mode is greater than that of the antisymmetric and (ii) the coupling between CN vibrators is very small ($\Delta\nu \approx 6$ cm^{-1} for **A5**).

The unique solution band of complex **A5** gives rise, in the solid-state Raman spectrum, to a strong band with a weak shoulder at lower frequency, the assignment of which to the antisymmetric mode seems plausible. Similar behaviour in the Raman spectra is evidenced in other cases (for instance, **A11**); in such cases, the value of Δν is always small (less than 10 cm^{-1}). A similar splitting with an intensity asymmetry is also observed in the infrared spectrum on moving from solution to the solid state. We believe it more probable that here the additional weak band is the symmetric mode. In contrast, the splitting in the solid-state Raman spectra appears, in some complexes (**A4** and **A13**), as two

Table 4. Vibrational data of the complexes studied.

	ν(CN) [cm^{-1}]				Ref.
	Infrared		Raman		
	Solution (CH_2Cl_2)	Solid (KBr disc)[a]	Solution ($CHCl_3$)	Solid (crystals)	
A1	2118 m	2131/2125 m, br (2123)		2131 s, ca. 2119 w, sh	this work
A2		2123			[12]
A3		2112			[12]
A4	2114 m	2118 m, br (2115)		2120 s, 2112 s	this work
A5	2115 m	ca 2120 m, br (2117)	2121 s	2119 s, 2111 w, sh	this work
A6		2119			[12]
A7		2108			[12]
A8		2118			[12]
A9		2126			[12]
A10	2111 m	2111 m		2110 s	this work
A11	2114 m	2122 m, br (2118)		2123 s, ca. 2114 w, sh	this work
A12		2121			[12]
A13	2108 m	2113 m (2112)		2115 s, 2110 s	this work
A14	2110 m	2114 m, 2103 w (2113)		2113 s, 2102 m	this work
B1	2082 m	2080 m (2080)			[12]
B2		2078			[12]
B3		2131			[12]
C1		2125			[12]
C2		2127			[12]
C3		2118			[12]
C4		2121			[12]
C5		2113			[12]
C6		2115			[12]
D1		2085			[12]
D2	2090 m	2083 s (2080)		2093 s	this work
D3		2072			[12]
D4		2069			[12]
D5		2066			[12]
D6		2167, 2156			[14]
E1	2071 m	2071 m, 2018 w (2071)			this work
E2	2069 m	2071 m, 2013 w (2070)	2091 m	2090 s	this work
E3	2068 m	2074 m, 2017 vw (2070)	2090 m	2097 s	this work
E4	2068 m	2072 m	2090 m	2092 s	this work
E5	2070 m	2068 m, 2013 vw (2068)		2090 s, 2086 s	this work
F1		2089 w, 2020 s			[9]
F2		2090 w, 2014 s,			[9]
F3	2068 w, 2017 m	2088 w, 2005 m (2088, 2007)			this work
F4		2086 w 2009 s			[14]

[a] The original frequencies reported in the literature are presented in parentheses.

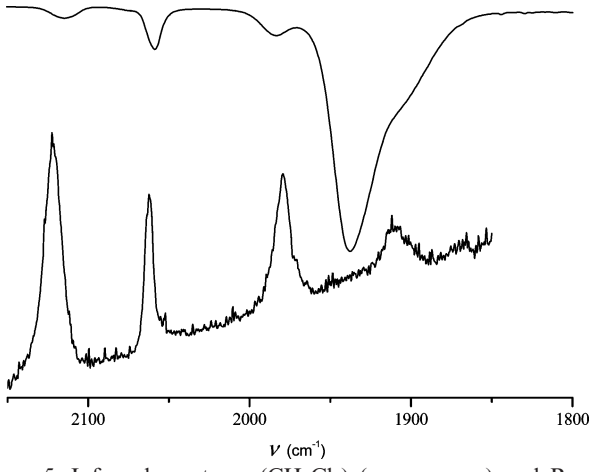

Figure 5. Infrared spectrum (CH_2Cl_2) (upper curve) and Raman spectrum ($CHCl_3$) (lower curve) of complex **A5**.

bands with nearly identical intensities. If adjacent CN vibrators scarcely couple within a molecule then intermolecular coupling will surely be zero. The band doubling does not have a factor group origin. The most obvious explanation is the occupation of two symmetry non-equivalent sites within a single crystal form.[10]

The complexes of this series are interesting for testing the correspondence between the structure determined in the solid state by X-ray diffraction and the structure in solution, the latter determined by ^{1}H NMR spectroscopy (all the other complexes have little solubility in appropriate solvents and too many different protons to enable a straightforward assignment). Reliable results have been obtained for two complexes of the **A** series, which have the general molecular formula $[(CO)_5MCNM'(bipy)_2NCM(CO)_5]$ but differ in their metal atoms (**A1**: M = Mo, M′ = Ni; **A5**: M = W, M′ = Co). The NMR spectroscopic data suggest the

same *cis* structure in solution, but an old sample of complex **A1**, prepared several years ago, has surprisingly given a ^{1}H NMR spectrum that strongly suggests a *trans* geometry (see Exp. Section for details). These results indicate that the central M′(bipy)$_2$ core is not rigid and that sometime the initial *cis* structure can be transformed into a more stable *trans* structure. In fact, in the present case, we note that the Ni^{II} d^8 ion has a well-recognised preference for a planar arrangement. This could be the driving force towards a *trans* structure, which can be considered a tetragonally elongated octahedron, when free from crystal constraints. On the other hand, the d^7 Co^{II} ion maintains a *cis* structure both in solution and the solid state.

Members of series **B** (three in number) are structurally similar to **A**: they too are 2+ cations but each member has a different central metal atom, always with two bipy ligands. Only the infrared spectra reported in the literature are available; two have a single band at around 2080 cm^{-1} but for the Mn compound it is at 2131 cm^{-1}. This is linked to the presence of CO groups on the terminal metal atoms; a similar pattern is seen for all the **C** species and for **D6**. All the species with CO groups, be they *cis* or *trans*, show frequencies that are higher than those of the other species in the present study.

The spectroscopic data for series **C** (*trans*, uncharged) have been reported in the literature. The infrared data obtained by using KBr discs are given; a single ν(CN) band appears with a frequency ranging from 2113 to 2127 cm^{-1}, in agreement with their *trans* structure and the presence of CO ligands.

Complex **D2** is probably representative of the **D** series. It has a single IR band, both when recorded in solution and in the solid state, and a single Raman band in the solid state (not coincident with the IR band; there is a shift of 10 cm^{-1}). The linear geometry is spectrally apparent.

Series **E** is novel in that in these complexes the CN coordinates to the central M′ atom through the carbon, not the nitrogen as for all other series, **F** excepted. Apart from this, the molecular arrangement is very similar to that of the **D** series, with a linear geometry, confirmed by crystal structure determinations of two of them. The literature reports for each complex a single infrared band at about 2068 cm^{-1} when recorded in KBr. Our corresponding infrared spectra show the same band, often with an additional weak band at 2013–2018 cm^{-1}. This additional band does not appear in the solution spectra. It seems to be that of an impurity, which, most probably, results from partial oxidation during the grinding with KBr. This would give rise to the corresponding complex of the **F** series (see below) and these exhibit a strong infrared absorption in the relevant frequency region. The solution spectra show a single absorption very close to, or coincident with, the strongest band in KBr. The Raman spectra of the solid have a single band at a frequency about 20 cm^{-1} higher than that of the infrared. This value seems to approximate an upper limit for the splitting between symmetric and antisymmetric modes. We were also able to record some Raman spectra for dissolved samples **E2–4**: they all show a single band not far from that found for the solid. Clearly, all the spectra are in accord with a linear geometry for the complexes.

The complexes of the **F** species, very similar to those of series **E** but with a charge 3+, show "anomalous" vibrational spectra, the splitting of spectral features from 50 to 90 cm^{-1} being much greater than occurs as a result of purely vibrational interactions (see below). The crystal structure reported above confirms that they are linear but not centrosymmetric molecules with two intrinsically different CpFe(dppe) units. We believe that the two vibrational features are strongly localised in the two CN vibrators, the higher frequency assigned to the ν(CN) of the α unit (Table 3) very similar to that of the parent **E** complex, the lower frequency to the ν(CN) of the β unit in which the oxidation process occurs.

An important feature common to all the experimental spectra, whether for species with a *cis* or *trans* geometry, is that the symmetric mode has a higher frequency than the antisymmetric. Unexpected are the very low Raman intensity of the antisymmetric mode and the very low infrared intensity of the symmetric mode in the *cis* complexes. The question of the origin of this pattern remains, however. The Raman is the easier. We have commented elsewhere[4] that the derived polarisability tensor of the CN stretching vibration is ellipsoidal. Were it accurately spherical the intensity of the antisymmetric Raman feature would be zero. The weakness of this feature is therefore understandable in terms of near-spherical bond polarisability tensors. The weakness of the symmetric feature in the infrared is more difficult to understand. Were the infrared intensities to be regarded as simple sums of bond transition dipoles oriented along the bond axes, two bands of comparable intensities would be predicted for *cis* complexes with an angle of around 90°. Because it is difficult to see why an additive bond dipole model should be inapplicable, the most evident explanation is that the dipole is not along the bond, but has a significant transverse component such that the interdipole angle is greater than 90°. Whatever the reason, the conclusion is clear: ν(CN) infrared and Raman spectra, particularly when considered separately, cannot be regarded as simple indicators of molecular geometry.

The frequency separation between the symmetric and the antisymmetric modes is a rough measure of the coupling between the two CN vibrators. For the *cis* structure (**A** series) the separation is usually small (the average is about 6 cm^{-1}); for the *trans* structures (**D** and **E** series), it is significantly larger (the maximum value observed is a little over 20 cm^{-1}). This agrees with the analysis of [M(CN)$_6$] complexes in which the effect of G-matrix coupling between M–C and C–N is reflected in the observed C–N couplings. This conclusion is relevant to the interpretation of the spectra of Prussian Blue because it means that the effects of *trans* coupling outweigh those of *cis* coupling in this family of compounds. Comparison of the **D** and **E** series indicates that the spectra are essentially independent of whether the coordination is CN or NC; the values of ν(CN) and Δν seem little affected.

ν(CO) Spectra

The complexes of the **A** (*cis*) and **C** (*trans*) series have two $M(CO)_5$ groups as terminal branches: do the corresponding vibrational features contain useful information on the molecular symmetry? An isolated $M(CO)_5$ unit exhibits C_{4v} symmetry and the ν(CO) modes transform as 2 A_1 (IR, Raman) + B_1 (Raman) + E (IR, Raman). Coupling between the two units seems unlikely but, were it to occur, would give rise to more complex spectra. The solution spectra, both infrared and Raman, of **A5** are shown in Figure 5. The experimental data were well reproduced by the calculations (details are available in the Supporting Information: Table 1SI and Figure 1SI). The infrared spectrum of the old sample of the **A1** complex, which in solution has a *trans* geometry, is nearly identical to that of the freshly prepared sample with *cis* geometry. This observation, along with the simplicity of the spectra, answers the above question: the vibrational coupling between the two $M(CO)_5$ units is negligible, whatever the geometry of the complex, and give no information on the molecular geometry.

Calculations

In previous papers on the vibrational spectra of cyanide complexes it has proved of value to view the data against a background of model DFT calculations. The conclusions were rather unexpected; in some considerable measure the frequency shifts observed were related, primarily, to electrostatic effects and the internal vibrational stark effect (IVSE) model was introduced to account for them.[8] Surprisingly, π interactions seemed relatively unimportant. It was of interest to extend these calculations to cover the present series and for this we selected the species **A5**. We have referred to this compound several times in the above discussion and it is one of the best characterised of the species studied. Additionally, it contains CO groups as terminal ligands and the prediction of their vibrational spectra provides something of an internal check on our interpretation of CN. Unfortunately, the crystal structure of **A5** is not available and so we compare the output of our calculations with the available data for **A12**, a complex with the same metal pattern as **A5** and for which the structure is known. As a second line of enquiry in the calculations we studied the phenomenon of bond localisation, and so the loss of the centre of symmetry, in linear complexes.

The geometrical structural data obtained from our calculations on **A5** are compared with the experimental data for **A12** in Table 5. Together with the modelling of the real system **A5**, we have examined four simple models with the aim of exploring the different bond contributions in the M–CN–M′ unit. Comparative results that we have obtained for the species, from CN^- to **A5**, are given in Table 6.

Table 5. Significant bond lengths and angles for $[(CO)_5WCNCo(bipy)_2CNW(CO)_5]$ (**A5**) and $[(CO)_5WCNCo(phen)_2CNW(CO)_5]$ (**A12**).

	Calculated **A5**	Experimental **A12**
d(W–C) [Å]	2.175	2.171(15)
d(C–N) [Å]	1.171	1.151(17)
d(N–Co) [Å]	1.942	2.096(11)
$[C(O)–W]_{eq.}$ (mean) [Å]	2.048	2.031
N–Co–N [°]	94.4	93.8
C–N–Co [°]	166.3	161.8(11)
W–C–N [°]	175.6	175.3(11)

The data for CN^- and $[NaCNNa]^+$ show the sensitivity of the CN bond length and vibrational frequency to the natural bond orbital (NBO) charges on C and N, recognised in the IVSE model. In $[WCNCo]^+$ there is a large increase in the p_{π^*} population (that in the p_π population remains essentially invariant through the series) with a corresponding change in bond length and frequency. The small change in q_C is such as to work in the opposite direction (a decreased repulsion between C and N). The p_{π^*} population is unrealistically large in $[WCNCo]^+$ and addition of a single CO ligand leads to a significant reduction in this population with a consequent increase in CN frequency and a shorter bond length in $[(CO)WCNCo]^+$. Addition of four more CO ligands to the W of $[(CO)WCNCo]^+$, addition of two bipy ligands to Co, dimerisation and charge neutrality to give **A5** further decreases the p_{π^*} population to a value that seems much more realistic. The concomitant changes in q_C and q_N are such that a weakly repulsive interaction is replaced by an attractive one. Both of these effects act to increase the CN frequency and shorten its bond length in **A5** relative to $[(CO)WCNCo]^+$. Of the two, the changes in q_C and q_N are the more dramatic and, we suspect, the more important, in keeping with the IVSE model.

We now turn to the problem of linear but not centrosysmmetric complexes. We have attempted a theoretical simulation by means of two simplified models, both based on the same core structure Fe–N–C–Fe–C–N–Fe. In one model the overall charge was 2+ (i) and, in the other, 3+ (ii), thus simulating the reduced and oxidised forms of the central cores of the two **E3** and **F3** complexes. The resulting calculated charge distributions were (i) Fe^a-(1.131)–N^a(–0.672)–C^a(0.007)–Fe(1.069)–C^b(0.007)–N^b-

Table 6. Comparative calculations on a series of cyanide species.

Species	q_C[a]	q_N[a]	$q_{M(-N)}$[a]	$q_{M(-C)}$[a]	p_π	p_{π^*}	*d*(CN) [Å]	ν(CN) [cm^{-1}]
CN^-	–0.245	–0.754			4	0	1.184	2139
$[NaCNNa]^+$	–0.126	–0.759	0.959	0.926	3.997	0	1.170	2247
$[WCNCo]^+$	–0.0878	–0.764	0.880	0.972	3.973	0.473	1.186	2038
$[(CO)WCNCo]^+$	–0.0581	–0.675	0.881	0.964	3.947	0.193	1.175	2154
A5	0.164	–0.595	1.016	–0.724	3.974	0.135	1.171	2218, 2225

[a] NBO charges.

(–0.672)–Fe^b(1.131) and (ii) Fe^a(1.541)–N^a(–0.783)–C^a-(0.121)–Fe(1.034)–C^b(0.190)–N^b(–0.816)–Fe^b(1.714). The asymmetry of the charge distribution in the 3+ species is evident. We conclude that this asymmetry is inherent in the system and not some artefact introduced, for example, by the crystalline environment or, indeed, by the presence of ligands.

Whereas in model (i) the symmetry of the structure is maintained and the two C–N bond lengths are identical, in model (ii) the C^b–N^b bond length is greater than that of the C^a–N^a (1.1745 vs. 1.1715 Å). Consequently, the two CN vibrations are coupled in model (i), showing two bands at 2289 (IR) and 2294 cm^{-1} (Raman), and this coupling is, as usual, small. In contrast, model (ii) gives rise to two bands, the frequencies of which are well separated (at 2196 and 2096 cm^{-1}), largely located at C^a–N^a and C^b–N^b, respectively. These calculations strongly support the suggestion[9] that the two terminal Fe atoms bear different positive charges and the two observed bands are to be separately assigned to the two CN groups. These two groups vibrate independently, that at the higher frequency corresponding to the CN attached to the Fe with lower charge.

Conclusions

The work described in this paper has provided some unexpected insights into the characteristics of the cyanide ligand when several are present. Although this work has been concerned with bridging cyanides, in retrospect, it seems that much the same considerations apply to terminal cyanides. It seems that the cyanide groups, in large measure, function independently. When several are bonded to the same metal atom and are symmetry related then, indeed, they vibrationally couple, albeit weakly and indirectly, through the C–M and M–C bonds that link them. It seems clear that otherwise identical metal atoms in different formal valence states (certainly in different electron distributions) can be linked by CN groups. The potential for such localisation is important in many areas of which bioinorganic chemistry is perhaps the most significant.

Although it has become customary to classify cyanide as a π-bonding ligand, the present work indicates that its involvement in π-backbonding is not dominant and may well show little variation. In previous papers we have shown that the most important influence on cyanide frequencies is that of the local electric field gradient (the IVSE model) and it seems that it is important in the present study. This has led us to extend our previous calculations[8] on the effect on ν(CN) of charged species bonded to C and N in the cyanide ligand. We used the model system q_2-C–N-q_1, with q_1 and q_2 variable positive charges placed at fixed distances from C and N. q_1 was allowed to change over a range for each fixed value of q_2. A plot of the data obtained for an extended range of q_1 and q_2 is illustrated in Figure 6.

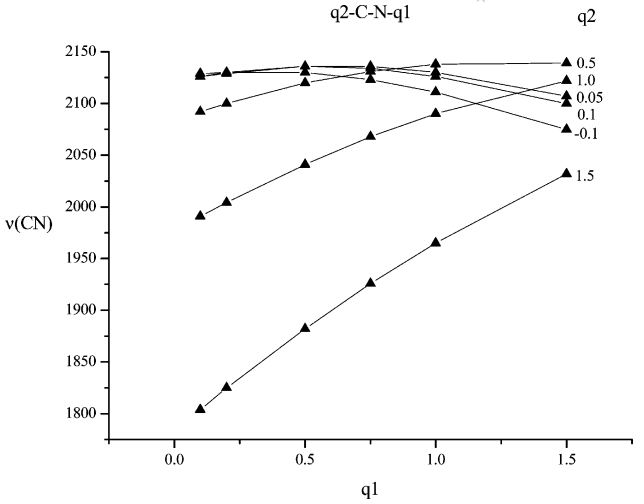

Figure 6. Plot of calculated ν(CN) values in the system q_2-C–N-q_1 against the values of q_1 charge. The value of q_2 was varied systematically and plots are given for the values indicated at the right of each curve. A high positive charge on a metal atom bonded to the C atom can lead to surprisingly low ν(CN) values.

The meaning of this plot is clear: by increasing q_1, ν(CN) can either increase or decrease, depending on the q_2 value. Of particular note is the prediction of the possibility of ν(CN) values much lower than might otherwise be regarded as reasonable. More generally, the plots account for the apparently random behaviour of the ν(CN) value with changes in the oxidation states of the metal atoms to which CN is coordinated.[13] That is, the IVSE model seems appropriate and, in its absence, historically, π-backbonding has been invoked in its place.[9,15] The fact that no general π-bonding model has emerged thus becomes understandable. So, discussions in the literature have tended to focus on particular examples and so are lacking in generality. What appears to be a general statement is that in most systems there are sufficient π/σ-bonding/antibonding orbitals available to support almost any discussion, even contradictory ones. It is our opinion that although π-bonding effects on frequencies must surely exist, it is difficult to distinguish them from the other effects we have considered and which surely are more important.

Experimental Section

Syntheses: The synthesis of the complexes was designed to target preferentially either a *cis* or a *trans* structure;[12] it was based on the double substitution of the two labile ligands (X) of an appropriate octahedral M′ complex with M species each of which contain a terminal CN ligand [Equation (1)].

$$2[M(L)_5CN]^{0/1-} + [M'(L')_4X_2] \rightarrow [(L)_5MCNM'(L')_4NCM(L)_5]^{2+/0} + 2X^- \quad (1)$$

The structure of the final complex is usually dictated by the structure of the octahedral M′ complex, that is, by the *cis* or *trans* positions of the two X ligands. To obtain *cis* complexes the starting material was [M′(Bipy)$_2$X$_2$] or [M′(phen)$_2$X$_2$], which have a *cis* configuration.[16] To obtain *trans* complexes the starting material was

$[M(Py)_4X_2]$, species that have a *trans* configuration because of a significant ligand steric effect.[17]

The complex $[(CO)_5MoCNNi(Bipy)_2NCMo(CO)_5]$ (**A1** in the Table 1) was prepared following a previously reported procedure.[12] $Na[Mo(CO)_5CN]$ (116 mg) was added to a solution of $[Ni(Bipy)_2(ClO_4)_2]$, prepared by the addition of 2,2′-bipyridine (32 mg) to $[Ni(ClO_4)_2{\cdot}6H_2O]$ (18 mg) in acetonitrile (14 mL). The solution turned violet and was stirred for 8 h. Then the solvent was removed under reduced pressure and the residue extracted with dichloromethane (16 mL) and filtered. The filtrate was layered with petroleum ether (20 mL). After a few days, crystals of the complex **A1** were collected and recrystallised by the same procedure as described before.

The complex $[Cp(dppe)FeNCRu(4\text{-}EtPy)_4CNFeCp(dppe)]^{3+}[PF_6^-]_3$ (**F3** in Table 1) was prepared by oxidising $[Cp(dppe)FeNCRu(4\text{-}EtPy)_4\text{-}CNFeCp(dppe)]^{2+}[PF_6^-]_2$ (**E3** in Table 1) with $[Cp_2Fe][PF_6]$ following the literature method.[9] $[Cp_2Fe][PF_6]$ (0.0052 g, molar ratio ca. 1:1) was added to a solution of **E3** (0.0293 g) in CH_2Cl_2 (3 mL). The mixture was stirred, filtered and layered in a small tube with *n*-hexane (5 mL). The tube was introduced into a larger Schlenk tube under an inert atmosphere and allowed to stand for a week. Small dark-red crystal were recovered; among them it was possible to select examples suitable for X-ray diffraction. Any other attempts, by changing the reactant concentrations or the layered solvent (cyclohexane, benzene), did not improve the quality of the crystals.

Vibrational Spectra: Raman spectra were collected by using two different instruments. With a Bruker RFS 100 FT-Raman spectrophotometer equipped with a Nd:YAG laser (1064 nm) operated at 50–100 mW, spectra were collected in dichloromethane or chloroform in a quartz standard cuvette at 2 cm^{-1} resolution. The acquisition required between 3000 and 10000 scans. A Jobin Yvon Labram 800 HR Raman microscope was also employed. Measurements were carried out using a He–Ne 633 nm laser (20 mW). Spectra were collected with 300–450 acquisitions, each of 70–160 s.

Infrared spectra were recorded with a Bruker EQUINOX 55 FT-IR spectrophotometer equipped with a Globar source and DLaTGS detector. Both CH_2Cl_2 solutions (standard liquid sampling cell, 0.1 cm path, NaCl) and 13 mm KBr pellets were used. The spectra were usually acquired with 32 scans at 2 cm^{-1} resolution.

NMR Spectra: Routine NMR spectra were acquired with a JEOL EX400 spectrometer operating at 400 MHz for ^1H NMR. The spectrum of **A1** (old sample) shows two doublets (at ca. 8.66 and 8.43 ppm), which correspond to the two different protons of the bipy groups, and two triplets (at ca. 7.84 and 7.33 ppm), which correspond to the other H species. This strongly suggests that the two bipy ligands are identical, that is, that the structure is *trans*. In contrast, the spectrum of **A5** (freshly prepared sample) shows both eight poorly resolved NMR peaks (at ca. 9.6, 8.7, 8.6_5, 8.5, 8.3, 8.0, 7.6_5, 7.2_5), which suggests that the two bipy groups are different, that is, a *cis* structure.

X-ray Structure Determination: Single-crystal diffraction data were collected with an Oxford Xcalibur CCD area detector diffractometer using graphite-monochromated Mo-K_α (λ = 0.71069 Å) radiation. Data reduction and absorption corrections were performed using Crysalis RED 1.171.26 (Oxford Diffraction). The structures were solved by direct methods using SIR2004,[18] and refined by full-matrix least-squares analysis using SHELX-

Table 7. Crystal structure determination of **F3** and **A1**.

	F3	**A1**
Empirical formula	$C_{92}H_{94}F_{18}Fe_2N_6P_6Ru$	$C_{36}H_{16}Mo_2N_2NiO_{10}$
Formula weight	2024.32	889.83
Temperature [K]	120(3)	293(2)
Wavelength [Å]	0.71073	0.71073
Crystal system	$P\bar{1}$	$C2/c$
Space group	triclinic	monoclinic
Unit cell dimensions		
a [Å]	13.985(2)	22.5068(7)
b [Å]	14.809(2)	11.1386(3)
c [Å]	23.143(2)	15.4946(6)
α [°]	76.510(11)	
β [°]	83.425(11)	103.799(3)
γ [°]	75.255(13)	
Volume [$Å^3$]	4499.8(11)	3772.3(2)
Z	2	3
Density (calculated) [Mg/m^3]	1.494	0.369
Absorption coefficient [mm^{-1}]	0.677	0.300
$F(000)$ [mm^3]	2072	414
Crystal size [mm]	$0.3 \times 0.2 \times 0.05$	$0.2 \times 0.1 \times 0.05$
θ range for data collection [°]	3.73–23.40	4.55–31.76
Index ranges	$-14 \le h \le 14$	$-33 \le h \le 33$
	$-16 \le k \le 14$	$-16 \le k \le 16$
	$-25 \le l \le 24$	$-22 \le l \le 22$
Reflections collected	37984	53735
Independent reflections	9945	6191
Completeness to	θ = 30.50° 75.6%	θ = 31.76° 96.2%
Refinement method	full-matrix least-squares on F^2	
Data/restraints/parameters	9945/0/1108	6191/0/231
Goodness-of-fit on F^2	1.114	1.118
Final R indices [$I > 2\sigma(I)$]	R_1 = 0.0765, $wR2$ = 0.1695	R_1 = 0.0583, $wR2$ = 0.1401
R indices (all data)	R_1 = 0.1565, $wR2$ = 0.2277	R_1 = 0.1364, $wR2$ = 0.1926
Largest diff. peak and hole [$e Å^{-3}$]	2.063 and –0.805	2.034 and –0.547

97.[19] Hydrogen atoms were generated in calculated positions using SHELX-97. Table 7 lists the crystallographic data.

CCDC-769676 (for **A1**), -724344 (for **F3**) contain the supplementary crystallographic data for this paper. These data can be obtained free of charge from The Cambridge Crystallographic Data Centre via www.ccdc.cam.ac.uk/data_request/cif.

Calculations: The computational method used DFT theory. Hybrid B3LYP functionals with a 6-31g(d,p) basis set were used for light elements and a LANL2DZ effective core potential basis set was used for Fe, Co and W. All the calculations were performed with the Gaussian 03[20] package on a Linux workstation. All the systems were optimised and both harmonic vibrational frequencies and intensities calculated. Atomic charge and population analyses were obtained by a natural bond orbital (NBO) analysis. We performed an analysis of complex **A5**, representative of the *cis* complexes studied in this work, which has good infrared and Raman spectra available. It is also similar to compound **A12** for which the single-crystal structure has been reported.[12]

Supporting Information (see also the footnote on the first page of this article): Figure S1 shows the calculated infrared and Raman spectra of the complex **A12**, Figure S2 shows the crystal packing of the complex **A1** and Figure S3 shows the crystal packing of the complex **F3**.

Acknowledgments

Many thanks are due to Dr M. R. Chierotti (Dipartimento di Chimica IFM, Università di Torino) for recording the NMR spectra and to Prof. D. Viterbo (Dipartimento di Scienze e Tecnologie Avanzate, Università del Piemonte Orientale) for helpful discussion.

[1] a) K. R. Dunbar, R. A. Heintz, *Prog. Inorg. Chem.* **1997**, *45*, 283–391; b) C. A. Bignozzi, J. R. Schoonover, F. Scandola, *Prog. Inorg. Chem.* **1997**, *44*, 1–95; c) O. Kahn, *Molecular Magnetism, New Magnetic Materials* (Eds.: K. Itoh, M. Kinoshita), Gordon & Breach, Amsterdam, **2000**; d) M. Verdaguer, N. Galvez, R. Garde, C. Desplanches, *Electrochem. Soc. Interface* **2002**, *11*, 28; e) P. W. Atkins, *Catalysis and electrocatalysis at nanoparticle surfaces*, Marcel Dekker, New York, **2003**; f) D. M. DeLongchamp, P. T. Hammond, *Adv. Funct. Mater.* **2004**, *14*, 224–232.

[2] a) B. I. Swanson, L. H. Jones, *J. Chem. Phys.* **1971**, *55*, 4174–4180; b) B. I. Swanson, J. J. Rafalko, *Inorg. Chem.* **1976**, *15*, 249–253; c) B. I. Swanson, L. H. Jones, *Inorg. Chem.* **1974**, *13*, 313–316; d) L. H. Jones, B. I. Swanson, G. J. Kubas, *J. Chem. Phys.* **1974**, *61*, 4650–4655.

[3] M. Verdaguer, A. Bleuzen, V. Marvaud, J. Vaissermann, M. Seuleiman, C. Desplanches, A. Scuiller, C. Train, R. Garde, G. Gelly, C. Lomenech, I. Rosenman, P. Veillet, C. Cartier, F. Villain, *Coord. Chem. Rev.* **1999**, *190–192*, 1023–1047.

[4] S. F. A. Kettle, G. L. Aschero, E. Diana, R. Rossetti, P. L. Stanghellini, *Inorg. Chem.* **2006**, *45*, 4928–4937.

[5] a) L. H. Jones, *J. Chem. Phys.* **1962**, *36*, 1209–1215; b) W. P. Griffith, G. T. Turner, *J. Chem. Soc. A* **1970**, 858–862; c) L. H. Jones, M. N. Memering, B. I. Swanson, *J. Chem. Phys.* **1971**, *54*, 4666–4671.

[6] a) W. P. Griffith, P. M. Kiernan, J.-M. Brégeault, *J. Chem. Soc., Dalton Trans.* **1978**, 1411–1417; b) A. Müller, R. Jostes, W. Eltzner, C.-S. Nie, E. Diemann, H. Bögge, M. Zimmermann, M. Dartmann, U. Reinsch-Vogell, S. Che, S. J. Cyvin, B. N. Cyvin, *Inorg. Chem.* **1985**, *24*, 2872–2884; c) H. Chun, E. M. Maes, R. S. Czernuszewicz, I. Bernal, *Polyhedron* **2001**, *20*, 2597–2607.

[7] C. P. Horwitz, D. F. Shriver, *Adv. Organomet. Chem.* **1984**, *23*, 219–305.

[8] S. F. A. Kettle, E. Diana, E. Boccaleri, P. L. Stanghellini, *Inorg. Chem.* **2007**, *46*, 2409–2416.

[9] T. Sheng, H. Vahrenkamp, *Eur. J. Inorg. Chem.* **2004**, 1198–1203.

[10] T. Sheng, H. Vahrenkamp, *Inorg. Chim. Acta* **2004**, *357*, 1739–1747.

[11] G. N. Richardson, U. Brand, H. Vahrenkamp, *Inorg. Chem.* **1999**, *38*, 3070–3079.

[12] T. Sheng, Ph. D. Thesis, Albert-Ludwigs-Universität, Freiburg im Breisgau, Germany, **2002**.

[13] This is also evidenced in the IR spectra of some Prussian Blue like compounds that show the sequence M–CN–M′ in which, with the same M, the oxidation state of M′ is changed. For example, in systems in which M = Fe^{III}, ν(CN) increases, moving from M′ = Co^{II} to M′ = Co^{III}, but remains roughly constant when M = Fe^{II} and M′ = Cu^{II} or Cu^{III}. In contrast, when M = Mn^{III}, the ν(CN) decreases passing from M′ = Mn^{II} to M′ = Mn^{III}.[14]

[14] a) S. N. Ghosh, *J. Inorg. Nucl. Chem.* **1974**, *36*, 2465–2466; b) W. E. Buschmann, J. M. Miller, *Inorg. Chem.* **2000**, *39*, 2411–2421; c) P. Franz, C. Ambrus, A. Hauser, D. Chernyshov, M. Hostettler, J. Hauser, L. Keller, K. Krämer, H. Stoeckli-Evans, P. Pattison, H. B. Bürgi, S. Decurtins, *J. Am. Chem. Soc.* **2004**, *126*, 16472–16477; d) Q. Kong, X. Chen, J. Yao, D. Xue, *Nanotechnology* **2005**, *16*, 164–168.

[15] N. Zhu, H. Vahrenkamp, *Chem. Ber./Recueil* **1997**, *130*, 1241–1252.

[16] E. D. McKenzie, *Coord. Chim. Rev.* **1971**, *6*, 187–216.

[17] G. J. Long, P. J. Clarke, *Inorg. Chem.* **1978**, *17*, 1394–1401.

[18] A. Altomare, M. C. Burla, M. Camalli, G. L. Cascarano, C. Giacovazzo, A. Guagliardi, A. G. Moliterni, G. Polidori, R. Spagna, *J. Appl. Crystallogr.* **1999**, *32*, 115.

[19] G. M. Sheldrick *SHELXL-97*, University of Göttingen, Germany, **1997**.

[20] M. J. Frisch, G. W. Trucks, H. B. Schlegel, G. E. Scuseria, M. A. Robb, J. R. Cheeseman, J. A. Montgomery, Jr., T. Vreven, K. N. Kudin, J. C. Burant, J. M. Millam, S. S. Iyengar, J. Tomasi, V. Barone, B. Mennucci, M. Cossi, G. Scalmani, N. Rega, G. A. Petersson, H. Nakatsuji, M. Hada, M. Ehara, K. Toyota, R. Fukuda, J. Hasegawa, M. Ishida, T. Nakajima, Y. Honda, O. Kitao, H. Nakai, M. Klene, X. Li, J. E. Knox, H. P. Hratchian, J. B. Cross, V. Bakken, C. Adamo, J. Jaramillo, R. Gomperts, R. E. Stratmann, O. Yazyev, A. J. Austin, R. Cammi, C. Pomelli, J. W. Ochterski, P. Y. Ayala, K. Morokuma, G. A. Voth, P. Salvador, J. J. Dannenberg, V. G. Zakrzewski, S. Dapprich, A. D. Daniels, M. C. Strain, O. Farkas, D. K. Malick, A. D. Rabuck, K. Raghavachari, J. B. Foresman, J. V. Ortiz, Q. Cui, A. G. Baboul, S. Clifford, J. Cioslowski, B. B. Stefanov, G. Liu, A. Liashenko, P. Piskorz, I. Komaromi, R. L. Martin, D. J. Fox, T. Keith, M. A. Al-Laham, C. Y. Peng, A. Nanayakkara, M. Challacombe, P. M. W. Gill, B. Johnson, W. Chen, M. W. Wong, C. Gonzalez, J. A. Pople, *Gaussian 03*, *Revision D.01*, Gaussian, Inc., Wallingford CT, **2004**.

Received: March 8, 2010
Published Online: July 13, 2010

DOI: 10.1002/ejic.201000067

Iron(II) Spin-Transition Complexes with Dendritic Ligands, Part II[‡]

YongLi Wei,[a] Prashant Sonar,[b] Matthias Grunert,[a] Joachim Kusz,[a,c] A. Dieter Schlüter,[b] and Philipp Gütlich*[a]

Dedicated to Professor Rolf W. Saalfrank on the occasion of his 70th birthday

Keywords: Spin crossover / Iron / Dendrimers / Moessbauer spectroscopy / Magnetic properties

The dendritic triazole-based complexes $[Fe(G1\text{-}BOC)_3](triflate)_2 \cdot xH_2O$ (**1**; G1-BOC = *tert*-butyl {3-[3-(3-*tert*-butoxycarbonylaminopropyl)-5-([1,2,4]triazol-4-ylcarbamoyl)-phenyl]propyl}carbamate, triflate = $CF_3SO_3^-$), $[Fe(G1\text{-}BOC)_3](tosylate)_2 \cdot xH_2O$ (**2**; tosylate = *p*-$CH_3PhSO_3^-$), $[Fe(G1\text{-}DPBE)_3](triflate)_2 \cdot xH_2O$ {**3**; G1-DPBE = 3,5-bis(3,5-didodecaoxybenzyloxy)-*N*-[1,2,4]triazol-4-ylbenzamide}, $[Fe(G1\text{-}DPBE)_3](tosylate)_2 \cdot xH_2O$ (**4**) and $[Fe(G1\text{-}DPBE)_3](BF_4)_2 \cdot xH_2O$ (**5**) were designed and synthesized. Magnetic and thermal properties of these novel complexes were characterized by magnetic susceptibility measurements, ^{57}Fe Mössbauer spectroscopy and thermogravimetric analysis or differential scanning calorimetry, respectively. All dendritic complexes under study show different spin-transition behaviour with respect to the nature of different dendritic ligands and counteranions. Complexes **1** and **2** have pronounced effects of a spin-state change during the first heating process and gradual spin-transition properties for further temperature treatments, whereas **3** and **4** exhibited a very sharp spin-state change in the first heating procedures. Complex **5** showed a gradual spin-transition curve. In this paper, we report how the magnetic properties of these complexes are correlated with noncoordinated water molecules and their effects on spin states.

Introduction

Dendritic materials are interesting due to their unique macromolecular monodispersed nature, generation-dependent properties and the possibilities they offer for anchoring various groups for functionalization. These materials have received much attention recently with regards to fundamental research and because of their applications in various fields.[1–3] For example, incorporation of metals in a dendritic moiety may provide an opportunity to generate new metallodendrimer materials,[4–8] dendritic boxes and other supramolecular dendritic arrangements.[9–11] These metallodendrimers can be used as soluble catalysts for various organic reactions. There are a few reports in the literature: aryl–nickel(II) dendrimers have been used as an effective catalyst for the Karasch addition reaction of polyhaloalkanes to olefins,[12] P-based polypalladium complexes were used for the electrochemical reaction of CO_2 to CO[13,14] and iron dendritic complexes were used as spatially encumbered models of nonheme iron proteins.[15] Our motivation also falls in the same line to make metal–dendritic-system-based complexes with various interesting properties dependent on different ligands, metal ions and counteranions.

It is well documented that iron(II)-containing dendritic complexes may exhibit thermal spin-crossover (SCO) behaviour. This particular unique property with an accompanying change of colour and magnetic behaviour is very useful for various applications such as display devices, optical switches and magneto-optical storage systems.[16,17] Spin crossover is related to its electronic transition between $t_{2g}^6e_g^0$ [low spin (LS)] and $t_{2g}^4e_g^2$ [high spin (HS)]. In some cases, this electronic transition causes a switching of colour of the complexes with respect to its transition state. The electron transition can be triggered by using external perturbations such as change of temperature, pressure, light irradiation and magnetic field.[16a,18,19] There are numerous examples of the SCO behaviour of organometallic complexes using various ligands but very few reports about using dendritic ones. Still, it is quite challenging to design and synthesize novel ligands that can show synergic effects in terms of thermal and spin-crossover properties. Among the reported wide range of ligand systems, 4-R-substituted 1,2,4-triazoles were the most studied, in which the functional R group may be any kind of aliphatic or aromatic

[‡] Part I: Ref.[21]

[a] Institut für Anorganische Chemie und Analytische Chemie, Johannes Gutenberg Universität Mainz, Staudingerweg 9, 55099 Mainz, Germany
Fax: +49-6131-3922990
E-mail: guetlich@uni-mainz.de
[b] Laboratory of Polymer Chemistry, Department of Materials, Swiss Federal Institute of Technology, ETH Zürich, HCI J541 8093 Zürich, Switzerland
E-mail: ads@mat.ethz.ch
[c] University of Silesia, Institute of Physics, ul. Uniwersytecka 4, 40007 Katowice, Poland

organic moiety. Its combination with iron to provide the $Fe^{II}N_6$ spin-crossover chromophore is the most attractive one due to its relatively high chemical stability and striking colour change upon spin transition[20] that originates either from the dd HS/LS bands or the more intensive metal-to-ligand charge-transfer (MLCT) bands, which in many cases overlap the thermochromic effect associated with the dd HS/LS bands.

Earlier we published the first part of this study using various triazole-based ligand systems combined with iron(II) and its spin transition.[21] In this second part, our main focus is the utilization of various triazole-based dendritic ligands (as shown in Figure 1) for making iron(II) complexes with different counteranions to arrive at a structure–property relationship with respect to its spin-crossover behaviour. We have synthesized and characterized various triazole dendritic ligands and their iron(II) complexes, all the while keeping SCO behaviour as the main objective. This study is an extension of our earlier work[21] and also a comparative study with that of some of the previously reported dendritic iron(II) complexes by Fujigaya et al. (see structure **B** in Figure 1).[22] They highlighted a generation number (*n*) dependency of the abruptness of the spin-state change with temperature and showed that [(G1-trz)Fe] (trz = triazole) was the best-behaved complex in terms of the spin-crossover properties (cooperativity) in terms of eventual applications.[21] We have chosen different counteranions such as triflate ($CF_3SO_3^-$) and tosylate (p-$CH_3PhSO_3^-$) because of their interesting influences on spin-crossover behaviour.[23–25] The G1-PBE [PBE = poly(benzyl ether)] dendritic triazole-based complexes (see structure **A** in Figure 1) are already covered in our earlier publication. In this paper, we are mainly focussing on two dendritic triazole ligands (structures **B** and **C** in Figure 1) with different dendritic branches attached to triazole and their iron(II) complexes. Structural differences of dendritic ligands play a crucial role in "tuning" the thermal and magnetic properties of iron(II) complexes because of differences in the connection between the triazole ring and the dendron (NH–C=O and CH_2 spacing). Some important rules for the design and the synthesis of the dendritic ligands and their iron(II) complexes with magnetic thermal properties are discussed in this paper.

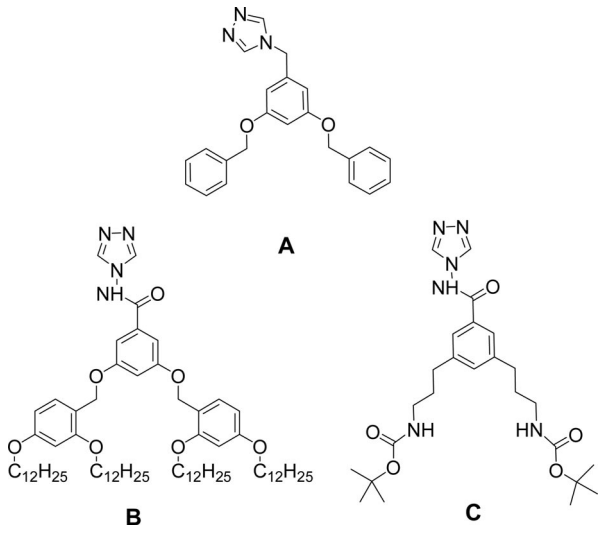

Figure 1. Perspective molecular structures of different dendritic triazoles: G1-PBE (**A**),[21] G1-DPBE (**B**) and G1-BOC (**C**).

Results and Discussion

Synthesis of the Dendritic Triazole Ligands

The first-generation dendritic triazole G1-BOC (**C**), was synthesized by heating to reflux the corresponding *tert*-butoxycarbonyl (BOC)-protected dendron **D**[26] with 4-amino-1,2,4-triazole (atrz) in the presence of diphenyl (2,3-dihydro-2-thioxo-3-benzooxazolyl) phosphonate (DBOP) as a catalyst in a mixture of triethylamine and dry THF under nitrogen (Scheme 1). The reaction was worked up by using standard extraction techniques and the compound was isolated from the organic phase. The crude product was purified by column chromatography and the final compound was obtained in 72% yield. The ligands A and B were synthesized according to previously reported publications of Sonar et al.[21] and Fujigaya et al.,[22] respectively. The dendritic triazoles in Figure 1 were prepared on the gram scale as analytically pure compounds. The purity of the materials was confirmed by elemental analysis, MALDI-TOF spectrometry and NMR spectroscopy.

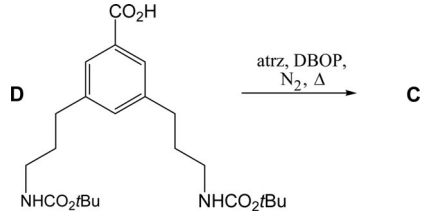

Scheme 1.

Synthesis of the Iron(II) Complexes with Dendritic Triazoles

All the iron(II) complexes with dendritic triazoles, $[Fe(G1\text{-}BOC)_3](triflate)_2 \cdot xH_2O$ (**1**), $[Fe(G1\text{-}BOC)_3](tosylate)_2 \cdot xH_2O$ (**2**), $[Fe(G1\text{-}DPBE)_3](triflate)_2 \cdot xH_2O$ {**3**; G1-DPBE = 3,5-bis(3,5-didodecaoxybenzyloxy)-*N*-[1,2,4]triazol-4-ylbenzamide}, $[Fe(G1\text{-}DPBE)_3](tosylate)_2 \cdot xH_2O$ (**4**) and $[Fe(G1\text{-}DPBE)_3](BF_4)_2 \cdot xH_2O$ (**5**), were synthesized in high yield. Ascorbic acid was used as antioxidant during the synthesis of all complexes to avoid the oxidation of iron(II) ions. The reactions were carried out using methanol and THF solvent mixtures (1:5) at room temperature. After completion of the reaction, we did not observe any precipitate formation in the solvent mixture, which may be due to similar solubility behaviour of dendritic triazole and its complexes at room temperature. Due to this reason, we could not purify the final iron(II) complexes, as it was difficult to separate the products by precipitation from the reaction solution. After modifying the synthesis procedure, we

were able to separate the pure dendritic triazole iron(II) complexes at very low temperature. Specifically for the G1-BOC-based iron(II) complexes, when the solvent of the reaction mixture was partially removed, the remaining reaction solution segregated easily into two layers. After cooling in liquid nitrogen to around –100 °C, the pink solid G1-BOC-based iron(II) complex was recovered as a product at the bottom of the flask. The same procedure was carried out several times to get higher yields. For other dendritic triazole-based iron(II) complexes, we used the same procedure as mentioned above and it was much easier to obtain pure complexes in higher yields.

Powder X-ray Diffraction Experiments of the Dendritic Triazole Iron(II) Complexes

The powder X-ray diffraction experiments were carried out at various temperatures (first at 300 K, then at 250, 300, 350 and again at 300 K, respectively) using fresh samples of $[Fe(G1\text{-}BOC)_3](tosylate)_2 \cdot xH_2O$ (**2**) and $[Fe(G1\text{-}DPBE)_3](tosylate)_2 \cdot xH_2O$ (**4**) to compare the effect of different dendritic triazoles. The X-ray powder diffraction pattern shows in each case a single strong diffraction peak beside some small diffraction peaks. The broad halo peak appeared at about 2θ–20° and originated from the voluminous dendritic branches attached to triazole. It was not possible to determine the crystal structures because only eight diffraction peaks of the poorly structured complexes under study could be recorded.

Figure 2 shows the X-ray powder diffraction pattern measured in the 2θ range between 2 and 20° at various temperatures for $[Fe(G1\text{-}BOC)_3](tosylate)_2 \cdot xH_2O$ (**2**). As shown in Figure 2 (a), the diffraction pattern at 300 K shows the strong peak at 2θ = 3.440°, whereas some other small peaks appear at the positions of 2θ = 5.975, 6.912, 12.546 and 13.874°. After cooling the samples to 250 K, the strong diffraction signal changes its position from 2θ = 3.440° to 2θ = 3.281°. This temperature effect was also noticed for other small diffraction peaks at the positions 5.812, 6.729, 12.386 and 13.715° (Figure 2, b). When the sample is heated again to the original temperature at 300 K, the position of the strong signal changes only a little (to 2θ = 3.243°). Other small peaks appear at 5.788, 6,738, 12.334 and 13.718° (Figure 2, c), respectively. All these signals can be indexed as (1,0), (1,1), (2,0), (3, 1) and (4,0) and belong to a two-dimensional hexagonal lattice with lattice parameters *a* equal to 29.71, 31.15 and 31.51 Å for 300, 250 and 300 K, respectively. After heating the iron(II) complexes again to 350 K, the complex shows a strong diffraction peak at 2θ = 3.247° and only two small peaks appear at positions at 5.805 and 6.743° (Figure 2, d). During the heating and cooling cycles, we observed the irreversibility of the appearances of the peak. This is due to the loss of water after heating to 350 K [see the thermogravimetric analysis (TGA) and differential scanning calorimetric (DSC) measurements below]. By cooling again to 300 K, the strong peak was observed at position 2θ = 3.306° and two small peaks remained at positions 5.906 and 6.845° (Figure 2, e). These peaks can be indexed as (1, 0), (1, 1) and (2, 0) and belong to a two-dimensional hexagonal lattice with lattice parameters *a* equal to 31.47 and 30.91 Å for 350 and 300 K, respectively.

The G1-DPBE-based iron(II) complex $[Fe(G1\text{-}DPBE)_3](tosylate)_2 \cdot xH_2O$ (**4**) was also analyzed by X-ray powder diffraction under similar conditions to the first sample measurement. (Figure 3). The X-ray diffraction pattern was first analyzed at 300 K using a fresh sample of **4**. The peak appeared at 2θ = 4°; other small peaks were also observed at various positions at 6.199, 6,988, 8.405 and 12.382°. These can be indexed in two-dimensional hexagonal lattice as (2, 1), (3, 0), (3, 1) and (4, 2), respectively (Figure 3, a). On cooling this sample to 250 K, the small peaks appeared at positions 4.674, 6,209, 7.032, 8.422 and 12.425°, which can be indexed as (2,0), (2,1), (3,0), (3,1) and (4,2), respectively (Figure 3, b). After heating the sample again to 300 K, the

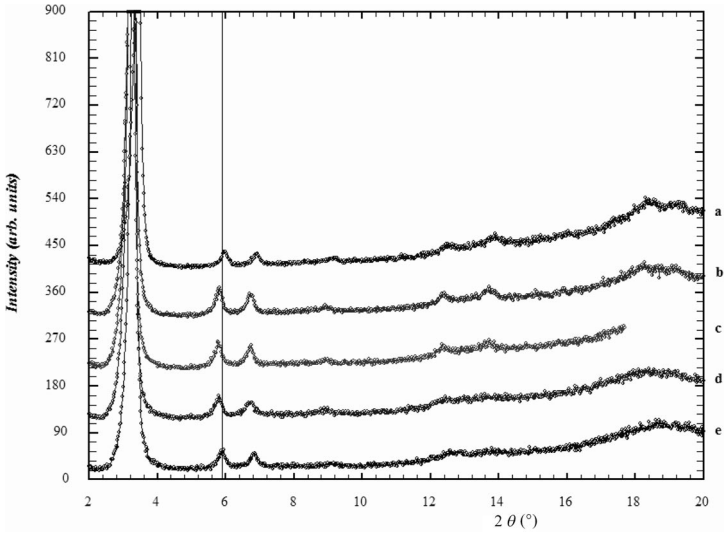

Figure 2. X-ray powder diffraction pattern of a fresh sample of **2** measured at (a) 300, (b) 250 and (c) 300 K after cooling and (d) 350 and (e) at 300 K after heat treatment. The vertical line shows the changes in the 2θ position of diffraction peak (1).

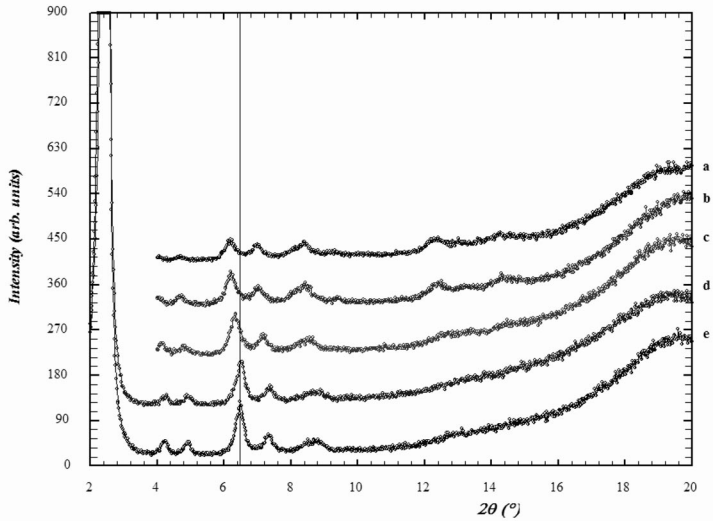

Figure 3. X-ray powder diffraction pattern of a fresh sample of **4** measured at (a) 300, (b) 250 and (c) 300 K after cooling and (d) 350 and (e) at 300 K after heat treatment. The vertical line shows the changes in the 2θ position of the diffraction peak.

small peaks appeared at positions 4.131, 4.767, 6.338, 7.171 and 8.543° and this is indexed as (1,1), (2,0), (2,1), (3,0) and (3,1), respectively (Figure 3, c). During the next heating cycle from 300 to 350 K, the complex showed a strong peak at 2θ = 2.476°. Small peaks at this temperature were observed at positions 4.262, 4.909, 6.516, 7.376 and 8.695°, which can be indexed as (1,0), (1,1), (2,0), (2,1), (3,0) and (3,1), respectively (Figure 3, d). After cooling the sample from 350 to 300 K, the first strong peak appeared at position 2θ = 2.458° and the small peaks appeared at positions 4.228, 4.926, 6.485, 7.341 and 8.793°. The smaller peaks can be indexed as (1,0), (1,1), (2,0), (2,1), (3,0) and (3,1), respectively (Figure 3, e).

All visible peaks can be indexed in a two-dimensional hexagonal lattice with lattice parameters a equal to 43.64, 43.56, 42.68, 41.14 and 41.50 Å for 300, 250, 300, 350 and again 300 K, respectively. Similar results were obtained for the liquid-crystalline dendritic triazole iron(II) complexes reported by Fujigaya[22] and Seredyuk.[27] Our earlier paper on this work also reported some common observations.[21]

Magnetic Measurements of the Dendritic Triazole Iron(II) Complexes

The magnetic properties of **1** were investigated with a superconducting quantum interference device (SQUID) magnetometer at variable temperatures following the sequence 150→350→1.7→350 K. The results are plotted as $\chi_M T$ versus T in Figure 4 (a). For a first heating process from 150 to 250 K, the $\chi_M T$ curve shows a gradual increase in the $\chi_M T$ values. After heating above 250 K, the curve ends in a plateau with an $\chi_M T$ value around 2.8 $cm^3 K mol^{-1}$, which is about 20% below that expected for the spin-only value of iron(II) in the high-spin state. On cooling, the $\chi_M T$ values match perfectly those of the heating branch in the temperature between 350 and 250 K. When the temperature is lowered from 250 K down to 1.7 K, the $\chi_M T$ value initially remains constant and then, at about 210 K, starts to lower more gradually compared to the first heating process. It finally reaches a value of 0.28 $cm^3 K mol^{-1}$ at 1.7 K. The spin-transition temperature T_{SC} (at which 50% of all complex molecules actively involved in the thermal spin transition have changed the spin states from high spin to low spin on cooling) of complex **1** is about 30 K. After the first heating process, the $\chi_M T$ curves in both cooling and heating directions are completely reversible and no hysteresis was observed. The shape of the $\chi_M T$ curves in this case, and somewhat similar also in the cases of Figure 4 (b and d), resemble very much the curves for thermal variation of the high-spin fraction in SCO systems with low-spin transition temperatures (i.e., with small energy gaps between HS and LS states). It has been proposed that in such cases the SCO characteristics, or rather the magnetic response functions $\chi_M T$, may be essentially determined by the molecular vibrations due to the closeness of the effective vibrational gap to the electronic gap.[28]

The magnetic properties of **2** were studied following the temperature sequence of 200→350→6→350 K. The $\chi_M T$ versus T values are shown in Figure 4b. In the first heating process from 200 to 350 K, the $\chi_M T$ values increase from 1.7 (at 200 K) to 2.45 $cm^3 K mol^{-1}$ (at 305 K). In the temperature range 280–305 K, the $\chi_M T$ values change sharply and merge into a plateau with a $\chi_M T$ value of 2.8 $cm^3 K mol^{-1}$. After this first heating process, the $\chi_M T$ versus T curve shows a gradual spin transition upon cooling from 350 to 6 K, at which point the $\chi_M T$ value reaches 0.5 $cm^3 K mol^{-1}$. The second heating curve from 6 to 350 K matches well with the cooling curve but cannot reproduce the same sharp transition that was observed during the first heating process.

The magnetic properties of the freshly synthesized iron(II) complex **3** were characterized by following the temperature sequence of 80→350→5.5→350 K; the results

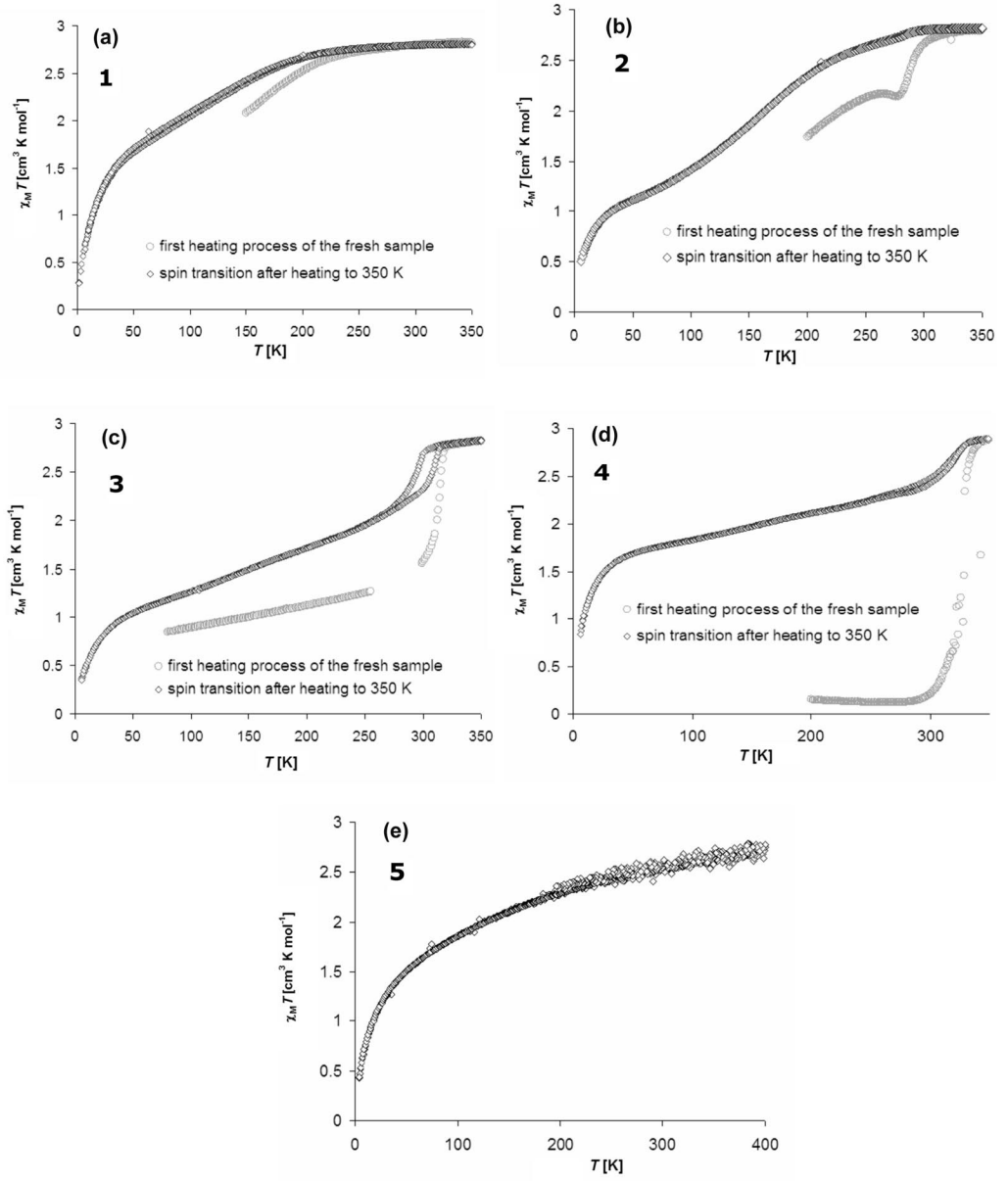

Figure 4. Thermal dependence of $\chi_M T$ of complexes (a) **1**, (b) **2**, (c) **3**, (d) **4** and (e) **5**.

are shown in Figure 4 (c). The $\chi_M T$ values increase mildly with increasing temperature in the region 80 to 350 K, starting from an $\chi_M T$ value of 0.85 $cm^3 K mol^{-1}$ at 80 K. Apparently, the thermal spin transition is very gradual due to weak cooperativity between the complex molecules in this material. After crossing the temperature from 300 K onward, the spin state changes very sharply and merges into a plateau with an $\chi_M T$ value of 2.8 $cm^3 K mol^{-1}$ at 320 K. Upon cooling from 350 to 5.5 K, the $\chi_M T$ value remains nearly constant between the 350 and 300 K zone but on further cooling down to 280 K, $\chi_M T$ decreased rather gradually from 2.7 to 2.2 $cm^3 K mol^{-1}$. At 50 K an $\chi_M T$ value of 1.0 $cm^3 K mol^{-1}$ was recorded. Below 50 K the $\chi_M T$ value dropped down to 0.35 $cm^3 K mol^{-1}$ at 5.5 K most likely due to the well-known zero-field-splitting effect. In the second heating process from 5.5 to 350 K, the transition curve matches very well that of the cooling mode. The $\chi_M T$ values start rising sharply between 5.5 and 50 K. Further heating leads to much more gradual spin transition until the sample is heated up to 300 K. During this cycle the $\chi_M T$ values change from 1.0 to 2.3 $cm^3 K mol^{-1}$. Another sharp transition appeared between 300 and 317 K, at which the $\chi_M T$ values change from 2.3 to 2.8 $cm^3 K mol^{-1}$. A hysteresis loop of around 15 K width has been observed in the temperature region between 270 and 300 K.

The magnetic characteristics of **4** were measured in the temperature sequence of 200→350→6→350 K, as shown in Figure 4 (d). During the first heating step from 200 to 350 K, this iron(II) complex shows an extremely sharp spin-state change from the low-spin to the high-spin state. The $\chi_M T$ values change from 0.15 to 2.9 $cm^3 K mol^{-1}$ within a relatively narrow temperature range of 290 to 350 K. Dur-

ing the subsequent cooling and heating processes, the $\chi_M T$ versus T curve is much more gradual relative to the first heating process. As the temperature is lowered from 350 to 300 K, $\chi_M T$ first remains constant and then decreases more strongly between 330 and 300 K; the $\chi_M T$ values decrease from 2.4 to 1.7 $cm^3 K mol^{-1}$. With a further decrease in temperature down to 6 K, the $\chi_M T$ values decrease to 0.84 $cm^3 K mol^{-1}$, thereby revealing an incomplete HS→LS conversion. The drop of $\chi_M T$ at temperatures below 50 K is again most likely due to the occurrence of zero-field splitting of the remaining HS iron(II) ions. There was no obvious difference in the $\chi_M T$ values between the cooling and heating curves and hysteresis was not observed.

Figure 4 (e) shows the thermal dependence of the $\chi_M T$ values of the iron(II) complex **5**. The magnetic properties were measured in the temperature regime between 400 and 4 K following the sequence of 330→4→400 K. At room temperature, the $\chi_M T$ value is 2.5 $cm^3 K mol^{-1}$, which points to the presence of a small fraction of low-spin molecules. Cooling the sample leads to a gradual $\chi_M T$ curve with values of 1.5 $cm^3 K mol^{-1}$ at 50 K and 0.44 $cm^3 K mol^{-1}$ at 4 K. The $\chi_M T$ versus T response is completely reversible. During these measurements we did not find any plateau despite heating the sample up to 400 K. The $\chi_M T$ value at 400 K was around 2.7 $cm^3 K mol^{-1}$.

From all these measurements of the dendritic triazole complexes under study, it is quite clear that the magnetic behaviour depends on various factors such as the nature of the counteranions, the structure of the dendrons attached to the triazoles and the type of the spacer between the triazole nitrogen and the dendron (NH–C=O and CH_2 spacing).

^{57}Fe Mössbauer Spectroscopy Study of the Dendritic Triazole Iron(II) Complexes

The measured Mössbauer spectra of all dendritic triazole iron(II) complexes under study are shown in Figure 5. The corresponding hyperfine parameters obtained from least-squares fitting to Lorentzians are collected in Table 1.

A representative Mössbauer spectrum of complex **1** recorded at 80 K is shown in Figure 5 (a). The spectrum shows two quadruple doublets. The best fits could be obtained with isomer shift δ = 0.55 mm s^{-1} and quadrupole splitting ΔE_Q = 0.28 mm s^{-1} for the inner doublet, which is typical for iron(II) in the low-spin state, whereas the parameter values δ = 1.17 mm s^{-1} and ΔE_Q = 3.35 mm s^{-1} for the doublet that consists of the outer two lines that are assigned to the high-spin state of the iron(II) site. The large quadrupole splitting mainly arises from a noncubic valence electron contribution to the electric field gradient and calls for a compressed octahedral coordination sphere around iron(II) sites. The area ratio A_{HS}/A_{HS+LS} (A_{HS} = area of the HS doublet; A_{HS+LS} = total area of the HS and LS doublets) shows that still 70% of HS exists in the sample at 80 K. The estimation is based on the assumption that the Lamb–Mössbauer factors for HS and LS states are similar.

The Mössbauer spectrum of complex **2** recorded at 80 K is displayed in Figure 5 (b). The fitted parameters are δ = 0.54 mm s^{-1} and ΔE_Q = 0.31 mm s^{-1} with reference to the low-spin state and δ = 1.16 mm s^{-1} and ΔE_Q = 3.42 mm s^{-1} for the high-spin state of the iron(II) sites. These parameter values are typical for LS and HS iron(II) sites in $Fe^{II}N_6$ core complexes. The area fraction of about 35% of HS in the sample of **2** at 80 K is much lower than that of **1** at the same temperature. This can be explained by the hydrogen-bonding interaction being more dominant in compound **2** than in **1**, which plays a crucial role in stabilizing the LS state.[29] A structural proof was given by single-crystal X-ray diffraction on a trinuclear triazole iron(II) SCO compound.[30]

The Mössbauer spectra of **3** (fresh sample) were recorded at 80 and 4 K, respectively, and the fitted spectra are shown in Figure 5 (c). The parameters obtained from the fitting procedure of the 80 K spectrum are δ = 0.49 mm s^{-1} and ΔE_Q = 0.21 mm s^{-1} for the LS state and δ = 1.19 mm s^{-1} and ΔE_Q = 3.30 mm s^{-1} for the HS state of iron(II). The area fraction A_{HS}/A_{HS+LS} comes out to be γ = 0.36 at 80 K and only slightly lower with γ = 0.29 at 4 K.

The Mössbauer spectra of **4** (fresh sample) were also recorded at 80 and 4 K, as shown in Figure 5 (d). At 80 K the spectrum shows a major doublet (with area fraction of 94%) with an isomer shift of 0.47 mm s^{-1} and a quadrupole splitting of 0.21 mm s^{-1}, which is assigned to the iron(II) LS sites. The minor contribution of 6% with isomer shift of 1.16 mm s^{-1} and a large quadrupole splitting of 3.50 mm s^{-1} refers to high-spin iron(II) sites. Corresponding to the SQUID data, the value of 0.15 $cm^3 K mol^{-1}$ (at 200 K) of a fresh sample at low temperature probably arises from a small fraction of HS sites located at hydrated chain-end positions.[22,31] Therefore, the average degree of polymerization (D_p) can be estimated to be about 37 using the equation $D_p = 2\chi T_{HS}/\chi T_{LS}$.[27] However, with Mössbauer spectroscopy data it is possible to calculate D_p at very low temperatures, at which the zero-field splitting prevails in many instances and vitiates the determination of the magnetic susceptibilities that originate from the spin transition. It turned out that the 6% of iron(II) in the HS state determined by Mössbauer spectroscopy at 80 K had converted totally (to less than two percent, which is approximately the detection limit of Mössbauer spectroscopy) into low spin upon further cooling; the spectrum recorded at 4 K contains no more resonances of Fe^{II} in the HS state. By taking an error limit of maximum 2% in the high-spin signal into account, we can estimate that the average chain length would contain about one hundred iron(II) centres.

An estimate of D_p was possible only for complex **4**, because it was the only one among the five compounds under study that showed an extended plateau in the $\chi_M T$ versus T plot of the low-spin phase. For the other complexes, it cannot be decided whether the residual high-spin species in the low-temperature region arise mainly from iron(II) complexes at the end of the iron–triazole chains or whether other influences are operative such as various kinds of defects in the crystal lattice that are responsible for the incomplete spin transition.

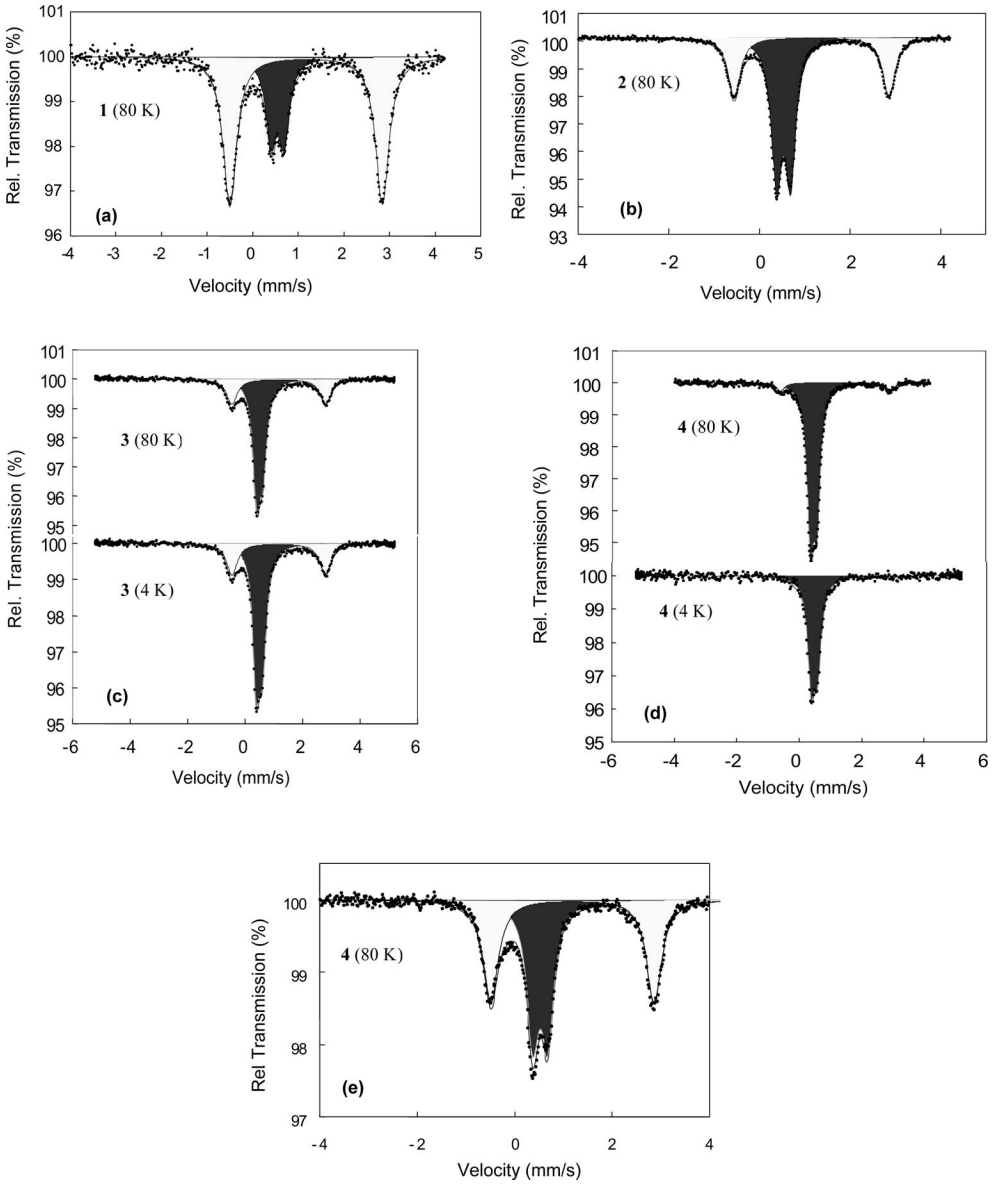

Figure 5. ^{57}Fe Mössbauer spectra of the iron(II) dendritic complexes (a) **1**, (b) **2**, (c) **3**, (d) **4** and (d) **5** at the temperatures indicated in the figures.

Table 1. ^{57}Fe Mössbauer spectrum parameters for all the iron(II) complexes under study.

Complexes	Low-spin state				High-spin state			
	T [K]	δ [mm s^{-1}]	ΔE_Q^{LS} [mm s^{-1}]	$\Gamma/2$ [mm s^{-1}]	δ [mm/s]	ΔE_Q^{HS} [mm s^{-1}]	$\Gamma/2$ [mm s^{-1}]	A_{HS}/A_{HS+LS} [%]
$[Fe(G1\text{-}BOC)_3](triflate)_2 \cdot xH_2O$ (**1**)	80	0.55	0.28	0.14	1.17	3.35	0.18	70
$[Fe(G1\text{-}BOC)_3](tosylate)_2 \cdot xH_2O$(**2**)	80	0.54	0.31	0.14	1.16	3.42	0.17	35
$[Fe(G1\text{-}DPBE)_3](triflate)_2 \cdot xH_2O$ (**3**)	80	0.49	0.21	0.15	1.19	3.30	0.21	36
$[Fe(G1\text{-}DPBE)_3](triflate)_2 \cdot xH_2O$ (**3**)	4	0.49	0.21	0.17	1.17	3.26	0.24	29
$[Fe(G1\text{-}DPBE)_3](tosylate)_2 \cdot xH_2O$ (**4**)	80	0.47	0.21	0.13	1.16	3.50	0.16	6
$[Fe(G1\text{-}DPBE)_3](tosylate)_2 \cdot xH_2O$ (**4**)	4	0.48	0.21	0.15	–	–	–	0
$[Fe(G1\text{-}DPBE)_3](BF_4)_2 \cdot xH_2O$ (**5**)	80	0.53	0.31	0.15	1.19	3.35	0.19	49

A sample of complex **5** showed nearly half of low-spin and high-spin states at 80 K as can be distinguished from Figure 5 (e). The parameters for the complex molecules in the LS state are δ = 0.53 mm s^{-1} and ΔE_Q = 0.31 mm s^{-1}, whereas for those in the HS state these values are δ = 1.19 mm s^{-1} and ΔE_Q = 3.35 mm s^{-1}. It is worth noting that the relatively large quadrupole splitting of 3.35 mm s^{-1} for HS-Fe^{II} sites, which seems to arise mainly from a noncubic distribution of valence electrons around the iron(II) centres, points to a relatively high symmetry (close to O_h) of the

FeN_6 chromophore despite the bulkiness of the dendritic ligands. There appears to be little perturbation of the FeN_6 cores that leads to a rather small lattice contribution to the electric field gradient, which usually opposes the valence electron contribution.

Thermal Properties of the Dendritic Triazole Iron(II) Complexes

The TGA and DSC curves of the iron(II) complexes **1** to **5** are presented in Figures 6 and 7, respectively. The TGA curves of **1** and **2** show similar weight-loss profiles (see Figure 6, a and b). Both complex compounds started to show weight loss at around 50 °C and had weight loss of about 5 and 6% when the temperature reached around 100 °C. The weight can be attributed to the loss of about five and six molecules of water from the iron(II) complexes **1** and **2**. In each complex there are two regions of sharp weight loss above 150 °C, which can be attributed to the decomposition of the alkyl chain of the complexes. During water release, the DSC curves show strong endothermic peaks around 70 °C and one further peak at about 150 °C. Both signals

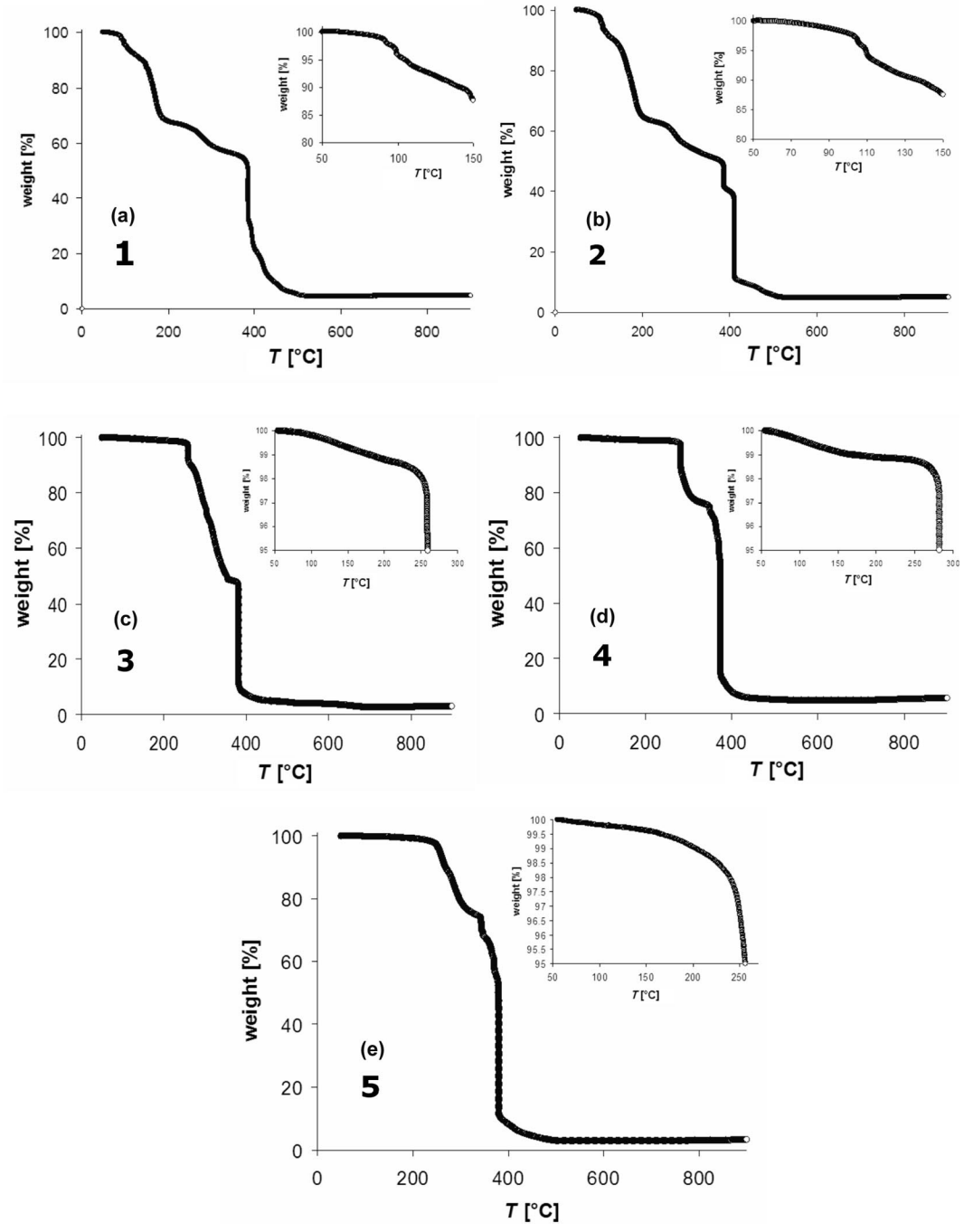

Figure 6. TGA data of the iron(II) dendritic complexes (a) **1**, (b) **2**, (c) **3**, (d) **4** and (e) **5**.

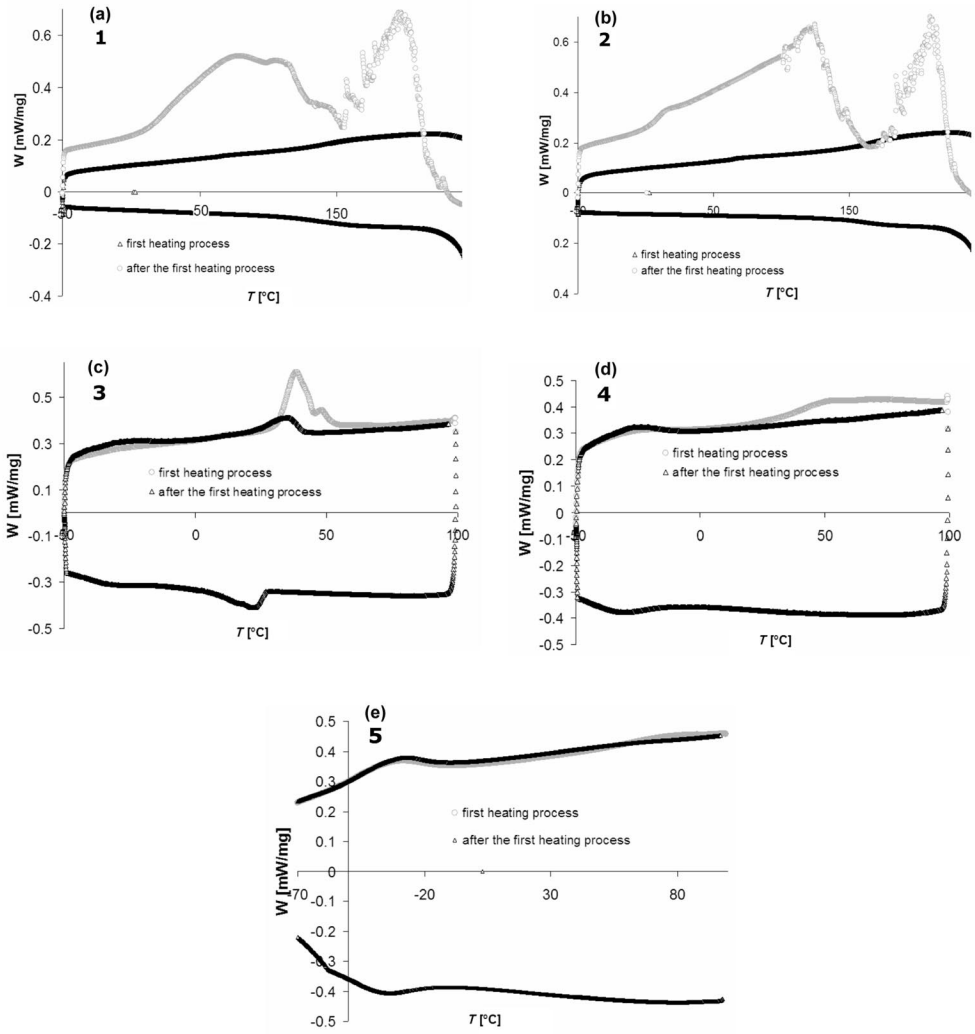

Figure 7. DSC data of the iron(II) dendritic complexes (a) **1**, (b) **2**, (c) **3**, (d) **4** and (e) **5**.

are of rather complicated shape, which points to the occurrence of a combination of water release and structural rearrangement. The latter peak around 150 °C might be due to decomposition of the compound. After the first heating process, there were no endothermic or exothermic peaks detected in the range between 50 and 250 °C. Only a small change in the slope of the curve can be recognized around 150° for compound **1** and at about 170 °C for compound **2**, which probably indicates small structural changes due to alkyl-chain-length reduction. The calculation of the enthalpy and entropy of the heating and cooling processes was not possible due to the overlap of the signals in the calorimetric data.

The results obtained from the thermal analysis are in agreement with the interpretation of the magnetic properties. Water loss detected by TGA indicates a drastic change of spin state in the magnetic response function $\chi_M T$ versus T, which is irreversible due to the loss of noncoordinated water. The complex signals around 70 °C observed by DSC further confirm the irreversible nature due to structural rearrangement of the fresh sample into a thermodynamically more stable configuration. Therefore, the thermally induced release of noncoordinated water molecules alters markedly the magnetic behaviour of these complex compounds.

In the first heating branch of complex **3**, there were two sharp endothermic peaks in the DSC curve observed at 40 and 50 °C (Figure 7, c). These changes are in accordance with the sharp increases in the $\chi_M T$ versus T curve in the same temperature region. After the first warming, the $\chi_M T$ versus T curve is irreversible because of loss of crystal water. This complex shows about 1.3% loss of weight before decomposition of the sample starts above 250 °C, as seen in the TGA curve (Figure 6, c). The declining mass of the iron(II) complex assigns a loss of about 2.7 molecules of water. During the second cycle of DSC, the calorimetric feature showed much weaker endothermic and exothermic peaks. The different temperature peak maxima in the second cycle of DSC can be attributed to the observed small hysteresis in the $\chi_M T$ curves. In this case, it seems that the change of spin state is a direct consequence of the release of water and would probably not occur without it. There-

fore, the increasing $\chi_M T$ values are not an indication of thermal spin transition, but moreover an irreversible change of spin state.

In the case of **4**, the effect of loss of water on the spin state is even more pronounced relative to the other complexes. The TGA data (Figure 6, d) signal the loss of water around 60 °C, which amounts to 1.6 molecules of water per formula unit. As an immediate consequence, this complex shows abrupt and irreversible change of spin state from low spin to high spin at about 60 °C. The DSC data did not show any noticeable change, which is most likely due to the fact that an extra dried sample was used particularly for this DSC analysis. After the synthesis of this complex, the sample was dried under high vacuum for a long time. The TGA curve of **5** is shown in Figure 6 (e). The gradual weight loss of the complex is due to evaporation of the solvent from the complex. The weight loss between 200 and 250 °C is related to the decomposition of the compound. The water content of the fresh complex is less than 1%, which corresponds to the loss of less than one molecule of water per formula unit. A rapid loss in weight due to decomposition of the complex was observed in the temperature range of 250–380 °C. The DSC curve of **5** showed moderate and broad (ΔT of around 50 °C) exothermic and endothermic peaks at about –30 °C during heating and cooling cycles. These peaks not only arise from a HS→LS transition but also presumably from structural rearrangements.[32]

From all these observations it is clear that in each series of complexes, the abruptness of spin-state changes is more pronounced in the freshly prepared tosylate-based iron(II) complexes than in the triflate compounds. The only exception is **5**, which showed a gradual change of spin state. This is most likely due to the absence or little content of noncoordinated water in this complex. Kahn et al. previously reported this kind of gradual change of spin state as a function of temperature, which they suggested to arise from a combination of thermal spin-state change and dehydration process.[23] The dehydrated complex is stable under normal conditions, and the sharp spin-state change is not reversible after the heating process. The influence of noncoordinated water on the spin state is much more pronounced in the G1-DPBE derivatives in which the difference in the magnetic behaviour between a fresh sample and a heated one is more evident than in the others. For example, the freshly prepared sample of **4** was diamagnetic at the beginning and became paramagnetic after heating. Thus the observed spin-state change that occurred above room temperature was driven by the release of the noncoordinated water molecules upon heating, and this procedure is not reversible. The dehydrated forms of the iron(II) complexes do no show abrupt spin-state changes around room temperature but rather a gradual and reversible thermal spin crossover below room temperature. This can be understood as a consequence of changes of lattice parameters due to loss of water. In this compound the loss of water is particularly small, whereas the changes of the two-dimensional hexagonal lattice parameters *a* are remarkably strong, which supports the aforementioned explanation. It is conceivable that the structure of a thermally cycled sample has a different hydrogen-bonding network than a sample before thermal treatment. For the complex **4**, the lattice parameter *a* is bigger for the LS state, which is consistent with similar compounds reported in the literature.[33] Complex **5** shows a significant loss of water below 350 K; it is therefore difficult to correlate the lattice parameter *a* with the spin-state change.

According to the results of the TGA measurements, the content of noncoordinated water molecules per formula unit is different in all the complex compounds under study and amounts to $x = 5$ in **1**, $x = 6$ in **2**, $x = 2.7$ in **3**, $x = 1.6$ in **4** and $x = 1$ in **5**. As these numbers are only approximate estimates, which most likely vary from one preparation to another of one and the same compound, we have preferred not to articulate the water content in the chemical formulae of the five systems under study. The common feature in all cases, however, is the more or les dramatic change of spin state on losing water by warming the substance.

Fujigaya et al. published[22] a report on (G*n*-trz)Fe-based (n = 0–2) dendritic triazole complexes that showed spin-transition dependence on the generation number (n) of the dendritic unit. They observed a similar behaviour for their (G1-trz)Fe complexes with a most abrupt spin transition. We also selected the same triazole dendritic ligands for making iron(II) complexes with different counteranions and tried to correlate the influence of various anions on the spin-transition behaviour. From the behaviour of the $\chi_M T$ versus T function, it is clear that noncoordinated water molecules play a crucial role. Attention should be drawn to the possibility that the ligand influences strongly depend on how the noncoordinated water interacts with the ligands through hydrogen bonding. It is known that if water is hydrogen-bonded to the ligand through N–H···OH_2 interaction close to the coordinating triazole ring of the ligand, the complex tends to stabilize in the LS state; if the hydrogen bonding occurs in the mode N···H_2O, the HS state is favoured.[29] Comparing the magnetic properties of [Fe(G1-DPBE)$_3$](A)$_2$·$x$$H_2O$ (A = triflate and tosylate) and the complexes [Fe(G1-BOC)$_3$](A)$_2$·$x$$H_2O$ (A = triflate and tosylate), the NH groups indeed exist in both structures (G1-BOC and G1-DPBE complexes), whereas the earlier studied G1-PBE derivatives do not have such NH groups. The influence of water in both derivatives {[Fe(G1-DPBE)$_3$](A)$_2$·$x$$H_2O$ (A = triflate and tosylate) and [Fe(G1-BOC)$_3$](A)$_2$·$x$$H_2O$ (A = triflate and tosylate)} seems to be much more predominant than in the earlier studied G1-PBE derivatives because of the formation of N–H···OH_2 hydrogen-bonding interaction that involves the noncoordinated water molecules. Furthermore, G1-BOC-based dendritic triazole has three –NH groups in the structure, among which only one is connected to the triazole ring. In this case, the –NH group connected to the triazole ring in G1-BOC-based iron(II) complexes is less suited to the formation of N–H···OH_2 hydrogen bonding than the –NH group in G1-DPBE. As a result, G1-DPBE derivatives show much more abrupt spin transition in the first warming procedure. On the contrary,

the magnetic properties of G1-PBE derivatives show almost no difference between the fresh sample and the heated one.

Conclusion

We have synthesized first-generation dendritic triazole-based ligands and their iron(II) complexes with different counteranions. Their thermal, magnetic and spin-transition properties were studied in detail using various characterization techniques. All complexes showed spin-transition behaviour that is dependent on the coordinated water molecules present in the iron(II) complex. Spin-state conversion was triggered by thermally induced water release and a gradual spin transition took place after a first heat treatment to 350 K. The $[Fe(G1\text{-}DPBE)_3](BF_4)_2{\cdot}xH_2O$ (**5**) iron(II) complex shows exceptional behaviour due to lack or little content of crystal water in the initial sample. Therefore, this particular iron(II) complex did not show any change in the spin-state change behaviour between initial and first heating cycle, whereas complexes **1** to **4** clearly show noticeable changes in magnetic behaviour upon heating. The influence of noncoordinated water is more predominant in iron(II) complexes with tosylate than with triflate anions. Similar effects are also observed for G1-DPBE-based iron(II) complexes than G1-BOC-based derivatives. The nature of the counteranions and the type of dendritic ligands play an important role for the magnetic behaviour as reflected by the $\chi_M T$ versus T curve and by variable-temperature Mössbauer spectroscopy.

Experimental Section

Materials and Characterization: Commercially available chemicals were reagent grade and used without further purification. The synthesis of dendritic ligands were published by Fujigaya et al.[22] and Sonar et al.[21] ^{1}H (300 MHz) and ^{13}C (62.5 MHz) NMR spectroscopy was carried out on a Bruker spectrometer at room temperature. Elemental analysis (C, H, N and S Analyzer) and mass spectrometry (Ionspec Ultrima spectrometer) techniques were utilized for the confirmation and purity of the samples. 1*H*-1,2,4-triazole-1-propanenitrile was synthesized from 1*H*-1,2,4-triazole and acrylonitrile as described in the literature.[31] Infrared spectra were recorded by using a Brooker Tensor 27 with samples prepared as pellets in KBr. DSC measurements were performed on Perkin–Elmer, Norwalk, Connecticut, whereas TGA analyses were carried out on TA Instruments, New Castle, Delaware. The elemental analyses of all complexes were performed on a Vario EL (Elemental) for C, H, N and S determination. For structural investigations powder X-ray diffraction were recorded at 300, 250 K and then again at 300, 350 and 300 K, with Cu-K_α radiation using a PANalytical X'Pert PRO diffractometer equipped with the Paar HTK 1200. The temperature-dependent magnetic susceptibilities were measured on a MPMS SQUID device of Quantum Design. The magnetic data were corrected for magnetization of the sample holder and diamagnetic contributions. ^{57}Fe Mössbauer spectroscopy was carried out at 80 K using a constant-acceleration conventional spectrometer with a nitrogen cryostat. The source used was ^{57}Co in a Rh matrix with an activity of about 10 mCi kept at room temperature. For measurements at 4 K the samples were immersed in helium gas in a helium cryostat. In this case the used source was ^{57}Co in a Rh matrix with an activity of about 5 mCi kept at 4 K. It was impossible to record Mössbauer spectra at room temperature within acceptable measuring time because of the softness of the material with too low Debye temperatures. The isomer shift values are given with reference to α-iron.

Synthesis of Ligands and Complexes

Synthesis of G1-BOC (A): Triethylamine (1 mL, 6.88 mmol), 4-amino-1,2,4-triazole (0.89 g, 10.6 mmol) and diphenyl (2,3-dihydro-2-thioxo-3-benzoxazolyl) phosphonate (DBOP) (2.63 g, 6.87 mmol) were added to a solution of **A′** (3.00 g, 6.88 mmol) in 150 mL of THF at room temperature. The mixture was heated at reflux overnight and allowed to cool to room temperature. The organic solvent was evaporated and the crude compound purified by column chromatography using hexane/ethyl acetate mixture as eluent (gradient from 100:0 to 90:10). The fraction was collected and the solvents evaporated to dryness to give compound **5** as white powder (yield: 72%, 2.50 g). ^{1}H NMR ($CDCl_3$): δ = 8.56 (s, 2 H, Trz), 7.61 (s, 2 H, Ph), 7.33 (s, 1 H, Ph), 4.70 (s, 3 H, NH), 3.09 (t, 4 H, $2CH_2$), 2.73 (t, 4 H, $2CH_2$), 1.86 (t, 2 H, 2CH), 1.32 (s, 18 H, $6CH_3$) ppm. ^{13}C NMR ($CDCl_3$): δ = 168.14, 157.92, 143.65, 134.45, 131.31, 126.14, 79.72, 48.90, 40.35, 33.35, 31.96, 30.82, 28.69, 24.07 ppm. MALDI-TOF calcd. for $C_{25}H_{38}N_6O_5$: $[M + H]^+$ 502.62; found 502. $C_{25}H_{38}N_6O_5$ (502.61): calcd. C 59.74, H 7.62, N 16.72; found C 59.14, H 7.09, N 16.28.

Synthesis of $[Fe(G1\text{-}BOC)_3](triflate)_2{\cdot}xH_2O$ (1): A solution of $Fe(triflate)_2{\cdot}6H_2O$ (0.13 mmol, 0.062 g) and ascorbic acid [0.014 g; to prevent iron(II) from oxidation] in methanol (1 mL) were added dropwise to a solution of G1-BOC (0.4 mmol, 0.2012 g) in methanol (2 mL) at 60 °C while stirring. The reaction mixture was stirred for one hour at 60 °C and then was cooled down to room temperature. The solvent was removed under reduced pressure, and the colourless colloidal substance precipitated on cooling with liquid nitrogen. The product was fast-washed with cold MeOH and THF and dried in vacuo; yield 93%. $C_{77}H_{114}F_6FeN_{18}O_{21}S_2$ (1861.81): calcd. C 49.63, H 6.12, N 13.53, S 3.44; found C 47.15, H 5.93, N 12.10, S 4.14. IR (KBr pellets): $\tilde{\nu}$ = 2978.6 (m, CH_3), 2936.0 (–CH_2–), 758.8, 715.2, 640.1 (m, substituted Ar), 3365.8, 1690.2 (s, –CONH–), 1029.8 (s, CF_3), 1277.9, 1251.5 (m, R–SO_3^-), 1524.5, 1455.1, 1394.2, 1367.4, 1168.8 (triazole) cm^{-1}.

Synthesis of $[Fe(G1\text{-}BOC)_3](tosylate)_2{\cdot}xH_2O$ (2): A similar procedure as described above was employed to obtain the complex **2**, except for the quantity of the $Fe(tosylate)_2{\cdot}6H_2O$ salt (0.068 g, 0.13 mmol); yield 96%. $C_{89}H_{128}FeN_{18}O_{21}S_2$ (1906.07): calcd. C 56.03, H 6.72, N 13.22, S 3.36; found C 54.66, H 6.96, N 11.31, S 3.33. IR (KBr pellets): $\tilde{\nu}$ = 2977.4 (m, CH_3) 2932.6 (–CH_2) 684.0, 625.1 (m, substituted Ar) 3358.0, 1692.5 (s, –CONH–) 1275.1, 1251.5 (m, R–SO_3^-), 1523.7, 1453.6, 1392.7, 1366.2, 1170.7 (triazole) cm^{-1}.

Synthesis of $[Fe(G1\text{-}DPBE)_3](triflate)_2{\cdot}xH_2O$ (3): A methanol solution of $Fe(triflate)_2{\cdot}6H_2O$ (0.0310 g, 0.067 mmol) that contained a small amount of ascorbic acid was added dropwise to a solution of G1-DPBE (0.227 g, 0.2 mmol) in 20 mL of THF at 70 °C. The reaction mixture was stirred at this temperature for about 30 min, then cooled down to room temperature. The solvent was partially removed under reduced pressure until the solution was separated into two layers. The pink gelatine-form product was cooled with liquid nitrogen, washed with cold methanol and was dried under vacuum; yield 89%. $C_{215}H_{348}F_6FeN_{12}O_{27}S_2$ (3767.13): calcd. C 68.49, H 9.24, N 4.46, S 1.70; found C 69.13, H 10.27, N 4.40, S 2.39. IR (KBr pellets): $\tilde{\nu}$ = 1606.2, 1594.8 (s, Ar), 2921.3, 2853.6 (–CH_2–), 813.4, 720.8, 681.3, 639.9 (m, substituted Ar), 1074.0 (s,

C–O), 1699.0 (s, –CONH–), 1157.2 (s, CF_3), 1252.8 (m, R–SO_3^-), 1465.3, 1377.7, 1349.5, 1327.7, 1174.6 (triazole) cm^{-1}.

Synthesis of [Fe(G1-DPBE)$_3$](tosylate)$_2$·*x*H$_2$O (4): A similar procedure was employed to prepare **4** using Fe(tosylate)$_2$·6H$_2$O (0.0338 g, 0.067 mmol) and G1-DPBE (0.2271 g, 0.2 mmol); yield 93%. $C_{227}H_{362}FeN_{12}O_{27}S_2$ (3811.39): calcd. C 71.47, H 9.50, N 4.41, S 1.68; found C 71.31, H 9.51, N 4.30, S 1.79. IR (KBr pellets): $\tilde{\nu}$ = 1599.3 (s, Ar), 2923.5, 2853.3 (–CH_2–), 683.7 (m, substituted Ar), 1054.6 (m, C–O) 1696.4 (s, –CONH–), 1217.3 (m, R–SO_3^-), 1466.0, 1378.5, 1348.9, 1326.2, 1164.5 (triazole) cm^{-1}.

Synthesis of [Fe(G1-DPBE)$_3$](BF$_4$)$_2$·*x*H$_2$O (5): The same procedure as for **4** was employed to prepare **5** using Fe(BF$_4$)$_2$·6H$_2$O (0.0231 g, 0.067 mmol) and G1-DPBE (0.2252 g, 0.2 mmol), and was dried under vacuum; yield 90%. $C_{223}H_{348}B_2F_8FeN_{12}O_{21}$ (3762.72): calcd. C 70.23, H 9.62, N 4.61; found C 70.28, H 9.50, N 4.41.

Acknowledgments

We are thankful to B. Mathiasch for the performance of infrared spectroscopy, to M. Colussi for help with DSC and TGA measurements and to Dr. Christian Baerlocher for the XRD measurements (ETH Zürich). We acknowledge the financial support from the Deutsche Forschungsgemeinschaft (DFG), Priority Program no. 1137 ("Molecular Magnetism").

[1] D. J. Díaz, G. D. Storrier, S. Bernhard, K. Takada, H. D. Abruña, *Langmuir* **1999**, *15*, 7351–7354.
[2] G. R. Newkome, C. N. Moorefield, F. Vögtle, *Dendrimers and Dendrons: Concepts, Syntheses, Applications*, VCH, Weinheim, **2001**. J. M. J. Fréchet, D. A. Tomalia (Eds.), *Dendrimers and Other Dendritic Polymers*, Wiley, Chichester, **2001**.
[3] F. Zeng, S. C. Zimmerman, *Chem. Rev.* **1997**, *97*, 1681–1712.
[4] D. A. Tomalia, A. M. Naylor, W. A. Goddard III, *Angew. Chem. Int. Ed. Engl.* **1990**, *29*, 138–175.
[5] M. Fischer, F. Vögtle, *Angew. Chem. Int. Ed.* **1999**, *38*, 884–905.
[6] J.-M. J. Fréchet, *Science* **1994**, *263*, 1710–1715.
[7] M. Benito, O. Rossell, M. Seco, G. Segalés, V. Maraval, R. Laurent, A.-M. Caminade, J.-P. Majoral, *J. Organomet. Chem.* **2001**, *622*, 33–37.
[8] E. C. Constable, C. E. Housecroft, M. Neuburger, S. Schaffner, L. J. Scherer, *Dalton Trans.* **2004**, 2635–2642.
[9] C. Díaz, M. Barbosa, Z. Godoy, *Polyhedron* **2004**, *23*, 1027–1035.
[10] M. T. Reetz, G. Lohmer, R. Schwickardi, *Angew. Chem. Int. Ed. Engl.* **1997**, *36*, 1526–1539.
[11] F. G. A. Jansen, E. M. M. de Brabander-van den Berg, E. W. Meiser, *Recl. Trav. Chim. Pays-Bas* **1995**, *114*, 225–230.
[12] J. W. J. Knapen, A. W. van der Made, J. C. de Wilde, P. W. N. M. van Leeuven, P. Wijkens, D. M. Grove, G. van Koten, *Nature* **1994**, *372*, 659–663.
[13] a) A. Miedaner, C. J. Curtis, R. M. Barkley, D. L. DuBois, *Inorg. Chem.* **1994**, *33*, 5482–5490; b) A. M. Herring, B. D. Steffey, A. Miedaner, S. A. Wander, D. L. DuBois, *Inorg. Chem.* **1995**, *34*, 1100–1109.
[14] M. Slany, M. Bardaji, A.-M. Caminade, B. Chaudret, J. P. Majoral, *Inorg. Chem.* **1997**, *36*, 1939–1945.
[15] M. Enomoto, T. Aida, *J. Am. Chem. Soc.* **2002**, *124*, 6099–6108.
[16] a) *Topics in Current Chemistry*, vol. 233–235, *Spin Crossover in Transition Metal Compounds*, parts I–III (Eds.: P. Gütlich, H. A. Goodwin), Springer, Berlin, Heidelberg, **2004**; b) P. Gütlich, A. Hauser, H. Spiering, *Angew. Chem. Int. Ed. Engl.* **1994**, *33*, 2024–2054; *Angew. Chem.* **1994**, *106*, 2109–2141.
[17] J.-F. Létard, P. Guionneau, L. Goux-Capes, *Top. Curr. Chem.* **2004**, *235*, 221–249.
[18] a) O. Kahn, *Curr. Opin. Solid State Mater. Sci.* **1996**, *1*, 547–556; b) P. Gütlich, Y. Garcia, T. Woike, *Coord. Chem. Rev.* **2001**, *219–221*, 839–879; c) A. Bousseksou, G. Molnár, J.-P. Tuchagues, N. Menéndez, E. Codjovi, F. Varret, *C. R. Chim.* **2003**, *6*, 329–334; d) J. A. Real, A. B. Gaspar, V. Niel, M. C. Muñoz, *Coord. Chem. Rev.* **2003**, *236*, 121–141; e) A. Bousseksou, F. Varret, M. Goiran, K. Boukheddaden, J.-P. Tuchagues, *Top. Curr. Chem.* **2004**, *235*, 65–84 and references cited therein; f) E. König, *Struct. Bonding (Berlin)* **1991**, *76*, 51–152; g) P. Gütlich, Y. Garcia, H. A. Goodwin, *Chem. Soc. Rev.* **2000**, *29*, 419–427.
[19] L. Salmon, A. Bousseksou, B. Donnadieu, J.-P. Tuchagues, *Inorg. Chem.* **2005**, *44*, 1763–1773.
[20] P. J. van Koningsbruggen, *Top. Curr. Chem.* **2004**, *233*, 123–149.
[21] P. M. Sonar, C. M. Grunert, Y.-L. Wei, J. Kusz, P. Gütlich, A. D. Schlüter, *Eur. J. Inorg. Chem.* **2008**, 1613–1622.
[22] T. Fujigaya, D.-L. Jiang, T. Aida, *J. Am. Chem. Soc.* **2005**, *127*, 5484–5489.
[23] O. Kahn, C. J. Martinez, *Science* **1998**, *279*, 44–48.
[24] E. Codjovi, L. Sommier, O. Kahn, C. Jay, *New J. Chem.* **1996**, *20*, 503–505.
[25] Y. Garcia, P. J. van Koningsbruggen, E. Codjovi, R. Lapouyade, O. Kahn, L. Rabardel, *J. Mater. Chem.* **1997**, *7*, 857–858.
[26] A. Zhang, L. L. Okrasa, T. Pakula, A. D. Schlüter, *J. Am. Chem. Soc.* **2004**, *126*, 6658–6666.
[27] M. Seredyuk, A. B. Gaspar, V. Ksenofontov, S. Reiman, Y. Galyametdinov, W. Haase, E. Rentschler, P. Gütlich, *Chem. Mater.* **2006**, *18*, 2513–2519; A. B. Gaspar, M. Seredyuk, P. Gütlich, *Coord. Chem. Rev.* **2009**, *253*, 2399–2413.
[28] J.-P. Tuchagues, A. Bousseksou, G. Molnar, J. J. McGarvey, F. Varret, *Top. Curr. Chem.* **2004**, *235*, 85–103.
[29] M. Sorai, J. Ensling, K. M. Hasselbach, P. Gütlich, *Chem. Phys.* **1977**, *20*, 197–208; K. H. Sugiyarto, H. A. Goodwin, *Aust. J. Chem.* **1988**, *41*, 1645–1648; K. H. Sugiyarto, K. Weitzner, D. C. Graig, H. A. Goodwin, *Aust. J. Chem.* **1997**, *50*, 869–873.
[30] Y. Garcia, P. Guionneau, G. Bravic, D. Chasseau, J. A. K. Howard, O. Kahn, V. Ksenofontov, S. Reiman, P. Gütlich, *Eur. J. Inorg. Chem.* **2000**, 1531–1538.
[31] J. J. A. Kolnaar, G. Dijk, H. Kooijiman, A. L. Spek, V. G. Ksenofontov, P. Gütlich, J. G. Haasnoot, J. Reedijk, *Inorg. Chem.* **1997**, *36*, 2433–2440.
[32] Y. Garcia, P. J. van Koningsbruggen, R. Lapouyade, L. Fournès, L. Rabardel, O. Kahn, V. Ksenofontov, G. Levchenko, P. Gütlich, *Chem. Mater.* **1998**, *10*, 2426–2433.
[33] T. Fujigaya, D.-L. Jiang, T. Aida, *J. Am. Chem. Soc.* **2003**, *125*, 14690–14691.

Received: January 22, 2010
Published Online: July 14, 2010

DOI: 10.1002/ejic.201000304

[FeFe]-Hydrogenase Models: Overpotential Control for Electrocatalytic H_2 Production by Tuning of the Ligand π-Acceptor Ability

Fengwei Huo,[a] Jun Hou,*[a,b] Guicai Chen,[b] Dongming Guo,[a] and Xiaojun Peng*[b]

Keywords: Bioinorganic chemistry / Hydrogenase / Phosphanes / Carbonyldiiron compounds / Phosphane ligands

In the search for synthetic competitive catalysts that function with hydrogenase-like capability, a series of (Pyrrol-1-yl)-phosphane-substituted diiron complexes [(μ-pdt)$Fe_2(CO)_5$L] [pdt = propanedithiolate, L = Ph_2PPyr (**2**), $PPyr_3$ (**4**); Pyr = pyrrolyl] and [(μ-pdt)$Fe_2(CO)_4L_2$] [L = Ph_2PPyr (**3**), $PPyr_3$ (**5**)] were prepared as functional models for the active site of Fe-only hydrogenase. The structures of these complexes were fully characterized by spectroscopy and X-ray crystallography. In the IR spectra the CO bands for complexes **2**–**5** are shifted to higher energy relative to those of complexes with "traditional" phosphane ligands, such as PPh_3, PMe_3, and PTA (1,3,5-triaza-7-phosphaadamantane), indicating that (pyrrol-1-yl)phosphanes are poor σ-donors and better π-acceptors. The electrochemical properties of complexes **2**–**5** were studied by cyclic voltammetry in CH_3CN in the absence and presence of the the weak acid HOAc. The reduction potentials of these complexes show an anodic shift relative to other phosphane-substituted derivatives. All of the complexes can catalyze proton reduction from HOAc to H_2 in CH_3CN at their respective Fe^IFe^0 level. Complex **4** is the most effective electrocatalyst, which catalytically generates H_2 from HOAc at –1.66 V vs. Fc^+/Fc with only ca. 0.2 V overpotential in CH_3CN.

Introduction

Hydrogen has attracted remarkable interest as a clean and highly efficient energy carrier of the future.[1] However, presently expensive platinum-containing catalysts are used to efficiently catalyze hydrogen evolution from the reduction of protons and electrons.[2] Therefore, the search for less expensive and more efficient catalysts to replace platinum-based materials is an important goal for hydrogen energy applications.[3,4]

[FeFe]-hydrogenase ([FeFe]-H_2ase) can efficiently catalyze the reversible reduction of protons to hydrogen with high rates up to 6000 molecules of H_2 per second per mmol.[5–7] The active site, which generates H_2, consists of a 2Fe2S unit bridged to a 4Fe4S cluster by a cystein-S bridge, as revealed by X-ray structure determinations[8,9] and IR spectroscopic studies[10,11] illustrated in Figure 1A. The two Fe atoms in the 2Fe2S unit are coordinated by CO and CN^-, as well as a bridging 1,3-dithiolato ligand.[12,13] Please note that the L ligand has not been identified with certainty, and it is possibly H_2O, H or vacant based on different redox states.

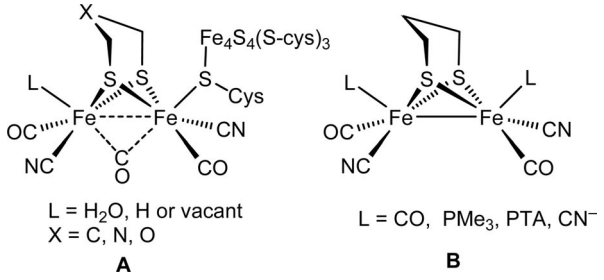

Figure 1. Active site of [Fe]H_2ase (A) and the synthetic Fe^IFe^I electrocatalysts for H_2 production (B).

Since the elucidation of the structures of [FeFe]-H_2ase, there have been numerous attempts aimed at the synthesis of diiron complexes that mimic the active site of [FeFe]-H_2ase in the past few years.[14–18] Mono- and disubstituted diiron complexes for electrocatalytic H_2 production were developed (Figure 1B).[19–24] However, the Fe^IFe^I catalysts synthesized so far require the harsh conditions of either strong acids (i.e., HOTs or $HClO_4$)[21–25] or a relatively high overpotential (0.5–1.0 V).[19,20] As is well known, [FeFe]-H_2ase can generate H_2 at neutral pH and at low potential (ca. –0.8 V vs. Fc^+/Fc). Thus, the major challenge now is to search for synthetic competitive catalysts with a low overpotential that function with [FeFe]-H_2ase-like capability under mild conditions for both proton and electron sources.

Theoretic[26,27] and experimental[19,28–30] studies indicate that the ligands at the diiron core have an important influence on the electrocatalytic capabilities of the 2Fe2S com-

[a] Key Laboratory for Precision & Non-traditional Machining of the Ministry of Education, Dalian University of Technology
Dalian 116024, P. R. China
Fax: +86-411-84706059
E-mail: junhou@dlut.edu.cn
[b] State Key Laboratory of Fine Chemicals, Dalian University of Technology
Dalian 116012, P. R. China
E-mail: pengxj@dlut.edu.cn

plexes. In this context, numerous σ-donor-ligand-substituted diiron complexes, [(μ-pdt)$Fe_2(CO)_5$L] and [(μ-pdt)-$Fe_2(CO)_4L_2$] [L = PMe_3, PMe_2Ph, PPh_3, $P(OEt)_3$, CN^-, 1,3,5-triaza-7-phosphaadamantane (PTA)] have been extensively investigated.[19,20,28–30] (Pyrrol-1-yl)phosphanes have been widely used to tune metal reactivity and selectivity in homogeneous catalysis because of their exceptional π-acceptor character.[31] Some (Pyrrol-1-yl)phosphane-substituted rhodium complexes, [Rh(acac)(CO)L] and [RhH(CO)L] (acac = acetylacetonato), were reported for hydroformylation with higher yields and better selectivity.[32,33] However, to the best of our knowledge, there is as yet no report on the use of (pyrrol-1-yl)phosphane-substituted diiron dithiolates as [FeFe]-H_2ase model complexes. This led us to explore 2Fe2S synthetic catalysts with small overpotentials by tuning ligand π-acceptor ability using (pyrrol-1-yl)phosphane ligands. Thus, we herein report on (pyrrol-1-yl)phosphane mono- and disubstituted diiron complexes formed by CO/L exchange reaction to study the influence of (pyrrol-1-yl)phosphanes on structure and electrochemical properties. The issue of overpotential in proton reduction by these complexes is also discussed.

Results and Discussion

Preparation and Spectroscopic Characterization of Complexes 2–5

These new complexes were obtained in moderate yield by refluxing toluene solutions of **1** with (pyrrol-1-yl)phosphane. The preparation of these phosphane-substituted diiron complexes is summarized in Scheme 1.

The reaction of **1** with 1 mol-equiv. of Ph_2PPyr in refluxing toluene for 48 h gave monosubstituted complex **2** in good yield. Disubstituted complex **3** as a major product together with a small amount of monosubstituted complex **2** was obtained by refluxing a solution of **1** with 2 equiv. of Ph_2PPyr for 48 h. In a similar way, complexes **4** and **5** were prepared in refluxing toluene by treatment of **1** with 1 and 2 equiv. of $PPyr_3$, respectively. However, the preparation of $PPyr_3$-substituted complexes is relatively more difficult than that of Ph_2PPyr-substituted derivatives, presumably because of the electronic effect. The reactivity of $PPyr_3$ is unusual as compared to that of alkylphosphanes. For instance, PPh_3 and PMe_3 can readily react with **1** to give mono- and disubstituted derivatives.[30] These observations are consistent with a greatly reduced nucleophilicity for the phosphorus atom in $PPyr_3$, presumably due to aromatic delocalization of the nitrogen lone pair into the ring.[31]

The products obtained in analytically pure form are soluble in CH_2Cl_2, THF, and acetone. All complexes are air- and thermally stable in the solid state but moderately sensitive in solution, and were characterized by IR and NMR spectroscopy as well as HR mass spectrometry, as detailed in the Experimental Section. The HR-MS analyses are in good agreement with the supposed molecular weight. The resonances of the 1,3-propanedithiolato methylene hydrogen and carbon atoms in their characteristic regions show a high-field shift as compared to the all-CO complex **1**, because of the shield effects of the aromatic rings at the bulky tertiary phosphane ligands. The IR spectra of complexes **2**–**5** exhibit three major ν_{CO} bands in the region 2056–1962 cm^{-1}. All compounds were identified by X-ray structure determinations.

Molecular Structures of Complexes 2–5

The crystal structures of **2**–**5** were determined by X-ray crystallography and are shown in Figure 2. Selected bond lengths and bond angles are listed in Table 1.

The 2Fe2S centers of all complexes are six-coordinate and exhibit square-pyramidal geometries. The Fe–Fe distances [2.5222(10) Å in **2**, 2.5188(6) Å in **3**, 2.523(2) Å in **4**, and 2.5237(8) Å in **5**] are in good agreement with those found in tertiary phosphane-substituted diiron analogues.[19,20,30,34]

In monosubstituted derivatives **2** and **4**, the coordination configurations are nearly identical with the tertiary phosphane monosubstituted derivatives [(μ-pdt)$Fe_2(CO)_5$L] [L =

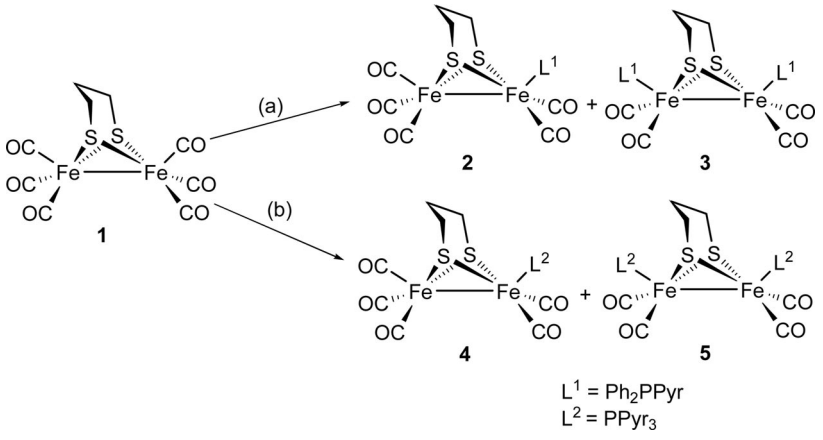

Scheme 1. (a) for **2**, Ph_2PPyr (1 equiv.), toluene, reflux, 48 h; for **3**, Ph_2PPyr (2 equiv.), toluene, reflux, 72 h; (b) for **4**, $PPyr_3$ (1 equiv.), toluene, reflux, 48 h; for **5**, $PPyr_3$ (2 equiv.), toluene, reflux, 72 h.

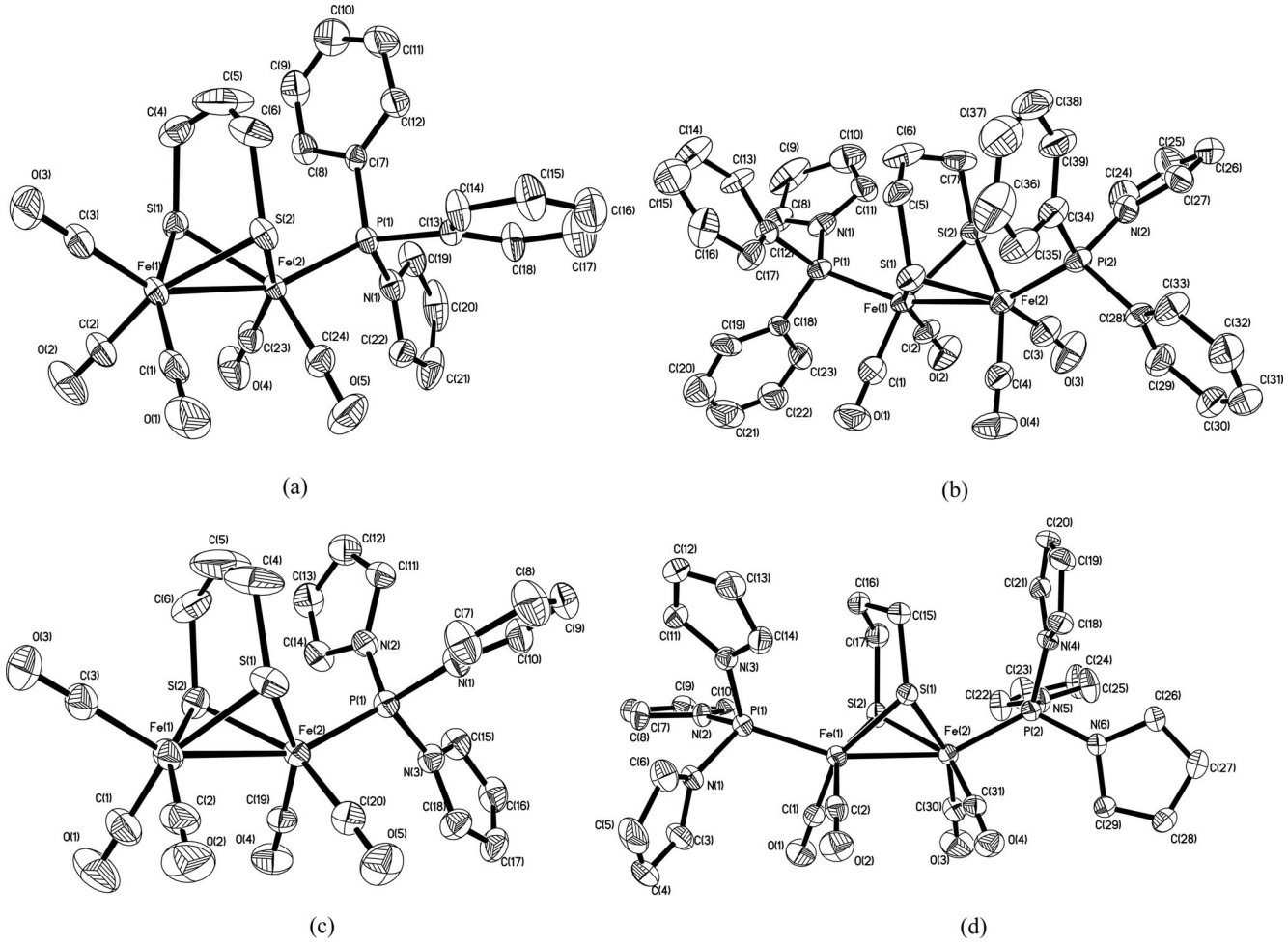

Figure 2. ORTEP (ellipsoids at 30% probability level) view of **2** (a), **3** (b), **4** (c), and **5** (d).

Table 1. Selected bond lengths and angles for **2**–**5**.

	2	**4**		**3**	**5**
Bond lengths [Å]					
Fe(1)–Fe(2)	2.5222(10)	2.5188(6)	Fe(1)–Fe(2)	2.523(2)	2.5237(8)
Fe(1)–S(1)	2.2609(15)	2.2486(8)	Fe(1)–S(1)	2.274(3)	2.2768(12)
Fe(1)–S(2)	2.2594(15)	2.2584(8)	Fe(1)–S(2)	2.270(3)	2.2778(12)
Fe(2)–S(1)	2.2636(15)	2.2617(7)	Fe(2)–S(1)	2.268(3)	2.2733(12)
Fe(2)–S(2)	2.2635(15)	2.2563(8)	Fe(2)–S(2)	2.263(3)	2.2509(12)
Fe–P_{ap}	2.2247(1)	2.1661(7)	Fe–P_{ap}[c]	2.215(8)	2.1725(1)
Fe–$C_{CO,ap}$	1.802(6)	1.801(3)	Fe–$C_{CO,ba}$[d]	1.767(6)	1.769(2)
Fe–$C_{CO,ba}$[a]	1.774(4)	1.783(1)	P–N	1.746(2)[e]	1.709(3)[f]
P–N	1.761(4)	1.7096(2)[b]			
Bond angles [°]					
Fe(1)–S(1)–Fe(2)	67.76(4)	67.90(2)	Fe(1)–S(1)–Fe(2)	67.50(9)	67.37(3)
Fe(1)–S(2)–Fe(2)	67.79(5)	67.82(2)	Fe(1)–S(2)–Fe(2)	67.64(9)	67.73(4)
P(1)–Fe(2)–Fe(1)	156.96(5)	155.11(2)	P(1)–Fe(1)–Fe(2)	158.29(9)	160.60(4)
P(1)–Fe(2)–S(1)	110.99(5)	108.11(3)	P(2)–Fe(2)–Fe(1)	154.16(10)	154.01(4)
P(1)–Fe(2)–S(2)	106.94(6)	107.22(3)	P(1)–Fe(1)–S(1)	109.10(12)	110.74(4)
S(1)–Fe(2)–Fe(1)	56.07(4)	55.80(2)	P(1)–Fe(1)–S(2)	110.19(11)	111.86(5)
S(2)–Fe(2)–Fe(1)	56.03(4)	56.13(2)	S(1)–Fe(1)–Fe(2)	56.14(9)	56.25(3)
			S(2)–Fe(1)–Fe(2)	56.06(8)	55.63(3)

[a] Average of five Fe–$C_{CO,ba}$ bonds. [b] Average of three P–N bonds. [c] Average of two Fe–P_{ap} bonds. [d] Average of four Fe–$C_{CO,ba}$ bonds. [e] Average of two P–N bonds. [f] Average of six P–N bonds.

PMe_3, PMe_2Ph, PPh_3, $P(OEt)_3$].[30] The phosphane moieties Ph_2PPyr and $PPyr_3$ occupy apical positions around the Fe atoms, and are roughly *trans* to the Fe–Fe bond. The Fe–P distance of 2.1661(7) Å in **4** is slightly shorter by 0.06 Å than that of 2.2247(14) Å in **2**, consistent with the poor donor (or good acceptor) ability of the $PPyr_3$ ligand. One phenyl ring in **2** and one pyrrolyl ring in **4** are nearly facing the dithiaferracyclohexane ring similar to the PPh_3-coordinating complex.[30] The angles of C(4)–S(1)–Fe(2) [113.13(11)°] and C(6)–S(2)–Fe(2) [114.88(13)°] for **4** are slightly larger than the corresponding angles of C(4)–S(1)–Fe(1) [111.37(16)°] and C(6)–S(2)–Fe(1) [110.70(11)°]. This indicates that the bulk ligand $PPyr_3$ around the diiron unit in **4** causes the dithiaferracyclohexane ring to slant towards the $Fe(CO)_3$ unit. The larger differences between the C(6)–S(2)–Fe(2) [115.1(2)°] vs. C(6)–S(2)–Fe(1) [109.8(2)°] angles for **2** and C(4)–S(1)–Fe(2) [116.0(2)°] vs. C(4)–S(1)–Fe(2) [110.1(2)°] angles for **4** further confirm the steric interactions when $PPyr_3$ is replaced by Ph_2PPyr. The angles of P(1)–Fe(2)–Fe(1) in **2** and **4** are ca. 8.1° and 6.1° larger than the C(3)–Fe(1)–Fe(2) angles, respectively. The average Fe(2)–$C_{CO,ba}$ distance of 1.781(2) Å for **4** is 0.02 Å longer than that of **2** [1.760(2) Å], and the corresponding length of C–O bonds [av. 1.139(13) Å] for **4** is shorter than that of **2** [av. 1.143(6) Å]. These features demonstrate that the introduction of the π-acceptor phosphane ligand decreases the electron donation of the iron centers and thereby leads to weaker π-back-bonding from the iron atoms to the carbonyl atoms. It is noteworthy that the average C–O bond length of 1.136 in **4** is in significant agreement with that reported for [(μ-pdt)$Fe_2(CO)_6$] (av. 1.136 Å),[34] indicative of the similar electronic effects of both the $PPyr_3$ ligand and CO.

The average Fe–P bond lengths of 2.215(8) Å in **3** and 2.1725(12) Å in **5** are in good agreement with that in phosphane-disubstituted analogues; the Fe–P bond length of **5** is ca. 0.04 Å shorter than that of **3**, further indicative of the better π-acceptor character of the $PPyr_3$ ligand relative to Ph_2PPyr. In the case of **3** and **5**, two aromatic rings face the propanedithiolato bridge, consistent with the fact that the ^1H NMR signals for the methylene protons of the 1,3-propanedithiolato bridge significantly shift to high field due to the shield effects of the aromatic rings.

An interesting structural feature of disubstituted complexes **3** and **5** is that the phosphane ligands are in apical/apical (ap/ap) position and *trans* to the Fe–Fe bond, contrary to that of [(μ-pdt)$Fe_2(CO)_4(PTA)_2$] featuring a ba/ba coordination mode.[20] This observation is identical to that found for PMe_2Ph-[30] and *t*BuNC-disubstituted[35] derivatives. We note that PMe_3 and cyano-disubstituted complexes [(μ-pdt)$Fe_2(CO)_4(PMe_3)_2$] and [(μ-pdt)$Fe_2(CO)_4(CN)_2]^{2-}$ possess an ap/ba configuration.[36,37] It can be inferred that the steric interactions of bulk phosphane with the dithiaferracyclohexane ring are not the main factor in the rearrangement and that electronic effects probably play a key role. That is, the better electron-donating ligands favor rearrangements into the ba/ba or ap/ba configuration, whereas the ligands with better π-acceptor capability prefer the ap/ap coordination mode.

In $PPyr_3$-substituted diiron complexes **4** and **5**, as expected, the nitrogen geometries are planar, with a sum of angles at N ranging from 358.6(9)° to 360.01(6)°. The bond lengths within the pyrrole rings are also similar to those found in the free ligand.[38]

π-Acceptor Ability of (Pyrrol-1-yl)phosphanes

In the IR spectra the ν_{CO} bands in the CO region provide a powerful tool for evaluating the structural and electronic changes of carbonyl transition-metal complexes.[39] The IR data of the CO bands for complexes **2**, **3**, **4**, and **5** are listed in Table 2. The spectra of the all-CO parent complex **1** and its PPh_3-monosubstituted derivative [(μ-pdt)$Fe_2(CO)_5PPh_3$] (**6**) are also included for comparison purposes. Compared with the all-CO parent complex **1**, the ν_{CO} bands of **2**–**5** shift to lower frequencies, indicating an increase of electron density on the iron cores when a CO ligand is replaced by a $Ph_2PPyr/PPyr_3$ ligand. The monosustituted series of diiron complexes **2**, **4**, and **6** shows a steady increase of ν_{CO} with an increasing degree of replacement of the phenyl groups by pyrrol-1-yl groups. It can be seen that the IR ν_{CO} bands of **6** shift by an average of 50 cm^{-1} to lower frequencies, whereas the ν_{CO} bands of complexes **2** and **4** shift to lower wavenumbers by ca. 32 cm^{-1} and 18 cm^{-1}, respectively. This indicates that the pyrrol-1-yl group plays a key role in decreasing the π-back-bonding of electrons from the metal cores to the CO ligands. The ν_{CO} bands in **4** are higher than those of complexes **2** and **6**, showing that complex **4** has a better π-acceptor ability and a poorer donor ability. In addition, the values of ν_{CO} for **4** and **5** are significantly higher than those found for alkylphosphane-substituted derivatives, [(μ-pdt)$Fe_2(CO)_5L$] and [(μ-pdt)$Fe_2(CO)_4L_2$] (L = PMe_3, PMe_2Ph, PTA).[20,30] For instance, the CO stretching frequency of **5** is shifted to higher energy by nearly 45 cm^{-1} upon replacement of PMe_3 by $PPyr_3$. The shifts to higher frequencies for **4** and **5** indicate a significantly reduced degree of π-back-bonding donation from the iron atoms to the carbonyl ligands in these diiron complexes and therefore demonstrate either a strong π-acceptor ability or a poor σ-donor character of the $PPyr_3$ ligand. As expected, the CO stretching frequencies of **4** are very close to those of **1**, indicative of a similar π-acceptor ability of the $PPyr_3$ and CO ligands. This effect has also been observed in other $PPyr_3$-substituted carbonylmetal complexes.[40] Thus, the π-acceptor capabilities of these phosphane ligands exhibit the following trend: CO ≈ $PPyr_3$ > PhPPyr > PPh_3. As described for $PPyr_3$-substituted carbonylmetal complexes by

Table 2. Summary of IR ν_{CO} bands for diiron complexes.

Complex	ν_{CO} [cm^{-1}]
1	2072(m), 2034(s), 1997(s)
2	2049(s), 1991(s), 1964(w)
3	2008(s), 1964(m), 1947(s)
4	2056(s), 2003(s), 1990(w)
5	2028(s), 1984(m), 1970(s)
6	2044(s), 1981(s), 1930(m)

Moloy et al., the good π-acceptor ability of $PPyr_3$ is attributed to the aromatic delocalization of the nitrogen lone pair into the five-membered rings.[31]

Electrochemistry of Complexes 2–5

The cyclic voltammograms of complexes **2**–**5** shown in Figure 3 were recorded in CH_3CN solution (with 0.1 M nBu_4NPF_6 as electrolyte), they were initiated from the open circuit potential and scanned in the cathodic direction as indicated in Figure 3. A summary of the redox potentials for **2**–**5** and the parent all-CO complex **1** and its PPh_3 derivatives, [(μ-pdt)$Fe_2(CO)_5PPh_3$] (**6**), is given in Table 3. It has been demonstrated that complexes **2** and **3** display two irreversible oxidation peaks, whereas **4** and **5** show one irreversible oxidation peak. In publications, those reported for ADT-, PDT-, and ODT-bridged (ODT = oxadithiolato) analogs,[19–21,30,41,42] were assumed to be the oxidation events of Fe^IFe^I to $Fe^{II}Fe^I$ and $Fe^{II}Fe^I$ to $Fe^{II}Fe^{II}$, respectively. In all cases discussed in this paper, it is noticeable that the 1st oxidation for complexes **2**–**5** exhibits a current intensity ca. twice that of the corresponding 1st reduction event, which was confirmed as a one-electron process by bulk electrolysis (vide infra).

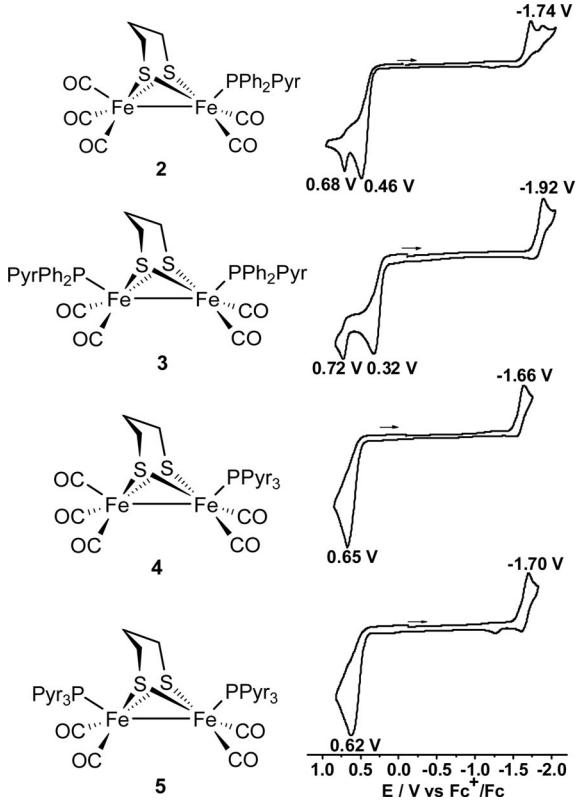

Figure 3. Cyclic voltammograms of complexes **2**, **3**, **4**, and **5** in CH_3CN solution (0.1 M nBu_4NPF_6) at a potential scan rate of 100 mV s^{-1}.

Therefore, we assume the 1st oxidation of complexes **2**–**5** is either a two-electron process of Fe^IFe^I to $Fe^{II}Fe^{II}$ or a combined result of two overlapping processes of Fe^IFe^I to $Fe^{II}Fe^I$ and $Fe^{II}Fe^I$ to $Fe^{II}Fe^{II}$. Further oxidation of these complexes probably arises from the degradation of oxidized species or the ligand redox process, which is beyond the scope of this article.

Table 3. Redox potentials for phosphane derivatives of **1**.

Complex	E_{pc} [V]	E_{pa} [V]	E_{pa} [V]
	Fe^IFe^I/Fe^0Fe^I	$Fe^IFe^I/Fe^{II}Fe^I$	$Fe^{II}Fe^I/Fe^{II}Fe^{II}$
1	–1.62	0.84	–
2	–1.74	0.46	0.68
3	–1.92	0.32	0.72
4	–1.66	0.65	–
5[a]	–1.70	0.62	–
6	–1.84	–0.40	–

[a] Complex **5** was somewhat soluble in CH_3CN.

Complexes **2**, **3**, **4**, and **5** exhibit an electrochemically irreversible reduction at –1.74 V, –1.92 V, –1.66 V, and –1.70 V, respectively. Bulk electrolysis of complexes **2**–**5** at each reduction potential shows a net consumption of ca. 0.95 electrons per molecule, demonstrating these reduction events are one-electron reduction processes from Fe^IFe^I to Fe^0Fe^I. However, for the electron counting of the 1st reduction process of the parent complex **1**, whether it is a one-electron process or a two-electron process, is disputable.[19–21,30,41–44] For most model complexes including ADT, PDT, and ODT derivatives, the concerned reduction event was considered to be a one-electron process.

In comparison to complex **1**, the first reduction potentials of complexes **2**–**5** are shifted to a relatively more negative value, consistent with the increase of electron density at the diiron core upon replacement of CO by the better donor ligands. Noticeably, the reduction potentials of **4** and **5** show a minor negative shift by only 40 mV and 80 mV, respectively, as compared to complex **1**. The minor shift suggests that the $PPyr_3$ ligand is a somewhat weaker π-acceptor in comparison to CO and therefore, slightly affects the redox capability of these diiron complexes. On the other hand, the reduction shifts are smaller than those observed for complex **6** and other reported phosphane-substituted diiron complexes.[19,20,30,42] Within the series of **2**, **4**, and **6**, we can see that the reduction potentials gradually shift to more positive potentials with displacement of the phenyl ring by the pyrrol-1-yl group, consistent with the change trends of the IR ν_{CO} bands.

In all cases, a linear dependence of the peak currents (i_p) on the square root of the scan rate ($v^{1/2}$) in CH_3CN solution indicates the electron-transfer reactions are diffusion-controlled.[45]

Electrocatalytic Proton Reduction to H_2

The behavior of electrocatalytic proton reduction to H_2 by **2**–**5** has been investigated by cyclic voltammetry in the absence and presence of the weak acid HOAc. The cyclic voltammograms recorded in CH_3CN solutions with different acetic acid concentrations (0–20 mM) are shown in

Figure 4. As can be seen, when 1 mM of HOAc was added, an obvious increase in the current intensity of the first reduction peak at –1.74 V, –1.92 V, –1.66 V, and –1.70 V for **2**–**5**, respectively, was observed. The height of the reduction peak in each CV shows a further increase with the sequential increments of acid concentration. The current height change at their respective reduction peak displays a good linear dependence on the concentrations of HOAc. In addition, the reduction potentials slightly move to more cathodic values with increasing acid concentration. All of these features are clearly indicative of a catalytic proton reduction process.[19–21,30,41–43,46] The CVs of complexes **2**–**5** indicate they are electrocatalytically active at the first reduction potentials for proton reduction from HOAc. The electrocatalytic properties of complexes **2**–**5** are very similar to that of [(μ-pdt)$Fe_2(CO)_5$PTA] reported by Darensbourg and coworkers,[20] which also shows the first reduction peak is catalytically active in the presence of a weak acid (HOAc). To further confirm the evolution of hydrogen at the first reduction peak, bulk electrolyses in CH_3CN solutions for **2**–**5** were performed in a gas-tight H-type cell as described in the Experimental Section. The electrolysis of complexes **2**, **3**, **4**, and **5** was carried out at –1.80 V, –1.98 V, –1.72 V, and –1.76 V, respectively, in the presence of HOAc (50 mM). When 12 C of charge had passed through the cell, a sample of gas was collected and analyzed by gas chromatography, showing hydrogen is the sole gaseous product.

By using the standard potential (–1.46 V vs. Fc^+/Fc) reported by Evans et al. for the HOAc reduction in CH_3CN,[47] the overpotentials of complexes **2**–**5** are 0.28, 0.46, 0.2, and 0.24 V, respectively. Darensbourg and coworkers reported H_2 evolution by electrolysis catalyzed by complex [(μ-pdt)$Fe_2(CO)_5$PTA] at –1.94 V vs. Fc^+/Fc with ca. 0.48 V overpotential for H_2/H^+ (HOAc).[20,48] It is noteworthy that complex **4** can electrocatalytically generate H_2 in weak acid at –1.66 V with only ca. 0.2 V overpotential. This potential is quite similar to that of [(μ-S-2-$RCONHC_6H_4)_2Fe_2(CO)_6$] (R = 4-FC_6H_4) reported by Sun and co-workers.[49] Although hexacarbonyldiiron azadithiolate complexes, [{(μ-$SCH_2)_2N(2$-$C_4H_3O)$}$Fe_2(CO)_6$] and [{(μ-$SCH_2)_2N(4$-$BrC_6H_4)$}$Fe_2(CO)_6$], can catalyze the H_2 production at lower potentials (ca. –1.13 to –1.48 V vs. Fc^+/Fc),[24,25] a strong acid ($HClO_4$) is needed. A summary of the overpotentials for **2**–**5** and diiron dithiolates is given in Table 4. To the best of our knowledge, in terms of reduction overpotential, complex **4** is the most energy-efficient diiron electrocatalyst for the H_2 production in the presence of a weak acid (HOAc) based on ligand-substituted 2Fe2S biomimics. Complex **4** with the best catalytic capability for proton reduction displays a catalytic potential very close to that of the noble metal Pt. In our previous work, we reported (pyrrolidin-1-yl)phosphane monosubstituted complex [(μ-pdt)$Fe_2(CO)_5P(NC_4H_8)_3$] can also catalyze the H_2 production in the presence of HOAc at –1.98 V with a relatively high overpotential (ca. 0.52 V).[29] However, its peak current is higher than that of **4**. Thus, it seems that a low overpotential is achieved at the cost of low rates of catalysis. Further experiments will be performed to confirm this in

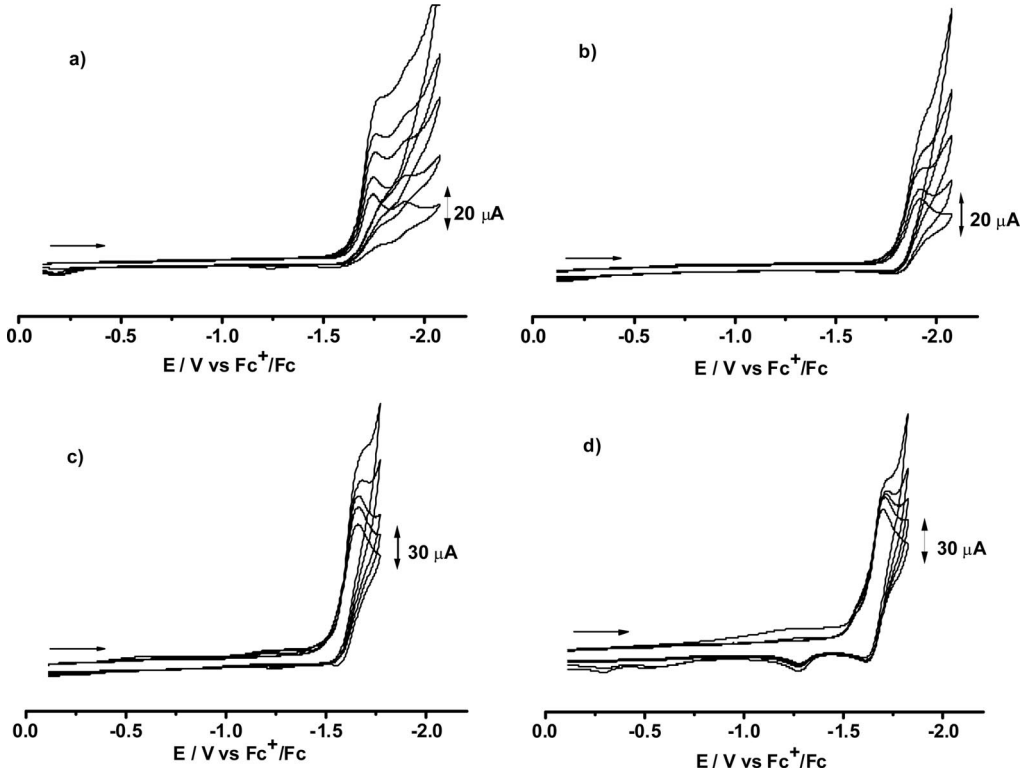

Figure 4. Successive cyclic voltammograms of 1.0 mM solution of **2** (a), **3** (b), **4** (c), **5** (d) with HOAc (0, 1, 5, 10, and 20 mM) in CH_3CN (0.1 M nBu_4NPF_6 as supporting electrolyte) at a potential scan rate of 100 mV s^{-1}.

future work. This significant electrocatalytic feature of **4** as well as of the analogues **2**, **3**, and **5** are interpreted as follows. On replacement of the CO ligand by the $PPyr_3$ ligand (or $PPyr_2Ph$ and $PPyrPh_2$), the low potential at the first reduction is maintained due to the small donating ability of the phosphane ligands relative to the CO ligand. The reduced species (Fe^IFe^0 level) of **4** provides a strong base for proton uptake, whereas that of **1** at its Fe^IFe^0 level is not a strong enough nucleophile to react with the proton, because the six strongly π-accepting CO ligands decrease the nucleophilicity of the diiron core. In contrast, the $PPyr_3$ ligand (or $PPyr_2Ph$ and $PPyrPh_2$) with a smaller π-acceptor ability modulates the nucleophilicity of the diiron core of the reduced species (Fe^IFe^0 level) of **4** at a functional level for H_2 production.

Table 4. Summary of overpotential for phosphane-substituted 2Fe2S complexes.

Complex	E_{pc} [V] Fe^IFe^I/Fe^0Fe^I	$E_{overpotential}$ [V]
1	–1.62	0.16
2	–1.74	0.28
3	–1.92	0.46
4	–1.66	0.20
5	–1.70	0.24
6	–1.84	0.38
$[(\mu\text{-pdt})Fe_2(CO)_5PTA]$	–1.94	0.48
$[(\mu\text{-S-2-RCONHC}_6H_4)_2Fe_2(CO)_6]$[a]	–1.66	0.20

[a] R = 4-FC_6H_4.

On the basis of the electrochemical observations described above and similar cases of phosphane-substituted 2Fe2S complexes previously reported,[19–21,30,41–43] an ECCE (electrochemical/chemical/chemical/electrochemical) mechanism for the electrocatalytic proton reduction process by **2**–**5** could be proposed, as presented in Scheme 2. The Fe^IFe^I complex initially undergoes an electrochemical reduction to generate a one-electron reduced intermediate Fe^IFe^0, which is singly protonated to form a hydride species $Fe^IFe^{II}H$ in the presence of HOAc. After a further protonation of $Fe^IFe^{II}H$ and a second electroreduction event, hydrogen is evolved, and the starting material is reclaimed to fulfill the catalytic cycle. Our results also show that the one-electron reductive level Fe^0Fe^I is electrocatalytically active.

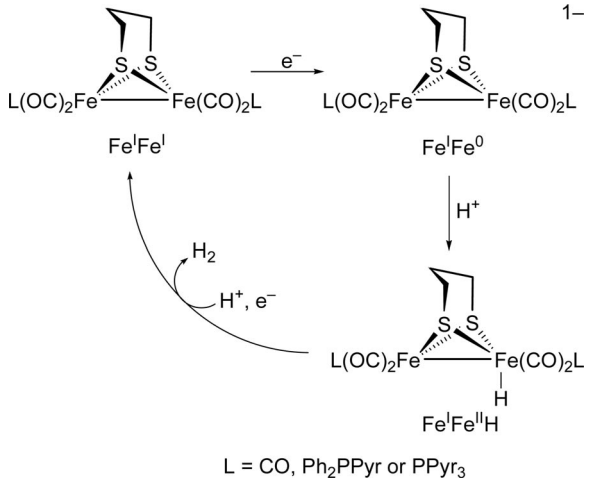

Scheme 2. Proposed ECCE mechanism for catalytic proton reduction to H_2 by complexes **2**–**5**.

Conclusions

In the search for synthetic competitive catalysts that function with [Fe]-H_2ase-like capability, a series of π-acceptor (pyrrol-1-yl)phosphane-substituted diiron complexes **2**–**5** were prepared as functional models for the Fe-only hydrogenase. This work explored the derivative chemistry of the precursor $[(\mu\text{-}S_2R)Fe_2(CO)_6]$ by replacement of CO with the exceptional π-acceptor (pyrrol-1-yl)phosphane ligands and developed applications of (pyrrol-1-yl)phosphanes in bio-organometallic chemistry and catalysis.

In the presence of the weak acid HOAc complexes **2**–**5** can catalyze proton reduction to H_2 at the first reduction level Fe^IFe^0. The most effective electrocatalyst is the $PPyr_3$-substituted complex **4**. As compared to that of other σ-donor phosphane-substituted diiron complexes (most of them catalyze proton reduction at the Fe^0Fe^0 level with high overpotentials), the introduction of (pyrrol-1-yl)phosphane ligands maintains the reduction of **2**–**5** at relatively positive potentials due to the ligand π-acceptor character and improves the electrocatalytic ability. Since minor ligand π-acidity modulation has a significant influence on the proton reduction of these diiron models, the approach as exemplified by complexes **2**–**5** is worthy of further investigation in future functional biomimetic designs of [FeFe]-H_2ase. In contrast to electron-rich diiron models supported by multiple donors, diiron models with an appropriate π-acidity ligand have two main advantages: (a) enhanced stability towards O_2 and, therefore, easy operation; (b) in terms of thermodynamics, small overpotentials for electrocatalytic H_2 production.

Electrocatalytic proton reduction to H_2 at moderate overpotentials in the presence of the weak acid HOAc was achieved through replacement of CO by moderate π-acceptor (pyrrol-1-yl)phosphanes. Ligand $PPyr_3$ may be utilized as a surrogate for CO in the diiron systems. The pyrrol-1-yl groups are amenable to further modification so that it should be possible to prepare water-soluble electrocatalysts. Further investigations are underway to improve the proton affinity of the diiron complexes by a built-in proton relay site and to develop more advanced and effective electrocatalysts for proton reduction.

Experimental Section

Materials and Techniques: Unless noted otherwise, all reactions and operations were carried out under nitrogen by using standard Schlenk techniques. All solvents were dried and distilled prior to use according to standard methods. Pyrrole and Et_3N were distilled from Na and stored under nitrogen. The following materials were commercial chemicals and used without further purification: 1,3-propanedithiol, PCl_3, Ph_2PCl, and $[Fe(CO)_5]$. The starting materials P(pyrrol-1-yl)$_3$ ($PPyr_3$), Ph_2P(pyrrol-1-yl) (Ph_2PPyr), and [(μ-

pdt)$Fe_2(CO)_6$] were synthesized according to literature procedures.[31,50] [(μ-pdt)$Fe_2(CO)_5PPh_3$] (**6**) was prepared according to the literature[30] as an IR and electrochemistry reference complex. Infrared spectra were recorded with a Nicolet FT-IR spectrophotometer as solutions with CaF_2 plates. ^1H, ^{13}C and ^{31}P NMR were collected with a Varian INOVA 400 M NMR spectrometer. The ^1H and ^{13}C spectra were normally referenced to TMS, and the ^{31}P spectra were referenced to 85% H_3PO_4. HR-MS data acquisition was carried out with a GCT-MS instrument (Micromass, England). Elemental analysis was performed with a PE 2400 II Elemental Analyzer (Perkin–Elmer).

Synthesis of [(μ-pdt)$Fe_2(CO)_5$L] (2) (L = Ph_2PPyr): PPh_2(pyrrol-1-yl) (0.83 g, 3.3 mmol) in toluene (30 mL) was added to a red solution of [(μ-pdt)$Fe_2(CO)_6$], **1** (1.27 g, 3.3 mmol) in toluene (50 mL) through a syringe. The reaction mixture was refluxed until TLC indicated there was no remaining carbonyl complex of the starting material. The solvent was removed under vacuum, and the resultant dark red residue was purified by column chromatography on silica gel eluting with CH_2Cl_2/hexane (1:5, v/v). A red solid was obtained by recrystallization from *n*-pentane/CH_2Cl_2 at –30 °C. Yield: 1.20 g (68%). Crystals suitable for X-ray studies were grown from a mixed CH_2Cl_2/hexane solution. $C_{24}H_{20}Fe_2NO_5PS_2$ (608.92): calcd. C 47.32, H 3.31, N 2.30; found C 47.51, H 3.20, N 2.48. IR (in CH_2Cl_2): $\tilde{\nu}_{CO}$ = 2049, 1991, 1964 cm^{-1}. ^1H NMR ($CDCl_3$): δ = 1.53 (m, 4 H), 1.84 (m, 2 H), 6.44 (s, 2 H), 7.19 (s, 2 H), 7.52 (m, 10 H) ppm. ^{13}C NMR ($CDCl_3$): δ = 212.6, 209.2, 137.4, 137.0, 131.6, 131.5, 131.1, 128.9, 128.8, 126.5, 112.6, 29.9, 22.1 ppm. ^{31}P NMR ($CDCl_3$): δ = 116.25 ppm. HR-MS (EI): calcd. for $[M]^+$ 608.9247; found 608.9219.

Synthesis of [(μ-pdt)$Fe_2(CO)_4L_2$] (3) (L = Ph_2PPyr): PPh_2(pyrrol-1-yl) (1.40 g, 5.6 mmol) in toluene (50 mL) was added to a red solution of [(μ-pdt)$Fe_2(CO)_6$], **1** (1.07 g, 2.8 mmol) in toluene (50 mL) through a syringe. The reaction mixture was refluxed until TLC indicated there was no remaining carbonyl complex of the starting material. The solvent was removed under vacuum, and the resultant dark red residue was purified by column chromatography on silica gel eluting with CH_2Cl_2/hexane (1:2, v/v). A red solid was obtained by recrystallization from *n*-pentane/CH_2Cl_2 at –30 °C. Yield: 1.4 g (61%). Crystals suitable for X-ray studies were grown from a mixed CH_2Cl_2/hexane solution. $C_{39}H_{34}Fe_2N_2O_4P_2S_2$ (832.01): calcd. C 56.27, H 4.12, N 3.37; found C 56.16, H 4.28, N 3.56. IR (in CH_2Cl_2): $\tilde{\nu}_{CO}$ = 2008, 1964, 1947 cm^{-1}. ^1H NMR (400 MHz, $CDCl_3$): δ = 0.81 (br., 6 H), 6.35 (s, 4 H), 7.19 (s, 4 H), 7.42 (m, 20 H) ppm. ^{13}C NMR (400 MHz, $CDCl_3$): δ = 213.8, 138.0, 137.6, 131.5, 130.7, 128.7, 126.6, 112.2, 29.8, 19.6 ppm. ^{31}P NMR (400 MHz, $CDCl_3$): δ = 113.17 ppm. HR-MS (EI): calcd. for $[M]^+$ 832.0134; found 832.0156.

Synthesis of [(μ-pdt)$Fe_2(CO)_5$L] (4) (L = $PPyr_3$): Complex **4** was prepared acording to a procedure similar to that described above for **2**. A mixture of **1** (1.0 g, 2.58 mmol) with P(pyrrol-1-yl)$_3$ (0.591 g, 2.58 mmol) in toluene (80 mL) was refluxed for 72 h. After solvent evaporation, the resultant dark red residue was purified by column chromatography on silica gel. The monosubstituted complex **4** was obtained after eluting with CH_2Cl_2/hexane (1:10, v/v). Following further recrystallization from *n*-pentane/CH_2Cl_2 at –30 °C, a dark red solid was obtained. Yield: 0.95 g (63%). Crystals suitable for X-ray studies were grown from a mixed CH_2Cl_2/hexane solution. $C_{20}H_{18}Fe_2N_3O_5PS_2$ (586.91): calcd. C 40.91, H 3.09, N 7.16; found C 41.02, H 3.15, N 7.05. IR (in CH_2Cl_2): $\tilde{\nu}_{CO}$ = 2056, 2003, 1990 cm^{-1}. ^1H NMR (400 MHz, $CDCl_3$): δ = 1.64 (m, 4 H), 1.92 (m, 2 H), 6.40 (s, 6 H), 6.90 (s, 6 H) ppm. ^{13}C NMR (400 MHz, $CDCl_3$): δ = 210.5, 210.4, 208.4, 123.7, 123.6 113.7, 113.6, 29.5, 22.6 ppm. ^{31}P NMR (400 MHz, $CDCl_3$): δ = 140.58 ppm. HR-MS (EI): calcd. for $[M]^+$ 586.9124; found 586.9153.

Synthesis of [(μ-pdt)$Fe_2(CO)_4L_2$] (5) (L = $PPyr_3$): Complex **5** was prepared according to a procedure similar to that described above for **3**. A mixture of **1** (2.4 g, 6.20 mmol) with P(pyrrol-1-yl)$_3$ (3.0 g, 13.1 mmol) in toluene (120 mL) was refluxed for 72 h. TLC showed the main product was the disubstituted complex **5** with a small amount of a mixture with the starting material **1** and the monosubstituted complex **4**. Following solvent evaporation, the resultant dark red residue was purified by column chromatography on silica gel. The starting material **1** was eluted with hexane, and the monosubstituted complex **4** was obtained after eluting with CH_2Cl_2/hexane (1:10, v/v). The disubstituted complex **5** was obtained with CH_2Cl_2/hexane (1:4, v/v) as elute. Following further recrystallization from *n*-pentane/CH_2Cl_2 at –30 °C, an orange solid was obtained. Yield: 2.5 g (51%). Crystals suitable for X-ray studies were grown from a mixed CH_2Cl_2/hexane solution. $C_{31}H_{30}Fe_2N_6O_4P_2S_2$ (787.99): calcd. C 47.23, H 3.84, N 10.66; found C 47.41, H 3.71, N 10.82. IR (in CH_2Cl_2): $\tilde{\nu}_{CO}$ = 2028, 1984, 1970 cm^{-1}. ^1H NMR (400 MHz, $CDCl_3$): δ = 0.90 (s, 2 H), 1.31 (s, 4 H), 6.40 (s, 12 H), 6.94 (s, 12 H) ppm. ^{13}C NMR (400 MHz, $CDCl_3$): δ = 211.0, 123.7, 113.6, 29.0, 21.2 ppm. ^{31}P NMR (400 MHz, $CDCl_3$): δ = 138.60 ppm. HR-MS (EI): calcd. for $[M]^+$ 787.9944; found 787.9967.

X-ray Structure Determinations: The single-crystal X-ray data were collected with a Siemens SMART CCD diffractometer. The data were collected at 293 K by using graphite-monochromated Mo-K_α radiation (λ = 0.71073 Å) with the ω-2θ scan mode. Data processing was accomplished with the SAINT processing program.[51] Intensity data were corrected for absorption with empirical methods. The structure was solved by direct methods and refined on F_o^2 against full-matrix least squares using the SHELXTL-97 program package.[52] All of the non-hydrogen atoms were refined anisotropically. Hydrogen atoms were located by geometrical calculation, but their positions and thermal parameters were fixed during the structure refinement. A summary of the crystallographic data and structural determinations is provided in Table 5. CCDC-617988 (for **2**), -617989 (**3**), -617990 (**4**), and -617991 (**5**) contain the supplementary crystallographic data for this paper. These data can be obtained free of charge from The Cambridge Crystallographic Data Center via www.ccdc.cam.ac.uk/data_request/cif

Electrochemistry: Acetonitrile used for electrochemical measurements was distilled from P_2O_5 and freshly distilled from CaH_2 under N_2. Measurements were made with a BAS 100 B/W electrochemical workstation controlled by a PC running BAS 100W 2.0 software.[??] ((<=AUTHOR: Please add reference for software!)) The working electrode was glassy carbon (Bioanalytical Systems) of diameter 3 mm, successively polished with 3 μm and 1 μm alumina and sonicated in ion-free water for 15 min prior to use. The counter electrode was a platinum wire. The experimental reference electrode was a non-aqueous Ag/Ag^+ electrode (0.01 M $AgNO_3$/0.1 M nBu$_4$NPF$_6$ in CH_3CN). The supporting electrolyte was 0.1 M nBu$_4$NPF$_6$ (Fluka, electrochemical grade). Ferrocene was used as an internal reference. All potentials are reported relative to Fc^+/Fc. During the electrocatalytic experiments under argon, increments of acid were added by microsyringe. Bulk electrolysis experiments were performed under argon with a BAS 100 B/W electrochemical analyzer, and carried out on a glassy carbon rod (A = 3.14 cm^2) in a gas-tight H-type electrolysis cell containing ca. 18 mL of CH_3CN solution. Gas chromatography was performed with a GC 920 instrument equipped with a thermal conductivity detector (TCD) under isothermal conditions with argon as a carrier gas.

Table 5. X-ray crystallographic data for **2**–**5**.

	2	**3**	**4**	**5**
Empirical formula	$C_{24}H_{20}Fe_2NO_5PS_2$	$C_{39}H_{34}Fe_2N_2O_4P_2S_2$	$C_{20}H_{18}Fe_2N_3O_5PS_2$	$C_{31}H_{30}Fe_2N_6O_4P_2S_2$
M_r [g mol^{-1}]	609.20	832.44	587.16	788.37
λ [Å]	0.71073	0.71073	0.71073	0.71073
Crystal system	monoclinic	monoclinic	triclinic	tetragonal
Space group	$P2_1/c$	$P2(1)$	$P\bar{1}$	$P4(3)$
a [Å]	9.2405(17)	9.373(3)	9.2604(19)	19.042(3)
b [Å]	17.439(3)	16.816(5)	9.646(2)	19.042(3)
c [Å]	16.549(3)	12.407(4)	14.459(3)	9.6956(19)
α [°]	90	90	91.520(3)	90
β [°]	102.025(3)	98.333(5)	100.732(3)	90
γ [°]	90	90	106.683(3)	90
V [Å^3]	2608.3(8)	1934.9(10)	1211.2(4)	3515.8(10)
Z	4	2	2	4
T [K]	293	293	293	293
$\rho_{calcd.}$ [g cm^{-3}]	1.551	1.429	1.610	1.489
μ [mm^{-1}]	1.369	0.982	1.472	1.079
F [000]	1240	856	596	1616
Total reflections	6099	6542	5394	7226
Reflections observed	3296	3938	4545	5019
Parameters	316	460	298	424
Goodness-of-fit on F^2	0.947	1.011	1.092	1.017
R_1[a] [$I > 2\sigma(I)$]	0.0653	0.0800	0.0398	0.0426
$wR2$[b] [$I > 2\sigma(I)$]	0.1240	0.1444	0.1127	0.0619
Max. peak/hole [e Å^{-3}]	0.860/–0.574	0.782/–0.326	0.569/–0.739	0.322/–0.251

[a] $R_1 = (\Sigma||F_o| - |F_c||)/(\Sigma|F_o|)$. [b] $wR2 = [\Sigma w(F_o^2 - F_c^2)^2/\Sigma w(F_o^2)^2]^{1/2}$.

Acknowledgments

We are grateful to the National Natural Science Foundation of China (Project 20472012) and the China Postdoctoral Science Foundation (Project 20090450105).

[1] R. F. Service, *Science* **2004**, *305*, 958–961.
[2] U. Koelle, *New J. Chem.* **1992**, *16*, 157–169.
[3] R. Cammack, *Nature* **1999**, *397*, 214–215.
[4] M. Y. Darensbourg, *Nature* **2005**, *433*, 589–591.
[5] M. W. W. Adam, *Biochim. Biophys. Acta* **1990**, *1020*, 115–145.
[6] J. W. Peters, *Curr. Opin. Struct. Biol.* **1999**, *9*, 670–676.
[7] M. Frey, *ChemBioChem* **2002**, *3*, 152–160.
[8] J. W. Peters, W. N. Lanzilotta, B. J. Lemon, L. C. Seefeldt, *Science* **1998**, *282*, 1853–1858.
[9] Y. Nicolet, C. Piras, P. Legrand, C. E. Hatchikian, J. C. Fontecilla-Camps, *Structure* **1999**, *7*, 13–23.
[10] A. L. De Lacey, C. Stadler, C. Cavazza, E. C. Hatchikian, V. M. Fernandez, *J. Am. Chem. Soc.* **2000**, *122*, 11232–11233.
[11] Z. Chem, B. J. Lemon, S. Huang, D. J. Swartz, J. W. Peters, K. A. Bagley, *Biochemistry* **2002**, *41*, 2036–2043.
[12] Y. Nicolet, A. L. deLacey, X. Vernède, V. M. Fernandez, E. C. Hatchikian, J. C. Fontecilla-Camps, *J. Am. Chem. Soc.* **2001**, *123*, 1596–1601.
[13] H.-J. Fan, M. B. Hall, *J. Am. Chem. Soc.* **2001**, *123*, 3828–3829.
[14] J. D. Lawrence, H. Li, T. B. Rauchfuss, M. Bénard, M.-M. Rohmer, *Angew. Chem. Int. Ed.* **2001**, *40*, 1768–1771.
[15] M. Razavet, S. C. Davies, D. L. Hughes, C. J. Pickett, *Chem. Commun.* **2001**, 847–848.
[16] T. Liu, M. Y. Darensbourg, *J. Am. Chem. Soc.* **2007**, *129*, 7008–7009.
[17] D. J. Evans, C. J. Pickett, *Chem. Soc. Rev.* **2003**, *32*, 268–275.
[18] C. Tard, X. Liu, S. K. Ibrahim, M. Bruschi, L. D. Gioia, S. C. Davies, X. Yang, L.-S. Wang, G. Sawers, C. J. Pickett, *Nature* **2005**, *433*, 610–613.
[19] D. Chong, I. P. Georgakaki, R. Mejia-Rodriguez, J. Sanabria-Chinchilla, M. P. Soriaga, M. Y. Darensbourg, *Dalton Trans.* **2003**, 4158–4163.
[20] R. Mejia-Rodriguez, D. Chong, J. H. Reibenspies, M. P. Soriaga, M. Y. Darensbourg, *J. Am. Chem. Soc.* **2004**, *126*, 12004–12014.
[21] F. Gloaguen, J. D. Lawrence, T. B. Rauchfuss, *J. Am. Chem. Soc.* **2001**, *123*, 9476–9477.
[22] F. Gloaguen, J. D. Lawrence, T. B. Rauchfuss, M. Bénard, M.-M. Rohmer, *Inorg. Chem.* **2002**, *41*, 6573–6582.
[23] S. J. Borg, T. Behrsing, S. P. Best, M. Razavet, X. Liu, C. J. Pickett, *J. Am. Chem. Soc.* **2004**, *126*, 16988–16999.
[24] S. Ott, M. Kritikos, B. Åkermark, L. Sun, R. Lomoth, *Angew. Chem. Int. Ed.* **2004**, *43*, 1006–1009.
[25] S. Jiang, J. H. Liu, L. Sun, *Inorg. Chem. Commun.* **2006**, *9*, 290–292.
[26] J. W. Tye, M. Y. Darensbourg, M. B. Hall, *Inorg. Chem.* **2006**, *45*, 1552–1559.
[27] C. Greco, M. Bruschi, P. Fantucci, L. De Gioia, *Eur. J. Inorg. Chem.* **2007**, 1835–1843.
[28] J. W. Tye, J. Lee, H.-W. Wang, R. Mejia-Rodriguez, J. H. Reibenspies, M. B. Hall, M. Y. Darensbourg, *Inorg. Chem.* **2005**, *44*, 5550–5552.
[29] J. Hou, X. J. Peng, Z. Y. Zhou, S. G. Sun, X. Zhao, S. Gao, *J. Organomet. Chem.* **2006**, *691*, 4633–4640.
[30] P. Li, M. Wang, C. He, G. Li, X. Liu, C. Chen, B. Åkermark, L. Sun, *Eur. J. Inorg. Chem.* **2005**, 2506–2513.
[31] K. G. Moloy, J. L. Petersen, *J. Am. Chem. Soc.* **1995**, *117*, 7696–7710.
[32] S. Serron, J. Huang, S. P. Nolan, *Organometallics* **1998**, *17*, 534–539.
[33] A. M. Trzeciak, T. Głowiak, R. Grzybek, J. J. Ziółkowski, *J. Chem. Soc., Dalton Trans.* **1997**, 1831–1837.
[34] E. J. Lyon, I. P. Georgakaki, J. H. Reibenspies, M. Y. Darensbourg, *Angew. Chem. Int. Ed.* **1999**, *38*, 3178–3180.
[35] J. L. Nehring, D. M. Heinekey, *Inorg. Chem.* **2003**, *42*, 4288–4292.
[36] X. Zhao, I. P. Georgakaki, M. L. Miller, J. C. Yarbrough, M. Y. Darensbourg, *J. Am. Chem. Soc.* **2001**, *123*, 9710–9711.
[37] F. Gloaguen, J. D. Lawrence, M. Schmidt, S. R. Wilson, T. B. Rauchfuss, *J. Am. Chem. Soc.* **2001**, *123*, 12518–12527.

[38] J. L. Atwood, A. H. Cowley, W. E. Hunter, S. K. Mehrota, *Inorg. Chem.* **1982**, *21*, 1354–1356.
[39] K. Nakamoto, *Infrared and Raman Spectra of Inorganic and Coordination Compounds*, part B ("Applications in Coordination, Organometallic, and Bioinorganic Chemistry"), 5th ed., John Wiley & Sons, New York, **1997**, pp. 126–148.
[40] J. Castro, A. Moyano, M. A. Pericàs, A. Riera, M. A. Maestro, J. Mahía, *Organometallics* **2000**, *19*, 1704–1712.
[41] L. C. Song, Z. Y. Yang, H. Z. Bian, Y. Liu, H. T. Wang, X. F. Liu, Q. M. Hu, *Organometallics* **2005**, *24*, 6126–6135.
[42] L. C. Song, J. H. Ge, X. G. Zhang, Y. Liu, Q. M. Hu, *Eur. J. Inorg. Chem.* **2006**, 3204–3210.
[43] F. Gloaguen, D. Morvan, J.-F. Capon, P. Schollhammer, J. Talarmin, *J. Electroanal. Chem.* **2007**, *603*, 15–20.
[44] M. H. Cheah, C. Tard, S. J. Borg, X. M. Liu, S. K. Ibrahim, C. J. Pickett, S. P. Best, *J. Am. Chem. Soc.* **2007**, *129*, 11085–11092.
[45] A. J. Bard, L. R. Faulkner, *Electrochemical Methods*, John Wiley & Sons, New York, **1980**, p. 218.
[46] I. Bhugun, D. Lexa, J.-M. Savéant, *J. Am. Chem. Soc.* **1996**, *118*, 3982–3983.
[47] G. A. N. Felton, R. S. Glass, D. L. Lichtenberger, D. H. Evans, *Inorg. Chem.* **2006**, *45*, 9181–9184.
[48] C. M. Thomas, O. Rudiger, T. Liu, C. E. Carson, M. B. Hall, M. Y. Darensbourg, *Organometallics* **2007**, *26*, 3976–3984.
[49] Z. Yu, M. Wang, P. Li, W. B. Dong, F. J. Wang, L. C. Sun, *Dalton Trans.* **2008**, 2400–2406.
[50] L. E. Bogan, D. A. Lesch, T. B. Rauchfuss, *J. Organomet. Chem.* **1983**, *250*, 429–438.
[51] *Software packages SMRT and SAINT*, Siemens Analytical X-ray Instruments Inc., Madison, WI, **1996**.
[52] *SHELXTL*, version 5.1, Siemens Industrial Automation, Inc., Madison, WI, **1997**.

Received: March 16, 2010
Published Online: July 9, 2010

DOI: 10.1002/ejic.201000420

Synthesis, Electrochemical Behavior, and Self-Assembly of Metallocene-Functionalized Thiofluorenes

Katrin Döring,[a] Nirmalya Ballav,[b][‡] Michael Zharnikov,*[b] and Heinrich Lang*[a]

Keywords: Metallocenes / Thiols / Fused ring systems / Self-assembly / Monolayers / Cyclic voltammetry

With a view to preparing organometallics for the fabrication of self-assembled monolayers (SAMs) and their possible electrochemical applications, we report the synthesis and characterization of ferrocene- and ruthenocene-functionalized thiofluorenes **4b** and **6b**, respectively. These sandwich compounds were accessible through a consecutive synthesis methodology. 9,9-Dimethyl-2,7-diiodofluorene (**1**) with *t*BuLi, S_8, and Me(CO)Cl gave 9,9-dimethyl-2-iodo-7-thioacetylfluorene (**2**), which, with Mc–C≡CH [**3**: Mc = (η^5-C_5H_4)(η^5-C_5H_5)Fe (Fc); **5**: Mc = (η^5-C_5H_4)(η^5-C_5H_5)Ru (Rc)] following the Sonogashira C–C cross-coupling protocol, produced the corresponding metal alkynyl-fluorenes Mc–C≡C–9,9-$FluMe_2$–$SC(O)CH_3$ (**4a**: Mc = Fc; **6a**: Mc = Rc; Flu = fluorenyl). Addition of NH_4OH/HCl gave thiols Mc–C≡C–9,9-$FluMe_2$–SH (**4b**: Mc = Fc; **6b**: Mc = Rc). Compounds **4b**, **6b**, and the related precursors were characterized electrochemically by cyclic voltammetry (CV). For comparison, the CV data of several biphenyl analogues of **4b** and **6b** are also reported and thus the oxidation processes of the Fc, Rc, and sulfur units have been studied. The ability of **4b** and **6b** to form SAMS was demonstrated by the fabrication of such films on Au(111) substrates. These films were subsequently characterized by X-ray photoelectron spectroscopy and near-edge X-ray absorption fine structure spectroscopy. The spectroscopic data for the **4b**/Au and **6b**/Au films suggest the formation of contaminant-free SAMs with relatively high packing density (2.0×10^{14} and 2.2×10^{14} molecules/cm^2, respectively).

Introduction

During the last two decades, the self-assembly of thiols on various metal and semiconductor substrates has received considerable attention. With an appropriate molecular architecture this process results in the formation of self-assembled monolayers (SAMs).[1–6] This architecture consists of a combination of three essential building blocks, namely a head group (in the given case –SH), which covalently binds to the substrate, a spacer (e.g., an alkyl or oligophenyl chain), which provides intermolecular interactions and drives the self-assembly, and a tail group (e.g., –OH or $–CO_2H$), which, after the formation of a SAM, defines the surface properties of the entire system. A broad flexibility in the design of the target molecules for SAM-like systems, and thiol-based SAMs in particular, leads to numerous practical applications in the areas of nanotechnology, bio-engineering, electronics, etc.[6] Among other possible architectures, thiols with redox-active tail groups (e.g., ferrocenyl,[7–13] ruthenocenyl,[14] or other[15–17] moieties) can be used as potential candidates for SAM formation on suitable substrates (e.g., coinage metals or GaAs).[18–36] The corresponding molecular films can then be used in different electrochemical applications with the substrate itself acting as a positive or negative electrode depending on the need. In particular, these films can serve as active electrochemical templates for which factors governing the rate of electron transfer across interfacial barriers can be precisely monitored and controlled. Furthermore, thiolate SAMs of ferrocenyl/isoquinoline-functionalized DNA probes on a Au electrode have recently been used for electrochemical genotyping.[36]

In view of the above notion, we recently reported the synthesis and characterization of metallocene-terminated biphenyl ethynyl thiols Mc–C≡C–C_6H_4–C_6H_4–SH [**8b**: Mc = (η^5-C_5H_4)(η^5-C_5H_5)Fe; **9b**: Mc = (η^5-C_5H_4)(η^5-C_5H_5)Ru] and their use as molecular constituents for the preparation of homogeneous, conformal, and mixed SAMs on Au substrates.[28,31,37] In these molecules, the electrochemically active Mc moieties are connected to the thiol head-group through a biphenyl-alkynyl unit, which is considered to be a relatively good molecular conductor, a prerequisite for the fast transfer of electrochemical signals to the substrate.[37] As an alternative to the biphenyl-alkynyl unit, a dialkylfluorenyl moiety can be considered, which differs from bi-

[a] Technische Universität Chemnitz, Fakultät für Naturwissenschaften, Institut für Chemie, Lehrstuhl für Anorganische Chemie,
Straße der Nationen 62, 09111 Chemnitz, Germany
Fax: +49-371-531-21219
E-mail: heinrich.lang@chemie.tu-chemnitz.de
[b] Universität Heidelberg, Institut für Angewandte Physikalische Chemie,
Im Neuenheimer Feld 253, 69120 Heidelberg, Germany
Fax: +49-6221-54 6199
E-mail: michael.zharnikov@urz.uni-heidelberg.de
[‡] Present address: Laboratory for Micro and Nanotechnology, Paul Scherrer Institute,
5232 Villigen, Switzerland

phenyl by a $C[(CH_2)_nCH_3]_2$ connectivity in the biphenyl backbone.[37,38] This connectivity fixes the phenylene units relative to each other in a planar conformation, in contrast to biphenyl in which possible rotation around the inner biphenyl carbon–carbon bond can hinder the overlap between the phenylene π systems, which reduces the efficiency of the transport properties of the biphenyl moiety. The dihedral angle of biphenyl in the gas phase is ca. 39°,[39] whereas the dihedral rotation is believed to be lifted in the 3D solid phase.[40,41] Fluorene is frequently used as a building block for molecular wires.[42,43] According to break junction measurements, its conductivity is comparable, although slightly inferior, to that of biphenyl.[44,45] In addition, the change in the molecular backbone could also affect the packing and orientation of the molecules in the corresponding SAMs upon assembly of the target molecules on a suitable substrate. Note that fluorene is a suitable building block for the SAM constituents; in particular, it has previously been shown that fluorene-based thiols form SAMs on gold.[39,46–48]

In this paper we present straightforward methodologies for the synthesis of different metallocene-functionalized thiofluorenes [Mc–C≡C–9,9-FluMe_2–SR: Mc = ferrocenyl (Fc), ruthenocenyl (Rc); R = H, $C(O)CH_3$; Fc = (η^5-C_5H_4)(η^5-C_5H_5)Fe; Rc = (η^5-C_5H_4)(η^5-C_5H_5)Ru; Flu = fluorenyl] and also describe their electrochemical behavior in the molecular state. Furthermore, the use of Mc–C≡C–9,9-FluMe_2–SR compounds as molecular constituents for the formation of SAMs on Au(111) substrates is demonstrated and discussed. The films obtained were characterized by several complementary spectroscopic techniques, namely by X-ray photoelectron spectroscopy (XPS) and near-edge X-ray absorption fine structure (NEXAFS) spectroscopy. The results for the Mc–C≡C–9,9-FluMe_2–SR compounds are compared with the analogous data of non-interlinked biphenyl metallocene alkynes.[28] Note that the CMe_2 unit was chosen as a unit of connectivity,[37,38] on the one hand, for synthetic reasons[49] and, on the other hand, for the small size of the methyl group relative to longer alkanes, which is important for efficient molecular packing.

Results and Discussion

Synthesis

The metallocene-based thioacetyls and thiols Mc–C≡C–9,9-FluMe_2–SR [Mc = Fc: **4a**: R = C(O)Me; **4b**: R = H; Mc = Rc: **6a**: R = C(O)Me; **6b**: R = H; Fc = (η^5-C_5H_4)(η^5-C_5H_5)Fe; Rc = (η^5-C_5H_4)(η^5-C_5H_5)Ru; Flu = fluorenyl] were prepared as outlined in reaction (1) and Scheme 1, respectively.

Iodo-functionalized 9,9-dimethylfluorene-thioacetyl **2** [reaction (1)] was accessible by the consecutive treatment of 9,9-dimethyl-2,7-diiodofluorene (**1**)[50] with *t*BuLi, $^1/_8S_8$, and MeC(O)Cl in tetrahydrofuran at –80 °C. After appropriate work-up, compound **2** was isolated as a colorless oil in 54% yield (see Exp. Sect.).

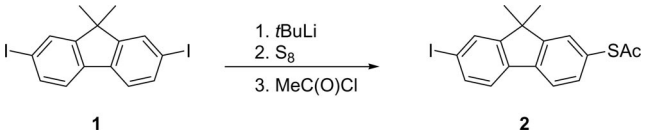

1 **2** (1)

Organometallics **4** and **6** were prepared by the synthetic methodology outlined in Scheme 1. Compounds Mc–C≡C–9,9-FluMe_2–SAc [**4a**: Mc = Fc; **6a**: Mc = Rc; Ac = C(O)Me] were accessible by treating 9,9-dimethyl-2-iodo-7-thioacetylfluorene (**2**) with Mc–C≡CH (**3**: Mc = Fc; **5**: Mc = Rc) in a 1:1 molar ratio following the Sonogashira carbon–carbon cross-coupling protocol.[51,52] Addition of NH_4OH followed by HCl to **4a** and **6a** afforded by concomitant precipitation of NH_4Cl the appropriate thiol end-grafted compounds Mc–C≡C–9,9-FluMe_2–SH **4b** (Mc = Fc) and **6b** (Mc = Rc; Scheme 1), respectively, which, after appropriate work-up, were isolated as orange (**4a**, **4b**) or yellow solid materials (**6a**, **6b**) in 45–99% yields (see Exp. Sect.).

Compounds **4a** and **6a** are stable towards air and moisture, whereas the corresponding thiols **4b** and **6b** must be kept under inert gas to avoid decomposition. All com-

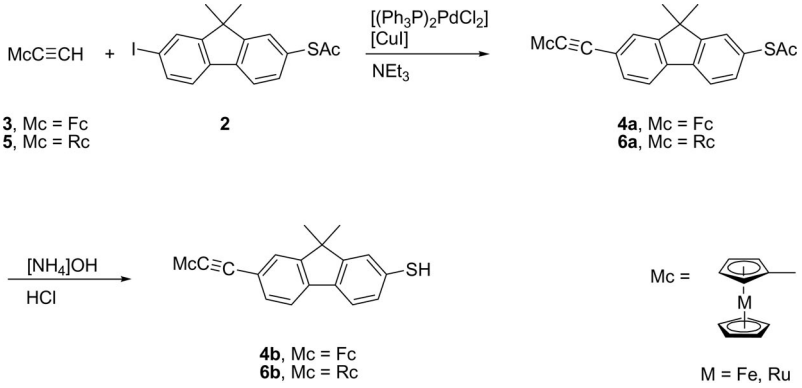

Scheme 1. Synthesis of **4** and **6** from **2** and Mc–C≡CH [Mc = Fc (**3**), Rc (**5**); Fc = (η^5-C_5H_4)(η^5-C_5H_5)Fe; Rc = (η^5-C_5H_4)(η^5-C_5H_5)Ru; Ac = C(O)Me].

pounds dissolve in common polar solvents including dichloromethane and tetrahydrofuran.

Compounds **2**, **4**, and **6** were characterized by elemental analysis, spectroscopy [IR, ^{1}H, ^{13}C(^{1}H) NMR], and mass spectrometry (ESI-TOF).

Structural information concerning the thioester and thiol moieties in **2**, **4**, and **6** was obtained by IR spectroscopy (see Exp. Sect.). Compounds **2**, **4a**, and **6a** show a characteristic ν_{CO} vibration at around 1700 cm^{-1} independent of the substituents at the 2-position of the fluorenyl moiety. Furthermore, a typical C≡C stretching frequency at 2206 cm^{-1} (**4a**, **6a**) was observed for Mc–C≡C–9,9-FluMe$_2$–SAc. Acetyl exchange in **4a** and **6a** for a hydrogen atom to give **4b** and **6b**, respectively, is indicated by very prominent resonance signals and vibrations of the SAc and SH groups, which allowed the progress of the reaction to be monitored by NMR {i.e., ^{1}H NMR: **4a**, **6a**: δ = 2.45 ppm [SC(O)Me]; **4b**, **6b**: δ = 3.56 ppm (SH)} and IR spectroscopy (ν_{CO}: **4a**, **6a**: $\tilde{\nu}$ = 1700 cm^{-1}; ν_{SH}: **4b**, **6b**: $\tilde{\nu}$ = 2561 cm^{-1}; $\nu_{C\equiv C}$: **4a**, **6a**: $\tilde{\nu}$ = 2206 cm^{-1}; **4b**: $\tilde{\nu}$ = 2198 cm^{-1}; **6b**: $\tilde{\nu}$ = 2202 cm^{-1}).

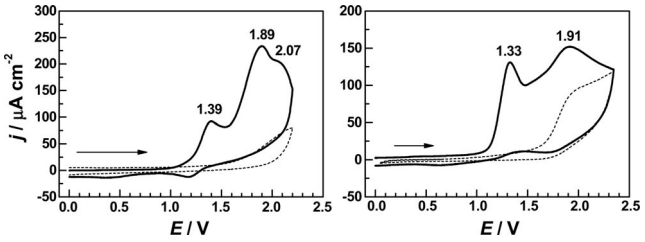

Figure 1. Cyclovoltammograms of **1** (left) and **7** (right) in dichloromethane at 25 °C {[nBu$_4$N]PF$_6$ supporting electrolyte (0.1 M), scan rate 100 mV s^{-1}; dashed line: blank supporting electrolyte solution only}.

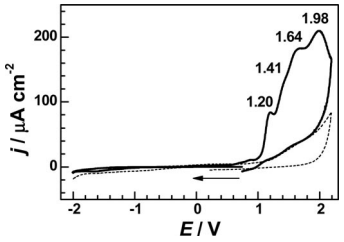

Figure 2. Cyclovoltammogram of **2** in dichloromethane at 25 °C {[nBu$_4$N]PF$_6$ supporting electrolyte (0.1 M), scan rate 100 mV s^{-1}; dashed line: blank supporting electrolyte solution only}.

Electrochemical Behavior

Compounds **1**, **2**, **4a**, **4b**, **6a**, **6b**, and 9,9-dimethylfluorene (**7**; synthesized according to ref.[53]) were studied by cyclic voltammetry to determine the redox behavior of the ferrocenyl and ruthenocenyl sandwich units as well as the thiol and thioacetyl groups.

The starting material I–FluMe$_2$–I (**1**) exhibits three oxidation potentials at $E_{p,ox}$ = 1.39, 1.89, and 2.07 V (Figure 1). Oxidation of the iodo substituent has been reported for the structurally related 4,4′-diiodobiphenyl with two current peaks at $E_{p,ox}$ = 1.65 and 1.76 V, respectively.[54,55] For comparison, 9,9-dimethylfluorene (**7**) was studied by cyclic voltammetry under similar conditions. Two irreversible oxidation events located at $E_{p,ox}$ = 1.33 and 1.91 V were observed (Figure 1). These are in the same range as the potential peaks for **1**. This is in agreement with the data found in the literature for similar compounds, that is, fluorene and 9,9-diethylfluorene, for which the main irreversible oxidation peak was observed at $E_{p,ox}$ = 1.32 V with a peak located at $E_{p,ox}$ = 1.6 V (vs. a silver/silver chloride electrode).[56] As can be seen from the literature, a dimer is produced during the oxidation of the fluorene.[56] Similar redox processes were found for 9,9-dimethyl-2-phenylfluorene, which has been explained by the doping/dedoping process of a polymer coating the electrode.[57]

For molecule **2** irreversible oxidation events were found at $E_{p,ox}$ = 1.20, 1.41 (shoulder), 1.64, and 1.98 V (Figure 2). In comparison with the similar biphenyl compound I–C$_6$H$_4$–C$_6$H$_4$–SAc,[54] the first potential can be assigned to the oxidation of the thioacetyl unit,[55] the following events most likely being associated with the fluorenic entity.[56,57]

For ferrocenes **4a** and **4b** events at $E°$ = 0.09 V (ΔE = 0.10 V) (**4a**) and 0.07 V (ΔE = 0.12 V) (**4b**; Figure 3) for the Fc/Fc$^+$ redox couple are typical. Compared with Fc–C≡CH (**3**) [$E°$ = 0.11 V (ΔE = 0.08 V)],[58] the ferrocenyl unit in **4** is easier to oxidize. Irreversible oxidation processes were observed at $E_{p,ox}$ = 1.18, 1.58, and 1.90 V for **4a** and $E_{p,ox}$ = 0.99, 1.35, and 1.88 V for **4b** (Figure 3). The ferrocenyl moiety becomes irreversible only when the potential is chosen to be more positive than $E_{p,ox}$ = 1.18 (**4a**) or 0.99 V (**4b**).

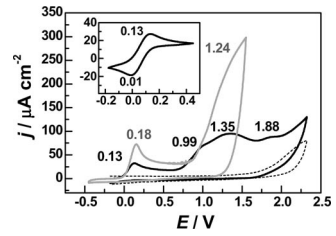

Figure 3. Cyclovoltammogram of **4b** (black line) and **8b** (grey line) in dichloromethane at 25 °C {[nBu$_4$N]PF$_6$ supporting electrolyte (0.1 M), scan rate 100 mV s^{-1}; dashed line: blank supporting electrolyte solution only; inset: cyclovoltammogram of the ferrocenyl acquired at the same conditions between –0.2 and 0.4 V}.

For the isostructural ruthenocene compounds, an irreversible oxidation event was found for the ruthenocene/ruthenocenium redox couple at $E_{p,ox}$ = 0.58 (**6a**) and 0.53 V (**6b**; Figure 4). This is also typical of ruthenocenes, for example, Rc–C≡C–C$_6$H$_4$–C$_6$H$_4$–SR [R = H, C(O)Me][31] or [Ru(η^5-C$_5$H$_5$)$_2$],[59] whereas compounds like [Ru(η^5-C$_5$H$_4$PPh$_2$)$_2$)][60,61a] and [Ru(η^5-C$_5$Me$_5$)(C$_{13}$Me$_8$H)][62] show a reversible oxidation character. The supporting electrolyte and cyclopentadienyl substituents of the ruthenocene compounds may affect the redox behavior.[60–65]

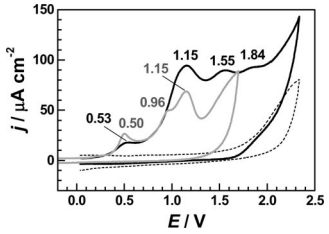

Figure 4. Cyclovoltammogram of **6b** (black line) and **9b** (grey line) in dichloromethane at 25 °C {[nBu$_4$N]PF$_6$ supporting electrolyte (0.1 M), scan rate 100 mV s^{-1}; dashed line: blank supporting electrolyte solution only}.

Furthermore, irreversible oxidations were observed at $E_{p,ox}$ = 1.24, 1.71, and 1.95 V for **6a** and at $E_{p,ox}$ = 1.15, 1.55, and 1.84 V for **6b** (Figure 4). Comparison of these values with the potentials of **4a** and **4b** indicate that **4** is easier to oxidize than **6**, as can also be seen by comparing Fc–C≡CH [$E°$ = 0.11 V (ΔE = 0.08 V)][58] with Rc–C≡CH ($E_{ox,p}$ = 0.61 V).[31]

Comparative Assessment of the Electrochemical Behavior

Mc–C≡C–C$_6$H$_4$–C$_6$H$_4$–SR versus Mc–C≡C–9,9-FluMe$_2$–SR

A comparison of the redox behavior of the fluorenyl compounds **4** and **6** with the related biphenyl molecules Mc–C≡C–C$_6$H$_4$–C$_6$H$_4$–SR [**8**: Mc = Fc; **9**: Mc = Rc; R = H, C(O)Me] studied earlier[31,37] was made. The ferrocene/ferrocenium couples of **4a** and **4b** are comparable to the related compounds **8a** [$E°$ = 0.18 V (ΔE = 0.14 V); Mc = Fc; R = C(O)Me] and **8b** [$E°$ = 0.04 V (ΔE = 0.09 V); Mc = Fc; R = H; Figure 3].[37] It can be seen that the –SH-terminated molecules **4b** and **8b** are easier to oxidize than the analogous S–C(O)Me-protected compounds **4a** and **8a**, which corresponds to the increased electron density in the ferrocenyl unit.

The sulfur oxidations in the biphenyl molecules take place at $E_{p,ox}$ = 1.42 (**8a**) and 1.24 V (**8b**; Figure 3).[37] In the case of the fluorenyl compounds, three irreversible oxidations were found corresponding to sulfur and fluorene (see above). Even though the sulfur oxidation cannot be clearly identified, the consequence of the inductive effects of the sulfur atoms [–SH, –S–C(O)Me] can be acknowledged.

The isostructural ruthenocenes **6** and **9** show, however, irreversible oxidation of the ruthenocene/ruthenocenium redox couple at $E_{p,ox}$ = 0.58 (**6a**), 0.53 (**6b**), 0.58 [**9a**: Mc = Rc, R = C(O)Me], and 0.50 V (**9b**: Mc = Rc, R = H; Figure 4).[31] The influence of the different sulfur end-groups in the related ferrocene compounds can also be seen for the ruthenocene molecules.

Furthermore, the cleavage of the sulfur–carbon bond of –S–C(O)Me in **9a** was observed at $E_{p,ox}$ = 1.30 V, whereas with –SH in **9b** this event occurred at $E_{p,ox}$ = 0.96 V (Figure 4).[31] This tendency is also noticeable in the corresponding fluorenyl compounds **6a** and **6b** as well as in the ferrocenyl compounds.

It could be shown that the ferrocenyl and ruthenocenyl oxidation events in the fluorenyl and biphenyl compounds are comparable. Even though the oxidation processes for the sulfur –S–C(O)Me and –SH units cannot be clearly identified in Mc–C≡C–9,9-FluMe$_2$–SR, the inductive effects can be verified.

Self-Assembly

XPS

The formation of SAMs upon the adsorption of molecules of **4b** and **6b** onto Au substrates was confirmed by XPS spectroscopic analyses. XPS spectra for the combined C1s/Ru3d, S 2p, and Fe 2p$_{3/2}$ binding energy ranges are presented in Figure 5 (a–c) for SAMs of **4b** and **6b** on Au along with the corresponding spectral fits. Both the C 1s and C1s/Ru3d spectra for **4b**/Au and **6b**/Au exhibit the main C 1s emission signal at ca. 284.4 eV, which is related to the biphenyl backbone and the cyclopentadienyl (μC_p) rings of Fc and Rc.[28,31,32] The C 1s peaks of the films of **4b** and **6b** are somewhat broader than that for the biphenyl thiol SAM.[28] Such an effect has also been observed recently for the SAMs of Fc–C≡C–C$_6$H$_4$–C$_6$H$_4$–SH [**8b**: Fc = (η^5-C$_5$H$_4$)(η^5-C$_5$H$_5$)Fe] and Rc–C≡C–C$_6$H$_4$–C$_6$H$_4$–SH [**9b**: Rc = (η^5-C$_5$H$_4$)(η^5-C$_5$H$_5$)Ru].[28,31] The broadening of the C 1s photoemission does not necessarily imply a lower homogeneity of the **4b** and **6b** films compared with the biphenyl dithiol film but rather reflects the fact that the C 1s peak for this type of SAM contains additional contributions from the μC_p rings, the C–S bond, and the shake-up-like excitation in the aromatic moiety.[28] Further contributions from the C≡C and CMe$_2$ groups cannot be neglected. Figure 5 (a) shows no spectral features related to CO, C=O, or CO$_2$H moieties and even correlates with the observed O 1s XPS spectra (not shown) recorded for both **4b**/Au and **6b**/Au. The Ru 3d$_{5/2,3/2}$ doublets at ca. 280.4 (Ru 3d$_{5/2}$) and ca. 284.6 eV (Ru 3d$_{3/2}$) are observed in the **6b**/Au spectrum, which can be assigned to the central Ru atom of the ruthenocenyl moiety.[66] The Ru 3d$_{3/2}$ component coincides with the C 1s main emission and could only be resolved on the basis of the well-distinguished Ru 3d$_{5/2}$ component, the known Ru3d$_{5/2}$/Ru3d$_{3/2}$ spin-orbit coupling, and the branching ratio. As for **4b**/Au, additional information is provided by the observation of the Fe 2p$_{3/2}$ XPS signal shown in Figure 5 (c), which is characteristic of Fe in the ferrocenyl moiety.[32,66] The XPS spectral features of C 1s, Ru 3d, and Fe 2p$_{3/2}$ observed in this study are quite similar to the XPS spectra of SAMs of **8b** and **9b**.[28,31,32] The S 2p spectra of both **4b**/Au and **6b**/Au in Figure 5 (b) exhibit a broad S 2p$_{3/2,1/2}$ doublet at 162.0 eV (S 2p$_{3/2}$), which can be assigned to the well-known thiolate species covalently bonded to metal substrates.[67,68]

On the basis of the intensity ratios of the C 1s and Au 4f XPS signals and the standard attenuation lengths of these emissions,[69] effective film thickness values for **4b**/Au and **6b**/Au were estimated to be 14.5 and 16.5 Å, respectively (accuracy ±5%). Notably, these values are similar to those

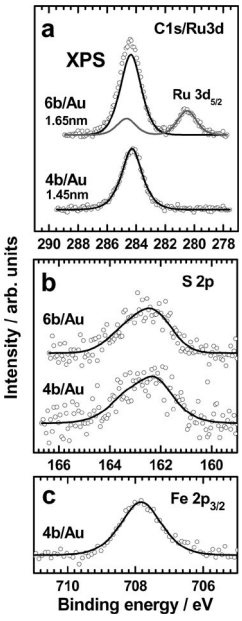

Figure 5. XPS spectra of **4b**/Au and **6b**/Au at various binding energy regions: (a) C1s and Ru3d (b) S 2p, and (c) Fe $2p_{3/2}$. Film thicknesses are also provided in (a).

of **8b** (18.9 Å) and **9b** (15.9 Å),[28,31] which implies that likewise the Mc–C≡C–C_6H_4–C_6H_4–SH and Mc–C≡C–9,9-$FluMe_2$–SR molecules in the corresponding films have an upright orientation. One can also use these values to assess the approximate packing density of **4b**/Au and **6b**/Au by using our recently published approach.[70] As the reference film, the SAM of dodecanethiolate on Au was used with a molecular density of 4.63×10^{14} cm^{-2} (an area per molecule of 21.6 $Å^2$) and an effective thickness of ca. 15 Å. Table 1 summarizes the film thicknesses and molecular densities of the SAMs of **4b**, **6b**, **8b**, and **9b** on Au and shows all these SAMs to have a comparable packing density. Thus, fluorene compounds can be effectively used as molecular constituents for the preparation of contaminant-free SAMs on suitable substrates with relatively high packing density.

Table 1. Film thickness and packing density data for the SAMs **4b**, **6b**, **8b**, and **9b**.

SAMs on Au	Number of atoms (excluding H)	Thickness [Å] (measured)	Molecular density [10^{14} molcm^{-2}]
4b	29	14.5	2.0
6b	29	16.5	2.2
8b	26	18.9	2.9
9b	26	15.9	2.4

NEXAFS Spectroscopy

Along with XPS, complementary information on the composition and chemical identity of the target films can be provided by NEXAFS data. NEXAFS spectra give an insight into the electronic structures of the target films by probing the electronic structure of the unoccupied molecular orbitals of the film constituents.[71] The superimposed carbon K-edge and ruthenium M-edge NEXAFS spectra of **4b**/Au and **6b**/Au as well as the Fe L-edge spectrum of **4b**/Au acquired at the magic angle of X-ray incidence (55°) are presented in Figure 6 (a). These spectra are independent of the molecular orientation on the surface.[71] The spectrum of **4b**/Au shows a π_1* resonance at ca. 285.1 eV, which is characteristic of the biphenyl unit of the fluorenyl moiety.[39] In addition, π*-like resonances at about 285.6 and ca. 287.3 eV can be observed, which are related to the $4e_{1g}$ and $3e_{2u}$ orbitals of the ferrocenyl moiety, respectively.[28,72–74] As a result of the structural similarity of **4b** and **6b**, the spectrum of **6b**/Au shows the same π_1* resonance of the biphenyl unit of the fluorenyl moiety at 285.1 eV,[71] whereas the resonances at 285.6 (weak) and 287.3 eV can be assigned to the $4e_{1g}$ and $3e_{2u}$ orbitals of ruthenocene.[31] The $4e_{1g}$ resonance for ruthenocene is weaker than that for ferrocene, however, such weak resonances are typical of metallocene compounds and may also be found in the spectra of nickelocene or cobaltocene.[72,74] The residual resonance at ca. 286.3 eV is associated with the $4e_{1g}$ orbital of ruthenocene.[73,74] At even higher photon energies, the spectral features of **4b**/Au and **6b**/Au look similar and exhibit almost identical σ* resonances, which reflects the structural resemblance of the ferrocenyl and ruthenocenyl moieties. To further support C K-edge NEXAFS data, the Fe L-edge spectrum of **4b**/Au is presented in Figure 6 (b). The spectrum clearly exhibits π* characteristic resonances of the $4e_{1g}$ and $3e_{2u}$ orbitals of the ferrocenyl moiety at both the L_2- and L_3-edges.[32,68,75] Our NEXAFS data for **4b**/Au and **6b**/Au agree well with the NEXAFS data recently reported[28,31] for **8b**/Au and **9b**/Au, respectively, which, together with the XPS data, suggest that **4b** and **6b** are suitable candidates for the fabrication of SAMs on the Au substrate.

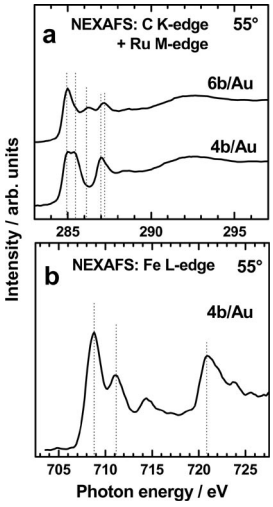

Figure 6. Carbon K-edge and iron L-edge NEXAFS spectra of **4b** and **6b** SAMs on Au(111) acquired at an X-ray incident angle of 55°. Characteristic resonances are marked by dotted lines.

Conclusions

Ferrocenyl- and ruthenocenyl-functionalized thiofluorenes **4b** and **6b**, respectively, have been synthesized. Each of

these molecules comprises electroactive moieties, a conductive fluorene backbone, and a thiol anchoring group. The electrochemical characteristics of **4b** and **6b** were studied in detail and compared with Fc–C≡C–C_6H_4–C_6H_4–SR [R = C(O)CH_3, H] and Rc–C≡C–C_6H_4–C_6H_4–SR [R = C(O)CH_3, H]. In agreement with expectation, the cyclovoltammetric data revealed reversible redox events for the ferrocenyl-based compounds, whereas the corresponding redox events for the ruthenocenyl-based compounds were found to be irreversible. Furthermore the oxidation events for the fluorenyl building block as well as for the different sulfur end-groups (–S–C(O)Me and –SH) are presented. To ensure the effective self-assembly of **4b** and **6b**, these molecules were assembled on the Au(111) substrate and the resulting films were characterized by XPS and NEXAFS spectroscopy. The complementary results from these spectroscopic techniques suggest the formation of densely packed and contaminant-free SAMs of both **4b** and **6b** on the Au substrate. **4b**/Au and **6b**/Au showed an upright orientation of the molecular backbones and covalent anchoring of the thiol end-group. In view of the unique redox behavior of ferrocene and ruthenocene, we plan to carry out electrochemical experiments on these SAMs in the near future. We also plan to perform in-depth structural characterizations of **4b**/Au and **6b**/Au, in particular, their molecular orientation by using angle-dependent NEXAFS spectroscopy.

Experimental Section

General: All reactions were carried out under purified nitrogen using standard Schlenk techniques. *n*-Hexane and tetrahydrofuran were purified by distillation from sodium/benzophenone ketyl, dichloromethane was purified by distillation from phosphorus pentoxide, and triethylamine was dried by distillation from KOH. Ethanol and dimethylformamide were used without further purification. Infrared spectra were recorded with a Nicolet FT-IR 200 spectrometer. NMR spectra were recorded with a Bruker Avance 250 spectrometer. ^{1}H NMR spectra were recorded at 250.130 MHz (internal standard, relative to $CDCl_3$, δ = 7.26 ppm) and $^{13}C\{^1H\}$ NMR spectra at 62.902 MHz (internal standard, relative to $CDCl_3$, δ = 77.16 ppm). Chemical shifts are reported in δ units (parts per million) downfield from tetramethylsilane with the solvent as the reference signal. Cyclovoltammograms (CV) were recorded in a dried single compartment cell purged with purified argon at 25 °C. Platinum wires served as working and counter electrodes. A non-aqueous saturated calomel electrode served as reference electrode. For ease of comparison, all potentials have been converted into the ferrocene/ferrocenium couple [Cp_2Fe/Cp_2Fe^+] [Cp_2Fe = (η^5-C_5H_5)$_2$-Fe] as the reference ($E°$ = 0.00 V).[76,77] Electrolyte solutions were prepared from freshly distilled dichloromethane solutions and [nBu$_4$N]PF_6 (dried under oil-pump vacuum at 120 °C, c = 0.1 M). The organometallic complexes were added at c = 1 mM. CVs were recorded at a scan rate of 100 mV s^{-1} using a Radiometer Analytical PGZ 100 VoltaLab instrument. Elemental analyses were performed with a Flashea instrument (Thermo Electron Corporation). Melting points were determined with a Gallenkamp MFB 595 010 M melting-point apparatus by using sealed nitrogen-purged capillaries. ESI-TOF (electrospray ionization, time-of-flight) mass spectra were recorded in dichloromethane with a micrOTOF QII spectrometer from Bruker Daltonik.

Chemical Synthesis

General Remarks: 9,9-Dimethyl-2,7-diiodofluorene (**1**),[50] Fc–C≡CH (**3**),[78] and Rc–C≡CH (**5**)[79] were prepared following published procedures. All other chemicals are commercially available and were used as received.

Synthesis of 2: *t*BuLi (1.6 M, 8.33 mL, 13.33 mmol) was slowly added to 9,9-dimethyl-2,7-diiodofluorene (**1**; 3.00 g, 6.66 mmol) dissolved in tetrahydrofuran (150 mL) at –80 °C. After 10 min of stirring at this temperature, sulfur (0.21 g, 6.66 mmol) dissolved in tetrahydrofuran (100 mL) was added dropwise and stirring was continued for 45 min at 0 °C. Afterwards, the reaction solution was cooled to –80 °C and MeC(O)Cl (0.52 g, 6.66 mmol) was added in a single portion. After warming the reaction mixture overnight to 25 °C all volatile materials were removed by rotary evaporation followed by the addition of water (25 mL). The reaction mixture was extracted three times with dichloromethane (25 mL) and the combined layers were dried with magnesium sulfate. After removal of all volatiles under an oil-pump vacuum the residue was purified by column chromatography [column size: 20 × 3 cm, silica gel, *n*-hexane/toluene = 1:3 (v/v)]. Molecule **1** was eluted first (colorless band) followed by the title compound (colorless band). Evaporation of the solvents under an oil-pump vacuum gave a colorless oil; yield 1.42 g (3.58 mmol, 54% based on **1**).

IR (KBr): $\tilde{\nu}$ = 2959 (w), 2921 (w), 2858 (w), 1701 (vs, $\nu_{C=O}$), 1596 (w), 1560 (w), 1462 (w), 1447 (m), 1397 (m), 1349 (w), 1263 (m), 1213 (w), 1121 (s), 1093 (s), 1053 (w), 1002 (w), 945 (m), 882 (w), 837 (w), 811 (vs, $\delta_{aryl\text{-}H}$), 793 (m), 736 (m), 669 (w), 614 (m), 526 (w), 494 (w), 438 (w) cm^{-1}. ^{1}H NMR ($CDCl_3$): δ = 1.49 (s, 6 H, CH_3), 2.46 [s, 3 H, SC(O)CH_3], 7.34–7.83 (m, 6 H, C_6H_3) ppm. $^{13}C\{^1H\}$NMR ($CDCl_3$): δ = 26.6 (CH_3), 30.0 [SC(O)CH$_3$], 46.8 (C-CH_3), 93.5 (C-I), 120.5 (C_6H_3), 121.9 (C_6H_3), 126.9 ($^iC/C_6H_3$), 128.4 (C_6H_3), 131.8 (C_6H_3), 133.25 (C_6H_3), 136.01 (C_6H_3), 137.6 ($^iC/C_6H_3$), 139.18 ($^iC/C_6H_3$), 153.4 ($^iC/C_6H_3$), 155.7 ($^iC/C_6H_3$), 193.4 (C=O) ppm. MS (ESI): m/z = 394.99 [M + H]$^+$. $C_{17}H_{15}IOS$ (394.27): calcd. C 51.79, H 3.83; found C 51.97, H 3.95.

Synthesis of 4a: [$(PPh_3)_2PdCl_2$] (29.83 mg, 0.04 mmol, 5 mol-%) and CuI (16.19 mg, 0.08 mmol, 10 mol-%) were added to Fc–C≡CH (**3**; 0.21 g, 1.02 mmol) and **2** (0.33 g, 0.85 mmol) dissolved in triethylamine (20 mL) at 25 °C. After 24 h of stirring at 60 °C all volatiles were removed under an oil-pump vacuum and the title compound was purified by column chromatography [column size: 25 × 2 cm, silica gel, *n*-hexane/dichloromethane = 1:1 (v/v)]. After eluting the starting material **3** (orange band), molecule **4a** was eluted as an orange band. Evaporation of all solvents under an oil-pump vacuum gave an orange-brown solid; yield 0.18 g (0.38 mmol, 45% based on **2**).

M.p. 97 °C. IR (KBr): $\tilde{\nu}$ = 3101 (w, $\nu_{aryl\text{–}H}$), 2961 (m), 2923 (s), 2852 (m), 2206 (w, $\nu_{C\equiv C}$), 1701 (vs, $\nu_{C=O}$), 1654 (s, $\nu_{C=C}$), 1559 (m), 1458 (m), 1401 (m), 1262 (s), 1104 (vs), 1025 (m), 948 (m), 886 (m), 821 (vs, $\delta_{aryl\text{-}H}$), 739 (m), 612 (m), 530 (w), 473 (w) cm^{-1}. ^{1}H NMR ($CDCl_3$): δ = 1.52 (s, 6 H, CH_3), 2.45 [s, 3 H, SC(O)CH_3], 4.27 (s, pseudo-t, 7 H, C_5H_5, C_5H_4), 4.53 (pseudo-t, $^3J_{HH}$ = 1.7 Hz, 2 H, C_5H_4), 7.39–7.50 (m, 6 H, C_6H_3) ppm. $^{13}C\{^1H\}$NMR ($CDCl_3$): δ = 27.1 (CH_3), 30.3 [SC(O)CH$_3$], 47.2 (C-CH_3), 65.5 ($^iC/C_5H_4$), 69.0 ($^\beta C/C_5H_4$), 70.1 (C_5H_5), 71.6 ($^\alpha C/C_5H_4$), 86.5 (C≡C-C_6H_3), 89.0 (C≡C-C_6H_3), 120.4 (C_6H_3), 120.9 (C_6H_3), 123.4 ($^iC/C_6H_3$), 125.8 (C_6H_3), 126.7 ($^iC/C_6H_3$), 128.9 (C_6H_3), 130.8 (C_6H_3), 133.6 (C_6H_3), 137.9 ($^iC/C_6H_3$), 140.2 ($^iC/C_6H_3$), 153.9 ($^iC/C_6H_3$), 154.8 ($^iC/C_6H_3$), 194.5 (C=O) ppm. MS (ESI): m/z = 476.08 [M]$^+$. $C_{29}H_{24}FeOS$ (476.41): calcd. C 73.11, H 5.08; found C 73.26, H 5.12.

Synthesis of 4b: Thioacetate **4a** (92.0 mg, 0.19 mmol) was dissolved in tetrahydrofuran (2 mL) and a 25% aq. NH_4OH solution

(65.7 mg, 1.93 mmol) was added in a single portion at 25 °C. After 20 min of stirring at this temperature, the reaction mixture was acidified with 3 M HCl (1 mL) and was then extracted three times with 15 mL portions of dichloromethane. After evaporation of the solvent of the combined organic fractions under an oil-pump vacuum an orange-brown solid was obtained; yield 83.0 mg (0.19 mmol, 99% based on **4a**).

M.p. 96 °C. IR (KBr): $\tilde{\nu}$ = 3080 (w, ν_{aryl-H}), 2958 (s), 2921 (s), 2852 (m), 2561 (w, ν_{S-H}), 2198 (w, $\nu_{C\equiv C}$), 1654 (m, $\nu_{C=C}$), 1447 (s), 1407 (m), 1262 (s), 1209 (w), 1104 (s), 1078 (m), 1024 (m), 996 (m), 923 (w), 882 (w), 814 (vs, δ_{aryl-H}), 739 (m), 665 (w), 526 (m), 478 (m), 453 (m) cm^{-1}. ^{1}H NMR ($CDCl_3$): δ = 1.48 (s, 6 H, CH_3), 3.56 (s, 1 H, SH), 4.25 (pseudo-t, $^3J_{HH}$ = 1.7 Hz, 2 H, C_5H_4), 4.26 (s, 5 H, C_5H_5), 4.52 (pseudo-t, $^3J_{HH}$ = 1.7 Hz, 2 H, C_5H_4), 7.24–7.64 (m, 6 H, C_6H_3) ppm. ^{13}C{^{1}H}NMR ($CDCl_3$): δ = 27.1 (CH_3), 47.0 (*C*-CH_3), 65.6 (^{i}C/C_5H_4), 68.9 ($^\beta$C/C_5H_4), 70.1 (C_5H_5), 71.5 ($^\alpha$C/C_5H_4), 86.6 (C≡*C*-C_6H_3), 88.7 (*C*≡C-C_6H_3), 119.8 (C_6H_3), 120.8 (C_6H_3), 122.6 (^{i}C/C_6H_3), 124.2 (C_6H_3), 125.7 (C_6H_3), 128.5 (C_6H_3), 129.7 (^{i}C/C_6H_3), 130.7 (C_6H_3), 136.8 (^{i}C/C_6H_3), 138.3 (^{i}C/C_6H_3), 153.3 (^{i}C/C_6H_3), 155.0 (^{i}C/C_6H_3) ppm. MS (ESI): *m*/*z* = 434.07 [M]$^+$. $C_{27}H_{22}FeS$ (434.37): calcd. C 74.66, H 5.10; found C 74.56, H 5.37.

Synthesis of 6a: Thioacetate **6a** was synthesized following the same procedure as that used for the preparation of **4a** {Rc–C≡CH (**5**; 0.23 g, 0.90 mmol), **2** (0.29 g, 0.75 mmol), triethylamine (20 mL), [$(PPh_3)_2PdCl_2$] (26.51 mg, 0.03 mmol, 5 mol-%), CuI (14.38 mg, 0.07 mmol, 10 mol-%)}. After appropriate work-up [column size: 25 × 2 cm, silica gel, *n*-hexane/dichloromethane = 1:3 (v/v)], complex **6a** was obtained as a yellow solid; yield 0.20 g (0.38 mmol, 51% based on **2**).

M.p. 85 °C. IR (KBr): $\tilde{\nu}$ = 3098 (w, ν_{aryl-H}), 3048 (w), 2958 (m), 2917 (w), 2852 (w), 2206 (w, $\nu_{C\equiv C}$), 1701 (vs, $\nu_{C=O}$), 1686 (s), 1655 (m, $\nu_{C=C}$), 1560 (m), 1459 (m), 1405 (m), 1348 (w), 1260 (vs), 1242 (vs), 1156 (m), 1119 (s), 1099 (vs), 1021 (w), 997 (m), 943 (w), 923 (w), 886 (w), 809 (vs; δ_{aryl-H}), 739 (m), 719 (w), 690 (w), 612 (m), 514 (w), 432 (m) cm^{-1}. ^{1}H NMR ($CDCl_3$): δ = 0.88 (t, *n*-hexane), 1.26 (m, *n*-hexane), 1.49 (s, 6 H, CH_3), 2.44 [s, 3 H, SC(O)CH_3], 4.60 (pseudo-t, $^3J_{HH}$ = 1.7 Hz, 2 H, C_5H_4), 4.64 (s, 5 H, C_5H_5), 4.92 (pseudo-t, $^3J_{HH}$ = 1.7 Hz, 2 H, C_5H_4), 7.33–7.76 (m, 6 H, C_6H_3) ppm. ^{13}C{^{1}H}NMR ($CDCl_3$): δ = 14.2 (*n*-hexane), 22.8 (*n*-hexane), 27.0 (CH_3), 30.3 [SC(O)*C*H$_3$], 31.7 (*n*-hexane), 47.2 (*C*-CH_3), 70.8 ($^\beta$C/C_5H_4), 71.9 (C_5H_5), 72.1 (^{i}C/C_5H_4), 73.7 ($^\alpha$C/C_5H_4), 86.4 (C≡*C*-C_6H_3), 87.9 (*C*≡C-C_6H_3), 120.4 (C_6H_3), 120.9 (C_6H_3), 123.2 (^{i}C/C_6H_3), 125.8 (C_6H_3), 126.7 (^{i}C/C_6H_3), 128.9 (C_6H_3), 130.7 (C_6H_3), 133.6 (C_6H_3), 137.9 (^{i}C/C_6H_3), 140.2 (^{i}C/C_6H_3), 153.9 (^{i}C/C_6H_3), 154.8 (^{i}C/C_6H_3), 194.5 (C=O) ppm. MS (ESI): *m*/*z* = 521.06 [M + H]$^+$. $C_{29}H_{24}ORuS\cdot\frac{1}{2}n$-hexane (564.70): calcd. C 68.05, H 5.53; found C 68.31, H 5.69.

Synthesis of 6b: The same procedure as used for the synthesis of **4b** was applied to the preparation of **6b** [compound **6a** (0.10 g, 0.19 mmol), 25% aq. NH_4OH (65.2 mg, 1.91 mmol, 0.3 mL)]. After appropriate work-up, compound **6b** was obtained as a yellow solid; yield 89.9 mg (0.18 mmol, 98% based on **6a**).

M.p. 85 °C. IR (KBr): $\tilde{\nu}$ = 3096 (w, ν_{aryl-H}), 3056 (w), 2956 (m), 2922 (m), 2855 (m), 2680 (w), 2561 (w, ν_{S-H}), 2202 (w, $\nu_{C\equiv C}$), 1599 (w), 1459 (m), 1449 (m), 1406 (s), 1385 (m), 1361 (w), 1261 (s), 1213 (w), 1201 (w), 1152 (w), 1133 (w), 1099 (s), 1021 (s), 997 (m), 918 (w), 886 (w), 809 (vs, δ_{aryl-H}), 757 (w), 736 (m), 514 (w), 457 (m), 430 (m) cm^{-1}. ^{1}H NMR ($CDCl_3$): δ = 0.88 (t, *n*-hexane), 1.26 (m, *n*-hexane), 1.53 (s, 6 H, CH_3), 3.55 (s, 1 H, SH), 4.60 (pseudo-t, $^3J_{HH}$ = 1.7 Hz, 2 H, C_5H_4), 4.64 (s, 5 H, C_5H_5), 4.92 (pseudo-t, $^3J_{HH}$ = 1.7 Hz, 2 H, C_5H_4), 7.33–7.67 (m, 6 H, C_6H_3) ppm. ^{13}C{^{1}H}NMR ($CDCl_3$): δ = 14.2 (*n*-hexane), 22.8 (*n*-hexane), 27.1 (CH_3), 31.7 (*n*-hexane), 46.9 (*C*-CH_3), 70.8 ($^\beta$C/C_5H_4), 71.9 (C_5H_5), 72.1 (^{i}C/C_5H_4), 73.7 ($^\alpha$C/C_5H_4), 86.5 (C≡*C*-C_6H_3), 87.5 (*C*≡C-C_6H_3), 119.7 (C_6H_3), 120.8 (C_6H_3), 122.4 (^{i}C/C_6H_3), 124.1 (C_6H_3), 125.6 (C_6H_3), 127.3 (^{i}C/C_6H_3), 128.5 (C_6H_3), 130.6 (C_6H_3), 136.7 (^{i}C/C_6H_3), 138.2 (^{i}C/C_6H_3), 153.2 (^{i}C/C_6H_3), 154.9 (^{i}C/C_6H_3) ppm. MS (ESI): *m*/*z* = 479.05 [M + H]$^+$. $C_{27}H_{22}RuS\cdot\frac{1}{2}n$-hexane (522.67): calcd. C 68.93, H 5.59; found C 68.95, H 5.36.

Preparation of SAMs of 4b and 6b on Au: The gold substrates were prepared by thermal evaporation of 200 nm of gold onto polished single crystal silicon (100) wafers (Silicon Sense) primed with a 5 nm titanium adhesion layer. The evaporated films were polycrystalline with a grain size of 20–50 nm for Si or a terrace size of 100–200 nm for mica as observed by atomic force microscopy and scanning tunneling microscopy. The grain surfaces predominantly possess a (111) orientation.[67,80] The SAMs were formed by immersion of the freshly prepared gold substrate into a 1 mmol solution of the target compounds **4b** and **6b** in dimethylformamide at room temperature for 24 h. After immersion, the samples were carefully rinsed with dimethylformamide followed by pure ethanol, blown dry with argon, and kept in argon-filled containers until characterization.

Characterization of the SAMs

4b/Au and **6b**/Au were characterized by XPS and NEXAFS spectroscopy at room temperature. The measurements were carried out under UHV conditions at a base pressure better than $1.5\cdot10^{-9}$ mbar. XPS measurements were performed by using a Mg-K_α X-ray source and an LHS 11 analyzer and the spectra acquisition was carried out in normal emission geometry with an energy resolution of ca. 0.9 eV. The X-ray source was positioned ca. 1.5 cm away from the samples and operated at a power of 260 W. The binding energy scale was referenced to the Au $4f_{7/2}$ peak of gold at 84.0 eV.[66] In addition to chemical identification, XPS data were used to estimate effective thicknesses of the target SAMs on the basis of the I_{C1s}/I_{Au4f} intensity ratios, assuming a standard exponential attenuation of the photoelectron signal and by using the attenuation lengths reported in ref.[69]. As a reference, SAMs of nonsubstituted alkanethiols, namely dodecanethiolate on a Au substrate with a known thickness was fabricated by a standard procedure.[81] NEXAFS spectroscopy[71] measurements were performed with the HE-SGM beamline of the synchrotron storage ring BESSY II in Berlin, Germany. The spectra were acquired at the C K-edge and the Fe L-edge in the partial electron yield mode with a retarding voltage of –150 and –400 V, respectively. Linear-polarized synchrotron light (polarization factor of ca. 82%) with an energy resolution of ca. 0.40 eV was used. Raw NEXAFS spectra were normalized to the incident photon flux by division through a spectrum of a clean, freshly sputtered Au sample. The photon energy scale was calibrated to the pronounced π_1* resonance of highly oriented pyrolytic graphite (HOPG) at 285.38 eV.[82]

Acknowledgments

M. Z. and N. B. thank M. Grunze for the support of this work, Ch. Wöll for the technical cooperation at BESSY II, and the BESSY II staff for their assistance during the NEXAFS experiments. Financial support from the Deutsche Forschungsgemeinschaft (DFG) and the Fonds der Chemischen Industrie is gratefully acknowledged.

[1] R. G. Nuzzo, D. L. Allara, *J. Am. Chem. Soc.* **1983**, *105*, 4481.

[2] A. Ulman, *An Introduction to Ultrathin Organic Films: Langmuir-Blodgett to Self-Assembly*, Academic Press, New York, **1991**.
[3] a) A. Ulman, *Chem. Rev.* **1996**, *96*, 1533; b) A. Ulman (Ed.), *Thin films: self-assembled monolayers of thiols*, Academic Press, San Diego, **1998**.
[4] F. Schreiber, *Prog. Surf. Sci.* **2000**, *65*, 151.
[5] F. Schreiber, *J. Phys. Condens. Matter* **2004**, *16*, R881.
[6] J. C. Love, L. A. Estroff, J. K. Kriebel, R. G. Nuzzo, G. M. Whitesides, *Chem. Rev.* **2005**, *105*, 1103.
[7] M. Kazemekaite, A. Bulovas, V. Smirnovas, G. Niaura, E. Butkus, V. Razumas, *Tetrahedron Lett.* **2001**, *42*, 7691.
[8] T. Kondo, T. Kanai, K. Uosaki, *Langmuir* **2001**, *17*, 6317.
[9] Q. Li, G. Mathur, S. Gowda, S. Surthi, Q. Zhao, L. Yu, J. S. Lindsey, D. F. Bocian, V. Misra, *Adv. Mater.* **2004**, *16*, 133.
[10] J. F. Smalley, H. O. Finklea, C. E. D. Chidsey, M. R. Linford, S. E. Creager, J. P. Ferraris, K. Chalfant, T. Zawodzinsk, S. W. Feldberg, M. D. Newton, *J. Am. Chem. Soc.* **2004**, *125*, 2004.
[11] U. Siemeling, D. Rother, C. Bruhn, H. Fink, T. Weidner, F. Träger, A. Rothenberger, D. Fenske, A. Priebe, J. Maurer, R. Winter, *J. Am. Chem. Soc.* **2005**, *127*, 1102.
[12] P. K. Eggers, H. M. Zareie, M. N. Paddon-Row, J. J. Gooding, *Langmuir* **2009**, *25*, 11090.
[13] M. Frasconi, A. D'Annibale, G. Favero, F. Mazzei, R. Santucci, T. Ferri, *Langmuir* **2009**, *25*, 12937.
[14] T. Vallant, W. Simanko, H. Brunner, U. Mayer, H. Hoffmann, R. Schmid, K. Kirchner, *Organometallics* **1999**, *18*, 3744.
[15] Z. Li, I. Pobelov, B. Han, T. Wandlowski, A. Błaszczyk, M. Mayor, *Nanotechnology* **2007**, *18*, 044018.
[16] N. Weibel, A. Błaszczyk, C. von Hänisch, M. Mayor, I. Pobelov, T. Wandlowski, F. Chen, N. Tao, *Eur. J. Org. Chem.* **2008**, *1*, 136.
[17] N. Weibel, A. Mishchenko, T. Wandlowski, M. Neuburger, Y. Leroux, M. Mayor, *Eur. J. Org. Chem.* **2009**, 6140.
[18] H. Ju, D. Leech, *Langmuir* **1998**, *14*, 300.
[19] T. Morita, S. Kimura, *J. Am. Chem. Soc.* **2003**, *125*, 8732.
[20] A. S. Viana, M. Kalaji, L. M. Abrantes, *Langmuir* **2003**, *19*, 9542.
[21] G. Valincius, G. Niaura, B. Kazakevičiene, Z. Talaikytė, M. Kažemėkaitė, E. Butkus, V. Razumas, *Langmuir* **2004**, *20*, 6631.
[22] J. P. Collman, N. K. Devaraj, C. E. D. Chidsey, *Langmuir* **2004**, *20*, 1051.
[23] L. Wei, K. Padmaja, W. J. Youngblood, A. B. Lysenko, J. S. Lindsey, D. F. Bocian, *J. Org. Chem.* **2004**, *69*, 1461.
[24] R. C. Chambers, C. E. Inman, J. E. Hutchison, *Langmuir* **2005**, *21*, 4615.
[25] J. He, S. M. Lindsay, *J. Am. Chem. Soc.* **2005**, *127*, 11932.
[26] R. D. Rohde, H. D. Angew, W.-S. Yeo, R. C. Bailey, J. R. Heath, *J. Am. Chem. Soc.* **2006**, *128*, 9518.
[27] S. Sarkar, S. Sampth, *Langmuir* **2006**, *22*, 3388.
[28] A. Shaporenko, K. Rössler, H. Lang, M. Zharnikov, *J. Phys. Chem. B* **2006**, *110*, 24621.
[29] N. Ballav, T. Weidner, K. Rößler, H. Lang, M. Zharnikov, *ChemPhysChem* **2007**, *8*, 819.
[30] P. G. Hoertz, J. R. Niskala, P. Dai, H. T. Black, W. You, *J. Am. Chem. Soc.* **2008**, *130*, 9763.
[31] T. Weidner, K. Rössler, P. Ecorchard, H. Lang, M. Grunze, M. Zharnikov, *J. Electroanal. Chem.* **2008**, *621*, 159.
[32] T. Weidner, N. Ballav, M. Zharnikov, A. Priebe, N. J. Long, J. Maurer, R. Winter, A. Rothenberger, D. Fenske, D. Rother, C. Bruhn, H. Fink, U. Siemeling, *Chem. Eur. J.* **2008**, *14*, 4346.
[33] L. L. Norman, A. Badia, *J. Am. Chem. Soc.* **2009**, *131*, 2328.
[34] F. Goujon, C. Bonal, B. Limoges, P. Malfreyt, *Langmuir* **2009**, *25*, 9164.
[35] A. Paul, R. M. Watson, P. Lund, Y. Xing, K. Burke, Y. He, E. Borguet, C. Achim, D. H. Waldeck, *J. Phys. Chem. C* **2009**, *112*, 7233.
[36] a) R. Ikeda, S. Kitagawa, J. Chiba, M. Inouye, *Chem. Eur. J.* **2009**, *15*, 7048; b) R. Ikeda, S. Kobayashi, J. Chiba, M. Inouye, *Chem. Eur. J.* **2009**, *15*, 4822.
[37] K. Rößler, T. Rüffer, B. Walfort, R. Packheiser, R. Holze, M. Zharnikov, H. Lang, *J. Organomet. Chem.* **2007**, *692*, 1530.
[38] A. Shaporenko, M. Brunnbauer, A. Terfort, M. Grunze, M. Zharnikov, *J. Phys. Chem. B* **2004**, *108*, 14462.
[39] A. Shaporenko, M. Elbing, A. Błaszczyk, C. von Ha1nisch, M. Mayor, M. Zharnikov, *J. Phys. Chem. B* **2006**, *110*, 4307.
[40] J. Trotter, *Acta Crystallogr.* **1962**, *14*, 1135.
[41] A. Hargreaves, S. H. Rizvi, *Acta Crystallogr.* **1962**, *15*, 365.
[42] X. Chen, A. B. Braunschweig, M. J. Wiester, S. Yeganeh, M. A. Ratner, C. A. Mirkin, *Angew. Chem.* **2009**, *121*, 5280.
[43] M. Mayor, *Angew. Chem.* **2009**, *121*, 5691.
[44] D. Vonlanthen, A. Mishchenko, M. Elbing, M. Neuburger, T. Wandlowski, M. Mayor, *Angew. Chem. Int. Ed.* **2009**, *48*, 8886.
[45] A. Mishchenko, D. Vonlanthen, V. Meded, M. Bürkle, C. Li, I. V. Pobelov, A. Bagrets, J. K. Viljas, F. Pauly, F. Evers, M. Mayor, T. Wandlowski, *Nano Lett.* **2010**, *10*, 156.
[46] B. de Boer, H. Meng, D. F. Perepichka, J. Zheng, M. M. Frank, Y. J. Chabal, Z. Bao, *Langmuir* **2003**, *19*, 4272.
[47] W. Jiang, N. Zhitenev, Z. Bao, H. Meng, D. Abusch-Magder, D. Tennant, E. Garfunkel, *Langmuir* **2005**, *21*, 8751.
[48] X. Zeng, C. Wang, A. S. Batsanov, M. R. Bryce, J. Gigon, B. Urasinska-Wojcik, G. J. Ashwell, *J. Org. Chem.* **2010**, *75*, 130.
[49] J.-Y. Cho, B. Domercq, S. Barlow, K. Y. Suponitsky, J. Li, T. V. Timofeeva, S. C. Jones, L. E. Hayden, A. Kimyonok, C. R. South, M. Weck, B. Kippelen, S. R. Marder, *Organometallics* **2007**, *26*, 4816.
[50] K. Okumoto, Y. Shirota, *Chem. Mater.* **2003**, *15*, 699.
[51] A. Elangovan, Y.-H. Wang, T.-I. Ho, *Org. Lett.* **2003**, *5*, 1841.
[52] R. A. Batey, M. Shen, A. J. Lough, *Org. Lett.* **2002**, *4*, 1411.
[53] N. Lardiés, I. Romeo, E. Cerrada, M. Laguna, P. J. Skabara, *Dalton Trans.* **2007**, 5329.
[54] H. Lang, K. Döring, D. Taher, U. Siegert, B. Walfort, T. Rüffer, R. Holze, *J. Organomet. Chem.* **2009**, *694*, 27.
[55] K. Rößler, Diploma Thesis, Technical University of Chemnitz, Germany, **2005**.
[56] P. Hapiot, C. Lagrost, F. Le Floch, E. Raoult, J. Rault-Berthelot, *Chem. Mater.* **2005**, *17*, 2003.
[57] J. Rault-Berthelot, M. Cariou, J. Tahri-Hassani, *J. Electroanal. Chem.* **1996**, *402*, 203.
[58] P. Štěpnička, L. Trojan, J. Kubišta, J. Ludvík, *J. Organomet. Chem.* **2001**, *637–639*, 291.
[59] D. Obendorf, H. Schottenberger, K. Wurst, N. Schuler, G. Laus, *J. Organomet. Chem.* **2005**, *690*, 811.
[60] C. Nataro, A. N. Campbel, M. A. Ferguson, C. D. Incarvito, A. L. Rheingold, *J. Organomet. Chem.* **2003**, *673*, 47.
[61] a) M. G. Hill, W. M. Lamanna, K. R. Mann, *Inorg. Chem.* **1991**, *30*, 4687; b) M. Sato, G. Maruyama, A. Tanemura, *J. Organomet. Chem.* **2002**, *655*, 23; c) M. Sato, T. Nagata, A. Tanemura, T. Fujihara, S. Kumakura, K. Unoura, *Chem. Eur. J.* **2004**, *10*, 2166; d) M. Sato, Y. Kubota, Y. Kawata, T. Fujihara, K. Unoura, A. Oyama, *Chem. Eur. J.* **2006**, *12*, 2282.
[62] P. Bazinet, K. A. Tupper, T. D. Tilley, *Organometallics* **2006**, *25*, 4286.
[63] B. M. Ramachandran, S. M. Trupia, W. E. Geiger, P. J. Carroll, L. G. Sneddon, *Organometallics* **2002**, *21*, 5078.
[64] J. C. Swarts, A. Nafady, J. H. Roudebush, S. Trupia, W. E. Geiger, *Inorg. Chem.* **2009**, *48*, 2156.
[65] M. Lohan, P. Ecorchard, T. Rueffer, F. Justaud, C. Lapinte, H. Lang, *Organometallics* **2009**, *28*, 1878.
[66] J. F. Moudler, W. E. Stickle, P. E. Sobol, K. D. Bomben, J. Christian (Eds.), *Handbook of X-ray Photoelectron Spectroscopy*, Perkin–Elmer Corp., Eden Praire, MN, **1992**.
[67] K. Heister, M. Zharnikov, M. Grunze, L. S. O. Johansson, *J. Phys. Chem. B* **2001**, *105*, 4058.
[68] P. E. Laibinis, G. M. Whitesides, D. L. Allara, Y. Tao, A. N. Parikh, R. G. Nuzzo, *J. Am. Chem. Soc.* **1991**, *113*, 7152.
[69] C. L. A. Lamont, J. Wilkes, *Langmuir* **1999**, *17*, 3689.

[70] N. Ballav, P. Koelsch, M. Zharnikov, *J. Phys. Chem. C* **2009**, *113*, 18312.
[71] J. Stöhr, *NEXAFS Spectroscopy*, Springer, Berlin, **1992**.
[72] E. Ruehl, A. P. Hitchcock, *J. Am. Chem. Soc.* **1989**, *111*, 5069.
[73] A. P. Hitchcock, A. T. Wen, E. Ruehl, *Chem. Phys.* **1990**, *147*, 51.
[74] E. Ruehl, C. Heinzel, H. Baumgartel, A. P. Hitchcock, *Chem. Phys.* **1993**, *169*, 243.
[75] M. Himmelhaus, I. Gauss, M. Buck, F. Eisert, C. Woell, M. Grunze, *J. Electron Spectrosc. Relat. Phenom.* **1998**, *92*, 139.
[76] A conversion of given electrode potentials to the standard normal hydrogen electrode scale is possible: H. Strehlow, W. Knoche, H. Schneider, *Ber. Bunsen Ges. Phys. Chem.* **1973**, *77*, 760.
[77] G. Gritzner, J. Kuta, *Pure Appl. Chem.* **1984**, *56*, 461.
[78] D. J. Wold, R. Haag, M. A. Rampi, D. Frisbie, *J. Phys. Chem. B* **2002**, *106*, 2813.
[79] M. D. Rausch, A. Siegel, *J. Org. Chem.* **1969**, *34*, 1994.
[80] F. Köhn, Diploma Thesis, Universität Heidelberg, Germany, **1998**.
[81] N. Ballav, A. Shaporenko, S. Krakert, A. Terfort, M. Zharnikov, *J. Phys. Chem. C* **2007**, *111*, 7772.
[82] P. E. Batson, *Phys. Rev. B* **1993**, *48*, 2608.

Received: April 16, 2010
Published Online: July 16, 2010

DOI: 10.1002/ejic.201000501

Comparative Study of the Luminescence Properties and Relative Stability of a Series of Europium(III) Complexes Bearing One to Four Coordinated Azaxanthone Groups

David Parker,*[a] James W. Walton,[a] Laurent Lamarque,[b] and Jurriaan M. Zwier[b]

Keywords: Europium / Luminescence / Lanthanides / Macrocycles

The synthesis and spectral properties are reported of a set of four europium(III) complexes containing between one and four 3-azaxanthone sensitising chromophores. Each complex is based on a macrocyclic cyclen core. The emission and aqueous solution ^{1}H NMR spectral properties are compared, revealing information about the local complex symmetry on the experimental timescale. A C_2-symmetric mono-cationic complex shows an overall emission quantum yield of 10 % in HEPES buffer and exhibits the best relative stability profile in the presence of a million-fold excess of added metal salts or EDTA, as indicated by the time-dependence of overall europium emission, following indirect excitation of the 3-azaxanthone chromophore.

Introduction

Luminescent europium complexes have been studied intensively over the past twenty-five years as they are finding many applications as components of time-resolved assays,[1,2] as stains for living cells[3–6] or as responsive probes.[7–12] A sensitising group is incorporated into these systems to harvest incident light efficiently and typically absorbs light in the range 325–405 nm. Ideally, it possesses a small singlet-triplet energy gap and usually directly coordinates to the europium ion so that intramolecular energy transfer is optimised.[11,13–15] The number of sensitising moieties included in mononuclear systems is determined by consideration of ligand denticity, and by the steric demands imposed by its constitution and the size of any substituents. Amongst a plethora of such sensitising chromophores, azaxanthones have been examined recently as sensitisers[5,9,16–17] and have been integrated into a variety of ligands. They possess a weakly basic pyridyl nitrogen that can coordinate to the metal centre. The two constitutionally isomeric 3- and 1-azaxanthones are most readily available, e.g., **1a** and **2**. In the 1-azaxanthone system, **2**, the nitrogen is a slightly poorer σ-donor and is in a more sterically demanding environment due to the proximity of the α-oxygen. The isomeric 3-aza-system, **1**, is in a much less hindered environment and allows the possibility of the cooperative ligation of up to four pyridyl nitrogen atoms around the lanthanide ion, confirmed by recent X-ray characterisation of a cyclen-tetrakis(pyridylmethyl) Eu complex.[18] The cooperative ligation of three or more pyridyl nitrogen donors, in analogous systems based on **2**, creates highly unfavourable steric congestion.

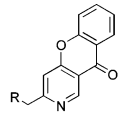

1a R = H
1b R = Br

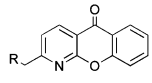

2

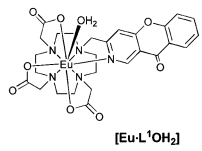

$[Eu{\cdot}L^1OH_2]$

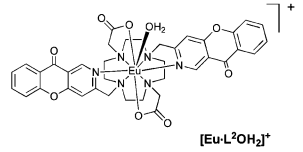

$[Eu{\cdot}L^2OH_2]^+$

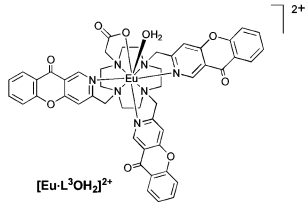

$[Eu{\cdot}L^3OH_2]^{2+}$

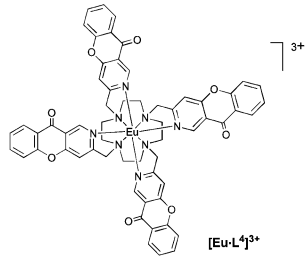

$[Eu{\cdot}L^4]^{3+}$

We have set out to compare the solution structure and relative stability of a series of four europium(III) complexes based on a cyclen core structure, incorporating between one and four 3-azaxanthone moieties; $[Eu{\cdot}L^1]$; $[Eu{\cdot}L^2]^+$; $[Eu{\cdot}L^3]^{2+}$ and $[Eu{\cdot}L^4]^{3+}$. This model study was undertaken with a view to assessing their suitability for further development as emissive probes.

[a] Department of Chemistry, Durham University,
South Road, Durham, DH1 3LE 1, UK
Fax: +44-191-334 2051
E-mail: david.parker@durham.ac.uk
[b] CISbio Bioassays International,
BP 84175, 30204 Bagnols-sur-Ceze, France

Supporting information for this article is available on the WWW under http://dx.doi.org/10.1002/ejic.201000501.

Synthesis and Spectroscopic Analysis

The complexes $[Eu{\cdot}L^1]$ and $[Eu{\cdot}L^2]Cl$ were prepared in a similar manner (Scheme 1), involving alkylation of the known precursors **3** and **4** with the benzylic halide, **1b**[5] (MeCN, K_2CO_3). Deprotection of the *tert*-butyl ester groups using trifluoroacetic acid was followed by complexation with $Eu(OAc)_3$ in water. In the case of $[Eu{\cdot}L^2]^+$, the complex was isolated as the chloride salt following anion exchange chromatography. The complexes were analysed by reverse-phase HPLC to confirm homogeneity (see Supporting Information). The di-cationic complex, $[Eu{\cdot}L^3]^{2+}$ was obtained by a similar overall process in which the mono-ethyl ester, **5** (stored as the di-protonated salt to inhibit lactamisation), was alkylated with three equivalents of **1b** (MeCN, K_2CO_3, 80%).

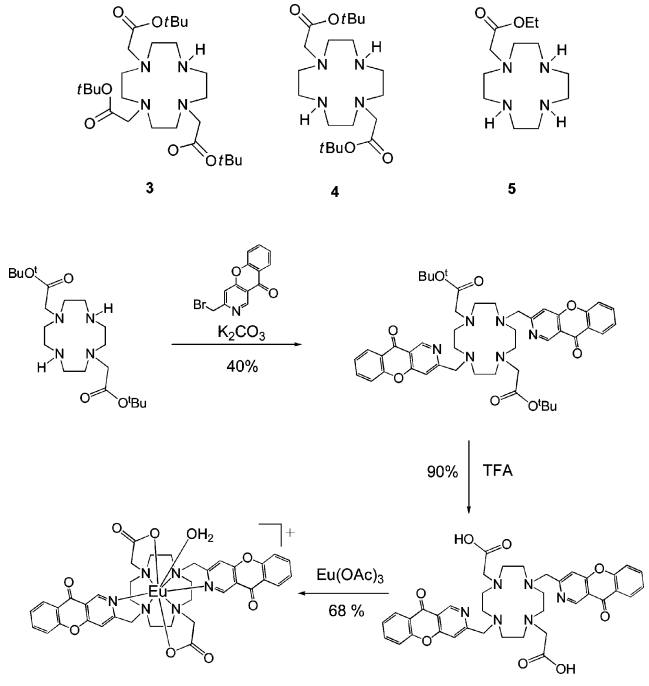

Scheme 1. Synthesis of $[Eu{\cdot}L^2]^+$.

Acid catalysed ester hydrolysis (pH 2.7, 100 °C, 2 h) followed by reaction with $Eu(OAc)_3$ at pH 5.5 allowed isolation of the complex $[Eu{\cdot}L^3]Cl_2$ as the chloride salt following anion exchange. Finally, the tetra-azaxanthonyl complex, $[Eu{\cdot}L^4]^{3+}$, was prepared by direct alkylation of cyclen (MeCN, K_2CO_3, 60%) and complexation was undertaken in acetonitrile using the europium triflate salt, prior to isolation of the more water-soluble chloride complex.

Proton NMR analysis of each complex was undertaken (400 MHz, D_2O pD 5.5) to assess the number of isomeric species in solution and verify the local symmetry on the NMR timescale. The neutral complex, $[Eu{\cdot}L^1]$, gave two sets of thirty paramagnetically shifted proton resonances in ratio 5:4. These correspond to the square-antiprismatic and twisted square-antiprismatic isomers that have been thoroughly documented previously in NMR analyses of related derivatives of DO3A (1,4,7,10-tetraazacyclododecane-1,4,7-triacetate).[19,20] The mono-cationic complex, $[Eu{\cdot}L^2]^+$, gave rise to two sets of 18 proton resonances, in ratio 6:5, consistent with the presence of two diastereoisomeric species with C_2 symmetry. The shifts of each set showed a strong correspondence with those observed for $[Eu{\cdot}L^1]$, in accord with this interpretation. For $[Eu{\cdot}L^4]^{3+}$, only one set of twelve paramagnetically shifted resonances was observed, consistent with local C_4 symmetry. Thus, the pyridyl H-6 proton resonated at +12.5 ppm, with the ring ethylene protons observed as a single shifted set of four resonances, at +30.0, +14.2, –10.9 and –29.1 ppm.

Absorption and emission spectroscopic data for each europium complex were obtained (Table 1). The lowest energy absorption of the parent chromophore 2-methyl-3-azaxanthone, **1a**, occurs at 324 nm (ε = 5.60 $mM^{-1}\,cm^{-1}$ MeOH) and is ascribed to an n–π* transition with some degree of ππ* character.

Table 1. Photophysical data for europium(III) complexes of L^1–L^4 (λ_{exc} 328 nm, pH 5.8).

Complex	ε /$mM^{-1}\,cm^{-1}$	ϕ_{em}^{Eu}	k_{H2O} /ms^{-1}	k_{D2O} /ms^{-1}	q[b]
$[Eu{\cdot}L^1]$[a]	2.50	6.9	1.67	0.51	1.1
$[Eu{\cdot}L^2]^+$	5.80	10	1.7	0.65	1.1
$[Eu{\cdot}L^3]^{2+}$	9.30	5.0	2.00	0.63	1.3
$[Eu{\cdot}L^4]^{3+}$	15.6	5.4	1.41	0.83	0.4

[a] In methanol solution, 2-methyl-3-azaxanthone has ε = 5.60 $mM^{-1}\,cm^{-1}$ (324 nm). [b] Values of the number of coordinated water molecules, q, (± 20%), were determined according to ref.[21].

In a more polar medium, this absorption shifted slightly to the red (328 nm) with a reduction in oscillator strength, as noted for the isomeric 1-azaxanthone series.[16] For the Eu complexes of L^1 to L^4, a rather broad absorption band was observed around 329 nm. Increasing the number of azaxanthone groups increased the overall extinction coefficient of the complex. Overall metal-based emission quantum yields were in the range 5–10%. Measurements of the variation of the radiative rate constant characterising Eu emission (590 nm) in water and D_2O allowed an assessment of the complex hydration state,[21] q. Each complex possesses one coordinated water molecule, except for $[Eu{\cdot}L^4]^{3+}$, which appears to lack a bound water (q = 0.4). In this case, the steric demand imposed by cooperative ligation of the pyridyl nitrogens must inhibit the approach of a water molecule to cap the eight coordinate polyhedron.

Analysis of the europium emission spectral profile of each complex allowed certain conclusions to be drawn (Figure 1). The observed transitions correspond to emission from the ^5D_o excited state to the ^7F_n ground-state manifold (n = 0–4 observed).

The ΔJ = 0 transition at 580 nm diminished in relative intensity over the series and was smallest for $[Eu{\cdot}L^4]^{3+}$ that is eight-coordinate in solution. A low intensity for the ΔJ = 0 transition in C_4-symmetric, eight-coordinate Eu complexes has been observed for related tetra-phosphinate complexes, based on cyclen and the intensity increased significantly in analogues where the axial symmetry was lifted.[22,23] The relative intensity of the electric-dipole allowed ΔJ = 2 transitions (around 620 nm) compared to the ΔJ = 1 magnetic-dipole allowed set (around 590 nm) was

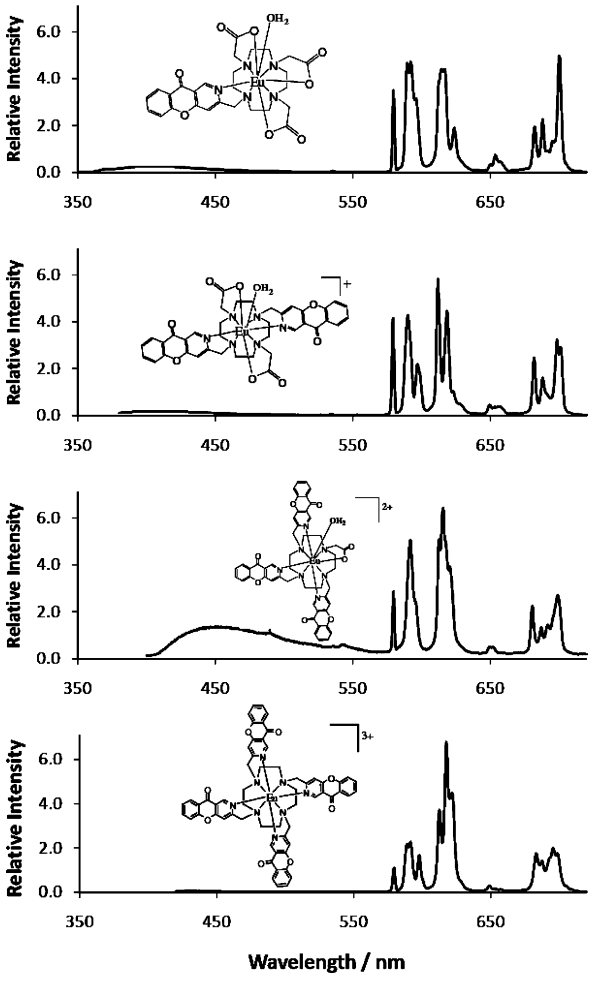

Figure 1. Emission spectra of the four europium complexes of L^1–L^4 (λ_{exc} 328 nm, 20 μM complex, pH 5.8, 293 K) showing ligand fluorescence around 450 nm and Eu emission (580–720 nm).

more or less constant for $[Eu{\cdot}L^1]$ to $[Eu{\cdot}L^3]^{2+}$, but increased markedly for $[Eu{\cdot}L^4]^{3+}$. The relative intensity of the hypersensitive $\Delta J = 2$ transition is determined both by symmetry and the polarisability of the capping axial donor, where present.[14,24] In this case, the modest change in the first three cases may be linked to the presence of a common, "capping" axial water molecule, that is absent for $[Eu{\cdot}L^4]^{3+}$.

Comparative Assessment of Complex Photoluminescence Stability

A series of experiments was undertaken to assess the relative stability of each complex to the presence of a million fold excess of Ca^{2+}, Mg^{2+}, Mn^{2+} or $[EDTA]^{2-}$. In this set, calcium and magnesium were chosen as common dications that can bind competitively to the macrocyclic ligand, the $MnCl_2$ acts as a strong reductant capable of quenching an intermediate excited state and EDTA serves as a competitive ligand for the Eu^{3+} ion. It has been used previously, in this sense, as a scavenging or competitive ligand.[25] In each case, the complex was present at 10 nM concentration in HEPES buffer, containing 0.1% bovine serum albumin, at pH 7.4 (Figure 2). Following excitation at 337 nm, the relative Eu emission intensity was measured at 15 min and after 18 h. The presence of added $CaCl_2$ or $MgCl_2$ did not significantly perturb the Eu emission intensity and caused some modest intensity enhancements that are difficult to rationalise. The effect of added $MnCl_2$ was more significant. This ion is readily oxidised in aqueous solution, and the quenching effect may be related to an electron transfer process that is expected to be more efficient the nearer the Mn^{2+} ion can get to the sensitising chromophore. Complexes that are sterically encumbered or cationic may be expected to inhibit the encounter of the Mn^{2+} aqua ion with the complex. The sensitivity to quenching by added $MnCl_2$ was greatest for the neutral complex, $[Eu{\cdot}L^1]$ compared to the cationic complexes, $[Eu{\cdot}L^2]^+$, $[Eu{\cdot}L^3]^{2+}$ and $[Eu{\cdot}L^4]^{3+}$. In a control experiment, the complex $[Eu{\cdot}L^1]$ (0.2 mM concentration) was excited directly at 397 nm, rather than indirectly at 337 nm via the sensitised emission process. The added $MnCl_2$ (added in increments up to a 1000-fold excess in this case) caused less than a 15% change in the measured emission intensity. Such behaviour accords with a quenching process in which the Mn^{2+} ion is oxidised by the excited state of the chromophore. Thus, the added reductant does not quench the metal excited state directly. A similar hypothesis,

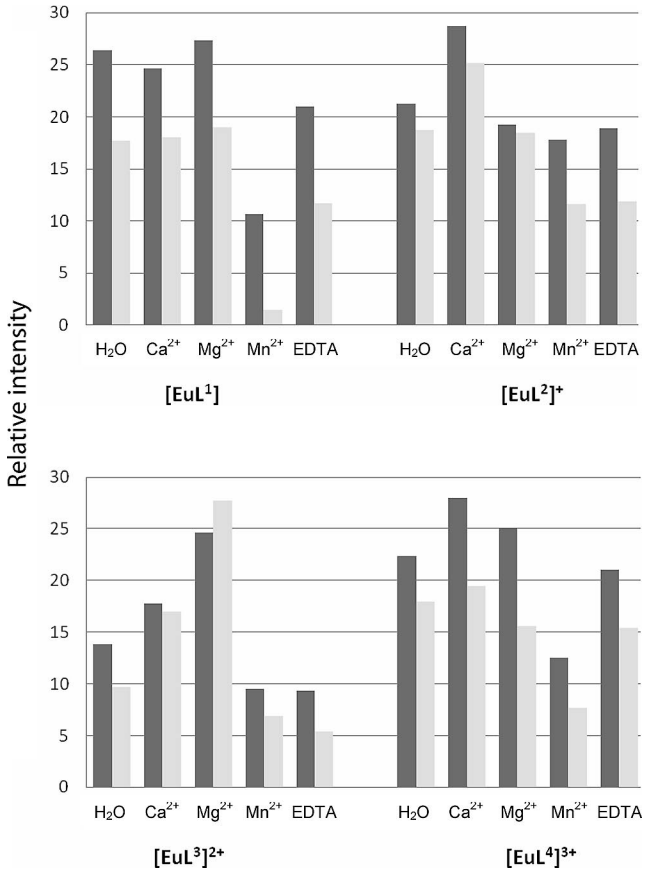

Figure 2. Changes in Eu emission intensity (± 20%) after 15 min (blue) or 18 h (red) in the presence of the stated additives (10 nM complex, 20 mM additive); intensity data for the upper pair have been scaled with respect to the lower set.

involving exciplex formation, has been put forward to account for the sensitivity of lanthanide emission towards electron-rich organic donors, such as urate, ascorbate or certain catecholates.[17,26,27]

In terms of stability with respect to *trans* complexation by excess $[EDTA]^{2-}$, $[Eu{\cdot}L^3]^{2+}$ was the least stable and the sterically hindered complex, $[Eu{\cdot}L^4]^{3+}$ appeared to be the most stable. What is more, for each complex examined, the diminution of Eu emission after an overnight incubation suggested that no complex completely resisted the exchange process that must involve dissociation of Eu and competitive re-association with EDTA.

Conclusions

Of the four complexes assessed in this comparative study, the C_2-symmetric system, $[Eu{\cdot}L^2]^+$, offers the most promising overall behaviour. It possesses the highest emission quantum yield and exhibits the best stability profile in the screening process used to establish the brightness of the Eu emission.

Experimental Section

General: All reagents were used as received from their respective suppliers. Acetonitrile was dried with calcium hydride. Air- or moisture-sensitive reactions were carried out under an atmosphere of argon. Thin-layer chromatography was carried out on silica plates (Merck 5554) or neutral alumina oxide plates (Merck Art 5550) and visualised under irradiation at 254 nm or iodine staining. Preparative column chromatography was carried out using silica (Merck silica gel 60, 230–400 mesh) or neutral aluminium oxide (Merck aluminium oxide 90, activity II–III, 70–230 mesh), soaked in ethyl acetate prior to use. ^{1}H- and ^{13}C-NMR spectra were recorded on a Varian VXR 400 (^{1}H at 399.97 MHz, ^{13}C at 100.61 MHz). Spectra were recorded in commercially available deuterated solvents. All chemical shifts are given in ppm and coupling constants in Hz. Electrospray mass spectroscopy was carried out on a VG Platform II (Fisons Instruments) and accurate masses recorded on a Thermo Finnigan LQT.

UV/Vis absorbance spectra were recorded on a Perkin–Elmer Lambda 900 UV/Vis/NIR spectrometer. Emission spectra were recorded on a ISA Joblin-Yvon Spex Fluorolog-3 luminescence spectrometer. Lifetime measurements were carried out using Perkin–Elmer LS55 spectrometer using FL Winlab software.

Analytical reverse phase HPLC was carried out on a Perkin–Elmer system at 295 K using a 150 × 4.66 mm 4 micron Phenomenex Synergi 4u Fusion-RP 80i column using an H_2O (+ 0.1% formic acid)/MeCN (+ 0.1% formic acid) solvent system with gradient elution program (Table 2).

Table 2. Gradient elution program for HPLC.

Time /min	H_2O + 0.1% HCO_2H	CH_3CN + 0.1% HCO_2H
0	95	5
2	95	5
15	0	100
17	0	100
22	95	5

Stability Assessment: Stock solutions of each of the four europium complexes were prepared in HEPES buffer (0.1 M, 0.1% BSA, pH 7.4), with an absorbance of 0.1 at 324 nm. Each solution was diluted a thousand times and 50 μL aliquots were added to a Greiner Costar half area 96 well plate. Each well was made up to 100 μL, by addition of 45 μL of the buffer solution and 5 μL of either water, or 400 mM aqueous solutions of $CaCl_2$, $MgCl_2$, $MnCl_2$ or Na_2EDTA. The emission intensity from each well at 620 nm was recorded on a RubyStar (BMG) plate reader using an integration window between 50 and 450 μs, following excitation at 337 nm. Each sample preparation was repeated and the mean value of the intensity measurements recorded.

Ligand and Complex Synthesis: The macrocyclic precursors **3** and **4** were prepared following literature methods.[4,16,19,27]

2-Bromomethyl-3-azaxanthone (1b)

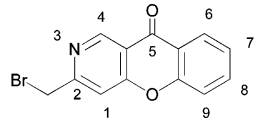

To a solution of 2-methyl-3-azaxanthone (1.48 g, 7.0 mmol) in carbon tetrachloride (50 mL) was added *N*-bromosuccinimde (1.87 g, 10.5 mmol) and dibenzoyl peroxide (40 mg, 0.17 mmol). The mixture was stirred and irradiated by a 100 W lamp for 14 h under argon. The reaction was monitored by ^{1}H-NMR and stopped after 14 h. The solvent was removed under reduced pressure and the crude product was dissolved in CH_2Cl_2 (30 mL) and washed with dilute aqueous K_2CO_3 solution (30 mL) to remove excess succinimide. The organic layer was dried with $MgSO_4$, filtered and the solvent removed under reduced pressure. Purification by column chromatography on silica [elution: toluene/CH_2Cl_2 (1:1), MeOH 0–2% using 0.1% increments] yielded a yellow solid (620 mg, 30%), m.p. 177–179 °C. NMR ($CDCl_3$): δ_H = 9.44 (s, 1 H, H^4), 8.31 (d, J = 8.4 Hz, 1 H, H^6), 7.77 (dd, J = 7.0, 8.4 Hz, 1 H, H^8), 7.53 (s, 1 H, H^1), 7.52 (d, J = 8.4 Hz, 1 H, H^9), 7.44 (dd, J = 7.0, 8.4 Hz, 1 H, H^7), 4.63 (s, 2 H, CH_2Br) ppm. δ_C = 175.9 (C^5), 162.1 (C^2), 161.9 (C$^{4'}$), 156.1 (C$^{9'}$), 150.9 (C^4), 135.9 (C^8), 127.0 (C^6), 125.4 (C^7), 123.2 (C$^{6'}$), 118.4 (C^9), 117.0 (C$^{1'}$), 112.1 (C^1), 33.0 (*C*H_2Br) ppm. *m*/*z* (HRMS$^+$) 291.9785 [M + H]$^+$ ($C_{13}H_9$ ^{81}BrNO$_2$ requires 291.9791), R_f = 0.57 [silica, toluene/CH_2Cl_2 (1:1) → MeOH 5%].

1,4,7-Tris(*tert*-butoxycarbonyl)-10-[2-methyl-3-azaxanthone]-1,4,7,10-tetraazacyclododecane: 1,4,7-Tris(*tert*-butoxycarbonyl)-1,4,7,10-tetraazacyclododecane (120 mg, 0.23 mmol), 2-bromomethyl-3-azaxanthone (67 mg, 0.23 mmol) and K_2CO_3 (16 mg, 0.12 mmol) were stirred in dry CH_3CN (3 mL) at 78 °C for 24 h under argon. The reaction was monitored by TLC to confirm that all the brominated starting material had been consumed. The solvent was removed under reduced pressure and the resultant solid was dissolved in CH_2Cl_2 (25 mL) and extracted with water (3 × 25 mL). The organic layer was dried with $MgSO_4$, filtered and the solvent was removed under reduced pressure. Purification by column chromatography on neutral alumina (CH_2Cl_2/MeOH; 0 to 5%) gave the product as a glassy yellow solid (145 mg, 87%). NMR ($CDCl_3$): δ_H = 9.39 (s, 1 H, H^4), 8.24 (d, J = 8.4 Hz, 1 H, H^6), 7.82 (s, 1 H, H^1), 7.77 (dd, J = 7.0, 8.4 Hz, 1 H, H^8), 7.48 (d, J = 8.4 Hz, 1 H, H^9), 7.41 (dd, J = 7.0, 8.4 Hz, 1 H, H^7), 4.76 (s, 2 H, H^a), 3.63 (s, 2 H, H^b), 3.49 (s, 4 H, H^f), 3.42–2.86 (m, 16 H, *cyclen Hs*), 1.41 (s, 9 H, H^e), 1.38 (s, 18 H, H^i) ppm. δ_C = 176.2 (C^5), 170.3 (*C*^{c}), 169.6 (C^g), 161.7 (C^2), 159.8 (C$^{4'}$), 156.1 (C$^{9'}$), 150.5 (C^4), 136.2 (C^8), 126.8 (C^6), 125.4 (C^7), 123.0 (C$^{6'}$), 118.6 (C^9), 117.2 (C$^{1'}$), 114.7 (C^1), 82.4 (C^h), 82.0 (C^d), 56.7 (C^b), 56.5 (C^f) 53.7 (C^a)

52.0–48.0 (*cyclen Cs*), 28.4 (C^e), 28.3 (Ci) ppm. *m/z* ($HRMS^+$) 724.4281 $[M + H]^+$ ($C_{39}H_{58}N_5O_8$ requires 724.4280), R_f = 0.4 (alumina, CH_2Cl_2 → MeOH 5%).

1,7-Bis(*tert*-butoxycarbonyl)-4,10-bis[2-methyl-3-azaxanthone]-1,4,7,10-tetraazacyclododecane: 1,7-Bis(*tert*-butoxycarbonyl)-1,4,7,10-tetraazacyclododecane (75 mg, 0.19 mmol), 2-bromomethyl-3-azaxanthone (108 mg, 0.37 mmol) and K_2CO_3 (26 mg, 0.19 mmol) were stirred in dry CH_3CN (3 mL) at 78 °C for 48 h under argon. The reaction was monitored by TLC to conform that all the brominated starting material had been consumed. The solvent was removed under reduced pressure and the resultant solid was dissolved in CH_2Cl_2 (25 mL) and extracted with water (3 × 25 mL). The organic layer was dried with $MgSO_4$, filtered and the solvent was removed under reduced pressure to give a glassy yellow solid which was purified by chromatography on neutral alumina (CH_2Cl_2/MeOH; 0 to 5%) to yield a glassy solid (61 mg, 40%). NMR ($CDCl_3$): δ_H = 9.42 (s, 2 H, H^4), 8.30 (s, 2 H, H^1), 7.98 (d, *J* = 8.4 Hz, 2 H, H^6), 7.41 (dd, *J* = 7.0, 8.4 Hz, 2 H, H^8), 7.10 (dd, *J* = 7.0, 8.4 Hz, 2 H, H^7), 6.62 (d, *J* = 8.4 Hz, 2 H, H^9), 3.94 (s, 4 H, H^a), 3.25 (s, 4 H, H^b), 3.00–2.80 (m, 16 H, *cyclen Hs*), 1.40 (s, 18 H, H^e) ppm. δ_C ($CDCl_3$) 176.3 (C^5), 171.1 (C^c), 167.6 (C^2), 162.0 ($C^{4'}$), 155.4 ($C^{9'}$), 150.1 (C^4), 135.2 (C^8), 126.4 (C^6), 124.6 (C^7), 122.6 ($C^{6'}$), 117.7 (C^9), 116.3 ($C^{1'}$), 111.1 (C^1), 81.2 (C^d), 60.5 (C^b), 56.9 (C^a), 55.0–52.0 (*cyclen Cs*), 28.4 (C^e) ppm. *m/z* ($HRMS^+$) 819.4084 $[M + H]^+$ ($C_{46}H_{55}N_6O_8$ requires 819.4076), R_f = 0.5 (alumina, CH_2Cl_2 → MeOH 5%).

Tri-*tert*-butyl 10-(Ethoxycarbonyl)-1,4,7,10-tetraazacyclododecane-1,4,7-tricarboxylate: Tri-*tert*-butyl 1,4,7,10-tetraazacyclododecane-1,4,7-tricarboxylate (270 mg, 0.572 mmol), ethyl bromoacetate (97 mg, 0.572 mmol) and K_2CO_3 (40 mg, 0.3 mmol) were stirred in dry CH_3CN (5 mL) at 78 °C for 36 h under argon. The solvent was removed under reduced pressure and the resultant solid was dissolved in CH_2Cl_2 (25 mL) and extracted with water (3 × 25 mL). The organic layer was dried with $MgSO_4$, filtered and the solvent was removed under reduced pressure. The residue was purified by column chromatography on silica (elution: CH_2Cl_2, MeOH 0–1% using 0.1% increments) to give the title compound as a yellow oil (244 mg, 77%). NMR ($CDCl_3$): δ_H = 4.14 (q, *J* = 7.2 Hz, 2 H, H^f), 3.47 (s, 2 H, H^d), 3.6–2.8 (m, 16 H, *cyclen Hs*), 1.45 (s, 27 H, H^a), 1.25 (t, *J* = 7.2 Hz, 3 H, H^g) ppm. δ_C ($CDCl_3$) 170.6 (C^e), 155.8 (C^c), 79.5 (C^b), 60.3 (C^d), 55.0 (C^f), 53.0–47.0 (*cyclen Cs*), 28.7 (C^a), 14.3 (C^g), *m/z* ($HRMS^+$) 559.3698 $[M + H]^+$ ($C_{27}H_{51}N_4O_8$ requires 559.3701), R_f = 0.6 (silica, CH_2Cl_2 → MeOH 5%).

1-(Ethoxycarbonyl)-1,4,7,10-tetraazacyclododecane (5): Tri-*tert*-butyl 10-(ethoxycarbonyl)-1,4,7,10-tetraazacyclododecane-1,4,7-tricarboxylate (219 mg, 0.39 mmol) was dissolved in CH_2Cl_2 (2 mL) and CF_3CO_2H (2 mL) was added. The mixture was stirred at 20 °C for 12 h under argon. The solvent and excess CF_3CO_2H were removed under reduced pressure and the residue was dissolved in dry CH_2Cl_2 (20 mL). The solution was dried with K_2CO_3 before being filtered and the solvent removed under reduced pressure to yield the product as a pale yellow oil (98 mg, 98%). NMR ($CDCl_3$): δ_H = 4.21 (q, *J* = 7.2 Hz, 2 H, H^f), 3.54 (s, 2 H, H^d), 3.3–2.8 (m, 16 H, *cyclen Hs*), 1.28 (t, *J* = 7.2 Hz, 3 H, H^g) ppm. δ_C ($CDCl_3$) 174.4 (C^e), 62.8 (C^d), 55.3 (C^f), 50.0–43.0 (*cyclen Cs*), 14.4 (C^g) ppm. *m/z* ($HRMS^+$) 259. 2129 $[M + H]^+$ ($C_{12}H_{27}N_4O_2$ requires 259.2129).

1-(Ethoxycarbonyl)-4,7,10-tris[2-methyl-3-azaxanthone]-1,4,7,10-tetraazacyclododecane: 1-(Ethoxycarbonyl)-1,4,7,10-tetraazacyclododecane (16 mg, 0.06 mmol), 2-bromomethyl-3-azaxanthone (70 mg, 0.24 mmol) and K_2CO_3 (25 mg, 0.18 mmol) were dissolved in dry MeCN (3 mL). The solution was stirred at 78 °C for 48 h under argon. The solvent was removed under reduced pressure and the yellow residue was dissolved in CH_2Cl_2 (20 mL). After washing with water (3 × 20 mL), the organic layer was dried with $MgSO_4$, filtered and the solvent was removed under reduced pressure. Purification by column chromatography on alumina (elution: CH_2Cl_2, MeOH 0–2% using 0.1% increments) gave the product as a yellow oil (43 mg, 80%). NMR ($CDCl_3$): δ_H = 9.38 (s, 2 H, H^4), 9.34 (s, 1 H, H^{4*}), 8.19 (d, *J* = 8.4 Hz, 1 H, H^{6*}), 8.13 (d, *J* = 8.4 Hz, 2 H, H^6), 7.75 (dd, *J* = 7.0, 8.4 Hz, 2 H, H^8), 7.68 (dd, *J* = 7.0, 8.4 Hz, 1 H, H^{8*}), 7.64 (s, 2 H, H^1), 7.58 (s, 1 H, H^{1*}), 7.52 (d, *J* = 8.4 Hz, 2 H, H^9), 7.46 (d, *J* = 8.4 Hz, 1 H, H^{9*}), 7.35 (dd, *J* = 7.0, 8.4 Hz, 2 H, H^7), 7.27 (dd, *J* = 7.0, 8.4 Hz, 1 H, H^{7*}), 4.09 (q, *J* = 7.2 Hz, 2 H, H^f), 3.91 (s, 4 H, H^a), 3.76 (s, 2 H, H^{a*}), 3.44 (s, 2 H, H^d), 3.1–2.8 (m, 16 H, *cyclen Hs*), 1.19 (t, *J* = 7.2 Hz, 3 H, H^g) ppm. δ_C = 176.1 (C^5), 171.4 (C^e), 170.6 (C^2), 161.8 ($C^{4'}$), 156.1 ($C^{9'}$), 150.3 (C^4), 135.6 (C^8), 126.8 (C^6), 125.0 (C^7), 122.8 ($C^{6'}$), 118.5 (C^9), 116.7 ($C^{1'}$), 112.2 (C^1), 60.7 (C^a), 55.8 (C^d), 55.0 (C^f), 54.0–48.0 (*cyclen Cs*), 14.5 (C^g) ppm. *m/z* ($HRMS^+$) 908.3377 $[M + Na]^+$ ($C_{51}H_{47}O_8N_7Na_1$ requires 908.3378), R_f = 0.40 (alumina, CH_2Cl_2 → MeOH 5%).

1,4,7,10-Tetrakis[2-methyl-3-azaxanthone]-1,4,7,10-tetraazacyclododecane (L^4): 1,4,7,10-Tetraazacyclododecane (18 mg, 0.10 mmol), 2-bromomethyl-3-azaxanthone (114 mg, 0.40 mmol) and K_2CO_3 (46 mg, 0.34 mmol) were dissolved in dry MeCN (4 mL). The solution was stirred at 78 °C for 72 h under argon. The solvent was removed under reduced pressure and the yellow residue was dissolved in CH_2Cl_2 (20 mL). After washing with water (3 × 20 mL), the organic layer was dried with $MgSO_4$, filtered and the solvent was removed under reduced pressure. Purification by column chromatography on alumina (elution: CH_2Cl_2, MeOH 0–1% using 0.1% increments) gave the product as a yellow oil (60 mg, 60%). NMR ($CDCl_3$): δ_H = 9.37 (s, 4 H, H^4), 8.10 (d, *J* = 8.4 Hz, 4 H, H^6), 7.76 (s, 4 H, H^1), 7.53 (dd, *J* = 7.0, 8.4 Hz, 4 H, H^8), 7.25 (dd, *J* = 7.0, 8.4 Hz, 4 H, H^7), 7.08 (d, *J* = 8.4 Hz, 4 H, H^9), 3.87 (s, 8 H, H^a), 3.00–2.80 (m, 16 H, *cyclen Hs*) ppm. *m/z* ($HRMS^+$) 1009.3678 $[M + H]^+$ ($C_{60}H_{49}O_8N_8$ requires 1009.3668), R_f = 0.56 (alumina, CH_2Cl_2 → MeOH 5%).

EuL^1: 1,4,7-Tris(*tert*-butoxycarbonyl)-10-[2-methyl-3-azaxanthone]-1,4,7,10-tetraazacyclododecane (55 mg, 0.10 mmol) was dissolved in CH_2Cl_2 (2 mL) and CF_3CO_2H (2 mL) was added. The mixture was stirred at 22 °C, under argon, for 12 h. Excess CF_3CO_2H and CH_2Cl_2 were removed under reduced pressure and the yellow residue was dissolved in CH_2Cl_2, which was again removed by reduced pressure to ensure the removal of all CF_3CO_2H. Deprotection of the O*t*Bu groups was confirmed by ^1H NMR, before the residue was dissolved in H_2O/CH_3OH (4:1 v/v, 5 mL). Addition of $Eu(OAc)_3$ (48 mg, 0.12 mmol) was followed by adjustment of the pH to 5.8, by the addition of NH_3, and the mixture was stirred at 60 °C for 48 h. After allowing the solution to cool to room temperature, the pH was raised to 10 by the addition of NH_3. The solution was stirred for 1 h causing excess Eu^{3+} to precipitate as $Eu(OH)_3$, which was removed by syringe filtration. Adjustment of the pH to 5.8 by the addition of CH_3CO_2H, followed by lyophilisation of the solvent, gave the title compound as a pale yellow solid (52 mg, 74%), *m/z* ($ESMS^+$) 703.9 $[M + H]^+$, 726.0 $[M + Na]^+$, 743.9 $[M + K]^+$, τ_{H2O} = 0.60 ms, τ_{D2O} = 1.98 ms, Φ_{H2O}^{em} = 6.9%, t_R = 8.57 min.

[EuL^2]Cl: 1,7-Bis(*tert*-butoxycarbonyl)-4,10-bis[2-methyl-3-azaxanthone]-1,4,7,10-tetraazacyclododecane (22 mg, 0.031 mmol) was dissolved in CH_2Cl_2 (2 mL) and CF_3CO_2H (2 mL) was added. The mixture was stirred at 22 °C, under argon, for 12 h. Excess CF_3CO_2H and CH_2Cl_2 were removed under reduced pressure and the yellow residue was redissolved in CH_2Cl_2. The solvent was,

again, removed under reduced pressure to ensure the removal of all CF_3CO_2H. Deprotection of the O*t*Bu groups was confirmed by ^{1}H-NMR before the residue was dissolved in H_2O/CH_3OH (4:1 v/v, 4 mL). Addition of $Eu(OAc)_3$ (15 mg, 0.037 mmol) was followed by adjustment of the pH to 5.8, by the addition of NH_3, and the mixture was stirred at 60 °C for 48 h. After allowing the solution to cool to room temperature, the pH was raised to 10 by the addition of NH_3. The solution was stirred for 1 h causing excess Eu^{3+} to precipitate as $Eu(OH)_3$, which was removed by syringe filtration. Adjustment of the pH to 5.8 by the addition of CH_3CO_2H, followed by lyophilisation of the solvent, gave the product as the acetate salt. The solid was converted into the chloride salt by stirring in H_2O for 1 h with Dowex 1 × 8 200–400 mesh Cl^-, which had been washed with 1 M HCl and neutralised with water. The Dowex was removed by filtration and the solvent lyophilised to yield the title compound as a pale yellow solid (28 mg, 66%), *m/z* (HRMS$^+$) 855.1798 $[M - Cl]^+$ ($C_{38}H_{36}O_8N_6{}^{151}Eu$ requires 855.1788), τ_{H2O} = 0.56 ms, τ_{D2O} = 1.54 ms, $\Phi_{H2O}{}^{em}$ = 10%, t_R = 8.91 min.

$[EuL^3]Cl_2$: 1-(Ethoxycarbonyl)-4,7,10-tris[2-methyl-3-azaxanthone]-1,4,7,10-tetraazacyclododecane (20 mg, 0.023 mmol) was dissolved in 2 mM HCl (4 mL) and the solution was stirred at 100 °C for 2 h. Removal of the OEt protecting group was confirmed by ^{1}H-NMR spectroscopy. The pH was raised to 5.0 using NaOH before $EuCl_3$ (9 mg, 0.028 mmol) was added and the mixture stirred at 60 °C for 40 h. After allowing to cool to room temperature, the pH was raised to 10 by the addition of aqueous ammonia solution (1 M). The solution was stirred for 1 h causing excess Eu^{3+} to precipitate as $Eu(OH)_3$, which was removed by syringe filtration. Adjustment of the pH to 5.8 by the addition of acetic acid, followed by lyophilisation of the solvent, and pumping of the residue under vacuum to gave $[EuL^2]^+$ as an off-white solid. Conversion to the choride salt used the ion exchange resin as described above. $\tau(H_2O)$ 0.50 ms, $\tau(D_2O)$ 1.61 ms, $\Phi_{H2O}{}^{em}$ = 5.0%, t_R = 8.71 min.

$[EuL^4]Cl_3$: L^4 (12 mg, 0.012 mmol) and $Eu(OTf)_3$ (6.5 mg, 0.011 mmol) were dissolved in CH_3CN (3 mL) at 78 °C, under argon, for 40 h. The solvent was removed under reduced pressure and the yellow residue was re-dissolved in CH_3CN (0.1 mL). This solution was dropped into Et_2O (10 mL) causing immediate precipitation of the product as the triflate salt. The pale yellow solid was converted into the chloride salt by stirring in H_2O for 1 h with Dowex 1 × 8 200–400 mesh Cl^-, which had been washed with 1 M HCl and neutralised with water. The Dowex was removed by filtration and the solvent lyophilised to yield a yellow solid (2 mg, 15%), *m/z* (HRMS$^+$) 588.1404 $[M - 3Cl + OH]^{2+}$ ($C_{60}H_{49}O_9N_8{}^{151}Eu$ requires 588.1405), τ_{H2O} = 0.71 ms, τ_{D2O} = 1.20 ms, $\Phi_{H2O}{}^{em}$ = 5.4%, t_R = 9.51 min.

Supporting Information (see also the footnote on the first page of this article): Selected HPLC analyses of Eu complexes and 1-H NMR spectra of selected complexes.

Acknowledgments

We thank the European Science Foundation (ESF), European Co-operation in the Field of Science and Technology (COST), ESF COST Action D38 for partial support.

[1] a) M. Gabourdes, V. Bourgine, G. Mathis, H. Bazin, B. Alpha-Bazin, *Anal. BioChem.* **2004**, *333*, 105; b) E. Lopez-Crapez, H. Bazin, J. Chevalier, E. Trinquet, J. Genier, G. Mathis, *Human Mutation* **2005**, *5*, 468; c) D. Maurel, L. Comps-Agar, C. Brock, M.-L. Rives, E. Bourrier, M. A. Ayoub, H. Bazin, N. Tinel, T. Durroux, L. Prezeau, E. Trinquet, J.-P. Pin, *Nat. Methods* **2008**, *5*, 561; d) H. Bazin, E. Trinquet, G. Mathis, *J. Biotechnol.* **2002**, *82*, 233.

[2] a) I. Hemmila, V. Laitala, *J. Fluoresc.* **2005**, *15*, 529; b) H. Harma, G. Sarrail, J. Kirjavainen, E. Martikkala, I. Hemmila, P. Hanninen, *Anal. Chem.* **2010**, *82*, 892.

[3] A. S. Chauvin, S. Comby, B. Song, C. D. Vandevyver, F. Thomas, J.-C. G. Bunzli, *Chem. Eur. J.* **2007**, *13*, 9515.

[4] R. A. Poole, G. Bobba, M. J. Cann, J.-C. Frias, D. Parker, R. D. Peacock, *Org. Biomol. Chem.* **2005**, *3*, 1013.

[5] G.-L. Law, C. Man, D. Parker, J. W. Walton, *Chem. Commun.* **2010**, *46*, 2391.

[6] E. J. New, D. Parker, D. G. Smith, J. W. Walton, *Curr. Opin. Chem. Biol.* **2010**, *14*, 238.

[7] R. Pal, D. Parker, L. C. Costello, *Org. Biomol. Chem.* **2009**, *7*, 1525.

[8] R. Pal, D. Parker, *Org. Biomol. Chem.* **2008**, *6*, 1020.

[9] A. Thibon, V. C. Pierre, *J. Am. Chem. Soc.* **2009**, *131*, 434.

[10] B. Song, G. Wang, M. Tan, J. Yuan, *J. Am. Chem. Soc.* **2006**, *128*, 13442.

[11] A. Thibon, V. C. Pierre, *Anal. Bioanal. Chem.* **2009**, *394*, 107.

[12] Y. Bretonniere, M. J. Cann, D. Parker, R. Slater, *Org. Biomol. Chem.* **2004**, *2*, 1624.

[13] S. Faulkner, L. S. Natrajan, W. S. Perry, D. S. Sykes, *Dalton Trans.* **2009**, 3890.

[14] D. Parker, *Chem. Soc. Rev.* **2004**, *33*, 156.

[15] S. N. Eliseeva, J.-C. G. Bunzli, *Chem. Soc. Rev.* **2010**, *39*, 189.

[16] P. Atkinson, K. S. Findlay, F. Kielar, R. Pal, D. Parker, R. A. Poole, H. Puschmann, S. L. Richardson, P. L. Stenson, A. L. Thompson, J. Yu, *Org. Biomol. Chem.* **2006**, *4*, 1707.

[17] G.-L. Law, D. Parker, S. L. Richardson, K.-L. Wong, *Dalton Trans.* **2009**, 8481.

[18] A. Wada, M. Watanabe, Y. Yamanoi, H. Nishihara, *Chem. Commun.* **2008**, 1671.

[19] S. Aime, M. Botta, A. S. Batsanov, J. A. K. Howard, M. P. Lowe, D. Parker, *New J. Chem.* **1999**, *23*, 669.

[20] P. Caravan, J. J. Ellison, T. J. McMurry, R. B. Lauffer, *Chem. Rev.* **1999**, *99*, 2293.

[21] A. Beeby, I. M. Clarkson, R. S. Dickins, S. Faulkner, D. Parker, M. Woods, L. Royle, A. S. de Sousa, J. A. G. Williams, M. Woods, *J. Chem. Soc. Perkin Trans. 2* **1999**, 493.

[22] D. Parker, R. S. Dickins, H. Puschmann, C. Crossland, J. A. K. Howard, *Chem. Rev.* **2002**, *102*, 1977.

[23] S. Aime, M. Botta, D. Parker, K. Senanayake, J. A. G. Williams, A. S. Batsanov, J. A. K. Howard, *Inorg. Chem.* **1994**, *33*, 4696.

[24] J. I. Bruce, R. S. Dickins, D. Parker, D. J. Tozer, *Dalton Trans.* **2003**, 1264.

[25] M. H. V. Werts, J. W. Verhoeven, J. W. Hofstraat, *J. Chem. Soc. Perkin Trans. 2* **2000**, 433.

[26] R. A. Poole, F. Kielar, D. Parker, S. L. Richardson, D. Parker, *Chem. Commun.* **2006**, 4084.

[27] F. Kielar, C. P. Montgomery, E. J. New, D. Parker, R. A. Poole, S. L. Richardson, P. A. Stenson, *Org. Biomol. Chem.* **2007**, *5*, 2975.

Received: May 4, 2010
Published Online: July 16, 2010

DOI: 10.1002/ejic.201000515

Reactions of Amine– and Phosphane–Borane Adducts with Frustrated Lewis Pair Combinations of Group 14 Triflates and Sterically Hindered Nitrogen Bases

George R. Whittell,[a] Edward I. Balmond,[a] Alasdair P. M. Robertson,[a] Sanjib K. Patra,[a] Mairi F. Haddow,[a] and Ian Manners*[a]

Keywords: Amines / Boron / Dehydrogenation / Lewis acids / Lewis bases

The ability of trialkyl Group 14 triflates in combination with amine and pyridine bases to dehydrogenate amine– and phosphane–borane adducts has been investigated. By using multinuclear NMR spectroscopy, it has been shown that $Me_2NH{\cdot}BH_3$ (**11**) is efficiently converted to $[Me_2N–BH_2]_2$ (**12**) by the so-called "frustrated Lewis pair" (FLP) of nBu$_3$SnOTf (**4**, $^-$OTf = $^-OSO_2CF_3$) and 2,2,6,6-tetramethylpiperidine (**6**). Within the scope of the study, exchange of the Lewis acid effects the rate of dehydrogenation in the order: **4** > Me_3SiOTf (**2**) > Et_3SiOTf (**3**). Exchange of the Lewis base for 2,6-di-*tert*-butylpyridine (**5**) has also been shown to reduce the rate of reaction, whereas 1,3-di-*tert*-butylimidazol-2-ylidene (**7**) reacted directly with **2** to afford 1,3-bis-*tert*-butyl-4-(trimethylsilyl)imidazolium triflate (**8**[OTf]). For FLP combinations for which dehydrogenation reaction times are longer, detectable quantities of $[H_2B(\mu\text{-}H)(\mu\text{-}NMe_2)BH_2]$ (**14**) are observed. Both the dehydrogenation reaction and competitive formation of this product are proposed to proceed by initial hydride abstraction by the Lewis acid, followed by deprotonation by the Lewis base, or combination with further dimethylamine–borane and elimination of $[Me_2NH_2]$OTf (**18**[OTf]), respectively. In contrast to **11**, $MeNH_2{\cdot}BH_3$ (**22**) was not found to cleanly dehydrogenate to either $[MeNH–BH_2]_3$ or $[MeN–BH]_3$ under the same conditions. An alternative reaction pathway was observed with either **2** or **4** and **6** with $Ph_2PH{\cdot}BH_3$ (**23**), resulting in *P*-silylation or *P*-stannylation of the phosphane–borane, respectively.

1. Introduction

The dehydrogenation of amine–borane adducts is of intense current interest for both the preparation of new polyaminoborane materials[1,2] and for utilisation in hydrogen storage[3] and hydrogen transfer applications.[4–32] Recent work has shown that, in addition to the thermally induced routes described in the 1950s that require temperatures above 100 °C, efficient processes mainly involving transition metal catalysis have been developed. The catalysts for these reactions can be heterogeneous or homogeneous in nature and have been shown to be successful for a variety of metal centers from the d-block.[33,34] Other Group 13–15 Lewis acid–Lewis base adducts such as phosphane–borane adducts have also been shown to undergo metal-catalyzed dehydrogenation to yield linear or cyclic oligomers or high-molecular-weight polymers.[35–38]

Led by key discoveries by Stephan and co-workers, much recent interest has focused on the metal-free activation of small molecules by exploiting the reactivity of mixtures containing sterically encumbered Lewis acids and bases.[39] By so preventing the adduct formation that is typical of these compounds, heterolytic bond cleavage of an additional substrate, such as hydrogen, becomes the dominant reaction pathway. This chemistry is often described as that of "frustrated Lewis pairs" (FLP) and has been shown to facilitate further useful reactions. For instance, the phosphonium or ammonium hydridoborates formed from hydrogen cleavage are catalytically active in the hydrogenation of imines, protected nitriles, aziridines,[40,41] enamines and silylenol ethers.[42] The FLP approach has also proved successful for the stoichiometric activation of many other small molecules, including olefins[43] and CO_2.[44,45] Based on these reports we were intrigued as to whether the FLP approach would also permit the efficient dehydrogenation of amine– and phosphane–borane adducts. In this respect we were initially encouraged by reports that ammonia[46] and catecholborane[47] can be successfully activated by this method. During the course of our work, however, Miller and Bercaw reported that the sterically bulky tertiary phosphane/borane Lewis pair of PtBu$_3$ and $B(C_6F_5)_3$ reacted with amine–borane adducts to afford the targeted dehydrogenated products and phosphonium hydridoborate salts.[48] Furthermore, this topic has recently been the subject of a theoretical study.[49]

With the exception of Bertrand's (alkyl)(amino)-carbenes[46] and some activity displayed by BPh_3 systems

[a] School of Chemistry, University of Bristol, Cantock's Close, Bristol BS8 1TS, United Kingdom
E-mail: ian.manners@bristol.ac.uk
Fax: +44-117-929-0509

towards hydrogen,[50] FLPs almost entirely contain $B(C_6F_5)_3$ (**1**) or a derivative thereof as the Lewis acid. Although the combination of large steric bulk and high Lewis acidity no doubt explain this observation, the cost of this compound compares to those of precious metal catalysts, and herein lies a limitation. There is no a priori reason why another Lewis acid may be ineffective as long as the aforementioned steric and electronic requirements are met. We, therefore, chose to initiate this study into the dehydrogenation of amine– and phosphane–borane adducts by employing less expensive Me_3SiOTf (**2**, $^-OTf = {}^-OSO_2CF_3$), Et_3SiOTf (**3**) and $n Bu_3SnOTf$ (**4**) as the Lewis acids. 2,6-Di-*tert*-butylpyridine (**5**), 2,2,6,6-tetramethylpiperidine (**6**) and 1,3-di-*tert*-butylimidazol-2-ylidene (**7**) were chosen as the sterically encumbered Lewis bases. In addition to preventing reaction with **2**, **3** and **4**, such steric bulk was deemed necessary to hinder competitive ligand-exchange chemistry with the amine and phosphane–borane adducts of interest. With the exception of **5**, these bases had previously been shown to be effective in the FLP activation of hydrogen.[51–54] During the course of our study, similar chemistry was reported for lutidine,[55] which also provided precedent for the use of a pyridine base.

2. Results and Discussion

2.1. Reactions of Trialkyl Group 14 Triflates with Lewis Bases

The mixing of **2**, **3** or **4** with a slight excess of either **5** or **6** in 1,2-dichlorobenzene at room temperature afforded no reaction as evidenced by ^{29}Si and ^{119}Sn NMR spectroscopy.[56,57] These combinations of Lewis acids and bases were therefore deemed appropriate for use in the FLP activation of amine and phosphane–borane adducts. 1,3-Di-*tert*-butylimidazol-2-ylidene (**7**), however, afforded a precipitate upon treatment with **2** in 1,2-dichlorobenzene. Recrystallisation of the solid from CH_2Cl_2/hexane produced crystals that were suitable for single-crystal X-ray diffraction (vide infra), and these were also analysed by multinuclear NMR spectroscopy. The ^1H NMR spectrum exhibited a highly deshielded proton resonance at $\delta = 9.19$ ppm, which was taken as indicative of an imidazolium environment. This signal integrated in a 1:1 ratio with respect to the olefin resonance at $\delta = 7.25$ ppm, and 1:9 with regard to that assigned to the Me_3Si group at $\delta = 0.49$ ppm. These data are consistent with protonation of the carbene centre and silylation of the carbon backbone. Support for the former deduction was provided by the absence from the $^{13}C\{^1H\}$ NMR spectrum of a signal that would be considered characteristic of a two-coordinate carbon atom ($\delta = 213.2$ ppm).[58] Further evidence for the latter can be taken from the resonance at $\delta = -6.2$ ppm in the $^{29}Si\{^1H\}$ NMR spectrum. The ^{19}F NMR spectrum indicated the inclusion of the triflate ion in the product by the presence of a singlet at $\delta = 78.2$ ppm.[59] In combination with mass spectrometry and elemental analysis, these data support the formation of 1,3-bis-*tert*-butyl-4-(trimethylsilyl)imidazolium triflate (**8**[OTf]) as depicted in Scheme 1.

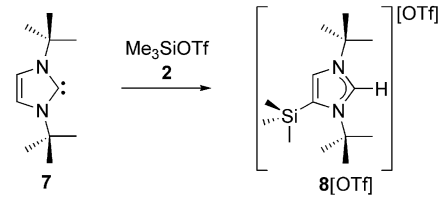

Scheme 1.

The molecular structure of **8**[OTf] was confirmed by single-crystal X-ray diffraction, for which a thermal-ellipsoid plot is presented in Figure 1. The compound crystallised in the orthorhombic space group $Pna2_1$ with one well-separated ion pair per asymmetric unit. The N1–C3 and N2–C3 bond lengths are 1.336(3) and 1.333(3) Å, respectively, which are closer to those found in 1,3-bis-*tert*-butylimidazolium cation (**9**) [1.325(4) and 1.328(4) Å][53] than in the corresponding carbene (**7**) [1.3665(18) and 1.3660(18) Å].[58] Furthermore, the N1–C3–N2 bond angle [109.9(2)°] is also more representative of **9** [107.4(3)°] than **7** [106.80(14)°]. These results clearly support the presence of a C3-bound proton in **8**[OTf]. The C1–C2 separation of 1.366(3) Å is significantly longer than the corresponding distances in **9** and **7** [1.342(2) and 1.343(4) Å, respectively], but comparable to that in 1,3-diisopropyl-4-(trimethylsilyl)-2-[(trimethylsilyl)imino]imidazoline (**10**) [1.347(4) Å],[60] which also contains a silylethylene backbone. It is presumably the steric pressure introduced by this substituent that is responsible for the observed elongation of the C=C bond. The remainder of the metrical parameters are also consistent with the structure determined by spectroscopic means and are included in the caption to Figure 1. It should be noted that this reaction is analogous to that observed between **7** and $B(C_6F_5)_3$ when the reagents were allowed to stand at room temperature.[53,54]

In order to provide a point of reference for the current study with respect to the literature, the abilities of the Group 14 triflates and N-donors to activate hydrogen were investigated. The reaction of **2** and **6** with H_2 (2 bar) in 1,2-dichlorobenzene was monitored by ^{29}Si NMR spectroscopy. After 18 h at 50 °C, however, the only signal apparent was that of the starting material **2** ($\delta = 43$ ppm).[56] The same result was observed for the reaction employing **2** and **5**; and when **4** and **6** were utilised, there was no conversion of the tin reagent (**4**) as evidenced by ^{119}Sn NMR spectroscopy.[57] At the time of this study there was no evidence to suggest that **5** was sufficiently nucleophilic to activate H_2, so the reaction was repeated with a Lewis acid known to facilitate this transformation with other Lewis bases. A solution of **1** and **5** that was exposed to H_2 (2 bar) only exhibited a resonance corresponding to the borane ($\delta = 55$ ppm)[61] after ca. 1 h at room temperature. On heating at 50 °C for ca. 18 h, however, two new signals were observed in the ^{11}B NMR spectrum, replacing that corresponding to the starting borane. The predominant signal ($\delta = -26$ ppm; $J_{BH} =$

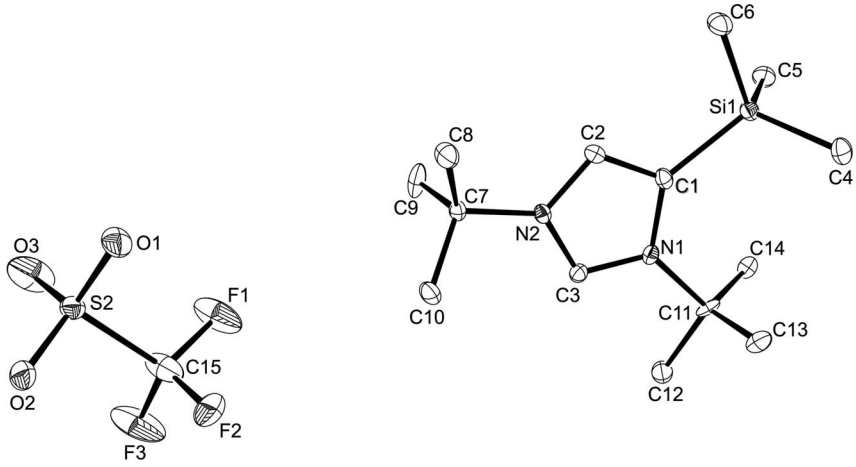

Figure 1. Molecular structure of **8**[OTf] with thermal ellipsoids at the 50% probability level. Hydrogen atoms have been omitted for clarity. Selected bond lengths [Å] and angles [°]: C1–C2 1.366(3), C1–Si1 1.895(2), C1–N1 1.410(3), C2–N2 1.372(3), C3–N1, 1.336(3), C3–N2 1.333(3); N1–C1–C2 104.7(2), C1–C2–N1 109.62(2), N1–C3–N2 109.9(2), C1–N1–C3 108.40(19), C2–N2–C3 107.38(19).

87 Hz), representing 80% of the soluble boron present, was consistent with the formation of $[HB(C_6F_5)_3]^-$ and thus H_2 activation.[50] It seems logical to conclude, therefore, that it is the lower electrophilicity of the Group 14 species that precludes the heterolysis of H_2 in this study. Compounds such as amine–borane adducts, however, may still be amenable to dehydrogenation by these combinations of reagents as the bonds to be cleaved are already polarised to facilitate the reaction.

2.2. Reactions of Dimethylamine– and Methylamine–Borane Adducts with Mixtures of Trialkyl Group 14 Triflates and N-Donor Bases

In previous investigations on amine–borane dehydrogenation we and others have found $Me_2NH{\cdot}BH_3$ (**11**) a convenient substrate to study, as it readily converts to $[Me_2N–BH_2]_2$ (**12**) in the presence of a broad range of catalysts.[34,62] A solution of **11** with a slight excess of **2** and **6** was prepared in 1,2-dichlorobenzene and the evolution of the mixture monitored by ^{11}B NMR spectroscopy. During the course of the reaction, the spectra obtained were typical of $Me_2NH{\cdot}BH_3$ dehydrogenation, displaying resonances assignable to the starting material [δ = –14 ppm (q, J_{BH} = 96 Hz)], **12** [δ = 4 ppm (t, J_{BH} = 111 Hz)] and the intermediate aminoborane, $Me_2N{=}BH_2$ {**13** [δ = 35 ppm (t, J_{BH} = 127 Hz)]}.[63] A side product assigned as $[H_2B(\mu\text{-}H)(\mu\text{-}NMe_2)BH_2]$ {**14** [δ = –19 ppm (td, J_{BH} = 129 Hz, J_{BH} = 31 Hz)]}[64] was also detected, albeit in small quantity. Reaction progress was accompanied by the precipitation of a colourless solid that was characterised as 2,2,6,6-tetramethylpiperidinium triflate ([**6**·H][OTf]) by ^1H and ^{19}F NMR spectroscopy.[65] The final reaction mixture was further analysed by ^{29}Si NMR spectroscopy, and this confirmed the expected conversion of **2** to Me_3SiH [**15** (δ = –15 ppm)] (Scheme 2).[66] The time taken for conversion of half the starting material ($t_{1/2}$) was 10.3 min, and this was lengthened considerably (3.66 h) on exchanging the Lewis base for **5**. Repeating the reaction with **6** but with **3** as the Lewis acid resulted in a modest lengthening of $t_{1/2}$ to 36.2 min under the same conditions. Finally, when **4** was used with the same amine, the reaction was ca. 86% complete by the time that the first NMR spectrum could be acquired (ca. 7 min). In all the reactions, when the formation of appropriate triflate salt and silane or stannane was taken into account, the product distribution was qualitatively the same as outlined above. It is noteworthy that the amount of the side product (**14**) formed relative to the product of dehydrogenation (**12**) became larger as $t_{1/2}$ increased, and this observation will be discussed in due course. In summary, the rate of the dehydrogenation increases as both the expected electro- and nucleophilicity of Lewis acid and base, respectively, increase.

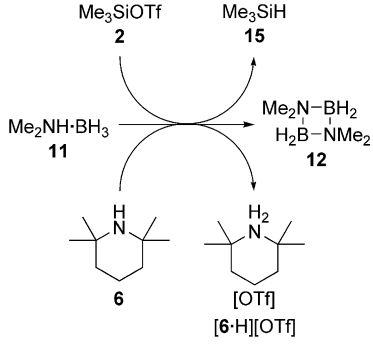

Scheme 2.

When proposing a mechanism for the above transformation, three possible alternatives need to be considered. Firstly, the Lewis acid and base may interact with the amine–borane in a concerted manner, similar to what has been proposed for the activation of H_2 by phosphanes and boranes.[67] Secondly, the Lewis base may deprotonate at the nitrogen atom with the Lewis acid abstracting a hydride from the resulting anion in a subsequent step. Alternatively, the converse is possible with hydride abstraction preceding

deprotonation. Mixtures of either **5** or **6** with **11** in 1,2-dichlorobenzene showed no signs of reaction under conditions comparable to those of dehydrogenation, as evidenced by ^{11}B NMR spectroscopy. When, for example, stannyl triflate **4** was treated with **11**, however, conversion to **14** was observed in the absence of any dehydrogenation by ^{11}B NMR spectroscopy. Only a broad resonance at $\delta \approx 0$ ppm and accounting for trace amounts of the soluble boron present was also observed in the ^{11}B NMR spectrum. We tentatively assign this signal to the boronium cation, $[H_2B(NHMe_2)(OTf)]$ (**16**), on account of the similarity in chemical shift with that of $[H_2B(NH_3)(OEt_2)]^+$ (δ = 0.21 ppm).[8] Attempts to isolate a model for **16** by hydride abstraction from $Me_3N{\cdot}BH_3$ (**17**), however, failed. During the course of the reaction of **4** with **11**, colourless crystals were observed to precipitate from the solution, and these were later characterised as $[Me_2NH_2]OTf$ (**18**[OTf]) by single-crystal X-ray diffraction[68] and ^1H and ^{19}F NMR spectroscopy. When these results are taken in conjunction with the formation of nBu$_3$SnH (**19**), from the initial hydride abstraction and as evidenced by a signal at δ = –89 ppm (J_{SnH} = 1526 Hz) in the ^{119}Sn NMR spectrum,[69] the full reaction stoichiometry can be described (Scheme 3).

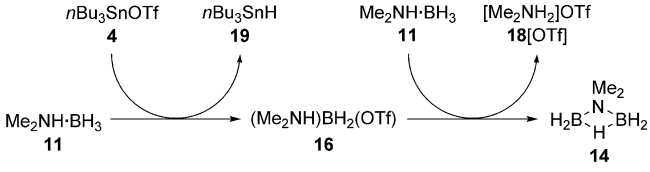

Scheme 3.

Baker, Dixon and co-workers have previously investigated the reaction of $H_3N{\cdot}BH_3$ (**20**) with the Lewis acid **1**.[8] They found that initial hydride abstraction was followed by interaction of the resulting borenium cation with another molecule of **20**. Subsequent loss of H_2 then afforded the coupled species $[H_2B(\mu\text{-}H)(\mu\text{-}NH_2)BH_2NH_3]^+$ (**21**) as the $[HB(C_6F_5)_3]^-$ salt, which could catenate further (Scheme 4). At Lewis acid additions of > 10 mol-%, however, the concentration of the cyclic cation **21** appeared high enough for the rate of an alternative reaction pathway to become significant (Scheme 5). It should be noted that this side-reaction effectively consumes ammonia–borane, but without liberation of hydrogen, and is analogous to what we observe with **4** and **11** (Scheme 3). In our dehydrogenation reactions, however, the presence of a strong base provides a low-activation-energy route to the formal dehydrogenation product. In the absence of this reagent or when deprotonation is slow, the boronium cation can interact with another molecule of **11** to afford the observed side reaction.

We attempted to extend this methodology to the dehydrogenation of $MeNH_2{\cdot}BH_3$ (**22**) with the aim of achieving selective removal of either 1 or 2 equiv. of H_2. The reactions of **22** with a mixture of **2** and **6**, by using both 1 and 2 mol-equiv. of the latter, however, afforded only a complex mixture of products as evidenced by ^{11}B NMR spectroscopy. Nonetheless, it is noteworthy that 2 equiv. of the FLP were required to consume all of **22** and that the dehydrogenation products $[MeNH{-}BH_2]_3$ and $[NMe{-}BH]_3$ were not significant components of the reaction mixture.[63]

2.3. Reactions of Diphenylphosphane–Borane Adduct with Mixtures of nBu$_3$SnOTf and Me$_3$SiOTf with 2,2,6,6-Tetramethylpiperidine

In light of our results regarding the dehydrogenation of secondary amine–borane adducts, we ventured to investigate the analogous reaction of $Ph_2PH{\cdot}BH_3$ (**23**). This reaction was of particular interest as phosphane–borane adducts are only sluggishly dehydrogenated by transition metal catalysts, thus necessitating high temperatures and long reaction times. As the mixture of **4** and **6** had been shown to dehydrogenate **11** in the shortest period of time, compound **23** was treated with this FLP reagent in slight excess. The white precipitate that so formed was collected and demonstrated to be [**6**·H][OTf] on the basis of ^1H and ^{19}F NMR spectroscopy. Removal of all volatiles from the filtrate afforded a colourless oil, which was also analysed by multinuclear NMR spectroscopy. The absence of resonances at δ = –40.0, 1.7 and 172 ppm in the ^{11}B, ^{31}P and ^{119}Sn NMR spectra, respectively, indicated complete consumption of both **4**[70] and **23**.[71] However, there were no

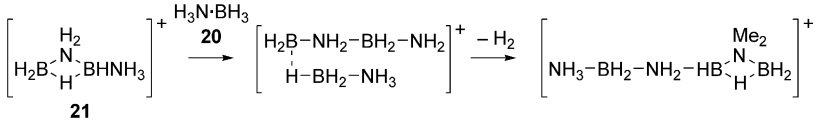

Scheme 4.

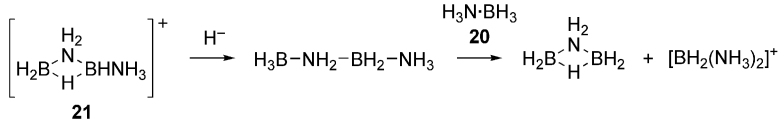

Scheme 5.

signals in the former two spectra that could be assigned to any of the expected dehydrogenation products, Ph_2PH–BH_2–PPh_2–BH_3, $[Ph_2P–BH_2]_3$ and $[Ph_2P–BH_2]_4$.[36] Further evidence for the occurrence of a reaction other than dehydrogenation was apparent from the observation of phosphorus-tin coupling ($J_{P\text{-}Sn}$ = 196 Hz) in both the ^{31}P and ^{119}Sn NMR spectra. Unfortunately, the oily nature of the product prevented further purification of the material and thus hampered elucidation of the structure. In order to obtain a crystalline product, we repeated the experiment using **2** as the Lewis acid. On employing the same procedure as utilised with stannyl triflate **4**, we also obtained an oil, but which crystallised on cooling and could be sublimed. The crystals obtained from the latter procedure were of a quality suitable for single-crystal X-ray diffraction, and this enabled the unambiguous determination of the molecular structure as $Ph_2P(SiMe_3)\cdot BH_3$ (**24**). This formulation is also consistent with the data from multinuclear NMR spectroscopy and mass spectrometry. Compound **24** crystallised in the monoclinic space group $P2_1/n$ with one molecule per asymmetric unit. There were no short intermolecular contacts, and a thermal ellipsoid plot along with selected metrical parameters is included in Figure 2. All bond lengths and angles are as expected, and the structural solution is included solely for the purpose of supporting product identification. The similarities in the ^{11}B and ^{31}P NMR spectra for **24** (δ_B = –39 ppm, δ_P = –23 ppm) and the product obtained with **4** (δ_B = –36 ppm, δ_P = –20 ppm) suggest that an analogous product was obtained when the latter was used as the Lewis acid. The reaction chemistry is depicted in Scheme 6.

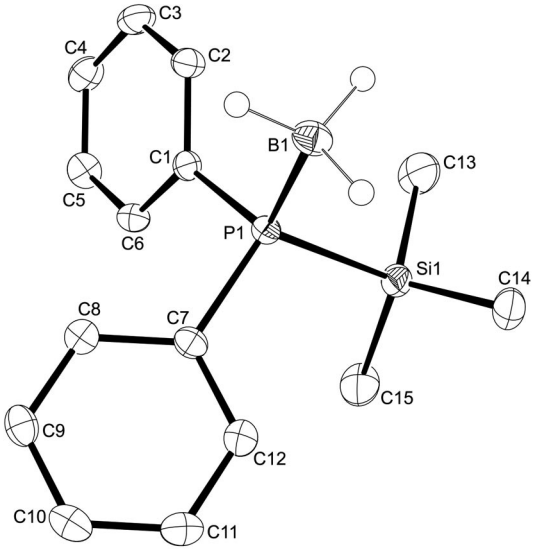

Figure 2. Molecular structure of **24** with thermal ellipsoids at the 50% probability level. Hydrogen atoms attached to carbon atoms have been omitted for clarity. Selected bond lengths [Å] and angles [°]: P1–B1 1.9389(17), P1–C1 1.8170(15), P1–C7 1.8172(15), P1–Si1 2.2831(6); C1–P1–C7 105.35(7), C1–P1–B1 112.83(7), C7–P1–B1 112.65(7), C1–P1–Si1 103.95(5), C7–P1–Si1 110.01(5), B1–P1–Si1 111.55(6).

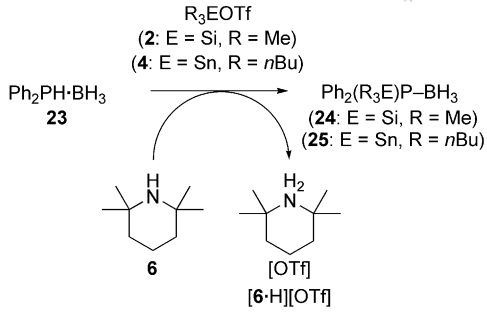

Scheme 6.

In contrast to the reaction with dimethylamine–borane (**11**), compound **23** neither reacts with Lewis acid **2** nor is deprotonated by Lewis base **6** in isolation. These results are consistent with functionalisation of the phosphane occurring by a concerted mechanism.

3. Conclusions

The FLP formed by nBu$_3$SnOTf (**4**) with 2,2,6,6-tetramethylpiperidine (**6**) was found to dehydrogenate $Me_2NH\cdot BH_3$ (**11**) both cleanly and rapidly to afford $[Me_2N–BH_2]_2$ (**12**), in addition to nBu$_3$SnH (**19**) and 2,2,6,6-tetramethylpiperidinium triflate ([**6**·H][OTf]). Formally exchanging the Lewis acid for either Me$_3$SiOTf (**2**) or Et$_3$SiOTf (**3**) still resulted predominantly in dehydrogenation, but accompanied by increasing relative quantities of $[H_2B(\mu\text{-}H)(\mu\text{-}NMe_2)BH_2]$ (**14**). A similar trend was also observed on exchanging the base for the less nucleophilic 2,6-di-*tert*-butylpyridine (**5**). The formation of both products is proposed to proceed by hydride abstraction from the amine–borane adduct by the Lewis acid. Selectivity is then determined by the relative activation energies for deprotonation of the resulting boronium cation vs. reaction with further **11**. In contrast to the reactivity with **11** and in the presence of **6**, compounds **2** and **4** both functionalised $Ph_2PH\cdot BH_3$ (**23**) by a formal deprotonation/substitution reaction. Studies suggest, however, that the E–O (E = Si or Sn) and P–H bonds are cleaved in a concerted process.

4. Experimental

4.1. General Considerations

All manipulations of air- and moisture-sensitive materials were carried out either under inert gas (nitrogen or argon) or in vacuo by using standard Schlenk-line and glove-box techniques. All reaction solvents were dried and degassed by means of a Grubbs-type solvent purification system immediately prior to use.[72] Deuterated solvents for NMR spectroscopy were purchased from the Cambridge Isotope Laboratories, dried and degassed by inert-gas distillation from appropriate drying agents (CaH_2 for $CDCl_3$ and NaK for C_6D_6), or used as received (D_3COD). Tris(pentafluorophenyl)-

borane was purchased from Boulder Scientific and purified in accordance with the literature.[73] Methylamine–borane,[63] diphenylphosphane–borane[71] and 1,3-bis-*tert*-butylimidazol-2-ylidene[58] were prepared according to literature methods. The remainder of the chemicals used within this research were purchased from Sigma Aldrich Ltd. NMR spectra were recorded at ambient temperature with either a Jeol JNM-ECP300/400 or JNM-LA300 spectrometer. Chemical shifts are reported relative to residual protio solvent (^{1}H), the deuterio solvent itself (^{13}C) or external $BF_3{\cdot}Et_2O$ (^{11}B), 85% H_3PO_4 (^{31}P), $CFCl_3$ (^{19}F), Me_4Si (^{29}Si) and Me_4Sn (^{119}Sn) standards. Spectra recorded in 1,2-dichlorobenzene and CH_2Cl_2 were acquired unlocked. Elemental analysis was performed with an Eurovector EA 3000 Elemental Analyser by Des Davis of the University of Bristol Microanalysis Laboratory. Mass spectrometry employing either electron ionisation (EI) or chemical ionisation (CI), were carried out with a VG Analytical AutoSpec mass spectrometer at the University of Bristol.

4.2. Reactions of Trialkyl Group 14 Triflates with Lewis Bases

In 1,2-dichlorobenzene (0.7 mL), 0.4 mmol of the respective Lewis acid and Lewis base were mixed. The solutions were then stirred at 20 °C for 2 h before identification of the components by ^{29}Si or ^{119}Sn NMR spectroscopy. Each of the Lewis acids, Me_3SiOTf (**2**) [66] [^{29}Si NMR (79.50 MHz, 1,2-$Cl_2C_6H_4$): δ = 43 ppm], Et_3SiOTf (**3**)[56] [^{29}Si NMR (79.50 MHz, 1,2-$Cl_2C_6H_4$): δ = 44 ppm] and $n$$Bu_3SnOTf$ (**4**)[70] [^{119}Sn NMR (98.16 MHz, 1,2-$Cl_2C_6H_4$): δ = 151 ppm] showed no reactivity with either 2,6-di-*tert*-butylpyridine (**5**) or 2,2,6,6-tetramethylpiperidine (**6**). Reaction of **2** (0.057 g, 0.26 mmol) with 1,3-di-*tert*-butylimidazol-2-ylidene (**7**, 0.043 g, 0.24 mmol) in 1,2-$Cl_2C_6H_4$ resulted in the rapid formation of a colourless precipitate. The solid was collected by filtration and recrystallised from CH_2Cl_2/hexane to afford pure 1,3-di-*tert*-butyl-4-(trimethylsilyl)imidazolium triflate (**8**[OTf], 0.075 g, 78%) as colourless crystals. ^{1}H NMR (400 MHz, $CDCl_3$): δ = 9.19 [d, J_{HH} = 4 Hz, 1 H, N(CH)N], 7.24 [d, J_{HH} = 4 Hz, 1 H, C(CH)N], 1.78 (s, 9 H, CH_3), 1.74 (s, 9 H, CH_3), 0.49 (s, 9 H, $SiCH_3$) ppm. ^{13}C{^{1}H} NMR (100.53 MHz, $CDCl_3$): δ = 136.7 [s, N(CH)N], 134.2 [s, C(*C*H)N], 128.7 [s, C*C*(N)Si], 120.8 (q, J_{CF} = 321 Hz, OTf), 61.8 [s, N*C*(CH_3)$_3$], 60.5 [s, N*C*(CH_3)$_3$], 30.7 [s, C(*C*H$_3$)$_3$], 29.8 [s, C(*C*H$_3$)$_3$], 1.3 [s, Si(CH_3)$_3$] ppm. ^{19}F NMR (376.12 MHz, $CDCl_3$): δ = –78.2 (s, OTf) ppm. ^{29}Si{^{1}H} NMR (79.50 MHz, $CDCl_3$): δ = –6.2 [s, Si(CH_3)$_3$] ppm. $C_{15}H_{29}F_3N_2O_3SSi$ (401.55): C 44.76, H 7.26, N 6.96; found C 44.49, H 7.08, N 7.22. MS (EI): *m*/*z* (%) = 253.2 (100) [M – OTf]$^+$, 197.1 (15) [M – OTf – C_4H_8]$^+$, 181.1 (64) [M – OTf – SiC_3H_8]$^+$, 141.1 (35) [M – OTf – C_4H_8 – C_4H_8]$^+$, 125.1 (55) [M – OTf – SiC_3H_8 – C_4H_8]$^+$, 69.0 (44) [M – OTf – SiC_3H_8 – C_4H_8 – C_4H_8]$^+$.

4.3. Attempted H_2 Heterolysis with Mixtures of Trialkyl Group 14 Triflates and N-Donor Bases

All reactions with dihydrogen were attempted in a manner analogous to that described with Me_3SiOTf (**2**) and 2,2,6,6-piperidine (**6**): A solution of **2** (0.081 mg, 0.36 mmol) and **6** (0.056 g, 0.39 mmol) was prepared in 1,2-$Cl_2C_6H_4$ (0.7 mL) in an NMR tube fitted with a greaseless stopcock (J. Young). The solution was then frozen at –196 °C, the tube evacuated and warmed to ambient temperature before hydrogen was admitted (2 bar). After 2 h at ambient temperature, the ^{29}Si NMR spectrum only indicated the present of **2** (δ =43 ppm).[66] The solution was then heated at 50 °C for 18 h before the analysis was repeated.

2 and 2,6-Di-*tert*-butylpyridine (5) with H_2: No reaction was apparent by ^{29}Si NMR spectroscopy at ambient temperature after 2 h or at 50 °C for a further 18 h. Only unreacted **2** was observed in solution (^{29}Si NMR: δ = 43 ppm).[66]

***n*Bu_3SnOTf (4) and 6 with H_2:** No reaction was apparent by ^{119}Sn NMR spectroscopy at ambient temperature after 2 h or at 50 °C after a further 18 h. Only unreacted **4** was observed in solution (^{119}Sn NMR: δ = 151 ppm).[70]

$B(C_6F_5)_3$ (1) and 5 with H_2: No reaction was apparent by ^{11}B NMR spectroscopy at ambient temperature after 2 h with only **1** (^{11}B NMR: δ = 58.6 ppm) being observed in solution.[61] The mixture was then heated to 50 °C for a further 18 h, after which analysis by ^{11}B NMR spectroscopy exhibited two signals: a minor peak corresponding to an unknown product (δ = 3.5 ppm) and a major peak arising from $[HB(C_6F_5)_3]^-$ (δ = –26 ppm; J_{BH} = 87 Hz).[50]

4.4.1. Dehydrogenation of $Me_2NH{\cdot}BH_3$ with Mixtures of Trialkyl Group 14 Triflates and N-Donor Bases

All dehydrogenation reactions were carried out as described in detail below for the reaction of $Me_2NH{\cdot}BH_3$ (**11**) with Me_3SiOTf (**2**) and 2,2,6,6-tetramethylpiperidine (**6**). The percentage composition values were calculated from integration of the ^{11}B NMR spectra. To a solution of **11** (0.025 g, 0.42 mmol) in 1,2-$Cl_2C_6H_4$ (0.35 mL) was added a solution of **2** (0.086 g, 0.39 mmol) and **6** (0.057 g, 0.40 mmol) in further 1,2-dichlorobenzene (0.35 mL). The reaction mixture was then stirred at 20 °C for 2 h, before the components of the mixture were identified by ^{11}B NMR spectroscopy. ^{11}B NMR (9.25 MHz, 1,2-$Cl_2C_6H_4$): δ = –22.2 (trace), –18.6 {td, J_{BH} = 129, J_{BH} = 31 Hz, [H_2B(μ-H)(μ-NMe_2)BH_2] (**14**), 3%}, –14.3 (q, J_{BH} = 96 Hz, **11**, 8%), 4.1 [t, J_{BH} = 111 Hz, (Me_2NBH_2)$_2$ (**12**), 89%] ppm. Reaction of **11** with **2** and **5**: ^{11}B NMR (9.25 MHz, 1,2-$Cl_2C_6H_4$): δ = –19.5 (td, J_{BH} = 129, J_{BH} = 31 Hz, **14**, 18%), –15.3 (q, J_{BH} = 96 Hz, **11**, 27%), –1.5 (br. s, 24%), 3.3 (t, J_{BH} = 111 Hz, **12**, 31%) ppm. Reaction of **11** with **3** and **6**: ^{11}B NMR (9.25 MHz, 1,2-$Cl_2C_6H_4$): δ = –22.1 (br. s, 4%), –18.6 (td, J_{BH} = 129, J_{BH} = 31 Hz, **14**, trace), –13.9 (q, J_{BH} = 96 Hz, **11**, 5%), 4.2 (t, J_{BH} = 111 Hz, **12**, 87%) ppm. Reaction of **11** with **4** and **6**: ^{11}B{^{1}H} NMR (9.25 MHz, 1,2-$Cl_2C_6H_4$): δ = –18.7 (td, J_{BH} = 129, J_{BH} = 31 Hz, **14**, 2%), 4.1 (t, J_{BH} = 111 Hz, **12**, 91%), 27.2 ppm [d, J_{BH} = 148 Hz, $BH(NMe_2)_2$, 7%].[74]

4.4.2. Dehydrogenation of $Me_2NH{\cdot}BH_3$ with Me_3SiOTf and 2,2,6,6-Tetramethylpiperidine for the Isolation of 2,2,6,6-Tetramethylpiperidine Triflate:

To a solution of **11** (0.025 g, 0.42 mmol) in 1,2-$Cl_2C_6H_4$ (0.35 mL) was added a solution of **2** (0.086 g, 0.39 mmol) and **6** (0.057 g, 0.40 mmol) in further 1,2-$Cl_2C_6H_4$ (0.35 mL) at 20 °C. The mixture was stirred for 2 h before being filtered through a glass-fibre pad. The white solid so collected was then dried in vacuo. ^{1}H NMR (399.7 MHz, D_3COD): δ = 1.83–1.76 (m, 2 H, CH_2); 1.67–1.63 (m, 4 H, CH_2); 1.42 (s, 12 H, CH_3) ppm. ^{19}F NMR (376.12 MHz, D_3COD): δ = –80.1 (s, OTf) ppm. A spectroscopically identical product was attained through the stoichiometric reaction of trifluoromethanesulfonic acid and 2,2,6,6-tetramethylpiperidine in 1,2-dichlorobenzene.

4.4.3. Determination of Reaction Rates for the Dehydrogenation of $Me_2NH{\cdot}BH_3$ with Mixtures of Lewis Acids and Lewis Bases:

The relative rates of dehydrogenation of **11** by using various mixtures of Lewis acids and Lewis bases were determined by recording ^{11}B NMR spectra as a function of time. The relative concentrations of reagent and product were subsequently determined by integration of the corresponding signals. The reactions were performed in NMR tubes fitted with greaseless stopcocks (J. Young) on a 0.4 mmol scale in 1,2-$Cl_2C_6H_4$ (0.7 mL).

4.4.4. Reactions of $Me_2NH{\cdot}BH_3$ with N-Donor Lewis Bases:

Compound **11** (0.023 g, 0.4 mmol) was combined with either **5** or **6** (0.4 mmol) in 1,2-$Cl_2C_6H_4$ (0.7 mL) and the mixture stirred at 20 °C for 2 h. In both cases no reactions were observed by ^{11}B

NMR spectroscopy, with only **11** being present in solution (–14 ppm).[63]

4.4.5. Reactions of $Me_2NH{\cdot}BH_3$ with Trialkyl Group 14 Triflates: Compound **11** (0.023 g, 0.4 mmol) was combined with either **2**, **3** or **4** (0.4 mmol) in 1,2-$Cl_2C_6H_4$ (0.7 mL) and the mixture stirred at 20 °C for 2 h. In each case, ^{29}Si or ^{119}Sn NMR spectroscopy indicated a mixture of unreacted Lewis acid along with the corresponding silane or stannane produced by hydride abstraction at the boron atom. For **2**: ^{29}Si NMR (79.5 MHz, 1,2-$Cl_2C_6H_4$): δ = –16 (Me_3SiH) ppm.[66] For **3**: ^{29}Si NMR (79.5 MHz, 1,2-$Cl_2C_6H_4$): δ = –2 (Et_3SiH) ppm.[56] For **4**: ^{119}Sn NMR (98.16 MHz, 1,2-$Cl_2C_6H_4$): δ = –89 (d, J_{SnH} = 1526 Hz, *n*BuSnH) ppm.[69] ^{11}B NMR spectroscopy indicated that the sole boron-containing product produced was [$H_2B(\mu\text{-}H)(\mu\text{-}NMe_2)BH_2$] (**14**). ^{11}B NMR (96.25 MHz, 1,2-$Cl_2C_6H_4$): δ = –19 (td, J_{BH} = 129, J_{BH} = 31 Hz) ppm.[64] When the reaction mixture was allowed to stand for ca. 1 d, colourless crystals formed that were suitable for single-crystal X-ray analysis. Comparison of the unit-cell parameters with the literature[68] demonstrated these to consist of [Me_2NH_2]OTf, and this formulation is consistent with the NMR spectra of the bulk sample. ^1H NMR (300 MHz, D_3COD): δ = 2.67 (s, 6 H, Me) ppm. ^{19}F NMR (282.09 Hz, D_3COD): δ = –80.0 (s, OTf) ppm.

4.5.1. Reaction of $MeNH_2{\cdot}BH_3$ with 1 equiv. of Me_3SiOTf and 2,2,6,6-Tetramethylpiperidine: To a solution of $MeNH_2{\cdot}BH_3$ (**22**, 0.023 g, 0.5 mmol) in CH_2Cl_2 (0.75 mL) was added a solution of Me_3SiOTf (**2**, 0.121 g, 0.55 mmol) and 2,2,6,6-tetramethylpiperidine (**6**, 0.076 g, 0.55 mmol) in further CH_2Cl_2 (0.75 mL). The mixture was then stirred at 20 °C for 2 h before study by ^{11}B NMR spectroscopy. $^{11}B\{^1H\}$ NMR (96.25 MHz, CH_2Cl_2): δ = –23.2 (4%), –22.2 (17%), –19.9 (3%), –19.0 (**22**, 6%),[63] –18.3 (4%), –8.3 to –4.7 (overlapping singlets, 41%), –1.8 (13%), 28.8 (2%), 32.4 ([MeN–BH]$_3$, 10%),[63] 41.2 (trace) ppm.

4.5.2. Reaction of $MeNH_2{\cdot}BH_3$ with 2 equiv. of Me_3SiOTf and 2,2,6,6-Tetramethylpiperidine: To a solution of **22** (0.023 g, 0.5 mmol) in dichloromethane CH_2Cl_2 (0.75 mL) was added a solution of **2** (0.242 g, 1.1 mmol) and **6** (0.152 g, 1.1 mmol) in CH_2Cl_2 (0.75 mL). The mixture was then stirred at 20 °C for 2 h before analysis by ^{11}B NMR spectroscopy. $^{11}B\{^1H\}$ NMR (96.25 MHz, CH_2Cl_2): δ = –22.8 (2%), –22.0 (2%), –18.2 (trace), –8.9 (49%), –5.5 (4%), –1.7 (13%), –1.0 (22%), 29.5 (trace), 32.4 ([MeN–BH]$_3$, 1%),[63] 41.3 (6%).

4.6.1. Reaction of $Ph_2PH{\cdot}BH_3$ with Me_3SiOTf and 2,2,6,6-Tetramethylpiperidine: To a solution of $Ph_2PH{\cdot}BH_3$ (**23**, 0.25 g, 1.23 mmol) in CH_2Cl_2 (1 mL) was added a solution of Me_3SiOTf (**2**, 0.31 g, 1.36 mmol) and 2,2,6,6-tetramethylpiperidine (**6**, 0.19 g, 1.36 mmol) in further CH_2Cl_2 (1 mL). The mixture was stirred at 20 °C for 2 h, upon which a colourless solid was seen to precipitate. After a further 2 h, the solid was collected by filtration and the solvent removed in vacuo to yield a colourless oil that solidified on cooling to –18 °C. The solid was sublimed at 45 °C (0.005 Torr) to afford crystals of (Me_3Si)$PPh_2{\cdot}BH_3$ (**24**, 0.28 g, 82%). ^{11}B NMR (96.25 MHz, $CDCl_3$): δ = –39.4 (dq, J_{BP} = 35, J_{BH} = 97 Hz) ppm. $^{31}P\{^1H\}$ NMR (121.44 MHz, $CDCl_3$): δ = –23.4 (br. m, Me_3SiPPh_2) ppm. ^1H NMR (300 MHz, $CDCl_3$): δ = 7.68–7.60 (m, 4 H, Ph), 7.47–7.40 (m, 6 H, Ph), 0.38 (d, J_{HP} = 6 Hz, 9 H, Me_3Si) ppm. $^{13}C\{^1H\}$ NMR (75.43 MHz, $CDCl_3$): δ = 133.2 (d, J_{CP} = 8 Hz, Ph), 130.3 (s, Ph), 128.8 (d, J_{CP} = 9 Hz, Ph), –2.4 (d, J_{CP} = 9 Hz, Me_3Si) ppm. $^{29}Si\{^1H\}$ NMR (59.60 MHz, $CDCl_3$): δ = 5.2 (d, J_{SiP} = 44 Hz, Me_3SiPPh_2) ppm. MS-CI+ (70 eV): *m*/*z* (%) = 271.1 (75) [M^+ – H], 258.1 (100), [M^+ – BH_3], 187.1 (44) [$H_2PPh_2^+$]; satisfactory elemental analysis could not be obtained.

4.6.2. Reaction of $Ph_2PH{\cdot}BH_3$ with Me_3SiOTf: To a solution of **23** (0.075 g, 0.62 mmol) in CH_2Cl_2 (1 mL) was added a solution of **2** (0.16 g, 0.68 mmol) in further CH_2Cl_2 (1 mL) and the mixture stirred at 20 °C for 2 h. ^{31}P and ^{11}B NMR spectroscopy indicated that no reaction had occurred, with **23** being the only apparent species in solution. $^{11}B\{^1H\}$ NMR (96.25 MHz, CH_2Cl_2): δ = –41.1 (d, J_{BP} = 45 Hz, BH_3) ppm. $^{31}P\{^1H\}$ NMR (121.44 MHz, CH_2Cl_2): δ = 1.5 (br. m, **23**) ppm.

4.6.3. Reaction of $Ph_2PH{\cdot}BH_3$ with 2,2,6,6-Tetramethylpiperidine: To a solution of **23** (0.075 g, 0.62 mmol) in CH_2Cl_2 (1 mL) was added a solution of **6** (0.1 g, 0.68 mmol) in further CH_2Cl_2 (1 mL) and the mixture stirred at 20 °C for 2 h. ^{31}P NMR and ^{11}B NMR spectroscopy indicated that ca. 5% of **23** had undergone an phosphane–amine exchange to afford **6**·BH_3,[75] with the concomitant liberation of diphenylphosphane. $^{11}B\{^1H\}$ NMR (96.25 MHz, CH_2Cl_2): δ = 41.1 (d, J_{PB} = 45 Hz, $Ph_2PH{\cdot}BH_3$), –22.8 (s, **6**·BH_3) ppm. $^{31}P\{^1H\}$ NMR (121.44 MHz, CH_2Cl_2): δ = 1.5 (br. m, $Ph_2PH{\cdot}BH_3$), –39.7 (s, Ph_2PH) ppm.[76]

4.6.4. Reaction of $Ph_2PH{\cdot}BH_3$ with *n*Bu_3SnOTf and 2,2,6,6-Tetramethylpiperidine: To a solution of **23** (0.1 g, 0.5 mmol) in CH_2Cl_2 (1 mL) was added a solution of *n*Bu_3SnOTf (**4**, 0.242 g, 0.55 mmol) and **6** (0.077 g, 0.55 mmol) in further CH_2Cl_2 (1 mL). The mixture was stirred at 20 °C for 2 h, resulting in the rapid formation of a colourless precipitate. After a further 2 h of stirring, the solid was collected by filtration and the solvent removed in vacuo to afford *n*$Bu_3SnPPh_2{\cdot}BH_3$ as a colourless oil (**25**, 0.22 g, 92%). $^{11}B\{^1H\}$ NMR (96.25 MHz, C_6D_6): δ = –36.4 (br. s, BH_3) ppm. $^{31}P\{^1H\}$ NMR (121.44 MHz, C_6D_6): δ = –20.1 (s, J_{SnP} = 196 Hz, *n*Bu_3SnPPh_2) ppm. ^1H NMR (300 MHz, C_6D_6): δ = 7.83–7.70 (m, 4 H, Ph), 7.12–6.97 (m, 6 H, Ph); 1.52–1.39 (m, 2 H, *n*Bu), 1.27–1.13 (m, 4 H, *n*Bu), 0.80 (t, J_{HH} = 7.16 Hz, 3 H, *n*Bu) ppm. $^{13}C\{^1H\}$ NMR (75.43 MHz, C_6D_6): δ = 134.0 (d, J_{CP} = 8.65 Hz, Ph), 130.4 (s, Ph), 129.3 (d, J_{CP} = 9.23 Hz, Ph), 29.6 (s, *n*Bu), 27.8 (s, *n*Bu), 14.1 (s, *n*Bu), 12.3 (s, *n*Bu) ppm. $^{119}Sn\{^1H\}$ NMR (98.16 MHz, C_6D_6): δ = 17.1 (d, J_{SnP} = 196 Hz, *n*Bu_3SnPPh_2) ppm. MS-CI+ (70 eV): *m*/*z* (%) = 490.2 (10) [M^+], 477.1 (38) [MH^+–BH_3], 291.1 (86) [*n*Bu_3Sn], 187.1 (100) [$H_2PPh_2^+$]; satisfactory elemental analysis could not be obtained due to the oily nature of the product.

4.7. X-ray Structural Characterization

Single-crystal X-ray structural study was performed with a CCD Bruker SMART APEX diffractometer equipped with an Oxford Instruments low-temperature attachment. Data were collected at 100(2) K by using graphite-monochromated Mo-K_α radiation (λ_α = 0.71073 Å). The frames were indexed, integrated, and scaled by using the SMART and SAINT software package,[77] and the data were corrected for absorption by using the SADABS program.[78] Pertinent crystallographic data for compounds **8**[OTf] and **24** are summarized in Table 1. The structure was solved and refined by using the SHELX suite of programs.[79] All molecular structures were generated by using ORTEP-3 for Windows Version 2.02.[80] The hydrogen atoms bonded to carbon atoms were included in geometrically calculated positions in the final stages of the refinement and were refined according to the typical riding model, whereas the hydrogen atoms attached to boron atoms were located and refined with isotropic thermal parameters. All non-hydrogen atoms were refined with anisotropic thermal parameters. CCDC-760847 (**8**[OTf]) and -761915 (**24**) contain the supplementary crystallographic data for this paper. These data can be obtained free of charge from The Cambridge Crystallographic Data Centre via www.ccdc.cam.ac.uk/data_request/cif.

Table 1. Crystallographic data and refinement parameters for **8**[OTf] and **24**.

	8[OTf]	**24**
Empirical formula	$[C_{14}H_{29}N_2Si][CF_3O_3S]$	$C_{15}H_{22}BPSi$
Formula mass	402.55	272.20
Crystal system	orthorhombic	monoclinic
Space group	$Pna2_1$	$P2_1/n$
a [Å]	17.5409(9)	8.9019(4)
b [Å]	9.6250(5)	15.6900(8)
c [Å]	12.1972(6)	11.7475(6)
α [°]	90	90
β [°]	90	95.635(3)
γ [°]	90	90
V [Å^3]	2059.27(18)	1632.85(14)
Z	4	4
$\rho_{calcd.}$ [g cm^{-3}]	1.298	1.107
μ [mm^{-1}]	2.57	2.24
$F(000)$	856	584
Reflections collected	18162	14637
independent	4225	3765
observed [$I>2\sigma(I)$]	4016	3026
No. of variables	236	178
Goodness-of-fit	1.052	1.017
Final R indices [$I>2\sigma(I)$][a]	R_1 = 0.0416 wR_2 = 0.1105	R_1 = 0.0358 wR_2 = 0.0783
R indices (all data)[a]	R_1 = 0.0473 wR_2 = 0.1123	R_1 = 0.0503 wR_2 = 0.0848

[a] $R_1 = \Sigma \||F_o| - |F_c|\|/\Sigma|F_o|$ with $F_o^2>2\sigma(F_o^2)$; $wR_2 = [\Sigma w(|F_o^2| - |F_c^2|)^2/\Sigma|F_o^2|^2]$.

Acknowledgments

I. M. thanks the Engineering and Physical Sciences Research Council (EPSRC) for financial support, the European Union for a Marie Curie Chair and the Royal Society for a Wolfson Research Merit Award. A. P. M. R. would like to acknowledge the EPSRC for a doctoral training award. S. K. P. thanks the European Union for a Marie Curie Postdoctoral Fellowship.

[1] A. Staubitz, A. P. Soto, I. Manners, *Angew. Chem. Int. Ed.* **2008**, *47*, 6212–6215.
[2] B. L. Dietrich, K. I. Goldberg, D. M. Heinekey, T. Autrey, J. C. Linehan, *Inorg. Chem.* **2008**, *47*, 8583–8585.
[3] C. W. Hamilton, R. T. Baker, A. Staubitz, I. Manners, *Chem. Soc. Rev.* **2009**, *38*, 279–293.
[4] C. A. Jaska, I. Manners, *J. Am. Chem. Soc.* **2004**, *126*, 2698–2699.
[5] F. Cheng, H. Ma, Y. Li, J. Chen, *Inorg. Chem.* **2007**, *46*, 788–794.
[6] Q. Xu, M. Chandra, *J. Power Sources* **2006**, *163*, 364–370.
[7] F. H. Stephens, V. Pons, R. T. Baker, *Dalton Trans.* **2007**, 2613–2626.
[8] F. H. Stephens, R. T. Baker, M. H. Matus, D. J. Grant, D. A. Dixon, *Angew. Chem. Int. Ed.* **2007**, *46*, 746–749.
[9] R. J. Keaton, J. M. Blacquiere, R. T. Baker, *J. Am. Chem. Soc.* **2007**, *129*, 1844–1845.
[10] M. T. Nguyen, V. S. Nguyen, M. H. Matus, G. Gopakumar, D. A. Dixon, *J. Phys. Chem. A* **2007**, *111*, 679–690.
[11] C. W. Yoon, L. G. Sneddon, *J. Am. Chem. Soc.* **2006**, *128*, 13992–13993.
[12] A. Staubitz, M. Besora, J. N. Harvey, I. Manners, *Inorg. Chem.* **2008**, *47*, 5910–5918.
[13] J. Spielmann, G. Jansen, H. Bandmann, S. Harder, *Angew. Chem. Int. Ed.* **2008**, *47*, 6290–6295.
[14] T. B. Marder, *Angew. Chem. Int. Ed.* **2007**, *46*, 8116–8118.
[15] S. Hausdorf, F. Baitalow, G. Wolf, F. O. R. L. Mertens, *Int. J. Hydrogen Energy* **2008**, *33*, 608–614.
[16] M. C. Denney, V. Pons, T. J. Hebden, D. M. Heinekey, K. I. Goldberg, *J. Am. Chem. Soc.* **2006**, *128*, 12048–12049.
[17] T. J. Hebden, M. C. Denney, V. Pons, P. M. B. Piccoli, T. F. Koetzle, A. J. Schultz, W. Kaminsky, K. I. Goldberg, D. M. Heinekey, *J. Am. Chem. Soc.* **2008**, *130*, 10812–10820.
[18] M. Kaess, A. Friedrich, M. Drees, S. Schneider, *Angew. Chem. Int. Ed.* **2009**, *48*, 905–907.
[19] A. Friedrich, M. Drees, S. Schneider, *Chem. Eur. J.* **2009**, *15*, 10339–10342.
[20] N. Blaquiere, S. Diallo-Garcia, S. I. Gorelsky, D. A. Black, K. Fagnou, *J. Am. Chem. Soc.* **2008**, *130*, 14034–14035.
[21] T. M. Douglas, A. B. Chaplin, A. S. Weller, *J. Am. Chem. Soc.* **2008**, *130*, 14432–14433.
[22] R. Dallanegra, A. B. Chaplin, A. S. Weller, *Angew. Chem. Int. Ed.* **2009**, *48*, 6875–6878.
[23] T. M. Douglas, A. B. Chaplin, A. S. Weller, X. Yang, M. B. Hall, *J. Am. Chem. Soc.* **2009**, *131*, 15440–15456.
[24] Y. Chen, J. L. Fulton, J. C. Linehan, T. Autrey, *J. Am. Chem. Soc.* **2005**, *127*, 3254–3255.
[25] J. L. Fulton, J. C. Linehan, T. Autrey, M. Balasubramanian, Y. Chen, N. K. Szymczak, *J. Am. Chem. Soc.* **2007**, *129*, 11936–11949.
[26] R. Rousseau, G. K. Schenter, J. L. Fulton, J. C. Linehan, M. H. Engelhard, T. Autrey, *J. Am. Chem. Soc.* **2009**, *131*, 10516–10524.
[27] M. Zahmakiran, S. Özkar, *Inorg. Chem.* **2009**, *48*, 8955–8964.
[28] Y. Jiang, H. Berke, *Chem. Commun.* **2007**, 3571–3573.
[29] Y. Jiang, O. Blacque, T. Fox, C. M. Frech, H. Berke, *Organometallics* **2009**, *28*, 5493–5504.
[30] Y. Kawano, M. Uruichi, M. Shimoi, S. Taki, T. Kawaguchi, T. Kakizawa, H. Ogino, *J. Am. Chem. Soc.* **2009**, *131*, 14946–14957.
[31] P. M. Zimmerman, A. Paul, Z. Zhang, C. B. Musgrave, *Angew. Chem. Int. Ed.* **2009**, *48*, 2201–2205.
[32] X. Yang, M. B. Hall, *J. Am. Chem. Soc.* **2008**, *130*, 1798–1799.
[33] T. J. Clark, K. Lee, I. Manners, *Chem. Eur. J.* **2006**, *12*, 8634–8648.
[34] P. Wang, X.-D. Kang, *Dalton Trans.* **2008**, 5400–5413.
[35] H. Dorn, R. A. Singh, J. A. Massey, A. J. Lough, I. Manners, *Angew. Chem. Int. Ed.* **1999**, *38*, 3321–3323.
[36] H. Dorn, R. A. Singh, J. A. Massey, J. M. Nelson, C. A. Jaska, A. J. Lough, I. Manners, *J. Am. Chem. Soc.* **2000**, *122*, 6669–6678.
[37] H. Dorn, J. M. Rodezno, B. Brunnhoefer, E. Rivard, J. A. Massey, I. Manners, *Macromolecules* **2003**, *36*, 291–297.
[38] T. J. Clark, J. M. Rodezno, S. B. Clendenning, S. Aouba, P. M. Brodersen, A. J. Lough, H. E. Ruda, I. Manners, *Chem. Eur. J.* **2005**, *11*, 4526–4534.
[39] D. W. Stephan, G. Erker, *Angew. Chem. Int. Ed.* **2010**, *49*, 46–76.
[40] P. A. Chase, G. C. Welch, T. Jurca, D. W. Stephan, *Angew. Chem. Int. Ed.* **2007**, *46*, 8050–8053.
[41] C. A. Preston, J. Titel, D. W. Stephan, *Chem. Commun.* **2008**, 1701–1703.
[42] P. Spies, S. Schwendemann, S. Lange, G. Kehr, R. Froehlich, G. Erker, *Angew. Chem. Int. Ed.* **2008**, *47*, 7543–7546.
[43] J. S. J. McCahill, G. C. Welch, D. W. Stephan, *Angew. Chem. Int. Ed.* **2007**, *46*, 4968–4971.
[44] C. M. Moemming, E. Otten, G. Kehr, R. Froehlich, S. Grimme, D. W. Stephan, G. Erker, *Angew. Chem. Int. Ed.* **2009**, *48*, 6643–6646.
[45] A. E. Ashley, A. L. Thompson, D. O'Hare, *Angew. Chem. Int. Ed.* **2009**, *48*, 9839–9843.
[46] G. D. Frey, V. Lavallo, B. Donnadieu, W. W. Schoeller, G. Bertrand, *Science* **2007**, *316*, 439–441.
[47] M. A. Dureen, A. Lough, T. M. Gilbert, D. W. Stephan, *Chem. Commun.* **2008**, 4303–4305.

[48] A. J. M. Miller, J. E. Bercaw, *Chem. Commun.* **2010**, *46*, 1709–1711.
[49] Y. Guo, X. He, Z. Li, Z. Zou, *Inorg. Chem.* **2010**, *49*, 3419–3423.
[50] G. C. Welch, D. W. Stephan, *J. Am. Chem. Soc.* **2007**, *129*, 1880–1881.
[51] V. Sumerin, F. Schulz, M. Nieger, M. Leskela, T. Repo, B. Rieger, *Angew. Chem. Int. Ed.* **2008**, *47*, 6001–6003.
[52] P. A. Chase, A. L. Gille, T. M. Gilbert, D. W. Stephan, *Dalton Trans.* **2009**, 7179–7188.
[53] D. Holschumacher, T. Bannenberg, C. G. Hrib, P. G. Jones, M. Tamm, *Angew. Chem. Int. Ed.* **2008**, *47*, 7428–7432.
[54] D. Holschumacher, C. Taouss, T. Bannenberg, C. G. Hrib, C. G. Daniliuc, P. G. Jones, M. Tamm, *Dalton Trans.* **2009**, 6927–6929.
[55] S. J. Geier, D. W. Stephan, *J. Am. Chem. Soc.* **2009**, *131*, 3476–3477.
[56] G. A. Olah, K. Laali, O. Farooq, *Organometallics* **1984**, *3*, 1337–1340.
[57] D. Farah, K. Swami, H. G. Kuivila, *J. Organomet. Chem.* **1992**, *429*, 311–334.
[58] A. J. Arduengo III, H. Bock, H. Chen, M. Denk, D. A. Dixon, J. C. Green, W. A. Herrmann, N. L. Jones, M. Wagner, R. West, *J. Am. Chem. Soc.* **1994**, *116*, 6641–6649.
[59] M. D. Barrera, Y. Cheburkov, W. M. Lamanna, *J. Fluorine Chem.* **2002**, *117*, 13–16.
[60] M. Tamm, D. Petrovic, S. Randoll, S. Beer, T. Bannenberg, P. G. Jones, J. Grunenberg, *Org. Biomol. Chem.* **2007**, *5*, 523–530.
[61] T. Beringhelli, D. Donghi, D. Maggioni, G. D′Alfonso, *Coord. Chem. Rev.* **2008**, *252*, 2292–2313.
[62] M. E. Sloan, T. J. Clark, I. Manners, *Inorg. Chem.* **2009**, *48*, 2429–2435.
[63] C. A. Jaska, K. Temple, A. J. Lough, I. Manners, *J. Am. Chem. Soc.* **2003**, *125*, 9424–9434.
[64] H. Nöth, B. Wrackmeyer, *Nuclear Magnetic Resonance Spectroscopy of Boron Compounds in NMR – Basic Principles and Progress* (Eds.: P. Diehl, E. Fluck, R. Kosfeld), Springer, Berlin, **1978**, vol. 14.
[65] Identification was made by comparison of the spectra with those obtained with an authentic sample prepared by reaction of **5** with HOTf.
[66] G. A. Olah, L. D. Field, *Organometallics* **1982**, *1*, 1485–1487.
[67] A. Rokob Tibor, A. Hamza, A. Stirling, T. Soos, I. Papai, *Angew. Chem. Int. Ed.* **2008**, *47*, 2435–2438.
[68] P. D. C. Dietzel, R. Dinnebier, M. Jansen, *Z. Anorg. Allg. Chem.* **2007**, *633*, 1410–1416.
[69] D. Crich, X.-Y. Jiao, Q. Yao, J. S. Harwood, *J. Org. Chem.* **1996**, *61*, 2368–2373.
[70] M. Arshadi, D. Johnels, U. Edlund, *Chem. Commun.* **1996**, 1279–1280.
[71] F. Dornhaus, M. Bolte, H.-W. Lerner, M. Wagner, *Eur. J. Inorg. Chem.* **2006**, 1777–1785.
[72] A. B. Pangborn, M. A. Giardello, R. H. Grubbs, R. K. Rosen, F. J. Timmers, *Organometallics* **1996**, *15*, 1518–1520.
[73] D. J. Parks, W. E. Piers, G. P. A. Yap, *Organometallics* **1998**, *17*, 5492–5503.
[74] D. K. Srivastava, L. K. Krannich, C. L. Watkins, *Inorg. Chem.* **1991**, *30*, 2441–2444.
[75] A. Flores-Parra, N. Farfan, A. I. Hernandez-Bautista, L. Fernandez-Sanchez, R. Contreras, *Tetrahedron* **1991**, *47*, 6903–6914.
[76] M. R. Crimmin, A. G. M. Barrett, M. S. Hill, P. B. Hitchcock, P. A. Procopiou, *Organometallics* **2007**, *26*, 2953–2956.
[77] *SAINT+ Software for CCD Diffractometers*, Bruker AXS, Madison, WI, **2000**.
[78] G. M. Sheldrick, *SADABS Program for Correction of Area Detector Data*; University of Göttingen, Göttingen, Germany, **1999**.
[79] a) *SHELXTL Package*, version 6.10, Bruker AXS, Madison, WI, **2000**; b) G. M. Sheldrick, *SHELXS-86 and SHELXL-97*, University of Göttingen, Göttingen, Germany, **1997**.
[80] L. J. Farrugia, *J. Appl. Crystallogr.* **1997**, *30*, 565.

Received: May 10, 2010
Published Online: July 21, 2010

DOI: 10.1002/ejic.201000278

Synthesis and Characterization of [FeFe]-Hydrogenase Models with Bridging Moieties Containing (S, Se) and (S, Te)

Mohammad K. Harb,[a] Helmar Görls,[a] Taka Sakamoto,[b] Greg A. N. Felton,[c] Dennis H. Evans,*[d] Richard S. Glass,*[b] Dennis L. Lichtenberger,*[b] Mohammad El-khateeb,[e] and Wolfgang Weigand*[a]

Dedicated to Prof. Reinhold Tacke on the occasion of his 60th birthday

Keywords: Iron / Hydrogenases / Tellurium / Selenium / Sulfur / Electrocatalysis

[FeFe]-hydrogenase-active-site models containing larger chalcogens such as Se or Te have exhibited greater electron richness at the metal centers and smaller gas-phase ionization energies and reorganization energies relative to molecules containing S atoms. Diiron complexes related to the much-studied molecule $[Fe_2(\mu\text{-}SC_3H_6S)(CO)_6]$ (**1**) have been prepared with one S atom replaced either by one Se atom to give $[Fe_2(\mu\text{-}SC_3H_6Se)(CO)_6]$ (**2**) or by one Te atom to give $[Fe_2(\mu\text{-}SC_3H_6Te)(CO)_6]$ (**3**). The molecules have been characterized by use of mass spectrometry and $^{13}C\{^1H\}$ NMR, $^{77}Se\{^1H\}$ NMR, IR, and photoelectron spectroscopic techniques along with structure determination with single-crystal X-ray diffraction, electrochemical measurements, and DFT calculations. He I photoelectron spectra and DFT computations of **2** and **3** show a lowering of ionization energies relative to those of the all-sulfur complex **1**, indicating increased electron richness at the metal centers that favors electrocatalytic reduction of protons from weak acids to produce H_2. However, chalcogen substitution from S to Se or Te also causes an increase in the Fe–Fe bond length, which disfavors the formation of a carbonyl-bridged "rotated" structure, as also shown by the photoelectron spectra and computations. This "rotated" structure is believed to be important in the mechanism of H_2 production. As a consequence of the competing influences of increased electron richness at the metals with less favorable "rotated" structures, the catalytic efficiency of the Se and Te molecules **2** and **3** is found to be comparable to that of molecule **1**.

Introduction

The importance of developing clean renewable energy sources and fuels is rising with the increasing depletion of global fossil fuel reserves and the increasing demand to reduce our carbon footprint. One potential alternative for fuel and energy storage is hydrogen gas. [FeFe]-hydrogenase is one of the enzymes that produce H_2 in nature,[1–3] and H_2 is one of cleanest renewable fuels available today.[4–11] Several [FeFe]-hydrogenase-active-site biomimetic compounds[12–32] containing dithiolato,[12–33] diselenolato,[33–38] or ditellurolato[33,39–41] bridging ligands have been prepared, characterized, and evaluated for the electrocatalytic production of H_2 from weak acids.

Recent spectroscopic and computational studies have revealed that substitution of S by Se or Te in the $Fe_2S_2(CO)_6$ core of [FeFe]-hydrogenase models results in lower ionization and reorganization energies for the Se or Te compounds,[35,39–42] which may lead to faster electron transfer rates and more active catalysts. However, the rate of catalytic reduction was found to be substantially diminished as the size of chalcogen increased,[39–41] which was in contrast to one previous finding.[35] Hence, further study on complexes containing heavier chalcogens rather than a S atom is warranted.

In this paper we elucidate the influence of the chalcogen on the electrocatalytic production of H_2 from [FeFe]-hydrogenase model complexes by utilizing mixed dichalcogenolato ligands. As a continuation of our previous studies in this area,[23–25,35,36,43] a series of homologous compounds **1** through **3** (Scheme 1) was prepared and evaluated with use of electrochemistry, photoelectron spectroscopy (PES), and density functional theory (DFT) calculations. Compounds

[a] Institut für Anorganische und Analytische Chemie, Friedrich-Schiller-Universität Jena, August-Bebel-Straße 2, 07743 Jena, Germany
[b] Department of Chemistry and Biochemistry, The University of Arizona, Tucson, AZ, 85721, USA
[c] Department of Chemistry, Oakland University, Rochester, MI, 48309, USA
[d] Department of Chemistry, Purdue University, West Lafayette, IN, 47907, USA
[e] Chemistry Department, Jordan University of Science and Technology, 22110 Irbid, Jordan
Supporting information for this article is available on the WWW under http://dx.doi.org/10.1002/ejic.201000278.

2 and **3** allow direct comparison with dithiolato compound **1**, extensively studied for its ability to catalyze the formation of H_2 from weak acids.

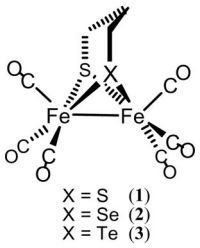

Scheme 1. Mixed dichalcogen [FeFe]-hydrogenase model compounds.

Results and Discussion

Reaction of 1,2-Thiaselenolane (4) and 1,2-Thiatellurolane (5) with $Fe_3(CO)_{12}$

Treatment of $Fe_3(CO)_{12}$ with 1,2-thiaselenolane (**4**) or 1,2-thiatellurolane (**5**) in THF under reflux resulted in the formation of diiron complexes $[Fe_2(\mu\text{-}SC_3H_6Se)(CO)_6]$ (**2**) or $[Fe_2(\mu\text{-}SC_3H_6Te)(CO)_6]$ (**3**), respectively (Scheme 2). Compounds **2** and **3** are air-stable in the solid state and for several hours in solution. These compounds have been characterized by IR, multinuclear NMR spectroscopy, mass spectrometry, and elemental analysis, as well as by X-ray crystallography. The ^1H NMR spectra of **2** and **3** exhibit three signals for the three different CH_2 moieties at 1.73 (CH_2), 2.11 (SCH_2), and 2.12 ($SeCH_2$) ppm for **2** and 1.46 (CH_2), 2.01 (SCH_2), and 2.29 ($TeCH_2$) ppm for **3**. The ^1H NMR resonances of the SCH_2 group in **2** and **3** are shifted upfield relative to that reported for the propanedithiolate (PDT) complex **1** (2.26 ppm).[21,32] The $SeCH_2$ and $TeCH_2$ proton resonances in **2** and **3** are also shifted to higher field relative to those reported for propanediselenolato (PDSe) (2.19 ppm)[36] and propaneditellurolato (PDTe) (2.3 ppm)[44] complexes. The $^{13}C\{^1H\}$ NMR spectra of **2** and **3** display three resonances at 13.1 ($SeCH_2$), 24.7 (SCH_2), and 30.3 ppm ($SeCH_2CH_2$) for **2** and at –9.4 ($TeCH_2$), 30.2 (SCH_2), 31.9 ($TeCH_2CH_2$) ppm for **3**. The ^{13}C resonance of $TeCH_2$ in **3** is significantly shifted to higher field relative to the respective resonances of SCH_2 and $SeCH_2$, which could be attributed to the "heavy atom" effect.[45] In addition, the expected resonances for the carbonyl groups were observed in the spectra. One signal was observed at δ = 132.9 ppm in the $^1H^{77}Se$ HMBC NMR spectrum of **2**, which was shifted upfield relative to those reported for PDSe (145 ppm).[36] The ^{125}Te NMR spectrum of **3** exhibits a signal at δ = 177 ppm. The mass spectra of **2** and **3** show the molecular ion peaks followed by several peaks obtained by loss of CO groups.

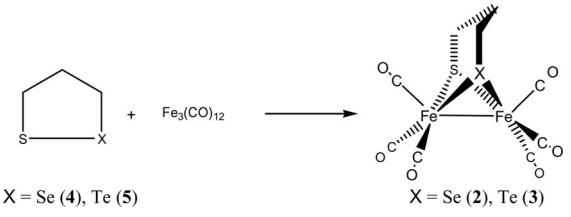

Scheme 2. The reaction of 1,2-thiaselenolane (**4**) and 1,2-thiatellurolane (**5**) with $Fe_3(CO)_{12}$ in THF.

The X-ray crystallographic structure analyses reveal the proposed structures of **2** and **3** as shown in Figures 1 and 2, and details of the crystal data are presented in Table 1. The central [2FeSX] (X = Se, Te) moieties of **2** and **3** are in the butterfly conformation, and the coordination geometry around the iron cores is rather similar to those reported for **1** and for the PDSe and PDTe complexes.[22,36,44] The Fe–Fe distances increase according to the trend **1** < **2** < PDSe < **3** < PDTe [with values of 2.5103(11) < 2.5373(9) < 2.5610(8) < 2.5736(10) < 2.633(1) Å, respectively], which is attributed to the increase in the atom size from S through Se to Te.[22,36,44] As observed in **1**, PDSe, and PDTe, the C2 methylene group of **2** and **3** is disordered over two positions with 50% probability.[22,36,44] Disorder also is likely between the location of the chalcogen atoms, especially in the case of the S and Se atoms of molecule **2**, where the Fe–Se and

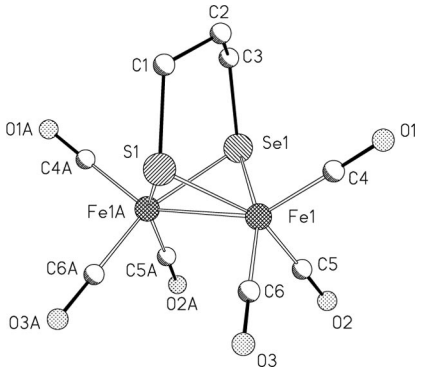

Figure 1. ORTEP drawing of $[Fe_2(\mu\text{-}SC_3H_6Se\text{-}\mu)(CO)_6]$ (**2**) at the 50% probability level (hydrogen atoms are omitted for clarity). Selected distances (Å) and angles (°): Fe1–Fe1A 2.5374(9), Fe1–S1 2.28(2), Fe1–Se1 2.332(4), Fe1–S1–Fe1A 67.7(7), Fe1–Se1–Fe1A 65.91(11).

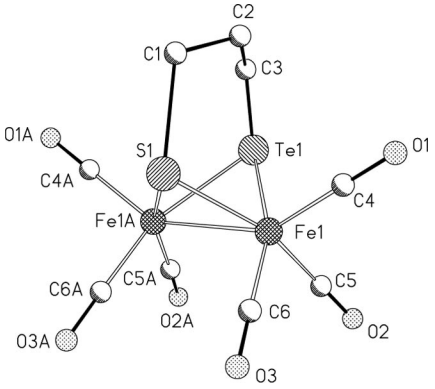

Figure 2. ORTEP drawing of $[Fe_2(\mu\text{-}SC_3H_6Te\text{-}\mu)(CO)_6]$ (**3**) at the 50% probability level (hydrogen atoms are omitted for clarity). Selected distances (Å) and angles (°): Fe1–Fe1A 2.574(1), Fe1–S1 2.256(7), Fe1–Te1 2.5074(9), Fe1–S1–Fe1A 69.5(3), Fe1–Te2–Fe1A 61.76(3).

Fe–S distances from the structure determination differ by only 0.01 Å despite the difference in the sizes of the Se and S atoms. The covalent radius of Se is 0.15 Å greater than that of S,[46] and the computations that are discussed later optimize the Fe–Se distance at a value 0.15 Å longer than the Fe–S distance; the Fe–chalcogen distance from the crystal structure determination is intermediate between the values optimized in the computations.

Table 1. Crystal data and refinement details for the X-ray structure determinations of compounds **2** and **3**.

Compound	**2**	**3**
Formula	$C_9H_6Fe_2O_6SSe$	$C_9H_6Fe_2O_6STe$
Fw ($g\,mol^{-1}$)	432.86	481.50
T (°C)	–90(2)	–90(2)
Crystal system	Monoclinic	Monoclinic
Space group	$P2_1/m$	$P2_1/m$
a (Å)	6.8382(4)	6.9666(4)
b (Å)	13.3846(8)	13.3599(8)
c (Å)	7.9201(3)	8.0803(3)
β (°)	108.323(3)	109.792(3)
Z	2	2
ρ ($g\,cm^{-3}$)	2.089	2.260
μ (cm^{-1})	49.19	42.32
Measured data	5614	4544
Data with $I > 2\sigma(I)$	1487	1402
Unique data/R_{int}	1636/0.0632	1676/0.0336
wR_2 (all data, on F^2)[a]	0.1327	0.0889
R_1 [$I > 2\sigma(I)$][a]	0.0477	0.0304
s[b]	1.043	1.018
Res. dens. ($e\,Å^{-3}$)	1.360/–1.691	0.637/–0.913
Absorpt. method	NONE	NONE
CCDC No.	726555	726556

[a] Definition of the R indices: $R_1 = (\Sigma||F_o| - |F_c||)/\Sigma|F_o|$; $wR_2 = \{\Sigma[w(F_o^2–F_c^2)^2]/\Sigma[w(F_o^2)^2]\}^{1/2}$ with $w^{-1} = \sigma^2(F_o^2) + (aP)^2 + bP$; $P = [2F_c^2 + \mathrm{Max}(F_o)^2]/3$. [b] $s = \{\Sigma[w(F_o^2 - F_c^2)^2]/(N_o - N_p)\}^{1/2}$.

The IR spectra of complexes **2** and **3** exhibit three strong absorption bands with a KBr disk and four strong absorption bands in Nujol in the range 2071–1988 cm^{-1} for **2** and 2065–1983 cm^{-1} for **3**. These data are in the typical range of such model complexes.[16,17,20,22,24,36,47–49] For comparison, the carbonyl stretching frequencies of the all-sulfur PDT molecule **1** measured under the same conditions are in the range 2074–1990 cm^{-1}. The down-shifting of the CO absorption bands to lower frequencies from **1** through **2** to **3** is an indication of the increased π back-donation between the diiron center and the CO ligand caused by the rising donor ability of the chalcogen from S through Se to Te. The shifts are about half that observed when both S atoms are replaced by heavier chalcogens in other [FeFe]-hydrogenase model compounds.[39–41]

Electrochemical Investigations

The electrochemical behavior of compounds **1**–**3** has been investigated along with the ability of these complexes to catalyze the reduction of the weak acid acetic acid to form dihydrogen and acetate. Figure 3 presents two voltammograms for each compound, one with an initial negative-going sweep (right) to investigate cathodic processes, and one with an initial positive-going sweep (left) to explore anodic reactions.

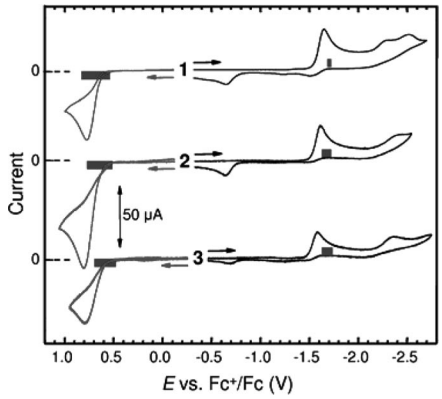

Figure 3. Voltammograms of ca. 1 mM **1**–**3** obtained in acetonitrile containing 0.10 M tetra-*n*-butylammonium hexafluorophosphate by using a glassy carbon working electrode (0.100 V/s). The gray bars represent the range of DFT-calculated oxidation and reduction potentials.

All three compounds show one principal cathodic peak near –1.6 V vs. Fc^+/Fc, whose height corresponds to slightly more than an overall one-electron reduction. The peak potentials are –1.652, –1.618, and –1.585 V for **1**, **2**, and **3**, respectively. The reduction is irreversible for **2** and **3** except at larger scan rates (1–5 V/s), where some chemical reversibility is observed and where the peak current function ($i_{p,c}/v^{1/2}$) decreases slightly, probably approaching the one-electron level as recently noted for μ-(1,2-ethanedithiolato)-diironhexacarbonyl (EDT).[50] Compound **1** shows some chemical reversibility even at 0.10 V/s (Figure 3). For all three compounds, additional cathodic processes are detected at potentials past –2 V.

On the return sweep of these voltammograms, an anodic peak is seen near –0.6 to –0.7 V, which is due to oxidation of a product formed at the first reduction peak. This peak is present, though smaller, in voltammograms where the scan is reversed just past the first cathodic peak.

Scans initiated in the positive direction (Figure 3) show an irreversible anodic peak whose height varies among the three compounds. The peak potentials are similar, +0.773, +0.802, and +0.791 for **1**, **2**, and **3**, respectively. Clearly, substitution of one of the sulfur atoms of **1** by selenium (**2**) or tellurium (**3**) has only a minor effect on the ease of oxidation of the complexes, as discussed with the photoelectron spectra and electronic structure of these molecules.

As noted above, however, there is a modest but significant increase in the ease of reduction along the series **1**–**3**, cathodic peak potentials moving to less negative values by about 67 mV. Almost exactly the same shift in potential was observed for a series of oxetane-containing dichalcogenolato $Fe_2(CO)_6$ complexes shown in Scheme 3, [(μ-$S_2C_5H_8O$){$Fe(CO)_3$}$_2$] (OxDT), [(μ-$Se_2C_5H_8O$){$Fe(CO)_3$}$_2$] (OxDSe), and [(μ-$Te_2C_5H_8O$){$Fe(CO)_3$}$_2$] (OxDTe), in which, however, both chalcogens were changed.[33]

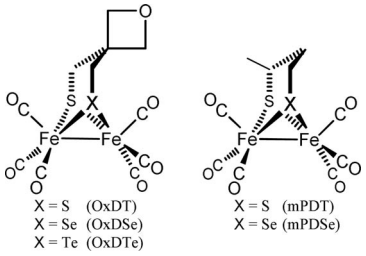

Scheme 3. [(μ-$X_2C_5H_8O$){$Fe(CO)_3$}$_2$] (X = S, Se, Te) and [{μ-$S(CH_2)_2CHCH_3S$}{$Fe(CO)_3$}$_2$] (X = S, Se).

Catalysis of the Reduction of a Weak Acid

Complexes similar to **1**–**3** are known to catalyze the reduction of acids.[51] A typical acid for the evaluation of catalytic efficiency is acetic acid (pK_a = 22.3 in acetonitrile[52]) and a typical observation for such a weak acid is that catalytic reduction does not take place at the reduction peak of the catalyst but at a rather more negative potential. Such is the case for all three of these complexes. As acid is added, the reduction peak of the catalyst is hardly affected, but there appears a new peak in the range –1.8 to –2.5 V, which grows in height more or less linearly with the concentration of acid. Results for 1 mM catalyst and 50 mM acetic acid are shown in Figure 4. For all complexes, the catalytic peak is rather drawn-out along the potential axis, and for compound **1** there is evidence for resolution of the catalytic peak into two or three separate processes (Figure 4).

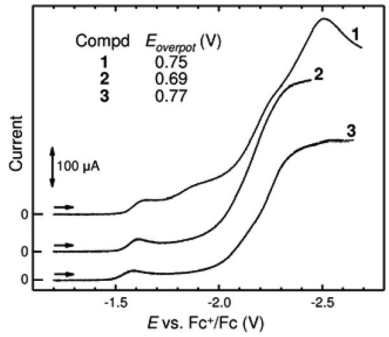

Figure 4. Voltammograms of ca. 1 mM **1**–**3** in the presence of 50 mM acetic acid. Other conditions as in Figure 3. Return scans are omitted for clarity. The overpotential, $E_{overpot}$, is the difference between the potential at which the catalytic current is half its maximum value and the standard potential for the reduction of acetic acid, –1.46 V.

It is difficult to evaluate the catalytic efficiency of these complexes, because considerable direct reduction of acetic acid occurs at the glassy carbon working electrode. The current obtained with 50 mM acetic acid alone (no catalyst) reaches 300 μA at –2.4 V.[53] However, the currents obtained for 50 mM acetic acid and 1 mM **1**–**3** greatly exceed this amount, so these complexes can be described as moderately good catalysts.

Another measure of efficiency is the overpotential, defined in this case as the difference between the potential at which the catalytic current is half its maximum value and the standard potential for the reduction of acetic acid in acetonitrile, –1.46 V. The overpotential, $E_{overpot}$, (shown in Figure 4) ranges from 0.69 to 0.77 V, not unlike other similar complexes.[51]

Photoelectron Spectroscopy

Photoelectron spectroscopy provides an experimental measure of the electron energies and molecular reorganization energies of the molecules and helps to quantify the trends in electronic structure in this series of molecules. The ionization energies also are well-defined energy quantities for validation of the electron energies from computational methods and provide a foundation for modeling the electrochemistry and chemical behavior (vide infra). The valence photoelectron spectra of these molecules are compared in Figure 5.

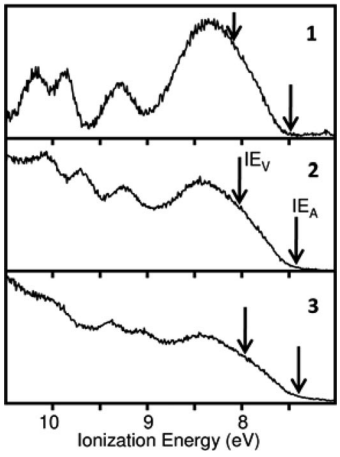

Figure 5. He I photoelectron spectra of **1**–**3**. The arrows near 7.5 eV are the DFT-calculated adiabatic ionization energies, IE_A, and the arrows near 8 eV are the DFT-calculated vertical ionization energies, IE_V. The energy difference between IE_V and IE_A for each molecule is the reorganization energy to the optimum geometry of the cation.

The general assignments of the ionizations are based on previously reported analogous compounds.[33,36,54] The energy region displayed in the spectra contains the valence ionizations from the Fe-based 3d orbitals and the chalcogen-based p orbitals. The first broad ionization profile of each molecule, from about 7.5 to 8.8 eV ionization energy, arises predominantly from combinations of the Fe d-based orbitals with a weak shoulder on the low-ionization-energy side corresponding to ionization from the HOMO of the molecule. The chalcogen-based valence p-orbital ionizations, S through Te, are expected to be observed in the higher-energy-ionization side of this region, on the basis of previously reported photoelectron spectra of chalcogen-containing [FeFe]-hydrogenase model compounds.[33,36,54] The second and third distinct ionization bands, above 9.0 eV, are assigned as having a mixture of chalcogen character and Fe d orbitals from previous studies.[33,36,54] These ionization energies decrease substantially with substitution from S through Se to Te, as expected from the decreasing

electronegativity of the atoms and the decreasing inherent stability of the atomic orbitals.

However, the leading ionization band changes very little with chalcogen substitution, except for the difference in the instrument's baseline scatter for the different data collections. A close examination of the band profile (Figure S2 in the Supporting Information) shows that the onsets of the ionization bands shift by only about 0.1 eV from molecule **1** (ca. 7.5 eV) to molecule **3** (ca. 7.4 eV). The onset of the ionization band typically approximates the adiabatic ionization energy for removal of an electron from the HOMO, in which the molecule has relaxed to the optimum geometry of the positive molecule ion. The spectra suggest that the expected lowering of the adiabatic ionization due to the increased electron richness at the metals from **1** through **2** to **3**, as evidenced by the decrease in carbonyl stretching frequencies, is counterbalanced somewhat by a decrease in the molecular reorganization energies. This suggestion is consistent with previous studies[33,36,54] and is examined further in the following section.

Computational Results

Electronic structure calculations can provide additional understanding of the electronic structure and chemical properties of a chemical system, provided the calculations are appropriately validated against experimental structures, spectroscopic observations, electrochemical measurements, and thermodynamic properties. The DFT computational methodology utilized in this study has previously been shown to give good quantitative agreement with the structures, carbonyl stretching frequencies, oxidation potentials, reduction potentials, bond energies, and p*K*a values of a variety of [FeFe]-hydrogenase model compounds.[33,36,54–56] It is important to re-examine the validity of a method for each new class of molecules.

For the particular case of the substitutions of S, Se, and Te atoms in the molecules of this study, the optimized geometries from the computations agree very well with the crystal structure determinations. Key structural parameters are compared in Table S1 in the Supporting Information. For molecule **1**, the largest deviations in bond lengths are about 0.02 Å, and angles are well within a degree, except for the averaged angles in the experimental structure of the propane linkage between the S atoms, which is 50% disordered between two conformations in the crystal, as noted earlier. Most important is the Fe–Fe distance, which agrees within 0.01 Å. Molecule **2** shows evidence of additional disorder through interchange of the S and Se atoms in the crystal, as discussed earlier. However, this disorder does not seriously affect the determination of the Fe–Fe distance, which the computations match within 0.001 Å. Similar disorder may be present for molecule **3**, and a relatively flat potential energy surface for bonding to Te has been noted earlier, but the calculated Fe–Fe distance still agrees with the experimental value within 0.02 Å. Both experimental results and computations show an increasing Fe–Fe distance from **1** through **2** to **3**.

Agreement between the experimental and optimized structures does not necessarily mean that the computations yield sufficiently reasonable electron distributions and energies. The carbonyl stretching frequencies are one measure that is sensitive to the electron richness at the metal center. The frequencies are obtained computationally from the multidimensional potential well about the equilibrium geometry of the molecule, and thus reflect the energy of small geometric distortions. Furthermore, the electronic coupling and interaction force constants between the carbonyl vibrations are reflected in both the splitting and the intensities of the IR absorptions. Simulation of carbonyl stretching frequencies has become an important contribution to the understanding of hydrogenase active sites and hydrogenase mimics.[57,58] Figure S1 in the Supporting Information shows the good agreement between the observed and simulated IR absorption frequencies and intensities, and most particularly the shift of the vibrations to lower frequency from **1** through **2** to **3** with increasing donor ability from S through Se to Te. The increased electron-donor ability of heavier chalcogens is also evidenced in the computations by the increasing positive charge on these atoms. The Voronoi deformation electron densities[59] in the vicinity of the chalcogens decreased by 0.06 e^- from S to Se and by 0.10 e^- from Se to Te.

The computations also agree with the observations in the photoelectron spectra. The HOMO is calculated to be predominantly the Fe–Fe σ bond, as shown in Figure 6 for molecule **2**. This orbital is followed closely by six orbitals composed predominantly of the $3d^6$ electrons of the two Fe centers with some mixing of chalcogen p character, all clustered within an energy range of less than 1 eV. The orbitals with primary chalcogen character are found after a gap of approximately 0.5 eV, similar to the pattern observed in the photoelectron ionizations. Figures of these orbitals for all molecules are provided in the Supporting Information. The calculated first vertical ionization energies (IE_V, obtained by the ΔSCF difference in energy from the neutral molecule to the positive ion without change in geometry) and adiabatic ionization energies (IE_A, obtained by the ΔSCF method with full geometry optimization of the positive ion to its global minimum) are indicated by the arrows in Figure 5. The vertical ionization energies (calculated at 8.08 eV for **1**, 8.02 eV for **2**, and 7.97 eV for **3**) are difficult to define experimentally, because of the large number of broad overlapping ionizations in this region, but

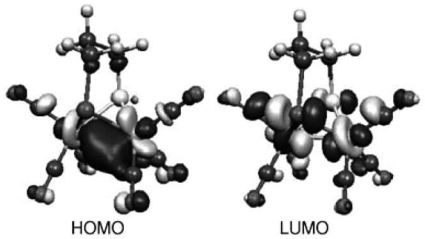

Figure 6. Highest-occupied and lowest-unoccupied molecular orbitals of **2**.

the agreement between the calculated adiabatic ionization energies (7.48 eV for **1**, 7.43 eV for **2**, and 7.40 eV for **3**) and the onset of ionization band intensity in each spectrum illustrates the success of the computational model for these molecules.

On the basis of the Fe–Fe bonding character in the HOMO of the neutral molecule, one might expect the primary geometry relaxation in the positive ion to be a lengthening of the Fe–Fe distance, and indeed this is found when geometry optimization of the positive ion begins with the structure of the neutral molecule. However, a wider search of the potential energy surface finds a structure with a semibridging carbonyl group to be the global minimum. The optimized structure of the cation in the gas phase, shown in Figure 7, may be viewed as a rotation by approximately 60° of one $Fe(CO)_3$ group, which creates a vacant axial coordination site at the iron center.[60–64] This structure has been observed before and has been termed the "rotated" structure.[54,65–70] The stabilization energy from the nonbridged "unrotated" structure to the rotated structure is 0.28 eV for **1**, 0.25 eV for **2**, and 0.21 eV for **3**. The decrease in stabilization energy to the semibridged structure through the series may be related to both the increasing Fe–Fe distance and the greater electron richness at the metal centers.

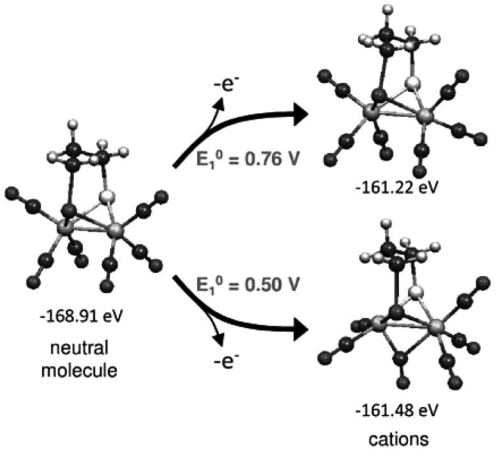

Figure 7. Calculated neutral and cation structures of molecule **2**. The cation structure without a bridging carbonyl group is at the top right, and the "rotated" cation structure with a semibridging carbonyl group is at the bottom right. The numbers in black are the gas-phase electronic energies, and the numbers in gray are the calculated solution oxidation potentials.

The total cation reorganization energy (ΔE_r) is the energy difference between the vertical ionization energy, IE_V, and the adiabatic ionization energy, IE_A. The ΔE_r energies are calculated to be 0.60 eV for **1**,[54] 0.58 eV for **2**, and 0.57 eV for **3**. The decrease in reorganization energies is visually apparent in Figure 5, where the energy separation between IE_V and IE_A decreases down the series. Also apparent in Figure 5 is the decrease in the vertical ionization energies, which follows the increase in electron richness at the metal centers from molecules **1** to **3**, but the decreasing reorganization energies reduces the shift (ca. 0.1 eV experimental, 0.08 eV calculated) of the adiabatic ionization energies through this series. The balance between these factors is important to the relative behavior of these molecules.

The largest contribution to the calculation of the electrochemical oxidation potentials is the adiabatic ionization energy, followed by differences in solvation energies and thermal contributions to the free energies of the neutral and ionized molecules. The calculated oxidation potentials of molecule **2** to the unrotated and rotated cation structures discussed above are shown in Figure 7 and compared with the cyclic voltammograms in Figure 3. An exact determination of the standard oxidation potential by cyclic voltammetry (CV) is not possible, because the process is not chemically reversible, and the rate of transformation to the rotated structure (with the lower oxidation potential) is not known, but the calculated oxidation potentials agree well with the region of oxidation processes in the voltammogram. Note also from Figure 7 that the 0.26 eV stabilization of the rotated structure relative to the unrotated structure of the cation is directly reflected in the difference of oxidation potentials to the two structures.

The calculated reduction potentials of molecule **2** are shown in Figure 8 and also compared with the cyclic voltammograms in Figure 3. The LUMO for accepting the electron consists mainly of the metal–metal antibonding interaction with some metal–chalcogen antibonding interaction of the chalcogen p orbitals, as shown in Figure 6. Similar to the removal of an electron from the HOMO, adding an electron into the LUMO also initiates geometric change. Various structures were explored for the anions of these molecules obtained by reduction, and the results suggest a complex thermodynamic and kinetic combination of reduction events. Reduction to the unrotated structure with an elongated metal–metal bond is favored initially, reduction to the rotated structure occurring at a more negative potential (more negative by 0.27 V for **1**, 0.21 V for **2**, and 0.18 V for **3**). The trend does not change if the conformation of the propane linker between the two chalcogens is changed from bending over the rotated iron, as shown in Figure 8, to bending over the unrotated iron. Reduction of the unrotated anion to the dianion at potentials more negative than –2 V leads directly to a structure with an extremely elongated metal–metal distance. However, the global minimum structure of the dianion has a bridging carbonyl ligand with one broken Fe–chalcogen bond, and reduction to this structure requires less negative potential than the first reduction of the neutral molecule to the anion. This is termed potential inversion and is similar to the process observed for the related molecule with a benzenedithiolato ligand.[55] Formation of the bridging carbonyl structure requires a substantial structural rearrangement of the nonbridging anion, such that kinetic factors become relevant on the CV time scale. Previously, **1** exhibited a greater-than-one-electron reduction under significantly slow CV scan rates.[71] Furthermore, the formation of the bridging dianion from a nonbridging anion through an energetically stable intermediate structure, becoming a two-electron reduction processes with decreased CV scan rates, was reported for EDT.[50] The reductions are not

chemically reversible, and the calculations indicate potential inversion with the second reduction, so it is difficult to compare directly the calculated potentials with the observed CV results. However, as Figure 3 shows, the calculated reduction potentials are in the region of reduction events, perhaps slightly too negative, and confirm that there is little shift in potential between the molecules. This occurs again, because of the decreasing reorganization energies with change in charge. Because of the complexity of these reduction processes, we do not attempt further modeling of the reductions in the presence of acids in this contribution.

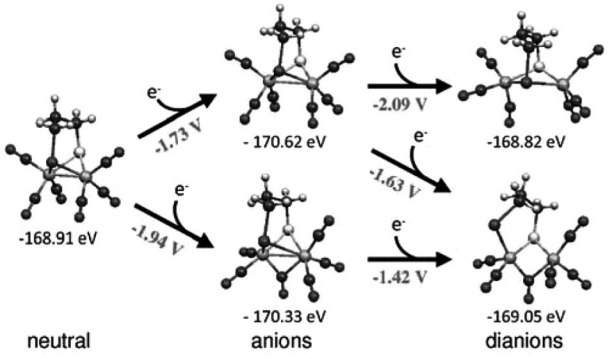

Figure 8. Calculated anion and dianion structures of molecule **2** with gas-phase electronic energies (black) and calculated solution reduction potentials (gray).

Conclusions

Synthesis and characterization of the mixed dichalcogenolato [FeFe]-hydrogenase model compounds related to the much-studied molecule $[Fe_2(\mu\text{-}SC_3H_6S)(CO)_6]$, where one sulfur atom is replaced by either a selenium atom or a tellurium atom, were successful. Combinations of experimental and computational analyses have provided useful insight into the electronic perturbations resulting from single chalcogen substitutions at the diiron core of the molecules. The crystal structures show the slight increase in the Fe–Fe distance with increasing size of the chalcogen atom. The increasing donor ability of chalcogens down the group and the corresponding greater electron richness at the iron centers in the molecules is evidenced spectroscopically by the lower carbonyl stretching frequencies and lower ionization energies for the molecules with heavier chalcogens. However, the influence of these electronic perturbations is muted for thermodynamic processes that involve a gain or loss of electrons from the molecules, such that the adiabatic ionization energies and initial oxidation and reduction potentials vary only slightly with chalcogen substitution. The reason is that the reorganization energy, ΔE_r, with electron transfer also decreases with substitution down the series, which counterbalances the influence of increasing electron richness at the metals. The longer Fe–Fe distances in the neutral molecules and the decreasing stabilization energies from the unrotated structure to the rotated structure with a semi-bridging carbonyl ligand in the ions are important factors in these trends. The computations agree well with these observations.

Reduction processes both with and without weak acid are studied to –2.7 V. Computations find that a number of structural transformations are possible for the anions and dianions that are formed in this range. A dianion structure with a bridging carbonyl and broken iron–chalcogen bond is found to be most stable in solution, suggesting an inversion of potential with the first reduction and the possibility for a greater-than-one-electron transfer in the first reduction peak, depending on the rate of transformation to the rotated structure with the broken iron–chalcogen bond. A slightly greater-than-one-electron process is observed in the first reduction peak for molecule **1** at the scan rate of this study, where the kinetic transformation may be favored over the heavier chalcogens by the shorter Fe–Fe distance and the greater reorganization energy. The thermodynamic and kinetic complexity of the reductions obviates a detailed structural and mechanistic modeling of the reduction of protons to H_2. Experimentally, the catalytic efficiency for the reduction of protons is found to be similar for the three molecules, with overall similar overpotentials and catalytic peak currents. This similarity is consistent with the balance between electronic structure and energy factors discussed above.

Experimental Section

General Comments: All reactions were performed by using standard Schlenk and vacuum-line techniques under an argon atmosphere. All solvents were purchased from Fisher Scientific and dried and distilled prior to use according to standard methods. $Fe_3(CO)_{12}$ (purchased from Aldrich) and other chemicals (purchased from Acros) were used without further purification. The ^1H, $^{13}C\{^1H\}$, $^{77}Se\{^1H\}$, and 2D NMR (^1H,^1H COSY, ^1H,^{13}C HSQC, ^1H,^{77}Se HMBC) spectra were recorded with a Bruker AVANCE 200 or 400 MHz spectrometer by using the solvent residual peak (^1H, $^{13}C\{^1H\}$ NMR) or a concentrated solution of SeO_2 in D_2O as reference. The ^{77}Se chemical shifts are reported relative to neat Me_2Se [$\delta(Me_2Se) = \delta(SeO_2) + 1302.6$ ppm].[72] The ^{125}Te chemical shift was measured vs. external PhTeTePh and converted to that of Me_2Te. Mass spectra were recorded with a FINNIGAN MAT SSQ 710 instrument. IR spectra were measured with a Perkin–Elmer System 2000 FTIR spectrometer and in Nujol with a Thermo Nicolet Avatar ESP 380 FTIR spectrometer utilizing the OMNIC version 6.1 software. Elemental analyses were performed with a LECO CHNS-932 apparatus. Silica gel 60 (0.015-0.040 mm) was used for column chromatography, TLC was done with Merck TLC aluminum sheets (Silica gel 60 F_{254}). Bis(bromomethyl) selenide,[73] bis(bromomethyl) sulfide,[53] 1,2-thiaselenolane (**4**),[74] and 1,2-thiatellurolane (**5**)[74] were prepared according to literature protocols. Yield calculations were based on the substoichiometric utilized chemicals or on $Fe_3(CO)_{12}$ for the diiron complexes.

$[Fe_2(\mu\text{-}SC_3H_6Se)(CO)_6]$ (2): Triirondodecacarbonyl (0.10 g, 0.20 mmol) and **4** (0.03 g, 0.20 mmol) were heated at reflux in THF (30 mL) for one hour. The solvent was removed from the resulting brown-red mixture under reduced pressure. The obtained solid was dissolved in a minimum amount of hexane and column chromatographed (SiO_2/hexane). From the major red fraction, **2** was ob-

tained as a red solid (0.06 g, 69%). $C_9H_6Fe_2O_6SSe$ (433.77): calcd. C 24.97, H 1.40, S 7.41; found: C 25.09, H 1.36, S 7.23. IR (KBr disk): $\tilde{\nu}_{C\equiv O}$ = 2070 (s), 2030 (vs), 1993 (s), (Nujol) 2071 (s), 2031 (vs), 2000 (s), 1988 (s), 1977 (m) cm^{-1}. ^1H NMR (400 MHz, $CDCl_3$): δ = 1.73 (m, 2 H, $SeCH_2CH_2$), 2.11 (m, SCH_2), 2.12 (m, $SeCH_2$) ppm. $^{13}C\{^1H\}$ NMR (100 MHz, $CDCl_3$): δ = 13.1 ($SeCH_2$), 24.7 (SCH_2), 30.3 ($SeCH_2CH_2$), 208.2 (CO) ppm. ^1H ^{77}Se HMBC NMR (76 MHz, $CDCl_3$): δ = 132.9 ppm. DEI-MS: *m*/*z* = 434 $[M]^+$, 406 $[M - CO]^+$, 350 $[M - 3CO]^+$, 294 $[M - 5CO]^+$, 266 $[M - 6CO]^+$.

$[Fe_2(\mu\text{-}STeC_3H_6Te)(CO)_6]$ (3): Triirondodecacarbonyl (0.10 g, 0.20 mmol) and **5** (0.04 g, 0.2 mmol) in THF (30 mL) were heated at reflux. After one hour, the green solution became red-brown, and it was then allowed to cool to room temperature. The THF solvent was removed, and the obtained solid was dissolved in a minimum amount of hexane and column chromatographed (SiO_2/hexane). The red fraction containing complex **3** (0.03 g, 31%) was collected, and the hexane was removed. $C_9H_6Fe_2O_6STe{\cdot}0.67$hexane (540.84): calcd. C 28.97, H 2.87, S 5.95; found: C 28.83, H 2.43, S 6.34. IR (KBr disk): $\tilde{\nu}_{C\equiv O}$ = 2063 (s), 2024 (vs), 1989 (vs), (Nujol) 2065 (s), 2026 (vs), 1996 (s), 1983 (s), 1971 (m) cm^{-1}. ^1H NMR (400 MHz, $CDCl_3$): δ = 1.46 (m, 2 H, $TeCH_2CH_2$), 2.01 (m, 2 H, SCH_2), 2.29 (m, 2 H, $TeCH_2$) ppm. $^{13}C\{^1H\}$ NMR (100 MHz, $CDCl_3$): δ = –9.4 ($TeCH_2$), 30.2 (SCH_2), 31.9 ($TeCH_2CH_2$), 209.1 (CO) ppm. ^{125}Te NMR (158 MHz, $CDCl_3$): δ = 177 ppm. DEI-MS: *m*/*z* = 482 $[M]^+$, 454 $[M - CO]^+$, 426 $[M - 2CO]^+$, 398 $[M - 3CO]^+$, 370 $[M - 4CO]^+$, 342 $[M - 5CO]^+$, 314 $[M - 6CO]^+$.

Crystal Structure Determination: The intensity data for the compounds were collected with a Nonius KappaCCD diffractometer, by using graphite-monochromated Mo-K_α radiation. Data were corrected for Lorentz and polarization effects, but not for absorption effects.[75,76] The structures were solved by direct methods (SHELXS)[77] and refined by full-matrix least-squares techniques against F_o^2 (SHELXL-97).[78] All hydrogen atoms were included at calculated positions with fixed thermal parameters. All non-hydrogen atoms were refined anisotropically.[77] The (S, Se) and (S, Te) positions in **2** and **3** are superimposed. Crystallographic data (excluding structure factors) has been deposited with the Cambridge Crystallographic Data Centre. CCDC-726555 (for **2**) and -726556 (for **3**) contain the supplementary data for this paper. These data can be obtained free of charge from The Cambridge Crystallographic Data Centre via www.ccdc.cam.ac.uk/data_request/cif.

Electrochemical Measurements: Instrumentation and the source and treatment of solvent and supporting electrolyte have been reported earlier.[79] All potentials are reported vs. the potential of the ferrocenium/ferrocene (Fc^+/Fc) couple measured in acetonitrile. Voltammetric experiments were conducted at 298 K, by using approximately 1.0 mM of each compound in acetonitrile containing 0.10 M Bu_4NPF_6 on a Glassy Carbon working Electrode (GCE), under an Ar atmosphere. The area of the GCE was determined to be 0.0707 cm^2 from cyclic voltammetric studies of the oxidation of ferrocene in acetonitrile by using 2.5×10^{-5} cm^2/s as its diffusion coefficient.[79]

Photoelectron Spectroscopy: Photoelectron spectra were recorded by using an instrument that features a 36 cm radius hemispherical analyzer (McPherson),[80] with a custom-designed photon source, sample cells, detection, and control electronics. Calibration and data analysis were described previously.[81] In the figures of the photoelectron spectra, the spectra obtained with the He I source photons are represented by solid black lines. Both samples sublimed cleanly, with no visible changes in the spectra during data collection after initial observation of ionizations from the diiron complexes. The sublimation temperatures (at 10^{-5} Torr) were 37–39 and 40–44 °C for complexes **2** and **3**, respectively.

Density Functional Theory (DFT) Calculations: Computational methods have been developed previously for this class of diiron hexacarbonyl systems with S and Se heteroatoms in the bridging positions and validated by their ability to account for geometric structures, adiabatic ionization energies, carbonyl stretching frequencies, pK_a values, oxidation and reduction potentials, and other electrochemical parameters, as well as metal–metal and pertinent metal–ligand bond energies.[36,54–56] DFT calculations were carried out with the Amsterdam density functional (ADF2009.01b) package.[82,83] Geometry optimizations and frequency calculations (with no imaginary frequencies in the final geometries) were carried out by using the VWN functional with the Stoll correction implemented.[84] All electronic energies were obtained with the OPBE functional.[85] Comparison of the OPBE functional to other common functionals found it to be the best for the prediction of nuclear magnetic constants[86] and the only functional to correctly predict the spin states of seven different iron complexes.[85] All calculations utilized a triple-ζ Slater type orbital (STO) basis set with one polarization function (TZP) for H, C, O, Fe, S, Se, and Te. Relativistic effects by the zero-order regular approximation (ZORA)[87,88] were also applied during all calculations. The frozen-core approximation was used for the inner core of all heavy atoms. The theoretical stretching frequencies and IR absorption intensities for all species were calculated analytically with the same computing method as for the geometry optimizations and scaled by a factor of 1.002. For the simulated IR spectra in Figure S1, the linewidths are adjusted by a constant factor to approximate the linewidths in the experimental spectra. Figures of the optimized geometries and molecular orbital plots were created with the program Molekel.[89]

Supporting Information (see footnote on the first page of this article): Comparison of the experimental IR spectra (in Nujol) in the carbonyl stretching region (solid lines) with calculated IR spectra (dashed lines) for each of **1**–**3** (Figure S1); He I photoelectron spectra of the first ionization bands of molecules **1** (blue), **2** (green), and **3** (red) (Figure S2); calculated neutral and cation structures of **1** (Figure S3); highest occupied and lowest unoccupied orbitals, calculated structures (Figures S4–S13); calculated geometries (Tables S1–S11).

Acknowledgments

Financial support for this work was provided for M. K. H. by the Deutscher Akademischer Austausch Dienst (DAAD) and by the National Science Foundation through the Collaborative Research in Chemistry program, Grant No. CHE 0527003, (D. H. E., R. S. G. and D. L. L.).

[1] M. Frey, *ChemBioChem* **2002**, *3*, 153–160.
[2] P. M. Vignais, B. Billoud, *Chem. Rev.* **2007**, *107*, 4206–4272.
[3] A. L. De Lacey, V. M. Fernandez, M. Rousset, R. Cammack, *Chem. Rev.* **2007**, *107*, 4304–4330.
[4] Y. Nicolet, C. Cavazza, J. C. Fontecilla-Camps, *J. Inorg. Biochem.* **2002**, *91*, 1-8.
[5] S. Shima, O. Pilak, S. Vogt, M. Schick, M. S. Stagni, W. Meyer-Klaucke, E. Warkentin, R. K. Thauer, U. Ermler, *Science* **2008**, *321*, 572–575.
[6] R. Cammack, M. Frey, R. Robson, *Hydrogen as a Fuel: Learning from Nature*, Taylor & Francis, London, **2001**.
[7] R. Coontz, B. Hanson, *Science* **2004**, *305*, 957–975.
[8] A. Melis, L. Zhang, M. Forestier, M. L. Ghirardi, M. Seibert, *Plant Physiol.* **2000**, *122*, 127–136.

[9] P. C. Hallenbeck, J. R. Benemann, *Int. J. Hydrogen Energy* **2002**, *27*, 1185–1193.
[10] P. Tamagnini, R. Axelsson, P. Lindberg, F. Oxelfelt, R. Wunschiers, P. Lindblad, *Microbiol. Mol. Biol. Rev.* **2002**, *66*, 1–20.
[11] T. Happe, A. Hemschemeier, M. Winkler, A. Kaminski, *Trends Plant Sci.* **2002**, *7*, 246–250.
[12] a) X. Zhao, I. P. Georgakaki, M. L. Miller, J. C. Yarbrough, M. Y. Darensbourg, *J. Am. Chem. Soc.* **2001**, *123*, 9710–9711; b) M. Y. Darensbourg, E. J. Lyon, J. J. Smee, *Coord. Chem. Rev.* **2000**, *206–207*, 533–561; c) D. J. Evans, C. J. Pickett, *Chem. Soc. Rev.* **2003**, *32*, 268–275; d) W. Lubitz, B. Tumas, *Chem. Rev.* **2007**, *107*, 3900–3903; e) L.-C. Song, *Acc. Chem. Res.* **2005**, *38*, 21–28; f) X. Liu, S. K. Ibrahim, C. Tard, C. J. Pickett, *Coord. Chem. Rev.* **2005**, *249*, 1641–1652; g) J.-F. Capon, F. Gloaguen, P. Schollhammer, J. Talarmin, *Coord. Chem. Rev.* **2005**, *249*, 1664–1676; h) J.-C. Fontecilla-Camps, A. Volbeda, C. Cavazza, Y. Nicolet, *Chem. Rev.* **2007**, *107*, 4273–4303; i) D. M. Heinekey, *J. Organomet. Chem.* **2009**, *694*, 2671–2680.
[13] X. Zhao, C. Chiang, M. L. Miller, M. V. Rampersad, M. Y. Darensbourg, *J. Am. Chem. Soc.* **2003**, *125*, 518–524.
[14] F. Gloaguen, J. D. Lawrence, M. Schmidt, S. R. Wilson, T. B. Rauchfuss, *J. Am. Chem. Soc.* **2001**, *123*, 12518–12527.
[15] J. D. Lawrence, H. Li, T. B. Rauchfuss, M. Benard, M. Rohmer, *Angew. Chem. Int. Ed.* **2001**, *40*, 1768–1771.
[16] H. Li, T. B. Rauchfuss, *J. Am. Chem. Soc.* **2002**, *124*, 726–727.
[17] S. Ott, M. Kritikos, B. Åkermark, L. Sun, *Angew. Chem. Int. Ed.* **2003**, *42*, 3285–3288.
[18] M. Razavet, S. C. Davies, D. L. Hughes, J. E. Barclay, D. J. Evans, S. A. Fairhurst, X. Liu, C. J. Pickett, *Dalton Trans.* **2003**, 586–595.
[19] C. Tard, X. Liu, S. K. Ibrahim, M. Bruschi, L. De Gioia, S. C. Davies, X. Yang, L.-S. Wang, G. Sawers, C. J. Pickett, *Nature* **2005**, *433*, 610–613.
[20] L.-C. Song, Z.-Y. Yang, H.-Z. Bian, Q.-M. Hu, *Organometallics* **2004**, *23*, 3082–3084.
[21] S. Ezzaher, J.-F. Capon, F. Gloaguen, F. Y. Pétillon, P. Schollhammer, J. Talarmin, N. Kervarec, *Inorg. Chem.* **2009**, *48*, 2-4.
[22] D. Seyferth, G. B. Womack, M. K. Gallagher, *Organometallics* **1987**, *6*, 283–294.
[23] U.-P. Apfel, Y. Halpin, H. Görls, J. G. Vos, B. Schweizer, G. Linti, W. Weigand, *Chem. Biodivers.* **2007**, *4*, 2138–2148.
[24] J. Windhager, M. Rudolph, S. Bräutigam, H. Görls, W. Weigand, *Eur. J. Inorg. Chem.* **2007**, 2748–2760.
[25] J. Windhager, H. Goerls, H. Petzold, G. Mloston, G. Linti, W. Weigand, *Eur. J. Inorg. Chem.* **2007**, 4462–4471.
[26] L.-C. Song, Z.-Y. Yang, H.-Z. Bian, Y. Liu, H.-T. Wang, X.-F. Liu, Q.-M. Hu, *Organometallics* **2005**, *24*, 6126–6135.
[27] S. Ezzaher, J.-F. Capon, F. Gloaguen, F. Y. Pétillon, P. Schollhammer, J. Talarmin, *Inorg. Chem.* **2007**, *46*, 3426–3428.
[28] P. Orain, J.-F. Capon, N. Kervarec, F. Gloaguen, F. Pétillon, R. Pichon, P. Schollhammer, J. Talarmin, *Dalton Trans.* **2007**, 3754–3756.
[29] T.-T. Zhang, M. Wang, N. Wang, P. Li, Z.-Y. Liu, L.-C. Sun, *Polyhedron* **2009**, *28*, 1138–1144.
[30] D. Morvan, J.-F. Capon, F. Gloaguen, F. Y. Pétillon, P. Schollhammer, J. Talarmin, J. Yaouanc, F. Michaud, N. Kervarec, *J. Organomet. Chem.* **2009**, *694*, 2801–2807.
[31] L.-C. Song, X. Luo, Y.-Z. Wang, B. Gai, Q.-M. Hu, *J. Organomet. Chem.* **2009**, *694*, 103–112.
[32] E. J. Lyon, I. P. Georgakaki, J. H. Rabenspies, M. Y. Darensbourg, *Angew. Chem. Int. Ed.* **1999**, *38*, 3178–3180.
[33] M. K. Harb, U.-P. Apfel, J. Kübel, H. Görls, G. A. N. Felton, T. Sakamoto, D. H. Evans, R. S. Glass, D. L. Lichtenberger, M. El-khateeb, W. Weigand, *Organometallics* **2009**, *28*, 6666–6675.
[34] S. Gao, J. Fan, S. Sun, X. Peng, X. Zhao, J. Hou, *Dalton Trans.* **2008**, 2128–2135.
[35] U.-P. Apfel, Y. Halpin, M. Gottschaldt, H. Görls, J. G. Vos, W. Weigand, *Eur. J. Inorg. Chem.* **2008**, 5112–5118.
[36] M. K. Harb, T. Niksch, J. Windhager, H. Görls, R. Holze, L. T. Lockett, N. Okumura, D. H. Evans, R. S. Glass, D. L. Lichtenberger, M. El-khateeb, W. Weigand, *Organometallics* **2009**, *28*, 1039–1048.
[37] L.-C. Song, B. Gai, H.-T. Wang, Q.-M. Hu, *J. Inorg. Biochem.* **2009**, *103*, 805–812.
[38] M. K. Harb, J. Windhager, A. Daraosheh, H. Görls, L. T. Lockett, N. Okumura, D. H. Evans, R. S. Glass, D. L. Lichtenberger, M. El-khateeb, W. Weigand, *Eur. J. Inorg. Chem.* **2009**, 3414–3420.
[39] J. C. Guillemin, G. Bajor, E. Riague, B. Khater, T. Veszpremi, *Organometallics* **2007**, *26*, 2507–2518.
[40] A. F. Cozzolino, N. E. Gruhn, D. L. Lichtenberger, I. Vargas-Baca, *Inorg. Chem.* **2008**, *47*, 6220–6226.
[41] M. A. Cranswick, N. E. Gruhn, O. Oorhles-Steele, K. R. Ruddick, N. Burzlaff, W. A. Schenk, D. L. Lichtenberger, *Inorg. Chim. Acta* **2008**, *361*, 1122–1133.
[42] L.-C. Song, B. Gai, H.-T. Wang, Q.-M. Hu, *J. Inorg. Biochem.* **2009**, *103*, 805–812.
[43] J. Windhager, R. A. Seidel, U.-P. Apfel, H. Görls, G. Linti, W. Weigand, *Chem. Biodivers.* **2008**, *5*, 2023–2041.
[44] M. Shieh, M. H. Shieh, *Organometallics* **1994**, *13*, 920–924.
[45] G. A. Kalabin, V. M. Bzhezovskii, D. F. Kushnarev, A. G. Proidakov, *Zh. Org. Khim.* **1981**, *17*, 1143.
[46] B. Cordero, V. Gomez, A. E. Platero-Prats, M. Reves, J. Echeverria, E. Cremades, F. Barragan, S. Alvarez, *Dalton Trans.* **2008**, 2832–2838.
[47] J. D. Lawrence, T. B. Rauchfuss, S. R. Wilson, *Inorg. Chem.* **2002**, *41*, 6193–6195.
[48] L.-C. Song, B.-S. Yin, Y.-L. Li, L.-Q. Zhao, J.-H. Ge, Z.-Y. Yang, Q.-M. Hu, *Organometallics* **2007**, *26*, 4921–4929.
[49] L.-C. Song, Z.-Y. Yang, Y.-J. Hua, H.-T. Wang, Y. Liu, Q.-M. Hu, *Organometallics* **2007**, *26*, 2106–2110.
[50] G. A. N. Felton, B. J. Petro, R. S. Glass, D. L. Lichtenberger, D. H. Evans, *J. Am. Chem. Soc.* **2009**, *131*, 11290–11291.
[51] G. A. N. Felton, C. A. Mebi, B. J. Petro, A. K. Vannucci, D. H. Evans, R. S. Glass, D. L. Lichtenberger, *J. Organomet. Chem.* **2009**, *694*, 2681–2699.
[52] K. Izutsu in *Acid-Base Dissociation Constants in Dipolar Aprotic Solvents*, Blackwell Scientific Publishers, Oxford, UK, **1990**.
[53] E. Weissflog, M. Schmidt, *Z. Anorg. Allg. Chem.* **1977**, *437*, 146–148.
[54] B. J. Petro, A. K. Vannucci, L. T. Lockett, C. Mebi, R. Kottani, N. E. Gruhn, G. S. Nichol, P. A. J. Goodyer, D. H. Evans, R. S. Glass, D. L. Lichtenberger, *J. Mol. Struct.* **2008**, *890*, 281–288.
[55] G. A. N. Felton, A. K. Vannucci, J. Chen, L. T. Lockett, N. Okumura, B. J. Petro, U. I. Zakai, D. H. Evans, R. S. Glass, D. L. Lichtenberger, *J. Am. Chem. Soc.* **2007**, *129*, 12521–12530.
[56] G. A. N. Felton, A. K. Vannucci, N. Okumura, L. T. Lockett, D. H. Evans, R. S. Glass, D. L. Lichtenberger, *Organometallics* **2008**, *27*, 4671–4679.
[57] J. W. Tye, M. Y. Darensbourg, M. B. Hall, *J. Comput. Chem.* **2006**, *27*, 1454–1462.
[58] J. W. Tye, M. Y. Darensbourg, M. B. Hall, *Inorg. Chem.* **2008**, *47*, 2380–2388.
[59] C. F. Guerra, J. W. Handgraaf, E. J. Baerends, F. M. Bickelhaupt, *J. Comput. Chem.* **2004**, *25*, 189–210.
[60] J. W. Peters, *Curr. Opin. Struct. Biol.* **1999**, *9*, 670–676.
[61] Y. Nicolet, C. Piras, P. Legrand, C. Hatchikian, J. C. Fontecilla-Camps, *Struct. Fold. Des.* **1999**, *7*, 13–23.
[62] M. W. Adams, *Biochim. Biophys. Acta* **1990**, *1020*, 115–145.
[63] M. W. W. Adams, L. E. Mortenson, *Biochim. Biophys. Acta Bioenerg.* **1984**, *766*, 51–61.
[64] J. Chen, D. K. Blanchard, *Biochem. Biophys. Res. Commun.* **1978**, *84*, 1144–1150.
[65] J. I. van der Vlugt, T. B. Rauchfuss, C. M. Whaley, S. R. Wilson, *J. Am. Chem. Soc.* **2005**, *127*, 16012–16013.
[66] A. K. Justice, G. Zampella, L. De Gioia, T. B. Rauchfuss, J. I. van der Vlugt, S. R. Wilson, *Inorg. Chem.* **2007**, *46*, 1655–1664.

[67] A. K. Justice, G. Zampella, L. De Gioia, T. B. Rauchfuss, *Chem. Commun.* **2007**, 2019–2021.
[68] A. K. Justice, T. B. Rauchfuss, S. R. Wilson, *Angew. Chem. Int. Ed.* **2007**, *46*, 6152–6154.
[69] T. Liu, M. Y. Darensbourg, *J. Am. Chem. Soc.* **2007**, *129*, 7008–7009.
[70] C. M. Thomas, M. Y. Darensbourg, M. B. Hall, *J. Inorg. Biochem.* **2007**, *101*, 1752–1757.
[71] S. J. Borg, T. Behrsing, S. P. Best, M. Razavet, X. Liu, C. J. Pickett, *J. Am. Chem. Soc.* **2004**, *126*, 16988–16999.
[72] R. C. Burns, M. J. Collins, R. J. Gillespie, G. J. Schrobilgen, *Inorg. Chem.* **1986**, *25*, 4465–4469.
[73] E. Weissflog, *Phosphorus Sulfur Silicon Relat. Elem.* **1980**, *8*, 87–88.
[74] E. Block, E. V. Dikarev, R. S. Glass, J. Jin, B. Li, X. Li, S. Zhang, *J. Am. Chem. Soc.* **2006**, *128*, 14949–14961.
[75] B. V. Nonius, *COLLECT, Data Collection Software*, **1998**.
[76] Z. Otwinowski, W. Minor, "Processing of X-ray Diffraction Data Collected in Oscillation Mode" in *Methods in Enzymology, Vol. 276* (Ed.: C. W. Carter Jr.,), Elsevier, New York, **1997**, pp. 307–326.
[77] G. M. Sheldrick, *Acta Crystallogr., Sect. A* **1990**, *46*, 467–473.
[78] G. M. Sheldrick, *SHELXL-97 (Release 97-2)*, University of Göttingen, Germany, **1997**.
[79] N. A. Macías-Ruvalcaba, D. H. Evans, *J. Phys. Chem. B* **2005**, *109*, 14642–14647.
[80] K. Siegbahn, C. Nordling, A. Fahlman, R. Nordberg, K. Hamrin, J. Hedman, G. Johansson, T. Bergmark, S. E. Karlsson, I. Lindgren, B. Lindberg, *Nova Acta Regiae Societatis Scientiarum Upsaliensis* **1967**, *20*, 282.
[81] M. A. Cranswick, A. Dawson, J. J. A. Cooney, N. E. Gruhn, D. L. Lichtenberger, J. H. Enemark, *Inorg. Chem.* **2007**, *46*, 10639–10646.
[82] G. Te Velde, F. M. Bickelhaupt, E. J. Baerends, C. Fonseca Guerra, S. J. A. Van Gisbergen, J. G. Snijders, T. Ziegler, *J. Comput. Chem.* **2001**, *22*, 931–967.
[83] ADF2009.01b, **2009**.
[84] H. Stoll, C. M. E. Pavlidou, H. Preuss, *Theor. Chim. Acta* **1978**, *49*, 143–149.
[85] M. Swart, A. W. Ehlers, K. Lammertsma, *Mol. Phys.* **2004**, *102*, 2467.
[86] Y. Zhang, H. Lin, D. G. Truhlar, *J. Chem. Theory Comput.* **2007**, *3*, 1378–1398.
[87] E. van Lenthe, A. Ehlers, E. Baerends, *J. Chem. Phys.* **1999**, *110*, 8943–8953.
[88] E. van Lenthe, E. J. Baerends, J. G. Snijders, *J. Chem. Phys.* **1993**, *99*, 4597–4610.
[89] S. Portmann, H. P. Luthi, *Chimia* **2000**, *54*, 766–769.

Received: March 11, 2010
Published Online: July 15, 2010

DOI: 10.1002/ejic.201000384

"Tail–Tail Dimerization" of Ferrocene Amino Acid Derivatives

Daniel Siebler,[a] Christoph Förster,[a] and Katja Heinze*[a]

Keywords: Anhydrides / Conformational analysis / Electrochemistry / Metallocenes / Mixed-valent compounds

Acid anhydrides of N-protected 1′-aminoferrocene-1-carboxylic acid (Fca) have been prepared and spectroscopically characterized (protection group Boc, Fmoc, Ac; **4a**–**4c**). The structure of the Boc-derivative **4a** has been determined by single-crystal X-ray crystallography. An intramolecular N–H···O hydrogen bond involving the carbamate units results in a ring structure containing the two ferrocene units, the anhydride moiety, and the hydrogen bond. In the crystal, the individual molecules are connected by intermolecular N–H···O hydrogen bonds of the carbamate unit. Experimental and theoretical studies suggest that the ring motif is also a dominant species in solution. Electronic communication across the anhydride moiety is found to be very weak as judged from electrochemical, spectroscopic, and theoretical experiments.

Introduction

Oligoferrocenes have attracted enormous interest in the past years because of their applicability in molecular electronics and multi-redox catalysis.[1–4] Linear processable poly(ferrocenylenes) were pioneered by Manners, who obtained these compounds by the ring-opening polymerization of ER_2-bridged [1]ferrocenophanes (E = C, Si, Ge, Sn), and Wagner, who used BR_n linkers.[5–9]

Electronic communication between 1,1′-disubstituted ferrocene derivatives as part of larger systems could form the basis for well-defined molecular wires, which promotes continued research in this direction. With asymmetrical 1,1′-disubstituted ferrocenes, e.g. 1′-aminoferrocene-1-carboxylic acid (Fca),[10] several linkages are conceivable, which should lead to different communication channels. In "dimers" of Fca, a symmetrical ureylene bridge MeOOC–Fn–NH–CO–NH–Fn–COOMe ("head–head dimer"),[10b,11] an asymmetrical amide bridge ("head–tail dimer"),[10a,12,13] and a symmetrical anhydride bridge ("tail–tail" dimer) can be formed (Fn = 1,1′-disubstituted ferrocene) (Scheme 1). The different number, type, and hybridization of the bridging atoms (2–3; C, N, O atoms; formal sp^2, sp^3) and the preferred relative orientations of the ferrocene units are believed to modulate the communication pathways. Urea and amide bridges are reported to promote communication between the ferrocene subunits.[11–13] In Kraatz's amide-bridged [Fca-Ala] oligomers with intervening α-amino acids between the ferrocene units, electronic communication is not expected because of the blocking alanine moieties.[14] Most other ferrocene amides reported so far are conjugates with insulating α-amino acids.[15] For potential application in molecular electronics, oligomers of ferrocene should display sufficient electronic interaction. Thus, it is of significant interest whether oligomers of Fca should be assembled through amide bonds or through alternating ureylene/anhydride units for this purpose.

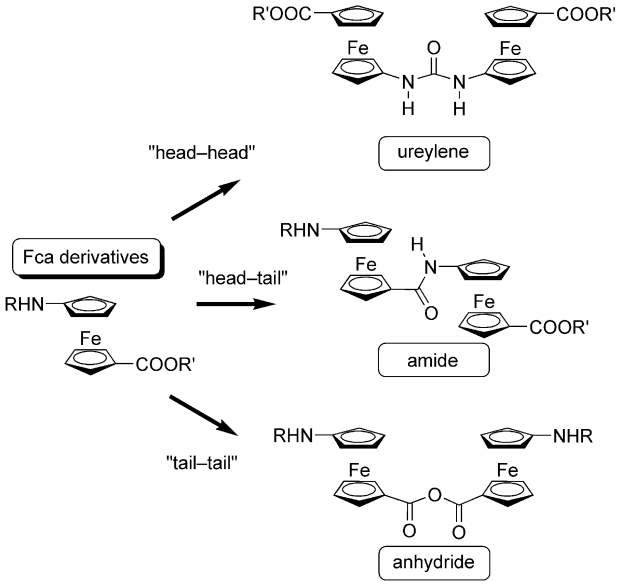

Scheme 1. Possible "dimers" of ferrocene amino acid fca.

In 2008, Stepnicka reported the formation of the anhydride of 2-diphenylphosphanyl-ferrocene-1-carboxylic acid by activation of the acid with *N*,*N*′-dicyclohexylcarbodiimide/4-dimethylaminopyridine (DCC/DMAP).[16] Several older reports are concerned with the formation of the parent Fc–CO–O–CO–Fc anhydride.[17] However, in contrast

[a] Institute of Inorganic Chemistry and Analytical Chemistry, Johannes Gutenberg University of Mainz, Duesbergweg 10–14, 55128 Mainz, Germany
Fax: +49-6131-39-27277
E-mail: katja.heinze@uni-mainz.de

Supporting information for this article is available on the WWW under http://dx.doi.org/10.1002/ejic.201000384.

to the ureylene-bridged "head–head" dimer of Fca[11] and "head–tail" amides of Fca,[10a,12,13] structural, conformational, and electrochemical data of bis(Fca anhydrides) are lacking in the literature.

Anhydrides are often encountered in peptide synthesis during activation of carboxylic acids by DCC, EDC [1-ethyl-3-(3-dimethylaminopropyl)carbodiimide] or acid chlorides.[16,20c] We have recently reported the activation of Fca as an acid fluoride by cyanuric fluoride for amide coupling,[13] similar to the formation of Fc-COF from Fc-COOH.[18] For certain applications, the acid chloride of Fca is required (e.g. for solid-phase peptide synthesis and for construction of longer oligomers).[12] In these cases, we prefer the in situ generation of the acid chloride of N-protected Fca derivatives by 1-chloro-*N*,*N*,2-trimethyl-1-propen-1-amine (Ghosez's reagent[19]) under quite neutral conditions (compatible with the amine protecting groups employed). During these activation and coupling procedures we also encountered the formation of aminoferrocene carboxylic acid anhydrides as side products. The results of our structural, conformational, electrochemical, and theoretical studies on such "tail–tail" Fca dimers are reported here (Scheme 1).

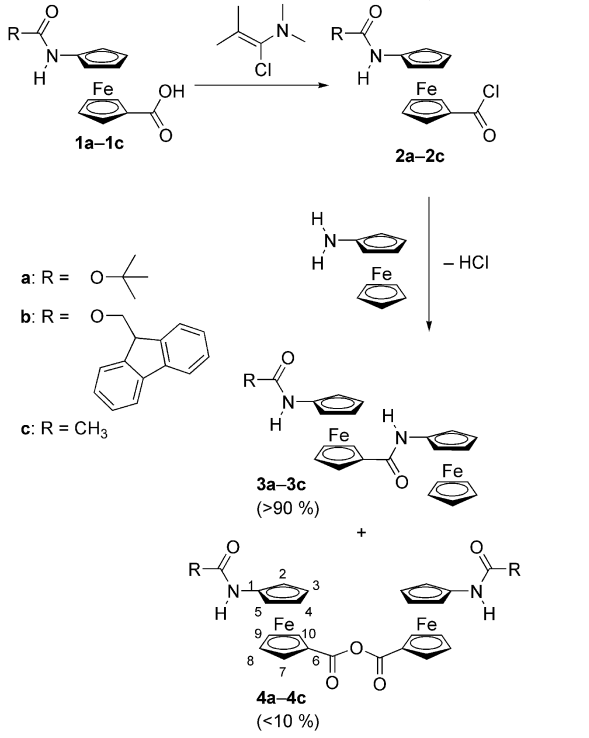

Scheme 2. Synthesis of **4a**–**4c** and atom numbering for NMR assignments.

Results and Discussion

For acid-labile Boc- and base-sensitive Fmoc protecting groups, neutral conditions are essential for the activation of *N*-Boc- and *N*-Fmoc-protected Fca derivatives. This can be accomplished by using 1-chloro-*N*,*N*,2-trimethyl-1-propen-1-amine (Ghosez's reagent[19]) in dichloromethane. Thus, *N*-Boc-, *N*-Fmoc-, or *N*-acetyl-protected Fca **1a**–**1c**[10b,10c] were treated with a slight excess Ghosez's reagent to generate the respective acid chlorides **2a**–**2c** in situ (Scheme 2). In order to prove the in situ formation of the acid chloride, the reaction of **1c** with Ghosez's reagent was conducted in an NMR tube. Quantitative formation of the acid chloride **2c** (without formation of anhydride **4c**) is shown by the $^{13}C\{^1H\}$ NMR spectrum of the reaction mixture. Especially the C^6-COCl resonance of **2c** at δ = 75.7 ppm is significantly different from the C^6-CO-O resonance of **4c** found at δ = 69.9 ppm (all other ^{13}C resonances appear at very similar chemical shifts, e.g. *C*OCl is observed at δ = 169.0 ppm). Amide-bridged ferrocenes **3a**–**3c** (from coupling with amino ferrocene) and anhydrides **4a**–**4c** were formed in the presence of HCl scavengers. In this respect, 2,4,6-collidine proved to be beneficial for anhydride formation (see Experimental Section). Anhydrides themselves are often only poor acylating agents so that these are unwanted side products in the synthesis of amides.[20] Amides **3a**–**3c** and analogous oligoamides were reported previously.[13] In these coupling reactions, the anhydrides **4a**–**4c** are usually obtained in less than 10% isolated yield after column chromatography. Higher yields of anhydrides **4a**–**4c** are achieved in the presence of 2,4,6-collidine and the absence of amines (see Experimental Section).

Mass spectrometric analyses confirm the dinuclear nature of **4a**–**4c** as molecular ion peaks are observed at the expected *m*/*z* ratios. UV/Vis spectroscopy of **4a**–**4c** in CH_2Cl_2 reveals the typical ferrocene absorption band at about λ_{max} = 460 nm, with extinction coefficients expected for dinuclear species of about ε = 1000 $M^{-1}cm^{-1}$ (Experimental Section). ^1H and ^{13}C NMR spectroscopic data prove the 1,1′-substitution at the ferrocene units and the presence of the respective protecting groups (Experimental Section). A single signal set is observed, which suggests rapidly interconverting species on the NMR time scale. Significant differences in the chemical shifts of the proton and carbon resonances are observed for nuclei in the vicinity of the protecting groups, e.g. $\delta(CO_{carbamate/amide})$ = 153.3, 153.9, 169.4 ppm; $\delta(C^1)$ = 98.8, 98.2, 97.1 ppm; δ(N*H*) = 6.36, 6.88, 7.60 ppm for **4a**–**4c**, respectively. The anhydride *C*O resonance is found at $\delta \approx$ 168 ppm throughout the series. Dilution of a $CDCl_3$ solution of **4a** slightly shifts the NH proton resonance of **4a** from δ = 6.37 ppm (50 mM) to δ = 5.99 ppm (6 mM), which suggests an intermolecular interaction or a mixed intra/intermolecular hydrogen-bonding situation with rapidly interconverting species. In the latter case, the chemical shift variation would be the result of averaging an intramolecular, concentration-independent hydrogen bond with an intermolecular, concentration-dependent hydrogen bond, i.e. in a certain species one NH group is temporarily engaged in an intramolecular hydrogen bond, while the second NH unit is engaged in an intermolecular hydrogen bond. The rather small chemical shift variation, $\Delta\delta$ = 0.38 ppm, points to such an intermediate situation (see Supporting Information). For comparison

Ac–Ala–Fca–Ala–OMe features a shift variation of $\Delta\delta$ = 0.74 ppm for the purely intermolecular interaction of a single NH group under comparable conditions.[15c]

The solid-state IR spectra of **4a**–**4c** display the characteristic symmetric and antisymmetric CO stretching vibrations of an anhydride unit at about 1765 and 1700 cm^{-1}, respectively, practically independent of the protecting group. The CO stretching vibration of the latter is found at 1709/1692, 1732, and 1668 cm^{-1}, characteristic for carbamates and amides, respectively. For **4a** and **4c**, these values suggest hydrogen bonds involving this CO group in the solid state. The NH stretching vibration is found well below 3400 cm^{-1} for **4a** and **4c**, which indicates that all the NH groups are hydrogen bonded in the solid state. This can be achieved by the intermolecular hydrogen bonds NH···O$C_{carbamate/amide/anhydride}$ or by a combination of inter- and intramolecular hydrogen bonds NH···O$C_{carbamate/amide/anhydride}$ (vide infra). In dilute CH_2Cl_2 solution and also for **4b** in the solid state, NH vibrations are observed both above and below 3400 cm^{-1}, which indicates the simultaneous presence of hydrogen-bonded and free NH groups.

Crystals of **4a** suitable for X-ray crystal structure analysis were grown from diethyl ether/petroleum ether (b.p. 40/60 °C) at –28 °C. Compound **4a** crystallizes in the monoclinic space group $P2_1/n$ as orange blocks. The two crystallographically different NH hydrogen atoms, H1 and H2, were located in the Fourier difference map and refined freely. The individual dinuclear molecules are connected by intermolecular hydrogen bonds N2–H2···O5_A (symmetry operation 1/2 – x, 1/2 + y, 1/2 – z) with N···O distances of 2.884(3) Å and an unconstrained NH···O angle of 162(2)°, to give helices along the crystallographic b axis (Figure 1). The intramolecular hydrogen bond N1–H1···O7 [N···O distance 2.903(3) Å; NH···O angle of 170(2)°] leads to a large ring containing the two ferrocene units (Fe1, Fe2), the anhydride moiety, and the N1–H1···O7 hydrogen bond (Figure 1). This ring motif has several consequences: (i) the ring twists the anhydride group by a O2–C101–C102–O3 torsion angle of ±57°, (ii) the ring forces the ferrocene units in an almost orthogonal relative orientation (as defined by the $Cp1_{center}$–$Cp2_{center}$–$Cp3_{center}$–$Cp4_{center}$ torsion angle of ±87°, Figure 1), and (iii) the Fe1 from Fe2 can be distinguished structurally and electronically. The Fe1 site bears the NH hydrogen donor group, and the Fe2 site carries the CO hydrogen acceptor group. The cyclopentadienyl rings at Fe1 and Fe2 are both oriented in an almost eclipsed fashion (C6–$Cp1_{center}$–$Cp2_{center}$–C1 ±90.8°; C11–$Cp3_{center}$–$Cp4_{center}$–C16 ±79.0°) with an approximate 1,2′-conformation.[21] The intramolecular Fe1···Fe2 distance is 6.43 Å. All other metrical data are unremarkable and within the common ranges. The intra- and intermolecular hydrogen bonds found in the solid state of **4a**, together with the solution IR and NMR spectroscopic data, are compatible with the assumption that intramolecular hydrogen bonds (rings) are also present to some degree in solution.

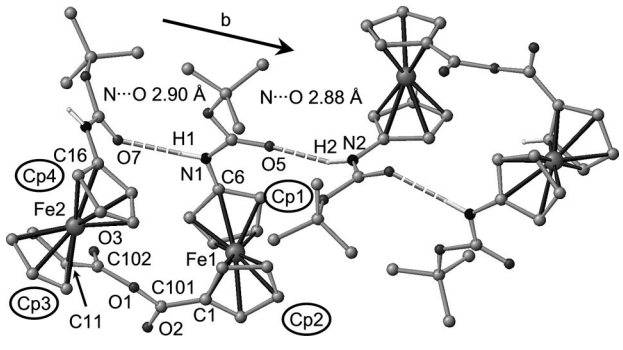

Figure 1. Molecular structure and connectivity of **4a** in the solid state.

The stability of ring motifs was probed by DFT calculations (B3LYP, LANL2DZ) on a model of **4c**.[12,13,15c,15e,22] The metrical data of the calculated ring conformation **4c**-r agree sufficiently well with the experimentally observed values for **4a** (N1···O7 2.84 Å; O2–C101–C102–O3 55°; Fe1···Fe2 7.26 Å). Only the relative orientation of the ferrocene moieties is calculated to be significantly smaller ($Cp1_{center}$–$Cp2_{center}$–$Cp3_{center}$–$Cp4_{center}$ 49°). The ring motif **4c**-r is found to be more stable than the non-hydrogen bonded form **4c**-o by 31 kJ mol^{-1}, which substantiates the assumption of ring formation and desymmetrization in solution (Figure 2).

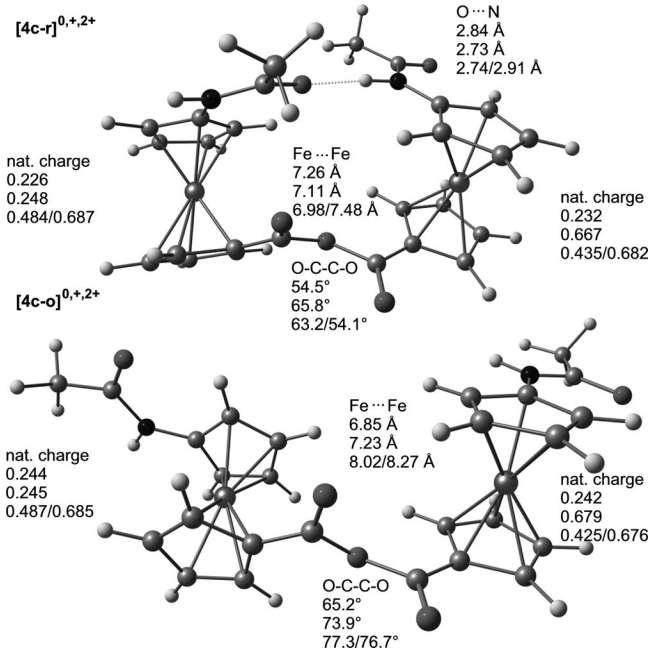

Figure 2. DFT-optimized structures of **4c**-r and **4c**-o and natural charges on iron for the neutral state, cations, and dications (singlet/triplet state).

Charging of the neutral complex to give the cation [**4c**]$^+$ and the dication [**4c**]$^{2+}$ and reoptimization of the geometries increases the Fe–Cp distances for the oxidized iron sites. For the monocations [**4c**-o]$^+$ and [**4c**-r]$^{2+}$, the calculated structures suggest charge-localized Fe^{II}/Fe^{III} mixed-valent systems with distances Fe^{III}–Cp(centroid) ≈ 1.80 Å and Fe^{II}–Cp(centroid) ≈ 1.73 Å. In the dications [**4c**]$^{2+}$, all Fe–

Cp(centroid) distances are found to be about 1.80 Å (triplet state) and 1.77 Å (singlet state). The triplet state of the dications $[\mathbf{4c}\text{-o}]^{2+}$ and $[\mathbf{4c}\text{-r}]^{2+}$ is calculated to be significantly more stable than the singlet state. Thus, the following discussion will refer to the triplet states of $[\mathbf{4c}\text{-o}]^{2+}$ and $[\mathbf{4c}\text{-r}]^{2+}$.

The calculations on **4c**/$[\mathbf{4c}]^{+}$ suggest that the ring motif remains more stable than the open form upon one-electron oxidation to $[\mathbf{4c}]^{+}$ $\{\Delta E = E([\mathbf{4c}\text{-r}]^{+}) - E([\mathbf{4c}\text{-o}]^{+}) = -53\ \mathrm{kJ\,mol^{-1}}\}$. However, the stability of the ring is dramatically reduced for the dication $[\mathbf{4c}]^{2+}$ $\{E([\mathbf{4c}\text{-r}]^{2+}) \approx E([\mathbf{4c}\text{-o}]^{2+})$ for the triplet state$\}$. The lower stability of the doubly charged ring is likely due to the increased coulomb repulsion between the two oxidized iron sites in $[\mathbf{4c}]^{2+}$. We were interested in seeing whether desymmetrization as a result of intramolecular hydrogen bonding has an influence on the charge (de-)localization in the mixed-valent cation $[\mathbf{4c}]^{+}$. To this end, NBO analyses were performed for **4c**-r, **4c**-o, $[\mathbf{4c}\text{-r}]^{+}$, $[\mathbf{4c}\text{-o}]^{+}$, $[\mathbf{4c}\text{-r}]^{2+}$, and $[\mathbf{4c}\text{-o}]^{2+}$. The calculated natural charges on iron are compiled in Figure 2. From these values, it can be deduced that $[\mathbf{4c}\text{-r}]^{+}$ is a rather charge-localized system with Fe^{III} at the NH donor and Fe^{II} at the carbonyl hydrogen acceptor site (Robin–Day class I–II[23]). Charge localization is also observed for the open form $[\mathbf{4a}\text{-o}]^{+}$. Thus, from the standpoint of charge (de-)localization, open forms and ring forms behave similarly in this case.

Indeed, electrochemical experiments (cyclic voltammetry, square-wave voltammetry, Figure 3) reveal only very small potential differences for the two expected oxidation waves for **4a**–**4c**. This attests only a very weak (if any) electronic communication between the two iron sites in $[\mathbf{4a}]^{+}$–$[\mathbf{4c}]^{+}$. Thus, it appears impossible to isolate pure samples of the mixed-valent cations $[\mathbf{4a}]^{+}$–$[\mathbf{4c}]^{+}$ because of the small comproportionation constant $K_C << 50$ ($\Delta E_{1/2} << 100$ mV, Experimental Section). For comparison, Kraatz's ureylene-bridged diferrocene dimethyl 1′,1′-ureylenebis(1-ferrocenecarboxylate) features $\Delta E_{1/2} = 137$ mV and $K_C = 207$[11] and our amide-bridged diferrocenes (with comparable substituents) feature $\Delta E_{1/2} = 123$ mV and $K_C = 120$ under comparable conditions (same counterions in the electrochemical experiments).[13] Thus, "head–head dimers" and "head–tail dimers" of Fca can be oxidized to class II mixed-valent cations with some degree of charge delocalization, while oxidation of "tail–tail dimers" of Fca gives rather localized class I–II mixed-valent systems. The latter finding might be due to the twisted anhydride bridge, which results in a poor communication pathway, and/or due to the structural asymmetry of the system with "hydrogen-donating" and "hydrogen-accepting" ferrocene units in the ring conformers. A larger splitting of the redox waves of carbamate **4a** is noted in comparison to that of **4b** (Figure 3).

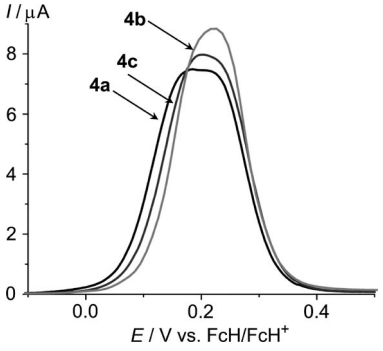

Figure 3. SWV of **4a**–**4c** in CH_2Cl_2/(nBuN)(PF_6).

Compound **4a** can be oxidized with $AgSbF_6$ in CH_2Cl_2 (Figure 4). Addition of 1 equiv. $AgSbF_6$ resulted in the appearance of the typical ferrocenium band at 825 nm (ε = 475 $\mathrm{M^{-1}\,cm^{-1}}$) and a very weak band at ca. 2150 nm ($\varepsilon \approx$ 25 $\mathrm{M^{-1}\,cm^{-1}}$). Addition of 2 equiv. $AgSbF_6$ approximately doubles the intensity of both(!) bands to 935 $\mathrm{M^{-1}\,cm^{-1}}$ at 815 nm and to 55 $\mathrm{M^{-1}\,cm^{-1}}$ at ca. 2150 nm, respectively. This excludes the interpretation of the weak NIR band as being due to an intervalence transition. Rather, it appears to be associated with the presence of ferrocenium ions bearing an NHR-substituted cyclopentadienyl ligand.

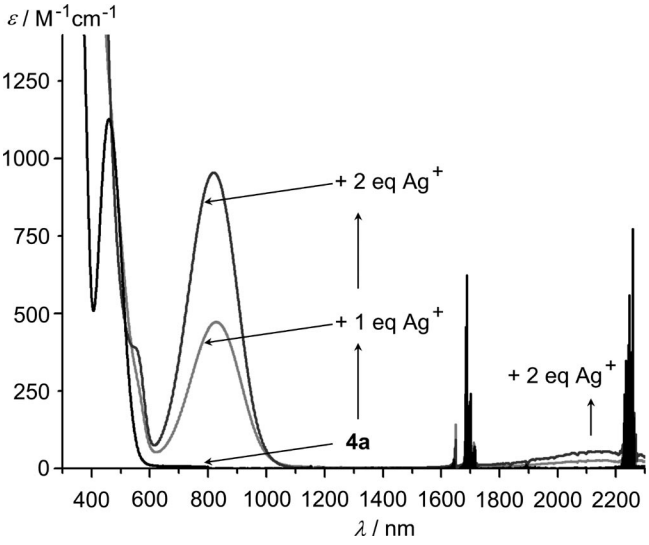

Figure 4. UV/Vis/NIR spectra of **4a** during oxidation with 0–2 equiv. $AgSbF_6$ in CH_2Cl_2.

To support this assumption, FcH, Fc–COOMe, AcNH–Fc, AcNH–Fn–COOMe, and BocNH–Fn–COOMe were oxidized with $AgSbF_6$ under the same conditions. The ferrocenium bands are observed at 621, 630, 759, 796, and 807 nm, respectively. For the latter three ferrocenium ions, an additional weak NIR band with $\lambda > 2000$ nm and $\varepsilon < 20\ \mathrm{M^{-1}\,cm^{-1}}$ is also observed, but for FcH^{+} and $[Fc\text{–}COOMe]^{+}$, no such band at about 2000 nm could be found (see Supporting Information). Thus, we assign the weak NIR bands of $[AcNH\text{–}Fc]^{+}$, $[AcNH\text{–}Fn\text{–}COOMe]^{+}$, $[BocNH\text{–}Fn\text{–}COOMe]^{+}$, and $[\mathbf{4a}]^{n+}$ to a transition that is associated with the N-substituted cyclopentadienyl ligand.

In order to assist band assignments, time-dependent DFT calculations (with the BVP86 functional and the DGDZVP2 basis set[24]) on geometry-optimized mononuclear ferrocenium cations $[AcNH\text{–}Fc]^{+}$ and $[AcNH\text{–}Fn\text{–}COOMe]^{+}$ have been performed. Transitions with non-vanishing intensities are calculated at 1928, 888, and 585 nm (f = 0.0001, 0.0071, 0.0015) for $[AcNH\text{–}Fc]^{+}$ and at

1909, 938, and 590 nm (f = 0.0001, 0.0062, 0.0010) for [AcNH–Fn–COOMe]$^+$, respectively, which nicely reproduces the experimental spectra (≈ 2200, 759, 551 nm and ≈ 2150, 796, 555 nm; see Supporting Information). The lowest-energy transition calculated (1928 nm) corresponds mainly to the d_{z^2} (HOMO; 62β) to $d_{x^2-y^2}$ (SOMO, 63β) electron excitation (Figure 5), while the next two high-intensity transitions result from the Cp ring (plus d_{xz}; 59β) and Cp ring (plus d_{xy}; 58β) to $d_{x^2-y^2}$ excitations.[25] The first weak transition gains some intensity from the admixture of the nitrogen p_z orbital to the $d_{x^2-y^2}$ orbital, thus introducing some charge-transfer character. For the very similar TDDFT spectrum of [AcNH–Fn–COOMe]$^+$ and a MO diagram of [AcNH–Fc]$^+$ see the Supporting Information.

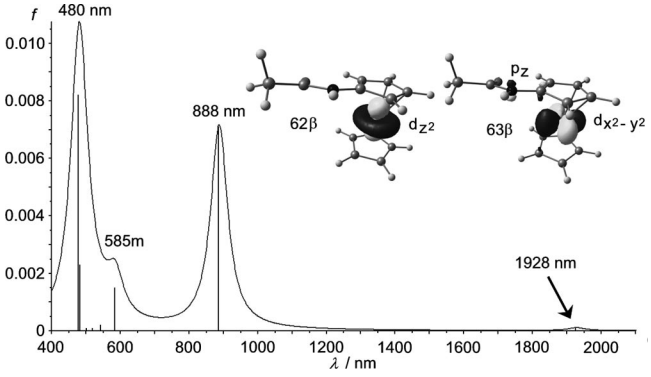

Figure 5. TDDFT-caclulated spectrum of [AcNH–Fc]$^+$ (Lorentzian line broadening with FWHM 60 cm^{-1}) and relevant Kohn–Sham molecular beta orbitals with an isosurface contour value of 0.06 a.u.

Thus, no IVCT bands have been observed for [**4a**]$^+$ up to 2300 nm, which is in accordance with the class I–II formulation of [**4a**]$^+$. Rather, the observed NIR bands at about 2000 nm are assigned to a charge-transfer admixed metal-centered HOMO to SOMO transition, which is supported by experimental and theoretical data.

Conclusions

We have shown that "tail–tail" dimers of N-protected Fca, namely the respective anhydrides, are formed from the corresponding acid chlorides in the presence of bases. The Boc-protected derivative **4a** has been structurally characterized by X-ray crystallography. A ring motif with an intramolecular hydrogen bond NH···OC is found, which desymmetrizes the molecule in the solid state. In solution, the hydrogen-bonded rings are in equilibrium with open forms. This is also supported by DFT calculations. Electrochemical experiments and chemical oxidation with $AgSbF_6$ reveal only weak (if any) electronic communication over the anhydride bridge, in contrast to the ureylene or amide bridges, which promote electronic communication. Observation of NIR bands both in singly and doubly oxidized systems is not indicative of intervalence transfer, but is assigned to a charge-transfer admixed metal-centered transition in these N-substituted ferrocenium salts. Thus, it is advisable to characterize not only the mixed-valent species but also the respective fully oxidized (or reduced) species in order to correctly assign the NIR bands of potential mixed-valent systems.

The weak electronic communication of the redox centers in Fca anhydrides might be due to the large twist of the anhydride unit, which prevents efficient electronic communication. Thus, the design principle of molecular wires based on Fca should focus on "head–tail" linked Fca (amide bridges) units rather than on alternating "head–head"/"tail–tail" linked Fca (ureylene/anhydride bridges) units. The amide strategy is currently being investigated in our laboratory in greater detail.

Experimental Section

General Procedures: All reactions were performed under argon atmosphere unless otherwise noted. Dichloromethane was dried with CaH_2 and distilled prior to use. All reagents were used as received from commercial suppliers (Acros, Sigma–Aldrich). BocNH–Fn–COOH, FmocNH–Fn–COOH and AcNH–Fn–COOH were prepared according to literature procedures.[10b,10c] NMR spectra were recorded on a Bruker Avance DRX 400 spectrometer at 400.31 MHz (^{1}H) and 100.07 MHz (^{13}C{^{1}H}). All resonances are reported in ppm vs. the solvent signal as internal standard $CDCl_3$ (^{1}H: δ = 7.26; ^{13}C: δ = 77.0 ppm). IR spectra were recorded with a BioRad Excalibur FTS 3100 spectrometer by using KBr cells in CH_2Cl_2 and as CsI disks. Electrochemical experiments were carried out on a BioLogic SP-50 voltammetric analyzer by using a glassy carbon working electrode, a platinum wire as counter electrode, and a 0.01 M $Ag/AgNO_3$ electrode as reference electrode. The measurements were carried out at a scan rate of 100 mV s^{-1} for cyclic voltammetry experiments and at 10 mV s^{-1} for square-wave voltammetry experiments by using 0.1 M (nBu$_4$N)(PF_6) as supporting electrolyte in CH_2Cl_2. Potentials are given relative to the ferrocene/ferrocenium couple ($E_{1/2}$ = 225 ± 5 mV under the experimental conditions). UV/Vis/NIR spectra were recorded on a Varian Cary 5000 spectrometer by using 1.0 cm cells (Hellma, suprasil). FD mass spectra were recorded on a FD Finnigan MAT90 spectrometer. Melting points were determined by using a Gallenkamp capillary melting point apparatus MFB 595 010 and were not corrected. Elemental analyses were performed by the microanalytical laboratory of the chemical institutes of the University of Mainz.

Crystal Structure Determination: Intensity data were collected with a Bruker AXS Smart1000 CCD diffractometer with an APEX II detector and an Oxford cooling system and corrected for absorption and other effects by using Mo-K_α radiation (λ = 0.71073 Å) at 173(2) K. The diffraction frames were integrated by using the SAINT package and most were corrected for absorption with MULABS.[26,27] The structure was solved by direct methods and refined by the full-matrix method based on F^2 by using the SHELXTL software package.[28,29] All non-hydrogen atoms were refined anisotropically. The positions of the hydrogen atoms were generated with appropriate geometric constraints and allowed to ride on their respective parent carbon atoms with fixed isotropic thermal parameters, with the exception of H1 and H2, which were located in the Fourier difference map and freely refined. $C_{32}H_{36}Fe_2N_2O_7$ (672.33); monoclinic, $P2_1/n$; a = 12.0908(6), b = 16.5040(8), c = 15.7260(8) Å; β = 106.850(2)°; V = 3003.3(3) Å^3; Z = 4, $D_{calcd.}$ = 1.487 g cm^{-3}; μ = 1.017 mm^{-1}; F(000) = 1400; θ = 2.47–27.50°; h, k, l = –15 to 15, –21 to 21, –20 to 20; reflections collected/unique

[$I \geq 2\sigma(I)$] = 33471/6901; 396 refined parameters; transmission factors, T_{min}/T_{max} = 0.84798/1.14278; Goodness-of-fit on F^2, S = 0.909; R [$I \geq 2\sigma(I)$]/R [all data] = 0.0409/0.0794; wR [$I \geq 2\sigma(I)$]/wR [all data] = 0.0688/0.0877; max./min. electron density = 0.462/–0.515 e Å^{-3}. CCDC-769441 contains the supplementary crystallographic data for this paper. These data can be obtained free of charge from The Cambridge Crystallographic Data Centre via www.ccdc.cam.ac.uk/data_request/cif.

Density Functional Calculations: These calculations were carried out with the Gaussian03/DFT series[30,31] of programs. For geometry optimizations, the B3LYP formulation of density functional theory was used that employs the LANL2DZ basis set. No symmetry constraints were imposed on the molecules. No solvent modeling was employed. All points were characterized as minima (N_{imag} = 0) by frequency analysis. Spin-unrestricted single-point TD-DFT calculations were performed by the BVP86 functional by using a DGDZVP2 basis set.

Synthesis of 4a: BocNH–Fn–COOH (390 mg, 1.13 mmol) was dissolved in CH_2Cl_2 (20 mL). 1-Chloro-*N*,*N*,2-trimethyl-1-propen-1-amine (150 μL, 1.13 mmol) and 2,4,6-collidine (0.5 mL, 3.78 mmol) were added by syringe. After the solution was stirred for 16 h at room temperature, it was diluted with CH_2Cl_2 (50 mL), and the organic phase was washed with aqueous saturated $NaHCO_3$ solution (2× 50 mL), aqueous 5% citric acid (3× 50 mL), and brine (1× 50 mL) and dried with $MgSO_4$. After the solvent was removed in vacuo, the residue was purified by chromatography on silica [3× 10 cm, petroleum ether (b.p. 40/60 °C)/diethyl ether, 1:2] to give 205 mg of the orange product (0.30 mmol, 54%). M.p. 167–168 °C. R_f = 0.73 [diethyl ether/petroleum ether (b.p. 40/60 °C) 4:1]. MS (FD): *m*/*z* = 672 ([M]$^+$, 100%). $C_{32}H_{36}N_2O_7Fe_2$ (672.33)·1/8CH_2Cl_2: C 56.50, H 5.35, N 4.10; found C 56.43, H 5.52, N 4.00. ^{1}H NMR (400 MHz, $CDCl_3$): δ = 6.36 (br. s, 2 H, NH), 4.84 (pt, 4 H, $H^{7,10}$), 4.70 (br. s, 4 H, $H^{2,5}$), 4.58 (pt, 4 H, $H^{8,9}$), 4.10 (pt, 4 H, $H^{3,4}$), 1.46 [s, 18 H, $C(CH_3)_3$] ppm (pt = pseudo-triplet = non-resolved doublet of doublets). $^{13}C\{^1H\}$ NMR (100 MHz, $CDCl_3$): δ = 168.4 (s, $CO_{anhydride}$), 153.3 (s, $CO_{carbamate}$), 98.8 (s, C^1), 80.1 [s, $C(CH_3)_3$], 74.0 (s, $C^{8,9}$), 72.0 (s, $C^{7,10}$), 69.9 (s, C^6), 66.1 (s, $C^{3,4}$), 62.2 (s, $C^{2,5}$), 28.2 [s, $C(CH_3)_3$] ppm. IR (CH_2Cl_2, c = 10^{-2} M): $\tilde{\nu}$ = 3431 (w, NH), 3351 (w, NH), 1765 (m, $CO_{anhydride,sym}$), 1724 (sh, $CO_{carbamate}$), 1708 (s, $CO_{anhydride,asym}$) cm^{-1}. IR (CsI): $\tilde{\nu}$ = 3320 (m, NH), 1767 (s, $CO_{anhydride,sym}$), 1709, 1692 (s, $CO_{carbamate}$, $CO_{anhydride,asym}$) cm^{-1}. UV/Vis (CH_2Cl_2): λ_{max} (ε) = 459 nm (1130 M^{-1} cm^{-1}). SWV (CH_2Cl_2; vs. FcH/FcH$^+$): $E_{1/2}$ = +0.15, +0.24 V.

Synthesis of 4b: FmocNH–Fn–COOH (570 mg, 1.22 mmol) was dissolved in CH_2Cl_2 (15 mL). 1-Chloro-*N*,*N*,2-trimethyl-1-propen-1-amine (160 μL, 1.21 mmol) and 2,4,6-collidine (0.8 mL, 6.05 mmol) were added by syringe. After the solution was stirred for 20 h at room temperature, it was diluted with CH_2Cl_2 (50 mL), and the organic phase was washed with aqueous saturated $NaHCO_3$ solution (2× 50 mL), aqueous 5% HCl (2× 50 mL), water (1× 50 mL), and brine (1× 50 mL) and dried with $MgSO_4$. After the solvent was removed in vacuo, the residue was purified by chromatography on silica [3× 10 cm, petroleum ether (b.p. 40/60 °C)/diethyl ether, 1:2; elution with diethyl ether] to give 150 mg of the orange product (0.16 mmol, 27%). M.p. 158–161 °C. R_f = 0.51 [diethyl ether/petroleum ether (b.p. 40/60 °C) 4:1]. MS (FD): *m*/*z* (%) = 916 (100) [M]$^+$. $C_{52}H_{40}N_2O_7Fe_2$ (916.57): C 68.14, H 4.40, N 3.06; found C 67.59, H 4.95, N 2.93. ^{1}H NMR (400 MHz, $CDCl_3$): δ = 7.74 (d, $^3J_{HH}$ = 7.4 Hz, 4 H, H^{Fmoc}), 7.64 (d, $^3J_{HH}$ = 6.1 Hz, 4 H, H^{Fmoc}), 7.37 (t, J_{HH} = 7.4 Hz, 4 H, H^{Fmoc}), 7.29 (t, J_{HH} = 7.5 Hz, 4 H, H^{Fmoc}), 6.88 (br. s, 2 H, NH), 4.88 (s, 4 H, $H^{7,10}$), 4.75 (s, 4 H, $H^{2,5}$), 4.57 (s, 4 H, $H^{8,9}$), 4.38 (br. s, 4 H, CH_2^{Fmoc}), 4.21 (t, 2 H, $^3J_{HH}$ = 6.4 Hz, CH^{Fmoc}), 4.09 (br. s, 4 H, $H^{3,4}$) ppm. $^{13}C\{^1H\}$ NMR (100 MHz, $CDCl_3$): δ = 168.4 (s, $CO_{anhydride}$), 153.9 (s, $CO_{carbamate}$), 143.8 (s, C^{Fmoc}), 141.3 (s, C^{Fmoc}), 127.7 (s, C^{Fmoc}), 127.1 (s, C^{Fmoc}), 125.2 (s, C^{Fmoc}), 119.9 (s, C^{Fmoc}), 98.2 (s, C^1), 74.0 (s, $C^{8,9}$), 72.1 (s, $C^{7,10}$), 69.9 (s, C^6), 67.0 (s, CH_2^{Fmoc}), 66.2 (s, $C^{3,4}$), 62.3 (s, $C^{2,5}$), 47.1 (s, CH^{Fmoc}) ppm. IR (CH_2Cl_2, c = 10^{-2} M): $\tilde{\nu}$ = 3423 (w, NH), 3331 (w, NH), 1763 (m, $CO_{anhydride,sym}$), 1732 (s, $CO_{carbamate}$), 1701 (s, $CO_{anhydride,asym}$) cm^{-1}. IR (CsI): $\tilde{\nu}$ = 3398 (m, NH), 3335 (m, NH), 1766 (s, $CO_{anhydride,sym}$), 1732 (s, $CO_{carbamate}$), 1707 (s, $CO_{anhydride,asym}$) cm^{-1}. UV/Vis (CH_2Cl_2): λ_{max} (ε) = 460 nm (1070 M^{-1} cm^{-1}). SWV (CH_2Cl_2; vs. FcH/FcH$^+$): $E_{1/2}$ = +0.19, +0.25 V.

Synthesis of 4c: AcNH–Fn–COOH (290 mg, 1.01 mmol) was suspended in CH_2Cl_2 (20 mL). 1-Chloro-*N*,*N*,2-trimethyl-1-propen-1-amine (130 μL, 1.00 mmol) and 2,4,6-collidine (0.5 mL, 3.78 mmol) were added by syringe. After the solution was stirred for 5 h at room temperature, it was diluted with CH_2Cl_2 (50 mL), and the organic phase was washed with aqueous saturated $NaHCO_3$ solution (2× 50 mL), aqueous 5% HCl (2× 50 mL), water (1× 50 mL), and brine (1× 50 mL) and dried with $MgSO_4$. After the solvent was removed in vacuo, the residue was purified by chromatography on silica (3× 10 cm, CH_2Cl_2/ethyl acetate; elution with ethyl acetate/thf, 10:1) to give 85 mg of the orange product (0.15 mmol, 30%). M.p. 102–104 °C. R_f = 0.09 [CH_2Cl_2/petroleum ether (b.p. 40/60 °C) 1:1]. MS (FD): *m*/*z* = 556 ([M]$^+$, 100%). $C_{26}H_{24}N_2O_5Fe_2$ (556.04)·$C_4H_8O_2$: C 55.93, H 5.01, N 4.35; found C 55.86, H 4.89, N 4.54. ^{1}H NMR (400 MHz, $CDCl_3$): δ = 7.60 (br. s, 2 H, NH), 4.87 (pt, 4 H, $H^{7,10}$), 4.83 (br. s, 4 H, $H^{2,5}$), 4.62 (pt, 4 H, $H^{8,9}$), 4.09 (pt, 4 H, $H^{3,4}$), 2.11 (s, 6 H, CH_3) ppm (pt = pseudo-triplet = non-resolved doublet of doublets). $^{13}C\{^1H\}$ NMR (100 MHz, $CDCl_3$): δ = 169.4 (s, CO_{amide}), 168.3 (s, $CO_{anhydride}$), 97.1 (s, C^1), 74.0 (s, $C^{8,9}$), 72.0 (s, $C^{7,10}$), 69.9 (s, C^6), 66.3 (s, $C^{3,4}$), 63.3 (s, $C^{2,5}$), 23.9 (s, CH_3) ppm. IR (CH_2Cl_2, c = 10^{-2} M): $\tilde{\nu}$ = 3431 (w, NH), 3342 (w, NH), 1771/1759 (s+sh, $CO_{anhydride,sym}$), 1699 (s, $CO_{anhydride,asym}$), 1687 (s, CO_{amide}) cm^{-1}. IR (CsI): $\tilde{\nu}$ = 3285 (m, NH), 1765 (s, $CO_{anhydride,sym}$), 1696 (s, $CO_{anhydride,asym}$), 1668 (s, CO_{amide}) cm^{-1}. UV/Vis (CH_2Cl_2): λ_{max} (ε) = 461 nm (1100 M^{-1} cm^{-1}). SWV (CH_2Cl_2; vs. FcH/FcH$^+$): $E_{1/2}$ = +0.17, +0.24 V.

Supporting Information (see footnote on the first page of this article): Cartesian coordinates of DFT-optimized **4c**-r, [**4c**-r]$^+$, and [**4c**-r]$^{2+}$ (singlet, triplet) and those of **4c**-o, [**4c**-o]$^+$ and [**4c**-o]$^{2+}$ (singlet, triplet) are presented. The $^{13}C\{^1H\}$ NMR spectrum of **1c** + Ghosez's reagent in $CDCl_3$ (formation of **2c**) and the comparison with the $^{13}C\{^1H\}$ NMR spectrum of **4c** in $CDCl_3$ is shown. The plot of δ(NH) vs. concentration of **4a** in $CDCl_3$, the Gaussian fits of the square-wave voltammograms of **4a**–**4c**, the UV/Vis/NIR spectra of various substituted ferrocenes during oxidation to the ferrocenium cations with $AgSbF_6$ in CH_2Cl_2, the results of the TD-DFT calculations on [AcNH–Fc]$^+$ and [AcNH–Fn–COOMe]$^+$, and the MO scheme of [AcNH–Fc]$^+$ are also given.

Acknowledgments

We thank Jovana-Maria Diesch for preparative assistance and the Deutsche Forschungsgemeinschaft for continuously supporting our work.

[1] M. Wagner, *Angew. Chem.* **2006**, *118*, 6060–6062; *Angew. Chem. Int. Ed.* **2006**, *45*, 5916–5918.

[2] K. A. Mahmoud, H.-B. Kraatz in *Frontiers in Transition Metal Containing Polymers* (Eds.: A. S. Abd-Aziz, I. Manners), p. 473, John Wiley & Sons, Inc. **2006**.

[3] D. A. Rider, I. Manners in *Frontiers in Transition Metal Containing Polymers* (Eds.: A. S. Abd-Aziz, I. Manners), p. 135, John Wiley & Sons, Inc. **2006**.

[4] I. Manners, *Adv. Organomet. Chem.* **1995**, *37*, 131–168.

[5] P. Nguyen, P. Gómez-Elipe, I. Manners, *Chem. Rev.* **1999**, *99*, 1515–1548.

[6] I. Manners, *Science* **2001**, *294*, 1664–1666.

[7] G. R. Whittell, I. Manners, *Adv. Mater.* **2007**, *19*, 3439–3468.

[8] J. B. Heilmann, M. Scheibitz, Y. Qin, A. Sundararaman, F. Jäkle, T. Kretz, M. Bolte, H.-W. Lerner, M. C. Holthausen, M. Wagner, *Angew. Chem.* **2006**, *118*, 934–939; *Angew. Chem. Int. Ed.* **2006**, *45*, 920–924.

[9] L. Kaufmann, J.-M. Breunig, H. Vitze, F. Schödel, I. Nowik, M. Pichlmaier, M. Bolte, H.-W. Lerner, R. F. Winter, R. H. Herber, M. Wagner, *Dalton Trans.* **2009**, 2940–2950.

[10] a) T. Okamura, K. Sakauye, N. Ueyama, A. Nakamura, *Inorg. Chem.* **1998**, *37*, 6731–6736; b) L. Barišić, V. Rapić, V. Kovač, *Croat. Chem. Acta* **2002**, *75*, 199–210; c) K. Heinze, M. Schlenker, *Eur. J. Inorg. Chem.* **2004**, 2974–2988.

[11] K. Mahmoud, Y.-T. Long, G. Schatte, H.-B. Kraatz, *J. Organomet. Chem.* **2004**, *689*, 2250–2255.

[12] K. Heinze, U. Wild, M. Beckmann, *Eur. J. Inorg. Chem.* **2007**, 617–623.

[13] K. Heinze, D. Siebler, *Z. Anorg. Allg. Chem.* **2007**, *633*, 2223–2233.

[14] S. Chowdhury, G. Schatte, H.-B. Kraatz, *Angew. Chem.* **2006**, *118*, 7036–7038; *Angew. Chem. Int. Ed.* **2006**, *45*, 6882–6884.

[15] a) L. Barišić, M. Dropučić, V. Rapić, H. Pritzkow, S. I. Kirin, N. Metzler-Nolte, *Chem. Commun.* **2004**, 2004–2005; b) L. Barišić, M. Čakić, K. A. Mahmoud, Y.-N. Liu, H.-B. Kraatz, H. Pritzkow, S. I. Kirin, N. Metzler-Nolte, V. Rapić, *Chem. Eur. J.* **2006**, *12*, 4965–4980; c) M. Čakić Semenčić, D. Siebler, K. Heinze, V. Rapić, *Organometallics* **2009**, *28*, 2028–2037; d) A. Lataifeh, S. Beheshti, H.-B. Kraatz, *Eur. J. Inorg. Chem.* **2009**, 3205–3218; e) D. Siebler, C. Förster, K. Heinze, *Eur. J. Inorg. Chem.* **2010**, 523–527; f) H.-B. Kraatz, *J. Inorg. Organomet. Polym. Mater.* **2005**, *15*, 83–106; g) K. A. Mahmoud, H.-B. Kraatz, *J. Inorg. Organomet. Polym. Mater.* **2006**, *16*, 201–210; h) D. R. van Staveren, N. Metzler-Nolte, *Chem. Rev.* **2004**, *104*, 5931–5985.

[16] M. Lamač, J. Cvačka, P. Štěpnička, *J. Organomet. Chem.* **2008**, *693*, 3430–3434.

[17] a) H. H. Lau, H. Hart, *J. Org. Chem.* **1959**, *24*, 280–281; b) E. M. Acton, R. M. Silverstein, *J. Org. Chem.* **1959**, *24*, 1487–1489; c) E. J. Kupchik, R. J. Kiesel, *J. Org. Chem.* **1966**, *31*, 456–461.

[18] T. H. Galow, J. Rodrigo, K. Cleary, G. Cooke, V. M. Rotello, *J. Org. Chem.* **1999**, *64*, 3745–3746.

[19] A. Devos, J. Remion, A.-M. Frisque-Hesbain, A. Colens, L. Ghosez, *J. Chem. Soc., Chem. Commun.* **1979**, 1180–1181.

[20] a) *Fmoc Solid Phase Peptide Synthesis* (Eds.: W. C. Chan, P. D. White), Oxford University Press, Oxford **2000**; b) H. Runqiu, W. Qingmin, *J. Organomet. Chem.* **2001**, *637–639*, 94–98; c) B. Schetter, B. Speiser, *J. Organomet. Chem.* **2004**, *689*, 1472–1480.

[21] S. I. Kirin, H.-B. Kraatz, N. Metzler-Nolte, *Chem. Soc. Rev.* **2006**, *35*, 348–354.

[22] a) M. Čakić Semenčić, K. Heinze, C. Förster, V. Rapić, *Eur. J. Inorg. Chem.* **2010**, 1089–1097; b) J. Lapić, S. Djaković, M. Cetina, K. Heinze, V. Rapić, *Eur. J. Inorg. Chem.* **2010**, 106–114; c) V. Kovač, K. Radolović, I. Habuš, D. Siebler, K. Heinze, V. Rapić, *Eur. J. Inorg. Chem.* **2009**, 389–399; d) S. Djaković, D. Siebler, M. Čakic Semencić, K. Heinze, V. Rapić, *Organometallics* **2008**, *27*, 1447–1453; e) J. Lapić, G. Pavlović, D. Siebler, K. Heinze, V. Rapić, *Organometallics* **2008**, *27*, 726–735; f) S. I. Kirin, U. Schatzschneider, D. Köster, D. Siebler, N. Metzler-Nolte, *Inorg. Chim. Acta* **2009**, *362*, 894–906; g) S. I. Kirin, U. Schatzschneider, X. de Hatten, T. Weyhermüller, N. Metzler-Nolte, *J. Organomet. Chem.* **2006**, *691*, 3451–3457.

[23] M. B. Robin, P. Day, *Adv. Inorg. Chem. Radiochem.* **1967**, *10*, 247–360.

[24] R. Warratz, H. Aboulfadl, T. Bally, F. Tuczek, *Chem. Eur. J.* **2009**, *15*, 1604–1617.

[25] Y. S. Sohn, D. N. Hendrickson, H. B. Gray, *J. Am. Chem. Soc.* **1971**, *93*, 3603–3612.

[26] SMART Data Collection and SAINT-Plus Data Processing Software for the SMART System (various versions), Bruker Analytical X-ray Instruments, Inc.: Madison, WI, **2000**.

[27] B. Blessing, *Acta Crystallogr., Sect. A* **1995**, *51*, 33–38.

[28] G. M. Sheldrick, *SHELXTL*, Version 5.1, Bruker AXS: Madison, WI, **1998**.

[29] G. M. Sheldrick, *SHELXL-97*, University of Göttingen, Göttingen, Germany, **1997**.

[30] M. J. Frisch, G. W. Trucks, H. B. Schlegel, G. E. Scuseria, M. A. Robb, J. R. Cheeseman, J. A. Montgomery Jr., T. Vreven, K. N. Kudin, J. C. Burant, J. M. Millam, S. S. Iyengar, J. Tomasi, V. Barone, B. Mennucci, M. Cossi, G. Scalmani, N. Rega, G. A. Petersson, H. Nakatsuji, M. Hada, M. Ehara, K. Toyota, R. Fukuda, J. Hasegawa, M. Ishida, T. Nakajima, Y. Honda, O. Kitao, H. Nakai, M. Klene, X. Li, J. E. Knox, H. P. Hratchian, J. B. Cross, V. Bakken, C. Adamo, J. Jaramillo, R. Gomperts, R. E. Stratmann, O. Yazyev, A. J. Austin, R. Cammi, C. Pomelli, J. W. Ochterski, P. Y. Ayala, K. Morokuma, G. A. Voth, P. Salvador, J. J. Dannenberg, V. G. Zakrzewski, S. Dapprich, A. D. Daniels, M. C. Strain, O. Farkas, D. K. Malick, A. D. Rabuck, K. Raghavachari, J. B. Foresman, J. V. Ortiz, Q. Cui, A. G. Baboul, S. Clifford, J. Cioslowski, B. B. Stefanov, G. Liu, A. Liashenko, P. Piskorz, I. Komaromi, R. L. Martin, D. J. Fox, T. Keith, M. A. Al-Laham, C. Y. Peng, A. Nanayakkara, M. Challacombe, P. M. W. Gill, B. Johnson, W. Chen, M. W. Wong, C. Gonzalez, J. A. Pople, *Gaussian 03, Revision D.01*, Gaussian, Inc., Wallingford CT, **2004**.

[31] E. D. Glendening, A. E. Reed, J. E. Carpenter, F. Weinhold, NBO version 3.1 is incorporated within this version of the Gaussian suite.

Received: April 7, 2010
Published Online: July 13, 2010

DOI: 10.1002/ejic.201000293

Supported and Free-Standing Sulfonic Acid Functionalized Mesostructured Silica Films with High Proton Conductivity

Ralf Supplit,[a] Ayae Sugawara,[a] Herwig Peterlik,[b] Ryuji Kikuchi,[a] and Tatsuya Okubo*[a]

Keywords: Mesostructure / Self-assembly / Proton conductivity / Sol–gel processes / Conducting materials / Template synthesis

Sulfonic acid functionalized silica films with 2D-hexagonal mesostructures of various channel sizes are prepared in a one-step synthesis. A successful combination of in situ oxidation of a mercapto-functionalized silane with an evaporation induced self-assembly (EISA) process in the presence of amphiphilic block copolymers allows the formation of a highly structured material with a sulfonation degree of 33 %. Analysis of the mesostructure by a combination of XRD, grazing-incidence small-angle X-ray scattering (GI-SAXS), and TEM shows that 2D-hexagonally ordered mesostructured films are obtained by optimization of the surfactant to silica precursor ratio. The tuneability of the mesochannel size is demonstrated by the use of three different surfactants. The complete oxidation of the mercapto group to sulfonic acid is confirmed by Fourier transform infrared spectroscopy (FTIR). The thermal stability of the material is investigated by coupled thermogravimetric analysis, differential temperature analysis, and mass spectrometry (TGA-DTA-MS). Alternating current (AC) impedance analysis of humidified samples shows high proton conductivity of up to 0.18 $S\,cm^{-1}$ at 60 °C and 95 % relative humidity.

Introduction

The combination of a high surface area and controllable pore size of mesostructured sol–gel materials has attracted considerable interest in the research communities of many different fields.[1,2] As the mesochannels of such materials are modified with functional groups the application range is further expanded.

A particularly interesting field is the application of functionalized mesostructured materials as electrolytes for fuel cells. Today, Nafion membranes are the most commonly used electrolytes in polymer electrolyte membrane fuel cells (PEMFC). Its high proton conductivity is derived from randomly oriented hydrophilic sulfonic acid functionalized channels in a hydrophobic fluorocarbon matrix. Depending on the degree of hydration, these channels have a diameter of several nanometers.[3] Sulfonic acid functionalized mesochannels can be deliberately designed in the form of a periodically structured network by sol–gel processing and surfactant templating to reach, or even outstrip, the proton-conducting features of Nafion.[4–8]

In addition, mesoporous silica with sulfonic acid groups has excellent properties as a heterogeneous catalyst for esterification,[9–15,24] condensation,[13–17] acylation,[11,15,18,19] acetylation,[18,20] Fries rearrangement of phenylacetate,[21] and protection of alcohols by tetrahydropyranylation.[22] In catalytic and solid electrolyte applications the local environment and the accessibility of the active functional groups is strongly dependent on the synthetic route, and therefore incorporation of the sulfonic acid moieties is a crucial step.

This functionalization can be achieved in several ways: one method is the postsynthetic impregnation of a preformed mesostructured silica matrix by reaction of the surface silanol groups with a sulfonic acid precursor, such as (3-mercaptopropyl)trimethoxysilane (MPTMS), followed by oxidation of the functional group by either hydrogen peroxide or nitric acid.[13,14,18,25,26] The use of a perfluorosulfonic acid precursor instead of MPTMS improved acid strength and catalytic performance.[11,23] A postsynthetic functionalization method for supported and free-standing mesostructured films rather than powders was reported by Athens et al. who prepared functionalized alumina–silica samples in a multistep synthesis.[23] Their product showed improved water retention at higher temperatures and reached stable conductivity values of up to 5×10^{-3} $S\,cm^{-1}$ at 50 % relative humidity at temperatures of up to 180 °C.

However, in addition to the high synthetic effort, the postsynthetic impregnation has another drawback. The material will usually have a decreasing functionalization degree from the outer surface of the material to the center of the mesochannels. Furthermore, the inner pore size is decreased which may eventually result in pore blocking. In this way the specific advantages of the mesoporous material may be

[a] Department of Chemical System Engineering, The University of Tokyo,
7-3-1 Hongo, Bunkyo-ku, 113-8656 Tokyo, Japan
E-mail: okubo@chemsys.t.u-tokyo.ac.jp
[b] Faculty of Physics, University of Vienna,
Strudlhofgasse 4, 1090 Vienna, Austria

diminished. These problems can be overcome by co-condensation of the silica precursor with mercapto-functionalized organosiloxane precursors that can then be oxidized to sulfonic acid in a second step. This synthesis was performed under acidic conditions with nonionic surfactants[10] and with ionic surfactants for mesostrucured silica[13,14] and ethane bridged silica.[24]

A direct one-step synthesis route to mesostructured silica doped with sulfonic acid was introduced by Margolese et al. In his method mercaptopropyl- or 2-(4-chlorosulfonylphenyl)ethyl groups are oxidized in situ in the presence of hydrogen peroxide.[27–30]

To date, several groups have reported the proton conductivity of sulfonic acid functionalized silica powders. The highest reported value was 0.2 $S cm^{-1}$ at 140 °C and 100% relative humidity (requires high pressure) that is a great improvement compared to Nafion, which reached only 6×10^{-5} $S cm^{-1}$ under the same experimental conditions.[31] However, the preparation of stable dense disks or thin films, required for fuel cell electrolytes, can be difficult. An application probably requires incorporation into a polymer matrix, which would significantly reduce proton conductivity and water uptake potential. Direct deposition of electrolyte films on electrode surfaces would therefore have obvious advantages. Feasibility of the use of a sol–gel film as a fuel cell electrolyte has already been demonstrated by Li et al. who prepared a fuel cell prototype from nonfunctionalized 650 nm thick silica sol–gel films deposited by spin coating on a porous electrode.[32] The relatively low power output of 51 $\mu W cm^{-2}$ was mostly attributed to the high resistance in the system. This problem could be solved by the use of sulfonic acid functionalized materials instead of pure silica to improve the conductivity by five orders of magnitude.[31] However, at present all co-condensation methods to prepare sulfonic acid functionalized silica involve hydrothermal synthetic conditions and can only be used for the preparation of powders. In this work, we present for the first time a simple EISA[33] method for the preparation of mesostructured sulfonic acid functionalized supported and free-standing silica films. With our novel approach, thin electrolyte films containing sulfonic acid groups can be directly applied to the electrode surface of fuel cell electrodes by the use of such simple techniques as dip, spin or spray coating. Thus, our new method is a significant step towards a desired application in fuel cell assemblies.

Synthesis

MPTMS was added to a prehydrolyzed sol of tetraethoxysilane (TEOS) in a molar ratio of 1:2. The sulfonic acid functionality was formed by in situ oxidation of MPTMS with hydrogen peroxide (Scheme 1) in an acid catalyzed sol–gel process.

A temperature increase of the sol, to approximately 50 °C, indicated the occurrence of a highly exothermic oxidation reaction, which happens concomitantly to the hydrolysis and condensation reactions that form the sol–gel network.

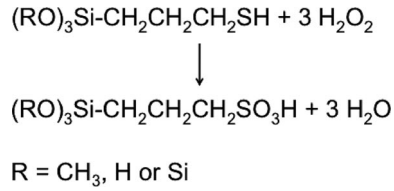

Scheme 1. In-situ oxidation of (3-mercaptopropyl)trialkoxysilane with hydrogen peroxide.

In this study three different surfactants were applied as templating agents: Brij-56 ($C_{16}EO_{10}$, B56), Sylanox 40-A80 ($EO_{17}PO_{12}C_{14}$, S40), and Pluronic-P123 ($EO_{20}PO_{70}EO_{20}$, P123). Supported films on glass slides were prepared by spin-coating from clear sols with a molar composition of TEOS/MPTMS/Surfactant/H_2O_2/H_2O/HCl/EtOH = 1:0.5:*S*:1.73:5:0.0082:11.7. Moulding the same sols in Teflon™ or polystyrene dishes gave free-standing films. Highly ordered mesostructures were obtained for samples prepared with *S* of 0.188 (B56), 0.079 (S40), and 0.034 (P123).

The samples prepared by moulding were labeled *B56-as-m*, *S40-as-m*, and *P123-as-m* and the supported films were denoted *B56-as-f*, *S40-as-f*, and *P123-as-f*, respectively. Surfactant extraction was performed in ethanol at 60 °C for 24 h,[29] and the resultant samples were labeled *B56-ex-f*, *S40-as-f*, *P123-as-f* and *B56-ex-m*, *S40-as-m*, and *P123-as-m*, respectively.

Chemical Characterization

FTIR analysis of all samples showed the typical bands expected for the silica network: Si–O stretching at 800, 1100, and 1200 cm^{-1}, Si–O bending at 950 cm^{-1}, and the O–H stretching vibrations of silanol groups and adsorbed water between 3100 and 3700 cm^{-1} (Figure 1). To investigate the oxidation of the mercapto group, a comparative sample with the label *SH-as* was prepared without addition of hydrogen peroxide under otherwise identical conditions. The successful oxidation of the mercapto group was confirmed by the disappearance of the absorption band of the SH group at 2565 cm^{-1} from the FTIR spectrum.

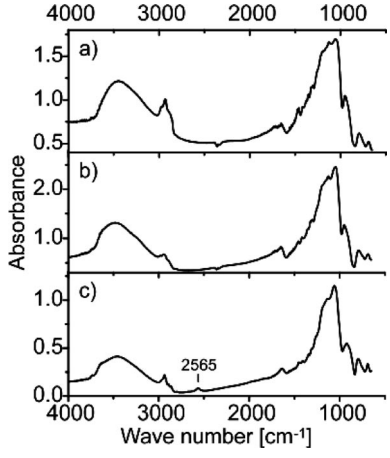

Figure 1. FTIR spectra of (a) *B56-as-m*, (b) *B56-ex-m* and (c) *SH-as*.

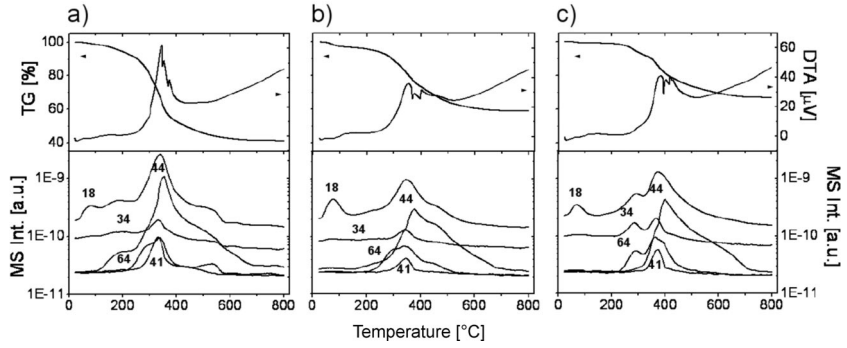

Figure 2. Coupled TGA-DTA-MS of (a) *B56-as-m*, (b) *B56-ex-m* and (c) *SH-as*.

Extraction of the surfactant was carried out in ethanol at 60 °C for 24 h.[29] This resulted in a reduction of the CH_2 vibration bands between 2800 and 3000 cm^{-1} to an intensity level close to the comparative sample prepared without surfactant. Therefore it only shows contributions of the propyl group of the functionalization in this region, indicating successful extraction of the surfactant.

The mass loss in the TGA (Figure 2, a and b) was 60%, and reduced to 40% after extraction. When we assume a fully condensed and oxidized network of the applied composition TEOS/MPTMS = 1:0.5 the composition of the surfactant-extracted sample would be $(SiO_2)_1(SiO_{1.5}CH_2CH_2CH_2SO_3H)_{0.5}$. A complete thermal decomposition of the organic moieties would leave only SiO_2 and result in a weight loss of 39%. The close agreement of this value to the experimental weight loss of 40% indicates a successful surfactant extraction.

For a detailed analysis of the mass peaks observed during the TGA we also measured the mercapto-functionalized comparative sample *SH-as* (Figure 2, c). Mass spectrometry allows us to identify the three main parts: in the first step up to 120 °C adsorbed water (mass number: 18) is evaporated. The second weight loss between 250 and 320 °C can be attributed to the cleavage of the carbon–sulfur bond of the mercaptopropyl group releasing SH_2 (34) and its oxidation products SO_2 (64) and water (18). In the third step between 330 and 405 °C the silicon–carbon bond cleaves releasing weight fragments of C_3H_5 (41), SH_2 (34), and their oxidation products SO_2 (64), water (18), and CO_2 (44). The long delay in the release of CO_2 up to 700 °C is explained by hydrocarbon species being trapped in inaccessible pores.

Among these samples, the surfactant extracted sample *B56-ex-m* (Figure 2, b) shows the highest weight loss and mass intensity of water (18) between 50–120 °C. This is attributed to the adsorbed water on the strongly hydrophilic pore surface of the sample. In contrast to the comparative sample, the second weight loss step with the release of SH_2 (34) is not observed. This indicates a successful oxidation of the mercapto group to sulfonic acid and demonstrates the advantage of direct synthesis over postsynthetic methods where it is usually not possible to achieve full oxidation.[29] The sample is thermally stable until around 230 °C when the carbon–sulfur bond of the propylsulfonic acid group is broken and SO_2 (64) is released. The next overlapping weight loss step starts at 300 °C, where the silicon–carbon bond breaks and C_3H_5 (41) and further SO_2 (64) are released.

The as-synthesized sample, *B56-as-m* (Figure 2, a), shows an additional weight loss starting at 120 °C that can be related to the decomposition of the polyoxyethylene chain of the surfactant by the mass peaks of CO_2 (44) and water (18). At around 250 °C the decomposition of the hydrocarbon part of the surfactant starts as indicated by a further increase in the mass numbers.

Structural Characterization

Nonionic surfactants were used as mesostructural templates in the sol–gel process. In a screening step films were prepared on glass slides by spin coating. The molar ratio of three different surfactants and the silica precursor was varied in the following ranges 0.047–0.285 (Brij-56), 0.020–0.117 (Sylanox 40-A80), and 0.005–0.034 (Pluronic P123).

XRD (Figure 3) shows sharp intense 01 diffractions for Brij-56 at *S* from 0.188 to 0.285, for Sylanox AS40 between 0.079 and 0.117, and for Pluronic P123 between 0.028 and 0.034. Interestingly, the *d*-spacing of the 01 plane gradually increases with increasing surfactant concentrations within these ranges. This can be explained by a more dense packing of the surfactant within the micellar rods that reduces the extent of shrinkage during drying.

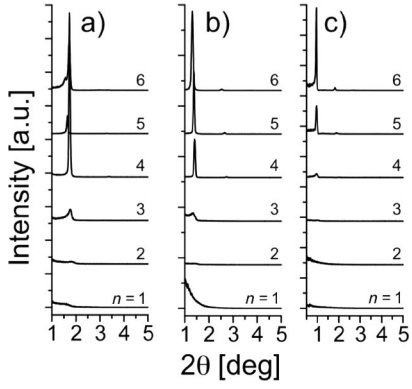

Figure 3. XRD diffraction patterns of sulfonic acid functionalized films templated with different surfactant molar ratios (a) Brij-56, $S = n \times 0.048$, (b) Sylanox 40-A80, $S = n \times 0.020$, (c) Pluronic P123, $S = n \times 0.0057$.

Free-standing films were prepared by molding in polystyrene or Teflon™ dishes with the optimized surfactant molar ratios of 0.188 (Brij-56), 0.079 (Sylanox 40-A80), and 0.034 (Pluronic P123, Figure 4), and showed analogue XRD patterns. The thickness can be varied between 50 and 300 μm by the amount of sol introduced into the mould. While the free-standing films usually crack into several pieces, fragments larger than 2 × 2 cm are easily obtained in all cases.

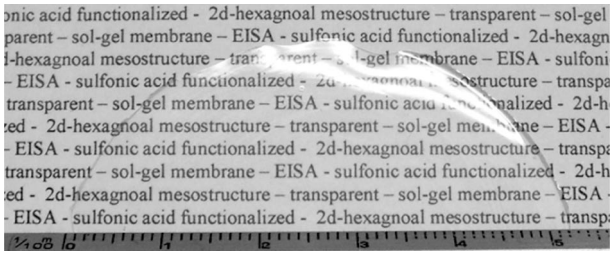

Figure 4. Photograph of *P123-as-m* (thickness 150 μm) with 2D-hexagonal mesostructure.

The mesostructure of films prepared by the EISA process is usually aligned with the most dense crystallographic plane parallel to the substrate plane.[34] This textural effect results in an intensity increase of the diffracted X-rays originating from this plane, whereas other orientations do not show any contribution to the diffraction pattern. In the case of a 2D-hexagonal mesostructure (with the unit cell as defined in Figure 5d) the 1D pattern observed on a standard Bragg–Brentano powder X-ray diffractometer only shows diffraction peaks originating from the 01 plane, which is parallel to the substrate.

This limitation can be overcome by the use of a 2D detector in a GI-SAXS setup (Figure 5). The presence of diffraction spots up to the third order indicates a high degree of long range order. From the diffraction pattern a distorted 2D-hexagonal mesostructure can be identified. The structure contraction is explained by the anisotropic shrinkage that occurs during the drying process preferentially in the direction perpendicular to the substrate plane. In a strict sense, this results in a reduction of symmetry from 2D-hexagonal (*p6 mm*) to 2D-centered rectangular (*c2 mm*), but for simplicity we will keep the 2D-hexagonal indexation. TEM (Figure 6) confirmed the distorted 2D-hexagonal mesostructure of the three samples. The images show a side view of the ordered channel structure with a viewing angle parallel to 01, 10 or equivalent diffraction planes.

In our previous studies we observed that a change in the volume ratio of silica to surfactant can result in the formation of different mesostructures,[35–37] which can be related to the phase diagram of the respective surfactant.[38] However, in this study the only observed mesostructure was (distorted) 2D-hexagonal. Molar ratios, for which other structures were expected, did not show any significant long range order.

The parallel orientation of the mesochannels to the substrate plane, as observed in this study, is obviously not desirable for application as a solid electrolyte membrane. However, such orientation is only observed on flat surfaces. Porous substrates, which could be a porous supporting matrix such as cellulose or silk as well as the electrode itself, would probably result in random channel orientations. A deliberate choice of surface structures such as conical holes may even give a perpendicular orientation of the 2D-hexagonal mesostructured channels.[39] Another way to overcome this alignment problem would be the use of interconnected 3D mesosphases, which may be accessed by additives[40,41] or drying induced phase transformations.[42–44]

As described above, effective surfactant extraction was achieved in ethanol. The samples described in this article

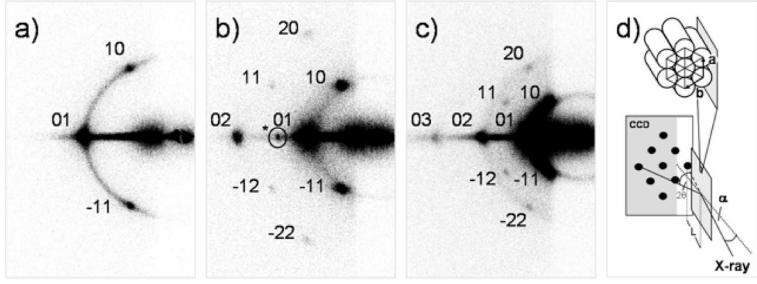

Figure 5. GI-SAXS diffraction pattern of sulfonic acid functionalized silica films: (a) *B56-as-f*, (b) *S40-as-f*, and (c) *P123-as-f*; the circle and the asterisk in (b) indicate a diffraction spot that is due to total reflection on the substrate surface followed by diffraction ($2\theta + 2\alpha$); (d) shows a schematic illustration of the GI-SAXS setup and the definition of the unit cell.

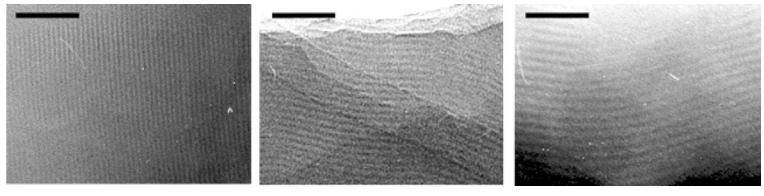

Figure 6. TEM images of scratched sulfonic acid functionalized mesostructured silica films templated with three different surfactants: left: *B56-as-f*, center: *S40-as-f*, and right: *P123-as-f*; scale bars 50 nm.

bear sulfonic acid groups on every third silicon atom. Thus, compared to nonfunctionalized silica films, reduced crosslinking and higher flexibility of the network are expected. However, GI-SAXS and XRD (Figure 7, d–g) analyses show that *S40-ex-f* and *B56-ex-f* still remain mesostructured even after removal of the surfactant. In the case of the sample *P123-ex-f* we were not able to measure a GI-SAXS pattern because the film was completely detached from the substrate.

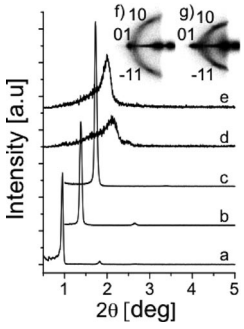

Figure 7. XRD patterns of (a) *P123-as-f*, (b) *S40-as-f*, (c) *B56-as-f*, (d) *S40-ex-f*, and (e) *B56-ex-f*; the inset shows the 2D GI-SAXS pattern of (f) *B56-ex-f* and (g) *S40-ex-f*; the intensities of d and e are multiplied by a factor of ten.

The XRD analysis of *S40-ex-f* and *B56-ex-f* (Figure 7d and e) shows that the degree of shrinkage varies significantly between these two samples. The *d*-spacing of the 01 plane of *B56-as-f* is reduced from 5.1 to 4.4 nm (14%), while *S40-as-f* shrank more than twice that much from 6.3 to 4.1 nm (35%). The decrease in intensity and the broadening of the diffractions in both samples indicates that the degree of order is reduced.

Proton Conduction and Ion Exchange Capacity

The conductivity is highly dependent on the presence of sulfonic acid groups and water. Titration of the acidity of the samples shows the amount of acid sites per gram (Table 1). These measured values are lower than the calculated amount of 6.8 mmol g^{-1} [for a fully condensed surfactant free sample of the applied composition "$(SiO_2)_1$-$(SiO_{1.5}CH_2CH_2CH_2SO_3\ H)_{0.5}$"]. This indicates that only about 30% of the sulfonic acid groups are accessible. However, when compared to Nafion membranes with 0.9 mmol g^{-1} the ion exchange capacity values are about 2.5 times higher and therefore high proton conductivity can be anticipated.

Table 1. Conductivity, ion exchange capacity (IEC), and water adsorption of as-synthesized and surfactant extracted samples.

Sample	H_2O adsorbed (60 °C/95%) [wt.-%]	IEC [mmol g^{-1}]	Conductivity (60 °C/95%) [S cm^{-1}]
B56-as-m	64	2.2	0.04
S40-as-m	68	1.9	0.09
P123-as-m	49	2.0	0.05
B56-ex-m	61	2.4	0.18
S40-ex-m	72	2.4	0.11
P123-ex-m	67	2.6	0.10

To control the humidity of the samples we applied saturated potassium sulfate salt solution that gives a relative humidity of 95% at 60 °C. The amount of water adsorbed on equilibrated samples used in the analysis was determined from the weight loss in the TGA after a holding time of one hour at 100 °C (Table 1).

Potentiostatic AC impedance measurements were performed to investigate the proton conduction of the as-synthesized and surfactant extracted samples. Because of the small thickness of the supported films and the high brittleness of the prepared membranes (especially in a high humidity atmosphere) we did not succeed in direct measurement. Thus, we had to use powdered samples in this investigation. However, we believe that for fuel cell applications, in which the electrolyte films may be deposited directly on the electrode surface or on porous supporting matrices, these practical problems could be easily overcome. The samples were equilibrated at 60 °C and 95% relative humidity for at least 48 h and pressed between two silver electrodes in a Teflon™ tube (2 mm diameter). In order to minimize surface effects at the electrode–sample interface we used small electrodes with diameters of 2 mm and high sample thickness of approximately 1 cm. Table 1 summarizes the conductivity values of the samples templated with the three different surfactants in as-deposited and surfactant extracted states. The as-synthesized samples showed high proton conductivities between 0.04 and 0.09 S cm^{-1}. After surfactant extractions these values are further improved to up to 0.18 S cm^{-1} making them highly competitive to commercially available Nafion membranes. Comparison of the different samples did not show a clear relation between proton conduction and channel size. However, it is important to realize that other factors such as the degree of mesostructural ordering also play an important role for the conduction mechanism. Therefore, the higher proton conduction of *B56-ex-m* may be explained by the better preservation of the mesostructure after the extraction process.

The conductivity values observed in this study are a significant improvement to materials of similar composition in the literature. The highest value reported for a sulfonic acid functionalized mesostructured silica reported so far is 0.2 S cm^{-1},[31] for a material prepared by hydrothermal synthesis using the ionic surfactant cetyltrimethylammonium bromide as a structure directing agent. However, this value was measured at 140 °C in 100% relative humidity (high pressure), whereas the value at 60 °C was less than 2×10^{-3} S cm^{-1}. Since they applied a similar ratio of MPTMS to TEOS in their experiments and measured similar ion exchange capacities (2.3 mmol g^{-1}), this improvement of two orders of magnitude has to be derived from the specific structure of the samples prepared by EISA. When water evaporates during the formation process, the hydrogen bonding interactions with the silica matrix are reduced. This results in phase separation of the hydrophilic polyoxyethylene groups and the silica matrix, which be-

comes more and more hydrophobic during the process. In this way the silica matrix rearranges to form a dense network without micropores.[45] When functionalized silica is used in an EISA process the same concept applies to the hydrophilic sulfonic acid groups. They will be directed to the inside of the mesochannels together with the hydrophilic polyoxyethylene groups of the surfactant to provide channels with a high density of sulfonic acid groups for increased proton conduction.

Conclusions

In conclusion, we have demonstrated a rapid one-step process for the formation of highly organized mesostructured functionalized supported and free-standing silica films, utilizing the EISA behavior of nonionic surfactants. The sulfonic acid functionalization was introduced by co-condensation of tetraethoxysilane with MPTMS (2:1) and in situ oxidation of the mercapto group by hydrogen peroxide. The mesostructural channel size was adjustable by the choice of different surfactants. The as-synthesized material showed a remarkable proton conductivity of up to 0.09 $S\,cm^{-1}$ (60 °C/95% relative humidity). Extraction of the surfactant increased the conductivity to up to 0.18 $S\,cm^{-1}$, but only supported films showed enough structural stability to survive the extraction process without cracking. Furthermore, its high ion exchange capacity of around 2.5 $mmol\,g^{-1}$ makes this material also interesting for application as a solid acid catalyst.

Experimental Section

Materials: Poly(ethylene oxide)-poly(propylene oxide)-poly(ethylene oxide) block copolymer (Pluronic-P123, $EO_{20}PO_{70}EO_{20}$), decaethylene glycol hexadecyl ether (Brij-56, $C_{16}EO_{10}$), and MPTMS were supplied by Aldrich. TEOS and ethanol (99.5%) were obtained from Wako chemicals. The lubricant Sylanox 40-A80 ($EO_{17}PO_{12}C_{14}$) was kindly donated by Dow Chemicals.

Sol Preparation: TEOS (61 g) was prehydrolyzed in a solution of ethanol (61 g, 99.5%) and dilute hydrochloric acid (5 mL, 0.07 N) at 60 °C for 90 min. The solution was cooled and stored at –20 °C. A portion of this stock solution (20 g) was combined with EtOH (14.5 g, 99.5%), HCl (0.35 g, 1 N), MPTMS (4.48 g), and hydrogen peroxide (5.36 g, 50%). The solution was stirred for one hour at room temperature with a magnetic Teflon™-coated stirrer bar at 500 RPM. During that time the temperature initially increased to about 50 °C but reached room temperature again after 60 min.

A comparative sample containing a mercapto functionality instead of sulfonic acid was prepared following the same procedure but replacing the hydrogen peroxide (50%, 5.36 g) with water (4.19 g).

Mesostructured Films: The surfactants were dissolved in the above prepared sol to obtain molar compositions of TEOS/MPTMS/Surfactant/H_2O_2/H_2O/HCl/EtOH = 1:0.5:*S*:1.73:5:0.0082:11.7. The molar ratio, *S*, of the surfactant was varied in the following ranges: 0.047< Brij-56 < 0.285, 0.020 < Sylanox 40-A80 < 0.117, and 0.0056< Pluronic P123 < 0.034. For example, highly ordered 2D-hexagonally structured films were produced from compositions of the sol (15 g) mixed with Brij-56 (2 g), Sylanox 40-A80 (2 g), or Pluronic-P123 (2.9 g) surfactant. Films were obtained by spin coating on glass substrates at 6000 rpm for 30 s. They were dried at room temperature for 24 h followed by aging at 60 °C for 6 h. Surfactant extraction was performed by immersing the films in EtOH at 60 °C for 24 h. Free-standing films were prepared by molding in polystyrene or Teflon™ dishes. The thickness of the films can be adjusted between 50 and 300 μm by the volume of sol used in the preparation. The dishes were partially covered to allow slow evaporation of the volatile compounds over a period of 2–3 d. The dry films were then aged at 60 °C for 6 h.

Low Angle XRD: Bragg–Brentano XRD measurements of supported and free-standing films were carried out with a MAC M03xHF22 (Bruker AXS) instrument using Cu-K_α radiation with an acceleration voltage of 40 kV and a current of 30 mA. The typical diffraction pattern was recorded between 1 and 5° (2θ) with a step size of 0.004° and a scan rate of $1°\,min^{-1}$.

GI-SAXS: GI-SAXS measurements were performed with a Bruker Nanostar with a Vantec 2000 detector (gas detector with microgap technology) and a sample to detector distance *L* of 111 cm. A rotating copper anode was used as a radiation source (wavelength 0.1542 nm). The primary beam was shielded with a beam stopper. Samples were aligned vertically at an incident angle α of 0.3° with respect to the beam (Figure 5d). The detector was calibrated with silver behenate as a reference standard. *d*-spacings were determined from the diffraction spots by analysis of the scattering pattern with the FIT2D software (A. P. Hammersley/ESRF).

TEM: TEM was performed with a JEOL JEM-2000EXII instrument. The samples were scratched from the films deposited on glass and applied directly to copper microgrids.

FTIR: FTIR Spectroscopy was performed with a Nicolet Magna IR-560 spectrometer. Samples were prepared by mixing 5 mg of powder (scratched from glass slides) with 200 mg of KBr in a mortar. Pellets of 1.2 cm diameter were obtained by pressing the powders at a pressure of 40 kN.

TGA-DTA-MS: Coupled TGA, DTA, and mass spectrometry was performed with a Rigaku TG 8120 Thermo Plus instrument with a ANELVI MOA200TS Quadruple Mass Spectrometer with a heating rate of $10\,K\,min^{-1}$. An 80/20 He/O_2 gas mixture was used as a carrier gas to simulate ambient atmosphere with minimum contamination of other gases.

Impedance Analysis: Electrochemical impedance analysis was performed with a Princeton VersaSTAT3 in the frequency range of 10 to 10^6 Hz. Samples were equilibrated at 60 °C and 95% relative humidity for at least 48 h. The powders were pressed (ca. 10 kN) between two silver electrodes of 2 mm diameter in a Teflon™ tube of 2 mm inner diameter. Contact with the electrodes was ensured by a spring. Data were analyzed with ZView software (Scribner Associates). The specific conductivity was calculated according to the formula $\sigma = (1/R)(L/A)$, where *R* is the resistance corresponding to the phase angle closest to zero at the low frequency end of the semicircle in the Nyquist plot, *L* the thickness of the sample between the electrodes, and *A* the cross-sectional contact area of the electrodes.

Ion Exchange Capacity (IEC): The scratched film samples (10 mg) were suspended in NaOH solution (5 mL, 0.01 N). The ion exchange capacity was determined by back titration to the neutral point with HCl (0.01 N).

Acknowledgments

The financial support of the Austrian Science Fund (FWF) project no. J2688 is greatly acknowledged. TEM was conducted at the Cen-

ter for Nano Lithography and Analysis, The University of Tokyo, supported by the Ministry of Education, Culture, Sports, Science and Technology (MEXT), Japan. We thank Takeo Yamaguchi and Taichi Ito for stimulating discussion and support. The donation of product samples by DOW chemicals is kindly acknowledged.

[1] J. S. Beck, J. C. Vartuli, W. J. Roth, M. E. Leonowicz, C. T. Kresge, K. D. Schmitt, C. T. W. Chu, D. H. Olson, E. W. Sheppard, *J. Am. Chem. Soc.* **1992**, *114*, 10834–10843.
[2] T. Yanagisawa, T. Shimizu, K. Kuroda, C. Kato, *Bull. Chem. Soc. Jpn.* **1990**, *63*, 988–992.
[3] K.-D. Kreuer, S. J. Paddison, E. Spohr, M. Schuster, *Chem. Rev.* **2004**, *104*, 4637–4678.
[4] S. Mikhailenko, D. Desplantier-Giscard, C. Danumah, S. Kaliaguine, *Microporous Mesoporous Mater.* **2002**, *52*, 29–37.
[5] F. Pereira, K. Valle, P. Belleville, A. Morin, S. Lambert, C. Sanchez, *Chem. Mater.* **2008**, *20*, 1710–1718.
[6] M. Aparicio, E. Lecoq, Y. Castro, A. Duran, *J. Sol-Gel Sci. Technol.* **2005**, *34*, 233–239.
[7] Y.-F. Lin, C.-Y. Yen, C.-C. M. Ma, S.-H. Liao, C.-H. Lee, Y.-H. Hsiao, H.-P. Lin, *J. Power Sources* **2007**, *171*, 388–395.
[8] R. Marschall, I. Bannat, J. Caro, M. Wark, *Microporous Mesoporous Mater.* **2007**, *99*, 190–196.
[9] I. K. Mbaraka, B. H. Shanks, *J. Catal.* **2006**, *244*, 78–85.
[10] Y.-F. Feng, X.-Y. Yang, Y. Di, Y.-C. Du, Y.-L. Zhang, F.-S. Xiao, *J. Phys. Chem. B J. Phys. Chem.* **2006**, *110*, 14142–14147.
[11] M. Alvaro, A. Corma, D. Das, V. Fornes, H. Garcia, *J. Catal.* **2005**, *231*, 48–55.
[12] J. A. Melero, G. Vicente, G. Morales, M. Paniagua, J. M. Moreno, R. Roldan, A. Ezquerro, C. Perez, *Appl. Catal. A* **2008**, *346*, 44–51.
[13] W. Van Rhijn, D. De Vos, W. Bossaert, J. Bullen, B. Wouters, P. Grobet, P. Jacobs, *Stud. Surf. Sci. Catal.* **1998**, *117*, 183–190.
[14] W. M. Van Rhijn, D. E. De Vos, B. F. Sels, W. D. Bossaert, P. A. Jacobs, *Chem. Commun.* **1998**, 317–318.
[15] J. A. Melero, R. van Grieken, *Leading Edge Catal. Res.* **2005**, 129–164.
[16] D. Dube, M. Rat, F. Beland, S. Kaliaguine, *Microporous Mesoporous Mater.* **2008**, *111*, 596–603.
[17] J. Yang, Q. Yang, G. Wang, Z. Feng, J. Liu, *J. Mol. Catal. A* **2006**, *256*, 122–129.
[18] S. Shylesh, S. Sharma, S. P. Mirajkar, A. P. Singh, *J. Mol. Catal. A* **2004**, *212*, 219–228.
[19] J. A. Melero, R. van Grieken, G. Morales, V. Nuno, *Catal. Commun.* **2004**, *5*, 131–136.
[20] J. A. Melero, R. Van Grieken, G. Morales, M. Paniagua, *Energy Fuels* **2007**, *21*, 1782–1791.
[21] R. van Grieken, J. A. Melero, G. Morales, *Appl. Catal. A* **2005**, *289*, 143–152.
[22] M. H. Lim, C. F. Blanford, A. Stein, *Chem. Mater.* **1998**, *10*, 467–470.
[23] G. L. Athens, Y. Ein-Eli, B. F. Chmelka, *Adv. Mater.* **2007**, *19*, 2580–2587.
[24] Q. Yang, M. P. Kapoor, N. Shirokura, M. Ohashi, S. Inagaki, J. N. Kondo, K. Domen, *J. Mater. Chem.* **2005**, *15*, 666–673.
[25] V. Dufaud, E. D. Mark, *J. Am. Chem. Soc.* **2003**, *125*, 9403–9413.
[26] K. Wilson, A. F. Lee, D. J. Macquarrie, J. H. Clark, *Appl. Catal. A* **2002**, *228*, 127–133.
[27] J. A. Melero, G. D. Stucky, R. van Grieken, G. Morales, *J. Mater. Chem.* **2002**, *12*, 1664–1670.
[28] J. A. Melero, R. Van Grieken, G. Morales, *Chem. Rev.* **2006**, *106*, 3790–3812.
[29] D. Margolese, J. A. Melero, S. C. Christiansen, B. F. Chmelka, G. D. Stucky, *Chem. Mater.* **2000**, *12*, 2448–2459.
[30] R. van Grieken, J. A. Melero, G. Morales, *Stud. Surf. Sci. Catal.* **2002**, *142B*, 1181–1188.
[31] R. Marschall, J. Rathousky, M. Wark, *Chem. Mater.* **2007**, *19*, 6401–6407.
[32] H. Li, T. Kunitake, *Chem. Lett.* **2006**, *35*, 640–641.
[33] C. J. Brinker, Y. Lu, A. Sellinger, H. Fan, *Adv. Mater.* **1999**, *11*, 579–585.
[34] D. Grosso, F. Cagnol, G. J. D. A. A. Soler-Illia, E. L. Crepaldi, H. Amenitsch, A. Brunet-Bruneau, A. Bourgeois, C. Sanchez, *Adv. Funct. Mater.* **2004**, *14*, 309–322.
[35] R. Supplit, N. Huesing, S. Gross, S. Bernstorff, M. Puchberger, *Eur. J. Inorg. Chem.* **2007**, 2797–2802.
[36] R. Supplit, N. Huesing, H. Bertagnolli, M. Bauer, V. Kessler, G. A. Seisenbaeva, S. Bernstorff, S. Gross, *J. Mater. Chem.* **2006**, *16*, 4443–4453.
[37] R. Supplit, N. Huesing, C. Fritscher, P. Jakubiak, V. G. Kessler, G. A. Seisenbaeva, S. Bernstorff, *Mater. Res. Soc. Symp. Proc.* **2005**, *847*, 177–182.
[38] P. C. A. Alberius, K. L. Frindell, R. C. Hayward, E. J. Kramer, G. D. Stucky, B. F. Chmelka, *Chem. Mater.* **2002**, *14*, 3284–3294.
[39] Y. Yamauchi, T. Nagaura, A. Ishikawa, T. Chikyow, S. Inoue, *J. Am. Chem. Soc.* **2008**, *130*, 10165–10170.
[40] S. P. Naik, W. Fan, T. Yokoi, T. Okubo, *Langmuir* **2006**, *22*, 6391–6397.
[41] S. P. Naik, T. Yokoi, W. Fan, Y. Sasaki, T.-C. Wei, H. W. Hillhouse, T. Okubo, *J. Phys. Chem. B* **2006**, *110*, 9751–9754.
[42] M. Ogura, H. Miyoshi, S. P. Naik, T. Okubo, *J. Am. Chem. Soc.* **2004**, *126*, 10937–10944.
[43] M. Ogura, H. Miyoshi, Y. Suzuki, S. Yamakita, T. Okubo, *Zeoraito* **2005**, *22*, 2.
[44] S. P. Naik, M. Ogura, H. Sasakura, Y. Yamaguchi, Y. Sasaki, T. Okubo, *Thin Solid Films* **2005**, *495*, 11–17.
[45] K. Yu, B. Smarsly, C. J. Brinker, *Adv. Funct. Mater.* **2003**, *13*, 47–52.

Received: March 15, 2010
Published Online: July 21, 2010

DOI: 10.1002/ejic.201000358

Helical Nanostructures of an Optically Active Metal-Free Porphyrin with Four Optically Active Binaphthyl Moieties: Effect of Metal–Ligand Coordination on the Morphology

Jitao Lu,[a] Lizhen Wu,[a] Jianzhuang Jiang,*[a,b] and Xiaomei Zhang*[a]

Keywords: Chirality / Porphyrinoids / Self-assembly / Optical activity / Nanostructures

An optically active metal-free porphyrin (**1**) with four chiral binaphthyl units attached at the *meso*-phenyl substituents through crown ether moieties has been designed, synthesized, and characterized. Its self-assembly behavior in the absence and presence of K^+ was comparatively investigated by electronic absorption and circular dichroism (CD) spectra, transmission electron microscopy (TEM), scanning electron microscopy (SEM), atom force microscopy (AFM), and energy-dispersive X-ray (EDX) spectroscopy. In the absence of K^+, metal-free porphyrin self-assembles into nanoparticles depending mainly on the van der Waals interaction among neighboring metal-free molecules. In the presence of K^+, additionally formed metal–ligand K–O_{crown} coordination bonds between K^+ and crown units of (*R*)- and (*S*)-**1** molecules, together with chiral discrimination of chiral side chains and intermolecular van der Waals interactions, induce a right-handed and left-handed helical arrangement in a stack of (*R*)- and (*S*)-**1** molecules, respectively, with an ordered "head-to-tail" internal molecular arrangement. This then further hierarchically self-assembles into highly ordered fibrous nanostructures with a helicity opposite to that of the original porphyrin stack. This clearly reveals the effect of the metal–ligand coordination bonding interaction on the morphology and handedness of self-assembled nanostructures.

Introduction

Nature is amazing when it comes to being able to create various kinds of functional architectures with a preferred helicity, such as DNA with a double-helix structure and motifs in protein with an α-coiled helical structure.[1] Inspired by the elegance of fascinating biological supramolecular structures, numerous artificial assemblies that comprise helical fibers and twisted ribbons of sugars,[2] helicenes,[3] metal complexes,[4] optically active π-conjugated systems,[5] and chiral block copolymers[6] have been fabricated with the assistance of noncovalent interactions such as hydrogen bonding, metal–ligand coordinate bonding, electrostatic interactions, van der Waals forces, and π–π stacking.

As one of the most important typical representative of π-conjugated systems, porphyrin compounds have been intensively studied over the past century due to their wide range of biological relevance and industrial applications.[7] In recent years, the self-assembly behavior and nanostructures of porphyrin compounds have attracted extensive research interest with an eye toward the construction of molecular-based electronic and optical devices such as electronic wires, switches, electroluminescence devices, field-effect transistors, and photovoltaic devices.[8] Hollow capsules with potential applications as drug-delivery agents were fabricated from a designed amphiphilic porphyrin compound.[9] Monomer, trimer, tetramer, and extended wirelike nanostructures were produced from a cyano-substituted porphyrin on a gold surface.[10] Very recently, the successful tuning control over the morphology of self-assembled nanostructures of porphyrin derivatives has been achieved by means of molecular design and synthesis through the introduction of metal–ligand coordination or hydrogen-bonding interactions according to this group.[11] Among these extensive investigations, great effort has been paid to the construction of helical supramolecular architectures with both achiral and, in particular, chiral porphyrin precursors due to their great potential applications.[11–15] This resulted in the synthesis of a large number of chiral porphyrins that contain different stereocenters such as chiral amino acids and chiral hydrocarbons. Nevertheless, some investigations have indicated that installing stereocenters into the periphery of a porphyrin molecule merely provides a possibility for the fabrication of helical supramolecular structures instead of ensuring it outright. Actually, quite a small fraction of nanostructures fabricated from porphyrin compounds with peripheral substituents that contain stereocenters exhibit helicity on the nanoscale.[16] In fact, some porphyrin compounds that bear peripheral chiral substituents with stereocenters that are even circular dichroism

[a] Department of Chemistry, Shandong University, Jinan 250100, China
E-mail: jianzhuang@ustb.edu.cn
[b] Department of Chemistry, University of Science and Technology Beijing, Beijing 100083, China
E-mail: jianzhuang@ustb.edu.cn

Supporting information for this article is available on the WWW under http://dx.doi.org/10.1002/ejic.201000358.

(CD) active at the supramolecular level do not display helical nanostructures, probably due to the lack of long-range molecular ordering as a result of the weak intermolecular interactions.[17] The delicate balance between noncovalent interactions and chiral discrimination during the self-assembly process therefore appears to play an important role in the fabrication of helical supramolecular nanostructures. This is indeed exemplified by the double-stranded helixes that have been fabricated from porphyrins decorated with optically active BisPYBOX [PYBOX = 2,6-bis(2-oxazolyl)-pyridine] units in the presence of oligomers that have two or three secondary dialkylammonium cations.[17b] However, synergistic interplay among noncovalent interactions and chiral discrimination during the self-assembly process and its effect on the morphology and dimension of nanostructures formed from porphyrin compounds still remains poorly understood.

It is well known that the significant absorption over the ultraviolet and visible region of porphyrin derivatives renders it possible to investigate the self-assembly process of these tetrapyrrole compounds, in particular chiral porphyrins, by means of electronic absorption and CD spectroscopy. However, at the molecular level quite a large number of porphyrins with peripheral subsitutents containing stereocenters do not display any circular dichroism signal in the whole absorption range of porphyrins. This is due to the weak perturbation of the central porphyrin core by the peripheral substituents with chiral stereocenters.[18] In this paper, we describe the synthesis and characterization of a novel optically active metal-free porphyrin. Optically active binaphthyl units were introduced onto the porphyrin periphery to enhance the asymmetric perturbation (Scheme 1). The self-assembly properties of this metal-free porphyrin were also comparatively studied. In the absence of K^+, both enantiomers of this optically active metal-free porphyrin self-assemble into nanoparticles. However, with the assistance of K^+, additional metal–ligand K–O_{crown} coordination bonds formed between K^+ and the crown moieties of the (*R*)- and (*S*)-**1** molecules, together with chiral discrimination of chiral side chains, induce a right-handed and left-handed helical arrangement in a stack of (*R*)- and (*S*)-**1** molecules with an ordered "head-to-tail" internal molecular arrangement, respectively, which then further hierarchically self-assembles into highly ordered fibrous nanostructures with the opposite helicity to the stack. This reveals the effect of the metal–ligand coordination bonding interaction on the morphology and handedness of self-assembled nanostructures. The results will be helpful in providing new insight into chiral information transfer and the expression of synthetic conjugated systems on the supramolecular level.

Results and Discussion

Synthesis and Characterization of Optically Active Metal-Free Porphyrin Enantiomers (*R*)- and (*S*)-1

To enhance the asymmetric perturbation to the porphyrin chromophore, optically active binaphthyl units were chosen to be attached onto the porphyrin ring through *meso*-attached benzene, thereby resulting in the target metal-free porphyrin enantiomers (*R*)- and (*S*)-**1** (Scheme 1). Meanwhile, crown ether substituents were also introduced between *meso*-attached benzene substituents and binaphthyl units, which were expected to provide an additional opportunity to tune the morphology and dimension of aggregates based on the formation of additional coordination bonding interactions between the crown ether units and the added K^+ ion. The metal-free porphyrin enantiomers (*R*)- and (*S*)-**1** were prepared from (*R*)/(*S*)-2,2′-dihydroxy-1,1′-binaphthyl derivatives **6**. As shown in Scheme 1, (*R*)-/(*S*)-**6** were obtained from the Williamson ether synthesis reaction between (*R*)-/(*S*)-2,2′-dihydroxy-1,1′-binaphthyl and 3,4-bis{2′-[2′′-(*p*-tolylsulfonyloxy)-ethoxy]ethoxy}benzaldehyde (**5**) generated from an aromatic nucleophilic substitution reaction and tosylation re-

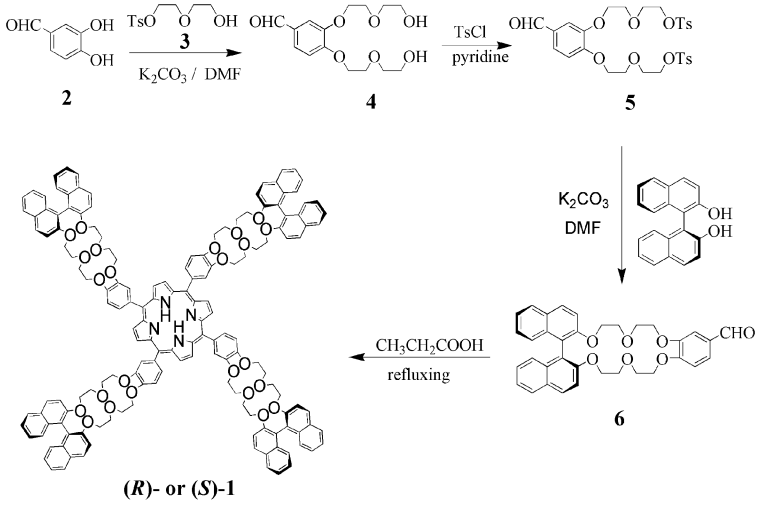

Scheme 1. Synthesis of optically active metal-free porphyrin enantiomers (*R*)- and (*S*)-(**1**).

action of 3,4-dihydroxybenzaldehyde. Then treatment of binaphthyl derivatives **6** in propionic acid, heated to reflux, with pyrrole led to the isolation of optically active metal-free porphyrin enantiomers (*R*)- and (*S*)-**1** in good yields. In line with the previous results, racemization of the corresponding optically active compounds at each reaction step under the depicted reaction conditions did not occur.[19] Satisfactory elemental analysis results were obtained for the newly prepared metal-free porphyrin enantiomers of **1** after purification through column chromatography followed by repeated recrystallization from chloroform/methanol (it is worth noting that the purple crystalline solid of **1** contains 0.5 equiv. solvated $CHCl_3$). The compound was further characterized by MALDI-TOF mass and ^1H NMR spectroscopic methods (Figures S1 and S2 in the Supporting Information). The MALDI-TOF mass spectrum of the compound clearly shows an intense signal for the protonated molecular ion $[M + H]^+$. The isotopic pattern closely resemble the simulated one, as shown in Figure S2. This compound was also characterized by electronic absorption and IR spectroscopy.

Electronic Absorption and CD Spectroscopy

The electronic absorption and circular dichroism spectra of the metal-free porphyrin derivatives (*R*)- and (*S*)-**1** in chloroform are shown in Figure 1. As can be seen from Figure 1B, similar to other metal-free porphyrins, compound **1** shows a typical molecular electronic absorption spectrum with the Soret band at 421 nm and Q bands at 511, 547, 582, and 637 nm, thereby revealing the nonaggregated molecular spectroscopic nature of the compound in $CHCl_3$. An intense band below 270 nm is also observed, which can be attributed to the absorption of binaphthyl groups with evidence by the observation of the corresponding CD signal in the same region for either (*R*)-**1** or (*S*)-**1** in their CD spectra (Figure 1A).[20] As clearly shown in the CD spectra of (*R*)- and (*S*)-**1**, the introduction of the optically active binaphthyl moieties through the crown ether unit onto the *meso*-attached phenyl groups of the porphyrin ring induces the appearance of CD signals of the porphyrin ligand in both the Soret and Q absorption regions (Figure 1A); this indicates an effective chiral information transfer from the optically active binaphthyl moieties to the porphyrin chromophore at the molecular level. In detail, in the case of (*S*)-**1**, the sign of the circular dichroism is negative over almost the entire Soret and Q bands, whereas conversely (*R*)-**1** shows a positive circular dichroism sign. According to the chiral exciton theory, (*S*)-**1** is right-handed, whereas (*R*)-**1** is left-handed on the basis of the circular dichroism pattern in the range of 250–270 nm. It is noteworthy that, despite the optically active binaphthyl groups being linked remotely to the porphyrin core, the circular dichroism intensity of **1** at the porphyrin Soret band [$\Delta\varepsilon$ = –3.0727 (λ = 421 nm, $c = 2\times10^{-6}$ mol L^{-1} in $CHCl_3$)] is not weaker than that of other optically active porphyrin derivatives,[21] thereby indicating the relatively stronger chiral perturbation of the optically active binaphthyl groups, which are believed to play important roles in the construction of helical nanostructures.

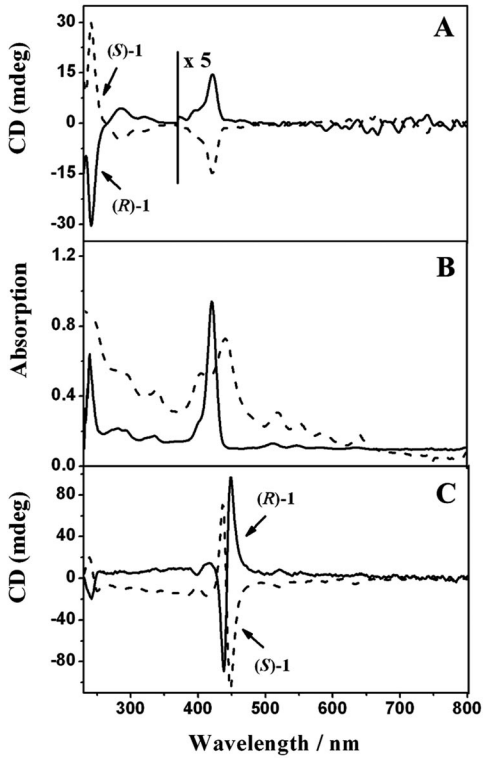

Figure 1. Circular dichrorism (CD) spectra of (*S*)- and (*R*)-**1** (A) as a dilute solution in chloroform and (C) their nanostructures formed in the presence of potassium ions dispersed in methanol. (B) Electronic absorption spectra of a dilute solution of metal-free porphyrin **1** in chloroform (solid line) and its nanostructures formed in the presence of potassium ions dispersed in methanol (dashed line).

The electronic absorption and circular dichroism spectra of the aggregates formed from (*R*)- and (*S*)-**1** in *n*-hexane in the absence and presence of potassium ions are also recorded and shown in Figures 1 and S3 (in the Supporting Information), respectively, which are different from the spectra of the corresponding compounds in $CHCl_3$. As shown in Figure S3A, in comparison with the electronic absorption spectra of homogeneous solutions of (*R*)- and (*S*)-**1** in chloroform, when (*R*)- and (*S*)-**1** self-assemble into aggregates, both the Soret and Q bands for (*R*)-**1** or (*S*)-**1** lose their intensity in the aggregate phase. In particular, the Soret band shifts to a longer wavelength with a maximum at 432 nm, and the Q band redshifts to 518, 553, 584, and 643 nm in *n*-hexane. In contrast, addition of K^+ induces further redshift for the porphyrin Soret band during the self-assembly process of **1**, with a maximum at 441 nm and a shoulder around 404 nm. This reveals the further enhanced intermolecular interaction due to the additionally introduced metal–ligand coordination bonds between crown ether units and K^+. The porphyrin Q absorption is redshifted to 518, 550, 582, and 638 nm. On the basis of Kasha's exciton theory,[22] redshifts in the main absorption

bands of compound **1** upon aggregation with and without the presence of K^+ reveals that the porphyrin molecules self-assemble into the *J* aggregates with a head-to-tail molecular arrangement in their nanostructures. However, observation of a larger degree of the redshift in the main electronic absorptions for (*R*)-**1** and (*S*)-**1** upon aggregation in the presence of K^+ indicates a stronger intermolecular interaction in the direction parallel to the porphyrin ring than in the aggregates formed in the absence of K^+ due to the formation of additional metal–ligand coordination bonds. These are expected to improve the chiral discrimination between adjacent porphyrin molecules, thus resulting in the formation of nanostructures with helicity. This was indeed verified by their circular dichroism spectroscopic and electronic microscopic results as detailed below.

In the circular dichroism spectra of aggregates fabricated from (*R*)- and (*S*)-**1** in the absence of K^+ (Figure S3A in the Supporting Information), both porphyrin enantiomers experience a similar intensity decrease in almost the whole Soret and Q regions upon aggregation. Nevertheless, no Cotton effect was observed in the circular dichroism spectra of (*R*)-**1** or (*S*)-**1** aggregates, thereby indicating the lack of effective chiral discrimination between the porphyrin molecules during the self-assembly process. However, perfect mirroring bisignate Cotton effect is observed with a zero crossing at 441 nm that is close to the absorption maximum (Figure 1C). According to the semiempirical method developed by Nakanishi and co-workers,[23] the sign of the coupling and the direction of dipole moments can be used to determine the chirality of stacked porphyrin molecules in aggregates. In general, the circular dichroism spectrum that features a bisignate Cotton effect showing positive features at longer wavelengths and negative ones at shorter wavelengths would indicate right-handed chirality of the dipole moments (positive chirality), whereas the opposite would be true for left-handed chirality (negative chirality). In the present case, the negative chirality of (*S*)-**1** aggregates corresponds to a left-handed stacking and the positive chirality of (*R*)-**1** aggregates indicates a right-handed stacking of chiral metal-free porphyrin molecules in aggregates. The formation of the supermolecular helicity, observed from the circular dichroism spectrum, is unequivocally confirmed by atom force microscopy (AFM) analysis of the (*R*)-**1** or (*S*)-**1** aggregates as detailed below.

Aggregate Morphology

The morphology of the aggregates formed was examined by transmission electron microscopy (TEM), scanning electron microscopy (SEM), and AFM. Samples were prepared by casting a drop of sample solution onto a carbon-coated grid. In line with the electronic absorption result, different morphologies were observed for nanostructures formed in the presence and absence of potassium ions. Figure 2A displays a large-area SEM image of nanostructures fabricated from (*R*)-**1** in the absence of potassium ions. As can be seen, spherical particles with an average radius of approximately 500 nm were formed from (*R*)-**1**. This is also true for (*S*)-**1**. A statistical analysis, conducted by measuring over 200 particles in this SEM image, indicated that the particles are quite uniform in dimension (Figure 2B). AFM was also used to evaluate the integrity of these nanoparticles on silica in the absence of solvent (Figure 2C), thereby showing that the height of these nanoparticles is in the range of 450–550 nm. This result is in good agreement with that observed by SEM.

Contrary to the self-assembly of metal-free porphyrin in the absence of K^+, both (*R*)- and (*S*)-**1** self-assemble into fibrous nanostructures with nanometer-sized diameter and micrometer-sized length in the presence of K^+ (Figure 3A and B). These fibrous nanostructures consist of bundles of single twisted strands, as clearly revealed by the magnified TEM image (Figure 3a). Further inspection with AFM indicates that these fibrous nanostructures with left- and right-handed helicity were formed from (*R*)- and (*S*)-**1** enantiomers, respectively, which are clearly revealed by two high-magnification AFM images chosen simultaneously from (*R*)- and (*S*)-**1** aggregates (Figure 3C and D). Careful analysis of a single fibrous nanostructure fabricated from (*R*)- and (*S*)-**1** enantiomers shows the average helical pitch to be about 125 nm with an angle (the angle of the groove with respect to the main fiber axis) of about 46°. It is worth noting that, as mentioned above, the circular dichroism spectroscopic results demonstrate that a right-handed and a left-handed helical arrangement was formed from (*R*)- and (*S*)-**1**, respectively, in a stack of the metal-free porphyrin molecules in aggregates. However, according to the AFM results, observation of nanostructures with opposite helicity to the stack fabricated from either the (*R*)- or the

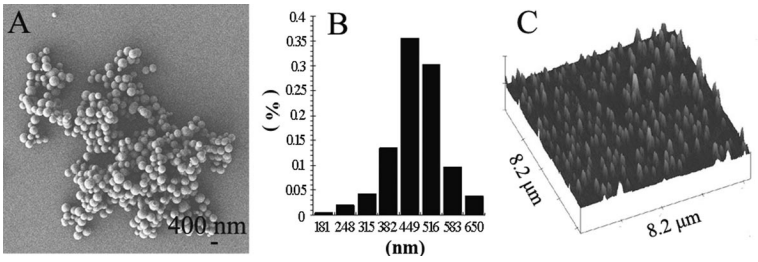

Figure 2. TEM and SEM images of nanostructures fabricated from optically active metal-free porphyrin **1** in the absence of K^+. (A) TEM image of nanoparticles formed from optically active metal-free porphyrin **1** in the absence of potassium ions. (B) Diameter distribution of nanoparticles. (C) Topographic AFM image of nanoparticles on silica.

(*S*)-**1** enantiomer clearly reveals the hierarchical self-assembly nature of this compound. In detail, the (*R*)-**1** molecules first self-assemble into one-dimensional right-handed helices with positive chirality depending on the synergistic interplay of intermolecular van der Waals interactions, additionally introduced metal–ligand coordination bonding, and chiral discrimination among neighboring porphyrin molecules, which, acting as elementary building blocks, further stack into highly ordered fibrous nanostructures with left-handed helicity (Figure 3C). In the case of the (*S*)-**1** enantiomer, the left-handed helices with negative chirality are formed at the first stage of aggregation and then stack into highly ordered nanofibers with right-handed helicity (Figure 3D).

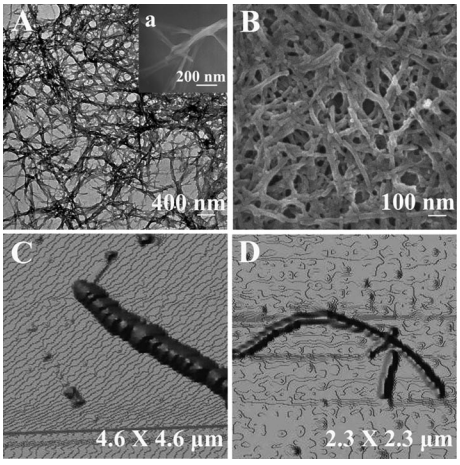

Figure 3. TEM, SEM, and topographic AFM images of nanostructures fabricated from optically active metal-free porphyrin **1** in the presence of K^+. (A) TEM image of nanostructures formed from optically active metal-free porphyrin **1** in the presence of potassium ions; (a) high-magnification TEM image of metal-free porphyrin **1** in the presence of K^+, which shows the nanostructures being formed by several fibers together. (B) SEM image of nanostructures formed from optically active metal-free porphyrin **1** in the presence of potassium ions. (C) AFM height image of a single left-handed fibrous nanostructure fabricated from (*R*)-**1**; (D) AFM height image of a single right-handed fibrous nanostructure fabricated from (*S*)-**1**.

Energy-Dispersive X-ray (EDX) Spectroscopy

To understand the role of potassium ions in the formation of nanofibers, EDX spectroscopy was used to detect the composition of the sample. Observation of the elemental signature for C, N, and O atoms in the EDX spectrum of the nanostrucutres fabricated from (*R*)- or (*S*)-**1** in the presence and absence of K^+ (Figure 4A and B) confirms the composition of nanoparticles and nanofibers from porphyrin derivative **1**. In addition, observation of the elemental signature for the potassium atom in addition to C, N, and O atoms in the EDX spectra of (*R*)- or (*S*)-**1** aggregates formed in the presence of K^+ (Figure 4A) indicates the existence and the coordination role of K^+ during the self-assembly process of the optically active porphyrin **1** enantiomers in the presence of K^+.

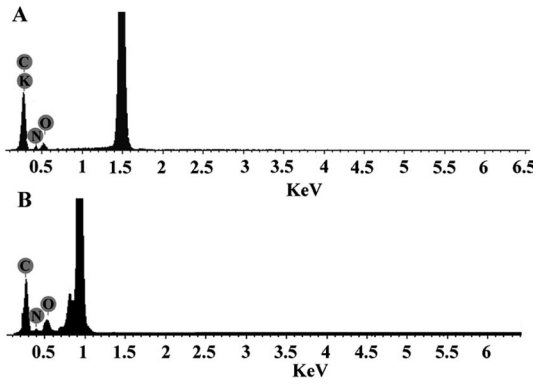

Figure 4. EDX spectrum of (A) nanostructures formed from optically active metal-free porphyrin **1** in the presence of potassium ions and (B) nanostructures formed from optically active metal-free porphyrin **1** in the absence of potassium ions.

X-ray Diffraction Patterns

The internal structure of self-assembled nanostructures was further investigated by X-ray diffraction (XRD) techniques (Figure 5). As can be seen from Figure 5A, in the absence of K^+, there exists no diffraction peak in the X-ray diffraction pattern of the nanoparticles self-assembled from metal-free porphyrin **1**, thereby indicating a lack of ordered molecular packing in this nanostructure due to the lack of effective intermolecular π–π interaction. In contrast, three broad diffraction peaks at 2θ = 1.26° (corresponding to 7.01 nm), 1.96° (4.51 nm), and 2.50° (3.53 nm) were observed in the X-ray diffraction pattern of the nanostructures fabricated from **1** in the presence of K^+, thereby indicating regular molecular stacking (Figure 5B). These peaks are ascribed to the refractions from the (001), (010), and (002) planes, respectively. On the basis of the geometry optimization and energy-minimized molecular structure of porphyrin **1** with the Gaussian 98 program at the B3LYP/6-31G(d) level,[24] the molecular dimensional size is 3.2 nm (length) × 4.5 nm (diagonal length) (Figure 5C). According

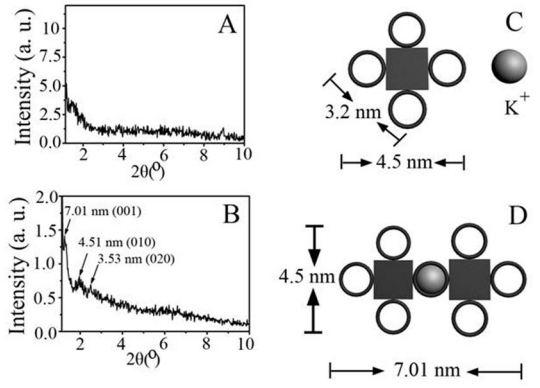

Figure 5. (A) XRD profile of the nanostructures fabricated from metal-free porphyrin **1** in the absence of K^+. (B) XRD profile of the nanostructures fabricated from metal-free porphyrin **1** in the presence of K^+. (C) Schematic representation of a metal-free porphyrin **1** molecule and K^+. (D) Schematic representation of a **1**/K^+ dimer.

to the XRD results and the simulated molecular structure, a unit cell that consists of two porphyrin molecules with cell parameters of a = 7.01 nm and b = 4.51 nm is given for compound **1** (Figure 5D).

Assembly Mechanism

On the basis of the experimental results described above, a formation mechanism of nanofibers from both enantiomers of metal-free porphyrin **1** in the presence of potassium ions was proposed and is depicted in Figure 6. As described above, to increase the chiral perturbation and intermolecular interaction, four bulky chiral binaphthyl units as well as crown ether moieties were incorporated onto the *meso*-attached phenyl groups of the porphyrin ring, which, however, interfere with the effective intermolecular π–π interaction, thereby preventing stacking of porphyrin molecules from assembling along one dimension to form one-dimensional nanostructures. As a result, nanoparticles were formed from both enantiomers of metal-free porphyrin **1** in the absence of potassium ion. However, in the event that K^+ ions were added to the system, additional metal–ligand coordination bonding interactions between K^+ and crown ether moieties facilitate the linear stacking of porphyrin molecules in a "head-to-tail" manner.[25] This, in combination with the van der Waals interaction between the porphyrin rings and the chiral discrimination among the optically active binaphthyl units during the self-assembly process, dominates the formation of a helix with a right- and a left-handed helical arrangement of (*R*)- and (*S*)-**1**, respectively, which then further hierarchically self-assembles into highly ordered fibrous nanostructures with a helicity opposite to that of the original porphyrin stack.

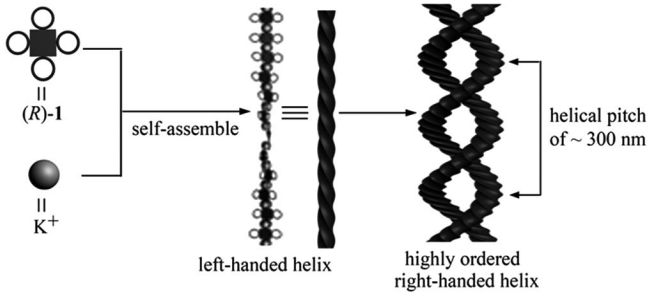

Figure 6. Schematic illustration of the hierarchical formation of nanofibers with right-handed helicity through a one-dimensional left-handed helix with negative chirality determined by the peripheral chiral side chains of the porphyrin ring in the molecule of the (*R*)-**1** enantiomer.

IR Spectra

IR spectroscopy was also employed to investigate the composition of the nanostructures. The IR spectra of the metal-free porphyrin itself, nanoparticles, and nanofibers of **1** are compared in Figure S4 in the Supporting Information. Similar features, except for the decreased intensity in the IR spectra of both nanoparticles and nanofibers relative to those of the metal-free porphyrin, unambiguously confirm the composition of both nanoparticles and nanofibers fabricated from the metal-free porphyrin. However, in the IR spectrum of the metal-free porphyrin, two relatively sharp absorptions at around 1260 and 1133 cm^{-1} are assigned to the symmetric and asymmetric C–O–C bonding stretching vibration, respectively. Similar absorption peaks at 1257 and 1134 cm^{-1} are also observed in the IR spectrum of nanoparticles fabricated from **1** in the absence of K^+. However, in the IR spectrum of the aggregates formed from **1** in the presence of K^+, these two absorption bands are broadened and shifted to a lower frequency at 1257 and 1124 cm^{-1}, respectively, thereby indicating the formation of coordination bonds between crown ether units and added K^+ ion. These results are in line with the electronic absorption result as detailed above.

Conclusion

We have designed and prepared both enantiomers of an optically active metal-free porphyrin decorated with four binaphthyl units linked at the *meso*-attached phenyl groups through crown ether moieties. The self-assembly properties of these two enantiomers were comparatively investigated in the absence and presence of potassium ions. Without adding K^+, both enantiomers self-assemble into nanoparticles. In the presence of K^+, additional metal–ligand $K–O_{crown}$ coordination bonds formed between K^+ and the crown units of (*R*)- and (*S*)-**1** together with chiral discrimination of chiral side chains, and intermolecular van der Waals interactions induce the formation of a right-handed and left-handed helix, respectively, with an ordered "head-to-tail" internal molecular arrangement at the first stage of aggregation; this then further hierarchically stacks into highly ordered fibrous nanostructures with the opposite helicity. The present results not only reveal the effect of additionally formed metal-coordination bonding on the morphology of self-assembled nanostructures but is also helpful in providing new insight into chiral information transfer and expression for synthetic conjugated systems at the supramolecular level.

Experimental Section

Measurements: Electronic absorption spectra were recorded with a Hitachi U-4100 spectrophotometer. MALDI-TOF mass spectra were taken with a Bruker BIFLEX III ultra-high resolution Fourier transform ion cyclotron resonance (FT-ICR) mass spectrometer with α-cyano-4-hydroxycinnamic acid as matrix. Q-TOF mass spectra were recorded with an Agilent Technologies 6510 mass spectrometer. All melting points were determined with an X-4 apparatus. ^1H and ^{13}C NMR spectra were recorded with a Bruker DPX 300 spectrometer. Elemental analyses were performed by the Beijing Institute of Chemistry. Circular dichroism (CD) measurements were carried out with a JASCO J-810 spectropolarimeter. Transmission electron microscopic (TEM) images were measured with a JEOL-100CX II electron microscope operated at 100 kV. High-resolution TEM (HRTEM) measurements and energy-dispersive

X-ray (EDX) spectra were performed with a JEOL-2010 instrument working at 200 kV. Scanning electron microscopic (SEM) images were obtained with a JEOL JSM-6700 F. Atom force microscopy (AFM) images were collected in air under ambient conditions by using the tapping mode with a Nanoscope III/Bioscope scanning probe microscope from Digital Instruments. For TEM imaging, a drop of sample solution was cast onto a carbon copper grid. For SEM imaging, Au (1–2 nm) was sputtered onto these grids to prevent a charging effect and to improve the image clarity.

Chemicals: DMF was freshly distilled just before use. 3,4-Dihydroxybenzaldehyde was purchased from Shanghai Zhixin Co. Both chloroform and methanol (HPLC grade) were purchased from Tianjin Kermel Co. Column chromatography was carried out on silica gel (Merck, Kieselgel 60, 70–230 mesh) with the indicated eluents. Optically pure (*R*)- and (*S*)-2,2′-dihydroxy-1,1′-binaphthyl (>99% *ee*) were obtained from Dalian Reagent Company. All the other chemicals were of reagent grade and used as received without further purification. 5-Tosyloxy-3-oxa-1-pentanol (**3**) was prepared according to a published procedure.[19b]

Nanostructure Fabrication: The self-assembled nanostructures of the optically active metal-free porphyrin were fabricated by the solution mixture method according to the following procedure.[26] A saturated solution of potassium acetate in *n*-hexane was injected into a solution of optically active metal-free porphyrin in chloroform (3×10^{-4} M) to give a solution with a final chloroform/*n*-hexane ratio of 1:1 (v/v) in a small flask. After the solution had slowly concentrated at room temperature, some loose aggregates remained at the bottom of the flask. Then a small amount of *n*-hexane was added into the flask to suspend the aggregates in the solvent. Successive drops of the solution were cast onto a grid (Cu with a carbon film). The aggregated behavior in the solid state was observed after the solvent was evaporated. The nanoparticles were prepared according to the same method except for using pure *n*-hexane instead of the saturated *n*-hexane solution of potassium acetate. The experimental results were stable and reproducible under the experimental conditions described above.

Preparation of 4: Potassium carbonate (3.79 g, 27.43 mmol) was added into a solution of 3,4-dihydroxybenzaldehyde (1.87 g, 13.6 mmol) and compound **3** (5.02 g, 29.88 mmol) in CH_3CN (169 mL). The mixture was heated at reflux under a nitrogen atmosphere for 16 h. After being cooled to room temperature, the mixture was concentrated under reduced pressure, and water (200 mL) was added. Then the product was extracted with dichloromethane (3×100 mL). The combined organic layers were washed with brine, dried with anhydrous sodium sulfate, filtered, and concentrated. The residue was purified by silica gel chromatography with ethyl acetate/petroleum ether (60–90 °C) (1:2) as eluent to give the product as a viscous oil (3.59 g, 84%). ^{1}H NMR (300 MHz, $CDCl_3$, 25 °C): δ = 3.69–3.76 (m, 8 H, OCH_2), 3.92–4.01 (m, 4 H, OCH_2), 4.21–4.26 (m, 4 H, OCH_2), 6.97–7.00 (d, J = 9 Hz, 1 H, Ar-H), 7.42–7.47 (m, 2 H, Ar-H), 9.84 (s, 1 H, CHO) ppm. ^{13}C NMR (100 MHz, $CDCl_3$, 25 °C): δ = 61.90, 68.17, 68.20, 68.51, 68.67, 72.28, 72.33, 110.80, 111.67, 112.10, 126.33, 129.77, 148.44, 153.56, 190.46 ppm. MS: calcd. for $C_{15}H_{23}O_7$ $[M + H]^+$ 315.1; found 315.1.

Preparation of 5: A solution of compound **4** (3.0 g, 9.42 mmol) in pyridine (6 mL) was cooled to –10 °C, and a solution of *p*-toluenesulfonyl chloride (4.0 g, 20.72 mmol) in pyridine (6 mL) was added dropwise whilst stirring. The mixture was then stirred at –10 °C for 2 h and at 0 °C for 12 h. The reaction mixture was poured onto ice, acidified with aqueous hydrogen chloride, and extracted with dichloromethane (3×100 mL). The combined organic layers were washed with water, dried with anhydrous sodium sulfate, and concentrated. The residue was purified by silica gel chromatography with ethyl acetate/petroleum ether (60–90 °C) (1:1) as eluent, thereby giving the product as a viscous oil (3.67 g, 61.7%). ^{1}H NMR (300 MHz, $CDCl_3$, 25 °C): δ = 2.38 (s, 6 H, CH_3), 3.75–3.83 (m, 8 H, OCH_2), 4.07–4.19 (m, 8 H, OCH_2), 6.96–6.98 (d, J = 8 Hz, 1 H, Ar-H), 7.28–7.33 (d, J = 20 Hz, 4 H, Ar-H), 7.37 (s, 1 H, Ar-H), 7.44–7.46 (d, J = 8 Hz, 1 H, Ar-H), 7.76–7.78 (d, J = 8 Hz, 4 H, Ar-H), 9.83 (s, 1 H, CHO) ppm. ^{13}C NMR (100 MHz, $CDCl_3$, 25 °C): δ = 21.31, 53.60, 60.25, 68.66, 68.70, 68.85, 69.40, 69.43, 69.45, 69.51, 111.89, 112.62, 126.61, 157.84, 129.81, 130.28, 132.93, 144.82, 149.01, 154.20, 190.53 ppm. MS: calcd. for $C_{29}H_{38}NO_{11}S_2$ $[M + NH_4]^+$ 640.2; found 640.2.

Preparation of (*R*)- or (*S*)-6: A mixture of compound **5** (3 g, 4.82 mmol), (*R*)- or (*S*)-2,2′-dihydroxy-1,1′-binaphthyl (1.15 g, 4.0210 mmol), and potassium carbonate (0.6 g, 4.35 mmol) in DMF (25 mL) was stirred at room temperature under nitrogen for 72 h. The reaction mixture was concentrated under reduced pressure, and the residue was shaken with water and extracted with dichloromethane (3×100 mL). The combined organic layers was washed with water (3×50 mL) and dried with anhydrous sodium sulfate. The solvent was removed by evaporation under reduced pressure, and the residue was purified by silica gel chromatography with ethyl acetate/petroleum ether (60–90 °C) (1:6) as eluent, thus leading to a white solid as the target compound **6** (0.63 g, 27.6%). ^{1}H NMR (300 MHz, $CDCl_3$, 25 °C): δ = 3.49–3.89 (m, 8 H, OCH_2), 3.90–4.23 (m, 8 H, OCH_2), 6.85–6.88 (d, J = 9 Hz, 1 H, Ar-H), 7.13–7.22 (m, 4 H, Ar-H), 7.27–7.43 (m, 6 H, Ar-H), 7.80–7.83 (m, 4 H, Ar-H), 9.83 (s, 1 H, CHO) ppm. ^{13}C NMR (100 MHz, $CDCl_3$, 25 °C): δ = 69.25, 69.45, 69.49, 69.55, 69.62, 69.76, 70.21, 70.30, 111.09, 111.95, 116.04, 120.60, 120.71, 123.58, 123.64, 215.35, 125.36, 126.15, 126.18, 126.61, 127.67, 127.70, 129.03, 129.06, 129.33, 129.38, 130.16, 134.04, 149.22, 154.14, 154.17, 154.21, 190.69 ppm. M.p. 80–83 °C. MS: calcd. for $C_{35}H_{36}NO_7$ $[M + NH_4]^+$ 582.2; found 582.2.

Preparation of (*R*)- and (*S*)-1: A solution of pyrrole (0.20 g, 3.0 mmol) in propionic acid (13 mL) was added dropwise to a solution of compound **5** (1.15 g, 2.0 mmol) in propionic acid (17 mL) at reflux for 30 min. Then the reaction mixture was cooled to room temperature. Methanol (100 mL) was added, and the solution was left standing overnight. The crystalline residue separated from the bulk solution was collected by filtration, washed with methanol, and then purified by silica gel chromatography. After the first green band eluted with chloroform, the desired metal-free porphyrin was subsequently eluted with chloroform/methanol (100:1) as eluent, thereby giving the product as a purple crystalline solid (1 g, 20%). Satisfactory elemental analysis results were obtained by repeated recrystallization from chloroform/methanol or chloroform/*n*-hexane. ^{1}H NMR (300 MHz, $CDCl_3$, 25 °C): δ = 3.60–3.87 (m, 32 H, OCH_2), 4.11–4.31 (m, 32 H, OCH_2), 7.18–7.36 (m, 33 H, Ar-H), 7.52–7.57 (m, 6 H, Ar-H), 7.76–7.84 (m, 6 H, Ar-H), 7.86–8 (m, 15 H, Ar-H), 8.93 (s, 8 H, Ar-H) ppm. M.p. 195–200 °C. MS: calcd. for $C_{156}H_{134}N_4O_{24}$ $[M + H]^+$ 2449.8; found 2449.6. $C_{156}H_{134}N_4O_{24}$·0.5$CHCl_3$ (2508.4): calcd. C 74.93, H 5.40, N 2.23; found C 74.59, H 5.07, N 2.15.

Supporting Information (see footnote on the first page of this article): Experimental and simulated isotopic patterns for the molecular ion of optically active metal-free porphyrin **1**. ^{1}H NMR spectroscopic data for the optically active metal-free porphyrin **1** recorded in $CDCl_3$. Electronic absorption spectra and CD spectra of a dilute solution of **1** in chloroform and its nanoparticle aggregates formed in the absence of potassium ions dispersed in methanol. Electronic absorption data for a dilute solution of **1** in chloroform. IR spectra

of optically active metal-free porphyrin itself, nanoparticles formed from optically active metal-free porphyrin in the absence of potassium ions, and nanofibers formed from optically active metal-free porphyrin in the presence of potassium ions in the region of 400–1800 cm^{-1} with 2 cm^{-1} resolution. Schematic illustration for the hierarchical formation of nanofibers with left-handed helicity through one-dimensional right-handed helix with negative chirality determined by the peripheral chiral side chains of porphyrin ring in the molecule of (*S*)-**1** enantiomer.

Acknowledgments

Financial support from the Natural Science Foundation of China (grant nos. 20931001 and 20801031), the Ministry of Education of China, the Independent Innovation Foundation of USTB and SDU, and the Beijing Municipal Commission of Education is gratefully acknowledged.

[1] a) R. A. Garoff, E. A. Litzinger, R. E. Connor, I. Fishman, B. A. Armitage, *Langmuir* **2002**, *18*, 6330–6337; b) M. Wang, G. L. Silva, B. A. Armitage, *J. Am. Chem. Soc.* **2000**, *122*, 9977–9986; c) R. F. Pasternack, A. Giannetto, P. Pagano, E. J. Gibbs, *J. Am. Chem. Soc.* **1991**, *113*, 7799–7800; d) K. C. Hannah, B. A. Armitage, *Acc. Chem. Res.* **2004**, *37*, 845–853; e) X. Chen, M. Liu, *J. Inorg. Biochem.* **2003**, *94*, 106–113.

[2] a) J. H. Fuhrhop, W. Helfrich, *Chem. Rev.* **1993**, *93*, 1565–1582; b) S. I. Tamaru, M. Nakamura, M. Takeuchi, S. Shinkai, *Org. Lett.* **2001**, *3*, 3631–3634; c) S. Tamaru, S. Uchino, M. Takeychi, M. Ikeda, T. Hatano, S. Shinkai, *Tetrahedron Lett.* **2002**, *43*, 3751–3755.

[3] a) C. Nuckolls, T. J. Katz, T. Verbiest, S. V. Elshocht, H. G. Kuball, S. Kiesewalter, A. J. Lovinger, A. Persoons, *J. Am. Chem. Soc.* **1998**, *120*, 8656–8660; b) J. M. Fox, T. J. Katz, S. V. Elshocht, T. Verbiest, M. Kauranen, A. Persoons, T. Thongpanchang, T. Krauss, L. Brus, *J. Am. Chem. Soc.* **1999**, *121*, 3453–3459.

[4] a) Z. Wu, G. Yang, Q. Chen, J. Liu, S. Yang, J. S. Ma, *Inorg. Chem. Commun.* **2004**, *7*, 249–252; b) S. Shinoda, T. Okazaki, T. N. Player, H. Misaki, K. Hori, H. Tsukube, *J. Org. Chem.* **2005**, *70*, 1835–1843; c) T. Kawamoto, B. S. Hammes, B. Haggerty, G. P. A. Yap, A. L. Rheingold, A. S. Borovik, *J. Am. Chem. Soc.* **1996**, *118*, 285–286.

[5] a) H. Engelkamp, S. Middlebeek, R. J. M. Nolte, *Science* **1999**, *284*, 785–788; b) D. Adam, P. Schumacher, J. Simmerer, L. Häusling, K. Siemensmeyer, K. H. Etzbach, H. Ringsdorf, D. Harrer, *Nature* **1994**, *371*, 141–143; c) J. Wu, M. D. Watson, L. Zhang, Z. Wang, K. Müllen, *J. Am. Chem. Soc.* **2004**, *126*, 177–186; d) V. Dehm, Z. Chen, U. Baumeister, P. Prins, L. D. A. Siebbeles, F. Würthner, *Org. Lett.* **2007**, *9*, 1085–1088.

[6] a) H. Goto, H. Q. Zhang, E. Yashima, *J. Am. Chem. Soc.* **2003**, *125*, 2516–2523; b) K. Morino, M. Oobo, E. Yashima, *Macromolecules* **2005**, *38*, 3461–3468; c) R. Nonokawa, E. Yashima, *J. Am. Chem. Soc.* **2003**, *125*, 1278–1283.

[7] K. Kadish, K. M. Smith, R. Guilard (Eds.), *The Porphyrin Handbook*, Academic Press, New York, **1999**.

[8] a) M. Kimura, H. Narikawa, K. Ohta, K. Hanabusa, *Chem. Mater.* **2002**, *14*, 2711–2717; b) X. Huang, F. Zhao, Z. Li, Y. Tang, F. Zhang, C. Tung, *Langmuir* **2007**, *23*, 5167–5172; c) A. de la Escosura, M. V. M. Díaz, P. Thoedarson, A. E. Rowan, R. J. M. Nolte, T. Torres, *J. Am. Chem. Soc.* **2003**, *125*, 12300–12308; d) P. Chen, X. Ma, M. Liu, *Macromolecules* **2007**, *40*, 4780–4784.

[9] Y. Li, X. Li, Y. Li, H. Liu, S. Wang, H. Gan, J. Li, N. Wang, X. He, D. Zhu, *Angew. Chem. Int. Ed.* **2006**, *45*, 3639–3643.

[10] T. Yokoyama, S. Yokoyama, T. Kamikado, Y. Yoshishige Okuno, T. Mashiko, *Nature* **2001**, *413*, 619–621.

[11] a) Y. Gao, X. Zhang, C. Ma, X. Li, J. Jiang, *J. Am. Chem. Soc.* **2008**, *130*, 17044–17052; b) Y. Gao, Y. Chen, R. Li, Y. Bian, X. Li, J. Jiang, *Chem. Eur. J.* **2009**, *15*, 13241–13252; c) G. Lu, Y. Chen, Y. Zhang, M. Bao, Y. Bian, X. Li, J. Jiang, *J. Am. Chem. Soc.* **2008**, *130*, 11623–11630; d) G. Lu, X. Zhang, X. Cai, J. Jiang, *Eur. J. Inorg. Chem.* **2010**, 753–757.

[12] a) H. Ogoshi, T. Mizutani, *Acc. Chem. Res.* **1998**, *31*, 81–89; b) X. Huang, K. Nakanishi, N. Berova, *Chirality* **2000**, *12*, 237–255.

[13] a) X. Huang, B. H. Richman, B. Borhan, N. Berova, K. Nakanishi, *J. Am. Chem. Soc.* **1998**, *120*, 6185–6186; b) G. Proni, G. Pescitelli, X. Huang, K. Nakanishi, N. Berova, *J. Am. Chem. Soc.* **2003**, *125*, 12914–12927; c) T. Kurtán, N. Nesnas, Y. Li, X. Huang, K. Nakanishi, N. Berova, *J. Am. Chem. Soc.* **2001**, *123*, 5962–5973; d) T. Kurtán, N. Nesnas, F. E. Koehn, Y. Li, K. Nakanishi, N. Berova, *J. Am. Chem. Soc.* **2001**, *123*, 5974–5982.

[14] a) D. Mansuy, *Coord. Chem. Rev.* **1993**, *125*, 129–142; b) J. P. Collman, X. Zhang, V. J. Lee, E. S. Uffelman, J. I. Brauman, *Science* **1993**, *261*, 1404–1411; c) Z. Gross, S. Ini, *J. Org. Chem.* **1997**, *62*, 5514–5521.

[15] E. Bellacchio, R. Lauceri, S. Gurrieri, L. M. Scolaro, A. Romeo, R. Purrello, *J. Am. Chem. Soc.* **1998**, *120*, 12353–12354.

[16] a) S.-i. Kawano, S.-i. Tamaru, N. Fujita, S. Shinkai, *Chem. Eur. J.* **2004**, *10*, 343–351; b) T. Sugimoto, T. Suzuki, S. Shinkai, K. Sada, *J. Am. Chem. Soc.* **2007**, *129*, 270–271; c) M. Wolffs, F. J. M. Hoeben, E. H. A. Beckers, A. P. H. J. Schenning, E. W. Meijer, *J. Am. Chem. Soc.* **2005**, *127*, 13484–13485.

[17] a) X. M. Guo, C. Jiang, T. S. Shi, *Inorg. Chem.* **2007**, *46*, 4766–4768; b) J.-H. Fuhrhop, C. Demoulin, C. Boettcher, J. Köning, U. Siggels, *J. Am. Chem. Soc.* **1992**, *114*, 4159–4169; c) S. Arimori, M. Takeuchi, S. Shinkai, *J. Am. Chem. Soc.* **1996**, *118*, 245–246; d) T. Ishi-I, J. H. Jung, S. Shinkai, *J. Mater. Chem.* **2000**, *10*, 2238–2240.

[18] a) S. Tamaru, M. Takeuchi, M. Sano, S. Shinkai, *Angew. Chem. Int. Ed.* **2002**, *41*, 853–856; b) S.-i. Tamaru, M. Nakamura, M. Takeuchi, S. Shinkai, *Org. Lett.* **2001**, *3*, 3631–3634.

[19] a) X. Zhang, A. Muranaka, W. Lv, Y. Zhang, Y. Bian, J. Jiang, N. Kobayashi, *Chem. Eur. J.* **2008**, *14*, 4667–4674; b) H. Liu, C. Chen, M. Ai, A. Gong, J. Jiang, F. Xi, *Tetrahedron: Asymmetry* **2000**, *11*, 4915–4922; c) H. Liu, Y. Liu, M. Liu, C. Chen, F. Xi, *Tetrahedron Lett.* **2001**, *42*, 7083–7086.

[20] a) N. Kobayashi, Y. Kobayashi, T. Osa, *J. Am. Chem. Soc.* **1993**, *115*, 10994–10995; b) N. Kobayashi, *Chem. Commun.* **1998**, *4*, 487–488.

[21] L. D. Bari, G. Pescitelli, G. Reginato, P. Salvadori, *Chirality* **2001**, *13*, 548–555.

[22] M. Kasha, H. R. Rawls, M. A. EI-Bayoumi, *Pure Appl. Chem.* **1965**, *11*, 371–392.

[23] a) N. Berova, K. Nakanishi, R. Woody, *Circular Dichroism: Princples and Applictions*, 2nd ed., Wily-VCH, New York, **2000**, pp. 337–382; b) A. L. Hofacker, J. R. Parquette, *Angew. Chem. Int. Ed.* **2005**, *44*, 1053–1057; c) M. Balaz, A. E. Holmes, M. Benedetti, P. C. Rodriguez, N. Berova, K. Nakanishi, G. Proni, *J. Am. Chem. Soc.* **2005**, *127*, 4172–4173; d) V. V. Borovkov, J. M. Lintuluoto, M. Fujiki, Y. Inoue, *J. Am. Chem. Soc.* **2000**, *122*, 4403–4407.

[24] M. J. Frisch, G. W. Trucks, H. B. Schlegel, G. E. Scuseria, M. A. Robb, J. R. Cheeseman, J. A. Montgomery Jr., T. Vreven, K. N. Kudin, J. C. Burant, J. M. Millam, S. S. Iyengar, J. Tomasi, V. Barone, B. Mennucci, M. Cossi, G. Scalmani, N. Rega, G. A. Petersson, H. Nakatsuji, M. Hada, M. Ehara, K. Toyota, R. Fukuda, J. Hasegawa, M. Ishida, T. Nakajima, Y. Honda, O. Kitao, H. Nakai, M. Klene, X. Li, J. E. Knox, H. P. Hratchian, J. B. Cross, C. Adamo, J. Jaramillo, R. Gomperts, R. E. Stratmann, O. Yazyev, A. J. Austin, R. Cammi, C. Pomelli, J. W. Ochterski, P. Y. Ayala, K. Morokuma, G. A. Voth, P. Salvador, J. J. Dannenberg, V. G. Zakrzewski, S. Dapprich, A. D. Daniels, M. C. Strain, O. Farkas, D. K. Malick, A. D. Rabuck, K. Raghavachari, J. B. Foresman, J. V. Ortiz, Q. Cui, A. G. Baboul, S. Clifford, J. Cioslowski, B. B. Stefanov, G. Liu, A. Liashenko, P. Piskorz, I. Komaromi, R. L. Martin, D. J.

Fox, T. Keith, M. A. Al-Laham, C. Y. Peng, A. Nanayakkara, M. Challacombe, P. M. W. Gill, B. Johnson, W. Chen, M. W. Wong, C. Gonzalez, J. A. Pople, *Gaussian 03*, Revision B.05, Gaussian, Inc., Pittsburgh, PA, **2003**.
[25] F. D'Souza, R. Chitta, S. Gadde, M. E. Zandler, A. L. McCarty, A. S. D. Sandanayaka, Y. Araki, O. Ito, *J. Phys. Chem. A* **2006**, *110*, 4338–4347.
[26] a) K. Balakrishnan, A. Datar, T. Naddo, J. Huang, R. Oitker, M. Yen, J. Zhao, L. Zang, *J. Am. Chem. Soc.* **2006**, *128*, 7390–7398; b) W. Su, Y. Zhang, C. Zhao, X. Li, J. Jiang, *ChemPhysChem* **2007**, *8*, 1857–1862; c) Y. Li, X. Li, Y. Li, H. Liu, S. Wang, H. Gan, J. Li, N. Wang, X. He, D. Zhu, *Angew. Chem. Int. Ed.* **2006**, *45*, 3639–3643; d) X. Gong, T. Milic, C. Xu, J. D. Batteas, C. M. Drain, *J. Am. Chem. Soc.* **2002**, *124*, 14290–14291.

Received: March 31, 2010
Published Online: July 13, 2010

DOI: 10.1002/ejic.201000377

Phosphorescent Cuprous Complexes with N,O Ligands – Synthesis, Photoluminescence, and Electroluminescence

Wei Sun,[a,b] Qisheng Zhang,[c] Li Qin,[b,c] Yanxiang Cheng,*[a] Zhiyuan Xie,[a] Canzhong Lu,*[c] and Lixiang Wang[a]

Keywords: Copper / N,O ligands / Phosphane ligands / Phosphorescence / Electroluminescence

Six heteroleptic cuprous complexes, [$\mathbf{L^1}$Cu(PPh_3)$_2$](BF_4) (**1a**), [$\mathbf{L^1}$Cu(DPEphos)](BF_4) (**1b**), [$\mathbf{L^2}$Cu(PPh_3)$_2$](BF_4) (**2a**), [$\mathbf{L^2}$Cu(DPEphos)](BF_4) (**2b**), [$\mathbf{L^3}$Cu(PPh_3)$_2$](BF_4) (**3a**), and [$\mathbf{L^3}$Cu(DPEphos)](BF_4) (**3b**) {$\mathbf{L^1}$ = diphenyl(2-pyridyl)phosphane oxide, $\mathbf{L^2}$ = diphenyl(8-quinolyl)phosphane oxide, $\mathbf{L^3}$ = diphenyl(2-pyridylmethyl)phosphane oxide, DPEphos = bis[2-(diphenylphosphanyl)phenyl] ether}, were prepared and fully characterized. The electronic absorption spectra and quantum chemical calculations indicate that the lowest excited states of these complexes can be assigned to the metal-to-ligand charge transfer (MLCT) transition. In poly(methyl methacrylate) (PMMA) films, these complexes exhibit blue-green to orange emissions with long lifetimes ranging from 7.5 to 28.6 μs. With wide energy-band gaps of 3.50 and 3.28 eV, complexes **3a** and **3b** emit efficiently in 20 wt.-% PMMA films with photoluminescence quantum efficiencies of 0.69 and 0.72, and emission maxima at 477 nm and 495 nm, respectively. Electroluminescent devices were fabricated with these N,O-based Cu^I complexes as emitters. The best device performance, with a peak current efficiency of 4.9 cd/A, was obtained for **3b**.

Introduction

Extensive efforts have been focused on N-heterocyclic Cu^I complexes for replacing phosphorescent transition metal complexes based on ruthenium or other noble metal ions in chemical sensors,[1] probes of biological systems,[2] and energy-conversion devices[3] due to their advantages such as having abundant resources, low cost, and nontoxic properties. However, these tetrahedral cuprous complexes always undergo a significant geometry change going from the ground to excited state corresponding to a change from d^{10} to d^9 as a result of MLCT transitions. The distortion of the excited state narrows the energy gap and increases the nonradiative decay of these Cu^I complexes.[4] Compared to classical $[Cu(N,N)_2]^+$ systems, mixed-ligand systems involving bulky phosphanes ($[Cu(N,N)(P,P)]^+$) exhibit improved emission properties, because the bulky and strong π-acidic phosphane ligands will sterically inhibit the excited-state distortion as well as enhance the energy level of the excited states by stabilizing of the Cu^I species.[5] In 2002, McMillin and co-workers reported the first example of a highly emissive mononuclear cuprous complex, $[Cu(dbp)(DPEphos)]^+$ (dbp = 2,9-di-*n*-butyl-1,10-phenanthroline), with an impressive quantum efficiency of 0.16[6] (0.26[3d]) in CH_2Cl_2 solution and 0.69[3a] in an PMMA film. Recently, a series of Cu^I complexes combining two bis(phosphane) ligands ($[Cu(P,P)_2]^+$) was also found to exhibit strong emission bands in both solid state and organic light-emitting diodes (OLEDs).[7]

Over the past few years, increasing attention has also been paid to luminescent Cu^I complexes based on asymmetric N,P ligands. These complexes display some unexpected properties perhaps due to the asymmetric electronic character of their ligands. Recently, Peter et al. reported several dinuclear and mononuclear Cu^I complexes supported by [P,N,P]$^-$ {bis[2-(diisobutylphosphanyl)phenyl]-amide}[8] and [P,N]$^-$ (amidophosphane) ligands[9] with unusually high quantum efficiencies, in the range of 0.16–0.70, in solution. More recently, our group and Tsukuda et al. reported a series of phosphorescent homo- and heteroleptic Cu^I complexes with asymmetric N,P ligands of 8-(diphenylphosphanyl)quinoline (dppq) and 2-methyl-8-(diphenylphosphanyl)quinoline.[10,11] The Cu^I complexes based on these iminophosphane ligands exhibit higher electro- and photochemical stability than those based on traditional diimine or diphosphane ligands.[11]

In the course of our studies on cuprous complexes with N,P ligands, we isolated an unexpected phosphorescent complex containing the oxidized N,P ligand, diphenyl(2-pyridyl)phosphane oxide. To the best of our knowledge, cu-

[a] State Key Laboratory of Polymer Physics and Chemistry, Changchun Institute of Applied Chemistry, Chinese Academy of Sciences,
Changchun 130022, P. R. China
E-mail: yanxiang@ciac.jl.cn
czlu@fjirsm.ac.cn
[b] The Graduate School, Chinese Academy of Sciences,
Beijing 100039, P. R. China
[c] State Key Laboratory of Structural Chemistry, Fujian Institute of Research on the Structure of Matter, Chinese Academy of Sciences,
Fuzhou 350002, P. R. China

prous complexes containing phosphane oxide coordinating ligands are few, and their luminescent properties have never been reported.[12] The unexpected finding motivated us to systematically explore the effects of the electronic character of the ligands on the photophysical properties of cuprous complexes. Herein, we report the synthesis of phosphorescent cuprous complexes containing phosphane oxide coordinating ligands, and the applications of these complexes in OLEDs.

Results and Discussion

Synthesis and Characterization

We synthesized six mixed-ligand Cu^I complexes of the type $[Cu(N,O)(P,P)](BF_4)$, where N,O is diphenyl(2-pyridyl)phosphane oxide (**L**^{1}), diphenyl(8-quinolyl)phosphane oxide (**L**^{2}) or diphenyl(2-pyridylmethyl)phosphane oxide (**L**^{3}), and P,P is DPEphos or a pair of PPh_3 ligands. The structures of the complexes are shown in Scheme 1. Complex **1a** was first obtained as a byproduct when we attempted to prepare the N,P Cu^I complex. In the following studies, all complexes were directly synthesized from the oxidized N,P ligands (N,O), in which ligand **L**^{2} was easily synthesized by the reaction of 8-(diphenylphosphanyl)quinoline with excess H_2O_2 in tetrahydrofuran (thf) at room temperature. The mixed-ligand complexes were obtained from two displacement reactions of $[Cu(CH_3CN)_4](BF_4)$. Crystals of the complexes were obtained through slow concentration and diffusion of solvents in moderate yields ranging from 47.2 to 86.6%, and characterized by ^{1}H NMR, ^{31}P NMR spectroscopy, and elemental analysis.

Significant upfield shifts are observed for the signal of the α-H atom of the pyridine or quinoline ring in all complexes compared to those of the free ligands in the ^{1}H NMR spectra, implying electron donation from the Cu ion and the phosphane auxiliary ligands to the N,O ligands. For instance, **1a** and **1b** exhibit signals at δ = 8.44 and 8.27 ppm, whereas **L**^{1} displays a signal at δ = 8.83 ppm. In comparison with $[Cu(dppq)(DPEphos)]^+$,[11] **2b** has almost the same signal for the α-H atom, but signals for other protons of the quinoline ring are shifted downfield due to the lower electron-donating ability of $-OPPh_2$ to the adjacent quinoline ring than that of $-PPh_2$. Additionally, signals in the upfield region for **3a** and **3b** indicate a higher electron density relative to **1a** and **1b**, which is attributed to the introduction of an electron-donating methylene unit.

In the course of our studies on cuprous complexes with N,P ligands, we noticed that significant ligand exchange or redistribution reactions sometimes occur. For instance, the homoleptic species $[Cu(dppq)_2](BF_4)$ has been observed in $CDCl_3$ solution alongside $[Cu(dppq)(PPh_3)_2](BF_4)$ in a ratio of 0.07:1, according to ^{1}H NMR spectra. However, signals for the homoleptic species have not been found in the ^{1}H NMR spectra of these N,O-based complexes probably due to their less crowded coordination environment.

Description of the Structures

The X-ray crystal structures of all N,O complexes have been determined. Selected bond lengths and angles are listed in Table 1, and views of the structures of the complexes showing the atom numbering appear in Figures 1, 2, 3, 4, 5, and 6.

The central copper atoms in all of the complexes are surrounded by one O and one N atom from the N,O ligands and two P atoms from phosphane ligands in a distorted tetrahedral geometry. The metallacycles consisting of the Cu, O, N, P, and one or two C atoms of the N,O ligands are found in either a half-chair or a boat conformation. The former is found in complexes **1a** and **1b** where the O atoms are out of the Cu–N–C–P near-plane. The latter conformation is seen in **2a** and **2b**, where the N and P atoms are out of the Cu–O–C–C near-plane, and in **3a** and **3b**, where the Cu and sp^3 C atoms are out of the O–P–N–C(sp^2) plane.[13]

There are two independent molecules of **1a** in the asymmetric unit of the crystal lattice. The largest deviations from ideal tetrahedral geometry (109.4°) are seen in the N–Cu–O bond angles [83.98(11)° for **1a** and 86.36(9)° for **1b**] due to the rigidity of **L**^{1}. With PPh_3 as the auxiliary ligand, **1a** has a larger P–Cu–P bond angle and longer Cu–N and Cu–P bonds than **1b**, which has a DPEphos auxiliary ligand, implying more steric congestion in **1a**. Similar changes in the P–Cu–P bond angle and the Cu–N and Cu–P bond lengths have also been found in other complexes described here and in $[Cu(N,N)(P,P)]^+$ systems reported previously.[6,14,15] The sum of the internal angles of the five-membered metallacycles of Cu–O–P(1)–C(5)–N and Cu–O–P(1)–C(1)–N are

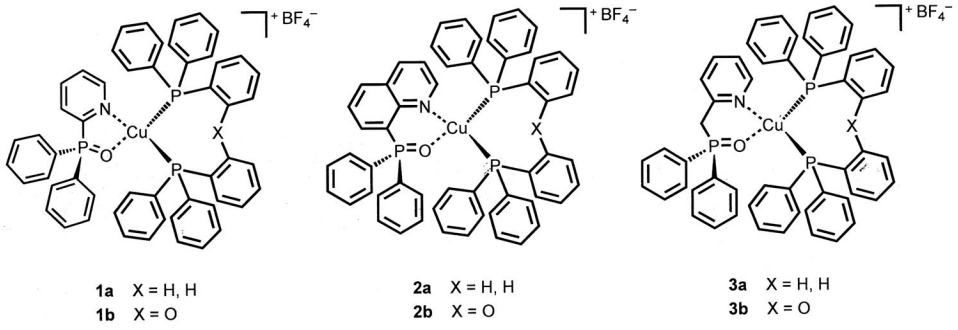

Scheme 1. Molecular structures of the Cu^I complexes.

Table 1. Selected bond lengths [Å] and angles [°] for **1a**, **1b**, **2a**, **2b**, **3a**, and **3b**.

	1a	**1b**	**2a**	**2b**	**3a**	**3b**
Cu–N	2.059(3)	2.044(3)	2.146(3)	2.129(3)	2.113(3)	2.065(2)
Cu–O	2.199(2)	2.171(2)	2.105(2)	2.117(2)	2.148(2)	2.230(2)
Cu–P(2)	2.2621(10)	2.2120(9)	2.2364(9)	2.2376(9)	2.2734(9)	2.2466(7)
Cu–P(3)	2.2390(10)	2.2611(9)	2.2906(9)	2.2787(9)	2.2595(9)	2.2657(7)
O–Cu–N	83.98(11)	86.36(9)	94.46(9)	97.22(10)	96.98(10)	93.22(8)
N–Cu–P(2)	114.01(8)	130.02(8)	116.04(8)	120.17(8)	106.47(8)	116.39(6)
O–Cu–P(2)	99.59(7)	109.68(6)	115.16(6)	114.47(7)	104.36(7)	116.50(5)
N–Cu–P(3)	121.34(8)	106.92(8)	103.17(7)	103.77(8)	108.07(8)	118.14(6)
O–Cu–P(3)	113.77(7)	104.64(6)	95.51(6)	102.59(7)	110.38(7)	94.19(5)
P(2)–Cu–P(3)	116.71(4)	113.46(3)	126.39(3)	115.74(3)	126.58(4)	114.22(2)
Σ metallacycle	537.07	534.98	689.04	686.46	688.83	675.01

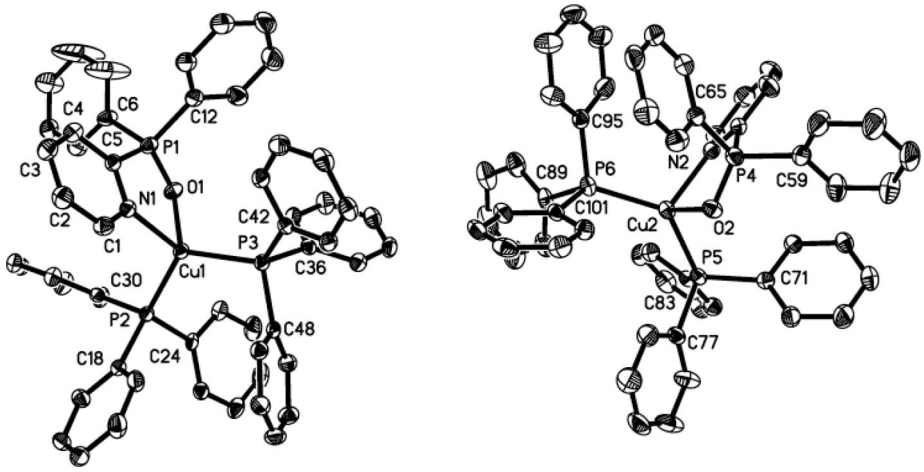

Figure 1. Crystal structure of the cation of **1a** with thermal ellipsoids at 30% probability. Solvent molecules, the anion, and H atoms are omitted for clarity.

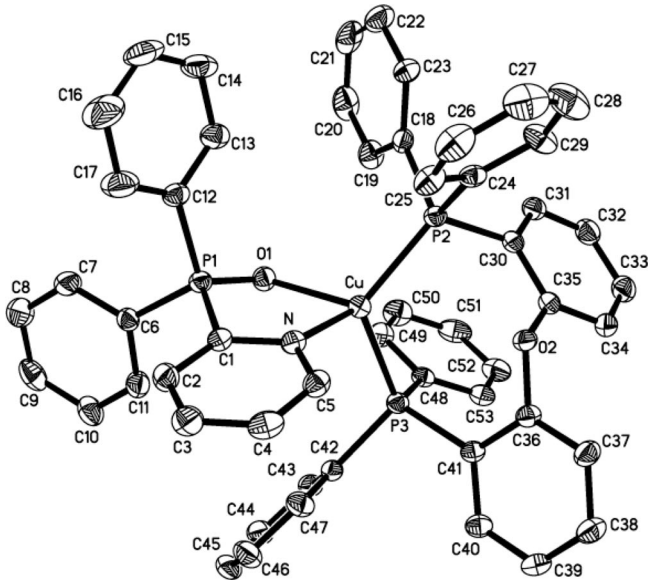

Figure 2. Crystal structure of the cation of **1b** with thermal ellipsoids at 30% probability. Solvent molecules, the anion, and H atoms are omitted for clarity.

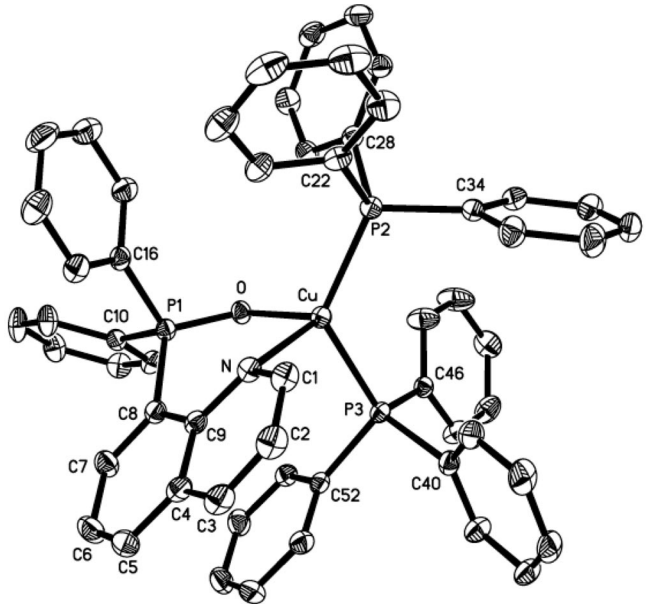

Figure 3. Crystal structure of the cation of **2a** with thermal ellipsoids at 30% probability. The anion and H atoms are omitted for clarity.

537.07 and 534.98° for **1a** and **1b**, respectively, which are slightly smaller than the value for a regular pentagon (540°), indicating the near coplanarity of the metallacycles.

The Cu–N bond for **2b** [2.129(3) Å] is 0.043 Å longer than that in the $[Cu(dppq)(DPEphos)]^+$ cation.[11] However, the average Cu–P bond for **2b** (2.258 Å) is 0.017 Å shorter

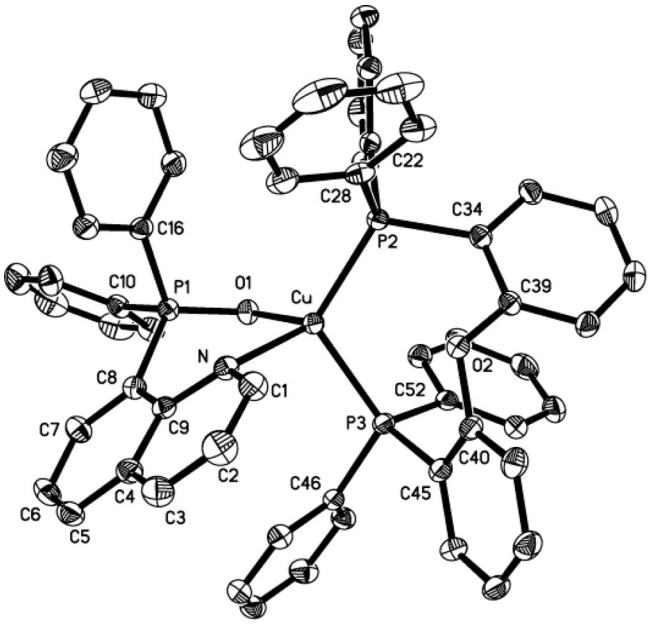

Figure 4. Crystal structure of the cation of **2b** with thermal ellipsoids at 30% probability. Solvent molecules, the anion, and H atoms are omitted for clarity.

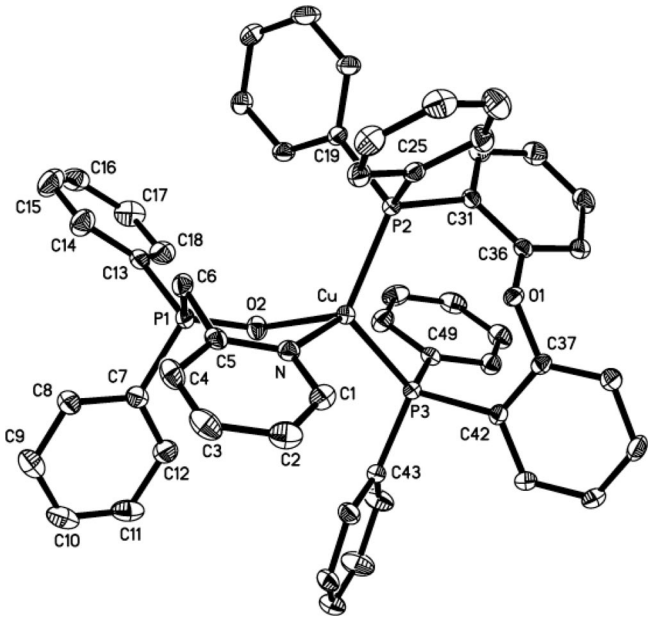

Figure 6. Crystal structure of the cation of **3b** with thermal ellipsoids at 30% probability. Solvent molecules, the anion, and H atoms are omitted for clarity.

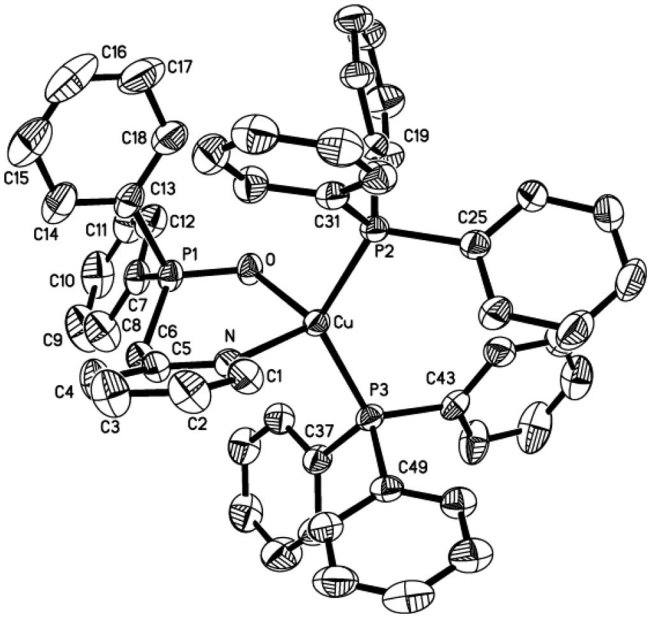

Figure 5. Crystal structure of the cation of **3a** with thermal ellipsoids at 30% probability. Solvent molecules, the anion, and H atoms are omitted for clarity.

than that in the analogous N,P complex, indicating that the N,O ligand is sterically less crowded than the corresponding N,P ligand. The sum of the internal angles of the metallacycle Cu–N–C(9)–C(8)–P(1)–O is 689.04 and 686.46° for complexes **2a** and **2b**, respectively, indicating significant distortion of the six-membered metallacycles.

Complexes based on L^3 tend towards ideal tetrahedral geometry compared to the complexes based on L^1. For example, the N–Cu–O bond angle of **3b** (93.22°) is 6.85° closer to the ideal tetrahedral value of 109.4° than that of **1b**. Furthermore, cuprous complexes based on L^3 show larger P–Cu–P bond angles and longer bonds than those in L^1-based complexes, suggesting that the coordination sphere of the central copper atoms is more congested for the complexes based on L^3. For example, the P–Cu–P bond angle for **3a** (126.58°) is 9.87° larger than that in **1a**. The Cu–N bond length in **3a** is 2.113(3) Å, which is 0.054 Å longer than that in **1a**, and the average Cu–P bond length in **3a** is 2.267 Å, which is 0.0159 Å longer than that in **1a**. The sums of the internal angles of the Cu–N–C(5)–C(6)–P(1)–O six-membered metallacycles are 688.83 and 675.01° for **3a** and **3b**, respectively, which are markedly different from the value of a regular hexagon (720°).

Photophysical Properties

The electronic absorption spectra of the Cu^I complexes in CH_2Cl_2 are shown in Figure 7. The intense UV absorption bands at 256–259 nm for **1a**, **1b**, **3a**, and **3b** and 267–274 nm for **2a** and **2b** are ascribed to the π-π* absorption bands of the N,O ligands. In addition to the high-energy absorption bands, weak, broad, low-energy shoulder bands are observed at around 355 nm for **1a** and **1b**, and around 385 nm for **2a** and **2b**, in agreement with the yellow color of these four complexes. These low-lying bands are attributed to the MLCT transitions involving the N-heterocyclic unit and the Cu^I ion, which are always observed in diimine (N,N) and iminophosphane (N,P) Cu^I complexes.[3f,6,11] However, the MLCT band was not detected in the colorless complexes **3a** and **3b**. To rationalize the feature qualitatively, DFT calculations were performed on **3b** by using 6-31+G** coupled to the LanL2DZ basis set. As shown in

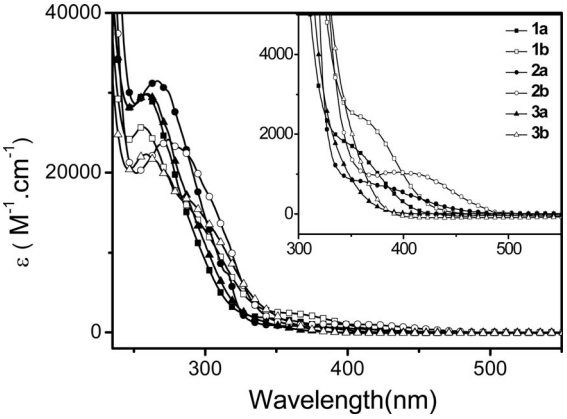

Figure 7. UV/Vis spectra of **1**–**6** in CH_2Cl_2 ($c \approx 10^{-5}$ M); inset: UV/Vis spectra in the low energy band.

Figure 8, the electron density in the highest occupied molecular orbital (HOMO) is mainly associated with the Cu^I center and the Cu–P σ-bonding orbital, whereas that of the lowest unoccupied molecular orbital (LUMO) is localized on the π-antibonding orbital of the pyridine ring. This implies that the lowest excited state of the complex **3b** is also attributed to the MLCT transition. The undetectable MLCT band for **3b** may be obscured by the strong π-π* absorption band nearby.

The energy-band gaps, estimated by the edge of the absorption bands, increase in the series $[\mathbf{L^3}Cu(PP)]^+ > [\mathbf{L^1}Cu(PP)]^+ > [\mathbf{L^2}Cu(PP)]^+$ (Figure 7), relating to the π-electron-accepting ability of the N-heterocycle on the N,O ligands. The energy-band gap of 2.56 eV for **2b** is narrower than that of $[Cu(dppq)(DPEphos)]^+$ (2.93 eV),[11] because the incorporation of the electron-withdrawing $–OPPh_2$ group[16] decreases the electron density of the quinoline ring and thus makes it easier to be reduced. The introduction of the electron-donating methylene group between the pyridine ring and the $–OPPh_2$ group[16] increases the electron density of the pyridine ring and enhances the energy-band gaps from 3.06 and 2.93 eV for **1a** and **1b** to 3.50 and 3.28 eV for **3a** and **3b**, respectively. According to the DFT calculations, **3b** shows a significantly higher LUMO energy level (–0.14685 Hartree) and a close HOMO energy level (–0.28709 Hartree) relative to those of $[Cu(NN)(PP)]^+$ systems [e.g. the analogous 2-(2′-pyridyl)benzimidazolylbenzene complex[15]].

In degassed CH_2Cl_2, complexes **3a** and **3b** emit with maxima at 556 and 558 nm, respectively, while emission maxima of 589 and 581 nm are observed for **1a** and **1b**, respectively (Table 2). The blueshift of the emission maxima is associated with the introduction of the electron-donating methylene unit to the pyridine rings in **3a** and **3b**. Meanwhile, the quantum efficiencies (ϕ) and lifetimes (τ) increase from 0.0005 (1.12 μs) and 0.0005 (1.05 μs) for **1a** and **1b** to 0.037 (2.15 μs) and 0.023 (1.71 μs) for **3a** and **3b**, respectively, due to the enlarged energy gap that decreases the nonradiative rate constant of the Cu^I complexes (energy-gap law). In addition, the complexes comprising the PPh_3 auxiliary ligand (**1a** and **3a**) have longer lifetimes and higher quantum efficiencies relative to the complexes with the DPEphos auxiliary ligand (**1b** and **3b**), which is different to observations in classical mixed-ligand (phenanthroline)Cu^I complexes[6] and consistent with a previous report of biquinoline systems.[3f] Emissions for **2a** and **2b** in degassed CH_2Cl_2 are too weak to be detected, owing to the narrow energy-band gaps that increase the nonradiative pathways.

The photophysical data in PMMA films with concentrations of 20 wt.-% are listed in Table 2. In a rigid matrix, the Cu^I complexes showed emission blueshifts of tens of

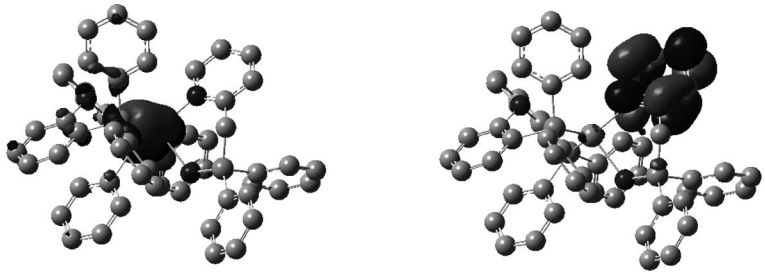

Figure 8. Calculated electron density of the HOMO (left) and LUMO (right) for **3b**.

Table 2. Photophysical performance of the cuprous complexes.

Complex	Solution (in degassed CH_2Cl_2)				Film (20 wt.-% in PMMA)		
	Abs. [nm][a], ($lg\varepsilon$)	λ [nm]	τ [μs][b]	Φ [%]	λ [nm]	τ [μs][c]	Φ [%]
1a	258 (4.5), 347 (3.2)	589	1.12	0.05	521	8.3	11.8
1b	256 (4.4), 358 (3.4)	581	1.05	0.05	527	7.5	12.7
2a	267 (4.5), 375 (2.9)		[d]		565	28.6	6.4
2b	274 (4.4), 395 (3.0)		[d]		573	14.9	6.4
3a	259 (4.5)	556	2.15	3.70	477	24.6	69.3
3b	258 (4.3)	558	1.71	2.26	495	18.6	71.9

[a] $c \approx 10$–5 M in CH_2Cl_2. [b] Fitted by single exponential. [c] Fitted by two exponentials, a pre-exponential weighted average lifetime (τ_{ave}) was used and calculated by the equation $\tau_{ave} = \Sigma(A_i\tau_i/\Sigma A_i)$, where A_i is the pre-exponential for the lifetime τ_i. [d] Too weak to be detected.

nanometers (54–79 nm), much higher quantum efficiencies and longer lifetimes (up to 28.6 μs) relative to the liquid phase.[3f,11] The quantum efficiencies of 0.69 for **3a** and 0.72 for **3b** are amongst the highest found for cuprous complexes[3a,3f,17] and significantly higher than those of **1a**, **1b**, **2a**, and **2b**. Furthermore, an absence of concentration quenching was observed in the complexes based on $\mathbf{L^3}$. For example, **3b** has an efficiency of 0.71 and an emission maximum of 501 nm in its neat film, similar to those in 20 wt.-% PMMA film. This may be associated with the bulky phosphane auxiliary ligand and $–OPPh_2$ that can effectively separate the π-electron acceptors (i.e. N-heterocycles) from each other and therefore avoid the nonradiative intermolecular energy transfer.

Electrophosphorescent Properties Characterization

Multilayer OLEDs with the configuration of indium tin oxide/poly(3,4-ethylenedioxythiophene)/emitting layer (≈ 50 nm)/bathocuproine (BCP) (20 nm)/Alq_3 (40 nm)/LiF (1 nm)/Al (≈ 100 nm) were fabricated to evaluate the electrophosphorescent properties of the cuprous complexes, as shown in Figure 9. The host materials utilized here include poly(9-vinylcarbazole) (PVK) that can match the phosphorescent materials with high energy-band gaps[3a,18] and 3,6-bis(carbazol-9-yl)-*N*-[4-(carbazol-9-yl)phenyl]carbazole (TCCz) that is suitable for phosphorescent materials with low energy-band gaps.[3f,19] The performance data of the OLEDs are listed in Table 3.

Table 3. Turn-on voltage (V_T), current efficiency (η_c), maximum brightness (B_{max}), and emission wavelength (λ_{max}) of the OLEDs.

Emitting layer	V_T [V]	η_c[a] [cd/A]	η_c[b] [cd/A]	B_{max} [cd/m^2]	λ_{max} [nm]
PVK:**1a**	8.7	0.39	0.30	211 (19.3 V)	535
PVK:**1b**	6.1	0.72	0.55	403 (13 V)	548
PVK:**2a**	9.3	0.32	0.22	124 (20.9 V)	620
PVK:**2b**	7.9	0.63	0.42	119 (16.7 V)	628
PVK:**3a**	9.3	0.33	0.23	124 (18.9 V)	522
PVK:**3b**	7.7	0.84	0.58	370 (14.9 V)	540
TCCz:**1b**	6.1	0.95	0.84	1502 (13.5 V)	541
TCCz:**2b**	8.5	1.57	1.08	846 (15.9 V)	612
TCCz:**3b**	8.7	0.29	0.26	508 (18.1 V)	609
3b	7.9	4.9	1.7	164 (12 V)	542

[a] Measured at 1 mA/cm^2. [b] Measured at 10 mA/cm^2.

Contrary to those of $[Cu(N,N)(P,P)]^+$ systems,[3a,3f] the electroluminescent (EL) spectra of the complexes based on $\mathbf{L^2}$ or $\mathbf{L^3}$ have large redshifts (≈ 50 nm) in PVK compared to their photoluminescent (PL) spectra in PMMA films, as shown in Figure 10. The reason for this is not very clear but could be related to the flexible six-membered ring of (N–C–C–P–O–Cu), which may vibrate under the electric field and cause a decrease in the excited-state energy.[17] Although the complexes with the PPh_3 auxiliary ligand have almost the same quantum efficiencies in PMMA film compared to the complexes based on DPEphos, the devices based on the former displayed lower performances. A similar result has been observed previously by our group and has been ascribed to the ligand dissociation reactions in solutions.[3f] It is likely that an undetectable ligand-dissociation reaction still occurs in these mixed-ligand systems in CH_2Cl_2.

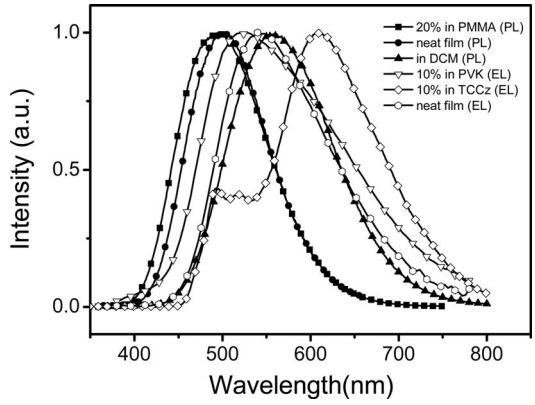

Figure 10. EL and PL spectra of **3b**.

With TCCz as the host material, the device performance of the complexes **1b** and **2b** are significantly improved in comparison with those with PVK. For instance, the current efficiency at 1.0 mA/cm^2 and the maximum brightness for **1b** increases from 0.72 to 0.95 cd/A and from 403 to 1502 cd/m^2, respectively. The improved performance of the devices based on TCCz may be attributed to the improved distribution of the cuprous complexes in TCCz than in PVK.[3f] The blueshifted EL spectra give further evidence for the lower aggregation level of the emitter in TCCz.

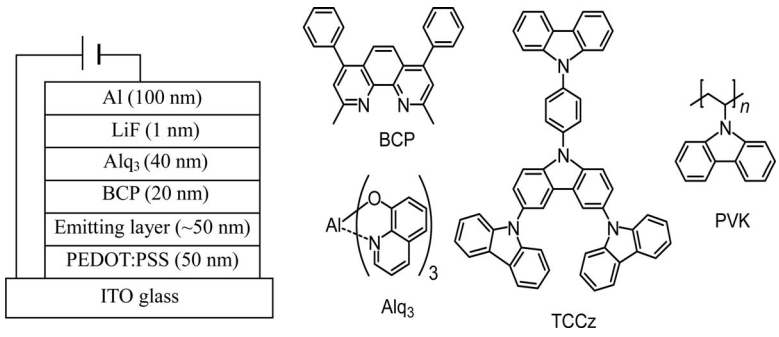

Figure 9. Device architecture (left) and molecular structures of the OLED materials (right).

However, TCCz is not a suitable host material for **3b**. As shown in Figure 10, the device based on a TCCz:**3b** emitting layer exhibited multiple emissions with the maximum at 609 nm, which is not from **3b** but probably from the exciplexes. DFT calculations reveal that **3b** has a relatively high LUMO level, while the LUMO level of TCCz is estimated to be 0.45 eV lower than that of PVK, judging from the cyclic voltammetry and absorption edge data. It may make the cuprous complex a less than an ideal center for electron direct-trapping in TCCz. In fact, the low current efficiency (0.8 cd/A at 1.0 mA/cm^2) and the impurities seen in the EL spectrum (Figure 10) suggest that **3b** has poor ability for charge capture even in PVK. For comparison, pure **3b** was used as the emitting layer in this device configuration. Unsurprisingly, the undoped device achieved an improved current efficiency of 4.9 cd/A at 1.0 mA/cm^2 with an EL spectrum almost identical to the PL spectrum of **3b** in CH_2Cl_2. We believe the EL performance of this complex can be further improved by optimizing the device configurations.

Conclusions

We report the synthesis and characterization of six mixed-ligand Cu^I complexes based on three N,O ligands. All of the complexes are easily prepared and stable in air. Similar to other mixed-ligands Cu^I complexes, they show the characteristic MLCT transition demonstrated by the electronic absorption spectra and DFT calculations. Their emissive colors depend on the electron-accepting ability of the N-heterocyclic unit in the N,O ligands. High PL efficiencies of about 0.70, without concentration quenching, were observed in these complexes (**3a** and **3b**) based on the ligand diphenyl(2-pyridylmethyl)phosphane oxide with a high π* level, implying that the cuprous complexes containing coordinated oxygen atoms are as effective phosphorescent emitters as the classical heteroleptic $[Cu(N,N)(P,P)]^+$ systems.

Experimental Section

General Considerations: The compounds $[Cu(CH_3CN)_4](BF_4)$,[20] diphenyl(2-pyridyl)phosphane oxide (**L^1**),[21] diphenyl(2-pyridylmethyl)phosphane oxide (**L^3**),[22] and 8-(diphenylphosphanyl)quinoline[23] were synthesized according to literature procedures. All other chemicals were of reagent grade and used without further purification. All solvents were dried and distilled by standard methods. ^{1}H NMR, with TMS as internal reference, and ^{31}P NMR spectra, with 85% H_3PO_4 as external reference were measured with a Bruker AV300 NMR spectrometer at room temperature. Elemental analyses were performed with a BioRad elemental analysis system. The UV/Vis and PL spectra were measured at room temperature with Perkin–Elmer Lambda 45 UV/Vis and Horiba Jobin–Yvon FluoroMax-4 spectrometers, respectively. The solution PL quantum efficiencies were measured and calculated by a relative method using $[Ru(bpy)_3](PF_6)_2$ (Φ = 0.042 in degassed water) as the standard.[24] The film samples were prepared by spin-coating a mixture of the Cu^I complex (20 wt.-%) and PMMA (80 wt.-%) in CH_2Cl_2 onto a quartz glass slide. The spectra were measured with the FluoroMax-4 spectrometer equipped with an integrating sphere and background-corrected by subtracting the spectrum obtained using a blank substrate, and subsequently corrected for the wavelength sensitivity of the fluorimeter and the spectra response of the sphere.[25] The film PL quantum efficiency was determined according to the method outlined by de Mello.[26] The luminescence-decay measurements were performed with the time-correlated single-photon counting (TCSPC) upgrade on the FluoroMax-4 spectrometer with a FluoroHub module. The lifetimes of solution samples were measured by TCSPC mode in conjunction with a nanoLED pulsed source (372 nm). The lifetimes of the PMMA film samples were measured by multi-channel scaling mode in conjunction with a spectraLED pulsed source (373 nm). Signals were collected with a FluoroHub module and analyzed by the DAS6 Decay Analysis software (HORIBA Jobin–Yvon).

Synthesis of the Ligand and the Cuprous Complexes

Synthesis of Diphenyl(8-quinolyl)phosphane Oxide (L^2): To 8-(diphenylphosphanyl)quinoline (0.60 g, 1.92 mmol) in thf (12 mL) was added an excess of 30% H_2O_2 at room temperature. The reaction mixture was stirred for 0.5 h. The solution was poured into water (ca. 30 mL) and extracted into CH_2Cl_2. The organic extract was dried with sodium sulfate, filtered, and concentrated to afford a yellow solid, which was purified by column chromatography to give **L^2**. Yield: 0.45 g (71.4%). ^{1}H NMR (300 MHz, $CDCl_3$, 298 K): δ = 7.36–7.50 (m, 7 H, Ar and quin-H3), 7.66 (m, 1 H, quin-H6), 7.80–7.87 (m, 4 H, Ar), 8.05 (d, $^3J_{H,H}$ = 8.1 Hz, 1 H, quin-H5), 8.19 (d, $^3J_{H,H}$ = 8.4 Hz, 1 H, quin-H4), 8.40 (dd, $^3J_{H,H}$ = 8.1 Hz, 1 H, quin-H7), 8.75 (dd, $^3J_{H,H}$ = 4.2 Hz, 1 H, quin-H2) ppm.

Synthesis of $[Cu(L^1)(PPh_3)_2](BF_4)$ (1a): Under nitrogen, $[Cu(CH_3CN)_4](BF_4)$ (0.157 g, 0.5 mmol) and PPh_3 (0.263 g, 1.0 mmol) were dissolved in CH_2Cl_2 (8 mL) and stirred for 1 h. **L^1** (0.139 g, 0.5 mmol) was added to the solution, and the mixture was stirred for 5 h. The solution was filtered, and the solvents were removed. The same procedure was applied in the synthesis of the complexes **1b**, **2a**, **2b**, **3a**, and **3b**. Recrystallization of the residue from CH_2Cl_2 and methanol (MeOH) gave yellow-green crystals of **1a**. Yield: 0.27 g (56.7%). ^{1}H NMR (300 MHz, $CDCl_3$, 298 K): δ = 7.09–7.18 (m, 26 H, Ar), 7.27–7.36 (m, 12 H, Ar), 7.55 (m, 2 H, Ar), 7.70 (m, 1 H, Py-H5), 7.82 (m, 1 H, Py-H4), 8.29 (m, 1 H, Py-H3), 8.44 (m, 1 H, Py-H6) ppm. ^{31}P NMR: δ = –34.25 (s, PPh_3), 0.69 (s, PO) ppm. $C_{53}H_{44}BCuF_4NOP_3 \cdot 0.2CH_2Cl_2$ (970.0): calcd. C 65.79, H 4.61, N 1.44; found C 65.85, H 4.32, N 1.48.

Synthesis of $[Cu(L^1)(DPEphos)](BF_4)$ (1b): Recrystallization of the residue from CH_2Cl_2 and MeOH gave yellow-green crystals of **1b**. Yield: 0.28 g (57.9%). ^{1}H NMR (300 MHz, $CDCl_3$, 298 K): δ = 6.72 (m, 2 H, Ar), 6.96 (t, $^3J_{H,H}$ = 7.5 Hz, 6 H, Ar), 7.05 (m, 6 H, Ar), 7.16–7.35 (m, 22 H, Ar), 7.49 (m, 3 H, Py-H5 and Ar), 7.81 (t, $^3J_{H,H}$ = 6.6 Hz, 1 H, Py-H4), 8.20 (d, $^3J_{H,H}$ = 4.8 Hz, 1 H, Py-H3), 8.27 (m, 1 H, Py-H6) ppm. ^{31}P NMR: δ = –48.00 (s, DPEphos), 0.91 (s, PO) ppm. $C_{53}H_{42}BCuF_4NO_2P_3$ (967.2): calcd. C 65.75, H 4.37, N 1.45; found C 65.94, H 4.00, N 1.44.

Synthesis of $[Cu(L^2)(PPh_3)_2](BF_4)$ (2a): Recrystallization of the residue from MeOH gave yellow crystals of **2a**. Yield: 0.30 g (61.2%). ^{1}H NMR (300 MHz, $CDCl_3$, 298 K): δ = 6.97–7.41 (m, 40 H, Ar), 7.51 (m, 2 H, quin-H3 and H6), 7.64 (t, $^3J_{H,H}$ = 6.3 Hz, 1 H, quin-H5), 8.38 (d, $^3J_{H,H}$ = 7.5 Hz, 1 H, quin-H4), 8.59 (m, 2 H, quin-H2 and H7) ppm. ^{31}P NMR: δ = –34.97 (s, PPh_3), 6.28 (s, PO) ppm. $C_{57}H_{46}BCuF_4NOP_3$ (1003.2): calcd. C 68.17, H 4.61, N 1.39; found C 67.77, H 4.61, N 1.53.

Synthesis of $[Cu(L^2)(DPEphos)](BF_4)$ (2b): Recrystallization of the residue from MeOH gave yellow crystals of **2b**. Yield: 0.24 g

Table 4. Crystallographic data for compounds **1a**, **1b**, **2a**, **2b**, **3a**, and **3b**.

	1a	1b	2a	2b	3a	3b
Empirical formula	$C_{109}H_{93}B_2Cl_7Cu_2F_8N_2O_2P_6$	$C_{56}H_{48}BCuF_4NO_3P_3$	$C_{57}H_{46}BCuF_4NOP_3$	$C_{58.5}H_{50}BCuF_4NO_{3.5}P_3$	$C_{55}H_{50}BCuF_4NO_2P_3$	$C_{55}H_{48}BCuF_4NO_3P_3$
Formula mass	2197.52	1002.19	1004.21	1066.26	1000.22	1014.20
Crystal system	monoclinic	triclinic	triclinic	triclinic	monoclinic	orthorhombic
Space group	*C*2/*c*	$P\bar{1}$	$P\bar{1}$	$P\bar{1}$	$P2_1/c$	$Pna2_1$
a [Å]	57.114(3)	12.7999(8)	12.3447(9)	12.2697(8)	12.8052(10)	33.5515(14)
b [Å]	12.7707(6)	14.0967(8)	13.1441(10)	14.1003(9)	22.1640(13)	9.2554(4)
c [Å]	27.2789(12)	14.3565(8)	16.4044(13)	15.6564(10)	17.9279(11)	15.6499(7)
α [°]	90	72.3360(10)	73.6520(10)	103.0970(10)	90	90
β [°]	91.1270(10)	75.0550(10)	83.6310(10)	97.4870(10)	95.555(5)	90
γ [°]	90	88.6640(10)	72.6630(10)	93.7190(10)	90	90
V [Å^3]	19892.9(15)	2380.6(2)	2437.1(3)	2603.2(3)	5064.3(6)	4859.8(4)
Z	8	2	2	2	4	4
$D_{calcd.}$ [g cm^{-3}]	1.467	1.398	1.368	1.360	1.312	1.386
Abs. coefficient [mm^{-1}]	0.780	0.621	0.604	0.573	0.582	0.609
Final *R* indices [$I > 2\sigma(I)$]:						
*R*1, *wR*2	0.0576, 0.1156	0.0545, 0.1549	0.0505, 0.1285	0.0581, 0.1580	0.0647, 0.1813	0.0346, 0.0809
R indices (all data):						
*R*1, *wR*2	0.1048, 0.1277	0.0713, 0.1642	0.0635, 0.1384	0.0761, 0.1724	0.0894, 0.2069	0.0384, 0.0830
GOF	0.997	1.003	1.015	1.015	1.057	1.016

(47.2%). ^{1}H NMR (300 MHz, $CDCl_3$, 298 K): δ = 6.64–7.31 (m, 38 H, Ar), 7.49 (td, $^3J_{H,H}$ = 7.2 Hz, 2 H, quin-H3 and H6), 7.62 (m, 1 H, quin-H5), 8.37 (d, $^3J_{H,H}$ = 7.5 Hz, 1 H, quin-H4), 8.47 (d, $^3J_{H,H}$ = 8.4 Hz, 1 H, quin-H7), 8.58 (d, $^3J_{H,H}$ = 8.4 Hz, 1 H, quin-H2) ppm. ^{31}P NMR: δ = –48.29 (s, DPEphos), 6.78 (s, PO) ppm. $C_{57}H_{44}BCuF_4NO_2P_3$ (1017.2): calcd. C 67.23, H 4.36, N 1.38; found C 66.96, H 4.36, N 1.24.

Synthesis of [Cu(L^3)(PPh$_3$)$_2$](BF$_4$) (3a): Recrystallization of the residue from MeOH gave colorless crystals of **3a**. Yield: 0.35 g (72.3%). ^{1}H NMR (300 MHz, $CDCl_3$, 298 K): δ = 3.75 (d, $^2J_{H,H}$ = –13.8 Hz, 2 H, CH_2), 6.83 (m, 1 H, Py-H3), 7.09–7.14 (m, 24 H, Ar), 7.31–7.46 (m, 12 H, Ar), 7.61–7.72 (m, 5 H, Ar and Py-H5), 7.89 (d, $^3J_{H,H}$ = 7.8 Hz, 1 H, Py-H4), 7.98 (d, $^3J_{H,H}$ = 4.8 Hz, 1 H, Py-H6) ppm. ^{31}P NMR: δ = –2.51 (s, PPh_3), 36.42 (s, PO) ppm. $C_{54}H_{46}BCuF_4NOP_3 \cdot CH_3OH$ (999.2): calcd. C 66.04, H 5.04, N 1.40; found C 65.84, H 4.82, N 1.24.

Synthesis of [Cu(L^3)(DPEphos)](BF$_4$) (3b): Recrystallization of the residue from MeOH gave colorless crystals of **3b**. Yield: 0.30 g (61.2%). ^{1}H NMR (300 MHz, $CDCl_3$, 298 K): δ = 3.77 (d, $^2J_{H,H}$ = –13.8 Hz, 2 H, CH_2), 6.77 (m, 3 H, Py-H3 and Ar), 6.91–7.02 (m, 5 H, Ar), 7.18–7.49 (m, 31 H, Ar), 7.69 (t, $^3J_{H,H}$ = 7.5 Hz, 1 H, Py-H5), 7.82 (d, $^3J_{H,H}$ = 7.5 Hz, 1 H, Py-H4), 8.02 (d, $^3J_{H,H}$ = 4.5 Hz, 1 H, Py-H6) ppm. ^{31}P NMR: δ = –17.02 (s, DPEphos), 37.09 (s, PO) ppm. $C_{54}H_{44}BCuF_4NO_2P_3 \cdot CH_3OH$ (1013.2): calcd. C 65.13, H 4.77, N 1.38; found C 65.30, H 4.41, N 1.12.

X-ray Crystallographic Studies: Data from selected crystals were collected with a Bruker Smart APEX diffractometer with a CCD detector, graphite monochromator, and Mo-K_α radiation (λ = 0.71073 Å). The intensity data were recorded in the ω-scan mode (187 K). Lorentz and polarization factors were used to correct the raw intensity data, and absorption corrections were performed by using the SADABS[27] program. The crystal structure was solved by using the SHELXTL program and refined by using full-matrix least squares.[28] All non-hydrogen atoms were refined anistropically. The positions of the hydrogen atoms attached to carbon atoms were fixed at their ideal positions. Details of crystal and structure refinement are shown in Table 4. CCDC-765391, -765392, -765393, and -765397, -765398, and -765399 contain the supplementary crystallographic data for complexes **1a**, **1b**, **3b**, **3a**, **2b**, and **2a**, respectively. These data can be obtained free of charge from The Cambridge Crystallographic Data Centre via http://www.ccdc.cam.ac.uk/data request/cif.

Density Functional Calculations: DFT calculations were performed by using the GAUSSIAN 03 software package[29] using a spin-restricted formalism at the B3LYP level. 6-31+G** was used to optimize the molecular geometry as a basis set for all elements, and Los Alamos ECP plus DZ (LANL2DZ) was used additionally for Cu. The HOMO and LUMO energies were determined by using minimized singlet geometries to approximate the ground states.

Acknowledgments

This work was supported by the National Natural Science Foundation of China (Nos. 20874098 and 50772113), the Natural Science Foundation of Fujian Province (No. 2007F3116), the Science Fund for Creative Research Groups (No. 20621401), and the 973 Project (2009CB623600).

[1] a) E. Cariati, J. Bourassa, P. C. Ford, *Chem. Commun.* **1998**, 1623–1624; b) H. V. R. Dias, H. V. K. Diyabalanage, M. A. Rawashdeh-Omary, M. A. Franzman, M. A. Omary, *J. Am. Chem. Soc.* **2003**, *125*, 12072–12073; c) L. F. Shi, B. Li, *Eur. J. Inorg. Chem.* **2009**, 2294–2302.

[2] a) D. R. McMillin, K. M. McNett, *Chem. Rev.* **1998**, *98*, 1201–1219; b) E. A. Lewis, W. B. Tolman, *Chem. Rev.* **2004**, *104*, 1047–1076.

[3] a) Q. S. Zhang, Q. G. Zhou, Y. X. Cheng, L. X. Wang, D. G. Ma, X. B. Jing, F. S. Wang, *Adv. Mater.* **2004**, *16*, 432–436; b) W. L. Jia, T. McCormick, Y. Tao, J. P. Lu, S. N. Wang, *Inorg. Chem.* **2005**, *44*, 5706–5712; c) Q. S. Zhang, Q. G. Zhou, Y. X. Cheng, L. X. Wang, D. G. Ma, X. B. Jing, F. S. Wang, *Adv. Funct. Mater.* **2006**, *16*, 1203–1208; d) N. Armaroli, G. Accorsi, M. Holler, O. Moudam, J. F. Nierengarten, Z. Y. Zhou, R. T. Wegh, R. Welter, *Adv. Mater.* **2006**, *18*, 1313–1316; e) Z. S. Su, G. B. Che, W. L. Li, W. M. Su, M. T. Li, B. Chu, B. Li, Z. Q. Zhang, Z. Z. Hu, *Appl. Phys. Lett.* **2006**, *88*, 213508 (1–3); f) Q. S. Zhang, J. Q. Ding, Y. X. Cheng, L. X. Wang, Z. Y. Xie,

X. B. Jing, F. S. Wang, *Adv. Funct. Mater.* **2007**, *17*, 2983–2990; g) N. Robertson, *ChemSusChem* **2008**, *1*, 977–979.
[4] a) D. V. Scaltrito, D. W. Thompson, J. A. O'Callaghan, G. J. Meyer, *Coord. Chem. Rev.* **2000**, *208*, 243–266; b) N. Armaroli, *Chem. Soc. Rev.* **2001**, *30*, 113–124; c) N. Armaroli, G. Accorsi, F. Cardinali, A. Listorti, *Top. Curr. Chem.* **2007**, *280*, 69–115; d) A. Lavie-Cambot, M. Cantuel, Y. Leydet, G. Jonusauskas, D. M. Bassani, N. D. McClenaghan, *Coord. Chem. Rev.* **2008**, *252*, 2572–2584.
[5] A. Barbieri, G. Accorsi, N. Armaroli, *Chem. Commun.* **2008**, 2185–2193.
[6] a) D. G. Cuttell, S. M. Kuang, P. E. Fanwick, D. R. McMillin, R. A. Walton, *J. Am. Chem. Soc.* **2002**, *124*, 6–7; b) S. M. Kuang, D. G. Cuttell, D. R. McMillin, P. E. Fanwick, R. A. Walton, *Inorg. Chem.* **2002**, *41*, 3313–3322.
[7] O. Moudam, A. Kaeser, B. Delavaux-Nicot, C. Duhayon, M. Holler, G. Accorsi, N. Armaroli, I. Se'guy, J. Navarro, P. Destruel, J. Nierengarten, *Chem. Commun.* **2007**, 3077–3079.
[8] S. B. Harkins, J. C. Peters, *J. Am. Chem. Soc.* **2005**, *127*, 2030–2031.
[9] A. J. M. Miller, J. L. Dempsey, J. C. Peters, *Inorg. Chem.* **2007**, *46*, 7244–7246.
[10] T. Tsukuda, C. Nishigata, K. Arai, T. Tsubomura, *Polyhedron* **2009**, *28*, 7–12.
[11] L. Qin, Q. S. Zhang, W. Sun, J. Y. Wang, C. Z. Lu, Y. X. Cheng, L. X. Wang, *Dalton Trans.* **2009**, 9388–9391.
[12] a) G. Pilloni, B. Corain, M. Degano, B. Longato, G. Zanotti, *J. Chem. Soc., Dalton Trans.* **1993**, 1777–1778; b) G. Pilloni, G. Valle, C. Corvaja, B. Longato, B. Corain, *Inorg. Chem.* **1995**, *34*, 5910–5918; c) P. Pinto, M. J. Calhorda, V. Félix, T. Avilés, M. G. B. Drew, *Monatsh. Chem.* **2000**, *131*, 1253–1265; d) H. Z. Liu, M. J. Calhorda, M. G. B. Drew, V. Félix, J. Novosad, L. F. Veiros, F. F. de Biani, P. Zanello, *J. Chem. Soc., Dalton Trans.* **2002**, 4365–4374.
[13] F. Hung-Low, A. Renz, K. K. Klausmeyer, *Eur. J. Inorg. Chem.* **2009**, 2994–3002.
[14] J. R. Kirchhoff, D. R. McMillin, W. R. Robinson, D. R. Powell, A. T. Mckenzie, S. Chen, *Inorg. Chem.* **1985**, *24*, 3928–3933.
[15] T. McCormick, W. L. Jia, S. N. Wang, *Inorg. Chem.* **2006**, *45*, 147–155.
[16] a) G. Hughes, M. R. Bryce, *J. Mater. Chem.* **2005**, *15*, 94–107; b) A. P. Kulkani, C. J. Tonzola, A. Babel, S. A. Jenekhe, *Chem. Mater.* **2004**, *16*, 4556–4573.
[17] A. Tsuboyama, K. Kuge, M. Furugori, S. Okada, M. Hoshino, K. Ueno, *Inorg. Chem.* **2007**, *46*, 1992–2001.
[18] a) Y. Kawamura, S. Yanagida, S. R. Forrest, *J. Appl. Phys.* **2002**, *92*, 87–93; b) A. Nakamura, T. Tada, M. Mizukami, S. Yagyu, *Appl. Phys. Lett.* **2004**, *84*, 130–132.
[19] J. Q. Ding, J. H. lü, Y. X. Cheng, Z. Y. Xie, L. X. Wang, D. G. Ma, X. B. Jing, F. S. Wang, *Adv. Funct. Mater.* **2008**, *18*, 2754–2762.
[20] G. J. Kubas, *Inorg. Synth.* **1979**, *19*, 90–92.
[21] G. R. Newkome, D. C. Hager, *J. Org. Chem.* **1978**, *43*, 947–949.
[22] G. Minghetti, S. Stoccoro, M. A. Cinellu, A. Zucca, M. Manassero, M. Sansoni, *J. Chem. Soc., Dalton Trans.* **1998**, 4119–4126.
[23] a) Y. C. Wang, C. W. Lai, F. Y. Kwong, W. Jia, K. S. Chan, *Tetrahedron* **2004**, *60*, 9433–9439; b) W. H. Sun, Z. L. Li, H. M. Hu, B. Wu, H. J. Yang, N. Zhu, X. B. Leng, H. G. Wang, *New J. Chem.* **2002**, *26*, 1474–1478.
[24] a) J. Van Houten, R. J. Watts, *J. Am. Chem. Soc.* **1976**, *98*, 4853–4858; b) W. L. Wallace, A. J. Bard, *J. Phys. Chem.* **1979**, *83*, 1350–1357.
[25] L. O. Pålsson, A. P. Monkman, *Adv. Mater.* **2002**, *14*, 757–758.
[26] J. C. de Mello, H. F. Wittmann, R. H. Friend, *Adv. Mater.* **1997**, *9*, 230–232.
[27] R. H. Blessing, *Acta Crystallogr., Sect. A* **1995**, *51*, 33–38.
[28] G. M. Sheldrick, *SHELXTL*, version 5.1, Bruker Analytical X-ray Systems, Inc., Madison, WI, **1997**.
[29] M. J. Frisch, G. W. Trucks, H. B. Schlegel, G. E. Scusseria, M. A. Robb, J. R. Cheeseman, J. A. Montgomery, T. Vreven, K. N. Kudin, J. C. Burant, J. M. Millam, S. S. Iyengar, J. Tomasi, V. Barone, B. Mennucci, M. Cossi, G. Scalmani, N. Rega, G. A. Petersson, H. Nakatsuji, M. Hada, M. Ehara, K. Toyota, R. Fukuda, J. Hasegawa, M. Ishida, T. Nakajima, Y. Honda, O. Kitao, H. Nakai, M. Klene, X. Li, J. E. Knox, H. P. Hratchian, J. B. Cross, C. Adamo, J. Jaramillo, R. Gomperts, R. E. Stratmann, O. Yazyev, A. J. Austin, R. Cammi, C. Pomelli, J. W. Ochterski, P. Y. Ayala, K. Morokuma, G. A. Voth, P. Salvador, J. J. Dannenberg, V. G. Zakrzewski, S. Dapprich, A. D. Daniels, M. C. Strain, O. Farkas, D. K. Malick, A. D. Rabuck, K. Raghavachari, J. B. Foresman, J. V. Ortiz, Q. Cui, A. G. Baboul, S. Clifford, J. Cioslowski, B. B. Stefanov, G. Liu, A. Liashenko, P. Piskorz, I. Komaromi, R. L. Martin, D. J. Fox, T. Keith, M. A. Al-Laham, C. Y. Peng, A. Nanayakkara, M. Challacombe, P. M. W. Gill, B. Johnson, W. Chen, M. W. Wong, C. Gonzalez, J. A. Pople, *Gaussian 03*, rev. B. 03, Gaussian, Inc. Pittsburgh, PA, **2003**..

Received: April 5, 2010
Published Online: July 9, 2010

DOI: 10.1002/ejic.201000165

Synthesis, Characterisation and Luminescent Properties of Mixed-Ligand Copper(I) Complexes Incorporating *N*-Thiophosphorylated Thioureas and Phosphane Ligands

Maria G. Babashkina,[a] Damir A. Safin,*[a] Axel Klein,*[a] and Michael Bolte[b]

Keywords: Chelate complexes / Copper / Crystal Structure / Luminescence / Phosphanes / Thiourea

The potassium salts of $H_2NC(S)NHP(S)(OiPr)_2$ (HL^I) or *o*-$C_6H_4[NHC(S)NHP(S)(OiPr)_2]_2$ (H_2L^{II}) react with $[Cu(PPh_3)_3I]$ or a mixture of CuI and $Ph_2P(CH_2)_{1-3}PPh_2$ or $Ph_2P(C_5H_4FeC_5H_4)PPh_2$ in aqueous $EtOH/CH_2Cl_2$ to give mononuclear complexes $[Cu(PPh_3)L^I]$ (**1**), $[Cu\{Ph_2P(CH_2)_2PPh_2\}L^I]$ (**2**), $[Cu\{Ph_2P(CH_2)_3PPh_2\}L^I]$ (**3**) or $[Cu\{Ph_2P(C_5H_4FeC_5H_4)PPh_2\}L^I]$ (**4**), or dinuclear complexes $[Cu_2(Ph_2PCH_2PPh_2)L^I_2]$ (**5**), $[Cu_2(PPh_3)_2L^{II}]$ (**6**), $[Cu_2\{Ph_2P(CH_2)_2PPh_2\}_2L^{II}]$ (**7**), $[Cu_2\{Ph_2P(CH_2)_3PPh_2\}_2L^{II}]$ (**8**), $[Cu_2\{Ph_2P(C_5H_4FeC_5H_4)PPh_2\}_2L^{II}]$ (**9**) or $[Cu_2(Ph_2PCH_2PPh_2)L^{II}]$ (**10**). The structures of these compounds were investigated by ^1H and $^{31}P\{^1H\}$ NMR, UV/Vis spectroscopy and elemental analysis. The crystal structures of H_2L^{II}, **1**, **3**–**6**, **8** and **10** were determined by single-crystal X-ray diffraction. The luminescent properties of complexes **1**–**10** in the solid state are reported.

Introduction

In preceding papers we described heteroligand complexes of Cu^I with a number of *N*-thiophosphorylated thioureas and thioamide $RC(S)NHP(S)(OiPr)_2$ [R = morpholin-4-yl, piperidin-1-yl,[1] (1-naphthyl)NH,[2] NH_2 (HL^I),[1,3] (pyridin-2-yl)NH, (pyridin-3-yl)NH, H_2N-6-Py-2-NH,[4] Ph, Et_2N,[5–7] $(EtO)_2P(O)CH_2C_6H_4$-4-NH,[8] MeNH, *i*PrNH, *t*BuNH, Me_2N, PhNH, 2,6-$Me_2C_6H_3NH$, 2,4,6-$Me_3C_6H_2NH$[9–11]] and triphenylphosphane or $Ph_2P(CH_2)_{1-3}PPh_2$ and $Ph_2P(C_5H_4FeC_5H_4)PPh_2$. We also showed that the reactions of alkaline salts of the tetrakis-thiourea containing a cyclam fragment with $[Cu(PPh_3)_3I]$ lead to the tetranuclear Cu^I complex $[\{Cu(PPh_3)_2\}_4$-(cyclam)] (Scheme 1).[12]

We have also described a number of *N*-(thio)phosphorylated bis(thio)ureas, which are potentially bridging ligands, and investigated their complexation properties towards various metal cations.[6,13–20] Only one dinuclear heteroligand complex of Cu^I with *N*-thiophosphoryl bis(thiourea), containing 1,10-diaza-18-crown-6, and PPh_3 (Scheme 1) has been described.[6] To the best of our knowledge there are no crystal structures of such types of complexes. Furthermore, we have described two Cu^I complexes

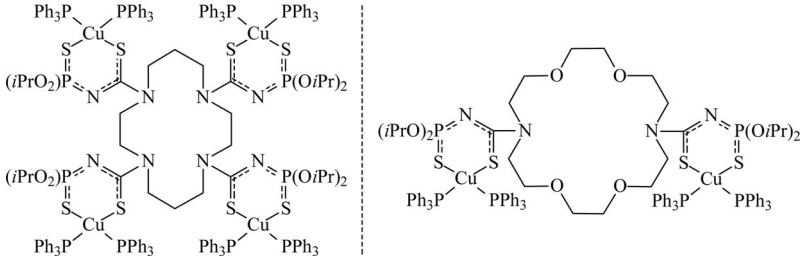

Scheme 1.

$[CuPPh_3\{RC(S)NP(S)(OiPr)_2\}]$ (R = H_2N-6-Py-2-NH,[4] $(EtO)_2P(O)CH_2C_6H_4$-4-NH[8]) containing one triphenylphosphane (PPh_3) ligand. A number of heteroligand Cu^I complexes containing both aryl-substituted pnictides and cyclic thioureas or pyridinethiolates have also been described.[21–23] A combination of these two types of ligands might lead to interesting and unusual photophysical and electrochemical properties.[24]

[a] Institut für Anorganische Chemie, Universität zu Köln, Greinstrasse 6, 50939 Köln, Germany
Fax: +49-221-4705196
E-mail: damir.safin@ksu.ru
axel.klein@uni-koeln.de
[b] Institut für Anorganische Chemie, J.-W.-Goethe-Universität, 60438 Frankfurt/Main, Germany

Supporting information for this article is available on the WWW under http://dx.doi.org/10.1002/ejic.201000165.

In this contribution we describe new heteroligand complexes of Cu^I with $H_2NC(S)NHP(S)(OiPr)_2$ (HL^I) and *o*-$C_6H_4[NHC(S)NHP(S)(OiPr)_2]_2$ (H_2L^{II}; Scheme 2) and phosphanes [PPh_3, $Ph_2P(CH_2)_{1-3}PPh_2$, $Ph_2P(C_5H_4FeC_5H_4)PPh_2$] along with their structural characterisation and luminescent properties. Mononuclear derivatives with non-bridging thiourea ligands and the phosphane ligands PPh_3, $Ph_2P(CH_2)_{1-3}PPh_2$ or $Ph_2P(C_5H_4FeC_5H_4)PPh_2$ have recently been described.[10,11]

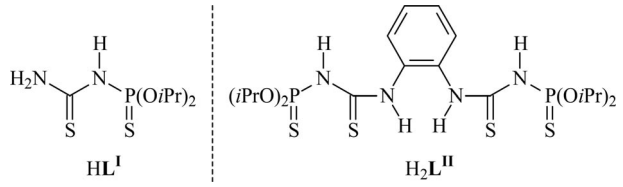

Scheme 2.

Results and Discussion

Synthesis

N-Thiophosphorylated thiourea HL^I was prepared as described previously.[1,3,25] *N*-Thiophosphorylated bis(thiourea) H_2L^{II} was prepared by addition of *o*-phenylenediamine to *O*,*O*′-diisopropylthiophosphoric isothiocyanate, $(iPrO)_2P(S)NCS$, similarly to the previously described method.[13] Reactions of the potassium salts of HL^I and H_2L^{II} with $[Cu(PPh_3)_3I]$ or a mixture of CuI and $Ph_2P(CH_2)_{1-3}PPh_2$ or $Ph_2P(C_5H_4FeC_5H_4)PPh_2$ in aqueous $EtOH/CH_2Cl_2$ led to the mononuclear complexes $[Cu(PPh_3)L^I]$ (**1**), $[Cu\{Ph_2P(CH_2)_2PPh_2\}L^I]$ (**2**), $[Cu\{Ph_2P(CH_2)_3PPh_2\}L^I]$ (**3**) or $[Cu\{Ph_2P(C_5H_4FeC_5H_4)PPh_2\}L^I]$ (**4**), or the dinuclear complexes $[Cu_2(Ph_2PCH_2PPh_2)L^I_2]$ (**5**), $[Cu_2(PPh_3)_2L^{II}]$ (**6**), $[Cu_2\{Ph_2P(CH_2)_2PPh_2\}_2L^{II}]$ (**7**), $[Cu_2\{Ph_2P(CH_2)_3PPh_2\}_2L^{II}]$ (**8**), $[Cu_2\{Ph_2P(C_5H_4FeC_5H_4)PPh_2\}_2L^{II}]$ (**9**) or $[Cu_2(Ph_2PCH_2PPh_2)L^{II}]$ (**10**) (Scheme 3).

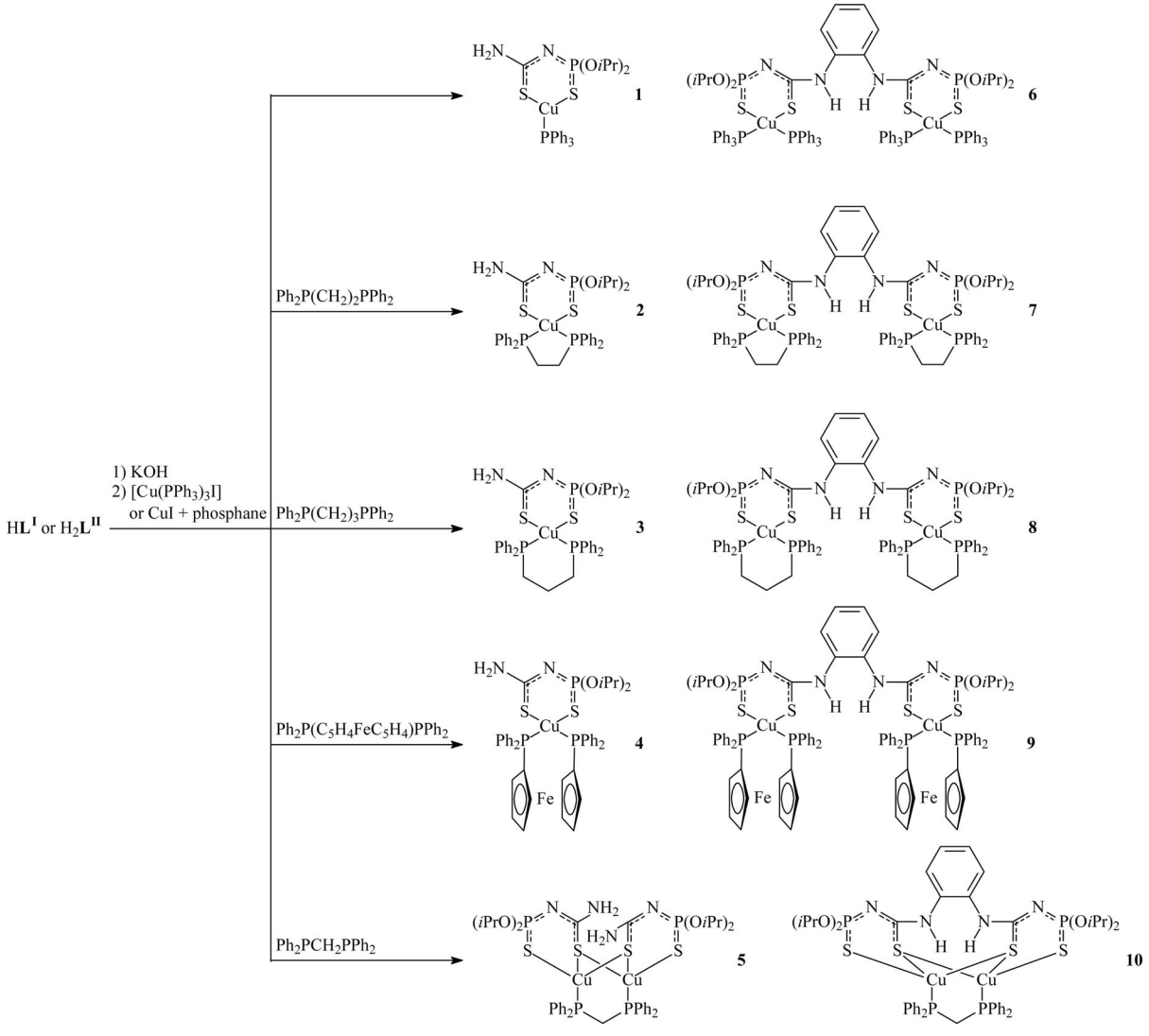

Scheme 3.

The complexes obtained are colourless crystalline powders, soluble in acetone, benzene, CH_2Cl_2, DMSO and DMF and insoluble in *n*-hexane. ^1H and $^{31}P\{^1H\}$ NMR spectroscopy indicated that the deprotonated thioureas $L^{I,II}$ are coordinated through the sulfur atoms of the thiocarbonyl and thiophosphoryl groups in all cases.

IR and NMR Spectroscopy and Photophysical Properties

The IR spectrum of H_2L^{II} contains a weak band centred at 652 cm^{-1} assigned to the P=S groups. The S=C–N fragment in the spectrum of the bis(thiourea) is shown as a band at 1553 cm^{-1}. There are two absorption bands at 3204 and 3422 cm^{-1} corresponding to the NH groups in the spectrum of H_2L^{II}, whereas a unique band at 3348–3369 cm^{-1} related to the (aryl)NH group is observed in the spectra of **6**–**10**. The IR spectra of the complexes contain a band at 594–616 cm^{-1} for the P=S group of the anionic forms $L^{I,II}$. These bands are shifted to low frequencies relative to the parent ligands as a result of coordination to the Cu^I ion. In the IR spectra of **1**–**10** there are bands at 1537–1562 cm^{-1} corresponding to the conjugated SCN fragment. In the IR spectra of **1**–**5** there are also a number of bands at 1609–1629, 3120–3137, 3241–3261 and 3483–3501 cm^{-1} corresponding to the NH_2 group. In addition, there is a broad intense band arising from the POC group at 988–1014 cm^{-1} in the spectra of H_2L^{II} and the complexes.

In the $^{31}P\{^1H\}$ NMR spectra of the complexes, the resonances in the range δ = 54.4–58.7 ppm correspond to the phosphorus atom of the thiophosphoryl group. These signals are shifted downfield relative to those in the spectra of HL^I and H_2L^{II}. The signals of the phosphorus atoms of PPh_3 in the spectra of the complexes **1** and **6** are found at δ = 0.4 and –1.5 ppm, respectively, whereas the signals for the phosphane phosphorus atoms in the $^{31}P\{^1H\}$ NMR spectra of the complexes **2**–**5** and **7**–**10** exhibit chemical shifts from δ = –22.4 to –10.6 ppm.

The ^1H NMR spectra of H_2L^{II} and **1**–**10** contain only signals that correspond to the proposed structures. The spectra contain a set of signals for the *i*Pr protons: signals for the CH_3 protons at δ = 0.85–1.47 ppm and signals for the CH protons at δ = 4.27–4.89 ppm. The signals for the aromatic ring and (aryl)NH protons are observed at δ = 6.70–8.29 ppm. Signals of the NH_2 group in the spectra of **1**–**5** are observed at δ = 5.33–5.72 ppm. In the ^1H NMR spectrum of H_2L^{II} the signal for the NHP proton is found at δ = 9.12 ppm. The signals for the NHP group proton are absent in the ^1H NMR spectra of **1**–**10**. This confirms the anionic character of the ligands in the complexes. The ^1H NMR spectra of **2**, **3**, **5**, **7**, **8** and **10** contain signals for the CH_2 protons of the phosphanes $Ph_2P(CH_2)_{1-3}PPh_2$ at δ = 1.56–2.97 ppm, whereas signals for the C_5H_4 protons in the spectra of **4** and **9** are observed at δ = 4.20–4.29 ppm.

The absorption spectra of the complexes **1**–**10** were studied in CH_2Cl_2 solution (Figure S1 in the Supporting Information), whereas their luminescent properties were investigated in the solid state at room temperature (Figure 1). The data are reported in Table 1. Complexes **2**–**5** and **7**–**10** show emission in the solid state. The origin of the emission is believed to be based on intraligand transitions centred on the thiophosphoryl component of the ligands, which are influenced by the nature of the phosphane. PPh_3 complexes did not exhibit any luminescence properties. One interesting point in this respect is the unusually low energy and intensity of the emission of the complexes **5** and **10**, which might be due to contributions from cluster-centred charge-transfer transition in these dinuclear aggregates, which show rather short Cu1···Cu2 distances.

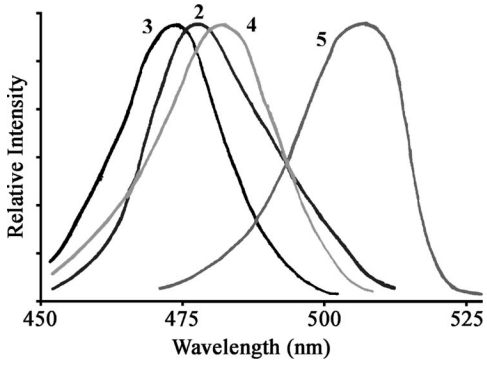

Figure 1. Emission spectra of **2**, **3**, **4** and **5**. The spectra of **7**–**10** are similar to the spectra of **2**–**5**, respectively. The excitation wavelength was chosen from the λ_{max} of the absorption.

Crystal Structures

Crystals of H_2L^{II}, **1**, **3**–**6**, **8** and **10** were obtained by slow evaporation of the solvent from their solutions in acetone/*n*-hexane (**1**) or CH_2Cl_2/*n*-hexane mixtures (1:5, v/v; see Exp. Sect.). The molecular structures of H_2L^{II}, **1**, **3**, **4**, **5**, **6**, **8** and

Table 1. UV/Vis absorption and emission maxima for complexes **1**–**10**.[a]

Complex	λ_{abs} [nm] (ε [$dm^3\,mol^{-1}\,cm^{-1}$])	λ_{em} [nm]	Complex	λ_{abs} [nm] (ε [$dm^3\,mol^{-1}\,cm^{-1}$])	λ_{em} [nm]
1	310 (10221)	no emission	**6**	304 (17631)	no emission
2	254 (19853), 302 (9632)	478	**7**	247 (31269), 306 (17564)	473
3	250 (19122), 307 (9471)	472	**8**	253 (28113), 306 (18103)	470
4	247 (19390), 310 (9718)	483	**9**	259 (33728), 311 (20824)	486
5	252 (3529), 373 (13382)	508	**10**	255 (3602), 379 (13127)	513

[a] Emission data obtained with excitation at λ of the long-wavelength absorption. The absorption spectra of the corresponding potassium salts show weak absorption bands at 289 (ε = 172 $dm^3\,mol^{-1}\,cm^{-1}$) (KL^I) and 297 nm (ε = 238 $dm^3\,mol^{-1}\,cm^{-1}$) (K_2L^{II}).

10 are shown in Figures 2, 3, 4, 5, 6, 7, 8, and 9, respectively. Selected bond lengths and angles are given in Tables 2 and 3.

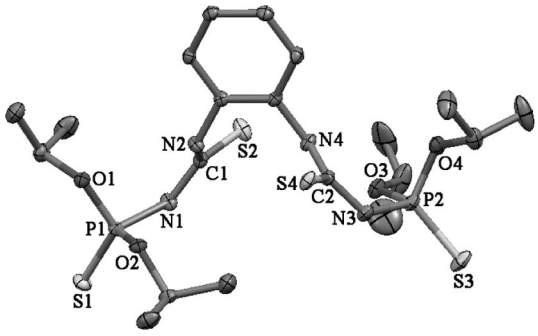

Figure 2. Thermal-ellipsoid representation of H_2L^{II} (hydrogen atoms have been omitted for clarity). Ellipsoids are drawn at the 30% probability level.

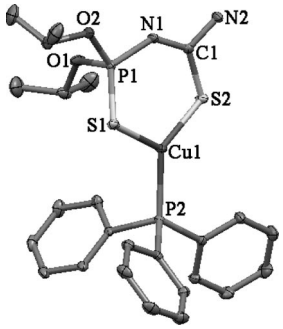

Figure 3. Thermal-ellipsoid representation of **1** (hydrogen atoms have been omitted for clarity). Ellipsoids are drawn at the 30% probability level.

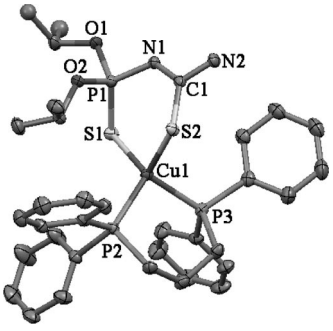

Figure 4. Thermal-ellipsoid representation of **3** (hydrogen atoms have been omitted for clarity). Ellipsoids are drawn at the 30% probability level.

The bis(thiourea) H_2L^{II} crystallises in the monoclinic space group *C*2/*c*. The parameters of the C=S, C–N, P–N and P=S bonds observed for H_2L^{II} (Table 2) are in the range typical for *N*-thiophosphorylated thiourea derivatives.[14] The two NC(S)N moieties show significant planarity (Figure 2). The two chelate backbones C(S)NP(S) are in

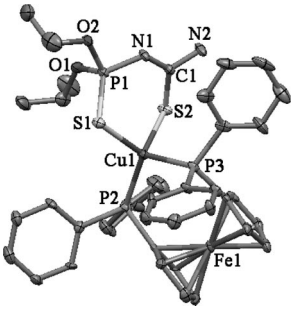

Figure 5. Thermal-ellipsoid representation of the independent molecule **A** of **4** (hydrogen atoms have been omitted for clarity). Ellipsoids are drawn at the 30% probability level.

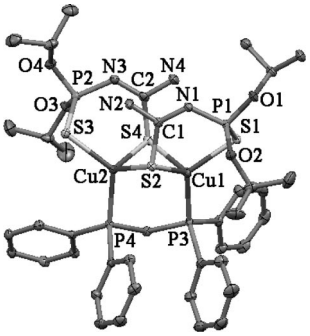

Figure 6. Thermal-ellipsoid representation of **5** (hydrogen atoms have been omitted for clarity). Ellipsoids are drawn at the 30% probability level.

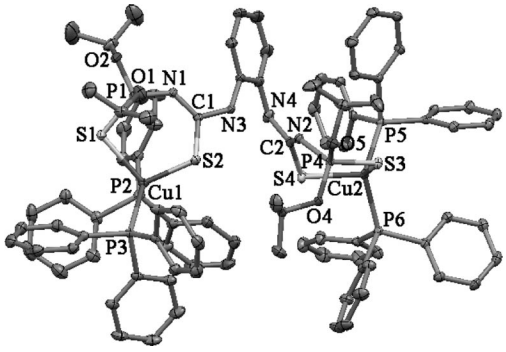

Figure 7. Thermal-ellipsoid representation of **6** (hydrogen atoms have been omitted for clarity). Ellipsoids are drawn at the 30% probability level.

an *anti* disposition relative to the phenylene spacer. Intra- and intermolecular hydrogen bonds of the type N–H···O–P and N–H···S=C, respectively, are present in the crystal of H_2L^{II} (Table 4). Intramolecular hydrogen bonds are formed between the oxygen atoms of the P–O groups and the hydrogen atoms of the (aryl)NH fragments, which in turn leads to an (*E*,*E*) conformation of the SCNP backbones. Intermolecular hydrogen bonds are formed between the hydrogen atom of one PNH group and the sulfur atom of the C=S group, and the same types of atoms of the two neighbouring molecules. As a result of the intermolecular hydrogen bonds (Table 4) a polymeric chain is formed in the crystal of H_2L^{II}.

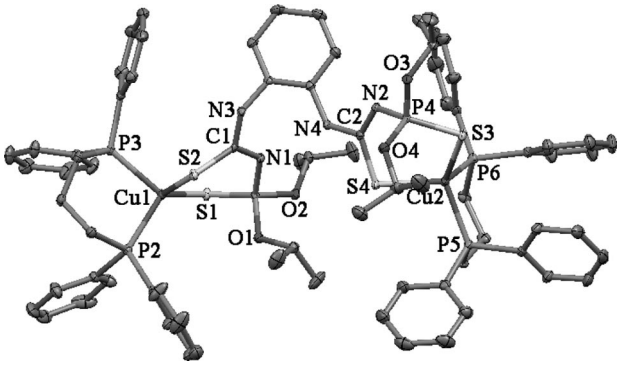

Figure 8. Thermal-ellipsoid representation **8** (hydrogen atoms have been omitted for clarity). Ellipsoids are drawn at the 30% probability level.

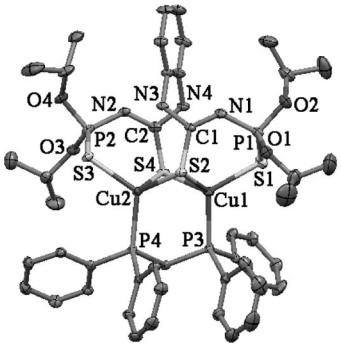

Figure 9. Thermal-ellipsoid representation of **10** (hydrogen atoms have been omitted for clarity). Ellipsoids are drawn at the 30% probability level.

Note that in our recent publication we published the synthesis of the complex $[Cu(PPh_3)_2L^I]$ (**11**), which contains two PPh_3 ligands.[1] Efforts to recrystallise **11** from a CH_2Cl_2/*n*-hexane mixture did not lead to crystals suitable for X-ray analysis, but according to the NMR spectroscopic data and elemental analysis, the material still contains two PPh_3 ligands. In the course of this work we tried to obtain crystals by the recrystallisation of **11** from an acetone/*n*-hexane mixture. Surprisingly, according to the NMR spectroscopic data and elemental analysis, the crystals obtained (suitable for X-ray diffraction) have the composition $[Cu(PPh_3)L^I]$ (**1**).

In the structure of **1** the geometry around the Cu atom is trigonal, formed by two S atoms and one PPh_3 ligand (Figure 3). The Cu–P bond [2.2127(7) Å, Table 2] is of practically the same length as observed for the complexes $[CuPPh_3\{RC(S)NP(S)(O\textit{i}Pr)_2\}]$ [R = H_2N-6-Py-2-NH,[4] $(EtO)_2P(O)CH_2C_6H_4$-4-NH[8]] with trigonally coordinated Cu^I. The six-membered CuSPNCS metallocycle has the conformation of a distorted boat. The fragment NC(S)NP is almost planar with the sulfur atom of the thiophosphoryl group deviating significantly from the average plane of this fragment; the torsion angle S1–P1–N1–C1 is 49.1(3)°.

In the structures of **3** and **4** the Cu^I cation is in a P_2S_2 tetrahedral environment formed by the two sulfur atoms of the deprotonated thiourea L^I ligand and the two phosphorus atoms of the $Ph_2P(CH_2)_3PPh_2$ or $Ph_2P(C_5H_4FeC_5H_4)$-PPh_2 molecule, respectively (Figures 4 and 5). The asymmetric unit of **4** contains two independent molecules. The Cu–S(C), Cu–S(P) and Cu–P bonds in **3** and **4** are markedly longer than those in **1** (Table 2). The S–Cu–S angle in **3** and

Table 2. Selected bond lengths [Å] and angles [°] for H_2L^{II}, **1**, **3**, and **4**.

	H_2L^{II}	**1**	**3**	**4**
C=S	1.6737(15), 1.6806(16)	1.752(3)	1.738(2)	1.730(9), 1.738(11)[a]
P=S	1.9133(6), 1.9162(6)	1.9594(9), 2.121(5)	1.9831(9)	1.987(3), 1.976(3)[a]
P–N	1.6775(14), 1.6838(14)	1.603(2)	1.602(2)	1.610(7), 1.609(7)[a]
P–O	1.5733(12), 1.5797(13), 1.5804(14), 1.5805(12)	1.578(2), 1.582(2)	1.588(2), 1.589(2)	1.593(6), 1.594(6), 1.578(6),[a] 1.583(6)[a]
C–N(P)	1.377(2)	1.314(3)	1.333(3)	1.316(10), 1.312(11)[a]
C–N	1.340(2), 1.343(2)	1.338(3)	1.335(3)	1.343(11), 1.356(12)[a]
Cu–S		2.2018(7)	2.3245(7)	2.325(3), 2.329(3)[a]
Cu–S(P)		2.2463(8), 2.376(5)	2.3559(6)	2.385(2), 2.358(2)[a]
Cu–P		2.2127(7)	2.2799(6), 2.2836(6)	2.280(2), 2.314(2), 2.296(2),[a] 2.300(2)[a]
S–C–N	122.21(12), 122.93(12)	115.0(2)	117.5(2)	116.2(6), 115.8(6)[a]
S–C–N(P)	120.61(12), 121.32(12)	129.0(2)	127.1(2)	127.1(7), 127.5(8)[a]
N–C–N	116.44(14), 116.46(13)	116.0(2)	115.4(2)	116.6(8), 116.6(9)[a]
C–N–P	127.93(12), 128.32(12)	130.7(2)	124.9(2)	125.3(6), 125.1(7)[a]
N–P–S	111.12(6), 111.86(6)	109.5(2), 121.94(9)	118.52(8)	119.1(3), 118.2(3)[a]
S–Cu–S		110.52(13), 115.86(3)	106.72(2)	106.21(9), 107.54(9)[a]
P–Cu–P			99.62(2)	110.68(9), 109.86(9)[a]
P–Cu–S		127.29(3)	107.96(2), 110.53(2)	104.22(9), 110.22(9), 101.70(9),[a] 116.24(9)[a]
P–Cu–S(P)	116.76(3), 121.15(12)	113.35(2), 118.27(2)	105.55(8), 118.87(9), 104.40(8),[a] 115.58(9)[a]	121.81(3), 124.53(3)[b]
Cu–S–C	107.21(8)	106.88(9)	103.6(3), 108.5(3)[a]	104.30(9), 99.72(9)[b]
Cu–S–P	86.9(2), 94.65(3)	96.90(3)	97.10(11), 93.08(11)[a]	98.38(3), 97.74(4)[b]
Cu–S–Cu				73.38(2), 69.95(2)

[a] Data for two independent molecules **A** and **B**. [b] Data for the Cu2–S4–C2(N4)–N3–P2(O3)(O4)–S3 backbone.

Table 3. Selected bond lengths [Å] and angles [°] for **5**, **6**, **8**, and **10**.

	5	**6**	**8**	**10**
C=S	1.769(3), 1.756(3)[a]	1.724(3), 1.733(3)	1.735(3), 1.741(3)	1.751(6), 1.774(5)
P=S	1.9934(10), 1.9917(10)[a]	1.9772(10), 1.9837(11)	1.9759(10), 1.9765(10)	1.987(2), 1.988(2)
P–N	1.617(2), 1.613(2)[a]	1.606(2), 1.624(2)	1.615(2), 1.622(2)	1.598(5), 1.599(5)
P–O	1.577(2), 1.583(2), 1.576(2),[a] 1.584(2)[a]	1.570(2), 1.576(2), 1.583(2)	1.571(2), 1.580(2), 1.5879(19), 1.590(2)	1.571(4), 1.574(4), 1.583(4), 1.584(4)
C–N(P)	1.326(3), 1.311(4)[a]	1.315(4), 1.318(4)	1.318(4), 1.325(4)	1.296(7), 1.313(8)
C–N	1.324(4), 1.346(4)[a]	1.355(4), 1.370(4)	1.358(3), 1.360(4)	1.347(8), 1.350(8)
Cu–S	2.3122(7), 2.5598(7), 2.3799(7),[a] 2.4309(7)[a]	2.3124(8), 2.3437(8)	2.3002(8), 2.3429(8)	2.3845(13), 2.4164(16), 2.4204(14), 2.5020(17)
Cu–S(P)	2.3236(7), 2.3250(8)[a]	2.3618(8), 2.3812(8)	2.2967(8), 2.3429(8)	2.3327(16), 2.3371(17)
Cu–P	2.2364(7), 2.2422(7)[a]	2.2756(9), 2.2960(8), 2.3121(8), 2.3155(9)	2.2472(8), 2.2593(8), 2.2702(8), 2.2808(9)	2.2277(16), 2.2355(15)
S–C–N	116.2(2), 115.3(2)[a]	114.4(2), 114.5(2)	114.0(2), 115.2(2)	117.0(5), 117.2(4)
S–C–N(P)	125.9(2), 127.0(2)[a]	127.7(2)	127.1(2), 127.6(2)	125.3(5), 126.2(5)
N–C–N	117.8(2), 117.6(3)[a]	117.8(3), 117.9(3)	117.7(2), 118.4(3)	116.8(5), 117.5(5)
C–N–P	124.6(2), 125.8(2)[a]	125.4(2), 125.5(2)	123.3(2), 126.5(2)	127.4(4), 128.5(4)
N–P–S	118.55(9), 116.80(9)[a]	117.78(10), 119.41(10)	116.46(9), 119.65(10)	113.9(2), 115.19(19)
S–Cu–S	98.10(2), 106.57(3), 108.96(2), 99.92(2),[a] 107.24(3),[a] 107.34(3)[a]	103.26(3), 104.27(3)	108.57(3), 110.49(3)	99.15(5), 100.57(5), 106.23(6), 115.15(6)
P–Cu–P		111.18(3), 121.11(3)	97.90(3), 99.81(3)	
P–Cu–S	122.16(3), 103.03(3)[a]	101.07(3), 105.63(3), 106.95(3), 121.47(3)	102.05(3), 103.03(3), 107.53(3), 112.21(3)	98.28(6), 104.58(5), 114.95(6), 120.35(6)
P–Cu–S(P)	116.76(3), 121.15(12)	101.19(3), 105.98(3), 113.02(3), 116.46(3)	107.17(3), 115.21(3), 123.04(3), 123.66(3)	116.22(6), 120.18(6)
Cu–S–C	107.21(8)	102.64(10), 102.84(10)	102.28(9), 104.29(9)	93.50(17), 95.03(17), 107.7(2), 107.92(19)
Cu–S–P	86.9(2), 94.65(3)	99.39(4), 102.05(4)	94.73(4), 95.81(4)	99.25(8), 99.85(7)
Cu–S–Cu				68.27(4), 70.27(4)

[a] Data for the Cu2–S4–C2(N4)–N3–P2(O3)(O4)–S3 backbone.

Table 4. Hydrogen-bond lengths [Å] and angles [°] for H_2L^{II}, **1**, **3**, **4**, **5**, **6**, **8**, and **10**.

	D–H···A	D–H	H···A	D···A	D–H···A
H_2L^{II}[a]	N1–H1···S2$^{\#1}$	0.79(2)	2.57(2)	3.3441(15)	170.0(18)
	N2–H2···O2	0.83(2)	2.31(2)	2.9644(17)	135.9(19)
	N3–H3···S4$^{\#2}$	0.81(2)	2.56(2)	3.3286(16)	158(2)
	N4–H4···O3	0.87(2)	2.22(3)	2.8957(18)	134(2)
1[b]	N2–H2A···N1$^{\#1}$	0.89(3)	2.23(3)	3.115(3)	172(3)
	N2–H2A···O2$^{\#1}$	0.89(4)	2.47(3)	2.999(3)	118(3)
3[c]	N2–H2B···N1$^{\#1}$	0.86(3)	2.37(3)	3.222(3)	172(2)
	N2–H2B···O1$^{\#1}$	0.86(3)	2.53(3)	3.099(3)	124(3)
4[d]	N2–H2A···N1$^{\#1}$	0.88	2.10	2.978(10)	172.4
	N2A–H2AA···N1A$^{\#2}$	0.88	2.34	3.166(11)	156.4
5[e]	N2–H2A···S3	0.86(3)	2.72(3)	3.503(3)	153(3)
	N2–H2B···N1$^{\#1}$	0.94(4)	2.32(4)	3.244(3)	167(3)
	N4–H4B···S1	0.83(4)	2.85(4)	3.561(3)	145(4)
6[f]	N3–H3···N2	0.69(3)	2.26(3)	2.851(4)	144(4)
	N4–H4···Cl1$^{\#1}$	0.77(4)	2.69(4)	3.437(4)	164(4)
8	N3–H3···S3	0.85(6)	2.72(6)	3.535(6)	161(5)
10[g]	N3–H3···S2$^{\#1}$	0.84(2)	2.83(3)	3.628(2)	158(3)
	N4–H4···N1	0.86(2)	2.15(3)	2.842(3)	137(3)

[a] Symmetry codes: #1: $-x + 1$, y, $-z + 3/2$; #2: $-x + 1$, $-y + 1$, $-z + 1$. [b] Symmetry codes: #1: $-x + 1$, $-y$, $-z$. [c] Symmetry codes: #1: $-x + 1$, $-y$, $-z + 1$. [d] Symmetry codes: #1: $-x + 1$, $-y + 1$, $-z$. [e] Symmetry codes: #1: $-x + 1$, $-y + 1$, $-z + 1$; #2: $-x + 1$, $-y + 1$, $-z + 2$. [f] Symmetry codes: #1: $-x + 1$, $-y + 1$, $-z + 1$. [g] Symmetry codes: #1: $-x + 1$, $-y + 2$, $-z + 1$.

4 is significantly smaller than that in **1**. The P–Cu–P angle in **4** is significantly larger than in **3** (Table 2), as expected for the replacement of the flexible $-(CH_2)_3-$ group by the ferrocenediyl unit.

In the dinuclear complex **5** the $Ph_2PCH_2PPh_2$ ligand bridges two Cu^I ions with two deprotonated thiourea groups coordinated to the Cu atoms through the thiophosphoryl and thiocarbonyl sulfur atoms of the ligand, the latter acting as a (μ,η^1,η^1)-Cu–S–Cu bridge, thus forming a dinuclear entity (Figure 6). Both Cu^I atoms in **5** are in a tetrahedral PS_3 environment. The same type of anionic thiourea ligand was observed in the structure of polynuclear Cu^I complexes.[1,3,7,9–11] The Cu1···Cu2 distance of 2.8355(4) Å is slightly longer than the sum of two van der Waals radii of Cu^I (2.80 Å).[26]

In the crystal, two molecules of the complexes **1** and **3**–**5** form centrosymmetric dimers as a result of intermolecular hydrogen bonds (Table 4). These intermolecular hydrogen bonds are formed by the hydrogen atom of the NH group and the nitrogen or oxygen (**1** and **3**) or solely nitrogen (**4** and **5**) atoms of the N–P–O*i*Pr group of a further molecule. In the crystal of **5** there are also intramolecular hydrogen bonds formed by the NH hydrogen atom of one molecule of L^I and the P=S sulfur atom of a second molecule of L^I (Table 4).

In the structures of **6** and **8**, each Cu^I cation is in a P_2S_2 tetrahedral environment formed by two sulfur atoms of the deprotonated *N*-thiophosphoryl bis(thiourea) L^{II} and two phosphorus atoms of two PPh_3 ligands (**6**) or one $Ph_2P(CH_2)_3PPh_2$ ligand (**8**; Figures 7 and 8). The Cu–S(C), Cu–S(P) and Cu–P bonds (Table 3) in **6** and **8** are similar to those found in the mononuclear analogues.[1–12] The S–Cu–S angles in **8** are significantly larger than those in **6**,

whereas the P–Cu–P angles in **8** are smaller than those in **6** (Table 3). In the crystals of **6** and **8** an intramolecular hydrogen bond is formed by the NH hydrogen atom of one pendant arm of L^{II} and the NPS nitrogen atom of the second pendant arm (Table 4). The second NH hydrogen atom of L^{II} forms an intermolecular hydrogen bond with the chlorine atom of a CH_2Cl_2 molecule in the crystal of **6** (Table 4). Two molecules of **8** form a centrosymmetric dimer in the crystal due to intermolecular hydrogen bonds between the second NH hydrogen atom of L^{II} and the C=S sulfur atom (Table 4). This type of intermolecular hydrogen bonding is typical of mononuclear analogues.[1–12]

The structure of **10** is similar to that of **5**. In the complex **10**, the deprotonated thiourea L^{II} coordinates two Cu^{I} atoms, which are also interconnected by two C=S sulfur atoms, forming an S_2Cu_2 four-membered ring (Figure 9). The $Ph_2PCH_2PPh_2$ ligand also bridges the two Cu^{I} atoms, thus completing a tetrahedral PS_3 environment. The Cu1···Cu2 distance [2.7629(10) Å] is slightly shorter than the sum of two van der Waals radii of Cu^{I}.[26] In the crystal of **10** there is an intramolecular hydrogen bond formed by the NH hydrogen atom of the pendant arm and the P=S sulfur atom of the second pendant arm (Table 4).

It is reasonable to assume that the formation of **5** and **10** is mainly caused by the rather small bite angle of $Ph_2PCH_2PPh_2$, which often does not allow for perfect chelate binding of metal cations and consequently leads to a bridging coordination, thus forming dinuclear structures[27] and often even promoting M–M bond formation.[28]

Conclusions

The potassium salts of L^{I} or L^{II} react with $[Cu(PPh_3)_3I]$ or a mixture of CuI and $Ph_2P(CH_2)_{1–3}PPh_2$ or $Ph_2P(C_5H_4FeC_5H_4)PPh_2$ to form mononuclear (**1**–**4**) or dinuclear (**5**–**10**) complexes. Recrystallisation of **1** from an acetone/*n*-hexane mixture leads to a complex with one PPh_3 molecule, whereas recrystallisation of **1** from a CH_2Cl_2/*n*-hexane mixture gave the product **11** with two PPh_3 ligands.[1] The formation of dinuclear complexes **5** and **10** is favoured by the small bite angle of $Ph_2PCH_2PPh_2$.

Complexes **2**–**5** and **7**–**10** exhibit emission in the solid state at ambient temperature, which can be assigned to ^{3}ILCT (or ^{3}MLCT) transitions. In contrast, **1** and **6** fail to emit under these conditions, probably due to fast relaxation.

Experimental Section

Physical Measurements: Infrared spectra were recorded with a Bruker IFS66*v*S spectrometer in the range 400–3600 cm^{-1}. NMR spectra were obtained with a Bruker Avance 300 MHz spectrometer at 25 °C. ^{1}H and $^{31}P\{^1H\}$ NMR spectra ($CDCl_3$) were recorded at 299.948 and 121.420 MHz, respectively. Chemical shifts are reported with reference to $SiMe_4$ (^{1}H) and H_3PO_4 ($^{31}P\{^1H\}$). Absorption spectra of 10^{-4} M (**1**–**5**) or 10^{-5} M (**6**–**10**) solutions in CH_2Cl_2 were measured with a Lambda-35 spectrometer. Fluorescence was measured with a Spex FluoroMax-3 spectrofluorimeter on solid samples at room temperature. Elemental analyses were performed with a CHNS HEKAtech EuroEA 3000 analyser.

Syntheses: *N*-Thiophosphorylated thiourea HL^{I} was prepared according to a previously described method.[25]

H_2L^{II}: A solution of *o*-phenylenediamine (0.540 g, 5 mmol) in anhydrous CH_2Cl_2 (15 mL) was treated under vigorous stirring with a solution of $(iPrO)_2P(S)NCS$ (0.263 g, 1.1 mmol) in the same solvent. The mixture was stirred for 1 h. The solvent was removed in vacuo, and the product was purified by recrystallisation from a CH_2Cl_2/*n*-hexane mixture (1:5, v/v). Yield: 2.758 g (94%). ^{1}H NMR: δ = 1.35–1.47 (m, 24 H, CH_3, *i*Pr), 4.89 (dsept, $^3J_{H,H}$ = 6.2, $^3J_{P,H}$ = 10.5 Hz, 4 H, OCH), 7.07–7.32 (m, overlapping with the solvent signal, C_6H_4 + NHP), 9.12 [br. s, 2 H, (aryl)NH] ppm. $^{31}P\{^1H\}$ NMR: δ = 53.0 (s) ppm. IR: $\tilde{\nu}$ = 652 (P=S), 993, 1003 (POC), 1553 (S=C–N), 3204, 3422 (NH) cm^{-1}. $C_{20}H_{36}N_4O_4P_2S_4$ (586.72): calcd. C 40.94, H 6.18, N 9.55; found C 41.01, H 6.12, N 9.48.

Complex 1: Complex **1** was prepared according to a previously described method,[1] but the residue was recrystallised from an acetone/*n*-hexane mixture (1:5, v/v). **1:** Yield: 0.264 g (91%). M.p. 141–142 °C. ^{1}H NMR ($CDCl_3$): δ = 1.30 (d, $^3J_{H,H}$ = 6.0 Hz, 6 H, CH_3, *i*Pr), 1.31 (d, $^3J_{H,H}$ = 6.1 Hz, 6 H, CH_3, *i*Pr), 4.75 (dsept, $^3J_{H,H}$ = 6.0, $^3J_{P,H}$ = 10.8 Hz, 2 H, OCH), 5.72 (br. s, 2 H, NH_2), 7.28–7.51 (m, 15 H, Ph) ppm. $^{31}P\{^1H\}$ NMR ($CDCl_3$): δ = 0.4 (s, 1 P, PPh_3), 54.4 (s, 1 P, NPS) ppm. IR: $\tilde{\nu}$ = 601 (P=S), 1008 (POC), 1546 (SCN), 1614, 3127, 3249, 3496 (NH_2) cm^{-1}. $C_{25}H_{31}CuN_2O_2P_2S_2$ (581.15): calcd. C 51.67, H 5.38, N 4.82; found C 51.82, H 5.29, N 4.90.

Complexes 2–5: A suspension of HL^{I} (0.128 g, 0.5 mmol) in aqueous ethanol (35 mL) was mixed with an ethanol solution of potassium hydroxide (0.031 g, 0.55 mmol). A mixture of CuI (0.095 g, 0.5 mmol) and $Ph_2P(CH_2)_nPPh_2$ (*n* = 1, 0.192 g; *n* = 2, 0.199 g; *n* = 3, 0.206 g; 0.5 mmol) or $Ph_2P(C_5H_4FeC_5H_4)PPh_2$ (0.277 g, 0.5 mmol) in CH_2Cl_2 (25 mL) was heated at reflux for 0.5 h and then added dropwise under vigorous stirring to the obtained potassium salt. The mixture was stirred for 1 h, and the resulting precipitate of KI was filtered off. The filtrate was concentrated until crystallisation started. Isolated crystals were obtained from a CH_2Cl_2/*n*-hexane mixture (1:5, v/v). **2:** Yield: 0.265 g (74%). M.p. 107–108 °C. ^{1}H NMR ($CDCl_3$): δ = 1.13–1.34 (m, 12 H, CH_3, *i*Pr), 2.25 (br. s, 2 H, CH_2), 4.73 (dsept, $^3J_{H,H}$ = 6.2, $^3J_{P,H}$ = 10.5 Hz, 2 H, OCH), 5.70 (br. s, 2 H, NH_2), 6.97–7.86 (m, overlapping with the solvent signal, Ph) ppm. $^{31}P\{^1H\}$ NMR ($CDCl_3$): δ = –12.4 (br. s, 2 P, PPh_2), 56.8 (s, 1 P, NPS) ppm. IR: $\tilde{\nu}$ = 607 (P=S), 1011 (POC), 1557 (SCN), 1611, 3120, 3241, 3491 (NH_2) cm^{-1}. $C_{33}H_{40}CuN_2O_2P_3S_2$ (717.28): calcd. C 55.26, H 5.62, N 3.91; found C 55.10, H 5.68, N 3.97. **3:** Yield: 0.314 g (86%). M.p. 92–93 °C. ^{1}H NMR ($CDCl_3$): δ = 1.15 (d, $^3J_{H,H}$ = 6.2 Hz, 6 H, CH_3, *i*Pr), 1.18 (d, $^3J_{H,H}$ = 6.1 Hz, 6 H, CH_3, *i*Pr), 1.56–1.97 (m, 2 H, CH_2), 2.36 (br. s, 4 H, CH_2), 4.67 (dsept, $^3J_{H,H}$ = 6.1, $^3J_{P,H}$ = 10.7 Hz, 2 H, OCH), 5.51 (br. s, 2 H, NH_2), 6.96–7.83 (m, overlapping with the solvent signal, Ph) ppm. $^{31}P\{^1H\}$ NMR ($CDCl_3$): δ = –19.8 (br. s, 2 P, PPh_2), 58.0 (s, 1 P, NPS) ppm. IR: $\tilde{\nu}$ = 610 (P=S), 1004 (POC), 1558 (SCN), 1621, 3132, 3258, 3501 (NH_2) cm^{-1}. $C_{34}H_{42}CuN_2O_2P_3S_2$ (731.31): calcd. C 55.84, H 5.79, N 3.83; found C 55.68, H 5.84, N 3.78. **4:** Yield: 0.345 g (79%). M.p. 174–175 °C. ^{1}H NMR ($CDCl_3$): δ = 1.19 (t, $^3J_{H,H}$ = 6.0 Hz, 12 H, CH_3, *i*Pr), 4.20 (br. s, 4 H, C_5H_4), 4.29 (br. s, 4 H, C_5H_4), 4.69 (dsept, $^3J_{H,H}$ = 6.2, $^3J_{P,H}$ = 10.3 Hz, 2 H, OCH), 5.33 (br. s, 2 H, NH_2), 7.21–7.76 (m, overlapping with the solvent signal, Ph) ppm. $^{31}P\{^1H\}$ NMR ($CDCl_3$): δ = –17.6 (br.

s, 2 P, PPh_2), 58.7 (s, 1 P, NPS) ppm. IR: $\tilde{\nu}$ = 612 (P=S), 996 (POC), 1553 (SCN), 1609, 3137, 3261, 3488 (NH_2) cm^{-1}. $C_{41}H_{44}CuFeN_2O_2P_3S_2$ (873.25): calcd. C 56.39, H 5.08, N 3.21; found C 56.54, H 4.99, N 3.26. **5:** Yield: 0.245 g (96%). M.p. 167–168 °C. ^1H NMR ($CDCl_3$): δ = 1.23 (d, $^3J_{H,H}$ = 6.2 Hz, 24 H, CH_3, *i*Pr), 2.90 (br. s, 4 H, CH_2), 4.64 (dsept, $^3J_{H,H}$ = 6.1, $^3J_{P,H}$ = 10.5 Hz, 4 H, OCH), 5.68 (br. s, 4 H, NH_2), 6.76–7.74 (m, overlapping with the solvent signal, Ph) ppm. $^{31}P\{^1H\}$ NMR ($CDCl_3$): δ = –10.6 (br. s, 2 P, PPh_2), 57.3 (s, 2 P, NPS) ppm. IR: $\tilde{\nu}$ = 616 (P=S), 994, 1013 (POC), 1538, 1562 (SCN), 1629, 3136, 3255, 3483 (NH_2) cm^{-1}. $C_{39}H_{54}Cu_2N_4O_4P_4S_4$ (1022.11): calcd. C 45.83, H 5.33, N 5.48; found C 46.04, H 5.27, N 5.42.

Complex 6: A suspension of H_2L^{II} (0.293 g, 0.5 mmol) in aqueous ethanol (35 mL) was mixed with an ethanol solution of potassium hydroxide (0.062 g, 1.1 mmol). A solution of $[Cu(PPh_3)_3I]$ (0.977 g, 1.0 mmol) in CH_2Cl_2 (25 mL) was added dropwise to the obtained potassium salt under vigorous stirring. The mixture was stirred for 1 h, and the resulting precipitate of KI was filtered off. The filtrate was concentrated until crystallisation started. Isolated crystals were obtained from a CH_2Cl_2/*n*-hexane mixture (1:5, v/v). Yield: 0.880 g (86%). ^1H NMR: δ = 1.19 (d, $^3J_{H,H}$ = 6.1 Hz, 12 H, CH_3, *i*Pr), 1.23 (d, $^3J_{H,H}$ = 6.1 Hz, 12 H, CH_3, *i*Pr), 4.75 (dsept, $^3J_{H,H}$ = 6.2, $^3J_{P,H}$ = 10.7 Hz, 4 H, OCH), 6.98–7.10 (m, 2 H, C_6H_4), 7.28–7.47 (m, 60 H, Ph), 7.58–7.70 (m, 2 H, C_6H_4), 7.77 [d, $^4J_{P,H}$ = 8.1 Hz, 2 H, (aryl)NH] ppm. $^{31}P\{^1H\}$ NMR: δ = –1.5 (s, 4 P, PPh_3), 54.4 (s, 2 P, NPS) ppm. IR: $\tilde{\nu}$ = 597 (P=S), 995 (POC), 1540 (SCN), 3348 (NH) cm^{-1}. $C_{92}H_{94}Cu_2N_4O_4P_6S_4$ (1760.96): calcd. C 62.75, H 5.38, N 3.18; found C 62.58, H 5.27, N 3.25.

Complexes 7–10: A suspension of H_2L^{II} (0.293 g, 0.5 mmol) in aqueous ethanol (35 mL) was mixed with an ethanol solution of potassium hydroxide (0.062 g, 1.1 mmol). A mixture of CuI (0.19 g, 1.0 mmol) and $Ph_2P(CH_2)_nPPh_2$ (*n* = 1, 0.384 g; *n* = 2, 0.398 g; *n* = 3, 0.412 g; 1.0 mmol) or $Ph_2P(C_5H_4FeC_5H_4)PPh_2$ (0.554 g, 1.0 mmol) in CH_2Cl_2 (25 mL) was heated at reflux for 0.5 h and then added dropwise to the obtained potassium salt under vigorous stirring. The mixture was stirred for 1 h, and the precipitate was filtered off. The filtrate was concentrated until crystallisation started. Isolated crystals were obtained from a CH_2Cl_2/*n*-hexane mixture (1:5, v/v). **7:** Yield: 0.671 g (89%). ^1H NMR: δ = 1.04 (br. s, 12 H, CH_3, *i*Pr), 1.14 (d, $^3J_{H,H}$ = 6.2 Hz, 12 H, CH_3, *i*Pr), 2.24 (br. s, 4 H, CH_2), 4.59 (br. s, 4 H, OCH), 6.76–7.98 [m, overlapping with the solvent signal, C_6H_4 + Ph + (aryl)NH] ppm. $^{31}P\{^1H\}$ NMR: δ = –13.2 (br. s, 4 P, PPh_2), 56.9 (s, 2 P, NPS) ppm. IR: $\tilde{\nu}$ = 594 (P=S), 1006 (POC), 1551 (SCN), 3362 (NH) cm^{-1}. $C_{72}H_{82}Cu_2N_4O_4P_6S_4$ (1508.64): calcd. C 57.32, H 5.48, N 3.71; found C 57.51, H 5.40, N 3.76. **8:** Yield: 0.561 g (73%). ^1H NMR: δ = 1.09 (d, $^3J_{H,H}$ = 6.0 Hz, 12 H, CH_3, *i*Pr), 1.18 (d, $^3J_{H,H}$ = 6.0 Hz, 12 H, CH_3, *i*Pr), 1.81 (br. s, 4 H, CH_2), 2.33 (br. s, 8 H, CH_2), 4.63 (dsept, $^3J_{H,H}$ = 6.1, $^3J_{P,H}$ = 10.6 Hz, 4 H, OCH), 6.81–7.70 [m, overlapping with the solvent signal, C_6H_4 + Ph + (aryl)-NH] ppm. $^{31}P\{^1H\}$ NMR: δ = –20.2 (br. s, 4 P, PPh_2), 56.6 (s, 2 P, NPS) ppm. IR: $\tilde{\nu}$ = 601 (P=S), 991 (POC), 1548 (SCN), 3353 (NH) cm^{-1}. $C_{74}H_{86}Cu_2N_4O_4P_6S_4$ (1536.70): calcd. C 57.84, H 5.64, N 3.65; found C 57.62, H 5.58, N 3.71. **9:** Yield: 0.710 g (78%). ^1H NMR: δ = 1.17 (d, $^3J_{H,H}$ = 6.1 Hz, 24 H, CH_3, *i*Pr), 4.25 (br. s, 16 H, C_5H_4), 4.65 (br. s, 4 H, OCH), 6.70–7.88 [m, overlapping with the solvent signal, C_6H_4 + Ph + (aryl)NH] ppm. $^{31}P\{^1H\}$ NMR: δ = –18.1 (br. s, 4 P, PPh_2), 58.1 (s, 2 P, NPS) ppm. IR: $\tilde{\nu}$ = 604 (P=S), 1014 (POC), 1552 (SCN), 3367 (NH) cm^{-1}. $C_{88}H_{90}Cu_2Fe_2N_4O_4P_6S_4$ (1820.58): calcd. C 58.06, H 4.98, N 3.08; found C 58.19, H 4.90, N 3.02. **10:** Yield: 0.378 g (69%). ^1H NMR: δ = 0.85 (br. s, 12 H, CH_3, *i*Pr), 1.11 (d, $^3J_{H,H}$ = 6.2 Hz, 12 H, CH_3, *i*Pr), 2.97 (br. s, 2 H, CH_2), 4.27 (br. s, 4 H, OCH), 7.06–7.38 (m, overlapping with the solvent signal, C_6H_4 + Ph), 8.29 [d, $^4J_{P,H}$ = 9.2 Hz, 2 H, (aryl)NH] ppm. $^{31}P\{^1H\}$ NMR: δ = –22.4 (s, 2 P, PPh_2), 54.9 (s, 2 P, NPS) ppm. IR: $\tilde{\nu}$ = 610 (P=S), 988 (POC), 1537, 1559 (SCN), 3369 (NH) cm^{-1}. $C_{45}H_{56}Cu_2N_4O_4P_4S_4$ (1096.19): calcd. C 49.31, H 5.15, N 5.11; found C 49.48, H 5.06, N 5.18.

Crystal Structure Determination and Refinement for H_2L^{II}, 1, 3–6, 8, 10: The X-ray diffraction data for crystals of H_2L^{II}, **1**, **3**–**6**, **8** and **10** were collected with a STOE IPDS-II diffractometer. The images were indexed, integrated and scaled by using the X-Area package.[29] Data were corrected for absorption by using the PLATON[30] program. The structures were solved by direct methods using the SHELXS[31] program and refined first isotropically and then anisotropically using SHELXL97.[31] Hydrogen atoms were revealed from $\Delta\rho$ maps and those bonded to C were refined by using a riding model. Hydrogen atoms bonded to N were freely refined in H_2L^{II}, **6** and **8**. In **10**, *U*(H) values were set to $1.2U_{eq}$(N), and N–H distances were restrained to 0.90(3) Å. All figures were generated by using the Mercury program.[32] CCDC-746321 (H_2L^{II}), -742126 (**1**), -742127 (**3**), -742128 (**4**), -742129 (**5**), -746318 (**6**), -746320 (**8**) and -746319 (**10**) contain the supplementary crystallographic data for this paper. These data can be obtained free of charge from The Cambridge Crystallographic Data Centre via www.ccdc.cam.ac.uk/data_request/cif. **H_2L^{II}:** $C_{20}H_{36}N_4O_4P_2S_4$, M_r = 586.71, monoclinic, space group *C*2/*c*, *a* = 20.9638(11), *b* = 11.7659(5), *c* = 25.9717(15) Å, β = 110.682(4)°, *V* = 5993.3(5) Å^3, *Z* = 8, ρ = 1.300 g cm^{-3}, μ(Mo-K_α) = 0.455 mm^{-1}, reflections: 18620 collected, 5240 unique, R_{int} = 0.0527, R_1(all) = 0.0368, wR_2(all) = 0.0847. **1:** $C_{25}H_{31}CuN_2O_2P_2S_2$, M_r = 581.12, monoclinic, space group $P2_1/n$, *a* = 18.5869(14), *b* = 8.3540(8), *c* = 19.9721(15) Å, β = 115.697(5)°, *V* = 2794.5(4) Å^3, *Z* = 4, ρ = 1.381 g cm^{-3}, μ(Mo-K_α) = 1.070 mm^{-1}, reflections: 36121 collected, 5191 unique, R_{int} = 0.0710, R_1(all) = 0.0534, wR_2(all) = 0.0709. **3:** $C_{34}H_{42}CuN_2O_2P_3S_2$, M_r = 731.27, monoclinic, space group $P2_1/n$, *a* = 16.4108(6), *b* = 12.2076(4), *c* = 20.0240(6) Å, β = 100.177(3)°, *V* = 3948.4(2) Å^3, *Z* = 4, ρ = 1.230 g cm^{-3}, μ(Mo-K_α) = 0.810 mm^{-1}, reflections: 20673 collected, 7208 unique, R_{int} = 0.0526, R_1(all) = 0.0483, wR_2(all) = 0.0873. **4:** $C_{41}H_{44}CuFeN_2O_2P_3S_2$, M_r = 873.20, triclinic, space group $P\bar{1}$, *a* = 11.5630(8), *b* = 19.9018(14), *c* = 22.1295(13) Å, α = 116.568(5), β = 99.682(5), γ = 90.364(5)°, *V* = 4470.7(5) Å^3, *Z* = 4, ρ = 1.297 g cm^{-3}, μ(Mo-K_α) = 1.035 mm^{-1}, reflections: 36215 collected, 15725 unique, R_{int} = 0.1939, R_1(all) = 0.1530, wR_2(all) = 0.1990. **5:** $C_{39}H_{54}Cu_2N_4O_4P_4S_4$, M_r = 1022.06, monoclinic, space group $P2_1/c$, *a* = 13.1707(5), *b* = 32.2392(13), *c* = 11.1962(4) Å, β = 98.891(3)°, *V* = 4696.9(3) Å^3, *Z* = 4, ρ = 1.445 g cm^{-3}, μ(Mo-K_α) = 1.262 mm^{-1}, reflections: 22460 collected, 8202 unique, R_{int} = 0.0490, R_1(all) = 0.0459, wR_2(all) = 0.0686. **6:** $C_{92}H_{94}Cu_2N_4O_4P_6S_4{\cdot}2CH_2Cl_2$, M_r = 1930.70, triclinic, space group $P\bar{1}$, *a* = 13.4500(5), *b* = 17.3046(7), *c* = 22.2429(8) Å, α = 74.416(3), β = 85.214(3), γ = 70.672(3)°, *V* = 4705.5(3) Å^3, *Z* = 2, ρ = 1.363 g cm^{-3}, μ(Mo-K_α) = 0.808 mm^{-1}, reflections: 50169 collected, 17546 unique, R_{int} = 0.0446, R_1(all) = 0.0639, wR_2(all) = 0.1201. **8:** $C_{74}H_{86}Cu_2N_4O_4P_6S_4{\cdot}CH_2Cl_2$, M_r = 1621.53, triclinic, space group $P\bar{1}$, *a* = 13.1235(5), *b* = 18.1183(6), *c* = 19.0561(7) Å, α = 69.187(3), β = 74.416(3), γ = 69.245(3)°, *V* = 3907.4(2) Å^3, *Z* = 2, ρ = 1.378 g cm^{-3}, μ(Mo-K_α) = 0.892 mm^{-1}, reflections: 68964 collected, 14595 unique, R_{int} = 0.0605, R_1(all) = 0.0584, wR_2(all) = 0.1125. **10:** $C_{45}H_{56}Cu_2N_4O_4P_4S_4$, M_r = 1096.14, monoclinic, space group $P2_1/c$, *a* = 13.8418(13), *b* = 33.901(3), *c* = 11.1897(10) Å, β = 98.988(7)°, *V* = 5186.3(8) Å^3, *Z* = 4, ρ = 1.404 g cm^{-3}, μ(Mo-K_α) = 1.148 mm^{-1}, reflections: 67245 collected, 9156 unique, R_{int} = 0.1228, R_1(all) = 0.1561, wR_2(all) = 0.1106.

Supporting Information (see footnote on the first page of this article): Absorption spectra of **1**–**10** in CH_2Cl_2.

Acknowledgments

This work was supported by the Russian Science Support Foundation. D. A. S. and M. G. B. thank the Deutscher Akademischer Austausch-Dienst (DAAD) for scholarships (Forschungsstipendien 2008/2009).

[1] F. D. Sokolov, M. G. Babashkina, D. A. Safin, A. I. Rakhmatullin, F. Fayon, N. G. Zabirov, M. Bolte, V. V. Brusko, J. Galezowska, H. Kozlowski, *Dalton Trans.* **2007**, 4693–4700.
[2] M. G. Babashkina, D. A. Safin, Ł. Szyrwiel, M. Kubiak, F. D. Sokolov, Y. V. Starikov, H. Kozlowski, *Z. Anorg. Allg. Chem.* **2009**, *635*, 554–557.
[3] R. C. Luckay, X. Sheng, C. E. Strasser, H. G. Raubenheimer, D. A. Safin, M. G. Babashkina, A. Klein, *Dalton Trans.* **2009**, 4646–4652.
[4] D. A. Safin, M. G. Babashkina, M. Bolte, F. D. Sokolov, V. V. Brusko, *Inorg. Chim. Acta* **2009**, *362*, 1895–1900.
[5] N. G. Zabirov, A. Yu. Verat, F. D. Sokolov, M. G. Babashkina, D. B. Krivolapov, V. V. Brusko, *Mendeleev Commun.* **2003**, *13*, 163–164.
[6] A. Y. Verat, F. D. Sokolov, N. G. Zabirov, M. G. Babashkina, D. B. Krivolapov, V. V. Brusko, I. A. Litvinov, *Inorg. Chim. Acta* **2006**, *359*, 475–483.
[7] M. G. Babashkina, A. I. Rakhmatullin, D. A. Safin, F. Fayon, F. D. Sokolov, A. Klein, D. B. Krivolapov, T. Pape, F. E. Hahn, unpublished results.
[8] D. A. Safin, M. G. Babashkina, T. R. Gimadiev, M. Bolte, M. V. Pinus, D. B. Krivolapov, I. A. Litvinov, *Polyhedron* **2008**, *27*, 2978–2982.
[9] F. D. Sokolov, M. G. Babashkina, F. Fayon, A. I. Rakhmatullin, D. A. Safin, T. Pape, F. E. Hahn, *J. Organomet. Chem.* **2009**, *694*, 167–172.
[10] D. A. Safin, M. G. Babashkina, M. Bolte, A. Klein, *CrystEngComm* **2010**, *12*, 134–143.
[11] D. A. Safin, M. G. Babashkina, M. Bolte, A. Klein, *Inorg. Chim. Acta* **2010**, *363*, 1897–1901.
[12] D. A. Safin, M. G. Babashkina, F. D. Sokolov, N. G. Zabirov, J. Galezowska, H. Kozlowski, *Polyhedron* **2007**, *26*, 1113–1116.
[13] F. D. Sokolov, V. V. Brusko, N. G. Zabirov, R. A. Cherkasov, *Russ. J. Gen. Chem.* **1999**, *69*, 1006–1007.
[14] F. D. Sokolov, V. V. Brusko, N. G. Zabirov, R. A. Cherkasov, *Curr. Org. Chem.* **2006**, *10*, 27–42.
[15] F. D. Sokolov, D. A. Safin, N. G. Zabirov, A. Yu. Verat, V. V. Brusko, D. B. Krivolapov, E. V. Mironova, I. A. Litvinov, *Polyhedron* **2006**, *25*, 3611–3616.
[16] F. D. Sokolov, D. A. Safin, M. G. Babashkina, N. G. Zabirov, V. V. Brusko, N. A. Mironov, D. B. Krivolapov, I. A. Litvinov, R. A. Cherkasov, B. N. Solomonov, *Polyhedron* **2007**, *26*, 1550–1560.
[17] F. D. Sokolov, D. A. Safin, M. Bolte, E. R. Shakirova, M. G. Babashkina, *Polyhedron* **2008**, *27*, 3141–3145.
[18] D. A. Safin, M. G. Babashkina, M. Bolte, A. Klein, *Polyhedron* **2009**, *28*, 1403–1408.
[19] D. A. Safin, M. G. Babashkina, F. D. Sokolov, S. V. Baranov, F. E. Hahn, T. Pape, *Z. Anorg. Allg. Chem.* **2009**, *11*, 1613–1619.
[20] R. C. Luckay, X. Sheng, C. E. Strasser, H. G. Raubenheimer, D. A. Safin, M. G. Babashkina, A. Klein, *Dalton Trans.* **2009**, 8227–8236.
[21] A. Kaltzoglou, P. J. Cox, P. Aslanidis, *Inorg. Chim. Acta* **2005**, *358*, 3048–3056.
[22] P. Aslanidis, P. J. Cox, S. Divanidis, A. C. Tsipis, *Inorg. Chem.* **2002**, *41*, 6875–6886.
[23] T. S. Lobana, R. Sharma, R. Sharma, S. Mehra, A. Castineiras, P. Turner, *Inorg. Chem.* **2005**, *44*, 1914–1921.
[24] V. W.-W. Yam, K. K.-W. Lo, C.-R. Wang, K.-K. Cheung, *J. Phys. Chem. A* **1997**, *101*, 4666–4672.
[25] E. S. Levchenko, I. N. Ghmurova, *Ukr. Khim. Zh. (Russ. Ed.)* **1956**, *22*, 523–526.
[26] J. E. Huheey, E. A. Keiter, R. L. Keiter (Eds.), *Inorganic Chemistry: Principles of Structure and Reactivity*, 4th ed., Harper Collins College Publishers, New York, **1993**.
[27] a) M. Dennehy, G. P. Tellería, O. V. Quinzani, G. A. Echeverría, O. E. Piro, E. E. Castellano, *Inorg. Chim. Acta* **2009**, *362*, 2900–2908; b) L. Ponikiewski, A. Rothenberger, *Inorg. Chim. Acta* **2008**, *361*, 43–48; c) C. Di Nicola, Effendy, C. Pettinari, B. W. Skelton, N. Somers, A. H. White, *Inorg. Chim. Acta* **2006**, *359*, 53–63.
[28] B. Nohra, E. Rodriguez-Sanz, C. Lescop, R. Réau, *Chem. Eur. J.* **2008**, *14*, 3391–3403.
[29] *X-Area, Area-Detector Control and Integration Software*, Stoe & Cie, Darmstadt, Germany, **2001**.
[30] A. L. Spek, *J. Appl. Crystallogr.* **2003**, *36*, 7–13.
[31] G. M. Sheldrick, *Acta Crystallogr., Sect. A* **2008**, *64*, 112–122.
[32] I. J. Bruno, J. C. Cole, P. R. Edgington, M. Kessler, C. F. Macrae, P. McCabe, J. Pearson, R. Taylor, *Acta Crystallogr., Sect. B* **2002**, *58*, 389–397.

Received: February 10, 2010
Published Online: July 15, 2010

DOI: 10.1002/ejic.201000344

Construction of a Hybrid Family Based on Lanthanide–Organic Framework Hosts and Polyoxometalate Guests

Xiaoyu Liu,[a,b] Yanyan Jia,[a] Yongfeng Zhang,[a] and Rudan Huang*[a]

Keywords: Metal–organic frameworks / Polyoxometalates / Organic–inorganic hybrid composites / Lanthanides

A series of 3D polyoxometalate (POM) based coordination polymers, namely, $Ln_4(pdc)_4[SiW_{12}O_{40}]\cdot xH_2O$ (Ln = Eu, Gd, Tb, Dy; x = 19, 13, 14, 18; H_2pdc = pyridine-2,6-dicarboxylate), have been hydrothermally synthesized and characterized by elemental analyses, IR spectroscopy, thermogravimetric analyses (TGA), XRD, and single-crystal X-ray diffraction analyses. Single-crystal X-ray diffraction reveals that they are all isostructural, and the Keggin polyanions $[SiW_{12}O_{40}]^{4-}$ are wrapped as noncoordinating guests in the nonlinear channels of the 3D host framework with $4^3\cdot6^2\cdot8$ topology that is formed by rare-earth metal ions and organic ligands. Furthermore, cyclic voltammetry (CV), ethanol-sorption properties, and catalytic properties are also discussed.

Introduction

Metal–organic frameworks (MOFs), a promising new class of materials, have attracted increasing attention due to their fascinating structural diversity and their potential for a wide variety of applications in various fields including catalysis, gas storage, selective absorption, magnetism, and optical materials.[1,2] In this respect, polyoxometalates (POMs), which are a significant family of metal-oxide clusters, are suitable and effective for the design and construction of functional organic–inorganic hybrid materials because of their diverse topological properties and great potential applications in catalysis, photochemistry, medicine, and magnetism.[3–5] The current applications of supported POMs as environmentally benign catalysts are widely applied in many different fields due to their high surface area, stability, and activity.[6] Many compounds have been used for supporting POMs such as activated carbon and ion-exchange resins. Since these supports have many shortcomings, the exploitation of other supports has become a new area of research interest. Undoubtedly, metal–organic frameworks are one of the optimal supports. Generally, this approach associates MOFs and POMs with their distinctive properties and merits, and leads to the generation of new materials with improved properties and functions. However, the rational design and construction of 3D porous organic–inorganic hybrid materials based on MOFs and POMs are still challenging.

Acting as linkers, lanthanide ions have received less attention than many high-dimensional POM-based organic–inorganic hybrid materials, which are structurally decorated with transition-metal ions or their coordination polymers.[7,8] Moreover, it is very interesting to investigate whether or not both early rare-earth metals and late rare-earth metals can construct MOFs to encapsulate POMs. Several accounts of progress have been made regarding this topic,[9,10] whereas high-dimensional rare-earth complex-network-encapsulating polyoxoanions are still scarce. Pyridine-2,6-dicarboxylate, an attractive multidentate ligand, has been selected as bridging ligand on account of its relatively high coordination numbers and versatile coordination behaviors.

In this paper, the topics being discussed include the synthesis, crystal structures, and properties of a series of 3D porous POM-based coordination polymers, namely, $Ln_4(pdc)_4[SiW_{12}O_{40}]\cdot xH_2O$ (Ln = Eu, Gd, Tb, Dy; x = 19, 13, 14, 18; H_2pdc = pyridine-2,6-dicarboxylate). Single-crystal X-ray structure analyses reveal that they are all isostructural, and that the Keggin polyanions $[SiW_{12}O_{40}]^{4-}$ are wrapped in the nonlinear channels of the 3D framework formed by rare-metal ions and organic ligands. In addition, their cyclic voltammetry (CV), ethanol-sorption properties, and catalytic properties are also discussed.

Results and Discussion

Synthesis and IR Spectroscopy

The successful preparation of compounds **1**–**10** depends upon the exploitation of hydrothermal techniques. Hydrothermal synthesis has recently been proven to be a particu-

[a] Department of Chemistry, School of Science, Beijing Institute of Technology,
5 South Zhongguancun Street, Haidian District, Beijing 100081, P. R. China
Fax: +86-10-68914780
E-mail: huangrd@bit.edu.cn
[b] Department of Biomedicine, Biochemical Engineering College of Beijing Union University,
Beijing 100023, P. R. China

Supporting information for this article is available on the WWW under http://dx.doi.org/10.1002/ejic.201000344.

larly effective technique in the preparation of organic–inorganic hybrid materials.[11] It is well known that many factors can influence the reaction, including the type of initial reactants, starting concentrations, pH values, reaction time, and temperature.[12] Many parallel experiments show that the type of initial reactants and the reaction time are crucial factors in the formation of the title compounds.

In the IR spectrum of compound **5**, the characteristic peaks at 971, 914, 802, and 758 cm^{-1} are attributed to the Keggin polyoxoanion, and the peaks at 1610, 1563, 1446 cm^{-1} are attributed to the carboxylic groups of pdc. Similar IR spectra are found in compounds **1**–**10**, and five compounds of them are shown in Figure S1 in the Supporting Information. It indicates that they are all isostructural, and XRD results prove our assumption.

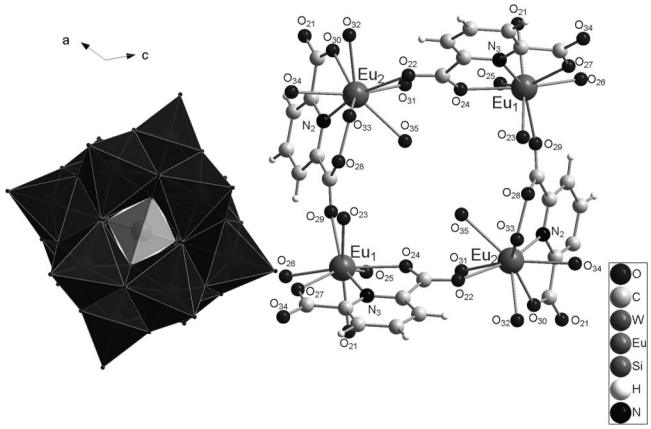

Figure 1. Polyhedral and ball-and-stick drawing of compound **5**. Hydrogen atoms and water molecules have been omitted for clarity.

Structure Description

Since all ten compounds are isomorphic, compound **5** has been selected as an example to describe their crystal structures. The structure of the well-known Keggin core is unexceptional, including a central $\{SiO_4\}$ tetrahedron surrounded by twelve $\{WO_6\}$ octahedrons arranged in four groups of three edge-sharing octahedral units $\{W_3O_{13}\}$. Each of the trinuclear units is in turn linked by corner sharing to each other and to the central $\{SiO_4\}$ tetrahedron. As shown in Figure 1, there are two crystallographically independent Eu^{III} atoms, and they are similar to the previous report.[13] The Eu1 ion is eight-coordinated by four oxygen atoms and a nitrogen atom from different pdc ligands, and three oxygen atoms from water molecules. The average Eu1–O(water) distance is 2.40 Å, which is longer than the average Eu1–O(pdc) distance of 2.39 Å and shorter than the average Eu1–N(pdc) distance of 2.50 Å. The Eu2 ion is different from the Eu1 ion; it is nine-coordinated by four oxygen atoms and a nitrogen atom from different pdc ligands, and four oxygen atoms from water molecules. The average Eu2–N(pdc) distance of 2.53 Å is longer than the average Eu2–O(water) distance of 2.43 Å. The average Eu2–O(pdc) distance is 2.47 Å. The Eu–O and Eu–N bond lengths are all within the normal ranges.[14]

In compound **5**, there are two kinds of cyclic units, as shown in Figure 2. One is that two nine-coordinated Eu^{III} and two eight-coordinated Eu^{III} ions are connected with the oxygen atoms of four pdc ligands to form a tetranuclear cyclic unit with dimensions of 9.40×8.34 Å. Moreover, one $[SiW_{12}O_{40}]^{4-}$ ion is linked by two such tetranuclear units through hydrogen bonding. The other is that four nine-coordinated Eu^{III} and four eight-coordinated Eu^{III} ions link oxygen atoms of eight pdc ligands to form a octanuclear cyclic unit with dimensions of $13.8 \times 15.3 \times 16.5 \times 17.5$ Å. All $[SiW_{12}O_{40}]^{4-}$ anions are located in cages formed by a tetranuclear cyclic unit and an octanuclear cyclic unit connecting each other (as shown in Figure 3).

The Keggin polyanions $[SiW_{12}O_{40}]^{4-}$ are wrapped in the nonlinear channels of the 3D framework (Figure S2 in the Supporting Information) formed by rare-metal ions and organic ligands; the extensive hydrogen-bonding interactions between guest molecules and the framework play an important role in stabilizing the 3D structure. As shown above, Eu^{III} can be defined as a four-connected node. It can been seen in Figure 4 that the 3D framework comprises a $(4^3 \cdot 6^2 \cdot 8)$ topology.

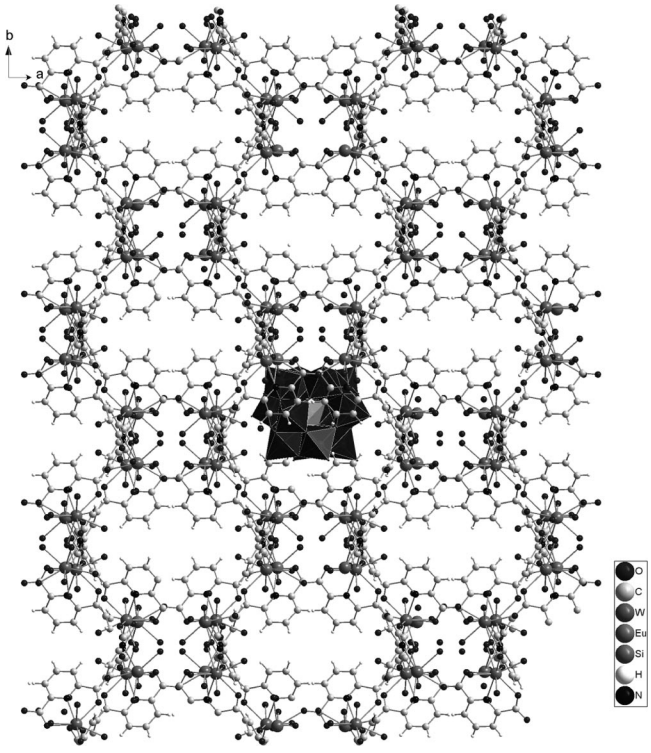

Figure 2. Tetranuclear cyclic unit and octanuclear cyclic unit in compound **5**.

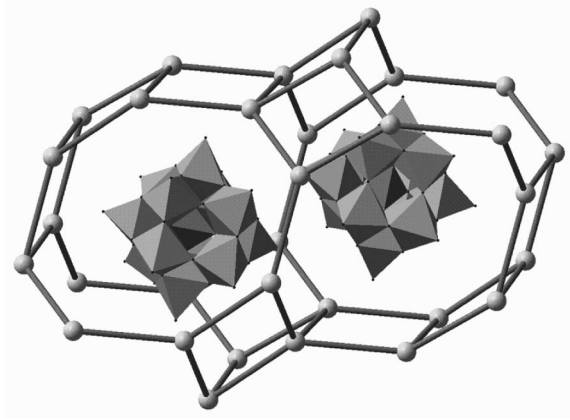

Figure 3. Cages formed by the tetranuclear cyclic and octanuclear cyclic unit.

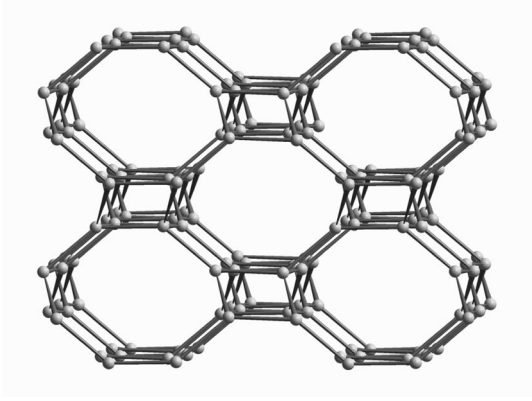

Figure 4. Representation of the $4^3 \cdot 6^2 \cdot 8$ topology network of compound **5** along the [001] direction.

Thermogravimetric Analyses (TGA)

The TG curve of compound **5** (Figure S3 in the Supporting Information) shows a 2.8% weight loss between 20 and 107 °C, in accord with crystallographic water (calculated value: 2.3%). From 107 to 137 °C, compound **5** loses its coordinated water with a 3.59% weight loss (calculated value: 3.24%). The 2.55% weight loss (calculated value: 2.48%) from 400 to 520 °C is ascribed to the decomposition of pdc molecules. When the temperature is higher than 586 °C, decomposition of the main framework occurs. Compounds **1**–**10** show similar weight-loss stages.

Powder X-ray Diffraction (PXRD)

The experimental and simulated PXRD patterns of compounds **1**–**10** are in comparatively good agreement with each other, thereby indicating the phase purity of the products. The differences in intensity may be due to the preferred orientation of the powder samples. Similar experimental PXRD patterns are found in compounds **1**–**10**; five compounds of them are shown in Figure S4 in the Supporting Information, and it has been proven that they are all isostructural. Enlightened by single-crystal X-ray diffraction and TG results, powder X-ray diffraction experiments were conducted to investigate the stability of compound **5** under different conditions (see Figure 5). Compound **5** loses all water when it is heated at 340 °C for 0.5 h, and the color turns from yellow to yellowish brown. When it is immersed in water for 24 h, it presents an interesting reversible course and its color returns to yellow. When it is heated at 500 °C for 0.5 h, it turns from yellow to brown. Except for few slight differences, by comparing these results it would seem that they match very well with each other. It may be attributed to the subtle change of the relative positions of some atoms in the crystal lattice. The main metal–organic frameworks of compound **5** remain stable when it is heated at a high temperature, which shows its excellent stability and potential for applications that require this characteristic.

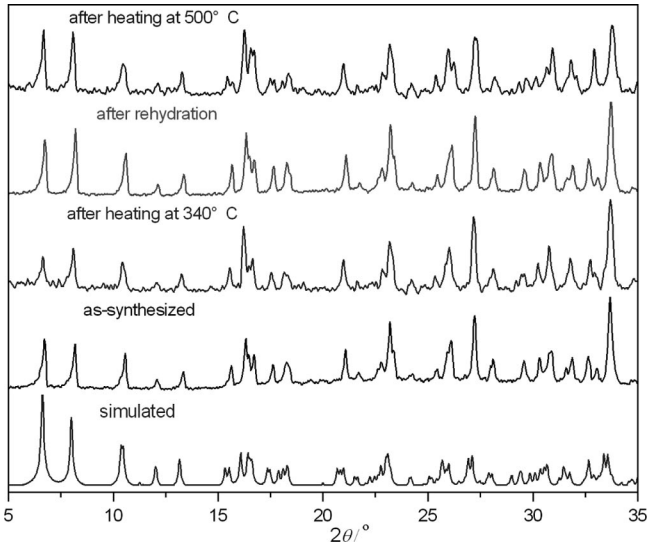

Figure 5. Powder XRD patterns of compound **5** after different treatment.

Photoluminescent Properties

Compounds **1**–**10** exhibit photoluminescent properties at ambient temperature. The maximum emission peak of compound **5** (Figure S5 in the Supporting Information) is located at 361 nm. The data of compound **5** is similar to H_2pdc, albeit slightly blueshifted, which shows that the luminescent behavior is ligand-based emission. The blueshift in the emission may be attributed to the chelating of the H_2pdc ligand to the metal ion, which effectively increases the rigidity of the ligand and reduces the loss of energy.[15] Compounds **1**–**10** exhibit photoluminescent properties similar to those of compound **5** (Figure 6).

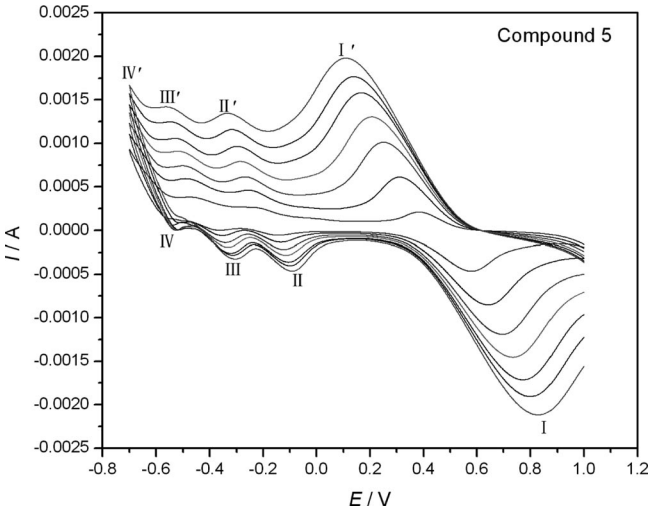

Figure 6. Cyclic voltammograms of **5**–CPE (CPE = carbon-paste electrode) in 1 M H_2SO_4 solution at different scan rates (from inner to outer: 0.025, 0.05, 0.075, 0.1, 0.125, 0.15, and 0.175 V s^{-1}).

Electrochemical Properties

The electrochemical behaviors of **5**–CPE at different scan rates in the potential range of +1.0 to –0.8 V have been studied. There exist four reversible redox peaks I–I′, II–II′, III–III′, and IV–IV′ with half-wave potentials $E_{½}$ = (E_{pa} + E_{pc})/2 = 0.472 (I–I′), –0.201 (II–II′), –0.418 (III–III′), –0.612 (IV–IV′) V (scan rate: 100 V s^{-1}), respectively. Three redox peaks II–II′, III–III′, and IV–IV′ with approximate electron ratios of 1:1:2 can be observed and attributed to polyanions $[SiW_{12}O_{40}]^{4-}$. Redox peaks II–II′, III–III′ correspond to two consecutive one-electron processes, and IV–IV′ corresponds to a two-electron process.[16] Redox peak I–I′ was assigned to the Eu centers with slight differences.[17] It may be attributed to the chelating of the H_2pdc ligand to the metal ion. When the scan rates were varied from 0.05 to 0.175 V s^{-1} for **5**–CPE, the peak potentials changed gradually: the cathodic peak potentials shifted toward the positive direction and the corresponding anodic peak potentials toward the negative direction with increasing scan rates. The peak currents are proportional to the scan rate, which indicates that the redox process of **5**–CPE is surface-controlled.[18] In addition, **5**–CPE is very stable. When the potential range was maintained between +1.0 and –0.8 V, the peak currents remained almost unchanged after several cycles. After **5**–CPE was stored at room temperature for about 1 month, the peak changed only slightly and could be renewed by adding some carbon paste.

Ethanol-Sorption Properties

Although polyanions $[SiW_{12}O_{40}]^{4-}$ are located in cages formed by octanuclear cyclic units, cages formed by tetranuclear units may have potential to sorb guest molecules. Similar work has been reported by some other researchers.[19] To test our estimation, compound **6** was used for gas-sorption measurements. As shown in Figure 7, the amount of ethanol sorption increases gradually with the increase of p/p_0 and increases suddenly at a definite pressure ($p/p_0 \approx 0.5$). Finally, it almost levels off at $p/p_0 \approx 0.8$. Whether ethanol can be sorbed into the compound depends on two factors. One is the lattice expansion energy (E_1[20]), whereas the other is ion-dipole and hydrogen-bonding interactions between the alcohols and the compound (E_{int}[21]). If ($E_{int} - E_1$) > 0, then ethanol can be sorbed into the compound. The process of desorption is similar to that of adsorption except for a slight shift. This type of hystereses can be attributed to host–guest interactions, and it causes the guest molecule to escape very slowly during desorption.

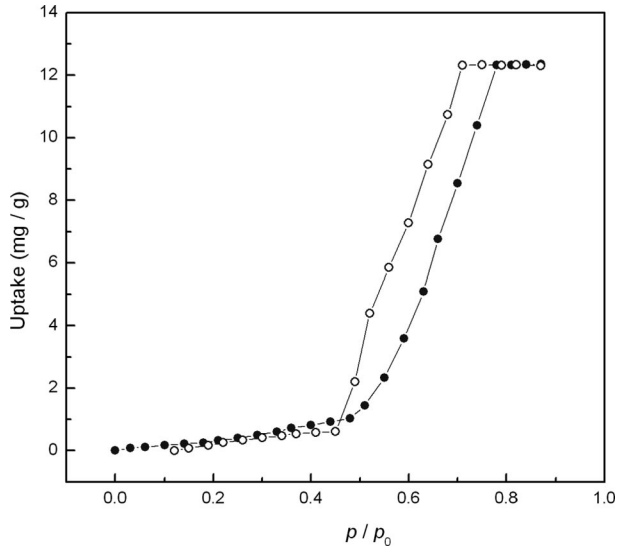

Figure 7. Ethanol adsorption–desorption of compound **6**. Filled and open symbols represent adsorption and desorption branches, respectively.

Catalytic Properties

Catalytic properties of POM-based coordination polymers have been reported over the past few years.[22] The synthesis of ethyl acetate was selected as a test reaction to assess the catalytic properties of compound **6**. As shown in Table 1, compound **6** is significantly more active and selective toward the synthesis of ethyl acetate than H_2SO_4. The synthesis of ethyl acetate cannot be carried out without any catalyst. Moreover, the UV/Vis spectrum (Figure 8) shows that the maximum absorption peak of $H_4SiW_{12}O_{40}$ is located at around 260 nm, but there is no apparent absorption peak for compound **6**. This result shows that there is no POM leaching from the MOF for compound **6** in aqueous solution. Therefore, it is reasonable to believe that an MOF-supported POM catalyst cannot experience a loss of activity or create any pollution problems. Compound **6** is in fact recyclable without any loss of catalytic activity and selectivity over 10 cycles.

Table 1. Results of the catalysis tests.

Catalyst	Conversion [mol%]	Selectivity [mol%]
$Gd_4(C_7H_3NO_4)_4[SiW_{12}O_{40}]\cdot 13H_2O$	>99	>99
H_2SO_4	80	81
None	0	0

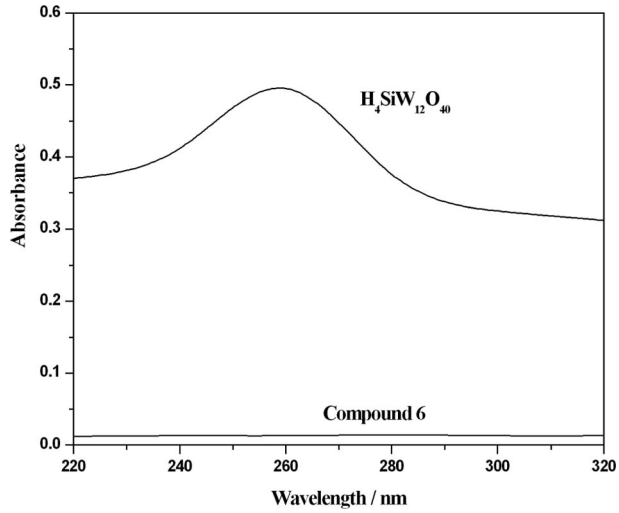

Figure 8. UV/Vis spectrum of compound **6** and $H_4SiW_{12}O_{40}$.

Conclusion

We have hydrothermally synthesized and characterized a series of 3D porous POM-based coordination polymers $Ln_4(pdc)_4[SiW_{12}O_{40}]\cdot xH_2O$ (Ln = Eu, Gd, Tb, Dy; x = 19, 13, 14, 18; H_2pdc = pyridine-2,6-dicarboxylate). These materials present striking thermostability and favorable catalytic properties. Although the nonlinear channels of the 3D host framework are filled with Keggin polyanions, these compounds still exhibit ethanol-sorption properties. If the polyanions could be successfully replaced by other anions without the host framework collapsing, more and more materials with improved properties and functions could be prepared. Furthermore, it has been proven that early rare-earth metals and late rare-earth metals can both construct metal–organic frameworks to encapsulate polyoxometalates.

Experimental Section

Materials and Methods: All reagents were purchased commercially and used without further purification. Infrared spectra were obtained (as KBr pressed pellets) with a Nicolet 170SXFT/IR spectrometer. Thermogravimetric analyses (TGA) were performed under nitrogen with a heating rate of 10 °C min^{-1} with a Perkin–Elmer TGA 7 thermogravimetric analyzer. The C, H, and N elemental analyses were performed with a Perkin–Elmer 2400 CHN elemental analyzer. Powder X-ray diffraction (PXRD) of samples were collected with a Japan Shimadzu XRD-6000 X-ray diffractometer equipped with graphite-monochromatized Cu-K_α radiation (λ = 0.154 nm) (40 kV, 30 mA, step 0.02 °, speed 5 ° min^{-1}). Fluorescence spectroscopy data were recorded with a Hitachi Model RF-5301PC spectrofluorometer equipped with a 450 W xenon lamp as the excitation source, and the measurements were performed at room temperature. All electrochemical measurements were carried out with a CHI 660 electrochemical workstation at room temperature. Cyclic voltammograms were recorded with a 384B polarographic analyzer. A typical three-electrode cell with a CPE working electrode, a platinum counter electrode, and a silver/silver chloride reference electrode was used for the voltammetry experiments. A Micromeritics ASAP 2010 surface area and porosity analyzer was used to measure ethanol sorption. The products of catalysis experiments were analyzed by GC (N2000).

Synthesis of $La_4(C_7H_3NO_4)_4[SiW_{12}O_{40}]\cdot 20H_2O$ (1): A mixture of $K_8[\alpha\text{-}SiW_{11}O_{39}]\cdot 13H_2O$ (0.1610 g, 0.05 mmol), $La(NO_3)_3\cdot 6H_2O$ (0.0866 g, 0.2 mmol), and pdc (0.0260 g, 0.15 mmol) was dissolved in distilled water (10 mL) at room temperature. After stirring for 30 min, the suspension was placed into a 25 mL Teflon-lined stainless-steel container and heated at 130 °C for 4 d. After slow cooling to room temperature, yellow block crystals were filtered, washed with distilled water, and dried in a desiccator at room temperature to give a yield of 56% based on W. $C_{28}H_{52}La_4N_4O_{76}SiW_{12}$ (4449.32): calcd. C 10.01, H 1.33, N 1.67; found C 10.04, H 1.38, N 1.60.

Synthesis of $Ce_4(C_7H_3NO_4)_4[SiW_{12}O_{40}]\cdot 16H_2O$ (2): A mixture of $H_4SiW_{12}O_{40}\cdot nH_2O$(0.282 g, 0.1 mmol), $Ce(NO_3)_3\cdot 6H_2O$ (0.0906 g, 0.2 mmol), and pdc (0.0290 g, 0.17 mmol) was dissolved in distilled water (10 mL) at room temperature. After stirring for 30 min, the suspension was placed into a 25 mL Teflon-lined stainless-steel container and heated at 130 °C for 4 d. After slow cooling to room temperature, colorless block crystals were filtered, washed with distilled water, and dried in a desiccator at room temperature to give a yield of 39% based on W. $C_{28}H_{44}Ce_4N_4O_{72}SiW_{12}$ (4382.20): calcd. C 10.00, H 1.34, N 1.63; found C 10.06, H 1.38, N 1.61.

Synthesis of $Nd_4(C_7H_3NO_4)_4[SiW_{12}O_{40}]\cdot 19H_2O$ (3): The preparation procedure was similar to that for **2**, except that $Ce(NO_3)_3\cdot 6H_2O$ was replaced by $Nd(NO_3)_3\cdot 6H_2O$. Colorless block crystals were filtered, washed with distilled water, and dried in a desiccator at room temperature to give a yield of 37% based on W. $C_{28}H_{50}N_4Nd_4O_{75}SiW_{12}$ (4398.68): calcd. C 9.97, H 1.53, N 1.67; found C 10.02, H 1.48, N 1.66.

Synthesis of $Sm_4(C_7H_3NO_4)_4[SiW_{12}O_{40}]\cdot 11H_2O$ (4): The preparation procedure was similar to that for **1**, except that $La(NO_3)_3\cdot 6H_2O$ was replaced by $Sm(NO_3)_3\cdot 6H_2O$. Colorless block crystals were filtered, washed with distilled water, and dried in a desiccator at room temperature to give a yield of 53% based on W. $C_{28}H_{34}N_4O_{67}SiSm_4W_{12}$ (4312.11): calcd. C 9.96, H 1.11, N 1.65; found C 10.01, H 1.18, N 1.68.

Synthesis of $Eu_4(C_7H_3NO_4)_4[SiW_{12}O_{40}]\cdot 19H_2O$ (5): The preparation procedure was similar to that for **1**, except that the $La(NO_3)_3\cdot 6H_2O$ was replaced by $Eu(NO_3)_3\cdot 6H_2O$. Colorless block crystals were filtered, washed with distilled water, and dried in a desiccator at room temperature to give a yield of 52% based on W. $C_{28}H_{50}Eu_4N_4O_{75}SiW_{12}$ (4484.85): calcd. C 10.02, H 1.63, N 1.63; found C 10.04, H 1.68, N 1.61.

Synthesis of $Gd_4(C_7H_3NO_4)_4[SiW_{12}O_{40}]\cdot 13H_2O$ (6): The preparation procedure was similar to that for **1**, except that $La(NO_3)_3\cdot 6H_2O$ was replaced by $Gd(NO_3)_3\cdot 6H_2O$. Colorless block crystals were filtered, washed with distilled water, and dried in a desiccator at room temperature to give a yield of 55% based on W. $C_{28}H_{38}Gd_4N_4O_{69}SiW_{12}$ (4397.91): calcd. C 9.98, H 1.13, N 1.62; found C 10.02, H 1.16, N 1.61.

Synthesis of $Tb_4(C_7H_3NO_4)_4[SiW_{12}O_{40}]\cdot 14H_2O$ (7): The preparation procedure was similar to that for **2**, except that $Ce(NO_3)_3\cdot$

Table 2. Crystal data and structural refinements for compounds **5**, **6**, **7**, and **8**.

	5	**6**	**7**	**8**
Empirical formula	$C_{28}H_{50}Eu_4N_4O_{75}SiW_{12}$	$C_{28}H_{38}Gd_4N_4O_{69}SiW_{12}$	$C_{28}H_{40}N_4O_{70}SiTb_4W_{12}$	$C_{28}H_{48}Dy_4N_4O_{74}SiW_{12}$
M_r	4484.85	4397.91	4496	4582.36
Crystal system	monoclinic	monoclinic	triclinic	monoclinic
Space group	*C*2/*c*	*C*2/*c*	*C*2/*c*	*C*2/*c*
a [Å]	30.418(6)	30.554(5)	30.342(6)	30.418(10)
b [Å]	16.302(3)	16.306(3)	16.219(3)	16.302(5)
c [Å]	21.780(4)	21.656(4)	21.787(4)	21.780(12)
α [°]	90	90	90	90
β [°]	133.83(3)	134.437(2)	134.13	133.826(3)
γ [°]	90	90	90	90
V [Å^3]	7792(3)	7704(2)	7695(3)	7792(6)
Z	4	4	24	50
$D_{calcd.}$ [mg m^{-3}]	3.823	3.792	2.781	4.449
F(000)	8000	7776	5736	8800
GOF	1.089	1.007	1.414	1.042
R_{int}	0.0863	0.0930	0.1195	0.0933
R_1[a] [$I > 2\sigma(I)$]	0.0766	0.1247	0.0763	0.0897
wR_2[b] (all data)	0.2075	0.2395	0.2003	0.2537

[a] $R_1 = \Sigma||F_o| - |F_c||/\Sigma|F_o|$. [b] $wR_2 = \Sigma[w(F_o^2 - F_c^2)^2]/\Sigma[w(F_o^2)^2]^{1/2}$.

$6H_2O$ was replaced by $Tb(NO_3)_3{\cdot}5H_2O$. Colorless block crystals were filtered, washed with distilled water, and dried in a desiccator at room temperature to give a yield of 34% based on W. $C_{28}H_{40}N_4O_{70}SiTb_4W_{12}$ (4496.17): calcd. C 10.01, H 1.21, N 1.67; found C 10.08, H 1.28, N 1.64.

Synthesis of $Dy_4(C_7H_3NO_4)_4[SiW_{12}O_{40}]{\cdot}18H_2O$ (8): The preparation procedure was similar to that for **1**, except that $La(NO_3)_3{\cdot}6H_2O$ was replaced by $Dy(NO_3)_3{\cdot}6H_2O$. Yellow block crystals were filtered, washed with distilled water, and dried in a desiccator at room temperature to give a yield of 50% based on W. $C_{28}H_{48}Dy_4N_4O_{74}SiW_{12}$ (4582.36): calcd. C 9.96, H 1.43, N 1.67; found C 9.98, H 1.41, N 1.61.

Synthesis of $Ho_4(C_7H_3NO_4)_4[SiW_{12}O_{40}]{\cdot}16H_2O$ (9): The preparation procedure was similar to that for **2**, except that $Ce(NO_3)_3{\cdot}6H_2O$ was replaced by $Ho(NO_3)_3{\cdot}6H_2O$. Colorless block crystals were filtered, washed with distilled water, and dried in a desiccator at room temperature to give a yield of 37% based on W. $C_{28}H_{44}Ho_4N_4O_{72}SiW_{12}$ (4481.44): calcd. C 9.98, H 1.34, N 1.64; found C 10.03, H 1.38, N 1.61.

Synthesis of $Er_4(C_7H_3NO_4)_4[SiW_{12}O_{40}]{\cdot}16H_2O$ (10): The preparation procedure was similar to that for **2**, except that $Ce(NO_3)_3{\cdot}6H_2O$ was replaced by $Er(NO_3)_3{\cdot}6H_2O$. Colorless block crystals were filtered, washed with distilled water, and dried in a desiccator at room temperature to give a yield of 36% based on W. $C_{28}H_{44}Er_4N_4O_{72}SiW_{12}$ (4490.76): calcd. C 10.00, H 1.36, N 1.67; found C 10.06, H 1.38, N 1.61.

Preparation of 5–CPE: A compound **5** modified carbon-paste electrode (CPE) was fabricated as follows: graphite powder (0.5 g) and compound **5** (30 mg) were mixed and ground together in an agate mortar with a pestle to achieve an even, dry mixture. Paraffin (0.3 mL) was then added to the mixture, which was stirred with a glass rod. The homogenized mixture was used to pack 3 mm inner-diameter glass tubes, and the surface was wiped with weighing paper. Electrical contact was established with a copper rod through the back of the electrode.

X-ray Crystallography: Intensity data of **1**–**10** were collected with a Bruker Smart Apex CCD area-detector diffractometer with graphite-monochromated Mo-K_α (λ = 0.71073 Å) radiation at room temperature. All absorption corrections were applied by using the multiscan program SADABS. The structures were solved by direct methods and refined on F^2 by full-matrix least squares using the SHELXTL-97 program package on a legend computer.[23] All non-hydrogen atoms were refined anisotropically. Hydrogen atoms were located in the calculated positions and refined by using a riding model. However, only the structures of compounds **5**, **6**, **7**, and **8** (Table 2) were obtainable; data of the other compounds were not sufficient for analysis. On the basis of IR and PXRD and elemental analyses, it can be proven that they are all isostructural. CCDC-753342 (**5**), -725110 (**6**), -752239 (**7**), and -752240 (**8**) contain the supplementary crystallographic data for this paper. These data can be obtained free of charge from The Cambridge Crystallographic Data Centre via www.ccdc.cam.ac.uk/data_request/cif.

Ethanol-Sorption Properties: A sample of compound **6** (0.250 g) was used for gas-sorption measurements at 77 K. Compound **6** was heated overnight under vacuum at 200 °C to remove guest solvent molecules from the framework. Before the measurement was taken, the sample was evacuated again by using the "outgas" function of the surface area analyzer for 10 h (at 200 °C for **6**).

Synthesis of Ethyl Acetate: A standard synthesis of ethyl acetate procedure was performed. A mixture of ethanol (9.5 mL), acetic acid (6 mL), and compound **6** (0.058 g) was placed into a three-neck flask and heated at 110 °C for 1 h. After the reaction was complete, the products were analyzed with GC. H_2SO_4 was selected as a reference; the procedure was similar to that for compound **6**.

Supporting Information (see footnote on the first page of this article): IR specta, X-ray powder diffraction patterns, emission spectra, and TGA curves.

Acknowledgments

This work was financially supported by the National Natural Science Foundation of China (nos. 20971014, 20771013, and 20476011).

[1] a) H. L. Li, M. Eddaoudi, M. O'Keeffe, O. M. Yaghi, *Nature* **1999**, *402*, 276–279; b) M. Eddaudi, J. Kim, N. Rosi, D. Vodak, J. Wachter, M. O'Keefee, O. M. Yaghi, *Science* **2002**, *295*, 469–472; c) N. W. Ockwig, O. Delgado-Friedrichs, M. O'Keeffe, O. M. Yaghi, *Acc. Chem. Res.* **2005**, *38*, 176–182; d) L. R. MacGillivray, G. S. Papaefstathiou, T. Friscic, T. D. Hamilton, D.-

K. Bucar, Q. L. Chu, D. B. Varshney, I. G. Georgiev, *Acc. Chem. Res.* **2008**, *41*, 280–291.

[2] a) W. Morris, C. J. Doonan, H. Furukawa, R. Banerjee, O. M. Yaghi, *J. Am. Chem. Soc.* **2008**, *130*, 12626–12627; b) Y. Z. Zheng, W. Xue, M. L. Tong, X. M. Chen, F. Grandjean, G. J. Long, *Inorg. Chem.* **2008**, *47*, 4077–4087; c) X. L. Wang, Y. F. Bi, B. K. Chen, H. Y. Lin, G. C. Liu, *Inorg. Chem.* **2008**, *47*, 2442–2448; d) Y. Q. Lan, S. L. Li, X. L. Wang, K. Z. Shao, Z. M. Su, E. B. Wang, *Inorg. Chem.* **2008**, *47*, 529–534.

[3] a) T. Yamase, M. T. Pope (Eds.), *Polyoxometalate Chemistry for Nano-Composite Design*, Kluwer Academic Publishers, Dordrecht, **2002**; b) T. Yamase, *Chem. Rev.* **1998**, *98*, 307–326; c) A. Müller, F. Peters, M. T. Pope, D. Gatteschi, *Chem. Rev.* **1998**, *98*, 239–272; d) C. L. Hill, *Chem. Rev.* **1998**, *98*, 1–2.

[4] a) S. T. Zheng, J. Zhang, G. Y. Yang, *Angew. Chem. Int. Ed.* **2008**, *47*, 3909–3913; b) R. Kawamoto, S. Uchida, N. Mizuno, *J. Am. Chem. Soc.* **2005**, *127*, 10560–10567; c) S. Uchida, N. Mizuno, *J. Am. Chem. Soc.* **2004**, *126*, 1602–1603; d) S. Uchida, R. Kawamoto, H. Tagami, Y. Nakagawa, N. Mizuno, *J. Am. Chem. Soc.* **2008**, *130*, 12370–12376.

[5] a) M. L. Wei, C. He, Q. Z. Sun, Q. J. Meng, C. Y. Duan, *Inorg. Chem.* **2007**, *46*, 5957–5966; b) C. H. Li, K. L. Huang, Y. N. Chi, X. Liu, Z. G. Han, L. Shen, C. W. Hu, *Inorg. Chem.* **2009**, *48*, 2010–2017; c) M. Nyman, C. R. Powers, F. Bonhomme, T. M. Alam, E. J. Maginn, D. T. Hobbs, *Chem. Mater.* **2008**, *20*, 2513–2521; d) M. Ibrahim, M. H. Dickman, A. Suchopar, U. Kortz, *Inorg. Chem.* **2009**, *48*, 1649–1654.

[6] a) V. Kogan, Z. Aizenshtat, R. Neumann, *Angew. Chem. Int. Ed.* **1999**, *38*, 3331–3334; b) J. Ettedgui, R. Neumann, *J. Am. Chem. Soc.* **2009**, *131*, 4–5.

[7] a) S. Reinoso, P. Vitoria, L. Lezama, A. Luque, J. M. Gutiérrez-Zorrilla, *Inorg. Chem.* **2003**, *42*, 3709–3711; b) S. Reinoso, P. Vitoria, L. S. Felices, L. Lezama, J. M. Gutiérrez-Zorrilla, *Inorg. Chem.* **2006**, *45*, 108–118; c) Y. P. Ren, X. J. Kong, X. Y. Hu, M. Sun, L. S. Long, R. B. Huang, L. S. Zheng, *Inorg. Chem.* **2006**, *45*, 4016–4023.

[8] a) C. Z. Lu, C. D. Wu, H. H. Zhang, J. S. Huang, *Chem. Mater.* **2002**, *14*, 2649–2655; b) S. Uchida, R. Kawamoto, T. Akatsuka, S. Hikichi, N. Mizuno, *Chem. Mater.* **2005**, *17*, 1367–1375.

[9] a) R. Copping, L. Jonasson, A. J. Gaunt, D. Drennan, D. Collison, M. Helliwell, R. J. Pirttijarvi, C. J. Jones, A. Huguet, D. C. Apperley, N. Kaltsoyannis, I. May, *Inorg. Chem.* **2008**, *47*, 5787–5798; b) P. Mialane, A. Dolbecq, E. Rivière, J. Marrot, F. Sécheresse, *Eur. J. Inorg. Chem.* **2004**, 33–36; c) X. J. Kong, Y. P. Ren, P. Q. Zheng, Y. X. Long, L. S. Long, R. B. Huang, L. S. Zheng, *Inorg. Chem.* **2006**, *45*, 10702–10711.

[10] a) J. Lu, E. H. Shen, Y. G. Li, D. H. Xiao, E. B. Wang, L. Xu, *Cryst. Growth Des.* **2005**, *5*, 65–67; b) E. H. Shen, J. Lu, Y. G. Li, E. B. Wang, C. W. Hu, L. Xu, *J. Solid State Chem.* **2004**, *177*, 4372–4376.

[11] a) M. Yuan, Y. G. Li, E. B. Wang, C. G. Tian, L. Wang, C. W. Hu, N. H. Hu, H. Q. Jia, *Inorg. Chem.* **2003**, *42*, 3670–3676; b) D. Q. Chu, J. Q. Xu, L. M. Duan, T. G. Wang, A. Q. Tang, L. Ye, *Eur. J. Inorg. Chem.* **2001**, 1135–1137.

[12] P. J. Hagrman, D. Hagrman, J. Zubieta, *Angew. Chem. Int. Ed.* **1999**, *38*, 2638–2684.

[13] S. K. Ghosh, P. K. Bharadwaj, *Inorg. Chem.* **2003**, *42*, 8250–8254.

[14] C. Qin, X. L. Wang, E. B. Wang, Z. M. Su, *Inorg. Chem.* **2005**, *44*, 7122–7129.

[15] a) J. Zhang, Y. B. Chen, S. M. Chen, Z. J. Li, J. K. Cheng, Y. G. Yao, *Inorg. Chem.* **2006**, *45*, 3161–3163; b) C. H. Li, K. L. Huang, J. M. Dou, Y. N. Chi, Y. Q. Xu, L. Shen, D. Q. Wang, C. W. Hu, *Cryst. Growth Des.* **2008**, *8*, 3141–3143.

[16] M. Sadakane, E. Steckhan, *Chem. Rev.* **1998**, *98*, 219–238.

[17] A. G. Atanasyants, A. N. Seryogin, *Hydrometallurgy* **1995**, *37*, 367–374.

[18] L. Cheng, X. M. Zhang, X. D. Xi, S. J. Dong, *J. Electroanal. Chem.* **1996**, *407*, 97–103.

[19] a) A. Lesbani, R. Kawamoto, S. Uchida, N. Mizuno, *Inorg. Chem.* **2008**, *47*, 3349–3357; b) K. Uehara, H. Nakao, R. Kawamoto, S. Hikichi, N. Mizuno, *Inorg. Chem.* **2006**, *45*, 9448–9453; c) S. Uchida, R. Kawamoto, N. Mizuno, *Inorg. Chem.* **2006**, *45*, 5136–5144; d) S. Uchida, M. Hashimoto, N. Mizuno, *Angew. Chem. Int. Ed.* **2002**, *41*, 2814–2817.

[20] L. Glasser, H. D. B. Jenkins, *J. Am. Chem. Soc.* **2000**, *122*, 632–638.

[21] P. W. Atkins, *Physical Chemistry*, Oxford University Press, Oxford, UK, **1990**, chapter 22.

[22] a) Y. Goto, K. Kamata, K. Yamaguchi, K. Uehara, S. Hikichi, N. Mizuno, *Inorg. Chem.* **2006**, *45*, 2347–2356; b) T. V. Kovalchuk, J. N. Kochkin, H. Sfihi, V. N. Zaitsev, J. Fraissard, *J. Catal.* **2009**, *263*, 247–257.

[23] a) G. M. Sheldrick, *SHELXS-97*, *Program for Crystal Structure Solution*, University of Göttingen, Germany, **1997**; b) G. M. Sheldrick, *SHELX-97*, *Program for Crystal Structure Refinement*, University of Göttingen, Germany, **1997**.

Received: March 28, 2010
Published Online: July 6, 2010

DOI: 10.1002/ejic.201000357

Platinum Complexes of Aromatic Selenolates

Amy L. Fuller,[a] Fergus R. Knight,[a] Alexandra M. Z. Slawin,[a] and J. Derek Woollins*[a]

Keywords: Platinum / Selenium / Heterocycles

Several synthetic methods are used to prepare naphthalene-based aromatic 1,2-diselenoles. A new one-pot synthesis starting from naphthalene is used to produce the known compound naphtho[1,8-*c*,*d*][1,2]diselenole (Se_2naph). Friedel–Crafts alkylation is used on Se_2naph to substitute either one *tert*-butyl group to form 2-*tert*-butylnaphtho[1,8-*c*,*d*][1,2]diselenole (mt-Se_2naph) or two *tert*-butyl groups to form 2,7-di-*tert*-butylnaphtho[1,8-*c*,*d*][1,2]diselenole (dt-Se_2naph). Bromination of mt-Se_2naph results in dibromination of the naphthalene ring, rather than reaction at selenium, to give 4,7-dibromo-2-*tert*-butylnaphtho[1,8-*c*,*d*][1,2]-diselenole (mt-Se_2naphBr_2). Reduction of the Se–Se bond in Se_2naph, mt-Se_2naph, dibenzo[*c*,*e*][1,2]diselenine (dibenzSe_2), or diphenyl diselenide (Se_2Ph_2) with $LiBEt_3H$, followed by in-situ addition of $[PtCl_2\{P(OPh)_3\}_2]$ yields the four-coordinate mono- and dinuclear platinum(II) bis(phosphite) complexes $[Pt(Se_2naph)\{P(OPh)_3\}_2]$ (**1**), $[Pt(mt\text{-}Se_2naph)\{P(OPh)_3\}_2]$ (**2**), $[Pt_2(dibenzSe_2)_2\{P(OPh)_3\}_2]$ (**3**), *cis*-$[Pt(SePh)_2\{P(OPh)_3\}_2]$ (**4**), and *trans*-$[Pt_2(SePh)_4\{P(OPh)_3\}_2]$ (**5**).

Introduction

The first synthesis of naphtho[1,8-*c*,*d*][1,2]diselenole (Se_2naph) was reported in 1977 by Meinwald et al. (Figure 1).[1] In their work, Se_2naph was synthesized by adding two equivalents of selenium powder to dilithionaphthalene and then exposing the reaction mixture to air to obtain the desired product in 18–22% yield. Today this preparation is still the most referenced procedure for making this compound. In 1988, Yui et al. reported a different synthetic route to Se_2naph, which involves the addition of sodium diselenide (Na_2Se_2) to 1,8-dichloronaphthalene, producing Se_2naph in a 69% yield.[2] Others have started with 1,8-dibromonaphthalene, synthesized 1,8-dilithionaphthalene, then added elemental selenium (as in Meinwald et al.'s procedure); however, low yields are reported (16%).[3] These reported procedures are, in reality, quite lengthy and present a number of synthetic hurdles, i.e. lengthy synthesis of 1,8-dichloro-[4] or 1,8-dibromonaphthalene.[5]

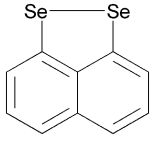

Figure 1. Naphtho[1,8-*c*,*d*][1,2]diselenole (Se_2naph).

In 1994, a synthetic procedure for the sulfur analog, naphtho[1,8-*c*,*d*][1,2]dithiole (S_2naph) was published using unsubstituted naphthalene as a starting material.[6] We have extended that synthesis to the selenium system and developed a facile, "one-pot" synthesis for Se_2naph. We have investigated substitution of this ring using Friedel–Crafts alkylation and report the synthesis of 2,7-di-*tert*-butylnaphtho[1,8-*c*,*d*][1,2]diselenole (dt-Se_2naph) and 2-*tert*-butylnaphtho[1,8-*c*,*d*][1,2]diselenole (mt-Se_2naph). Reaction of mt-Se_2naph with bromine gives 4,7-dibromo-2-*tert*-butylnaphtho[1,8-*c*,*d*][1,2]diselenole (mt-Se_2naphBr_2) (Figure 2).

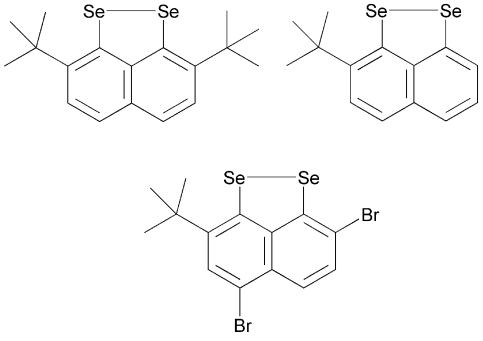

Figure 2. 2,7-di-*tert*-butylnaphtho[1,8-*c*,*d*][1,2]diselenole (dt-Se_2naph), 2-*tert*-butylnaphtho[1,8-*c*,*d*][1,2]diselenole (mt-Se_2naph), and 4,7-dibromo-2-*tert*-butylnaphtho[1,8-*c*,*d*][1,2]diselenole (mt-Se_2naphBr_2).

The crystal structure of Se_2naph has previously been reported,[7] along with several other compounds having an Se–Se bond; such as dibenzo[*c*,*e*][1,2]diselenine (dibenzSe_2) and diphenyl diselenide (Se_2Ph_2) (Figure 3).[8,9] Similar backbones in each of these compounds produce similar chemical environments for the selenium atoms. Although the compounds are structurally similar around the selenium atoms, there are major differences in the conformation that the backbone forces on the selenium substituents. As a result, the Se–Se bond length varies as a function of the flexi-

[a] School of Chemistry, University of St Andrews, St Andrews, Fife KY16 9ST, UK
E-mail: jdw3@st-and.ac.uk

bility of the diaryl backbone. Se_2naph has the longest Se–Se bond length at 2.3639(5) Å, followed by dibenzo[*c*,*e*][1,2]-diselenine (benzSe_2) [2.323(2) Å], and then diphenyl diselenide (Se_2Ph_2) [2.29(1) Å]. The direct relationship that can be drawn is the more rigid the backbone, the longer the Se–Se bond.

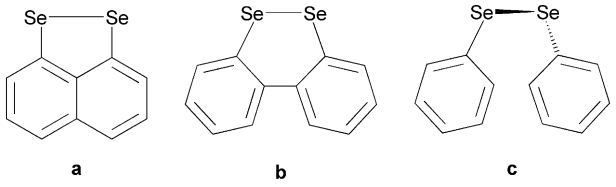

Figure 3. **a**: Naphtho[1,8-*c*,*d*][1,2]diselenole (Se_2naph), **b**: dibenzo-[*c*,*e*][1,2]diselenine (dibenzSe_2), and **c**: diphenyl diselenide (Se_2Ph_2).

These compounds can be used as ligands, by reducing the Se–Se bond to form dianionic *Se₂naph* or *dibenzSe₂* or monoanionic *SePh* (the reduced, negatively charged ligands are indicated by italics). There are very few metal complexes reported that have *Se₂naph* (or any naphthalene derivative) or *dibenzSe* as a ligand. These are limited to the platinum(II) bis(phosphane) complexes, [Pt(*Se₂naph*)(PPh_3)$_2$], [Pt(*Se₂naph*)(PMe_3)$_2$], and [Pt(*dibenzSe₂*)-(PPh_3)$_2$].[10,11] Furthermore, there are only a few reported mononuclear square-planar complexes having two *SePh* ligands. These include *cis*- and *trans*-[Pt(*SePh*)$_2$(PPh_3)$_2$], *trans*-[Pt(*SePh*)$_2${P(*n*Bu)$_3$}$_2$], and *trans*-[Pt(*SePh*)$_2$(PEt_3)$_2$]. Not only does *SePh* form mononuclear complexes, but there are several examples of the formation of dinuclear complexes with *SePh* moieties bridging the two metal centers (Figure 4).[11–13]

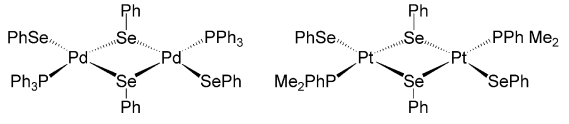

Figure 4. Known dinuclear complexes with bridging SePh ligands.

To date, there is only one reported "series" of related complexes. This series contains platinum bis-triphenylphosphane complexes with the general formula LPt(PPh_3)$_2$, where L is *Se₂naph*, *dibenzSe₂*, or two molecules of *SePh* (Figure 5). These complexes were not synthesized in a single laboratory, but have been reported independently by several groups. [Pt(PPh_3)$_2$(*Se₂naph*)], [Pt(PPh_3)$_2$(*dibenzSe₂*)], and *cis*-[Pt(PPh_3)$_2$(*SePh*)$_2$] were obtained via oxidative addition reactions with [Pt(PPh_3)$_4$] and the respective neutral diselenium compound.[10,11,14] These complexes are very similar around the Pt^{II} metal center despite the flexibility of the backbone.

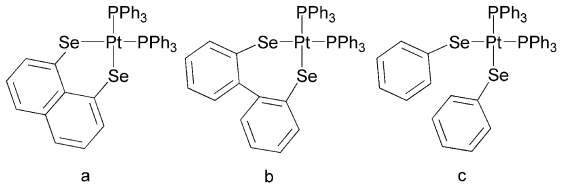

Figure 5. **a**: [Pt(PPh_3)$_2$(Se_2naph)], **b**: [Pt(PPh_3)$_2$(dibenzSe_2)], and **c**: *cis*-[Pt(PPh_3)$_2$($SePh)_2$].

In order to expand the number of di-selenium containing complexes and to obtain a series of these types of platinum complexes from which to draw structural insights, we have synthesized and characterized a new group of complexes produced by reactions using *cis*-[$PtCl_2${P(OPh)$_3$}$_2$] as a starting material. The resulting four-coordinate mono- and di-nuclear platinum(II) bis-phosphite complexes are [Pt(*Se₂naph*){P(OPh)$_3$}$_2$] (**1**), [Pt(*mt-Se₂naph*){P(OPh)$_3$}$_2$] (**2**), [Pt_2(*dibenzSe₂*)$_2${P(OPh)$_3$}$_2$] (**3**), *cis*-[Pt(*SePh*)$_2${P-(OPh)$_3$}$_2$] (**4**), and *trans*-[Pt_2(*SePh*)$_4${P(OPh)$_3$}$_2$] (**5**) (Figure 6). The X-ray structures of these compounds are reported along with a detailed comparison of their structures focusing on the geometry around the Pt^{II} metal center.

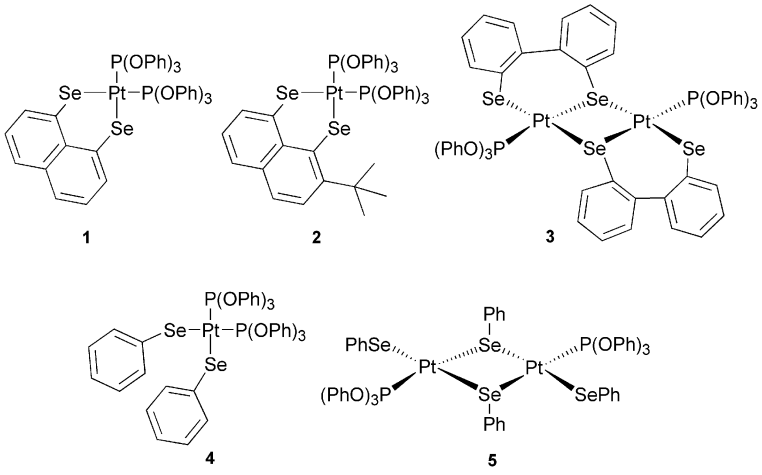

Figure 6. Complexes reported in this work: [Pt(*Se₂naph*){P(OPh)$_3$}$_2$] (**1**), [Pt(*mt-Se₂naph*){P(OPh)$_3$}$_2$] (**2**), [Pt_2(*dibenzSe₂*)$_2${P(OPh)$_3$}$_2$] (**3**), *cis*-[Pt(*SePh*)$_2${P(OPh)$_3$}$_2$] (**4**) and *trans*-[Pt_2(*SePh*)$_4${P(OPh)$_3$}$_2$] (**5**).

Results and Discussion

Several useful ligands have been prepared by novel synthetic methods in the course of this research. Naphtho[1,8-*c*,*d*][1,2]diselenole (Se_2naph) is synthesized using a one-pot reaction starting from naphthalene (26% yield). This synthesis was modelled after one reported by Ashe et al. for the sulfur analog naphtho[1,8-*c*,*d*][1,2]dithiole.[6] It was also found that substitution of the naphthalene ring in Se_2naph with either one *tert*-butyl group to form 2-*tert*-butylnaphtho[1,8-*c*,*d*][1,2]diselenole (mt-Se_2naph) or two *tert*-butyl groups to form 2,7-di-*tert*-butylnaphtho[1,8-*c*,*d*][1,2]diselenole (dt-Se_2naph) was possible via a standard Friedel–Crafts alkylation.[7,15] The addition of dibromine to mt-Se_2naph gave no reaction between selenium and bromine. Instead, electrophilic aromatic substitution dominates to produce the doubly substituted compound 4,7-dibromo-2-*tert*-butylnaphtho[1,8-*c*,*d*][1,2]diselenole (mt-Se_2naphBr_2) (Scheme 1). This is unusual, since reacting organoselenium compounds with dibromine generally results in oxidative addition with addition of the dibromine to the selenium atom, which adopts a "T-shaped" geometry.[16–18]

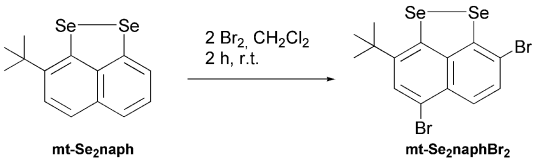

Scheme 1. The reaction scheme for the preparation of 4,7-dibromo-2-*tert*-butylnaphtho[1,8-*c*,*d*][1,2]diselenole (mt-Se_2naphBr_2).

The bromine selectivity can be explained by the electronic directing influence of selenium and the steric bulk of the *tert*-butyl group. Both selenium and *tert*-butyl groups donate electrons into the π-system, activating the naphthalene ring and directing incoming electrophiles to the *ortho* or *para* positions. The first attack at the position *para* to selenium would be sterically more favorable, keeping the two large bromine and *tert*-butyl groups further apart. However, the second substitution reaction is directed to the *ortho* position on the second ring to avoid the steric interaction with the first bromine atom.

A unique characteristic of these compounds is the selenium NMR spectroscopy. These compounds are made up of ^{77}SeSe, Se^{77}Se, and ^{77}Se^{77}Se isotopomers. Any selenium sample is a mixture of several stable isotopes, but only ^{77}Se, natural abundance of 7%, is NMR active. When the selenium atoms are in different chemical environments, the ^{77}Se NMR contains two major signals. For example, in mt-Se_2naph, the first two isotopomers give rise to singlets centered at 414 and 360 ppm, whilst the latter gives an AX spectrum with $J_{Se\text{-}Se}$ = 345 Hz (Figure 7). The peak at δ = 360 ppm corresponds to the selenium atom closest to the *tert*-butyl group, based on comparison to the ^{77}Se spectra of Se_2naph (δ = 420 ppm) and dt-Se_2naph (δ = 353 ppm). The ^{77}Se NMR spectrum of mt-Se_2naphBr_2, is similar, showing two shifts at 454 and 374 ppm, however, the peaks were broad and the $J_{Se\text{-}Se}$ could not be determined.

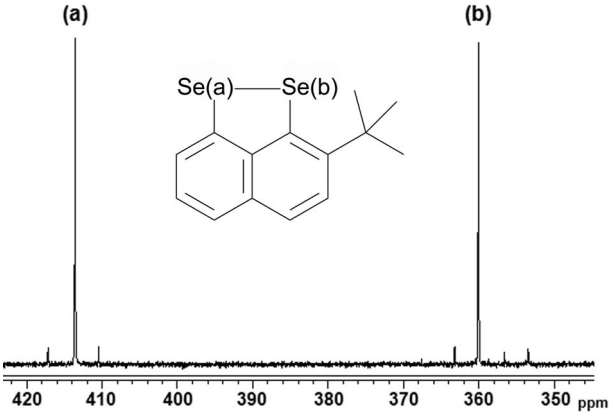

Figure 7. The ^{77}Se NMR for mt-Se_2naph.

X-ray structural characterization was conducted for dt-Se_2naph and mt-Se_2naphBr_2 (Table 1, Figure 8), however, mt-Se_2naph is a persistent oil and could not be crystallized.

Table 1. Selected interatomic distances [Å] and angles [°] for dt-Se_2naph and mt-Se_2naphBr_2.

	dt-Se_2naph[a]	mt-Se_2naphBr_2
Se(1)–Se	2.3383(5)	2.3388(14)
Se(1)–C(1)	1.934(3)	1.935(9)
Se(2)–C(9)		1.888(9)
Se(1)–Se(2)–C(9)		90.9(3)
Se(2)–Se(1)–C(1)	93.16(10)	93.9(2)
Se(1)–C(1)–C(2)	122.4(2)	122.0(7)
Se(1)–C(1)–C(10)	113.2(2)	114.4(6)
Se(2)–C(9)–C(8)		121.6(7)
Se(2)–C(9)–C(10)		119.1(7)
C(2)–C(1)–C(10)	124.3(3)	123.6(8)
C(10)–C(9)–C(8)		119.3(8)
C(1)–C(10)–C(9)	124.8(3)	121.7(8)
C(4)–C(5)–C(10)–C(1)	–0.9(2)	–1.0(5)
C(6)–C(5)–C(10)–C(9)	–0.9(2)	–1.0(5)
C(4)–C(5)–C(10)–C(9)	179.1(2)	180.0(10)
C(6)–C(5)–C(10)–C(1)	179.1(2)	180.0(10)
Mean plane deviations		
Se(1)	–0.1989(57)	–3.2451(39)
Se(2)		–3.3015(40)

[a] Se(2) is Se(1A), C(10) is C(6), C(9) is C(1A) and C(6) is C(4A)′.

The Se–Se bond lengths of dt-Se_2naph [2.3383(5) Å] and mt-Se_2naphBr_2 [2.3388(14) Å] are almost identical, but they are shorter than in Se_2naph, [2.3639(5) Å].[7] In dt-Se_2naph the selenium atoms are forced out of the plane, but this does not occur in Se_2naph or mt-Se_2naphBr_2. Despite the deviation from planarity of dt-Se_2naph, a comparison of torsion angles around the bridgehead carbon atoms of the backbone reveals little variation between Se_2naph, dt-Se_2naph and mt-Se_2naphBr_2 (Figure 9).

The crystal packing in Se_2naph, dt-Se_2naph and mt-Se_2naphBr_2 shows significant differences. Se_2naph forms herringbone π-stacks that are linked by an Se···Se interaction, with a π-π distance between naphthalene rings on

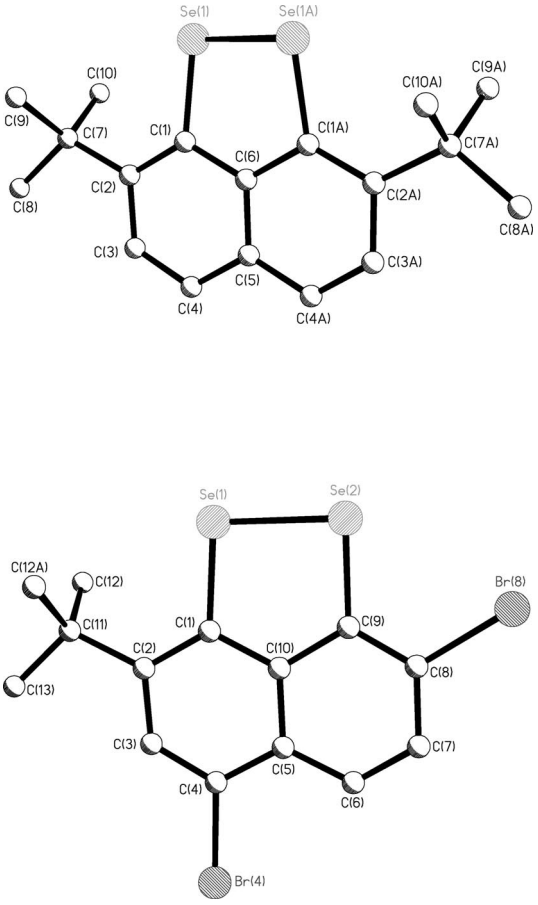

Figure 8. Molecular representation of mt-Se_2naph (top) and mt-Se_2naphBr_2 (bottom).

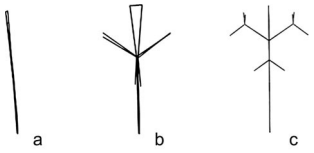

Figure 9. Out-of-plane deflections of a) Se_2naph, b) dt-Se_2naph, and c) mt-Se_2naphBr_2.

separate molecules of 3.81 Å.[7] However, due to the bulky *tert*-butyl arms, there are no intermolecular interactions between Se atoms in the crystal packing of dt-Se_2naph. In mt-Se_2naphBr_2, there is no intermolecular Se···Se interaction, however, there is a close intermolecular Br(4)···Br(8)′ contact [3.4790(13) Å]. This interaction and the resulting packing, is illustrated in Figure 10.

Reduction of the Se–Se bond in Se_2naph, mt-Se_2naph, or dibenzo[*c*,*e*][1,2]diselenine (dibenzSe_2) forms the dianion of those species {the presence of which, is denoted by italics in a molecular formula, e.g. [Pt(*mt-Se*$_2$*naph*)(P(OPh)$_3$)$_2$]}. The analogous reduction of diphenyl diselenide (Se_2Ph_2) gives monoanionic *SePh* (also indicated by italics). Formation of the anion is followed by in situ addition of [$PtCl_2${P(OPh)$_3$}$_2$], which yield the four-coordinate mono- and di-nuclear platinum(II) bis-phosphite complexes [Pt(*Se*$_2$*naph*){P(OPh)$_3$}$_2$] (**1**), [Pt(*mt-Se*$_2$*naph*){P(OPh)$_3$}$_2$] (**2**), [Pt$_2$(*dibenzSe*$_2$)$_2${P(OPh)$_3$}$_2$] (**3**), *cis*-[Pt(*SePh*)$_2${P(OPh)$_3$}$_2$] (**4**), and *trans*-[Pt$_2$(*SePh*)$_4${P(OPh)$_3$}$_2$] (**5**). Scheme 2 shows the reaction to form **1** and **2**.

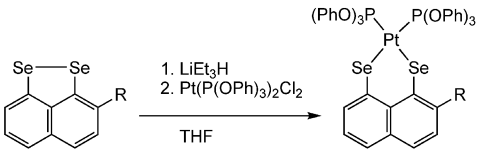

Scheme 2. Synthesis of **1** and **2**.

Complexes **1** and **2** have been fully characterized by elemental analysis, MS, IR, Raman, and ^{1}H, ^{13}C, ^{31}P, ^{77}Se, and ^{195}Pt NMR spectroscopy. We were unable to isolate bulk samples of complexes **3**–**5** and these complexes have been characterized by X-ray crystallography and multinuclear NMR spectroscopy.

The ^{31}P, ^{77}Se, and ^{195}Pt NMR spectroscopic data for **1**–**5** are given in Table 2 In its ^{31}P NMR spectrum, **1** displays a singlet at δ = 87 ppm, and both platinum ($J_{P,Pt}$ = 4711 Hz) and selenium ($J_{P\text{-}Se}$ = 28 Hz) satellites are visible. The ^{77}Se NMR contains a peak at δ = 140 ppm ($J_{Se\text{-}P}$ = 28 Hz) ($J_{Se\text{-}Pt}$ = 205 Hz). The ^{195}Pt NMR displays a triplet centered at –4711 ppm with selenium satellites visible ($J_{Pt,P}$ = 4711 Hz) ($J_{Pt\text{-}Se}$ = 205 Hz).

The ^{31}P NMR spectrum for **2** displays a typical [ABX]-pattern (A = P^{III}, X = Pt) indicative of direct coordination of two inequivalent phosphorus atoms to the platinum center. Both signals have platinum and selenium satellites; δ = 89 ($J_{P\text{-}P}$ = 68 Hz) ($J_{P,Pt}$ = 4686 Hz) ($J_{P\text{-}Se}$ = 19, 28); δ = 86 ($J_{P\text{-}P}$ = 68 Hz) ($J_{P,Pt}$ = 4669 Hz) ($J_{P\text{-}Se}$ = 35 Hz). The ^{77}Se NMR of **2** consists of two signals, each split by two inequivalent phosphorus atoms into a doublet of doublets with platinum satellites. The upfield peak at δ = 138 ppm is assigned to the ^{77}Se furthest from the *tert*-butyl arm by comparison with **1**. The ^{195}Pt NMR displays an apparent triplet

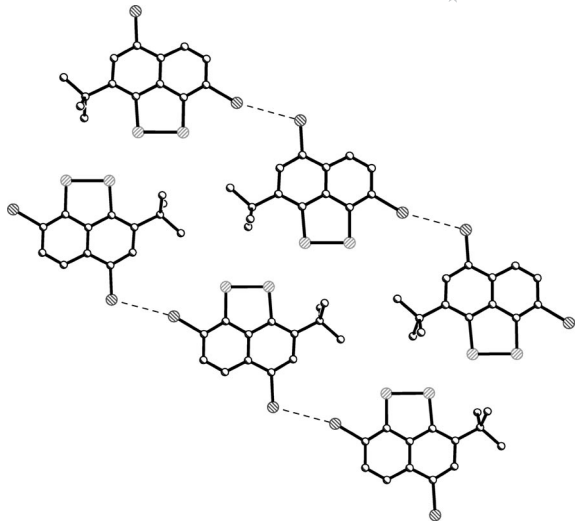

Figure 10. View of crystal packing in mt-Se_2naphBr_2 along the *b*-axis.

Table 2. NMR[a] data for complexes **1**–**5**.

	1	**2**[b]	**2**[c]	**3**	**4/5**
δ = ^{31}P [ppm]	87	89	86	85	84
$J_{P\text{-}P}$ [Hz]		68	68		
$J_{P,Pt}$ [Hz]	4711	4686	4669	4685	4724
$J_{P\text{-}Se}$ [Hz]	28	19, 28	35	21	28
δ = ^{77}Se	140 (t)	258 (dd)	138 (dd)	225 (t)	222 (t)
$J_{Se\text{-}P}$ [Hz]	28	19, 35	7, 28	21	28
$J_{Se\text{-}Pt}$ [Hz]	205	327	212	183	188
δ = ^{195}Pt	–4711 (t)	–4575 (dd)		–4570 (t)	–4075
$J_{Pt,P}$ [Hz]	4711	4979		4685	4729
$J_{Pt\text{-}Se}$ [Hz]	205			183	

[a] All NMR samples were prepared from crystalline samples in $CDCl_3$. [b] In complex **2**, two signals result from the ^{77}Se atom present in one of two inequivalent positions, either the position closest to or furthest away from the substituted *tert*-butyl arm. At this time, based on comparisons to complex **1**, it is thought that the ^{77}Se peak at δ = 138 ppm corresponds to the ^{77}Se atom furthest from the *tert*-butyl substituent. [c] See footnote [b].

(doublet of doublets with similar coupling constants) centered at –4575 ppm ($J_{Pt,P} \approx 4680$ Hz).

The NMR spectroscopic data for **3** indicates the mononuclear complex [Pt(*dibenzSe*$_2$){P(OPh)$_3$}$_2$] is the predominant species in solution.[19] The ^{31}P NMR for **3** displays a typical [AX]-pattern relating to the direct coordination of two equivalent phosphorus atoms to the platinum center and selenium satellites are also observed; δ = 85 ($J_{P,Pt}$ = 4685 Hz) ($J_{P\text{-}Se}$ = 21). The ^{77}Se NMR displays a triplet with platinum satellites at δ = 225 ($J_{Se\text{-}P}$ = 21 Hz) ($J_{Se\text{-}Pt}$ = 183 Hz). The ^{195}Pt NMR spectrum displays a triplet centered at –4570 ppm with selenium satellites visible ($J_{Pt,P}$ = 4685 Hz) ($J_{Pt\text{-}Se}$ = 183 Hz). We were unable to separate **4** and **5** and the ^{31}P, ^{77}Se, and ^{195}Pt NMR spectra were measured using samples that contained crystalline material of at least some crystals of both complexes, as determined by X-ray studies. The NMR spectroscopic data, however, are indicative of the presence in solution of just compound **4**.

The ^{31}P NMR spectrum displays a typical [AAX]-pattern with a single signal at δ = 85 ppm with platinum satellites ($J_{P,Pt}$ = 4724 Hz). As in **3**, the ^{77}Se NMR spectrum of **4/5** exhibits a triplet with platinum satellites; δ = 222 ($J_{Se\text{-}P}$ = 28 Hz) ($J_{Se\text{-}Pt}$ = 188 Hz). The ^{195}Pt NMR spectrum displays a triplet centered at –4075 ppm ($J_{Pt,P}$ = 4729 Hz).

The X-ray crystal structures of **1**, **2**, and **4a** are shown in Figure 11, while Figure 12 shows **3** and **5**. The X-ray analyses show that in every complex, the platinum center lies in a distorted square-planar environment.

The differing molecular structures of **4** and **5** were quite unexpected. As described above, the ^{31}P NMR clearly suggest that only one species is present in the solution after synthesis and purification of the reaction mixture. Crystallization using pentane diffusion into a dichloromethane solution produced orange block crystals, which were characterized by X-ray crystallography, revealing the monomeric

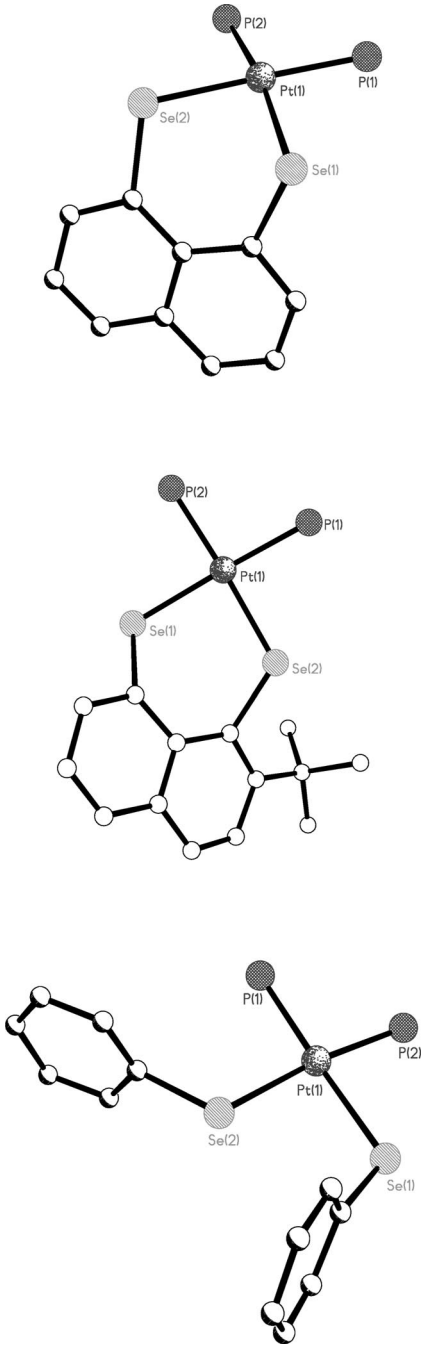

Figure 11. Molecular representations of the core atoms in **1** (top), **2** (middle), and one molecule of **4a** (bottom).

structure of **4**, however, this same solution also yielded crystals of binuclear **5**.

Complexes **1**, **2**, and **4** have strong similarities. Selected bond lengths and angles can be found in Table 3. Each of these complexes is monomeric, containing a four-coordinate Pt^{II} center having two –P(OPh)$_3$ ligands and two selenium ions from one or more of the selenium containing ligands. A comparison of bond lengths within this series of mononuclear complexes shows that all of these complexes have very similar Pt–P bond lengths ranging from 2.2232(13) Å to 2.2390(16) Å, with complex **2** having the

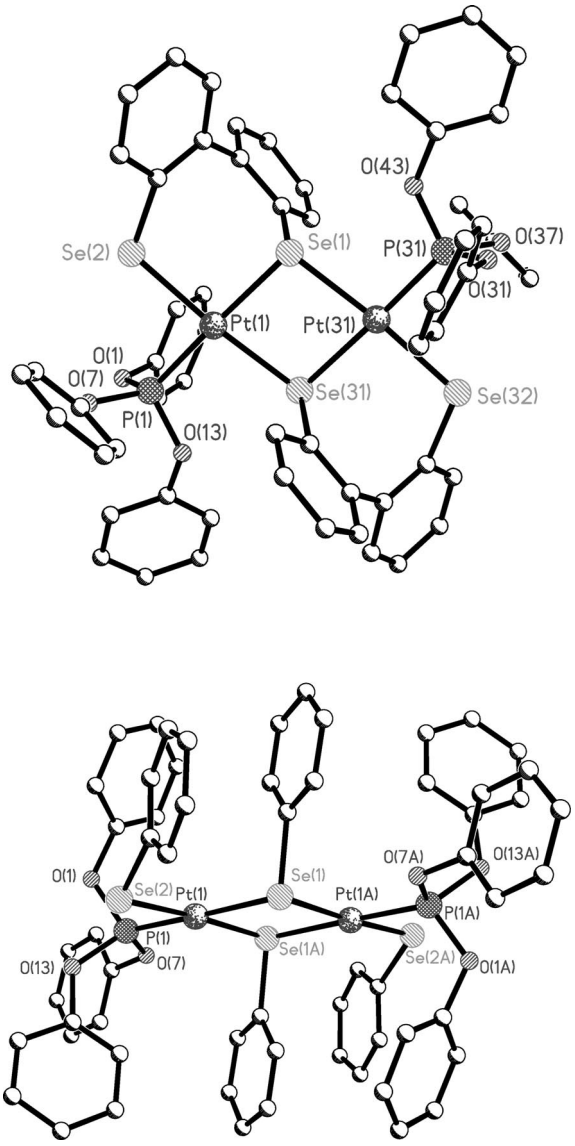

Figure 12. Molecular representations of **3** (top) and **5** (bottom).

shortest Pt–P bond length. The Pt–Se bond lengths have a larger difference. The Pt–Se bond lengths are longest in **4/4a** ranging from 2.481(2) Å to 2.463(2) Å, slightly shorter in **1** at 2.4600(7) Å and 2.4527(7) Å, and yet shorter in **2** at 2.4356(5) Å and 2.4256(5) Å. The short Pt–Se distances in **2** are possibly an effect of the electron donating *tert*-butyl arm on the naphthalene ring. It is noticeable on going from **1** to **2** the six membered $PtSe_2C_3$ ring changes substantially. In **1** the ring is essentially a boat conformation with a hinge at the Se···Se vector whilst in **2** the ring is a twisted chair conformation this difference presumably arises as a consequence of the sterically demanding *tert*-butyl group in **2**.

The Se(1)–Pt(1)–Se(2) bond angles increase from 85.55(2)° in **1**, to 87.47(7)° in **4** to 89.43(8)° in **4a**, and finally to 89.885(17)° in **2**. It is interesting that the only difference between **1** (the smallest angle) and **2** (the largest angle) is the substitution of the *tert*-butyl substituent on the naphthalene ring. The steric bulk of the *tert*-butyl group

Table 3. Selected interatomic distances [Å] and angles [°] for **1**, **2**, and **4** (**4**[1] is the second independent molecule of **4**).

	1	**2**	**4**	**4**[1]
Pt(1)–Se(1)	2.4600(7)	2.4356(5)	2.474(2)	2.481(2)
Pt(1)–Se(2)	2.4527(7)	2.4256(5)	2.463(2)	2.481(2)
Pt(1)–P(1)	2.2390(16)	2.2232(13)	2.229(5)	2.235(5)
Pt(1)–P(2)	2.2324(14)	2.2385(14)	2.224(4)	2.235(5)
Se(1)–C(1)	1.921(6)	1.914(5)	1.85(2)	1.87(2)
Se(2)–C	1.924(6)	1.930(4)	1.94(2)	
Se(1)–Pt(1)–Se(2)	85.55(2)	89.885(17)	87.47(7)	89.43(8)
Se(1)–Pt(1)–P(1)	91.19(4)	86.94(3)	177.85(13)	171.09(14)
Se(2)–Pt(1)–P(2)	88.80(4)	88.02(4)	173.70(14)	171.09(14)
P(1)–Pt(1)–P(2)	94.67(6)	95.29(4)	92.35(18)	99.3(2)
Se(1)–Pt(1)–P(2)	169.82(5)	176.93(3)	86.50(13)	86.11(15)
Se(2)–Pt(1)–P(1)	176.33(4)	175.08(3)	93.73(13)	86.11(15)
Pt(1)–Se(1)–C(1)	100.17(17)	107.59(13)	110.3(6)	105.0(6)
Pt(1)–Se(2)–C	107.63(18)	116.77(15)	112.8(5)	105.0(6)

pushes the selenium atom nearest to it out of the plane of the naphthalene ring, rendering the Se–Pt–Se bond angle larger than in **1**, where the selenium atoms may be constrained by a need to stay in the plane of the rings to participate in π-resonance. However, the size of the Se(1)–Pt(1)–Se(2) bond angle in **4** falls in the middle of the series of complexes, despite not being restricted by the backbone, as in **1** and **2**. The similarity of the bond angle (only ca. 4° difference) amongst the complexes is likely not coincidental, even if the ligands have no strong geometric preferences, the geometry of the complex is still limited by the tendency of Pt^{II} to be square planar.

Compared to **4** in the Se–Pt–Se angles, the *cis*-bond angles Se–Pt–P in the three complexes are universally similar. The Se(1)–Pt(1)–P(2) bond angle in **4** is 86.50(13)° and the Se(2)–Pt(1)–P(1) bond angle is 93.73(13)° with the Se(1)–Pt(1)–P(1) bond angle being 91.19(4)° and the Se(2)–Pt(1)–P(2) bond angle being 88.80(4)°. The bond angle differences in **2** are similar to the other two complexes, with the Se(1)–Pt(1)–P(1) bond angle being 86.94(3)° and the Se(2)–Pt(1)–P(2) bond angle being 88.02(4)°. The two *trans* Se–Pt–P bond angles of the three complexes likewise differ from each other by only a few degrees. The difference between the two angles is 7.5° in **1**, 4.2° in **4** and 1.8° in **2**.

The smallest of the *trans* Se–Pt–P bond angles occurs in **1**, with an angle of 169.82(5)°. Other than a bond angle of 173.40(14)° in **4**, all the other *trans* bond angles in all three complexes are very close to 176°. Like all the other angles, the P(1)–Pt(1)–P(2) bond angles of **1**, **2**, and **4** are very similar, except in **4b**, where it is the largest by 4° at 99.3(2)°. Somewhat strangely, the steric strain presented by the *tert*-butyl group in **2** and the greater degree of freedom allowed by the lack of a constraining background in **4** do not seem to cause much variation in the structure around the metal center. The metal center appears to be dictating the geometry and forcing the ligands to arrange themselves so that the complex has as close to a square planar motif it can.

Complexes **3** and **5** are different from the three just discussed, in that they each crystallize as a dinuclear complex with two four-coordinate Pt^{II} metal centers in a diamond

core motif. Each Pt^{II} ion in both complexes is coordinated by three selenium ions and one $-P(OPh)_3$ ligand. A list of selected bond lengths and angles for **3** and **5** are shown in Tables 4 and 5. The difference between the two coordination spheres is that **3** has dianionic bis-selenium ligands based on the biphenyl backbone, while the platinum centers in **5** are ligated by individual *SePh* ligands. One of the selenium atoms on the biphenyl in **3** is in a bridging position, which forces the ligand to twist and strain in order for the platinum to coordinate the other selenium atom. In **5**, the bridging and terminal positions are occupied by the *SePh* ligands instead.

Table 4. Selected interatomic distances [Å] and angles [°] for complex **3**.

Pt(1)–P(1)	2.202(2)	Pt(31)–P(31)	2.200(2)
Pt(1)–Se(2)	2.4370(10)	Pt(31)–Se(32)	2.4449(11)
Pt(1)–Se(31)	2.4582(10)	Pt(31)–Se(31)	2.4544(10)
Pt(1)–Se(1)	2.4569(10)	Pt(31)–Se(1)	2.4628(10)
Se(1)–C(19)	1.928(9)		
Se(31)–C(49)	1.944(10)		
Se(32)–C(56)	1.960(9)		
Se(2)–C(26)	1.922(10)		
P(1)–Pt(1)–Se(2)	88.50(7)	P(31)–Pt(31)–Se(32)	88.72(7)
P(1)–Pt(1)–Se(31)	93.86(7)	P(31)–Pt(31)–Se(1)	94.00(7)
Se(2)–Pt(1)–Se(1)	93.64(3)	Se(32)–Pt(31)–Se(31)	93.44(4)
Se(31)–Pt(1)–Se(1)	83.89(3)	Se(31)–Pt(31)–Se(1)	83.85(3)
Se(2)–Pt(1)–Se(31)	173.11(4)	Se(32)–Pt(31)–Se(1)	172.28(4)
P(1)–Pt(1)–Se(1)	177.60(7)	P(31)–Pt(31)–Se(31)	177.84(7)
C(19)–Se(1)–Pt(1)	93.9(3)	C(49)–Se(31)–Pt(31)	93.2(3)
C(19)–Se(1)–Pt(31)	106.5(3)	C(49)–Se(31)–Pt(1)	107.1(3)
Pt(1)–Se(1)–Pt(31)	96.04(3)	Pt(31)–Se(31)–Pt(1)	96.22(3)
C(26)–Se(2)–Pt(1)	110.1(3)	C(56)–Se(32)–Pt(31)	110.6(3)

Table 5. Selected interatomic distances [Å] and angles [°] for **5**.

Pt(1)–P(1)	2.186(2)	Pt(31)–P(31)	2.193(2)
Pt(1)–Se(2)	2.4493(9)	Pt(31)–Se(32)	2.4445(8)
Pt(1)–Se(1A)	2.4697(9)	Pt(31)–Se(3A)	2.4632(8)
Pt(1)–Se(1)	2.4771(8)	Pt(31)–Se(31)	2.4763(8)
Se(1)–Pt(1A)	2.4697(9)	Se(31)–Pt(3A)	2.4632(8)
Se(1)–C(19)	1.927(7)	Se(31)–C(49)	1.931(7)
Se(2)–C(25)	1.932(8)	Se(32)–C(55)	1.925(8)
P(1)–Pt(1)–Se(2)	85.83(6)	P(31)–Pt(31)–Se(32)	84.01(5)
P(1)–Pt(1)–Se(1A)	95.66(6)	P(31)–Pt(31)–Se(3A)	96.90(5)
Se(2)–Pt(1)–Se(1)	94.71(3)	Se(3A)–Pt(31)–Se(31)	84.07(3)
Se(1A)–Pt(1)–Se(1)	83.89(3)	Se(32)–Pt(31)–Se(31)	94.99(3)
Se(2)–Pt(1)–Se(1A)	175.74(3)	Se(32)–Pt(31)–Se(3A)	176.46(3)
P(1)–Pt(1)–Se(1)	178.57(5)	P(31)–Pt(31)–Se(31)	178.86(6)
C(19)–Se(1)–Pt(1A)	98.9(2)	C(49)–Se(31)–Pt(3A)	100.5(2)
C(19)–Se(1)–Pt(1)	104.2(2)	C(49)–Se(31)–Pt(31)	103.7(2)
Pt(1A)–Se(1)–Pt(1)	96.11(3)	Pt(3A)–Se(31)–Pt(31)	95.93(3)
C(25)–Se(2)–Pt(1)	106.6(2)	C(55)–Se(32)–Pt(31)	106.3(2)

Rather unsurprisingly, given their similar coordination spheres, the bond lengths in **3** and **5** are very similar throughout the complexes (Table 4, Table 5). The Pt–P bond lengths are similar at ca. 2.20 Å in **3** and ca. 2.19 Å in **5**. The Pt–Se bonds in both complexes differ depending on whether they are coordinated in a terminal or bridging fashion, but are again markedly similar between the two complexes. In **3**, the terminal Pt–Se bond lengths are ≈ 2.44 Å, whereas the bridging bond lengths are about 2.46 Å. In **5**, the terminal Pt–Se bond lengths are ca. 2.45 Å, and the bridging bond lengths are ca. 2.47 Å.

Like the bond lengths, the bond angles in **3** and **5** are very similar. Complex **3** has two obtuse angles and two acute angles around the platinum centers, which form a flattened X with a platinum atom in the center. The Se–Pt–Se bond angle of the diamond core is 83.89(3)°, and the bond *trans* to this, across the platinum center, is 88.50(7)°. The other two angles around the platinum center are ca. 94°. The Pt–Se–Pt bond bridging the diamond core is 96.04(3)°.

The bond angles in **5** track very closely to those in **3**. The Se–Pt–Se bond angle of the diamond core is 83.89(3)° and *trans* to this, the angle is 85.83(6)°. The other two angles around the platinum center are 94.71(3)° and 95.66(6)°. The bridging Pt–Se–Pt angles are both almost exactly 96°. From this data, it seems as though the visibly twisted biphenyl-based diselenium ligand is not responsible for the distortion of the geometry around the metal center in **3**, since the *SePh* ligands in **5** end up giving the complex an extremely similar set of bond lengths and angles without the ligand imposing a geometric restriction.

Experimental Section

General: All synthetic procedures were performed under nitrogen using standard Schlenk techniques unless otherwise stated, reagents were obtained from commercial sources and used as received. Dry solvents were collected from an MBraun solvent system. ^{1}H, ^{13}C, ^{31}P, and ^{77}Se spectra were recorded on a Jeol DELTA GSX270 spectrometer. ^{195}Pt spectra were obtained on a Bruker AVII400. Chemical shifts are reported in ppm and coupling constants (*J*) are given in Hz. IR (KBr pellet) and Raman spectra (powder sample) were obtained on a Perkin–Elmer system 2000 Fourier Transform spectrometer. Elemental analysis was performed by the University of St. Andrews, School of Chemistry Service. Positive-ion FAB mass spectra were performed by the EPSRC National Mass Spectrometry Service, Swansea. Precious metals were provided by Ceimig Ltd.

Synthetic Remarks: The compound *cis*-$[Pt\{P(OPh)_3\}_2Cl_2]$ was prepared by adding two equivalents of $P(OPh)_3$ to *cis*-$[PtCl_2(cod)]$ (cod = 1,5-cyclooctadiene) in dichloromethane at room temperature instead of by the procedure reported by Sabounchei et al.[20]

Synthesis of Naphtho[1,8-*c*,*d*][1,2]diselenole (Se_2naph): Crystalline naphthalene (6.10 g, 47.6 mmol) was added to a 500 mL round bottom Schlenk flask. The flask was evacuated and purged with nitrogen. Butyllithium (BuLi) (46.8 mL of 2.5 M in THF, 117 mmol) was added dropwise via syringe with stirring, followed by the slow addition of TMEDA (17.7 mL, 117 mmol). Upon addition, the flask became slightly warm and a white precipitate (pcc) formed. The pcc dissolved as the solution yellowed and then became increasingly darker until it was dark reddish in color. A reflux condenser was added to the flask, which was then warmed to ca. 70 °C for two hours. The mixture was allowed to cool to room temperature,

at which time the reflux condenser was replaced by a septum. The mixture was then cooled to –70 °C using a dry ice/acetone bath. Tetrahydrofuran (THF) (ca. 150 mL) was added dropwise via syringe. Selenium powder (11.1 g, 141 mmol) was then added at once. The reaction mixture was allowed to slowly warm to room temperature and was stirred overnight under nitrogen.

Caution! As the mixture warms to room temperature, the flask becomes slightly pressurized. Make sure the stopper is clipped and the flask is opened to nitrogen.

The next day, the flask was opened and the mixture was poured into a 2 separating funnel where ca. 500 mL of distilled water and ca. 300 mL of hexane was then added. It was difficult to see the separation line, but as the water layer was removed the line became more evident. The hexane layer, a clear purple solution, was collected. Silica gel was added to the organic layer and the solvent was evaporated. The silica gel/product was placed on top of a silica column and the product was eluted with hexane. The purple band was collected and the solvent evaporated. The purple solid was dissolved in a minimal amount of dichloromethane. The solution was then layered with hexane and placed in the freezer for recrystallization; yield 3.544 g, 26%. ^{1}H and ^{77}Se NMR matched those of the previous reported samples.[1]

Synthesis of 2,7-Di-*tert*-butylnaphtho[1,8-*c*,*d*][1,2]diselenole (dt-Se$_2$naph) and 2-*tert*-butylnaphtho[1,8-*c*,*d*][1,2]diselenole (mt-Se$_2$naph): 2,7-Di-*tert*-butylnaphtho[1,8-*c*,*d*][1,2]diselenole (dt-Se$_2$naph) and 2-*tert*-butylnaphtho[1,8-*c*,*d*][1,2]diselenole (mt-Se$_2$naph) were prepared by methods reported for the thiol analogues.[15,16] Se$_2$naph (0.38 g, 1.3 mmol), *tert*-butyl chloride (0.43 mL, 3.9 mmol), and CH_3NO_2 (ca. 7 mL), were added to a 100 mL round bottom Schlenk flask. The reaction was heated with stirring to about 80 °C and $AlCl_3$ (36 mg, 0.27 mmol) was added. The mixture continued to heat at about 80 °C for one hour. After the reaction cooled to room temperature, distilled water was added, which then was extracted with dichloromethane. The organic layer was removed, dried with $MgSO_4$, filtered, and the solvent was evaporated. These compounds were purified by column chromatography on silica gel elution using hexane, with mt-Se$_2$naph eluting first, then dt-Se$_2$naph, followed by starting material. dt-Se$_2$naph was crystallized by slow evaporation of a pentane solution to give orange blocks (17 mg, 3%). mt-Se$_2$naph is a dark red oil (104 mg, 23%), and finally 81 mg (21%) of the starting material was recovered.

mt-Se$_2$naph: ^{1}H NMR ($CDCl_3$): δ = 7.52–7.17 (m, 5 H), 1.53 (s, 9 H) ppm. ^{77}Se NMR ($CDCl_3$): δ = 414 (s), 414 (d, $J_{Se\text{-}Se}$ = 345 Hz), 360 (s), 360 (d, $J_{Se\text{-}Se}$ = 345 Hz) ppm. ^{13}C NMR ($CDCl_3$): δ = 144.3, 139.5, 138.8, 138.3, 136.5, 126.8, 125.8, 124.8, 123.3, 122.0, 36.5, 29.2 ppm. MS (TOF MS CI):*m*/*z* = 339 [^{78}Se, ^{80}Se], 341 [^{80}Se].

dt-Se$_2$naph: ^{1}HNMR ($CDCl_3$): δ = 7.52–7.44 (m, $J_{H,H}$ = 8, 21 Hz, 4 H), 1.56 (s, 18 H) ppm. ^{77}SeNMR ($CDCl_3$): δ = 353 (s) ppm. ^{13}CNMR ($CDCl_3$): δ = 144.05, 140.37, 136.99, 134.98, 125.82, 124.37, 36.66, 29.10 ppm. MS (TOF MS CI): *m*/*z* = 396 [^{78}Se, ^{80}Se], 398 [^{80}Se].

Synthesis of 4,7-Dibromo-2-*tert*-butylnaphtho[1,8-*c*,*d*][1,2]diselenole (Se$_2$naphBr$_2$): A solution of 2-*tert*-butylnaphtho[1,8-*c*,*d*][1,2]diselenole (mt-Se$_2$naph) (0.11 g, 0.33 mmol) in dichloromethane (10 mL) was cooled to 0 °C and slowly treated with bromine (0.11 g, 0.034 mL, 0.66 mmol). An analytically pure sample was obtained by crystallisation from diffusion of pentane into a dichloromethane solution of the product (0.1 g, 74%). IR (KBr tablet): $\tilde{\nu}_{max}$ = 3424 (br. s), 3069 (w), 2955 (s), 2854 (w), 1584 (w), 1568 (w), 1514 (w), 1482 (s), 1466 (vs), 1392 (s), 1361 (s), 1282 (s), 1218 (s), 1186 (w), 1147 (s), 1116 (vs), 996 (vs), 913 (s), 881 (s), 860 (w), 820 (s), 799 (s), 741 (s), 663 (w), 558 (w), 509 (w), 485 (w), 468 (w), 381 (w) cm^{-1}. ^{1}HNMR ($CDCl_3$): δ = 7.77–7.64 (m, 2 H, 3,5-H), 7.53–7.40 (m, 1 H, 6-H), 1.52 [s, 9 H, -C(CH_3)$_3$] ppm. ^{13}C NMR ($CDCl_3$): δ = 134.5 (s), 133.6 (s), 132.9 (s), 131.4 (s), 131.2 (s), 130.6 (s), 130.2 (s), 130.1 (s), 124.9 (s), 124.1 (s), 29.8 (s), 28.7 (s) ppm. ^{77}SeNMR ($CDCl_3$): δ = 454, 374 ppm. MS (TOF MS EI$^+$): *m*/*z* (%) =497.98 (100) [M$^+$].

Synthesis for [Pt(L){P(OPh)$_3$}$_2$], L = Se$_2$naph (1) and mt-Se$_2$naph (2): In a Schlenk tube, ca. 10 mL of dry THF was added to 1 mol-equiv. of **L**, the resulting purple solution was stirred for 10 min and then, 2 mol-equiv. of a 1 M solution of $LiBEt_3H$ in THF was added dropwise via syringe. Upon addition, the purple solution turned bright yellow and gas evolution was observed. This solution was stirred ca. 15 min and [Pt{P(OPh)$_3$}$_2$Cl$_2$] was added. The solution turned orange in color and was stirred 12 h, after which ca. 1 g of silica gel was added and the solvent was evaporated under vacuum. The flask containing the orange solid was opened to the air and the solid was placed on top of a short hexane-packed silica gel column. The column was eluted with hexane to remove any unreacted starting material and then washed with CH_2Cl_2. The CH_2Cl_2 band was collected and the solvent was removed under vacuum. Orange crystals were obtained for **1** (97 mg, 53%) and **2** (109 mg, 50%) after recrystallization from CH_2Cl_2 by pentane diffusion.

[Pt(*Se$_2$naph*){P(OPh)$_3$}$_2$] (1): Se$_2$naph (47 mg, 165 mmol), 0.33 mL of 1 M soln of $LiBEt_3H$ in THF, and [Pt{P(OPh)$_3$}$_2$Cl$_2$] (147 mg, 165 mmol). $C_{46}H_{36}O_6P_2PtSe_2{\cdot}CH_2Cl_2$: calcd. C 47.60, H 3.23; found C 47.79, H 3.10. FAB$^+$ MS: *m*/*z* = 1100 [M$^+$]. IR (KBr): $\tilde{\nu}_{max}$ = 1587, 1486, 1182, 1159, 918, 778, 757, 687, 596, 496 cm^{-1}. Raman: $\tilde{\nu}$ = 30720, 1591, 1538, 1333, 1007, 851, 733, 530, 200 cm^{-1}. All NMR samples were prepared from crystalline samples in $CDCl_3$. ^{1}H NMR: δ = 7.6 (d, $J_{H,H}$ = 7 Hz), 7.5 (d, $J_{H,H}$ = 7 Hz), 7.2–6.9 (m), 6.9 (t, $J_{H,H}$ = 7 Hz) ppm. ^{13}C NMR: δ = 150.9, 136.3, 135.1, 129.8, 126.9, 125.2, 124.7, 120.9 ppm. ^{31}P NMR: δ = 87 ppm ($J_{P,Pt}$ = 4711 Hz) ($J_{P\text{-}Se}$ = 28 Hz). ^{77}Se NMR: δ = 140 ppm (t, $J_{Se\text{-}P}$ = 28 Hz) ($J_{Se\text{-}Pt}$ = 205 Hz). ^{195}Pt NMR: δ = –4711 ppm (t, $J_{Pt,P}$ = 4711 Hz) ($J_{Pt\text{-}Se}$ = 205 Hz).

[Pt(*mt-Se$_2$naph*){P(OPh)$_3$}$_2$] (2): mt-Se$_2$naph (64 mg, 187 mmol), 0.37 mL of 1 M soln of $LiBEt_3H$ in THF, and [Pt{P(OPh)$_3$}$_2$Cl$_2$] (166 mg, 187 mmol). $C_{50}H_{44}O_6P_2PtSe_2{\cdot}0.5CH_2Cl_2$:: calcd. C 50.50, H 3.78; found C 50.51, H 3.49. FAB$^+$ MS: *m*/*z* = 1156 [M$^+$]. IR (KBr): $\tilde{\nu}_{max}$ = 1588, 1488, 1186, 1160, 922, 776, 756, 686, 595, 497 cm^{-1}. Raman: $\tilde{\nu}$ = 3066, 1595, 1586, 1515, 1340, 1007, 857, 733, 185 cm^{-1}. All NMR samples were prepared from crystalline samples in $CDCl_3$. ^{1}H NMR: δ = 7.4–7.0 (m), 6.9 (t, $J_{H,H}$ = 7 Hz)., 1.7 (s) ppm. ^{13}C NMR: δ = 151.0, 150.9, 147.0, 142.5, 132.9, 132.1, 131.9, 129.7, 129.6, 126.5, 125.5, 125.2, 125.0, 123.9, 123.2, 121.0, 120.9, 120.7, 120.6, 38.2, 31.6 ppm. ^{31}P NMR: δ = 89 ppm (d, $J_{P\text{-}P}$ = 68 Hz), ($J_{P,Pt}$ = 4686 Hz) ($J_{P\text{-}Se}$ = 19, 28) 86 ppm (d, $J_{P\ P}$ = 68 Hz), ($J_{P,Pt}$ = 4669 Hz) ($J_{P\ Se}$ = 35). ^{77}Se NMR: δ = 258 ppm (dd, $J_{Se\text{-}P}$ = 19, 35 Hz) ($J_{Se\text{-}Pt}$ = 329 Hz), 138 ppm (dd, $J_{Se\text{-}P}$ = 7, 28 Hz) ($J_{Se\text{-}Pt}$ = 212 Hz). ^{195}Pt NMR: δ = –4575 ppm (observed is apparent triplet $J_{Pt,P} \approx$ 4680 Hz).

Synthesis of [Pt$_2$(*dibenzSe$_2$*)$_2${P(OPh)$_3$}$_2$] (3): In a Schlenk tube, ca. 10 mL of dry THF was added to 1 mol-equiv. of dibenzSe$_2$, the resulting pale orange solution was stirred for 10 min and then 2 mol-equiv. of a 1 M solution of $LiBEt_3H$ in THF was added dropwise via syringe. Upon addition, the solution turned very pale yellow, then clear with gas evolution. This solution was stirred ca. 15 min and [Pt{P(OPh)$_3$}$_2$Cl$_2$] was added. The solution turned bright yellow in color and was stirred 12 h, after which time ca. 1 g of silica gel was added and the solvent was evaporated under vac-

uum. The flask containing the yellow solid was opened to the air and the solid was placed on top of a short hexane-packed silica gel column. The column was eluted with hexane to remove any unreacted starting material and then washed with 2:1 CH_2Cl_2/hexane. The resulting bright yellow band was collected and the solvent was removed under vacuum. X-ray quality crystals were obtained for **3** after recrystallization from CH_2Cl_2 by pentane diffusion. FAB^+ MS: *m/z* 1631 [M^+] (matches theoretical isotope profile for **3**). IR (KBr): $\tilde{\nu}_{max}$ = 1588, 1486, 1184, 1160, 1025, 922, 765, 687, 595, 491 cm^{-1}. Raman IR: $\tilde{\nu}$ = 3066, 1589, 1030, 1008 cm^{-1}. NMR samples were prepared from crystalline samples in $CDCl_3$. ^{31}P NMR: δ = 85 ppm ($J_{P,Pt}$ = 4685 Hz) ($J_{P\text{-}Se}$ = 21). ^{77}Se NMR: δ = 225 ppm (t, $J_{P\text{-}Se}$ = 21) ($J_{Pt\text{-}Se}$ = 183 Hz). ^{195}Pt NMR: δ = –4570 ppm (t, $J_{Pt,P}$ = 4685 Hz) ($J_{Pt\text{-}Se}$ = 183 Hz). The NMR spectroscopic data seem to suggest that the predominant species in solution is [Pt(dibenzSe$_2$){P(OPh)$_3$}$_2$].

Synthesis of *cis*-[Pt(*SePh*)$_2${P(OPh)$_3$}$_2$] (4) and [Pt$_2$(SePh)$_4${P(OPh)$_3$}$_2$] (5): In a Schlenk tube, ca. 10 mL of dry THF was added to 1 mol-equiv. of Se_2Ph_2, the resulting yellow solution was stirred for 10 min and then 2 mol-equiv. of a 1 M solution of $LiBEt_3H$ in THF was added dropwise via syringe. Upon addition, the solution turned pale yellow with gas evolution. This solution was stirred ca. 15 min and [Pt{P(OPh)$_3$}$_2$Cl$_2$] was added. The solution turned bright orange in color and was stirred 12 h, after which time ca. 1 g of silica gel was added and the solvent was evaporated. The flask containing the orange solid was opened to the air and the solid was placed on a small hexane silica gel column. The column was eluted with hexane to remove any unreacted starting material and then washed with 2:1 CH_2Cl_2/hexane. This orange band was collected and the solvent was removed under vacuum. Complexes **4** and **5** co-crystallized out of the same CH_2Cl_2 solution by pentane diffusion. Complex **4** is deep orange in color, almost red, whereas **5** is bright yellow. All data was obtained from crystalline solid that contained both **4** and **5**. $C_{48}H_{40}O_6P_2PtSe_2$ (**4**) (1127.80): calcd. C 51.12, H 3.57 and for $C_{60}H_{50}O_6P_2Pt_2Se_4$ (**5**) (1635.02): calcd. C 44.08, H 3.08; found C 44.62, H 2.81. FAB^+ MS: *m/z* 1635 [M^+] (matches theoretical isotope profile for **5**, but there are higher molecular ion peaks in the sample). IR (KBr): $\tilde{\nu}_{max}$ = 1587, 1485, 1183, 1156, 919, 784, 686, 601, 488 cm^{-1}. Raman IR: $\tilde{\nu}$ = 3063, 1597, 1576, 1220, 1169, 1071, 1001, 226, 178 cm^{-1}. NMR samples were prepared in $CDCl_3$. ^{31}P NMR: δ = 84 ppm. ($J_{P,Pt}$ = 4724 Hz) ($J_{P\text{-}Se}$ = 28 Hz). ^{77}Se NMR: δ = 222 ppm (t, $J_{P\text{-}Se}$ = 28 Hz) ($J_{Se\text{-}Pt}$ = 188 Hz). ^{195}Pt NMR: δ = –4075 ppm (t, $J_{Pt,P}$ = 4729 Hz). NMR spectroscopic data seem to suggest that the mononuclear species **4** exists in solution, rather than the dinuclear species **5**.

Table 6. Crystallographic data for compounds dt-Se_2naph, mt-Se_2naphBr_2 and **1**–**5**.

	dt-Se_2naph	mt-Se_2naphBr_2	1	2	3	4	5
Empirical formula	$C_{18}H_{22}Se_2$	$C_{14}H_{14}Br_2Se_2$	$C_{46}H_{36}O_6Se_2P_2Pt$	$PtC_{51}H_{46}O_6P_2Se_2Cl_2$	$C_{62}H_{50}Cl_4O_6P_2Pt_2Se_4$	$C_{146}H_{124}O_{18}P_6Pt_3Se_6Cl_4$	$C_{60}H_{50}O_6P_2Pt_2Se_4$
Formula weight	396.29	499.99	1099.74	1240.78	1800.78	3553.26	1634.96
Temperature [°C]	–148(1)	–148(1)	–148(1)	–148(1)	–180(1)	–148(1)	–180(1)
Crystal colour, habit	orange, block	red, prism	orange, block	yellow, platelet	yellow, prism	orange, block	yellow, prism
Crystal dimensions [mm^3]	0.55×0.40×0.30	0.09×0.06×0.06	0.22×0.15×0.07	0.41×0.14×0.10	0.20×0.20×0.20	0.52×0.10×0.06	0.10×0.03×0.03
Crystal system	orthorhombic	monoclinic	orthorhombic	monoclinic	monoclinic	monoclinic	triclinic
Lattice parameters	*a* = 11.333(11) Å	*a* = 9.638(7) Å	*a* = 13.3431(5) Å	*a* = 17.1347(5) Å	*a* = 12.0039(15) Å	*a* = 61.179(3) Å	*a* = 10.1847(12) Å
	b = 12.079(11) Å	*b* = 7.112(5) Å	*b* = 13.5580(5) Å	*b* = 26.5360(8) Å	*b* = 20.430(2) Å	*b* = 11.9162(4) Å	*b* = 13.7001(16) Å
	c = 12.029(11) Å	*c* = 10.499(8) Å	*c* = 22.8535(8) Å	*c* = 11.0032(3) Å	*c* = 25.009(3) Å	*c* = 18.9059(9) Å	*c* = 20.338(2) Å
	–	–	–	–	–	–	*α* = 83.840(7)°
	β = 90°	*β* = 94.263(15)°	*β* = 90°	*β* = 102.4922(8)°	*β* = 99.836(3)°	*β* = 98.6466(18)°	*β* = 82.868(7)°
	–	–	–	–	–	–	*γ* = 85.896(8)°
Volume [$Å^3$]	1647(3)	717.6(8)	4134.3(3)	4884.6(2)	6043.1(13)	13626.1(11)	2794.7(6)
Space group	*Pcca*	*P*2$_1$/*m*	*P*2$_1$2$_1$2$_1$	*Cc*	*Cc*	*C*2/*c*	*P*$\bar{1}$
Z value	4	2	4	4	4	4	2
$D_{calcd.}$ [g/cm^3]	1.598	2.314	1.767	1.687	1.979	1.732	1.943
F(000)	792	472	2144	2440	3440	6960	1560
m(Mo*Ka*) [cm^{-1}]	44.807	107.166	52.68	45.75	73.15	48.776	77.13
Number of reflections measured	13383	4132	43187	25442	19245	52775	18111
R_{int}	0.032	0.039	0.095	0.041	0.0453	0.329	0.047
Min.–max. transmissions	0.130–0.261	0.373–0.526	0.398–0.692	0.304–0.633	0.7102–1.0000	0.383–0.746	0.6118–1.0000
Independent reflections	1508	1362	9468	11089	8754	11981	9897
Observed reflection (no. variables)	1314 (94)	1267 (115)	8094 (515)	9956 (578)	7937 (722)	7175 (826)	7534 (688)
Reflection/parameter ratio	16.04	11.84	18.38	19.19	12.12	14.5	14.39
Residuals: R_1 [$I > 2.00s(I)$]	0.0385	0.0452	0.048	0.0345	0.0362	0.125	0.0453
Residuals: *R* (all reflections)	0.0444	0.0499	0.0629	0.042	0.0414	0.1953	0.067
Residuals: wR_2 (all reflections)	0.1011	0.1072	0.061	0.0543	0.0705	0.3989	0.0726
Goodness-of-fit indicator	1.093	1.181	1.051	0.987	0.874	1.145	0.975
Flack parameter	–	–	–0.006(5)	0.001(3)	–0.005(7)	–	–
Max. peak in final diff. map [$e/Å^3$]	0.83	0.66	2.59	1.54	1.744	6.56	1.807
Min. peak in final diff. map [$e/Å^3$]	–0.55	–0.99	–1.02	–0.70	–1.424	–10.18	–1.542

X-ray Crystallography: Crystal structure data for **1**, **2**, dt-Se_2naph and mt-Se_2naphBr_2 were collected using the St. Andrews Robotic Rigaku Saturn CCD diffractometer using Mo-K_α radiation (graphite monochromator optic, λ = 0.71073 Å), **4** was determined by using a Rigaku SCX-Mini whilst **3** and **5** were determined by using a Rigaku MM007 rotating anode and Mercury CCD. All data were corrected for absorption. The structure was solved by direct methods and refined by full-matrix least-squares methods on F^2 values of all data. Refinements were performed using SHELXTL (version 6.1, Bruker-AXS, Madison WI, USA, 2001). The experimental details including the results of the refinement are given in Table 6.

CCDC-759117 (for **1**), -759118 (for **2**), -759119 (for **3**), -759120 (for **4**), -759121 (for **5**), -759122 (for dt-Se_2naph), -759123 (for mt-Se_2naphBr_2) contain the supplementary crystallographic data for this paper. These data can be obtained free of charge from The Cambridge Crystallographic Data Centre via www.ccdc.cam.ac.uk/data_request/cif.

[1] J. Meinwald, D. Dauplaise, F. Wudl, J. J. Hauser, *J. Am. Chem. Soc.* **1977**, *99*, 255–257.

[2] K. Yui, Y. Aso, T. Otsubo, F. Ogura, *Bull. Chem. Soc. Jpn.* **1988**, *61*, 953–959.

[3] J. L. Kice, Y. Kang, M. B. Manek, *J. Org. Chem.* **1988**, *53*, 2435–2439.

[4] G. C. Hampson, A. Weissberger, *J. Chem. Soc.* **1936**, 393–398.

[5] S. Vyskocil, L. Meca, I. Tislerova, I. Cisarova, M. Polasek, S. R. Harutyunyan, Y. N. Belokon, M. J. Stead Russel, L. Farrugia, S. C. Lockhart, W. L. Mitchell, P. Kocovsky, *Chem. Eur. J.* **2002**, *8*, 4633–4648.

[6] A. J. Ashe III, J. W. Kampf, P. M. Savla, *Heteroat. Chem.* **1994**, *5*, 113–119.

[7] S. M. Aucott, H. L. Milton, S. D. Robertson, A. M. Z. Slawin, J. D. Woollins, *Heteroat. Chem.* **2004**, *15*, 530–542.

[8] J. D. Lee, M. W. R. Bryant, *Acta Crystallogr.* **1969**, *25*, 2094–2101.

[9] M. R. Bryce, A. Chesney, A. K. Lay, A. S. Batsanov, J. A. K. Howard, *J. Chem. Soc. Perkin Trans. 1* **1996**, 2451–2459.

[10] S. M. Aucott, H. L. Milton, S. D. Robertson, A. M. Z. Slawin, G. D. Walker, J. D. Woollins, *Chem. Eur. J.* **2004**, *10*, 1666–1676.

[11] S. M. Aucott, P. Kilian, S. D. Robertson, A. M. Z. Slawin, J. D. Woollins, *Chem. Eur. J.* **2006**, *12*, 895–902.

[12] R. Oilunkaniemi, R. S. Laitinen, M. Ahlgrén, *J. Organomet. Chem.* **2001**, *623*, 168–175.

[13] V. K. Jain, S. Kannan, R. J. Butcher, J. P. Jasinski, *J. Organomet. Chem.* **1994**, *468*, 285–290.

[14] V. P. Ananikov, I. P. Beletskaya, G. G. Aleksandrov, I. L. Eremenko, *Organometallics* **2003**, *22*, 1414–1421.

[15] M. Tesmer, H. Vahrenkamp, *Eur. J. Inorg. Chem.* **2001**, 1183–1188.

[16] V. Lippolis, F. Isaia, in: *Handbook of Chalcogen Chemistry, New Perspectives in Sulfur, Selenium and Tellurium* (Ed.: F. A. Devillanova), **2006**, p. 477.

[17] P. D. Boyle, S. M. Godfrey, *Coord. Chem. Rev.* **2001**, *223*, 265–299.

[18] W. Nakanishi, in: *Handbook of Chalcogen Chemistry, New Perspectives in Sulfur, Selenium and Tellurium* (Ed.: F. A. Devillanova), **2006**, p. 644.

[19] S. Ford, P. K. Khanna, C. P. Morley, M. D. Vaira, *J. Chem. Soc., Dalton Trans.* **1999**, 791–794.

[20] S. J. Sabounchei, A. Naghipour, *Molecules* **2001**, *6*, 777–783.

Received: March 31, 2010
Published Online: July 9, 2010

